

**LINEAR AND NONLINEAR FINITE ELEMENT ANALYSES OF
ANCHORAGE ZONES IN POST-TENSIONED CONCRETE STRUCTURES**

By
Songwut Hengprathanee

A DISSERTATION SUBMITTED TO THE FACULTY OF
VIRGINIA POLYTECHNIC INSTITUTE AND STATE UNIVERSITY
IN PARTIAL FULFILLMENT OF THE REQUIREMENTS FOR THE DEGREE OF
DOCTOR OF PHILOSOPHY
IN
CIVIL ENGINEERING

Carin L. Roberts-Wollmann, Chair
Thomas E. Cousins
Raymond H. Plaut
Gregor P. Wollmann
Donatus C. Ohanehi

September, 2004
Blacksburg, Virginia

Keywords: Prestressed concrete, Anchorage zones, Post-tensioned, Finite element analysis

Copyright 2004, Songwut Hengprathanee

LINEAR AND NONLINEAR FINITE ELEMENT ANALYSES OF ANCHORAGE ZONES IN POST-TENSIONED CONCRETE STRUCTURES

By
Songwut Hengprathanee

Committee Chair: Carin L. Roberts_Wollmann
Civil and Environmental Engineering

(ABSTRACT)

Linear and nonlinear finite element analyses are used for the investigation of rectangular anchorage zones with the presence of a support reaction. The investigation is conducted based on four load configurations consisting of concentric, inclined concentric, eccentric, and inclined eccentric loads. The method of model construction is illustrated thoroughly. The influence of several parameters, including anchorage ratio, inclination of prestressing load, eccentricity, magnitude of the reaction force, bearing plate ratio, and the location of the reaction force, is studied. Both graphical and numerical presentations of the results from each load configuration are given. Improved equations, which are modified from the equations presented in the AASHTO Standard Specifications (2002), are proposed. The results from the equations are compared to those from the finite element method. Nonlinear finite element analysis is used to verify the applicability of the equations and to study a new bursting steel arrangement.

Linear and nonlinear finite element analyses are also used for the study of non-rectangular anchorage zones. Four basic load configurations, including concentric, eccentric, inclined concentric, and inclined eccentric loads, are investigated. The shell element is selected for the construction of the finite element models. Several parameters, consisting of anchorage ratio, inclination of prestressing load, eccentricity, web thickness, ratio of web thickness to flange thickness, and flange width, are chosen for parametric studies. The results from the studies are presented graphically and numerically. Equations to calculate the bursting force and location of the force are developed from the Strut-and-Tie Model approach. The verification of the formulations and the investigation of bursting steel arrangement are conducted using nonlinear finite element analysis.

ACKNOWLEDGEMENTS

It is my deepest appreciation that I would like to express for the generosity, support, and continuing guidance of my advisor, Dr. Carin L. Roberts-Wollmann, during the last four years of my study at Virginia Tech. Her patience and encouragement have led me through the hard time of my study, which will never be forgotten. I also would like to extend my appreciation to Dr. Gregor P. Wollmann for his valuable advice and comments during the course of my study. I want to sincerely thank all my other dissertation committee members, Dr. Thomas E. Cousins, Dr. Raymond H. Plaut, and Dr. Donatus C. Ohanehi, for serving on my Doctoral committee.

I am indebted and wish to express my gratitude to Dr. Pornsak Pudhaphongsiriporn, who brought me to the educational world of structural engineering and also gave me the opportunity to study for my Master's and Doctoral degrees. Without his support, this present dissertation would never exist.

I wish to express my great thankfulness to Mr. Prakasit Manirojana, whom I respect as my brother, for his support and encouragement during my graduate study in the United States. His suggestions have successfully brought me through the hard decisions that I have made. I also wish to acknowledge my friends, Veerachai Kasuwan, Arichai Lalitkulanant, Pattharawut Khamchoo, Yodmanee Tepanon, Dr. Surachet Kanprachar, and many others, for their plentiful friendship.

Finally, I wish to express my forever gratefulness to my mother and father, who always make me proud of being their son for every single breath of my life. Their unmeasured and unquestionable love always gives me the courage to overcome obstacles. I also wish to gratefully thank my older brother, Songchai, for his sacrifice that bought me a chance to come to study in the United States, and my two younger brothers, Songphol and Songsak, for helping me with everything else during the period of my study. I also would like to give my thanks for all other members of my family for their love, support, and encouragement.

TABLE OF CONTENTS

LIST OF TABLES.....xi

LIST OF FIGURES.....xiv

CHAPTER 1 – INTRODUCTION.....1

1.1. Anchorage Zones in Prestressed Concrete Structures..... 1

1.2. Prestressed Concrete Structures..... 2

 1.2.1. Development of the Technology..... 2

 1.2.2. Basic Concepts..... 3

1.3. Anchorage Zone Design..... 6

 1.3.1. Previous Anchorage Zone Design..... 6

 1.3.2. Current Anchorage Zone Design Presented in AASHTO..... 8

 1.3.2.1.Strut-And-Tie Model (STM).....11

 1.3.2.2.Approximate Stress Analysis and Design..... 12

1.4. Literature Reviews..... 15

 1.4.1. Anchorage Zones..... 15

 1.4.1.1.Morsch (1924) and Guyon (1953)..... 15

 1.4.1.2.Yettram and Robbins (1969, 1970, and 1971)..... 17

 1.4.1.3.NCHRP Project 10-29 (1994)..... 17

 1.4.1.4.Roberts (1990)..... 18

 1.4.1.5.Burdet (1990)..... 19

 1.4.1.6.Sanders (1990)..... 22

 1.4.1.7.Wollmann (1992)..... 23

 1.4.2. Nonlinear Finite Element Analysis of Reinforced Concrete Structures..... 25

 1.4.2.1.Ngo and Scordelis (1967)..... 25

 1.4.2.2.Adeghe and Collins (1986)..... 26

 1.4.2.3.Al-Manaseer and Phillips (1987)..... 26

 1.4.2.4.Foster (1992)..... 29

 1.4.2.5.Foster, Budiono, and Gilbert (1996)..... 32

1.4.2.6.Foster and Rogowsky (1996, 1997).....	34
1.4.3. Other Works Using DIANA.....	36
1.4.3.1.Johansson (2000).....	36
1.4.3.2.Tabatabai and Mosalam (2000).....	37
1.4.3.3.Lundgren and Magnusson (2001).....	37
1.4.3.4.Kwan and Billington (2001).....	38
1.5. DIANA.....	38
1.5.1. Material Constitutive Models.....	39
1.5.1.1.Cracking and Crushing.....	39
1.5.1.2.Yielding of Reinforcing Steel.....	40
1.5.2. Element Types.....	40
1.5.2.1.Concrete Element.....	41
1.5.2.2.Embedded Steel Element.....	41
1.5.2.3.Steel Bearing Plate Element.....	42
1.5.2.4.Spring Connector Element.....	42
1.6. Objectives and Scope of this Study.....	42
1.6.1. Objectives.....	42
1.6.2. Scope.....	43
CHAPTER 2 – PRELIMINARY STUDIES USING NONLINEAR FEA.....	44
2.1. Study Compared to Foster and Rogowsky’s Research.....	44
2.2. Study Compared to Sander’s Experimental Work.....	48
CHAPTER 3 – RECTANGULAR SECTIONS WITH PRESENCE OF SUPPORT REACTIONS.....	52
3.1. Introduction.....	52
3.1.1. Objectives.....	52
3.1.2. Scope.....	53
3.2. Preparation of Work.....	54
3.2.1. Selection of the Model.....	54
3.2.2. Convergence Test.....	55
3.2.3. Location of Vertical Boundary Support.....	57
3.2.4. Location of Main Compressive Strut Line.....	59

3.3. Parameters.....	64
3.3.1. Anchorage Ratio (a/h).....	64
3.3.2. Inclination Angle of Prestressing Force (α).....	65
3.3.3. Eccentricity (e).....	66
3.3.4. Magnitude of Reaction Force (R).....	67
3.3.5. Bearing Plate Ratio (b/h).....	68
3.3.6. Location of Support Reaction (l).....	68
3.3.7. Summary.....	69
3.4. Load Configurations.....	69
3.4.1. Centrally Loaded Anchor Configuration.....	70
3.4.1.1.Elastic Stress Distribution.....	70
3.4.1.2.Bursting Force.....	74
3.4.1.3.Location of Bursting Force.....	84
3.4.2. Inclined Centrally Loaded Anchor Configuration.....	93
3.4.2.1.Elastic Stress Distribution.....	93
3.4.2.2.Bursting Force.....	98
3.4.2.3.Location of Bursting Force.....	114
3.4.3. Eccentrically Loaded Anchor Configuration.....	130
3.4.3.1.Elastic Stress Distribution.....	132
3.4.3.2.Bursting Force.....	136
3.4.3.3.Location of Bursting Force.....	142
3.4.4. Inclined Eccentrically Loaded Anchor Configuration.....	146
3.4.4.1.Elastic Stress Distribution.....	147
3.4.4.2.Bursting Force.....	150
3.4.4.3.Location of Bursting Force.....	162
3.5. Examples Using Nonlinear Analysis.....	170
3.5.1. Example Based on Wollmann’s Experimental Specimen.....	171
3.5.1.1.Problem Illustration.....	171
3.5.1.2.Nonlinear Analysis Result.....	172
3.5.2. Example Based on Precast Beam with Multi-Strand Tendon in PTI Manual.....	175
3.5.2.1.Problem Illustration.....	175
3.5.2.2.Design of Bursting Reinforcement.....	176

3.5.2.2.1.	<i>Design Using Approximate Equations Addressed in the AASHTO</i>	176
3.5.2.2.2.	<i>Design Using Strut-and-Tie Model Method</i>	178
3.5.2.2.3.	<i>Design Using New Approximate Equations</i>	185
3.5.2.3.	Nonlinear Analysis Result.....	186
3.5.2.4.	Nonlinear Analysis to Investigate the Reinforcement Arrangement.....	189
3.5.3.	Summary.....	191
3.6.	Discussions And Recommendations.....	192
3.6.1.	Design Recommendations.....	192
3.6.2.	Detailing Recommendations.....	193
 CHAPTER 4 – NON-RECTANGULAR SECTIONS.....		194
4.1.	Introduction.....	194
4.1.1.	Objectives.....	195
4.1.2.	Scope.....	195
4.2.	Preparation of Work.....	196
4.2.1.	Selection of Non-Rectangular Sections.....	196
4.2.2.	Model Construction.....	199
4.2.3.	Comparison of the Models.....	201
4.3.	Parameters.....	206
4.3.1.	Anchorage Ratio (a/h_w).....	206
4.3.2.	Inclination Angle of Prestressing Force (α).....	206
4.3.3.	Eccentricity (e).....	207
4.3.4.	Web Thickness (t_w).....	207
4.3.5.	Thickness Ratio of Flange and Web (t_f/t_w).....	207
4.3.6.	Flange Width (b_f).....	208
4.3.7.	Other Parameters.....	208
4.3.8.	Summary.....	208
4.4.	Load Configurations.....	209
4.4.1.	Concentrically Loaded Anchor Configuration.....	209
4.4.1.1.	Finite Element Results.....	209
4.4.1.1.1.	<i>Elastic Stress Distribution</i>	209
4.4.1.1.2.	<i>Bursting Force</i>	219
4.4.1.1.2.1.	<i>Symmetrical I-Section</i>	219

4.4.1.1.2.2.	<i>T-Section</i>	227
4.4.1.1.2.3.	<i>Unsymmetrical I-Section</i>	231
4.4.1.1.3.	<i>Location of Bursting Force</i>	234
4.4.1.1.3.1.	<i>Symmetrical I-Section</i>	234
4.4.1.1.3.2.	<i>T-Section</i>	242
4.4.1.1.3.3.	<i>Unsymmetrical I-Section</i>	246
4.4.1.2.	<i>Formulations</i>	248
4.4.1.2.1.	<i>Symmetrical I-Section</i>	251
4.4.1.2.2.	<i>T-Section</i>	264
4.4.1.2.3.	<i>Unsymmetrical I-Section</i>	271
4.4.2.	<i>Eccentrically Loaded Anchor Configuration</i>	276
4.4.2.1.	<i>Finite Element Results</i>	276
4.4.2.1.1.	<i>Elastic Stress Distribution</i>	276
4.4.2.1.2.	<i>Bursting Force</i>	282
4.4.2.1.2.1.	<i>Symmetrical I-Section</i>	282
4.4.2.1.2.2.	<i>T-Section</i>	284
4.4.2.1.2.3.	<i>Unsymmetrical I-Section</i>	286
4.4.2.1.3.	<i>Location of Bursting Force</i>	287
4.4.2.1.3.1.	<i>Symmetrical I-Section</i>	287
4.4.2.1.3.2.	<i>T-Section</i>	289
4.4.2.1.3.3.	<i>Unsymmetrical I-Section</i>	291
4.4.2.2.	<i>Formulations</i>	292
4.4.3.	<i>Inclined And Inclined Eccentrically Loaded Anchor Configurations</i>	301
4.4.3.1.	<i>Finite Element Results</i>	301
4.4.3.1.1.	<i>Elastic Stress Distribution</i>	301
4.4.3.1.2.	<i>Bursting Force</i>	307
4.4.3.1.3.	<i>Location of Bursting Force</i>	310
4.4.3.2.	<i>Formulations</i>	312
4.5.	<i>Examples Using Nonlinear Analysis</i>	323
4.5.1.	<i>Example Based on Sanders' Experimental Specimen</i>	323
4.5.1.1.	<i>Problem Illustration</i>	323
4.5.1.2.	<i>Nonlinear Analysis Result</i>	327

4.5.2. Example Based on Box Girder Bridge with Internal Tendons Presented in PTI Manual.....	335
4.5.2.1.Problem Illustration.....	336
4.5.2.2.Design of Bursting Reinforcement.....	336
4.5.2.3.Nonlinear Analysis Result.....	347
4.5.3. Summary.....	357
4.6. Discussions and Recommendations.....	358
4.6.1. Design Recommendations.....	359
4.6.1.1.Design Using Strut-and-Tie Model Method.....	359
4.6.1.2.Design Using Approximate Equations.....	362
4.6.2. Detailing Recommendations.....	362
CHAPTER 5 – MODIFIED RECOMMENDATIONS TO AASHTO.....	364
5.1. Design Recommendations for Rectangular Sections	364
5.2. Design Recommendations for Non-Rectangular Sections	366
5.2.1. Design Recommendations of the Web.....	367
5.2.2. Design Recommendations of the Flange.....	369
5.2.3. Design Recommendations Using the Strut-and-Tie Model Method.....	370
CHAPTER 6 – CONCLUSIONS.....	372
6.1. General Conclusions.....	372
6.1.1. Design of Rectangular Anchorage Zones with the Presence of a Support Reaction.....	373
6.1.2. Design of Non-Rectangular Anchorage Zones.....	374
6.2. Recommendations for Further Research.....	375
6.2.1. Experimental Research for Rectangular Anchorage Zone with a Support Reaction.....	375
6.2.2. Non-Rectangular Anchorage Zones.....	376
REFERENCES.....	377
APPENDIX A – GENERAL EXPRESSIONS.....	382
A.1.Centroid of Compressive Stress Diagram.....	382

A.2. Kern of Non-Rectangular Sections.....	383
A.3. Centroid of the Resultant Force.....	385
APPENDIX B – TABLES OF RESULTS.....	387
B.1. Comparison of T_{burst} on Horizontal and Inclined Strut Line.....	387
APPENDIX C – TENSILE STRESSES IN WEB.....	390
C.1. Tensile Stresses in the Web of Symmetrical I-Sections	390
APPENDIX D – DESIGN EXAMPLES OF NON-RECTANGULAR ANCHORAGE ZONES.....	391
D.1. Section with the Thickest Flange.....	391
D.2. Section with the Thinnest Web.....	394
D.3. Section with the Widest Flange.....	396
VITA.....	399

LIST OF TABLES

Table 3.1	COMPARISON OF ANGLE OF MAIN COMPRESSIVE STRUT.....	63
Table 3.2	SUMMARY OF PARAMETERS.....	69
Table 3.3	SLOPES OF STRAIGHT LINE FOR T_{burst}	83
Table 3.4	SLOPES OF STRAIGHT LINE FOR THE PREDICTION OF d_{burst}	92
Table 3.5	SLOPES OF STRAIGHT LINE FOR T_{burst} OF INCLINED CONCENTRIC LOAD.....	108
Table 3.6	COMPARISON OF THE RESULTS FOR CONCENTRIC LOAD WITH NO INCLINATION ANGLE.....	111
Table 3.7	COMPARISON OF THE RESULTS FOR CONCENTRIC LOAD WITH 6 DEGREE INCLINATION ANGLE.....	112
Table 3.8	COMPARISON OF THE RESULTS FOR CONCENTRIC LOAD WITH 9 DEGREE INCLINATION ANGLE.....	113
Table 3.9	SLOPES OF STRAIGHT LINE FOR THE PREDICTION OF d_{burst} INCLINED CONCENTRIC LOAD CASE.....	125
Table 3.10	COMPARISON OF d_{burst} FOR CONCENTRIC LOAD WITH NO INCLINATION ANGLE.....	127
Table 3.11	COMPARISON OF d_{burst} FOR CONCENTRIC LOAD WITH 6 DEGREE INCLINATION ANGLE.....	128
Table 3.12	COMPARISON OF d_{burst} FOR CONCENTRIC LOAD WITH 9 DEGREE INCLINATION ANGLE.....	129
Table 3.13	COMPARISON OF THE RESULTS FOR ECCENTRIC LOAD WITH NO INCLINATION ANGLE.....	159
Table 3.14	COMPARISON OF THE RESULTS FOR ECCENTRIC LOAD WITH 6 DEGREE INCLINATION ANGLE.....	160
Table 3.15	COMPARISON OF THE RESULTS FOR ECCENTRIC LOAD WITH 9 DEGREE INCLINATION ANGLE.....	161
Table 3.16	COMPARISON OF d_{burst} FOR ECCENTRIC LOAD WITH NO INCLINATION ANGLE.....	167
Table 3.17	COMPARISON OF d_{burst} FOR ECCENTRIC LOAD WITH 6 DEGREE INCLINATION ANGLE.....	168
Table 3.18	COMPARISON OF d_{burst} FOR ECCENTRIC LOAD WITH 9 DEGREE INCLINATION ANGLE.....	169
Table 3.19	EXPERIMENTAL DATA OF Beam3 FROM WOLLMANN'S RESEARCH (1992).....	171
Table 4.1	COMPARISON OF THE RESULTS FROM TWO MODELS.....	205

Table 4.2	SUMMARY OF PARAMETERS USED IN THE STUDY OF FLANGED SECTIONS....	208
Table 4.3	COMPARISON OF $d_{burst-web}$ FOR SYMMETRICAL I-SECTION USING EQUATION (a) SUBJECTED TO CONCENTRIC LOAD.....	255
Table 4.4	COMPARISON OF $d_{burst-web}$ FOR SYMMETRICAL I-SECTION USING EQUATION (b) SUBJECTED TO CONCENTRIC LOAD.....	256
Table 4.5	COMPARISON OF $T_{burst-web}$ AND $d_{burst-web}$ FOR SYMMETRICAL I-SECTION SUBJECTED TO CONCENTRIC LOAD.....	257
Table 4.6	COMPARISON OF $T_{burst-web}$ AND $d_{burst-web}$ FOR SYMMETRICAL I-SECTION SUBJECTED TO CONCENTRIC LOAD (continued).....	258
Table 4.7	COMPARISON OF $T_{burst-flg}$ AND $d_{burst-flg}$ FOR SYMMETRICAL I-SECTION SUBJECTED TO CONCENTRIC LOAD.....	263
Table 4.8	COMPARISON OF $T_{burst-flg}$ AND $d_{burst-flg}$ FOR SYMMETRICAL I-SECTION SUBJECTED TO CONCENTRIC LOAD (continued).....	264
Table 4.9	COMPARISON OF $T_{burst-web}$ AND $d_{burst-web}$ FOR T-SECTION SUBJECTED TO CONCENTRIC LOAD.....	269
Table 4.10	COMPARISON OF $T_{burst-flg}$ AND $d_{burst-flg}$ FOR T-SECTION SUBJECTED TO CONCENTRIC LOAD.....	271
Table 4.11	COMPARISON OF $T_{burst-web}$ AND $d_{burst-web}$ FOR UNSYMMETRICAL I-SECTION SUBJECTED TO CONCENTRIC LOAD.....	273
Table 4.12	COMPARISON OF $T_{burst-flg}$ AND $d_{burst-flg}$ FOR THE TOP FLANGE OF UNSYMMETRICAL I-SECTION SUBJECTED TO CONCENTRIC LOAD.....	275
Table 4.13	COMPARISON OF $T_{burst-flg}$ AND $d_{burst-flg}$ FOR THE BOTTOM FLANGE OF UNSYMMETRICAL I-SECTION SUBJECTED TO CONCENTRIC LOAD.....	275
Table 4.14	COMPARISON OF $T_{burst-web}$ AND $d_{burst-web}$ FOR SYMMETRICAL I-SECTION SUBJECTED TO ECCENTRIC LOAD.....	295
Table 4.15	COMPARISON OF $T_{burst-web}$ AND $d_{burst-web}$ FOR T-SECTION SUBJECTED TO ECCENTRIC LOAD.....	296
Table 4.16	COMPARISON OF $T_{burst-web}$ AND $d_{burst-web}$ FOR UNSYMMETRICAL I-SECTION SUBJECTED TO ECCENTRIC LOAD.....	296
Table 4.17	COMPARISON OF $T_{burst-flg}$ AND $d_{burst-flg}$ FOR THE TOP FLANGE OF SYMMETRICAL I-SECTION SUBJECTED TO ECCENTRIC LOAD.....	298
Table 4.18	COMPARISON OF $T_{burst-flg}$ AND $d_{burst-flg}$ FOR THE BOTTOM FLANGE OF SYMMETRICAL I-SECTION SUBJECTED TO ECCENTRIC LOAD.....	298
Table 4.19	COMPARISON OF $T_{burst-flg}$ AND $d_{burst-flg}$ FOR T-SECTION SUBJECTED TO ECCENTRIC LOAD.....	299
Table 4.20	COMPARISON OF $T_{burst-flg}$ AND $d_{burst-flg}$ FOR THE TOP FLANGE OF UNSYMMETRICAL I-SECTION SUBJECTED TO ECCENTRIC LOAD.....	300

Table 4.21 COMPARISON OF $T_{burst-flg}$ AND $d_{burst-flg}$ FOR THE BOTTOM FLANGE OF UNSYMMETRICAL I-SECTION SUBJECTED TO ECCENTRIC LOAD.....	300
Table 4.22 COMPARISON OF $T_{burst-web}$ AND $d_{burst-web}$ FOR SYMMETRICAL I-SECTION SUBJECTED TO INCLINED CONCENTRIC AND INCLINED ECCENTRIC LOAD.....	315
Table 4.23 COMPARISON OF $T_{burst-web}$ AND $d_{burst-web}$ FOR T-SECTION SUBJECTED TO INCLINED CONCENTRIC AND INCLINED ECCENTRIC LOAD.....	316
Table 4.24 COMPARISON OF $T_{burst-web}$ AND $d_{burst-web}$ FOR UNSYMMETRICAL I-SECTION SUBJECTED TO INCLINED CONCENTRIC AND INCLINED ECCENTRIC LOAD.....	316
Table 4.25 COMPARISON OF $T_{burst-web}$ AND $d_{burst-web}$ FOR UNSYMMETRICAL I-SECTION SUBJECTED TO INCLINED ECCENTRIC LOAD AND A SUPPORT REACTION	318
Table 4.26 COMPARISON OF $T_{burst-flg}$ AND $d_{burst-flg}$ FOR THE TOP FLANGE OF SYMMETRICAL I-SECTION SUBJECTED TO INCLINED CONCENTRIC AND INCLINED ECCENTRIC LOAD.....	319
Table 4.27 COMPARISON OF $T_{burst-flg}$ AND $d_{burst-flg}$ FOR THE BOTTOM FLANGE OF SYMMETRICAL I-SECTION SUBJECTED TO INCLINED CONCENTRIC AND INCLINED ECCENTRIC LOAD.....	320
Table 4.28 COMPARISON OF $T_{burst-flg}$ AND $d_{burst-flg}$ FOR THE FLANGE OF T-SECTION SUBJECTED TO INCLINED CONCENTRIC AND INCLINED ECCENTRIC LOAD.....	321
Table 4.29 COMPARISON OF $T_{burst-flg}$ AND $d_{burst-flg}$ FOR THE TOP FLANGE OF UNSYMMETRICAL I-SECTION SUBJECTED TO INCLINED CONCENTRIC AND INCLINED ECCENTRIC LOAD.....	322
Table 4.30 COMPARISON OF $T_{burst-flg}$ AND $d_{burst-flg}$ FOR THE BOTTOM FLANGE OF UNSYMMETRICAL I-SECTION SUBJECTED TO INCLINED CONCENTRIC AND INCLINED ECCENTRIC LOAD.....	322
Table 4.31 EXPERIMENTAL DATA OF F1 FROM SANDERS' RESEARCH (1990).....	325
Table B.1a CONCENTRIC LOAD CASE.....	388
Table B.1b INCLINED CONCENTRIC LOAD CASE.....	388
Table B.1c ECCENTRIC AND INCLINED ECCENTRIC LOAD CASE.....	389
Table D.1 COMPARISON FOR EXAMPLE D.1.....	394
Table D.2 COMPARISON FOR EXAMPLE D.2.....	396
Table D.3 COMPARISON FOR EXAMPLE D.3.....	398

LIST OF FIGURES

Fig. 1.1 STRESSES IN RECTANGULAR PRESTRESSED CONCRETE BEAM.....	4
Fig. 1.2 PRESTRESSED CONCRETE BEAMS.....	5
Fig. 1.3 ANCHORAGE ZONE.....	6
Fig. 1.4 ANCHORAGE ZONE ANALYSIS OF PRESTRESSED CONCRETE BODY.....	8
Fig. 1.5 TENSION IN ANCHORAGE ZONE.....	10
Fig. 1.6 STRUT-AND-TIE MODEL.....	12
Fig. 1.7 COMPRESSION STRUT IN STRUT-AND-TIE MODEL.....	12
Fig. 1.8 GUYON’S BURSTING STRESS DISTRIBUTION.....	13
Fig. 1.9 GUYON’S BURSTING FORCE DESIGN AID.....	16
Fig. 1.10 GUYON’S SYMMETRIC PRISM FOR ECCENTRICALLY LOADED ANCHORAGE ZONE.....	16
Fig. 1.11 MODIFIED STRUT-AND-TIE MODEL.....	23
Fig. 1.12 SPECIMENS TESTED BY WOLLMANN.....	24
Fig. 1.13 STRUT-AND-TIE MODELS FOR ECCENTRIC ANCHOR WITHOUT AND WITH REACTION FORCE.....	25
Fig. 1.14 TENSION STIFFENING MODEL USED IN AL-MANASEER AND PHILIPS’ STUDY.....	27
Fig. 1.15 SHEAR RETENTION FACTOR MODEL USED BY AL-MANASEER AND PHILIPS (1987).....	28
Fig. 1.16 STRESS-STRAIN RELATIONSHIP OF STEEL MODEL USED BY AL-MANASEER AND PHILIPS (1987).....	28
Fig. 1.17 UNIAXIAL STRESS-STRAIN RELATIONSHIP FOR CONCRETE USED BY FOSTER (1992).....	32
Fig. 1.18 FINITE ELEMENT MODEL USED IN FOSTER AND ROGOWSKY’S SERVICEABILITY ANALYSIS.....	35
Fig. 1.19 THE COMPARISON OF TRANSVERSE STRESS DISTRIBUTIONS.....	36
Fig. 2.1 TRANSVERSE BURSTING STRESS vs. RELATIVE DISTANCE FROM BEARING PLATE FOR $w/D = 0.20$	46
Fig. 2.2 TRANSVERSE BURSTING STRESS vs. RELATIVE DISTANCE FROM BEARING PLATE FOR $w/D = 0.40$	46
Fig. 2.3 TRANSVERSE BURSTING STRESS vs. RELATIVE DISTANCE FROM BEARING PLATE FOR $w/D = 0.60$	47

Fig. 2.4 TRANSVERSE BURSTING STRESS vs. RELATIVE DISTANCE FROM BEARING PLATE FOR $w/D = 0.80$	47
Fig. 2.5 SANDERS' SPECIMEN B4.....	48
Fig. 2.6 FINITE ELEMENT MODEL OF SANDERS' SPECIMEN B4.....	48
Fig. 2.7 THE EXPERIMENTAL STRAIN-LOAD RELATIONSHIP OF SPECIMEN B4.....	49
Fig. 2.8 THE STRAIN-LOAD RELATIONSHIP FROM PRELIMINARY STUDY MODEL LENGTH = $1.5h$ WITH 20 LOAD STEPS.....	49
Fig. 2.9 THE STRAIN-LOAD RELATIONSHIP FROM PRELIMINARY STUDY MODEL LENGTH = $2.5h$ WITH 20 LOAD STEPS.....	50
Fig. 2.10 THE STRAIN-LOAD RELATIONSHIP FROM PRELIMINARY STUDY MODEL LENGTH = $2.5h$ WITH 40 LOAD STEPS.....	50
Fig. 3.1 TYPICAL DIMENSIONS FOR FINITE ELEMENT MODELING.....	54
Fig. 3.2 ANCHORAGE ZONE WITH SUPPORT REACTION.....	54
Fig. 3.3 SPRING CONNECTION BETWEEN BEARING PLATE AND CONCRETE ELEMENT.....	55
Fig. 3.4 MODELS USED IN CONVERGENCE TEST.....	56
Fig. 3.5 CONVERGENCE TEST RESULT.....	56
Fig. 3.6 LOCATIONS OF VERTICAL ROLLER SUPPORT.....	57
Fig. 3.7 TENSILE STRESSES OF MODELS WITH DIFFERENT VERTICAL SUPPORT LOCATION.....	58
Fig. 3.8 COMPARISON OF MODEL WITH INCLINED STRUT LINE.....	60
Fig. 3.9 TYPICAL MODEL FOR THE STUDY OF ANCHORAGE ZONE WITH SUPPORT REACTION.....	61
Fig. 3.10 COMPARISON OF FINITE ELEMENT RESULTS PRESENTED BY BURDET (1990).....	65
Fig. 3.11 EFFECT OF INCLINED PRESTRESSING FORCE ON ANCHORAGE ZONE.....	65
Fig. 3.12 ECCENTRICALLY LOADED ANCHORAGE ZONE.....	67
Fig. 3.13 CONCENTRIC LOAD WITH $a/h = 0.20$ AND $R/P = 0.00$	70
Fig. 3.14 CONCENTRIC LOAD WITH $a/h = 0.20$, $l/h = 0.125$, AND $R/P = 0.05$	71
Fig. 3.15 CONCENTRIC LOAD WITH $a/h = 0.20$, $l/h = 0.125$, AND $R/P = 0.15$	72
Fig. 3.16 Y-Y STRESSES DUE TO REACTION LOAD WITH $l/h = 0.125$, $R/P =$ a) 0.05 AND b) 0.15.....	73
Fig. 3.17 BURSTING FORCE vs. ANCHORAGE RATIO ($b/h = 0.0$, $l/h = 0.125$).....	75
Fig. 3.18 BURSTING FORCE vs. ANCHORAGE RATIO ($b/h = 0.0$, $l/h = 0.25$).....	75
Fig. 3.19 BURSTING FORCE vs. ANCHORAGE RATIO ($b/h = 0.0$, $l/h = 0.50$).....	76
Fig. 3.20 BURSTING FORCE vs. LOCATION OF SUPPORT REACTION ($b/h = 0.0$).....	77
Fig. 3.21 STRESSES DUE TO REACTION LOAD WITH $R/P = 0.15$ AND $l/h = 0.50$	77

Fig. 3.22 BURSTING FORCE vs. BEARING PLATE RATIO ($l/h = 0.125$).....	78
Fig. 3.23 BURSTING FORCE vs. BEARING PLATE RATIO ($l/h = 0.25$).....	79
Fig. 3.24 BURSTING FORCE vs. BEARING PLATE RATIO ($l/h = 0.50$).....	79
Fig. 3.25 Y-Y STRESSES DUE TO REACTION LOAD WITH $R/P = 0.15$, $l/h = 0.25$, AND $b/h =$ a) 0.0, b) 0.125, AND c) 0.25.....	80
Fig. 3.26 BURSTING FORCE vs. REACTION RATIO ($l/h = 0.125$, $b/h = 0.0$).....	81
Fig. 3.27 BURSTING FORCE vs. REACTION RATIO ($l/h = 0.25$, $b/h = 0.0$).....	82
Fig. 3.28 BURSTING FORCE vs. REACTION RATIO ($l/h = 0.50$, $b/h = 0.0$).....	82
Fig. 3.29 COMPARISON OF FINITE ELEMENT RESULT AND MODIFIED EQUATION.....	83
Fig. 3.30 BURSTING FORCE LOCATION vs. ANCHORAGE RATIO ($b/h = 0.0$, $l/h = 0.125$).....	85
Fig. 3.31 BURSTING FORCE LOCATION vs. ANCHORAGE RATIO ($b/h = 0.0$, $l/h = 0.25$).....	85
Fig. 3.32 BURSTING FORCE LOCATION vs. ANCHORAGE RATIO ($b/h = 0.0$, $l/h = 0.50$).....	86
Fig. 3.33 COMPARISON OF d_{burst} WITH MODIFIED EQUATION.....	87
Fig. 3.34 BURSTING FORCE LOCATION vs. LOCATION OF SUPPORT REACTION ($R/P =$ 0.05).....	88
Fig. 3.35 BURSTING FORCE LOCATION vs. LOCATION OF SUPPORT REACTION ($R/P =$ 0.15).....	88
Fig. 3.36 BURSTING FORCE LOCATION vs. BEARING PLATE RATIO ($l/h = 0.50$).....	89
Fig. 3.37 BURSTING FORCE LOCATION vs. REACTION RATIO ($l/h = 0.125$, $b/h = 0.0$).....	90
Fig. 3.38 BURSTING FORCE LOCATION vs. REACTION RATIO ($l/h = 0.25$, $b/h = 0.0$).....	91
Fig. 3.39 BURSTING FORCE LOCATION vs. REACTION RATIO ($l/h = 0.50$, $b/h = 0.0$).....	91
Fig. 3.40 MODIFIED EQUATION OF d_{burst} FOR CONCENTRIC LOAD CONFIGURATION.....	92
Fig. 3.41 6 DEGREE INCLINED CONCENTRIC LOAD WITH $a/h = 0.20$, $R/P = 0.00$	94
Fig. 3.42 9 DEGREE INCLINED CONCENTRIC LOAD WITH $a/h = 0.20$, $R/P = 0.00$	95
Fig. 3.43 6 DEGREE INCLINED CONCENTRIC LOAD WITH $a/h = 0.20$, $R/P = 0.15$	96
Fig. 3.44 BURSTING FORCE AND INCLINATION ANGLE FOR CONCENTRIC LOAD.....	97
Fig. 3.45 VERTICAL STRESSES ON INCLINED CONCENTRICALLY LOADED ANCHORAGE ZONE.....	98
Fig. 3.46 BURSTING FORCE vs. ANCHORAGE RATIO FOR 6 DEGREE INCLINED CONCENTRIC LOAD ($b/h = 0.0$, $l/h = 0.125$).....	99
Fig. 3.47 BURSTING FORCE vs. ANCHORAGE RATIO FOR 6 DEGREE INCLINED CONCENTRIC LOAD ($b/h = 0.0$, $l/h = 0.25$).....	99
Fig. 3.48 BURSTING FORCE vs. ANCHORAGE RATIO FOR 6 DEGREE INCLINED CONCENTRIC LOAD ($b/h = 0.0$, $l/h = 0.50$).....	100

Fig. 3.49 BURSTING FORCE vs. ANCHORAGE RATIO FOR 9 DEGREE INCLINED CONCENTRIC LOAD ($b/h = 0.0, l/h = 0.125$).....	100
Fig. 3.50 BURSTING FORCE vs. ANCHORAGE RATIO FOR 9 DEGREE INCLINED CONCENTRIC LOAD ($b/h = 0.0, l/h = 0.25$).....	101
Fig. 3.51 BURSTING FORCE vs. ANCHORAGE RATIO FOR 9 DEGREE INCLINED CONCENTRIC LOAD ($b/h = 0.0, l/h = 0.50$).....	101
Fig. 3.52 BURSTING FORCE vs. LOCATION OF SUPPORT REACTION FOR 6 DEGREE INCLINED CONCENTRIC LOAD ($b/h = 0.0$).....	102
Fig. 3.53 BURSTING FORCE vs. LOCATION OF SUPPORT REACTION FOR 9 DEGREE INCLINED CONCENTRIC LOAD ($b/h = 0.0$).....	103
Fig. 3.54 BURSTING FORCE vs. BEARING PLATE RATIO FOR 6 DEGREE INCLINED CONCENTRIC LOAD ($l/h = 0.50$).....	104
Fig. 3.55 BURSTING FORCE vs. BEARING PLATE RATIO FOR 9 DEGREE INCLINED CONCENTRIC LOAD ($l/h = 0.50$).....	104
Fig. 3.56 BURSTING FORCE vs. REACTION RATIO FOR 6 DEGREE INCLINED CONCENTRIC LOAD ($l/h = 0.125, b/h = 0.0$).....	105
Fig. 3.57 BURSTING FORCE vs. REACTION RATIO FOR 6 DEGREE INCLINED CONCENTRIC LOAD ($l/h = 0.25, b/h = 0.0$).....	106
Fig. 3.58 BURSTING FORCE vs. REACTION RATIO FOR 6 DEGREE INCLINED CONCENTRIC LOAD ($l/h = 0.50, b/h = 0.0$).....	106
Fig. 3.59 BURSTING FORCE vs. REACTION RATIO FOR 9 DEGREE INCLINED CONCENTRIC LOAD ($l/h = 0.125, b/h = 0.0$).....	107
Fig. 3.60 BURSTING FORCE vs. REACTION RATIO FOR 9 DEGREE INCLINED CONCENTRIC LOAD ($l/h = 0.25, b/h = 0.0$).....	107
Fig. 3.61 BURSTING FORCE vs. REACTION RATIO FOR 9 DEGREE INCLINED CONCENTRIC LOAD ($l/h = 0.50, b/h = 0.0$).....	108
Fig. 3.62 EQUATION FOR BURSTING FORCE PREDICTION.....	109
Fig. 3.63 BURSTING FORCE LOCATION vs. INCLINATION ANGLE FOR CONCENTRIC LOAD (NO REACTION).....	115
Fig. 3.64 BURSTING FORCE LOCATION vs. ANCHORAGE RATIO FOR 6 DEGREE INCLINED CONCENTRIC LOAD ($b/h = 0.0, l/h = 0.125$).....	116
Fig. 3.65 BURSTING FORCE LOCATION vs. ANCHORAGE RATIO FOR 6 DEGREE INCLINED CONCENTRIC LOAD ($b/h = 0.0, l/h = 0.25$).....	116
Fig. 3.66 BURSTING FORCE LOCATION vs. ANCHORAGE RATIO FOR 6 DEGREE INCLINED CONCENTRIC LOAD ($b/h = 0.0, l/h = 0.50$).....	117
Fig. 3.67 BURSTING FORCE LOCATION vs. ANCHORAGE RATIO FOR 9 DEGREE INCLINED CONCENTRIC LOAD ($b/h = 0.0, l/h = 0.125$).....	117

Fig. 3.68 BURSTING FORCE LOCATION vs. ANCHORAGE RATIO FOR 9 DEGREE INCLINED CONCENTRIC LOAD ($b/h = 0.0, l/h = 0.25$).....	118
Fig. 3.69 BURSTING FORCE LOCATION vs. ANCHORAGE RATIO FOR 9 DEGREE INCLINED CONCENTRIC LOAD ($b/h = 0.0, l/h = 0.50$).....	118
Fig. 3.70 BURSTING FORCE LOCATION vs. LOCATION OF SUPPORT REACTION FOR 6 AND 9 DEGREE INCLINED CONCENTRIC LOADS AND $R/P = 0.05$	120
Fig. 3.71 BURSTING FORCE LOCATION vs. LOCATION OF SUPPORT REACTION FOR 6 AND 9 DEGREE INCLINED CONCENTRIC LOADS AND $R/P = 0.15$	120
Fig. 3.72 BURSTING FORCE LOCATION vs. BEARING PLATE RATIO FOR 6 DEGREE INCLINED CONCENTRIC LOAD ($l/h = 0.50$).....	121
Fig. 3.73 BURSTING FORCE LOCATION vs. REACTION RATIO FOR 6 DEGREE INCLINED CONCENTRIC LOAD ($l/h = 0.125, b/h = 0.0$).....	122
Fig. 3.74 BURSTING FORCE LOCATION vs. REACTION RATIO FOR 6 DEGREE INCLINED CONCENTRIC LOAD ($l/h = 0.25, b/h = 0.0$).....	122
Fig. 3.75 BURSTING FORCE LOCATION vs. REACTION RATIO FOR 6 DEGREE INCLINED CONCENTRIC LOAD ($l/h = 0.50, b/h = 0.0$).....	123
Fig. 3.76 BURSTING FORCE LOCATION vs. REACTION RATIO FOR 9 DEGREE INCLINED CONCENTRIC LOAD ($l/h = 0.125, b/h = 0.0$).....	123
Fig. 3.77 BURSTING FORCE LOCATION vs. REACTION RATIO FOR 9 DEGREE INCLINED CONCENTRIC LOAD ($l/h = 0.25, b/h = 0.0$).....	124
Fig. 3.78 BURSTING FORCE LOCATION vs. REACTION RATIO FOR 9 DEGREE INCLINED CONCENTRIC LOAD ($l/h = 0.50, b/h = 0.0$).....	124
Fig. 3.79 EQUATION FOR THE PREDICTION OF BURSTING FORCE LOCATION.....	125
Fig. 3.80 ANCHOR PLATES AT THE HIGHEST ECCENTRIC LOCATION.....	131
Fig. 3.81 ECCENTRIC LOAD WITH $e/h = 0.10, a/h = 0.10, R/P = 0.00$	133
Fig. 3.82 ECCENTRIC LOAD WITH $e/h = 0.40, a/h = 0.10, R/P = 0.00$	134
Fig. 3.83 STRESS IN Y-Y DIRECTION OF ECCENTRIC LOAD WITH e/h EQUAL TO a) +0.40, b) +0.10, c) -0.10, AND d) -0.40.....	135
Fig. 3.84 ECCENTRIC LOAD WITH $e/h = -0.40, a/h = 0.10, R/P = 0.15$	136
Fig. 3.85 BURSTING FORCE vs. LOCATION OF SUPPORT REACTION FOR ECCENTRIC LOAD AND $R/P = 0.05$ ($a/h = 0.20, b/h = 0.125$).....	138
Fig. 3.86 BURSTING FORCE vs. LOCATION OF SUPPORT REACTION FOR ECCENTRIC LOAD AND $R/P = 0.15$ ($a/h = 0.20, b/h = 0.125$).....	138
Fig. 3.87 BURSTING FORCE vs. BEARING PLATE RATIO FOR ECCENTRIC LOAD AND $R/P = 0.15$ ($a/h = 0.10, l/h = 0.25$).....	139
Fig. 3.88 BURSTING FORCE vs. REACTION FOR ECCENTRIC LOAD ($a/h = 0.20, l/h = 0.125$, and $b/h = 0.125$).....	140

Fig. 3.89 BURSTING FORCE vs. ECCENTRICITY RATIO FOR $R/P = 0.05$ ($a/h = 0.20$ and $b/h = 0.125$).....	141
Fig. 3.90 BURSTING FORCE vs. ECCENTRICITY RATIO FOR $R/P = 0.15$ ($a/h = 0.20$ and $b/h = 0.125$).....	141
Fig. 3.91 BURSTING FORCE LOCATION vs. LOCATION OF SUPPORT REACTION FOR ECCENTRIC LOAD AND $R/P = 0.05$ ($a/h = 0.20$, $b/h = 0.125$).....	143
Fig. 3.92 BURSTING FORCE LOCATION vs. LOCATION OF SUPPORT REACTION FOR ECCENTRIC LOAD AND $R/P = 0.15$ ($a/h = 0.20$, $b/h = 0.125$).....	143
Fig. 3.93 BURSTING FORCE LOCATION vs. BEARING PLATE RATIO FOR ECCENTRIC LOAD ($a/h = 0.10$, $l/h = 0.25$).....	144
Fig. 3.94 BURSTING FORCE LOCATION vs. ECCENTRICITY RATIO FOR $R/P = 0.05$ ($a/h = 0.20$, $b/h = 0.125$).....	145
Fig. 3.95 BURSTING FORCE LOCATION vs. ECCENTRICITY RATIO FOR $R/P = 0.15$ ($a/h = 0.20$, $b/h = 0.125$).....	146
Fig. 3.96 STRESS IN Y-Y DIRECTION OF 6 DEGREE INCLINED ECCENTRIC LOAD WITH e/h EQUAL TO a) +0.40, b) +0.10, c) -0.10, AND d) -0.40 ($R/P = 0.0$).....	148
Fig. 3.97 STRESS IN Y-Y DIRECTION OF 6 DEGREE INCLINED ECCENTRIC LOAD WITH e/h EQUAL TO a) +0.40, b) +0.10, c) -0.10, AND d) -0.40 ($l/h = 0.125$, $b/h = 0.125$, and $R/P = 0.15$).....	149
Fig. 3.98 BURSTING FORCE vs. LOCATION OF SUPPORT REACTION FOR 6 DEGREE INCLINED ECCENTRIC LOAD AND $R/P = 0.05$ ($a/h = 0.20$, $b/h = 0.125$).....	151
Fig. 3.99 BURSTING FORCE vs. LOCATION OF SUPPORT REACTION FOR 9 DEGREE INCLINED ECCENTRIC LOAD AND $R/P = 0.05$ ($a/h = 0.20$, $b/h = 0.125$).....	151
Fig. 3.100 BURSTING FORCE vs. LOCATION OF SUPPORT REACTION FOR 6 DEGREE INCLINED ECCENTRIC LOAD AND $R/P = 0.15$ ($a/h = 0.20$, $b/h = 0.125$).....	152
Fig. 3.101 BURSTING FORCE vs. LOCATION OF SUPPORT REACTION FOR 9 DEGREE INCLINED ECCENTRIC LOAD AND $R/P = 0.15$ ($a/h = 0.20$, $b/h = 0.125$).....	152
Fig. 3.102 BURSTING FORCE vs. BEARING PLATE RATIO FOR 6 DEGREE INCLINED ECCENTRIC LOAD AND $R/P = 0.15$ ($a/h = 0.10$, $l/h = 0.25$).....	154
Fig. 3.103 BURSTING FORCE vs. BEARING PLATE RATIO FOR 9 DEGREE INCLINED ECCENTRIC LOAD AND $R/P = 0.15$ ($a/h = 0.10$, $l/h = 0.25$).....	154
Fig. 3.104 BURSTING FORCE vs. ECCENTRICITY RATIO FOR 6 DEGREE INCLINED ECCENTRIC LOAD AND $R/P = 0.05$ ($a/h = 0.20$, $b/h = 0.125$).....	155
Fig. 3.105 BURSTING FORCE vs. ECCENTRICITY RATIO FOR 9 DEGREE INCLINED ECCENTRIC LOAD AND $R/P = 0.05$ ($a/h = 0.20$, $b/h = 0.125$).....	155
Fig. 3.106 BURSTING FORCE vs. ECCENTRICITY RATIO FOR 6 DEGREE INCLINED ECCENTRIC LOAD AND $R/P = 0.15$ ($a/h = 0.20$, $b/h = 0.125$).....	156
Fig. 3.107 BURSTING FORCE vs. ECCENTRICITY RATIO FOR 9 DEGREE INCLINED ECCENTRIC LOAD AND $R/P = 0.15$ ($a/h = 0.20$, $b/h = 0.125$).....	156

Fig. 3.108 EXAMPLE OF COMPARISON OF MODIFIED EQUATION FOR 9 DEGREE INCLINED ECCENTRIC LOAD AND $R/P = 0.05$ ($a/h = 0.20$, $b/h = 0.125$).....	157
Fig. 3.109 BURSTING FORCE LOCATION vs. LOCATION OF SUPPORT REACTION FOR 9 DEGREE INCLINED ECCENTRIC LOAD AND $R/P = 0.15$ ($a/h = 0.20$, $b/h = 0.125$).....	163
Fig. 3.110 BURSTING FORCE LOCATION vs. BEARING PLATE RATIO FOR 9 DEGREE INCLINED ECCENTRIC LOAD ($a/h = 0.10$, $l/h = 0.25$).....	163
Fig. 3.111 BURSTING FORCE LOCATION vs. ECCENTRICITY RATIO FOR 6 DEGREE INCLINED ECCENTRIC LOAD AND $R/P = 0.05$ ($a/h = 0.20$, $b/h = 0.125$).....	165
Fig. 3.112 BURSTING FORCE LOCATION vs. ECCENTRICITY RATIO FOR 9 DEGREE INCLINED ECCENTRIC LOAD AND $R/P = 0.05$ ($a/h = 0.20$, $b/h = 0.125$).....	165
Fig. 3.113 BURSTING FORCE LOCATION vs. ECCENTRICITY RATIO FOR 6 DEGREE INCLINED ECCENTRIC LOAD AND $R/P = 0.15$ ($a/h = 0.20$, $b/h = 0.125$).....	166
Fig. 3.114 BURSTING FORCE LOCATION vs. ECCENTRICITY RATIO FOR 9 DEGREE INCLINED ECCENTRIC LOAD AND $R/P = 0.15$ ($a/h = 0.20$, $b/h = 0.125$).....	166
Fig. 3.115 STRUCTURE USED FOR MODELING OF Beam3.....	172
Fig. 3.116 CRACKING STRAIN VECTORS ON FINITE ELEMENT MODEL OF Beam3.....	173
Fig. 3.117 VERTICAL BAR STRAINS IN SPECIMEN Beam3 FROM WOLLMAN'S STUDY (1992).....	174
Fig. 3.118 VERTICAL BAR STRAINS IN SPECIMEN Beam3 FROM NONLINEAR ANALYSIS.....	174
Fig. 3.119 TYPICAL DIMENSIONS OF THE MODEL.....	176
Fig. 3.120 MODEL FROM THE APPROXIMATE EQUATIONS.....	178
Fig. 3.121 STRUT-AND-TIE MODEL WITH A SUPPORT REACTION.....	179
Fig. 3.122 LOCAL NODE IN STRUT-AND-TIE MODEL.....	180
Fig. 3.123 LOCAL NODE AND FAN-SHAPED STRUTS.....	180
Fig. 3.124 FORCES IN STRUT-AND-TIE MODEL.....	182
Fig. 3.125 STRUT-AND-TIE MODEL WITH FAN-SHAPED STRUTS.....	184
Fig. 3.126 MODEL FROM THE STM METHOD AND NEW APPROXIMATE EQUATIONS.....	185
Fig. 3.127 CRACKING STRAIN VECTORS ON FINITE ELEMENT MODEL BASED ON APPROXIMATE EQUATIONS (MODEL 1).....	187
Fig. 3.128 CRACKING STRAIN VECTORS ON FINITE ELEMENT MODEL BASED ON STM AND NEW APPROACH (MODEL 2).....	187
Fig. 3.129 TENSILE STRAIN IN BURSTING STEEL BARS OF MODEL 1 AND 2.....	188
Fig. 3.130 MODELS FOR THE STUDY OF REINFORCEMENT ARRANGEMENT.....	190
Fig. 3.131 TENSILE STRAIN IN BURSTING STEEL BARS OF MODELS 3 AND 4.....	190
Fig. 3.132 CRACKING STRAIN VECTORS ON a) MODEL 3 AND b) MODEL 4.....	191
Fig. 4.1 FLANGED SECTIONS IN PRESTRESSED CONCRETE STRUCTURES.....	194

Fig. 4.2	STANDARD SECTIONS PRESENTED IN PCI BRIDGE DESIGN MANUAL (1997)....	197
Fig. 4.3	TRANSFORMED SECTIONS FOR THE PRESENT STUDY.....	198
Fig. 4.4	TYPICAL MODEL USED IN THE STUDY OF ANCHORAGE ZONE WITH FLANGED SECTION.....	200
Fig. 4.5	ANCHORAGE ZONE USED FOR COMPARISON OF THE MODELS WITH DIFFERENT TYPE OF ELEMENT.....	201
Fig. 4.6	FINITE ELEMENT MODEL USING BRICK ELEMENTS.....	202
Fig. 4.7	Y-Y STRESSES IN THE WEB OF THE MODEL WITH BRICK ELEMENT.....	202
Fig. 4.8	Z-Z STRESSES IN THE FLANGE PRESENTED IN THREE LAYERS.....	203
Fig. 4.9	FINITE ELEMENT MODEL USING SHELL ELEMENTS.....	204
Fig. 4.10	TENSILE STRESSES IN EACH MEMBER.....	204
Fig. 4.11	MODELS OF a) T-SECTION AND b) UNSYMMETRICAL I-SECTION.....	205
Fig. 4.12	TENSILE STRESSES IN THE MODEL WITH RECTANGULAR SECTION.....	210
Fig. 4.13	TENSILE STRESSES IN EACH MEMBER OF SYMMETRICAL I-SECTION MODEL WITH $b_f = 6.4$ in.....	212
Fig. 4.14	TENSILE STRESSES IN EACH MEMBER OF SYMMETRICAL I-SECTION MODEL WITH $b_f = 16.0$ in.....	212
Fig. 4.15	TENSILE STRESSES IN EACH MEMBER OF SYMMETRICAL I-SECTION MODEL WITH $b_f = 56.0$ in.....	213
Fig. 4.16	PRINCIPAL COMPRESSIVE STRESSES OF SYMMETRICAL I-SECTION MODEL WITH $b_f = 56.0$ in.....	214
Fig. 4.17	TENSILE STRESSES IN FLANGE OF SYMMETRICAL I-SECTION MODEL WITH $b_f = 6.4$ in. AND $t_f = 1.2$ in.....	214
Fig. 4.18	TENSILE STRESS DIAGRAMS IN FLANGE OF SYMMETRICAL I-SECTION MODEL WITH $b_f = 6.4$ in. AND $t_f = 1.2$ in.....	215
Fig. 4.19	TENSILE STRESSES IN EACH MEMBER OF T-SECTION MODEL WITH $b_f = 6.4$ in.....	216
Fig. 4.20	TENSILE STRESSES IN EACH MEMBER OF T-SECTION MODEL WITH $b_f = 16.0$ in.....	217
Fig. 4.21	TENSILE STRESSES IN EACH MEMBER OF T-SECTION MODEL WITH $b_f = 56.0$ in.....	217
Fig. 4.22	TENSILE STRESSES IN EACH MEMBER OF UNSYMMETRICAL I-SECTION MODEL WITH $b_{f1} = 16.0$ in. AND $b_{f2} = 8.0$ in.....	218
Fig. 4.23	WEB BURSTING FORCE vs. THICKNESS RATIO FOR SYMMETRICAL I-SECTION ($b_f = 6.4$ in.).....	220
Fig. 4.24	WEB BURSTING FORCE vs. THICKNESS RATIO FOR SYMMETRICAL I-SECTION ($b_f = 16.0$ in.).....	220

Fig. 4.25 WEB BURSTING FORCE vs. THICKNESS RATIO FOR SYMMETRICAL I-SECTION ($b_f = 56.0$ in.).....	221
Fig. 4.26 FLANGE BURSTING FORCE vs. THICKNESS RATIO FOR SYMMETRICAL I-SECTION ($b_f = 6.4$ in.).....	222
Fig. 4.27 FLANGE BURSTING FORCE vs. THICKNESS RATIO FOR SYMMETRICAL I-SECTION ($b_f = 16.0$ in.).....	222
Fig. 4.28 FLANGE BURSTING FORCE vs. THICKNESS RATIO FOR SYMMETRICAL I-SECTION ($b_f = 56.0$ in.).....	223
Fig. 4.29 WEB BURSTING FORCE vs. WEB THICKNESS FOR SYMMETRICAL I-SECTION ($b_f = 56.0$ in.).....	224
Fig. 4.30 WEB BURSTING FORCE vs. ANCHORAGE RATIO FOR SYMMETRICAL I-SECTION ($t_w = 1.5$ in.).....	225
Fig. 4.31 FLANGE BURSTING FORCE vs. ANCHORAGE RATIO FOR SYMMETRICAL I-SECTION ($t_w = 1.5$ in.).....	225
Fig. 4.32 WEB BURSTING FORCE vs. FLANGE WIDTH FOR SYMMETRICAL I-SECTION ($t_w = 1.5$ in.).....	226
Fig. 4.33 FLANGE BURSTING FORCE vs. FLANGE WIDTH FOR SYMMETRICAL I-SECTION ($t_w = 1.5$ in.).....	227
Fig. 4.34 WEB BURSTING FORCE vs. THICKNESS RATIO FOR T-SECTION ($b_f = 6.4$ in.).....	228
Fig. 4.35 WEB BURSTING FORCE vs. THICKNESS RATIO FOR T-SECTION ($a/h_w = 0.20$).....	229
Fig. 4.36 FLANGE BURSTING FORCE vs. THICKNESS RATIO FOR T-SECTION ($a/h_w = 0.20$).....	229
Fig. 4.37 BURSTING FORCE vs. ANCHORAGE RATIO FOR T-SECTION ($b_f = 6.4$ in. and $t_f/t_w = 1.4$).....	230
Fig. 4.38 BURSTING FORCE vs. FLANGE WIDTH FOR T-SECTION ($t_w = 1.5$ in.).....	231
Fig. 4.39 WEB BURSTING FORCE vs. FLANGE WIDTH RATIO ($a/h_w = 0.20$, $t_w = 1.5$ in., and $t_f/t_w = 1.40$).....	233
Fig. 4.40 FLANGE BURSTING FORCE vs. FLANGE WIDTH RATIO ($a/h_w = 0.20$, $t_w = 1.5$ in., and $t_f/t_w = 1.40$).....	233
Fig. 4.41 WEB BURSTING FORCE LOCATION vs. THICKNESS RATIO FOR SYMMETRICAL I-SECTION ($b_f = 6.4$ in.).....	235
Fig. 4.42 WEB BURSTING FORCE LOCATION vs. THICKNESS RATIO FOR SYMMETRICAL I-SECTION ($b_f = 16.0$ in.).....	235
Fig. 4.43 WEB BURSTING FORCE LOCATION vs. THICKNESS RATIO FOR SYMMETRICAL I-SECTION ($b_f = 56.0$ in.).....	236
Fig. 4.44 FLANGE BURSTING FORCE LOCATION vs. THICKNESS RATIO FOR SYMMETRICAL I-SECTION ($b_f = 6.4$ in.).....	237

Fig. 4.45 FLANGE BURSTING FORCE LOCATION vs. THICKNESS RATIO FOR SYMMETRICAL I-SECTION ($b_f = 16.0$ in.).....	237
Fig. 4.46 FLANGE BURSTING FORCE LOCATION vs. THICKNESS RATIO FOR SYMMETRICAL I-SECTION ($b_f = 56$ in.).....	238
Fig. 4.47 WEB BURSTING FORCE LOCATION vs. ANCHORAGE RATIO FOR SYMMETRICAL I-SECTION ($t_w = 1.5$ in.).....	239
Fig. 4.48 FLANGE BURSTING FORCE LOCATION vs. ANCHORAGE RATIO FOR SYMMETRICAL I-SECTION ($t_w = 1.5$ in.).....	240
Fig. 4.49 WEB BURSTING FORCE LOCATION vs. FLANGE WIDTH FOR SYMMETRICAL I-SECTION ($t_w = 1.5$ in.).....	241
Fig. 4.50 FLANGE BURSTING FORCE LOCATION vs. FLANGE WIDTH FOR SYMMETRICAL I-SECTION ($t_w = 1.5$ in.).....	241
Fig. 4.51 WEB BURSTING FORCE LOCATION vs. THICKNESS RATIO FOR T-SECTION ($b_f = 6.4$ in.).....	243
Fig. 4.52 WEB BURSTING FORCE LOCATION vs. THICKNESS RATIO FOR T-SECTION ($a/h_w = 0.20$).....	243
Fig. 4.53 FLANGE BURSTING FORCE LOCATION vs. THICKNESS RATIO FOR T-SECTION ($a/h_w = 0.20$).....	244
Fig. 4.54 BURSTING FORCE LOCATION vs. ANCHORAGE RATIO FOR T-SECTION ($b_f = 6.4$ in., $t_f/t_w = 1.4$, and $t_w = 5$ in.).....	245
Fig. 4.55 BURSTING FORCE LOCATION vs. FLANGE WIDTH FOR T-SECTION ($a/h_w = 0.20$, $t_f/t_w = 1.4$, and $t_w = 5$ in.).....	246
Fig. 4.56 WEB BURSTING FORCE LOCATION vs. FLANGE WIDTH RATIO ($a/h_w = 0.20$, $t_w = 1.5$ in., and $t_f/t_w = 1.40$).....	247
Fig. 4.57 FLANGE BURSTING FORCE LOCATION vs. FLANGE WIDTH RATIO ($a/h_w = 0.20$, $t_w = 1.5$ in., and $t_f/t_w = 1.40$).....	247
Fig. 4.58 SYMBOLS OF GEOMETRIC PROPERTIES AND RESULTANT FORCES IN MEMBERS OF FLANGED SECTIONS.....	250
Fig. 4.59 STRUT-AND-TIE MODEL FOR THE FORMULATION OF SYMMETRICAL I-SECTION.....	251
Fig. 4.60 WEB BURSTING FORCE LOCATION vs. FLANGE WIDTH FOR SYMMETRICAL I-SECTION ($t_w = 1.5$ in., $t_f/t_w = 1.4$, and $a/h_w = 0.20$).....	254
Fig. 4.61 STRUT-AND-TIE MODEL OF THE FLANGE FOR THE FORMULATIONS OF SYMMETRICAL I-SECTION.....	259
Fig. 4.62 k_f RATIO FOR THE TOP PORTION OF A FLANGED SECTION.....	262
Fig. 4.63 FLANGE BURSTING FORCE LOCATION AND k_f RATIO FOR SYMMETRICAL I-SECTION ($t_w = 1.5$ in., $t_f/t_w = 1.4$, and $a/h_w = 0.20$).....	262
Fig. 4.64 SIMPLIFIED STRUT-AND-TIE MODEL FOR SYMMETRICAL I-SECTION.....	265

Fig. 4.65 STRUT-AND-TIE MODEL FOR THE FORMULATIONS OF T-SECTION.....	266
Fig. 4.66 WEB BURSTING FORCE LOCATION vs. FLANGE WIDTH FOR T-SECTION ($t_w = 1.5$ in., $t_f/t_w = 1.4$, and $a/h_w = 0.20$).....	268
Fig. 4.67 STRUT-AND-TIE MODEL FOR THE FORMULATION OF UNSYMMETRICAL I-SECTION.....	272
Fig. 4.68 TENSILE STRESSES IN EACH MEMBER OF SYMMETRICAL I-SECTION MODEL WITH $b_f = 16.0$ in. AND $e/h_w = 0.10$	277
Fig. 4.69 TENSILE STRESSES IN EACH MEMBER OF SYMMETRICAL I-SECTION MODEL WITH $b_f = 16.0$ in. AND $e/h_w = 0.40$	278
Fig. 4.70 X-X STRESSES IN TOP FLANGE OF SYMMETRICAL I-SECTION MODEL WITH $b_f = 16.0$ in. AND $e/h_w = 0.40$	279
Fig. 4.71 TENSILE STRESSES IN EACH MEMBER OF T-SECTION MODEL WITH $b_f = 16.0$ in. AND $e/h_w = -0.10$	279
Fig. 4.72 TENSILE STRESSES IN EACH MEMBER OF T-SECTION MODEL WITH $b_f = 16.0$ in. AND $e/h_w = -0.40$	280
Fig. 4.73 X-X STRESSES IN TOP FLANGE OF T-SECTION MODEL WITH $b_f = 16.0$ in. AND $e/h_w = -0.40$	280
Fig. 4.74 TENSILE STRESSES IN EACH MEMBER OF UNSYMMETRICAL I-SECTION MODEL WITH $b_{f1} = 16$ in., $b_{f2} = 8$ in., AND $e/h_w = 0.40$	281
Fig. 4.75 BURSTING FORCE vs. FLANGE WIDTH FOR SYMMETRICAL I-SECTION WITH $e/h_w = 0.10$ ($a/h_w = 0.20$, $t_w = 5$ in., and $t_f/t_w = 1.10$).....	283
Fig. 4.76 BURSTING FORCE vs. FLANGE WIDTH FOR SYMMETRICAL I-SECTION WITH $e/h_w = 0.40$ ($a/h_w = 0.20$, $t_w = 5$ in., and $t_f/t_w = 1.10$).....	284
Fig. 4.77 BURSTING FORCE vs. FLANGE WIDTH FOR T-SECTION WITH $e/h_w = -0.10$ ($a/h_w = 0.20$, $t_w = 5$ in., and $t_f/t_w = 1.10$).....	285
Fig. 4.78 BURSTING FORCE vs. FLANGE WIDTH FOR T-SECTION WITH $e/h_w = -0.40$ ($a/h_w = 0.20$, $t_w = 5$ in., and $t_f/t_w = 1.10$).....	286
Fig. 4.79 BURSTING FORCE vs. FLANGE WIDTH RATIO WITH $e/h_w = -0.10$ ($a/h_w = 0.20$, $t_w = 5$ in., and $t_f/t_w = 1.10$).....	287
Fig. 4.80 BURSTING FORCE LOCATION vs. FLANGE WIDTH FOR SYMMETRICAL I-SECTION WITH $e/h_w = 0.10$ ($a/h_w = 0.20$, $t_w = 5$ in., and $t_f/t_w = 1.10$).....	288
Fig. 4.81 BURSTING FORCE LOCATION vs. FLANGE WIDTH FOR SYMMETRICAL I-SECTION WITH $e/h_w = 0.40$ ($a/h_w = 0.20$, $t_w = 5$ in., and $t_f/t_w = 1.10$).....	289
Fig. 4.82 BURSTING FORCE LOCATION vs. FLANGE WIDTH FOR T-SECTION WITH $e/h_w = -0.10$ ($a/h_w = 0.20$, $t_w = 5$ in., and $t_f/t_w = 1.10$).....	290
Fig. 4.83 BURSTING FORCE LOCATION vs. FLANGE WIDTH FOR T-SECTION WITH $e/h_w = -0.40$ ($a/h_w = 0.20$, $t_w = 5$ in., and $t_f/t_w = 1.10$).....	290

Fig. 4.84 BURSTING FORCE LOCATION AND FLANGE WIDTH RATIO WITH $e/h_w = -0.10$ ($a/h_w = 0.20$, $t_w = 5$ in., and $t_{f1}/t_w = t_{f2}/t_w = 1.1$).....	291
Fig. 4.85 FREE BODY FOR THE CALCULATION OF RESULTANT FORCES FOR ECCENTRIC LOAD CASE.....	293
Fig. 4.86 TENSILE STRESSES IN EACH MEMBER OF SYMMETRICAL I-SECTION MODEL WITH $b_f = 16.0$ in. SUBJECTED TO 6 DEGREE INCLINED CONCENTRIC LOAD.....	302
Fig. 4.87 TENSILE STRESSES IN EACH MEMBER OF SYMMETRICAL I-SECTION MODEL WITH $b_f = 16.0$ in. SUBJECTED TO 6 DEGREE INCLINED ECCENTRIC LOAD WITH $e/h_w = -0.10$	303
Fig. 4.88 TENSILE STRESSES IN EACH MEMBER OF SYMMETRICAL I-SECTION MODEL WITH $b_f = 16.0$ in. SUBJECTED TO 6 DEGREE INCLINED ECCENTRIC LOAD WITH $e/h_w = +0.10$	304
Fig. 4.89 TENSILE STRESSES IN EACH MEMBER OF T-SECTION MODEL WITH $b_f = 16.0$ in. SUBJECTED TO 6 DEGREE INCLINED ECCENTRIC LOAD WITH $e/h_w = -0.10$	305
Fig. 4.90 TENSILE STRESSES IN EACH MEMBER OF UNSYMMETRICAL I-SECTION MODEL WITH $b_f = 16.0$ in. SUBJECTED TO 6 DEGREE INCLINED ECCENTRIC LOAD WITH $e/h_w = -0.10$	306
Fig. 4.91 TENSILE STRESSES IN EACH MEMBER OF UNSYMMETRICAL I-SECTION MODEL WITH $b_f = 16.0$ in. SUBJECTED TO 6 DEGREE INCLINED ECCENTRIC LOAD AND A SUPPORT REACTION WITH $R/P = 0.15$, $b_{f1} = 16$ in., $b_{f2} = 8$ in., AND $e/h_w = -0.10$	307
Fig. 4.92 BURSTING FORCE vs. FLANGE WIDTH FOR INCLINED CONCENTRIC AND INCLINED ECCENTRIC LOAD, WEB AND TOP FLANGE ($a/h_w = 0.20$, $t_w = 5$ in., and $t_f/t_w = 1.10$).....	309
Fig. 4.93 BURSTING FORCE vs. FLANGE WIDTH FOR INCLINED CONCENTRIC AND INCLINED ECCENTRIC LOAD, BOTTOM FLANGE ($a/h_w = 0.20$, $t_w = 5$ in., and $t_f/t_w = 1.10$).....	309
Fig. 4.94 BURSTING FORCE LOCATION vs. FLANGE WIDTH FOR INCLINED CONCENTRIC AND INCLINED ECCENTRIC LOAD, WEB AND TOP FLANGE ($a/h_w = 0.20$, $t_w = 5$ in., and $t_f/t_w = 1.10$).....	311
Fig. 4.95 BURSTING FORCE LOCATION vs. FLANGE WIDTH FOR INCLINED CONCENTRIC AND INCLINED ECCENTRIC LOAD, BOTTOM FLANGE ($a/h_w = 0.20$, $t_w = 5$ in., and $t_f/t_w = 1.10$).....	311
Fig. 4.96 FREE BODY FOR THE CALCULATION OF RESULTANT FORCES INCLUDING SHEARING FORCES.....	313
Fig. 4.97 SPECIMEN F1 FROM SANDERS' EXPERIMENTAL WORK.....	324
Fig. 4.98 MODELS USED FOR NONLINEAR ANALYSIS EXAMPLE.....	326
Fig. 4.99 CRACKING STRAIN VECTORS IN MODEL SDTS01.....	328
Fig. 4.100 CRACKING STRAIN VECTORS IN MODEL SDTS02.....	328
Fig. 4.101 FLANGE REINFORCEMENT BURSTING STRAINS NEAR ANCHOR B FROM SANDERS' SPECIMEN F1 (SANDERS,1990).....	330

Fig. 4.102 FLANGE REINFORCEMENT BURSTING STRAINS DISTANT FROM SANDERS' SPECIMEN F1 (SANDERS,1990).....	330
Fig. 4.103 FLANGE REINFORCEMENT BURSTING STRAINS FROM MODEL SDTS01	331
Fig. 4.104 FLANGE REINFORCEMENT BURSTING STRAINS FROM MODEL SDTS02	331
Fig. 4.105 WEB REINFORCEMENT BURSTING STRAINS NEAR ANCHOR A FROM SANDERS' SPECIMEN F1 (SANDERS,1990).....	332
Fig. 4.106 WEB REINFORCEMENT BURSTING STRAINS NEAR ANCHOR B FROM SANDERS' SPECIMEN F1 (SANDERS,1990).....	332
Fig. 4.107 WEB REINFORCEMENT BURSTING STRAINS NEAR ANCHOR A FROM MODEL SDTS01.....	333
Fig. 4.108 WEB REINFORCEMENT BURSTING STRAINS NEAR ANCHOR B FROM MODEL SDTS01.....	333
Fig. 4.109 WEB REINFORCEMENT BURSTING STRAINS NEAR ANCHOR A FROM MODEL SDTS02.....	334
Fig. 4.110 WEB REINFORCEMENT BURSTING STRAINS NEAR ANCHOR B FROM MODEL SDTS02.....	334
Fig. 4.111 BOX GIRDER BRIDGE DETAILS AND DIMENSIONS.....	336
Fig. 4.112 REINFORCEMENT DETAILS FOR NONLINEAR ANALYSIS STUDY.....	346
Fig. 4.113 CRACKING STRAIN CONTOUR PLOTS FOR MODEL BASED ON PTI EXAMPLE..	348
Fig. 4.114 CRACKING STRAIN CONTOUR PLOTS FOR MODEL BASED ON PRESENT DESIGN EXAMPLE.....	349
Fig. 4.115 CRACKING STRAIN CONTOUR PLOTS FOR MODEL BASED ON THE MODIFICATION OF PRESENT DESIGN EXAMPLE.....	350
Fig. 4.116 TENSILE STRESSES IN THE WEB BURSTING STEEL FOR ALL LOAD STEPS FOR MODEL BASED ON PTI EXAMPLE.....	353
Fig. 4.117 TENSILE STRESSES IN THE WEB BURSTING STEEL FOR ALL LOAD STEPS FOR MODEL BASED ON PRESENT DESIGN EXAMPLE.....	354
Fig. 4.118 TENSILE STRESSES IN THE WEB BURSTING STEEL FOR ALL LOAD STEPS FOR MODEL BASED ON THE MODIFICATION OF PRESENT DESIGN EXAMPLE.....	354
Fig. 4.119 COMPARISON OF TENSILE STRESSES ALONG THE HORIZONTAL LINE AT THE FINAL LOAD STEP.....	355
Fig. 4.120 TENSILE STRESSES IN THE TOP FLANGE BURSTING STEEL FOR MODEL BASED ON PTI EXAMPLE.....	356
Fig. 4.121 TENSILE STRESSES IN THE TOP FLANGE BURSTING STEEL FOR MODEL BASED ON PRESENT DESIGN EXAMPLE.....	356
Fig. 4.122 STRUT-AND-TIE MODEL FOR A NON-RECTANGULAR SECTION.....	361

Fig. 5.1 STRUT-AND-TIE MODEL FOR ANCHORAGE ZONE WITH A SUPPORT REACTION.....	365
Fig. 5.2 TRANSFORMED NON-RECTANGULAR SECTION.....	367
Fig. 5.3 STRUT-AND-TIE MODEL FOR A NON-RECTANGULAR SECTION.....	371
Fig. A.1 COMPRESSIVE STRESS DIAGRAMS.....	382
Fig. A.2 PARAMETERS WITHIN NON-RECTANGULAR SECTION.....	383
Fig. A.3 FREE BODY FOR THE CALCULATION OF THE LOCATIONS OF RESULTANT FORCES.....	385
Fig. C.1 TENSILE STRESSES IN WEB OF SYMMETRICAL I-SECTION MODEL WITH THREE FLANGE WIDTHS.....	390
Fig. D.1 SECTION WITH THE THICKEST FLANGE.....	391
Fig. D.2 SECTION WITH THE THINNEST WEB.....	394
Fig. D.3 SECTION WITH THE WIDEST FLANGE.....	397

CHAPTER 1

INTRODUCTION

1.1 Anchorage Zones in Prestressed Concrete Structures

Prestressed concrete structures are designed based on the concept of self-equilibrating stresses within the structure. By using the ability of the concrete to withstand high compressive stresses, a large prestressing load is introduced to the structure at anchorage zones using prestressing tendons. The load results in the reduction or elimination of tensile stresses within the structure, resulting in an increase in the flexural capacity of the structure. Therefore, a prestressed concrete structure can have a longer span and more slender shape than that of a common reinforced concrete structure. Since a large prestressing load is introduced through the anchorage plate, the region ahead of the anchorage plate contains high compressive stresses immediately next to the plate and the compressive stresses are followed by tensile stresses normal to the tendon axis. Since the concrete cannot withstand the tensile stresses effectively, bursting reinforcement is required in the region in which the tensile stresses occur.

Ever since the AASHTO Standard Specifications 1994 first provided guidelines for anchorage zone design, which were adopted from the NCHRP project 10-29 (section 1.4.1.3), reasonable methods of anchorage zone design have been available for structural designers. However, the methods presented in the Specification have a limited range of applicability. The guideline cannot answer questions about some complex configurations of anchorage zones, such as an anchorage zone with a support reaction. Some researches (Leonhardt, 1964, and Wollmann, 1992) showed a significant influence of the support reaction on the behavior of bursting forces in prestressed concrete structures. Furthermore, the available methods of anchorage zone design were developed based on only a basic geometric configuration, which is a rectangular section. Insufficient information for a non-rectangular anchorage zone design is provided in the Specifications. Therefore, the present study focuses on the investigation of anchorage zones with a rectangular section subjected to

a support reaction, and anchorage zones with a non-rectangular section subjected to basic prestressing load configurations.

1.2 Prestressed Concrete Structures

1.2.1 Development of the Technology

In 1937, the first prestressed concrete bridge in the world was opened to traffic in the city of Aue, Germany. It was designed by Franz Dischinger, who was Germany's most experienced reinforced concrete designer at that time (Menn, 1990). The prestressing force was applied to the structure by using large-diameter reinforcing steel with low tensile strength, not bonded to the concrete. Due to the application of this large tensile force to the steel to generate the prestressing behavior and the lack of understanding of the phenomenon of creep and shrinkage in concrete, the strains in the bars were twice as large as the expected plastic strain. These unpredictable strains came from prestressing losses, which were acknowledged after further research. The strains eventually resulted in cracking and large deformations after the bridge had been in service for only 25 years. Although this bridge was carefully designed by a designer with a great knowledge in reinforced concrete structures, it verified that care and experience are not always sufficient in structural design and knowledge from new research discoveries is extremely significant.

In 1888, a new system using prestressed wires to eliminate the amount of cracking in slabs, planks, and beams was patented by a German engineer, W. Döring. After that, there were no further developments in the application of prestressing technique to the construction of concrete structures for some time. In 1928, a French engineer, Eugène Freyssinet, began the development of prestressing systems and finally in 1936 he introduced prestressing jacks and anchors, essential equipment required in the construction of prestressed concrete structures. Besides the jacks and anchors, Freyssinet also used high-strength wires bonded to concrete as prestressing reinforcement. Unfortunately, Freyssinet's systems were not widely

recognized in Germany at the time the construction of the prestressed concrete bridge in Aue began.

Freyssinet's ideas contributed to further developments in prestressing technology. Full prestressing is attained by the application of high compressive forces to a concrete element to eliminate tensile stresses, which cause cracking and deformations. The compressive forces are applied by stressing high strength wires and anchoring the wire to the concrete. As the prestressed concrete element becomes stronger due to increasing compressive strength, the ability of the structure to resist loads is also increased. The application of prestressing technique results in the reduction of dead weight due to the smaller required cross-sectional area of the structural components compared to that using a conventional reinforced concrete design method. Freyssinet also developed the methods of pre-tensioning and post-tensioning, which established the two major categories of prestressed concrete structures.

Based to some extent on Freyssinet's systems, Ulrich Finsterwalder invented a new post-tensioning system, the Dywidag system, which was widely used in Germany by the end of the 1940s. As a Dischinger student, Finsterwalder participated in the construction of the prestressed concrete bridge in Aue. Bars, like those used in the construction of the bridge in Aue, were also developed as part of the Dywidag system, except that these bars had a much higher tensile strength. Another system used in prestressed concrete construction was called Leoba. Fritz Leonhardt and W. Baur developed the system using a high-strength steel strand, which is manufactured from a group of high-strength steel wires, as prestressing steel. Prestressing remains popular, although prestressed concrete design requires more effort in the design procedure compared to a conventional reinforced concrete design.

1.2.2 Basic Concepts

Concrete can withstand high compressive stress; however, the tensile strength of concrete is only 8 to 20 percent of its compressive strength. To remain conservative in design, most designers of reinforced concrete structures neglect the tensile strength of concrete and use steel as the tension resisting component in the element. Service performance can be improved if the designer can eliminate the tensile stresses that occur in the concrete.

Prestressed concrete can be defined as a concrete structure with a preloaded compressive force to improve the ability to resist all external applied loads. The objective of the application of the preload is to eliminate high tensile stresses which will occur when the structure is in service. The preloading force or prestressing force can be applied to the concrete body by stretching prestressing steel (or tendons) to a specific stress level and anchoring the steel to the concrete body. By locking the steel at the position of the end surfaces of the beam using a special anchorage device, the tensile stresses in the steel create compressive stresses within the concrete body and result in the elimination of concrete tensile stresses (see Fig. 1.1).

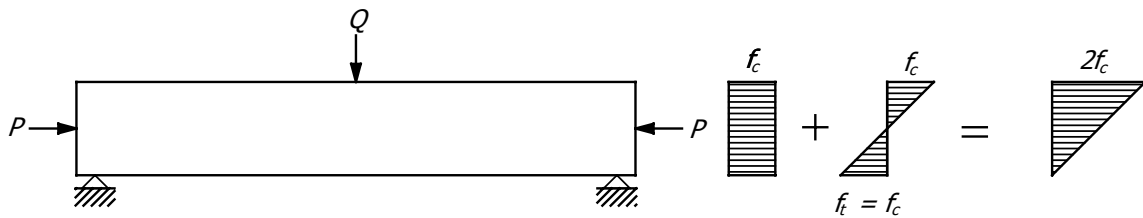


Fig. 1.1 STRESSES IN RECTANGULAR PRESTRESSED CONCRETE BEAM

Two methods to construct prestressed concrete beams are pre-tensioning and post-tensioning (see Fig. 1.2). In the pre-tensioning method, the tendons are stretched before casting of the concrete and the steel is released after the concrete reaches a specified strength. As the fresh concrete is placed, the space around the surface of the tendons is fully filled with concrete particles. When the concrete hardens, this creates perfect bonding between the concrete and the tendons. This bond allows the prestressing force to transfer from steel to concrete. Post-tensioning, which is the primary focus of the present research, differs from pre-tensioning in that post-tensioning requires the concrete to harden before the stressing of tendons. A duct or void is cast into the concrete element. After the concrete hardens, the tendon is threaded into the duct. At one end the tendon is anchored to the concrete. This method requires the tendons to be unbonded from the concrete in order to be stretched without any obstacle. At the other end, a jacking ram (or jack) is used to stretch the tendons. The force is then transferred into the bearing plate through a wedge plate. The individual strands are secured in conical holes in the wedge plate by two or three prong wedges.

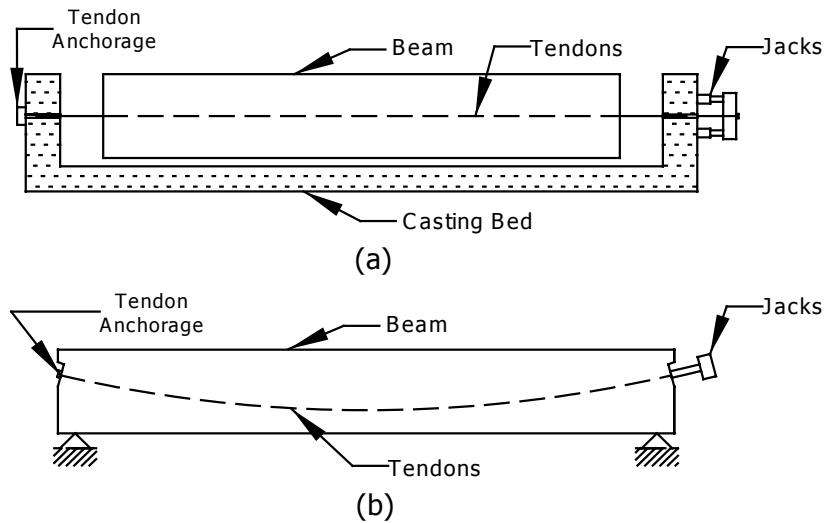


Fig. 1.2 PRESTRESSED CONCRETE BEAMS a) PRE-TENSIONED AND b) POST-TENSIONED

Eugène Freyssinet introduced a system for wedge-anchored high strength prestressing steel cable in 1940. The system has resulted in huge developments in the construction technology of prestressed concrete structures. The region into which the prestressing force is introduced, where very high local stresses develop under the bearing anchorage plate, and through which the forces spread into the cross-section of the structure, is the anchorage zone (see Fig. 1.3), which is defined in section 1.3.2. Prior to the publication of NCHRP Report 356 (Breen et al., 1994) and the Standard and LRFD Specifications of American Association of State Highway and Transportation Officials (AASHTO, 1994), reasonable anchorage zone design guidance had not been established. This lack of an appropriate design approach was reviewed in a survey conducted by Sanders (1990). The NCHRP report provides guidance on many anchorage zone configurations, however; further study of anchorage zones is still necessary and a more widely applicable design approach is still in demand.

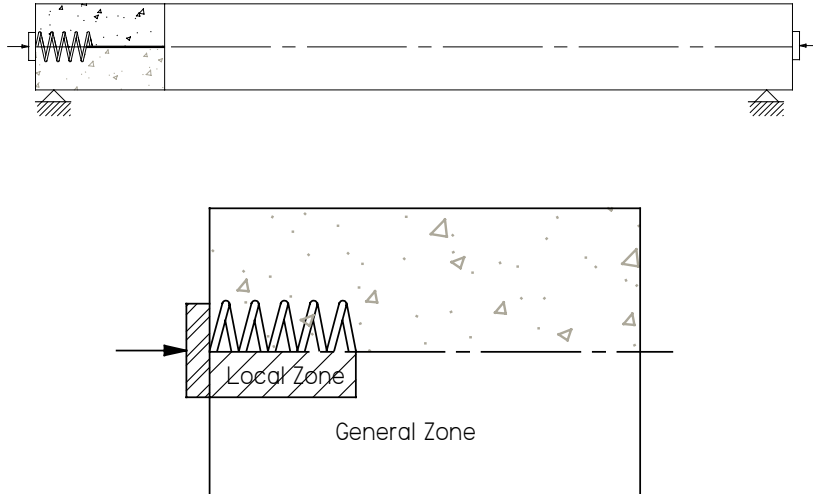


Fig. 1.3 ANCHORAGE ZONE

1.3 Anchorage Zone Design

1.3.1 Previous Anchorage Zone Design

Before the publication of NCHRP Report 356, anchorage zone design was conducted based primarily on published research. Gergely and Sozen (1967) introduced a method of anchorage zone design, which was based on equilibrium of an end-block after cracking was reached. The bursting crack was assumed to initiate at the loaded surface of the beam. The crack propagated along the centerline of the anchorage zone for an arbitrary length. The region of consideration began immediately ahead of the anchor and extended for a length larger than the beam depth (region 1-2-3-4 in Fig. 1.4). Assuming the horizontal crack occurs at the face 2-3, a free body diagram can be drawn as shown in Fig. 1.4b. The equilibrium state of the forces can be easily illustrated based on classical beam theory and the compressive characteristics of the concrete. The prestressing force P_i is the force immediately after the jack is released. The shear force V is resisted by aggregate interlocking of the cracking surface, and the compression force is present beyond the crack line to the end of the considered region. It is clear that the maximum moment, M_{max} , occurs at the level where the crack originated, therefore the tension force T can be calculated using the equation

$$T = \frac{M_{\max}}{h - x} \quad (1.1)$$

To be conservative, the strength of the reinforcing steel, f_s , is considered to be less than half of its yield strength ($f_s = 20,000$ psi). The required cross-sectional area, A_t , of the reinforcing steel is determined using the equation

$$A_t = \frac{T}{f_s} \quad (1.2)$$

The use of steel strength less than half of the yield strength of steel and the prestressing force P_i result in conservative anchorage zone design. It is recommended to distribute the reinforcing steel over the region from right under the anchor plate to the end of the crack line.

Because most prestressed concrete beams use end blocks, a rectangularly shaped section at the anchorage zone region, the bearing stress occurring in the region disperses freely through the body of the anchorage zone. The ACI Code Commentary, 318-83 (ACI, 1983), presented an allowable bearing stress, f_b , calculated with the following equations:

At release of the prestressing force:

$$f_b = 0.8f'_{ci} \sqrt{\frac{A_2}{A_1} - 0.2} \leq 1.25f'_{ci} \quad (1.3)$$

After all prestress losses:

$$f_b = 0.6f'_c \sqrt{\frac{A_2}{A_1}} \leq f'_c \quad (1.4)$$

where f'_{ci} is the compressive strength of the concrete at the time of initial prestress, f'_c is the nominal compressive strength, A_1 is the anchorage area, and A_2 is the area surrounding the anchor.

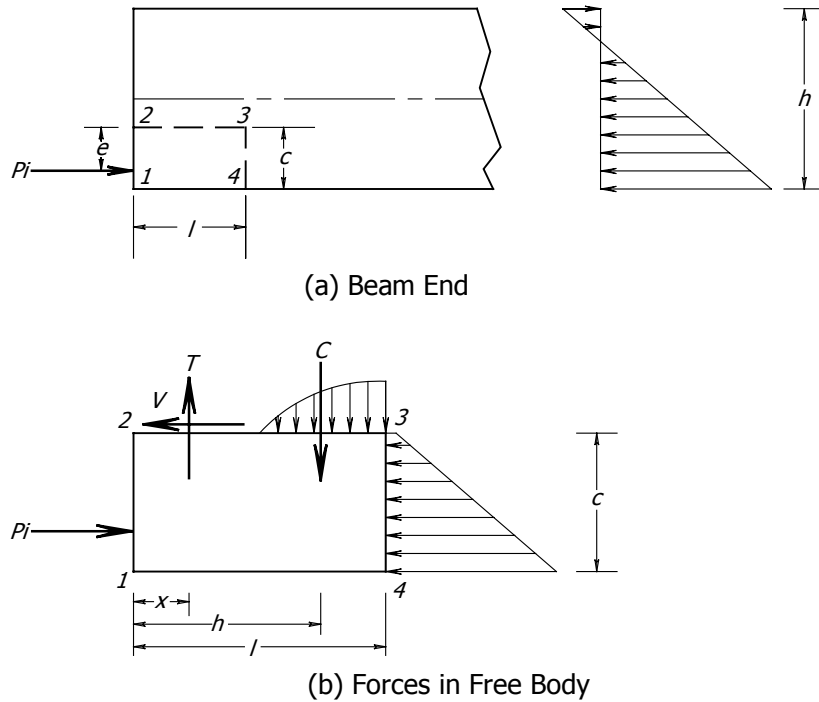


Fig. 1.4 ANCHORAGE ZONE ANALYSIS OF PRESTRESSED CONCRETE BODY

1.3.2 Current Anchorage Zone Design Presented in AASHTO

According to the AASHTO Standard Specifications (AASHTO, 1994), anchorage zones can be classified into two types: an anchorage zone at the end of a member and at an intermediate location within a member. For anchorage zones at the end of a member, the length of the anchorage zone is taken as less than one and one half of the depth of the section. For intermediate anchorage zones, the length of the anchorage zone is not less than the depth of the section. The body of the anchorage zone can be divided into two regions: local zone and general zone (see Fig. 1.3).

The local zone is the region covering and ahead of the anchorage device. The local zone transfers the prestressing force into the general zone. The primary design concern in the local zone is the very high bearing stress under the anchorage device. The main component of the local zone, besides the anchorage device and surrounding concrete, is spiral or tie confining reinforcement. A special anchorage device needs to pass an acceptance test, which is presented in the AASHTO Standard Specifications. The local zone is not the main area of

interest of this research, therefore the design of the local zone will not be explained in great detail.

The general zone is the region of concrete outside the vicinity of the local zone into which the high concentrated prestressing forces from the anchorage device spread throughout the region and become linearly distributed across the entire cross section at some location ahead of the anchorage device. This behavior of stress distribution can be described by using Saint Venant's principle. The AASHTO Specifications (1994) define the dimensions of the general zone to be the same as that stated for the overall anchorage zone. The design methods for the general zone may be selected from the following:

- Equilibrium-based plasticity models, generally referred to Strut-and-Tie Models;
- Elastic stress analysis based on elastic material properties, equilibrium equations, and strain compatibility;
- Other approximate methods such as approximate stress analyses and design presented in the specifications based on a study by Burdet (1990).

The code uses $0.7 \phi f'_{ci}$ as the upper bound for the factored concrete compressive strength for general zone design.

In the anchorage zone, several types of tensile stress can occur during the application of the prestressing force (see Fig. 1.5). Bursting stress is the tensile stress acting perpendicularly to the tendon path resulting from the spreading of the high compressive stresses outward from the tendon path. The integration of the bursting stresses along the tendon path provides the magnitude of the bursting force, which can be resisted using bursting reinforcement arranged in the proper location. The spalling stress is the tensile stress which occurs at the surface of the member, caused by the condition of compatibility of displacements. When the prestressing force is applied eccentrically to the section of the member, the spalling stress increases. Similar to the bursting force, the spalling force can be determined by integrating the spalling stress over the area in which the spalling stresses occur. In the case of highly eccentrically loaded anchorage zones (the prestressing force applied outside of the kern of the section), longitudinal edge tensile stresses may occur at the

longitudinal surface of the member. Methods for the calculation of reinforcing steel required to resist all tensile stresses is provided in the specifications (AASHTO, 1994).

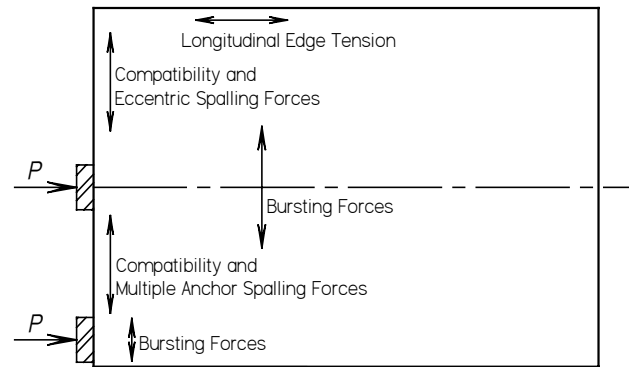


Fig. 1.5 TENSION IN ANCHORAGE ZONE

In design, the concrete compressive stress must be checked at the end of the local confining reinforcement or a distance ahead of the anchor equal to the anchorage device dimension, whichever is smaller. Bursting reinforcement to resist the bursting force in the anchorage zone must be provided over the full width of the cross-section and distributed along the longitudinal direction of the member to a distance equal to the smaller of $2.5d_{burst}$ and 1.5 of the depth of the section with the spacing no less than 24 times bar diameter or 300 mm (12 in.). The term d_{burst} is the distance from the loaded surface to the centroid of the total bursting forces in the anchorage zone. The centroid of the bursting reinforcement must be located at a distance of d_{burst} from the anchor.

For anchorage zones with eccentricity, 2 percent of the largest prestressing force in grouped anchors must be provided to resist the spalling stress. Special attention must be paid to the case of highly eccentrically loaded anchorage zones (center of the prestressing forces applied outside the kern of the section), for which longitudinal edge tension starts to occur. Based on the classical theory of elasticity, the longitudinal edge tensile force can easily be found. For the case of multiple anchorages, where the center-to-center spacing of adjacent anchorages is less than 40 percent of the depth of the section, 2 percent of the total prestressing force is used as the spalling force and minimum reinforcement must be provided. For spacings greater than 40 percent of the depth of the section, an analysis to determine the

spalling force is required. The reinforcement to resist the spalling force is arranged over the full width of the member in the direction being considered and must be continuous around the corner.

1.3.2.1 Strut-And-Tie Model (STM)

Strut-and-Tie Modeling is an equilibrium method based on the theory of plasticity. The method approximates the stress flow within a structure as an equivalent structure consisting of compression struts and tension ties connected at nodes (see Fig. 1.6). The dimensions of the struts can be calculated from the dimension of the anchorage plate at the surface of the member. The dimension of a tie will be equal to the area of bursting reinforcing steel used in the member. In anchorage zone design, strut-and-tie models are used to design the reinforcing steel. The method also requires the verification of the capacity of the compression struts in the model by checking the following components:

- The bearing capacity of the local zone including the effect of confining reinforcement;
- The compression strength of the strut perpendicular to the tendon path directly under the anchorage plate (plane AB in Fig. 1.7a);
- The node-strut interface compression capacity (plane BC in Fig. 1.7a);
- The local zone-general zone interface compression capacity (plane DE in Fig. 1.7a).

Schlaich et al. (1987) suggested that the deviation angle of members in strut-and-tie models from the principal stress path obtained from elastic analysis should not exceed 15 degrees.

For thin members, the dimension of struts parallel to the thickness of the member may be estimated from the linear variation from the lateral dimension of the anchorage plate to the total thickness of the section at a distance equal to the thickness of the member (see Fig. 1.7b). Besides the common pattern of strut-and-tie model generally used, there also are several patterns of strut-and-tie models such as multiple level STM, thrust-line STM, and multiple thrust-line STM (Burdet, 1990).

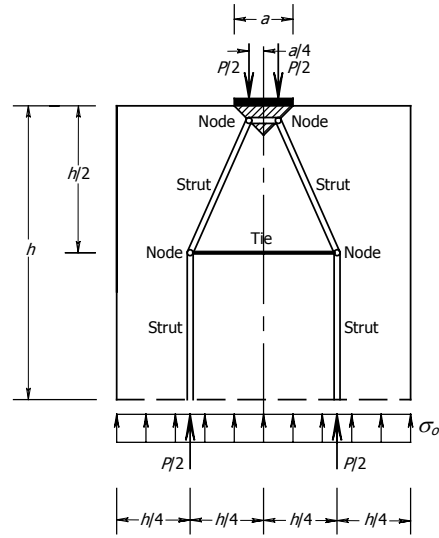
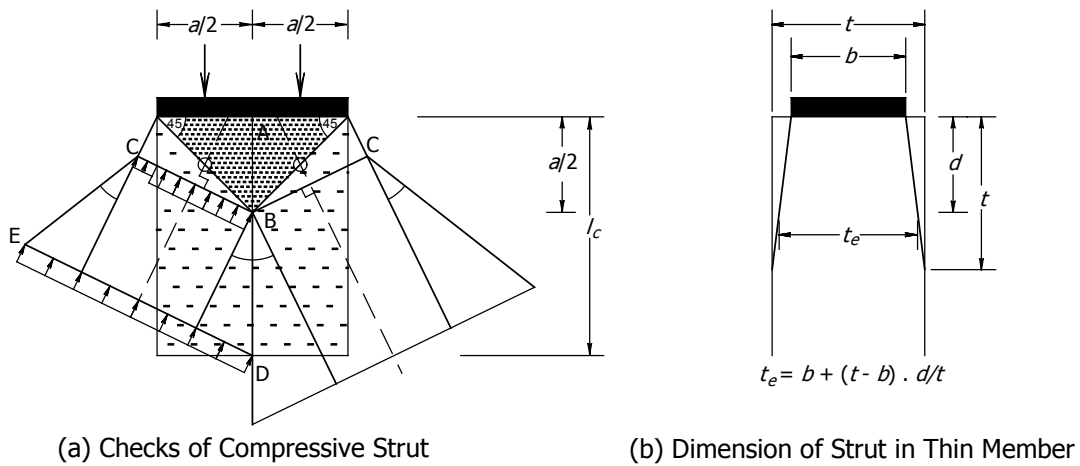


Fig. 1.6 STRUT-AND-TIE MODEL



(a) Checks of Compressive Strut

(b) Dimension of Strut in Thin Member

Fig. 1.7 COMPRESSION STRUT IN STRUT-AND-TIE MODEL

1.3.2.2 Approximate Stress Analysis and Design

Guyon (1953) studied the behavior of a concentric load applied over a rectangular body. In his study, a Fourier series method was used to solve for the relation between the tendon forces (P) and the ratio of the anchorage plate width to the section width (a_1/a_2 where a_1 is the anchor width and a_2 is the section depth, see Fig. 1.8). This relation was very influential in the design of anchorage zones.

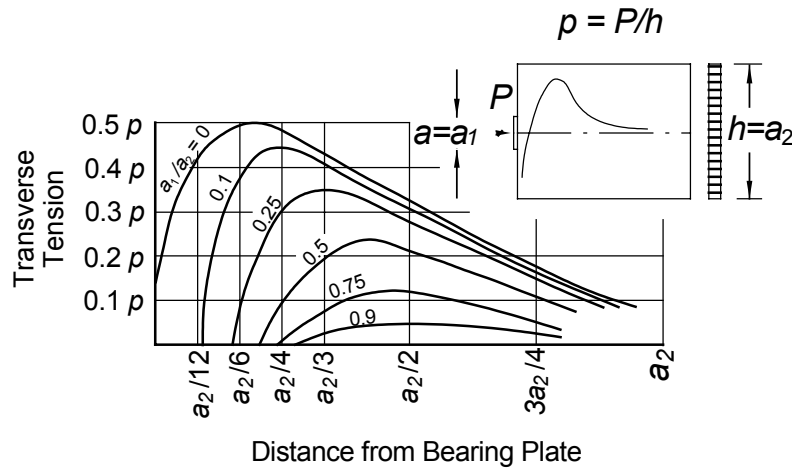


Fig. 1.8 GUYON'S BURSTING STRESS DISTRIBUTION

According to the AASHTO provisions (1994), the equation below can be used to calculate the bursting force and the location of the bursting steel centroid, respectively:

$$T_{burst} = 0.25 \Sigma P_u \left(1 - \frac{a}{h}\right) + 0.5 / \Sigma (P_u \sin \alpha) \quad (1.5)$$

$$d_{burst} = 0.5 (h - 2e) + 5e \sin \alpha \quad (1.6)$$

where T_{burst} is the bursting force in the anchorage zone acting ahead of the anchorage device and transverse axis (N), P_u is the factored tendon force (N), d_{burst} is the distance from the anchorage device to the centroid of the bursting force (T_{burst}) (mm), a is the lateral dimension of the anchorage device or group of devices in the direction considered (mm), e is the eccentricity of the anchorage device or group of devices, with respect to the centroid of the cross section, always taken as positive (mm), h is the lateral dimension of the cross section in the direction considered (mm), and α is the angle of inclination of a tendon force, with respect to the centerline of the member, positive for concentric tendons or if the anchor force points toward the centroid of the section, negative if the anchor force points away from the centroid of the section.

Some limitations of the application of these equations are listed as follows:

- Only applies to a rectangular cross section with its longitudinal dimension larger than its transverse dimension;
- No discontinuities within or ahead of anchorage zone;
- The minimum edge distance of the anchorage in the main plane of the member is larger than or equal to one and a half times the corresponding lateral dimension of the anchorage device (a);
- Only applies for one anchorage device or one group of closely spaced anchorage devices;
- The value of α is between -5 degrees and $+20$ degrees.

The determination of the longitudinal edge tension force can be obtained by considering the section of the member to be a beam subjected to a combined axial and flexural force. The magnitude of the longitudinal edge tension may be used as the spalling force at the surface of the member, but not less than 2 percent of the total factored tendon force.

The AASHTO provisions (1994) provide guidance for simple cases, but leave many questions unanswered. The presented equations were developed without considering the presence of a reaction force applied within the anchorage zone. The equations were developed based on two-dimensional linear elastic finite element analyses. The magnitude of T_{burst} and the location of its centroid may be highly influenced by the flanges of I- or T-beams. Cracking of the concrete significantly alters the distribution and magnitude of the bursting stresses. These areas of uncertainty in anchorage zone design will be investigated in this research program.

1.4 Literature Reviews

1.4.1 Anchorage Zones

1.4.1.1 Mörsch (1924) and Guyon (1953)

Mörsch (1924) developed methods of estimating sectional forces based on the theory of elasticity and the design of cross-sections based on allowable stresses under service loads. The methods ensure a sufficient level of safety and controlling of cracks in concrete structures. The most outstanding contribution of Mörsch was the development of the truss model, which is also recognized as the well-known truss analogy. The method gives an excellent illustration of the behavior of forces occurring in reinforced concrete structures. It became one of the most significant reference works of its time (Menn, 1990).

The first description of the effect of the bursting force on a concentrically loaded anchorage zone was presented by Mörsch. He presented a linear relationship between the bursting force and the ratio of the anchor plate to the section width (a/h or a_1/a_2 presented in Guyon's approach). Mörsch also introduced a model which was created based on the stress flow in a concentrically loaded body and later became the well-known Mörsch's strut-and-tie model (see Fig. 1.6). The model describes the flow of forces with a simple structure built from compression struts and tension ties. It was proved to be consistent with St. Venant's stress path. According to Fig. 1.6, the equation for the bursting force is:

$$T_{burst} = \frac{P}{4} \left[1 - \left(\frac{a}{h} \right) \right] \quad (1.7)$$

Besides the proposed design aid for concentrically loaded anchorage zones using the theory of elasticity (Fig. 1.8), Guyon (1953) also presented another design aid for the estimation of the tensile bursting force, using the ratio of the anchorage plate width to the section width (a_1/a_2) as shown in Fig. 1.9. In the case of eccentrically loaded anchorage zones, Guyon's symmetrical prism theory can be applied (see Fig. 1.10). The symmetrical prism states that the transverse dimension of the prism is equal to twice the smallest distance from the centerline of the tendon to the closest edge of the anchorage zone. This concept can

be adjusted to the case of multiple anchors within an anchorage zone as well. Guyon's investigation was referenced by many researchers and it was found to be reliable.

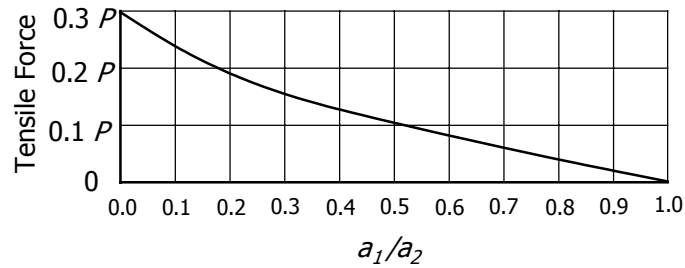


Fig. 1.9 GUYON'S BURSTING FORCE DESIGN AID

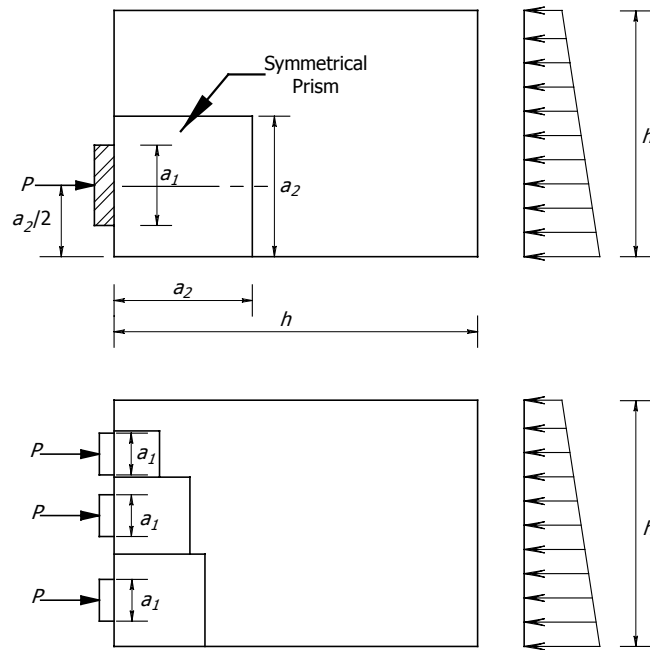


Fig. 1.10 GUYON'S SYMMETRIC PRISM FOR ECCENTRICALLY LOADED ANCHORAGE ZONE

Tesar (1932) presented an evaluation of spalling forces based on the study of a photoelastic body. For the application of eccentrically loaded anchorage zones, the spalling force can be found using the following expression:

$$T_s = (0.04 + |(a - a')/(a + a')|^3)P \quad (1.8)$$

where T_s is the spalling force, a is the smaller edge distance, and a' is the larger edge distance.

1.4.1.2 Yettram and Robbins (1969, 1970, and 1971)

In the study by Yettram and Robbins (1969, 1970, 1971), linear elastic finite element analysis was applied to the investigation of anchorage zones with the cases of concentric, eccentric, and multiple anchors. Both two- and three-dimensional studies were conducted using square-shaped plane stress and cubic solid elements, respectively. The results were used to compare to the elastic studies of Guyon (1953) and Iyengar (1961) and to the experimental results of Zieliński and Rowe (1960, 1962). In the concentric anchorage case, the distance of one and a quarter of the section depth was reported to be the location of uniform stress and the effect of Poisson's ratio is insignificant to the stress distribution. Guyon's symmetrical prism was also found to be reliable to determine the bursting stresses. The significant findings for the study of non-rectangular sections are that the extension of bursting stresses of non-rectangular sections is further than in rectangular sections and the flanges play an important role in reducing the spalling stresses. I-section members with end blocks were also investigated, and results indicated that the length of the end block is critical to the bursting stress in the member. A study of anchorage zones using a linear elastic finite element analysis method was also conducted by Egeberg (1968), whose results were compared with those proposed by Guyon (1953) and Magnel (1954).

1.4.1.3 NCHRP Project 10-29 (1994)

In the early 1990's, a research team at the University of Texas at Austin led by Professor John E. Breen, under the support of the National Cooperative Highway Research Program (NCHRP), conducted a research project of the anchorage zone in post-tensioned members. The research project was divided into two phases. The first phase of the project consisted of three major studies conducted by Roberts (1990), Sanders (1990), and Burdet (1990). Roberts carried out an investigation of the local anchorage zone in order to specify a design methodology and acceptance testing procedure. Sanders performed experimental

investigations of general anchorage zones parallel to the analytical investigations using linear elastic finite element method performed by Burdet.

The second phase included the studies by Falconer (1990) and Wollmann (1992). The main objective of the studies in this phase was to establish a basic design methodology for anchorage zones. In this phase, more complicated, but commonly used, configurations were investigated. Wollmann performed investigations of anchorage zones with the presence of a support reaction, intermediate anchorages in blisters and ribs, and anchorage of external tendons in diaphragms. Falconer conducted an investigation of multiple anchorages in flat slabs.

As a result of this research project, NCHRP report 356 (Breen et al., 1994) was published and the proposed design provisions for anchorage zones were submitted to the American Association of State Highway and Transportation Officials. These provisions were adopted and first included in the interim specifications of 1994. However, some configurations of anchorage zones, such as inclined prestressing force in anchorage zones with the presence of support reaction or non-rectangular T- and I-sections, still give rise to questions due to insufficient guidance found in the provisions. The applicability of equations (1.5) and (1.6) to the design of those configurations is also questioned.

1.4.1.4 Roberts (1990)

Roberts (1990) conducted an experimental study of the local anchorage zone in prestressed concrete members. The study consisted of three major categories: the evaluation of current testing methods for local zones, parametric studies, and the interaction between local zone and general zone. Twenty-eight physical tests were performed and several variables such as edge distance, spiral effect, auxiliary reinforcement influence, type of anchorage device, concrete strength, and the interface region were investigated.

The result of Roberts' study became the basis of the local anchorage zone design in the specifications. Roberts suggested the equation for the evaluation of local zone capacity:

$$P_n = 0.7 f'_c \sqrt{A/A_b} \times A_b + 4 f_{lat} A_{core} (1 - s/D)^2 \leq 3 f'_c A_b \quad (1.9)$$

where P_n is the nominal capacity of the anchorage device with confining reinforcement, A is the effective supporting area geometrically similar to the shape of the loaded anchorage plate, A_b is the bearing area, A_{core} is the area confined by the local confining reinforcing, s is the pitch or the spacing of the confining reinforcement, D is the diameter of confining reinforcement, and f_{lat} is the lateral confining strength taken as $2A_s f_y / sD$ for spiral and $A_s f_y / sD$ for ties where A_s is the cross-sectional area of confining steel. The full area of the bearing plate will be used if the slenderness ratio of the plate satisfies the equation

$$\frac{n}{t} \leq 0.073 \sqrt{\frac{E_b}{f_b}} \quad (1.10)$$

where n is the largest distance from the edge of the loading wedge plate to the outer edge of the bearing plate, t is the thickness of the bearing plate, E_b is the modulus of elasticity of the plate material, and f_b is the bearing pressure due to the prestressing force.

1.4.1.5 Burdet (1990)

Burdet (1990) conducted an analytical study using a linear elastic finite element method. The finite element program ABAQUS was selected to perform the analysis and the program PATRAN was used to generate the mesh of specimens. In the beginning of the study, Burdet performed a comparison between in-plane bursting stresses using two- and three-dimensional models. The result showed small differences between the two models and led to the reasonable use of a two-dimensional modeling method throughout the study. The study can be divided into three major categories: concentric, non-concentric, and multiple configurations. The category of non-concentric anchors consisted of eccentric, inclined, curved, and transverse loaded configurations.

Before the modeling of specimens, Burdet studied the effect of the modeling methods of the bearing plate, the element size used, and the difference of the results from two- and three-dimensional models. A bearing plate fully bonded to the supporting concrete influences the stress distribution in the anchorage zone and proved to be inaccurate. Therefore, bearing plates without bond were used along with the load uniformly applied over the plate. The size

of the elements used in the model came from a convergence study and was selected based on the factor of computational time. The two-dimensional model was also proven to be appropriate due to the simplicity and time saving as well.

In concentric configurations, parametric studies of the ratio of plate width to the section depth (a/h) and the bursting stresses were used to compare with those provided by Guyon (1953) and showed good agreement. The investigation of the spalling force from the study proved that the magnitude of the spalling force proposed by Guyon was almost twice as conservative as that from the study.

The results were also used to evaluate the applicability of strut-and-tie modeling. Burdet found that the most appropriate strut-and-tie model used for the design of concentric anchorage was the simplest model, which consists of two main struts running from the quarter point of the bearing plate to the quarter point of the end section and one tie connected at the position of changed angle in the struts. A dispersion angle of 26.5 degrees from the center of the plate to the quarter point of the section was found to be conservative for the design of anchorage zones with a/h greater than 0.15 and reasonably close for those with a/h less than 0.15. This also indicated the location of the centroid of bursting reinforcement. Burdet compared strut-and-tie models with the test results from the experimental study conducted by Sanders (1990) and found that the tensile strength in concrete plays an important role in the cracking behavior, which is not considered in strut-and-tie modeling.

In eccentric configurations, the stress distribution in anchorage zones was similar to that of the concentrically loaded model if the load was applied within the kern of the section, in which the ratio of eccentricity e to the section width h is equal to 0.167. If the load is applied outside of the kern, an additional tensile stress appears at the outer surface parallel to the tendon path. This stress is called the longitudinal edge tensile stress as previously mentioned in section 1.3.2. The magnitude of the bursting force decreases when the ratio of e/h increases. The study supported the applicability of the symmetrical prism theory proposed by Guyon (1953).

For the cases in which an inclined load was applied, the angles used in the models were 10 and 20 degrees and the tendon was curved if the angle was greater than 20 degrees. The maximum bursting stresses appeared perpendicular to and approximately along the tendon axis. Burdet observed that at a distance of 1.5 times the section width, transverse stresses still occur, which appear to be part of shearing stresses affected by the inclination of the load. As a result, Burdet proposed a formula used to calculate the bursting force, which is similar to equation (1.5) mentioned earlier, and also the expression to estimate the location of bursting reinforcement as shown in equation (1.6). For curved tendons, the models were designed to have angles of 10, 20, and 30 degrees with an eccentricity of 0 and 25 percent of the section width. The deviation force of the tendon, which is calculated from the ratio of the prestressing force to the radius of curvature of the tendon, was applied along the tendon line in the models. From the results of the analyses, Burdet concluded that transverse reinforcing steel should be provided on the outside of the curved tendon to reduce the effect of high tensile stresses based on the magnitude of the prestressing force.

In the study of multiple anchors, only configurations with two anchors were used, because it was believed to be more generally applicable than configurations with more than two anchors. Two groups of models, one with no eccentricity between the tendon axis and the centroid of two anchors and the other with an eccentric value, were created. After the analyses, the first group appeared to have two types of behavior. The ones with the position of each anchor falling within the quarter point of the section appeared to have tensile stresses approximately at the center of the anchorage zone. The others, which had the anchors outside their quarter point, had instead compressive stresses in the same region. In the models with the application of lateral force, the bursting stresses were greatly reduced. All analyses in the study were compared to the strut-and-tie model and experimental results from Sanders (1990).

Burdet (1990) also performed a series of analyses of a flanged section. The models were created from two plate bodies, one representing the web and connecting to the center of another which represented the flange, using shell elements. The stress distribution that occurs in the flange was observed to be larger in magnitude and extent than that in the web. The magnitude of the bursting force in each component of the section was smaller than that

in a rectangular section with similar dimensions. This study of flanged sections is the only study of non-rectangular sections conducted by Burdet. Further parametric studies of non-rectangular sections need to be performed.

1.4.1.6 Sanders (1990)

Sanders (1990) conducted experimental studies of several configurations of general anchorage zones with thirty-six specimens tested. Thirty-one specimens incorporated straight tendons, including seventeen concentric anchorage zones, six eccentric anchorage zones, and eight multiple anchorage zones. The other specimens investigated inclined and curved tendons. In this study, specimens were designed to cover all possible basic configurations which can be found in common prestressed concrete structures.

In the study of concentric anchorage zones, all specimens were designed to study the stress distribution in the bursting reinforcement and the behavior of anchorage zones without bursting reinforcement, as well as confining reinforcing steel, the presence of the tendon duct, the parameter of a/h , and the influence of lateral post-tensioning. One of Sanders' specimens was selected for preliminary study in the present research. Other tests of eccentric specimens were added to study the effect of eccentricity and were generally similar to the test series in concentric specimens. For the multiple anchorage tests, the study was divided into two groups consisting of specimens with a concentric axis and with an eccentric axis. The tests were identical to those in single anchorage tests. In the study of inclined anchorage and curved tendons, all four specimens were designed with special configurations with one curved tendon along with inclination at the bearing surface. Only one specimen in this series included two tendons.

Sanders showed that the methods to estimate the first cracking load using elastic analysis models proposed by Guyon (1953) as shown in Fig. 1.8 were reasonably accurate. The splitting tensile strength matched to the peak tensile stress of the same a/h ratio in order to find the magnitude of the prestressing load to cause cracking appeared to be unconservative. However, it was found later that using Ottosen's failure criterion (1977) to find the tensile stress (bursting stress) in each specimen could improve the prediction of cracking load to be

more conservative compared to the test result. As a result, Sanders suggested that using the value of $4.2\sqrt{f'_c}$ as the tensile strength of concrete to match the peak bursting stress given in Guyon's stress distribution model (Fig. 1.8) could give a conservative result.

For ultimate load prediction models, strut-and-tie models were adopted to evaluate the possible solution of calculation of the ultimate load. The ultimate tensile capacity of reinforcing steel must be checked and four checks of the compressive struts must be performed. The theory of beam-columns was used to explain the pattern of stress distribution in the case of the crack at the anchorage zone centerline propagating to the end of the specimen or 1.5 times the section width. This led to a modified version of strut-and-tie model. By assuming that the resulting force at the end of the specimen will be shifted in the direction of the crack (see Fig. 1.11), the dispersion angle of the compressive strut is reduced and this leads to the improved ultimate load of the anchorage zone. Using the modified strut-and-tie model reduces the amount of conservativeness compared to that using the regular strut-and-tie model.

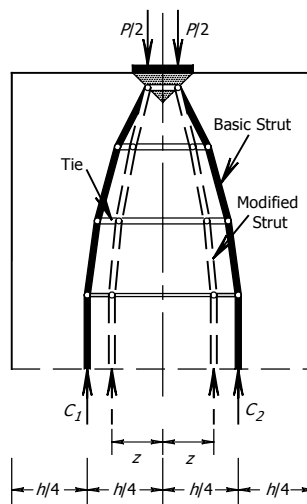


Fig. 1.11 MODIFIED STRUT-AND-TIE MODEL

1.4.1.7 Wollmann (1992)

Wollmann (1992) conducted an experimental study of anchorage zones with the presence of support reactions. Three specimens (see Fig. 1.12) were tested in the study and compared

to specimen B3 in Sanders' testing series. These three specimens had the same locations of the bearing plate and the supports. The specimen Beam2 had higher concrete strength than specimen Beam3 and both had vertical load applied at the middle of their spans which resulted in the ratio of reaction to prestressing load of 10%. Strut-and-tie modeling was used to determine the reinforcement in the specimens. The region used for the Strut-and-Tie Model extended from the support surface to the distance of one section depth. The centroid of the bursting reinforcement was located at the middle of this region. In the finite element analysis, the model showed the orientation of the main compression strut to be along the line from the center of the bearing plate to the centroid of the combined axial and flexural stress at the upper half of the end section. This was found to be consistent with the cracking pattern occurring on the tested specimens.

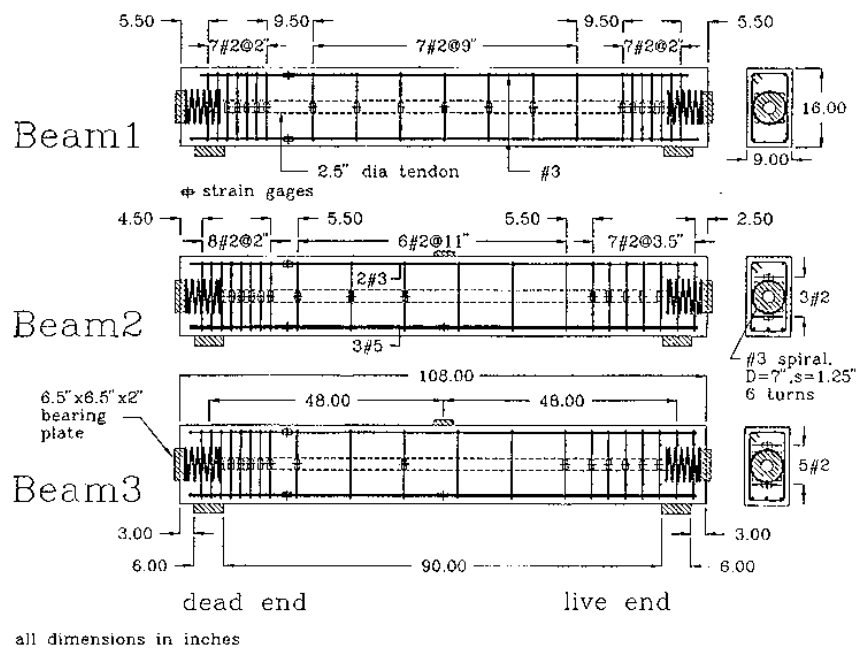


Fig. 1.12 SPECIMENS TESTED BY WOLLMANN

Based on the comparison of the results from all specimens, the length of the specimen seemed to have an influence on the transverse tensile strain. Wollmann suggested that the anchorage zone specimens should have the length designed to protect the extension of the crack to the end. Attention must be paid to the design of anchorage zones with the presence of support reaction with eccentricity using the expression in the specifications, equations

(1.5) and (1.6). Fig. 1.13 shows the difference of two strut-and-tie models without and with the presence of the reaction force. These more complicated configurations of the anchorage zone with support reaction require further investigation.

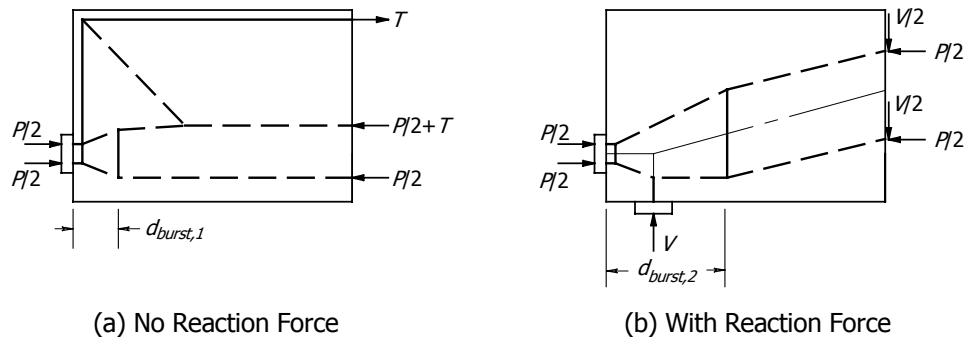


Fig. 1.13 STRUT-AND-TIE MODELS FOR ECCENTRIC ANCHOR WITHOUT AND WITH REACTION FORCE

1.4.2 Nonlinear Finite Element Analyses of Reinforced Concrete Structures

1.4.2.1 Ngo and Scordelis (1967)

Ngo and Scordelis (1967) used the finite element method to investigate the behavior of reinforced concrete beams. Based on the concept that concrete and reinforcing steel are separated from the perfect bonding state after the application of high loads to the member, linkage elements were used to account for the effects of bond slip which results in stress redistribution within the member after cracking occurs. The linkage element consisted of two linear springs, which had only mechanical properties and no physical dimension, and they were used as the connection between any two materials in the member without disturbing their geometry. A set of predefined cracks was located on the member based on the possible cracking pattern that can occur. However, the objective of the study was only to establish the feasibility and to examine the use of finite element method in the study of reinforced concrete structures. Since the study was published, the application of the finite element method to the investigation of reinforced and prestressed concrete structures has been gradually developed and refined.

1.4.2.2 Adeghe and Collins (1986)

Adeghe and Collins (1986) used a nonlinear finite element method to investigate the strain distribution in reinforcing steel in the bursting region of a rectangular body. Concrete properties were modeled based on the modified compression field theory proposed by Vecchio and Collins (1986), which presents a relationship between compression and tension in concrete under biaxial loading conditions. The results of the study showed that the dispersion angle of the principal stresses is flatter than that of the linear elastic analysis, which indicated that the design of bursting reinforcement based on linear elastic behavior will always be conservative. The other finding from the study is related to the arrangement of reinforcing steel in the member.

1.4.2.3 Al-Manaseer and Phillips (1987)

Al-Manaseer and Phillips (1987) conducted a numerical study of a nonlinear finite element analysis of reinforced concrete deep beams using quasi-material parameters, which were used to define the state of post-cracking related to smeared cracks. The study focused on two major effects: tension stiffening and interface shear retention (shear transfer at a cracked surface). By using parabolic isoparametric plane stress elements, the modeling of reinforced concrete properties was simplified. The immediate reduction of tensile stresses at cracking was introduced into the concrete property using a tension stiffening model similar to that proposed by Cope et al. (1979) (see Fig. 1.14). According to Fig. 1.14, σ and ε are stress and strain perpendicular to the direction of the crack, ε_{cr} is the cracking strain in concrete, f_t' is the concrete tensile strength, and α_1 and α_2 are material constants.

In the study of tension stiffening, the shear retention factor was kept as a constant number. The quantity α_1 was approximated from the ratio of yield strain of reinforcing steel and cracking strain of concrete, and fixed as a specific number. A set of α_2 values was selected and the results from each value were used to compare with the experimental result from the tests conducted by Ramakrishnan and Ananthanarayana (1978). It was found that the value of α_2 had a significant influence on the load-deflection curve. The closest value of α_2 to the experimental results was used for the study of shear retention parameters.

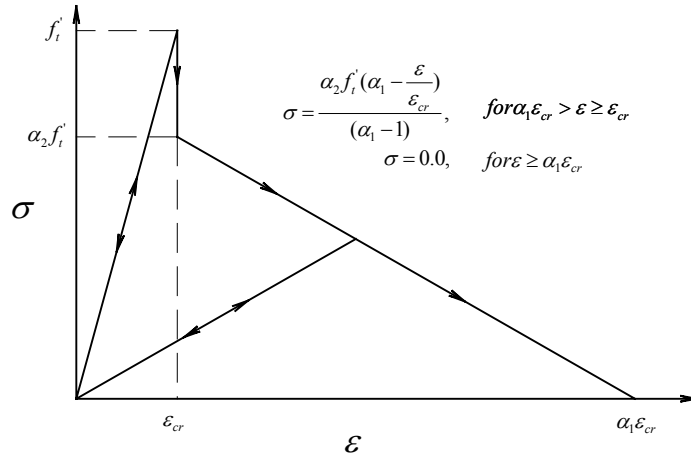


Fig. 1.14 TENSION STIFFENING MODEL USED IN AL-MANASEER AND PHILIPS' STUDY

In the shear retention factor (β) study, different values of β were selected. According to Al-Manaseer and Philips (1987), the shear retention factors can be found using the relation based on the concrete strain as shown in Fig. 1.15. The β_1 , β_2 , and β_3 are also material constants. The results from this study indicated the small influence due to the change of β values and the study led to the conclusion that the tension stiffening model has an influential effect on the behavior of reinforcement before the steel yields, but the shear retention factor establishes more the effect after yielding is reached.

In the studies of Al-manaseer and Philips (1987), the material properties of reinforcing steel which were used were based on the bilinear uniaxial stress-strain relationship allowing for isotropic strain hardening, as shown in Fig. 1.16, and can be expressed as

$$f_s = E_s (\varepsilon_s - \varepsilon_{pi}) \quad \text{for } f_s \leq f_{yi} \quad (1.11)$$

$$f_s = \frac{E_w}{E_s} (f'_s - f_{yi}) + f_{yi} \quad \text{for } f_s > f_{yi} \quad (1.12)$$

where $f'_s = E_s (\varepsilon_s - \varepsilon_{pi})$ when $f_s > f_{yi}$, f_s is the uniaxial stress of steel corresponding to ε_s , f_{y0} is the initial yield stress of steel, f_{yi} is the current yield stress of steel, E_s is the steel

modulus of elasticity, E_w is the steel hardening modulus of elasticity, ε_{y0} is the initial yield strain of steel, and ε_{pi} is the permanent plastic strain at current yield stress f_{yi} .

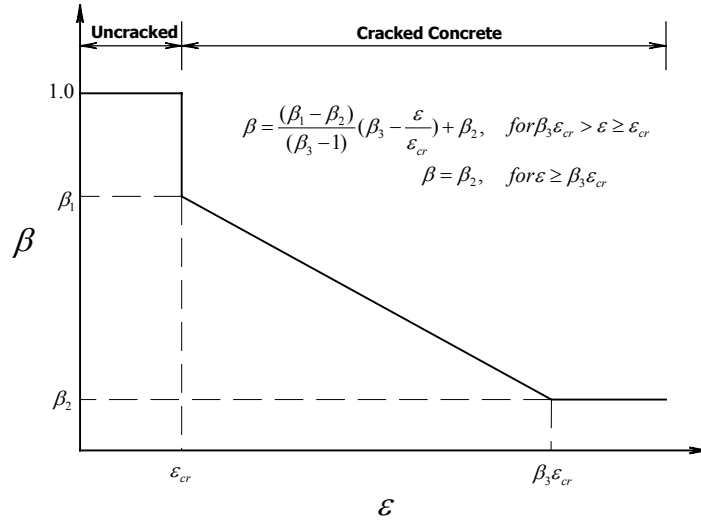


Fig. 1.15 SHEAR RETENTION FACTOR MODEL USED BY AL-MANASEER AND PHILIPS (1987)

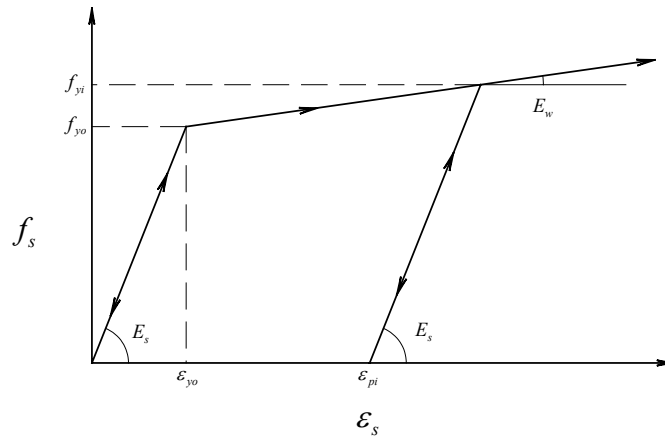


Fig. 1.16 STRESS-STRAIN RELATIONSHIP OF STEEL MODEL USED BY AL-MANASEER AND PHILIPS (1987)

For the nonlinear solution scheme, a modified Newton-Raphson iteration scheme was used in the analysis procedure and a force convergence criterion was selected with a tolerance of 2 percent. No arc length method or line-search, which helps to increase the computational speed, was applied. The study counted the total number of iterations to allow

the comparison of the results. The relation between the least number of iterations was noticed to coincide surprisingly well with the parameter that closely matched the experimental result. However, there is no confirmation of the existence of this relation addressed in the study.

1.4.2.4 Foster (1992)

Foster (1992) presented an investigation of an application of using the arc length method in the nonlinear analyses of three available experimental studies: the single span-deep beam by Ramakrishnan and Ananthanarayana (1978), the two-span deep beam by Ricketts (1985), and the shear panel by Vecchio and Collins (1986). The finite element program RECAP was used in the study. The study focused on the application of the new iteration scheme to nonlinear finite element analysis. Foster described a method to model material properties used to create the reinforced concrete bodies and used it in his later studies.

For the modeling of reinforced concrete used in the analyses, a three-node parabolic element with two Gauss point integration was used to form the element stiffness matrix for the reinforcing steel element, and an eight-node isoparametric plane stress element with 3x3 Gauss quadrature was used in the case of the concrete element. These two elements were assumed to be perfectly bonded to each other. Four states of the concrete element formulation were applied: undamaged, cracked, crushed, and simultaneously cracked and crushed. For the undamaged state, the formulation used the principle of equivalent uniaxial strains proposed by Darwin and Pecknold (1977) with a modification to account of a rotating crack model.

The purpose of using the equivalent uniaxial strain model was to predict the biaxial behavior of concrete by eliminating the Poisson effect. The equivalent uniaxial strain can be stated as the existing strain with zero stress in the opposite direction and can be found using the equation.

$$\varepsilon_{iu} = \sum_{i=1}^n \frac{\Delta\sigma_i}{E_{Ti}} \quad (1.13)$$

$$\sigma_i = \frac{\varepsilon_{iu} E_0}{1 + \left(\frac{E_0}{E_{sp}} - 2 \right) \frac{\varepsilon_{iu}}{\varepsilon_{ip}} + \left(\frac{\varepsilon_{iu}}{\varepsilon_{ip}} \right)^2} \quad (1.14)$$

where ε_{iu} is the equivalent uniaxial strain, σ_i is the principal stress in the i^{th} direction ($i = 1, 2$, 1 for tension and 2 for compression), E_0 is the tangent modulus at zero stress, E_{sp} ($= \sigma_{ip} / \varepsilon_{ip}$) is the secant modulus at the point of maximum compressive stress σ_{ip} , and ε_{ip} is the equivalent uniaxial strain at the maximum compressive stress. Equation (1.13) is applicable under a constant ratio of principal stresses, α ($= \sigma_1 / \sigma_2$), between iterations. The value of ε_{iu} is recalculated for each iteration at every load step, since the value of α may change when the stresses in an adjacent element redistribute due to cracking or crushing. The new ε_{iu} is calculated using the equation

$$\varepsilon_{iu} = \Delta\sigma_i \sum_{k=1}^m \frac{1}{(E_{Ti})_k}, \quad (i = 1, 2) \quad (1.15)$$

where m is the number of fictitious stress increments, $\Delta\sigma_i$ is the change in fictitious stress ($= \sigma_i / m$), and $(E_{Ti})_k$ is the tangent modulus for $\varepsilon_{iu} = (\varepsilon_{iu})_{k-1}$ and is calculated by differentiating equation (1.13) with respect to ε_{iu} . Foster suggests using m as calculated in the following equation:

$$m = \text{int}(100\sigma_i / \sigma_{ip}) + 1 \quad (1.16)$$

which will give less than 0.2% of stress error.

When a concrete element is subjected to a state of biaxial stress with both tension and compression, the formulations of the model change to those proposed by Vecchio and Collins (1986) with a modification on the tension side of the stress-strain curve (see Fig. 1.17). According to the modified compression field theory suggested by Vecchio and Collins, a cracked concrete element is treated as a new element with different material properties from its original model. Vecchio and Collins assert that both principal tensile and compressive

strains influence the peak compressive stress, σ_{ip} . The effect of tensile strain is that the concrete is softer and weaker than in its original state. The peak compressive stress can be found from

$$\sigma_{2p} = \gamma_1 f'_c \quad (1.17)$$

$$\gamma_1 = \frac{1}{0.8 - 0.34(\varepsilon_1/\varepsilon_0)} \leq 1.0 \quad (1.18)$$

where ε_0 is the strain at the undamaged state and is of the order of -0.002 . Equation (1.17) can be substituted into the parabolic compressive stress equation

$$\sigma_2 = \sigma_{2p} \left[\frac{2\varepsilon_2}{\varepsilon_0} - \left(\frac{\varepsilon_2}{\varepsilon_0} \right)^2 \right] \quad (1.19)$$

For tensile stress, the stress-strain curve used in the study was taken from the study by Al-Manaseer and Philips (1987) with a modification to account for the reduced concrete tensile strength due to the presence of cracking, and is presented by

$$\sigma_1 = \Gamma f_{cr} \quad (1.20)$$

where

$$\Gamma = \alpha_2 + \frac{(1 - \alpha_2)(\alpha_1 - \frac{\varepsilon_1}{\varepsilon_{cr}})}{(\alpha_1 - 1)} \leq 1.0 \quad \text{for } \varepsilon_1 < \alpha_1 \varepsilon_{cr} \quad (1.21)$$

$$\Gamma = \frac{\alpha_2 f'_t}{f_{cr}} \leq 1.0 \quad \text{for } \varepsilon_1 \geq \alpha_1 \varepsilon_{cr} \quad (1.22)$$

and f_{cr} is the concrete cracking stress at failure of the undamaged state, ε_{cr} is the concrete cracking strain ($= f_{cr}/E_0$), and α_1 and α_2 are material constants as previously mentioned.

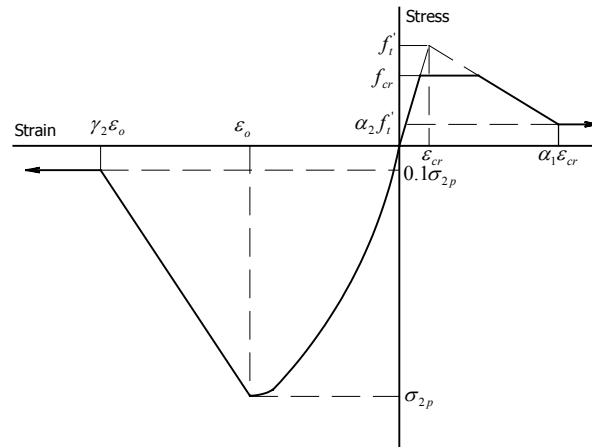


Fig. 1.17 UNIAXIAL STRESS-STRAIN RELATIONSHIP FOR CONCRETE USED BY FOSTER (1992)

In the study of the application of the arc length method, the displacement criterion was set with a convergence tolerance of 1%. According to the results, the arc length method is found to improve the computational stability and to reduce the required time to achieve convergence in each iteration step, and appears to be a better method compared to the modified Newton-Raphson iteration method alone. It is noticed that the method of the selection of material constants as well as shear retention parameters was not clearly explained in this study.

1.4.2.5 Foster, Budiono, and Gilbert (1996)

Foster et al. (1996) studied the finite element analyses of reinforced concrete structures using a rotating crack finite element model. The model included the effects of concrete cracking and crushing, crack rotation, tension softening, and bond-slip. The finite element program RECAP was also used for this study. The majority of the modeling method was similar to that of the previous study by Foster (1992), except for the method to account for the bond stress slip effect which was introduced into the stress-strain relationship of reinforcing steel, and the allowance of the rotation of principal stresses in the stiffness matrix formulation. The convergence criterion was also identical to that used in the arc length method study (Foster, 1992). The constitutive relationships of undamaged concrete were introduced in the model based on those proposed by Darwin and Pecknold (1977). In order

to allow rotation of principal stress axes, the following equation was adopted in the constitutive relationships:

$$\nu_1 E_2 = \nu_2 E_1 = \nu \sqrt{E_1 E_2} \quad (1.23)$$

where E and ν are the modulus of elasticity and Poisson's ratio in each principal direction, 1 and 2, respectively. This equation can be introduced in the stiffness matrix to achieve

$$D = \frac{1}{(1-\nu^2)} \begin{bmatrix} E_1 & \pm \nu \sqrt{E_1 E_2} & 0 \\ & E_2 & 0 \\ sym & & (1-\nu^2)G \end{bmatrix} \quad (1.24)$$

where G is the modulus of undamaged concrete and is expressed as

$$G = \frac{1}{4(1-\nu^2)} [E_1 + E_2 \pm 2\nu \sqrt{E_1 E_2}] \quad (1.25)$$

where the $E_1 E_2$ term is positive if $E_1, E_2 \geq 0$ and negative if $E_1, E_2 < 0$.

After the cracking state is reached, the fraction of the cracking modulus, G_{cr} , is replaced by the term $(1-\nu^2)G$ due to the assumption that the Poisson's ratio effect vanishes due to the cracks. The stiffness matrix can be rewritten as

$$D = \begin{bmatrix} E_1 & 0 & 0 \\ & E_2 & 0 \\ sym & & \beta G_{cr} \end{bmatrix} \quad (1.26)$$

where β is the shear retention parameter which is taken as 0.7 at cracking and linearly decreases to 0.3 at the strain of $10\varepsilon_{cr}$ and stays constant afterward. The results of the study showed a good correlation to the experimental data given by Foster (1992) and Budiono et al. (1993).

1.4.2.6 Foster and Rogowsky (1996, 1997)

Foster and Rogowsky (1996, 1997) investigated the bursting forces in concrete panels subjected to in-plane concentric loads. The same material property models of concrete and steel as introduced in the Foster et al. (1996) study were used in the modeling of concrete and reinforcing steel elements. The objectives of this study were to compare the bursting stress distributions from linear elastic finite element analyses with those from nonlinear finite element analyses in the case of service load behavior, and to investigate the bursting strain distributions in the case of ultimate load behavior of the concrete panels studied. Fig. 1.18 shows an example of the finite element models used in the serviceability analyses.

A three-node parabolic element with two Gauss point integration was used for the formulation of the stiffness matrix in the reinforcing steel. For the calculation of the stiffness matrix in concrete elements, an eight-node isoparametric plane stress element with a 3x3 Gauss quadrature was used. Due to the characteristics of the concrete panel, the region under the bearing plate, which in reality is usually strengthened with confining reinforcing steel (generally using a spiral), was modeled to have extra capacity beyond the regular concrete strength. The maximum confined concrete strength (f_c'') can be approximated using the following equation:

$$f_c'' = f_c' \times D/w \leq 2.5 f_c' \quad (1.27)$$

where D is the section width (a_2 or h as mentioned earlier), and w is the bearing plate width (a_1 or a). The concrete strength was $f_c' = 40$ MPa with an initial modulus of elasticity of $E_0 = 40,000$ MPa. Each steel bar had a yield strength $f_y = 400$ MPa with an initial modulus of elasticity of $E_0 = 200,000$ MPa and an area of $1,500 \text{ mm}^2/\text{m}$. The material constants, α_1 and α_2 , were chosen as 3.0 and 0.05, respectively. The shear retention parameter (β) was also the same as used in Foster et al. (1996). To eliminate the Poisson effect at the contact region between the bearing plate and the concrete surface, a set of short, stiff, spring elements was used to connect the nodes.

For the case of service load behavior, transverse stress distributions from the nonlinear analysis were plotted against those from linear elastic analysis for comparison. The transverse stresses are the combination of the force in the reinforcing steel distributed over its adjacent concrete region and the remaining concrete residual stresses. Fig. 1.19 shows an example of the comparison of the stress distributions based on linear elastic and nonlinear finite element analyses. As can be seen, the stress in the nonlinear analysis extends well beyond the position where the stress from the linear elastic analysis is dropping off. This flatter shape is consistent with the results of Adeghe and Collins (1986). Foster and Rogowsky (1996, 1997) stated that the bursting stress distribution followed that of the linear analysis prior to concrete cracking and changes to that of the nonlinear analysis when the maximum tensile stress reaches the tensile strength of concrete. The modified equation to calculate the bursting force based on Mörsh's equation was proposed as the following:

$$T_b = \frac{P}{4} \left[1 - \left(\frac{w}{D} \right)^{2/3} \right] \quad (1.28)$$

In the case of ultimate load analyses, Foster and Rogowsky concluded that the appropriate region for the arrangement of reinforcing steel begins approximately from 0.2 times the panel depth and extends to between 1.2 and 1.6 times the panel depth. In this study, the design of the bursting steel for each case study was proposed.

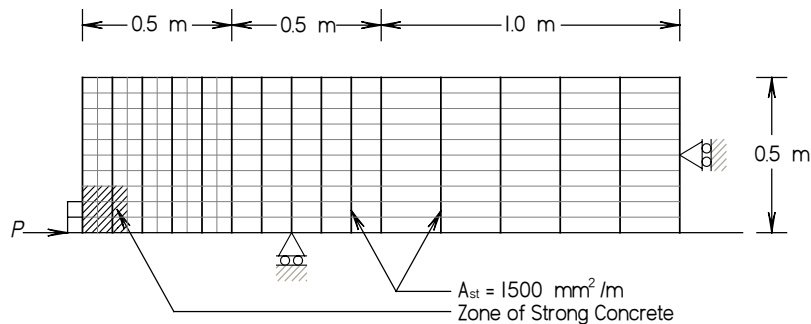


Fig. 1.18 FINITE ELEMENT MODEL USED IN FOSTER AND ROGOWSKY'S SERVICEABILITY ANALYSIS

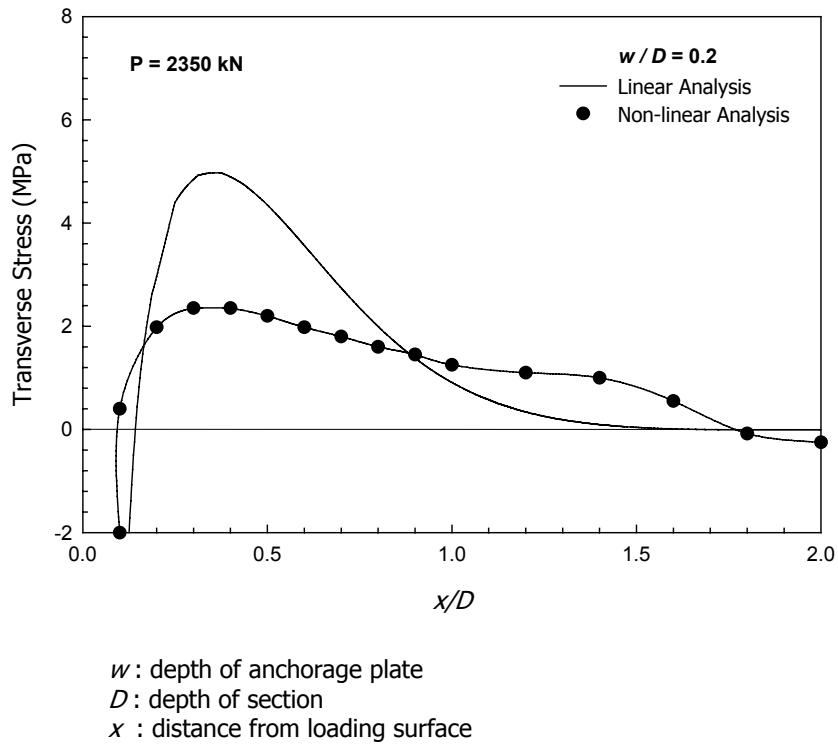


Fig. 1.19 THE COMPARISON OF TRANSVERSE STRESS DISTRIBUTIONS

1.4.3 Other Works Using DIANA

Due to the nature of the present study, a finite element program DIANA (DISplacement ANALyzer) was selected as the tool to investigate the behavior of anchorage zones with both linear and nonlinear analyses. The following literature review presents various works using the program.

1.4.3.1 Johansson (2000)

Johansson (2000) used nonlinear finite element analyses to evaluate a new reinforcement arrangement in frame corners which contained congested spliced bars at the frame corner. Cracking in concrete was modeled based on nonlinear fracture mechanics suggested by Hillerborg et al. (1976). The concrete in compression was modeled using the Drucker-Prager failure surface criterion. For reinforcing steel, the behavior was based on the Von Mises yield criterion. A two-dimensional plane stress element was used for concrete elements and

a truss element combined with an interface element was used for steel elements. The bond-slip effect was also used for the interaction between concrete and steel. There was good correlation between the results of the analyses and full-scale tests, and this encouraged the use of new reinforcement detailing examined in the analysis.

1.4.3.2 Tabatabai and Mosalam (2000)

Tabatabai and Mosalam (2000) proposed a method of using computational software to evaluate optimized reinforcement patterns in concrete structures. The study comprises three programs: ORCHID, DIANA, and ORDI. The first program ORCHID (Optimum Reinforced Concrete Highly Interactive Dimensioning) is used to determine the amount of reinforcing steel. ORCHID also provides a method to minimize the amount of reinforcing steel to achieve the most economical pattern of reinforcement in a structure. DIANA produces the nonlinear analysis result for each structure, which is reinforced based on the pattern given by ORCHID. The last program ORDI (ORchid/Diana Interface) performs the interface operation between these two programs and it also communicates with another nonlinear analyzer program if DIANA is replaced. Two basic structures, a one-way slab with fixed and pinned supports on each side and a deep beam with an opening, were selected as the illustrated examples. The cracking behavior of concrete was modeled based on constant tension cut-off, linear tension softening, and constant shear retention. The Von Mises yield criterion was used for the reinforcing steel. Neither strain hardening nor bond-slip effect were specified in the constitutive model of the materials. This study presented a powerful method using computational tools to improve the efficiency of a structure with the minimum amount of essential reinforcement. It was claimed to be useful for more complicated structures such as three-dimensional offshore caissons.

1.4.3.3 Lundgren and Magnusson (2001)

Lundgren and Magnusson (2001) conducted nonlinear three-dimensional finite element analyses to study the bonding behavior in reinforced concrete structures. Two models, lapped reinforcement splices in beams and anchorage in end regions, represent examples of structures with high bond stress regions. The assumption used in the study states that bond

stress depends not only on the slip effect, but also on the radial deformation between reinforcing steel and concrete. Various constitutive models available in DIANA were used to simulate the properties of materials. Compression based on Thorenfeldt's model (1987), a rotating crack model based on total strain, and Hordijk's tension softening model (1986) were used as the properties of concrete. Embedded reinforcement with the Von Mises yield criterion was used for the reinforcing steel. A bond slip model was introduced in the analyses by using special interface elements. The results agreed well with the experimental results based on the studies of Magnusson (2000). Besides normal strength concrete, high strength concrete was also investigated in the study.

1.4.3.4 Kwan and Billington (2001)

Kwan and Billington (2001) predicted cyclic behavior of structural concrete using nonlinear finite element analysis. The models were evaluated by comparing the simulations with a series of cyclically loaded physical tests of a concrete bridge bent cap beam-to-column connections conducted by Sritharan et al. (1996). After the evaluation, the results were used in another analysis. For material modeling, cracking of concrete was modeled using the smeared crack approach with the application of a linear descending tension softening curve and two types of shear retention parameters. The crushing effect was based on the Thorenfeldt model (1987). The Bauschinger effect, which represents the softening of the steel modulus due to reloading and unloading behavior, is not provided by DIANA. Therefore, a user-supplied subroutine was implemented to the model of steel using the model suggested by Su and Zhu (1994). The concrete element used an eight-node plane stress element with a variation of thickness. An embedded bar element was used as reinforcing steel. Many observations of the cyclic behavior were obtained.

1.5 DIANA

DIANA is a finite element program based on a displacement analysis approach. Besides the ability to perform linear elastic analysis, the program can also be used to perform

analyses with nonlinear behavior. The built-in constitutive models provide a variety of options for users to apply to the analyses of complicated problems such as reinforced concrete structures. The smeared crack model consisting of tension cut-off, tension softening, and shear retention helps users to establish the tension behavior in concrete and can be combined with other compressive plasticity-based models to establish the crushing behavior. If users prefer to model the behavior of cracking based on only one stress-strain relationship curve which contains both tension and compression behavior of concrete, the crack model based on total strain can help to fulfill this requirement. Various selections of element types available in the programs, including an embedded reinforcement bar element, allow users to choose an appropriate element to model any type of structure. In case the needed constitutive model is not available in the program, user-supplied subroutines can fulfill the need. The following sub-sections describe generally various items used in the present study.

1.5.1 Material Constitutive Models

Based on the nature of the material components of reinforced concrete structures, two significant constitutive models used in the study consist of concrete and reinforcing steel. Besides the compressive strength property in concrete, the nonlinear analysis procedure for concrete material requires the user to specify the tension behavior of concrete, which is essentially related to the phenomenon of cracking. With the selection of an embedded reinforcement element, the user can be conveniently assisted in placing the steel arbitrarily. The embedded reinforcement takes the responsibility of resisting the stresses after the limitation set in the concrete constitutive model becomes violated. Since the cracking model is used for concrete, the plasticity property of steel becomes extremely significant.

1.5.1.1 Cracking and Crushing

DIANA (2000) provides various methods to model cracking behavior. Cracking in concrete can be specified using the combination of tension cut-off, tension softening, and shear retention. Two options of tension cut-off, constant and linear, set the relationship between compressive and tensile strengths of the material. Five options of tension softening,

brittle, linear, multi-linear, Moelands', and Hordijk's nonlinear, give the user a choice to model the reduction behavior of tensile strength in concrete after the crack occurs. Three options of shear retention, full, constant, and variable, provide choices of shear transferring behavior after cracking. User-defined options can always fulfill the user's need if the available built-in options are found to be unsatisfactory.

The user can use the crack models based on a total strain option to establish the behavior of both cracking and crushing. Total strain describes the tensile and compressive behavior of a material using one stress-strain relationship. Some additional choices are provided in this option, which requires additional information of material parameters such as fracture energy, hardening modulus, and decaying factor. An example of a compression model is the behavior based on Thorenfeldt's compression curve.

1.5.1.2 Yielding of Reinforcing Steel

Two options of material properties are available for embedded reinforcement: Von Mises yielding model and user-supplied subroutine. By default, DIANA applies the perfect bond condition between reinforcement and concrete. If the user prefers to apply unbonded post-tensioning on a concrete model, an option of no bonding behavior can also be assigned. Besides these characteristics of steel, various hardening effect options can also be specified in the model. A yielding criterion is used for the material property of not only reinforcing steel but also other structural components which are made of steel, such as bearing plates.

1.5.2 Element Types

More than one hundred and sixty element types are available in the DIANA element library. Each of them is designed to fit in the modeling of any type of structure with specific characteristics. In structural engineering, one of the most generally used basic element types to simulate the characteristic of concrete medium is plane stress. DIANA provides both plane stress elements for two-dimensional modeling and shell elements for the creation of three-dimensional structures. Various choices for the number of nodes in an element are also supplied. Embedded reinforcing steel can be modeled using 3-node beam elements instead

of 2-node to provide more accuracy in the analysis. Some special connector elements such as spring elements are also provided.

1.5.2.1 Concrete Element

In the present study, an 8-node quadrilateral isoparametric plane stress element with 2x2 Gauss integration scheme CQ16M was selected as the concrete element in two-dimensional models. It is perfectly fitted to the task for the analysis of reinforced concrete structures with embedded reinforcement elements in case of nonlinear analysis. There was no unexpected error output from using the CQ16M element when a cracking constitutive model was assigned.

During the study of a non-rectangular anchorage zone, a comparison between the models created using the brick elements and the shell element is performed. A twenty-node solid brick element CHX60 was chosen for the model with brick elements. The model with shell elements was created using the shell element CQ40F. For the parametric study of non-rectangular anchorage zones, the shell elements CQ40F and CQ40S were chosen as concrete elements for linear elastic analysis and nonlinear analysis with embedded reinforcement modeled, respectively. Both CQ40F and CQ40S elements are alike as an 8-node quadrilateral isoparametric plane stress combined with plate bending element except that the CQ40S element can be modeled into a finite element body which contains an embedded reinforcement element. The bending behavior of the plate is based on the Mindlin-Reissner plate bending theory.

1.5.2.2 Embedded Steel Element

As previously mentioned, the embedded reinforcing bar can be inserted anywhere within the body of the concrete model. DIANA provides choices of BAR element and GRID element, whichever matches the user's desire. The reinforcement element is assigned to have a perfect bond to the concrete element unless the bonding condition is prescribed.

1.5.2.3 Steel Bearing Plate Element

To generate the behavior of transferring force from a metal plate onto the anchorage surface, a steel bearing plate is created using the plane stress element CQ16M with the steel material property used for the metal plate. In the case of three-dimensional modeling, the elements CQ40F and CQ40S were also used, depending upon the type of model.

1.5.2.4 Spring Connector Element

The connection between the steel bearing plate and the loading concrete surface was a set of spring elements with an extremely high stiffness. A simple 2-node translation spring element SP2TR was selected for this task. The reason for using this kind of connection between the steel bearing plate and the concrete surface, as previously mentioned in section 1.4.2.6, is to eliminate the Poisson effect which occurs if a perfect bond between the bearing plate and the concrete elements is intentionally assumed.

1.6 Objectives and Scope of this Study

1.6.1 Objectives

The present study consists of two investigations: the investigation of rectangular anchorage zones with the presence of support reaction and the investigation of non-rectangular anchorage zones with basic prestressing load configurations. The main objectives of this study are:

- To investigate the behavior of anchorage zones with the presence of support reaction and non-rectangular anchorage zones under four load configurations including concentric, eccentric, inclined, and inclined eccentric.
- To evaluate the applicability of the anchorage zone design methodologies addressed in the AASHTO Standard Specifications (2002) to the design of anchorage zones with a support reaction.

- To improve the formulations for the design of rectangular anchorage zones with a support reaction and produce the new formulations for the design of anchorage zones with non-rectangular sections.
- To study an effective bursting steel arrangement for anchorage zones using nonlinear finite element analysis.

1.6.2 Scope

After the background, literature review, and information about the selected finite element program DIANA have been presented in this chapter, the preliminary studies using nonlinear analysis are presented in Chapter 2. Two studies from the available published researches, the nonlinear finite element study of Foster and Rogowsky (1996, 1997) and the experimental study of Sanders (1990), are chosen for the evaluation of the selected finite element program DIANA. In Chapter 3, the parametric study of rectangular section with the presence of a support reaction is presented. The major focus is to investigate the applicability of the approximate equations presented in the AASHTO Specifications (2002) for the design of anchorage zones with a support reaction. Several parameters related to the anchorage zones are examined and the results from the study are used to improve the equations. The improvement of the Strut-and-Tie Model approach for the design of anchorage zones with a support reaction based on the information acquired in the finite element study is also proposed. A more simplified method of bursting steel arrangement than that presented in the Specifications is also examined using nonlinear finite element analysis. Chapter 4 presents the study of non-rectangular anchorage zones subjected to basic load configurations. The influence of the presence of the flange in the anchorage zones is investigated. The formulations for the design of non-rectangular anchorage zones are illustrated gradually. Effective bursting steel arrangements in both the web and the flange of non-rectangular anchorage zones are investigated using nonlinear finite element analysis. After all investigations have been demonstrated, improved methodologies for anchorage zone design, compared to those presented in the AASHTO Specifications (2002), are given in Chapter 5. The conclusions from the overall investigation in the present study are provided in Chapter 6. Additional information related to the study can be found in Appendices.

CHAPTER 2

PRELIMINARY STUDIES USING NONLINEAR FINITE ELEMENT ANALYSIS

In order to study the use of DIANA for conducting nonlinear analysis, two example models were created and used for comparison with those from the nonlinear finite element study of Foster and Rogowsky (1996, 1997) and the experimental result of a specimen from the study of Sanders (1990). As illustrated in section 1.4.2.6, Foster and Rogowsky performed a nonlinear analysis of a concrete panel subjected to a concentric load. The preliminary study of this part compares the results of bursting stresses obtained from nonlinear analyses using DIANA to the results of Foster and Rogowsky. The characteristics of the plots are investigated. In the second preliminary study, a specimen named B4 selected from Sanders' concentrically loaded reinforced concrete elements was modeled and a nonlinear analysis was performed to investigate reinforcing steel strain versus load behavior.

2.1 Study Compared to Foster and Rogowsky's Research

In this part of the preliminary studies, only the serviceability load behavior in Foster and Rogowsky's study was compared. Four models with different anchorage ratios (w/D or a/h where w or a are the plate width and D or h are the beam height) of 0.20, 0.40, 0.60, and 0.80 were created in DIANA using almost identical methods to those from the referenced study. However, due to insufficient information, some parameters and material properties in the new models were cautiously assumed. The dimensions of the confining concrete region of the new models, besides the one with w/D ratio of 0.20, were designed to have a square shape with the side length the same as the corresponding steel bearing plate. The reinforcement area of each bar element was determined by multiplying the distributed steel area of $1500 \text{ mm}^2/\text{m}$ to the influenced width of each steel element. The influenced width is the covered length taken from half of the distance between each bar on both sides of the considered bar.

The magnitudes of the material strength and the moduli of elasticity of both concrete and reinforcing steel remain the same. Because of the different input procedure for material properties, the constitutive model of the concrete was somewhat modified to be able to apply the built-in cracking behavior option in DIANA. Material constants describing the tension softening effect in the concrete (α_1 and α_2) used in the previous study (see section 1.4.2.6) were also used in this study. The study of Al-Manaseer and Philips (1987) indicated that the shear retention was insignificant if the material constant α_1 and α_2 values were appropriately selected. The Von Mises yield criterion was chosen for the constitutive model of the reinforcement. The numerical procedure for the nonlinear analysis of the new models consists of a modified Newton-Raphson iteration scheme with arc-length method and a similar convergence criterion as used in the previous study.

The transverse bursting stresses from the analyses were calculated with a similar method to that from the previous study, by combining the force in the reinforcing steel divided by its adjacent region of concrete and distributed concrete residual stresses taken from the same region. By taking the results from similar factors of applied load, the plots of transverse bursting stresses were created for all anchorage ratios. The results are identical to those of Foster and Rogowsky (see Figs. 2.1 to 2.4). As can be seen, the results from the present study look slightly different from those of the previous ones. The plots show similar stress distribution, which continues approximately to the location of 1.6 to 2.0 m from the surface. However, the bursting stresses from the new study begin at an earlier location with slightly lower peaks of maximum bursting stress. The areas under the curves are almost identical. It is noted that without modeling any bond-slip effect, the perfect bond assumption which is assigned to the interface relation of concrete and steel gives sufficient information about the behavior of the reinforced concrete panel after the cracking state is reached. Many possibilities, such as the modeling method of either material constitutive behavior or the assumed dimension of each component of the new models, may cause the difference in the results between these two studies. In conclusion, for the first preliminary study, DIANA gives a satisfying nonlinear analysis output compared to that of Foster and Rogowsky.

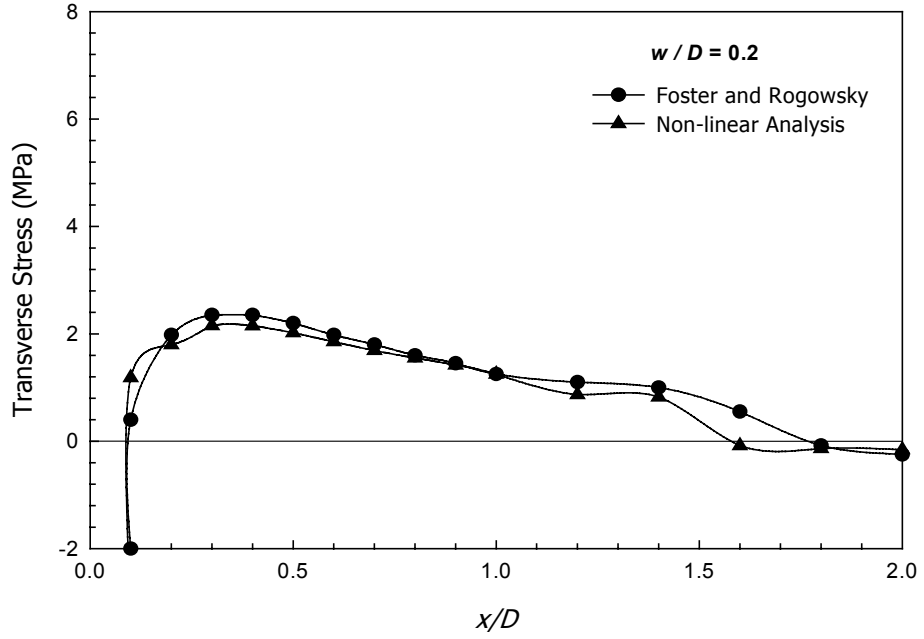


Fig. 2.1 TRANSVERSE BURSTING STRESS vs. RELATIVE DISTANCE FROM BEARING PLATE FOR $w/D = 0.20$

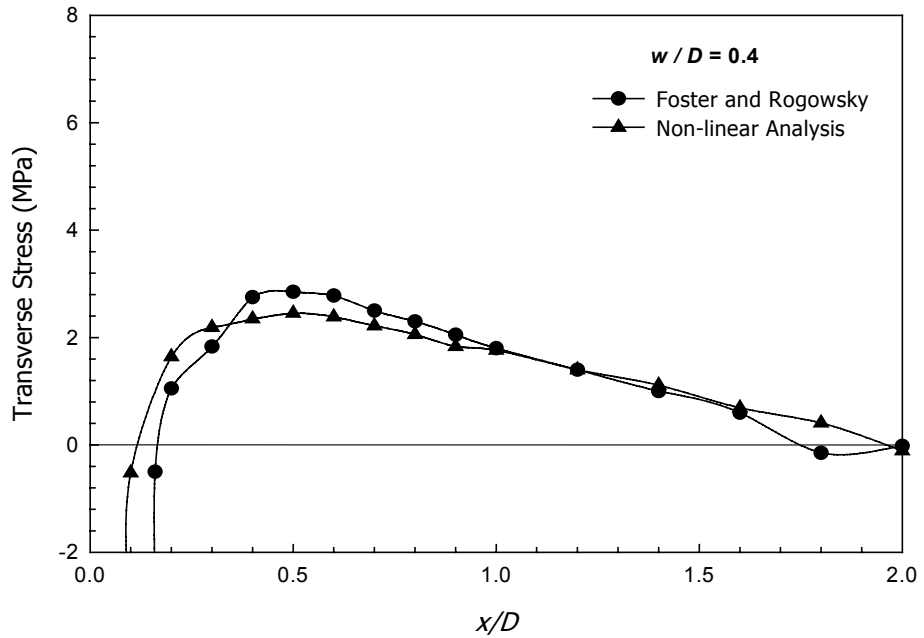


Fig. 2.2 TRANSVERSE BURSTING STRESS vs. RELATIVE DISTANCE FROM BEARING PLATE FOR $w/D = 0.40$

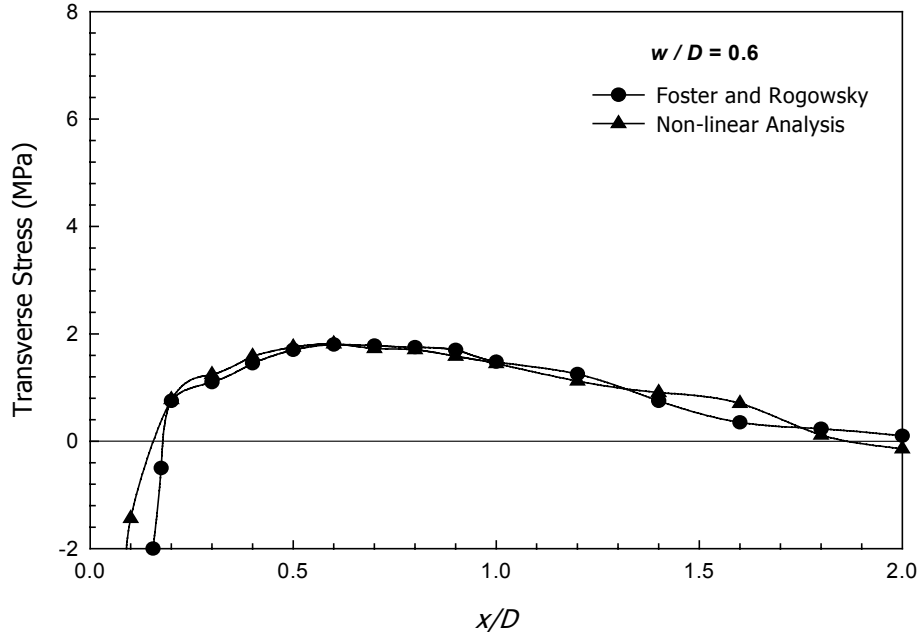


Fig. 2.3 TRANSVERSE BURSTING STRESS vs. RELATIVE DISTANCE FROM BEARING PLATE FOR $w/D = 0.60$

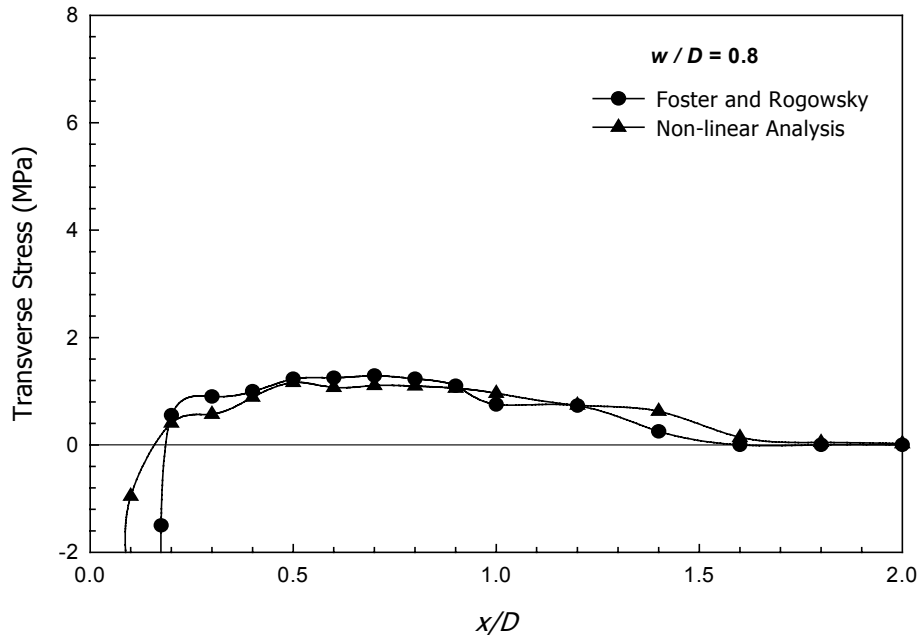


Fig. 2.4 TRANSVERSE BURSTING STRESS vs. RELATIVE DISTANCE FROM BEARING PLATE FOR $w/D = 0.80$

2.1 Study Compared to Sanders' Experimental Work

In the second preliminary study, the goal was to use DIANA to study the method to model an anchorage zone from a real specimen taken from available published research (Sanders, 1990). The specimen B4 from Sanders' specimens in the B-series, which are concentrically loaded, was selected (see Fig. 2.5). Using an 8-node isoparametric plane stress concrete element and 3-node beam element for embedded reinforcing steel, element size was designed to have a relative ratio of element size to the width of the specimen similar to that used in the first preliminary study. The new model material properties strictly followed the material information reported by Sanders (1990). The tensile strength of concrete was determined by using the value of $4.2\sqrt{f'_c}$ as suggested by Sanders. The compressive strength of the confined concrete region was calculated using equation (1.27). A tension softening characteristic curve with the same material constants (α_1 and α_2) as used in the first study was also applied for the cracking behavior of concrete. The iteration scheme and convergence criterion remained the same.

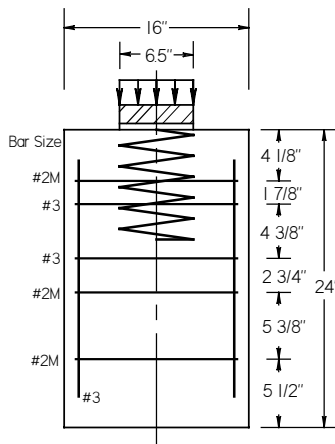


Fig. 2.5 SANDERS' SPECIMEN B4

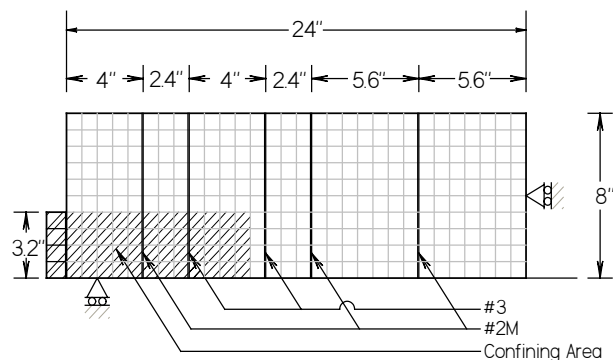


Fig. 2.6 FINITE ELEMENT MODEL OF SANDERS' SPECIMEN B4

The experimental result of specimen B4 is shown in Fig. 2.7 and the results from the second preliminary study are shown in Figs. 2.8 through 2.10. The differences in the characteristics of the strain-load curves from both studies are rather obvious, but the DIANA results show trends similar to the test results.

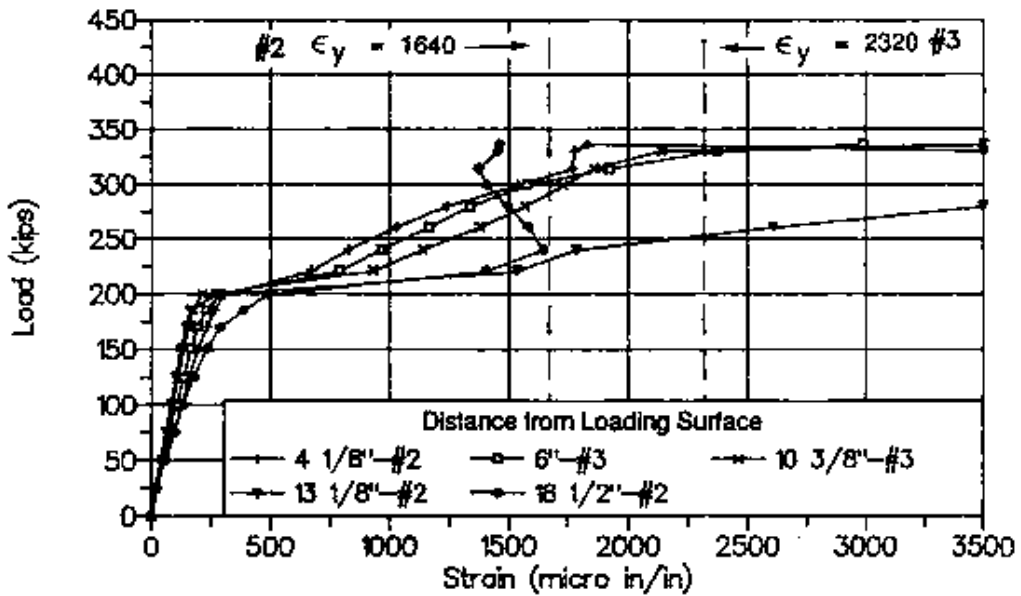


Fig. 2.7 THE EXPERIMENTAL STRAIN-LOAD RELATIONSHIP OF SPECIMEN B4

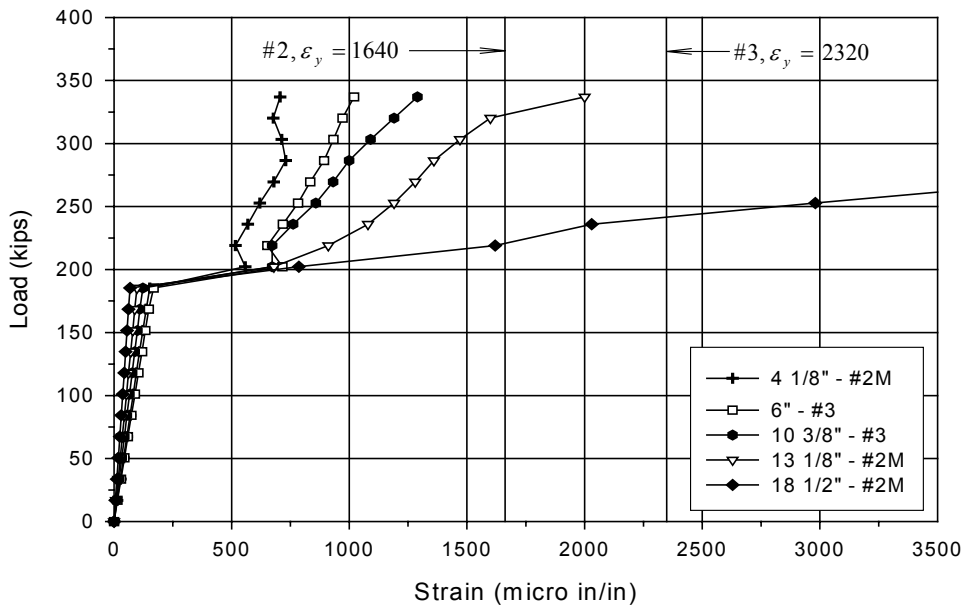


Fig. 2.8 THE STRAIN-LOAD RELATIONSHIP FROM PRELIMINARY STUDY
 MODEL LENGTH = $1.5h$ WITH 20 LOAD STEPS (h = SECTION WIDTH)

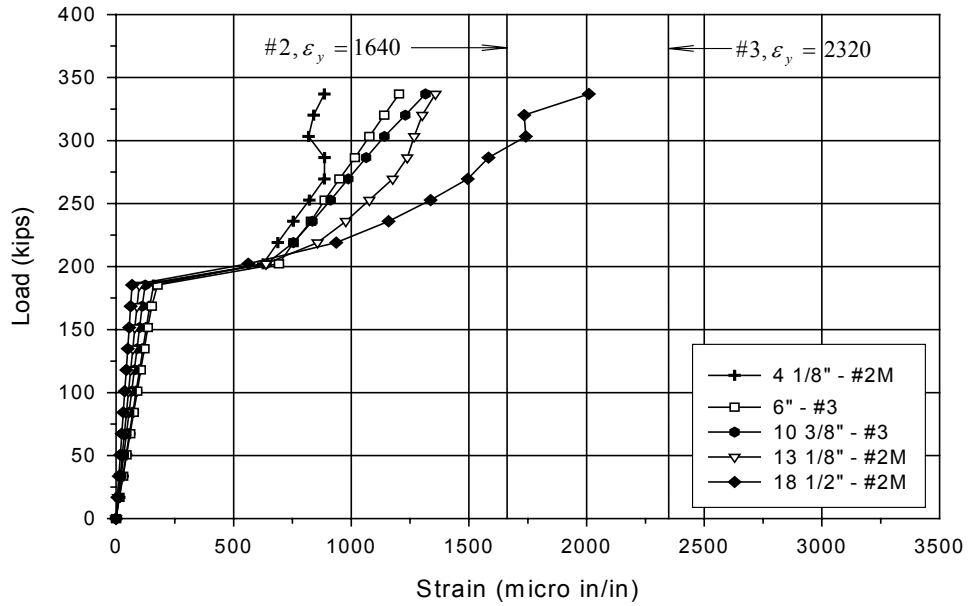


Fig. 2.9 THE STRAIN-LOAD RELATIONSHIP FROM PRELIMINARY STUDY
MODEL LENGTH = $2.5h$ WITH 20 LOAD STEPS (h = SECTION WIDTH)

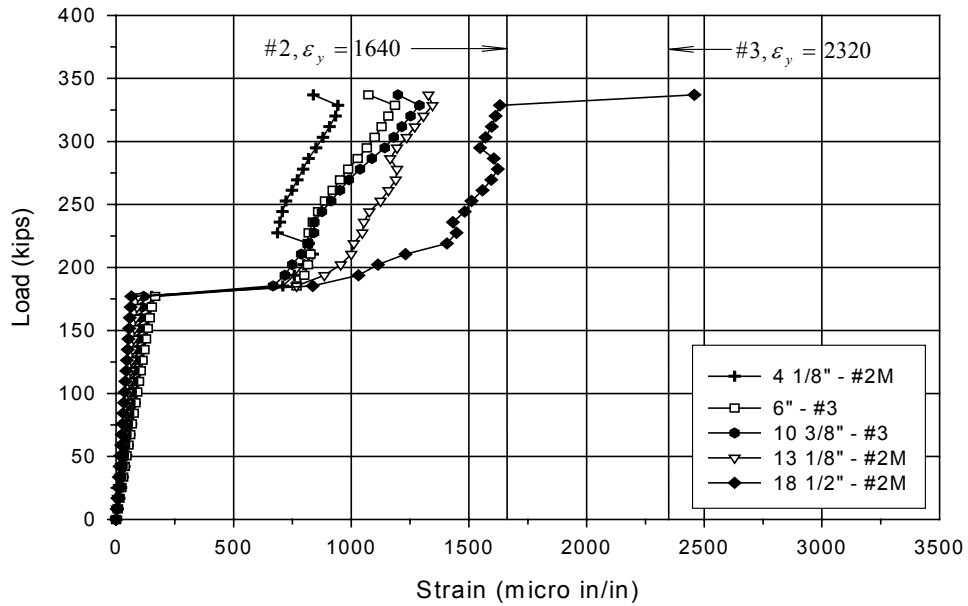


Fig. 2.10 THE STRAIN-LOAD RELATIONSHIP FROM PRELIMINARY STUDY
MODEL LENGTH = $2.5h$ WITH 40 LOAD STEPS (h = SECTION WIDTH)

In the experimental program, the ultimate load for specimen B4 was 337 kips and the first crack occurred at the load of 200 kips. All the steel in specimen B4 yielded except the #2M steel in the last layer, which showed a decreasing strain at loads larger than the first cracking load and then a small increase in strain after the load reached approximately 325 kips. The results of the nonlinear analyses differed from the experimental results in the magnitude of the first cracking load and the sequence of the steel bar with maximum to minimum strain.

The first cracking load determined by the new study is at a load of 185 kips for the models with 20 load steps and a load of 177 kips for the model with 40 load steps. For the models with 20 load steps, the one with a length of $1.5h$ showed that two bars yielded, which are #2M bars at the locations of $13 \frac{1}{8}$ in. and $18 \frac{1}{2}$ in. from the loaded surface. However, the model with a length of $2.5h$ had only one bar pass its yield strength at the last layer (#2M at $18 \frac{1}{2}$ in.). It is noted that with the same configuration of load and location of bars, the length of the model affects the nonlinear analysis result significantly. The longer model may provide more strength to the body than the shorter one, which causes the cracking strain to be smaller due to the continuation of the length.

The increase in the number of load steps gives the user more accurate information about the load. The curves in Fig. 2.10 are different from those in Fig. 2.9. The bar strains in the model with fewer load steps have a smoother change of slope. This illustrates the high sensitivity of the finite element analysis method to differences in the load iteration scheme. This confirms the idea of using the finite element method to study trends in the behavior of structures of interest or to predict roughly the magnitude of force relative to applied force. Non-linear finite element analysis should not be used to determine a specific value of stress or strain with the level of sophistication used in these models. The most significant assumptions in the nonlinear finite element modeling method are those used to establish the material constitutive models. As in Sanders' work, commonly used data such as compressive and splitting tensile strength of concrete and yield strength of steel are the only information given, which may limit the possible methods of modeling. Therefore, without sufficient information, it is good judgment for a user of a nonlinear finite element program to keep the complexity of the modeling method as simple as possible without losing the fundamental aspects of the material behavior.

CHAPTER 3

RECTANGULAR SECTIONS

WITH PRESENCE OF SUPPORT REACTIONS

3.1 Introduction

After Burdet's recommendations of anchorage zone design (1990), based on the study of rectangular sections of several configurations, were adopted into the AASHTO Standard Specifications (1994), they were acknowledged as conservative methods to design bursting reinforcement and were assumed to provide sufficient guidance for general anchorage zone design. However, in addition to the cases of inclined and eccentric load configurations, which are often found in the end regions of post-tensioned concrete girders, support reactions are also often found in this critical part of the structure. The support reaction was proven to have a significant effect on the bursting force according to the experimental study of Wollmann (1992) as mentioned in section 1.4.1.7. Unfortunately, only a few load configurations were investigated, and detailed recommendations for anchorage zones with support reactions have not yet been clearly addressed in any available code provisions. The study of anchorage zones of rectangular post-tensioned girders with the presence of a support reaction is the major focus of this chapter.

3.1.1 Objectives

The main objectives of this chapter are listed as follows:

1. To investigate the behavior of anchorage zones with a support reaction under various load configurations including concentric, eccentric, inclined, and inclined eccentric.
2. To investigate the effect of various parameters related to the anchorage zone with a support reaction. Parameters of the study comprise typical anchorage ratios (previously designated a/h), angle of inclination of prestressing load, magnitude of support reaction, support bearing plate ratio, and location of support reaction.

3. To evaluate the applicability of the method of determining the bursting force and the location of the force in the anchorage zone, equations (1.5) and (1.6), presented in the AASHTO Standard Specifications (2002), to the design of an anchorage zone with support reaction.
4. To determine a reinforcement detailing for bursting force resistance and to adjust the method of reinforcing steel arrangement presented in the AASHTO Standard Specifications (2002) if necessary.

3.1.2 Scope

This study focuses on the behavior of the bursting region in anchorage zones with a support reaction in order to examine the expressions used to determine the bursting force in the general anchorage zone and the location of bursting steel presented in the AASHTO Specifications. Four load configurations consisting of concentric, inclined concentric, eccentric, and inclined eccentric are investigated. The equations will be improved by including several parameters related to the design of the anchorage zone which the equations presented in the code exclude. A thorough comparison of the results from the former expressions and the newly found expressions is performed.

Because one of the methods for anchorage zone design allowed by the code is the use of the finite element method, this study also illustrates the step-by-step procedure of selecting the most appropriate finite element model for anchorage zones. The Strut-and-Tie Model (STM) method is also used to compare the results with those achieved from the newly found expressions. A new methodology for using the STM method to design an anchorage zone is investigated. Two example models of anchorage zones with a support reaction analyzed using the nonlinear finite element method are also given. The first example is to confirm the method of using the nonlinear finite element analysis to model the specimen Beam3 from Wollmann's study (1992). The second example is to compare the results of three design approaches: the approach presented in the code provisions, the STM method, and the newly developed approach. Finally, the arrangement of steel is investigated using the modified models of the second example in order to find a simpler method of handling the layout of reinforcement, which in the current code provisions are rather complicated.

3.2 Preparation of Work

3.2.1 Selection of the Model

At the beginning of the study, a typical detail of the finite element model used for the study must be selected. Based on the dimensions of the model used in the second preliminary study, the height of the model was chosen to match the specimens in the B-series of Sanders' experimental work. The full height of 16 in. was used instead of half of the height (8 in.) due to the unsymmetrical nature of the structure (see Fig. 3.1). A support reaction was located on the lower surface of the anchorage body. Therefore, when an eccentric prestressing load is applied, it must be considered to be applied on either the upper or the lower portion of the body (see Figs. 3.2a and 3.2b). This results in two completely different load configurations.

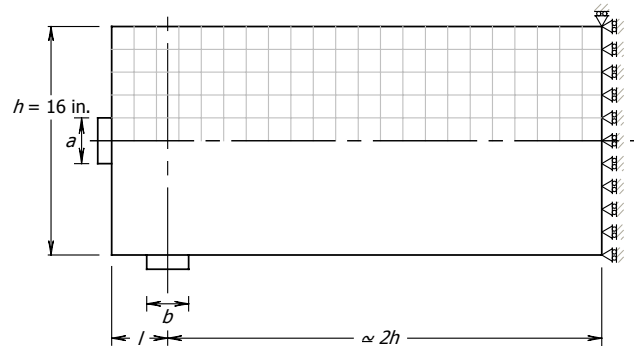


Fig. 3.1 TYPICAL DIMENSIONS FOR FINITE ELEMENT MODELING

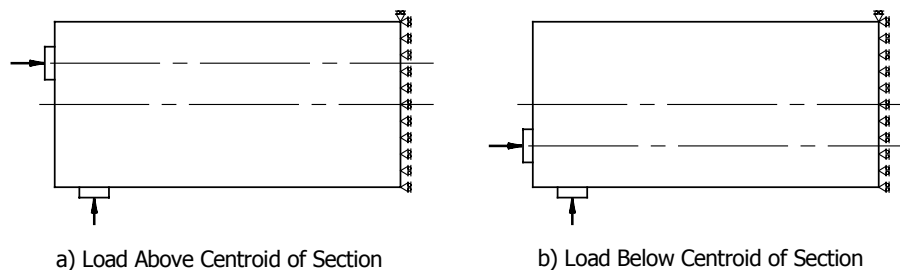


Fig. 3.2 ANCHORAGE ZONE WITH SUPPORT REACTION

The connection between the steel bearing plate and the concrete body is achieved by using spring elements as previously described in Chapter 1. A spring element with the length of 0.001 in. is connected from node to node within the bearing surface region to transfer force from the bearing plate in the direction of the spring axis to avoid Poisson's effect (see Fig. 3.3). For the case in which an inclined load is applied, the spring element cannot be used to transfer the shearing force to the the concrete element. The vertical component of the inclined load is applied directly onto the surface of the anchorage region of the concrete body.

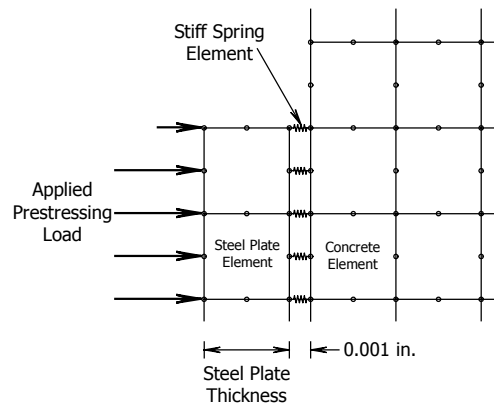


Fig. 3.3 SPRING CONNECTION BETWEEN BEARING PLATE AND CONCRETE ELEMENT

The length of the model is also significant. It must be carefully selected to avoid disturbances near the position of the vertical boundary support. For instance, if the vertical boundary support were located too close to the acting surface, the reaction of the vertical boundary support will affect the magnitudes of the bursting stresses and produce an unexpected result. The following subsections illustrate the method of choosing a typical model configuration in order to achieve an accurate result from the finite element analysis without resulting in excessive computational time and unnecessary effort.

3.2.2 Convergence Test

It is advisable to conduct a convergence test to verify that the most appropriate fineness of the mesh finite element has been selected before the subsequent investigation is performed. For the present study, a typical height of 16 in., as mentioned earlier, is used. In order to find

the most effective element size, three finite element models with the same structural dimensions but different mesh sizes were created (see Fig. 3.4). The models have an anchorage ratio (a/h) of 0.10 and a ratio of bearing plate of support reaction to section width (designated as b/h) of 0.125. The location of the support reaction (designated as l) was chosen as 2 in. from the prestressing surface. The magnitude of the support reaction is 5 percent of the prestressing load P . The bursting force along the horizontal line of each model was investigated and compared relative with one another. Fig. 3.5 shows the comparison of the results among these three models.

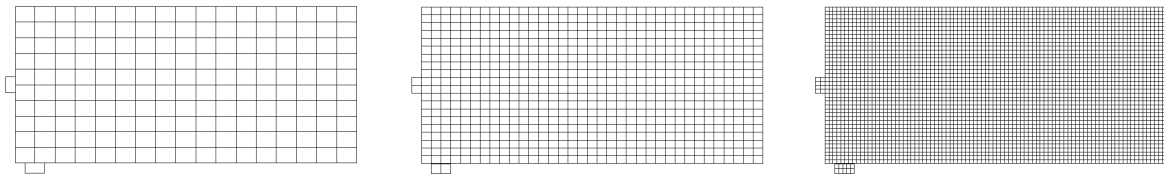


Fig. 3.4 MODELS USED IN CONVERGENCE TEST

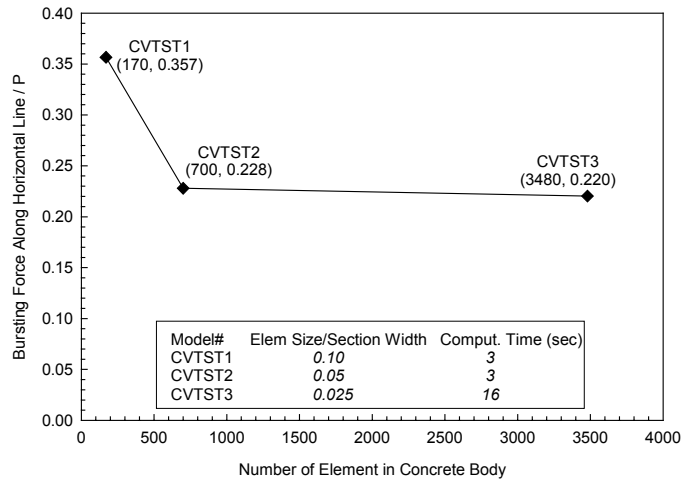


Fig. 3.5 CONVERGENCE TEST RESULT

As can be seen from Fig. 3.5, the model with the coarsest mesh (the number of elements is 170), which has an element size per section width ratio of 0.10, gives the ratio of bursting force on horizontal line per applied prestressing load of 0.357 which is largely different from those obtained from the other two models with finer meshes. The model with the number of elements equal to 700 gives only 3.38 percent difference of bursting force ratio compared to

the model with the finest mesh. The computational time required for a linear elastic analysis is as fast as that of the model with the coarsest mesh. Although the model with the largest number of elements may also require a small computational time, a very small element demands additional time for the modeling process if spring connections must be created between separated bodies such as the connection between the steel bearing plate and the concrete surface. As a result, the ratio of element size per section width of 0.05 (0.80 in. for the section width of 16 in.) was selected as the typical size of the element used for the present study.

3.2.3 Location of Vertical Boundary Support

In order to remain in equilibrium, the boundary condition of the model must include both vertical and horizontal boundary supports. In the present study, a horizontal roller support was fixed at each node at the end surface on the end line to model a symmetrical body with respect to the vertical axis. Only one vertical roller support is installed at the end of the model in order to provide the most realistic behavior. The position of this vertical support was suspected to have an effect on the value of bursting stresses due to vertical stress generated near its region. In this section, three finite element models were constructed with different locations of vertical roller support: at the top surface, at the horizontal centerline, and at the bottom surface of the anchorage zone model (see Fig. 3.6). A similar load configuration as well as other parametric ratios used in section 3.2.2 were applied. The length of the models was set to extend a distance of $2.0h$ from the edge of the bearing support plate.

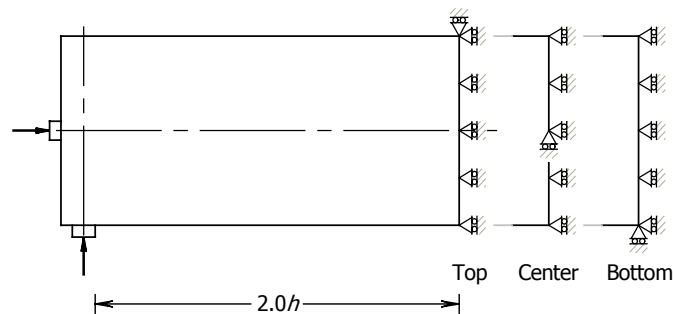


Fig. 3.6 LOCATIONS OF VERTICAL ROLLER SUPPORT

The plot of bursting stresses from each model was investigated and compared as shown in Fig. 3.7. According to the plots, the curves have similar characteristics which can be divided into two regions. The first region extends from the prestressing surface to a distance of approximately 25 in. The second region continues to the end of the model. The plots from the three models are identical until they enter the second region. The effect of the vertical boundary support is obvious in the three distinct patterns of transverse stresses. The model with the top vertical boundary support has compressive stresses under the support. The one with the support at mid-height of the section indicates very small stress values. The bottom vertical boundary support results in tensile transverse stresses above the support. Considering the region from the center of the support reaction to a distance of approximately $1.5h$, the bursting force calculated from each case has almost the same magnitude of about 0.227 times the prestressing load. Therefore, it can be concluded that the location of the vertical boundary support has no significant effect on the magnitude of the bursting force if the considered anchorage zone is extended to a distance of approximately $1.5h$ plus the distance from the support reaction to the loaded surface.

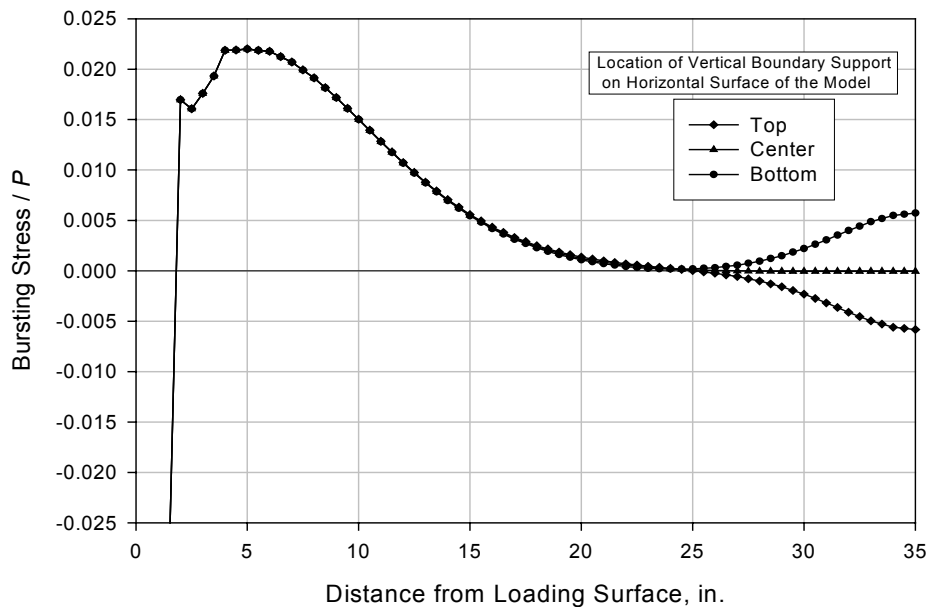


Fig. 3.7 TENSILE STRESSES OF MODELS WITH DIFFERENT VERTICAL SUPPORT LOCATION

3.2.4 Location of Main Compressive Strut Line

Since the alignment of the compressive strut line for an anchorage zone with a support reaction is not located horizontally (see Fig. 1.13b), the maximum tensile force cannot be determined from the stresses on the horizontal line passing through the center of the anchorage plate. In order to achieve the most accurate value of maximum tensile stress, the line representing the main compressive strut must be defined before the analysis takes place. Based on simple beam theory, the centroid of the resultant compressive stresses at the considered section, located at $1.5h$ from the center of the support reaction, can be determined. The line drawn from the center of the anchor plate to the resultant compressive force location is expected to give sufficient information of the maximum bursting stresses perpendicular to the line. A few models were created to verify this assumption.

A question to be answered was whether the considered section for determining the location of the centroid of the compressive force should be at a distance of $1.5h$ from the center or the edge of the support bearing plate. Because simple beam theory was used to locate the centroid, the height of the centroid varies linearly as the location of the considered section moves. The effect of the width of the support bearing plate on the bursting force was studied and is presented in the following section. To check the effectiveness of the assumption of placing the main compressive strut on an inclined line, a linear elastic finite element analysis was compared to the photo-elastic study of Sargious (Leonhardt, 1964). Fig. 3.8a shows the results of Sargious' study of inclined concentric force applied with an anchorage ratio of 0.20 onto a panel subjected to a support reaction with a magnitude of 20 percent of the prestressing load located at a distance of $1/6$ times the panel width. Fig. 3.8b shows the results of a finite element model created for comparison.

The main strut line used in the finite element model was determined from the centroid of the compressive stresses at the location of $1.5h$ from the center of the reaction. This line has smaller angle with respect to a horizontal line than in Sargious' study. The results from the finite element study are given in Figs. 3.8b and 3.8c. As can be seen in Fig. 3.8b, the magnitude of the bursting force from the finite element analysis is less than that given by

Sargious. The location of the centroid of the bursting force determined from the finite element analysis is located further, at $0.68h$, from the anchorage surface.

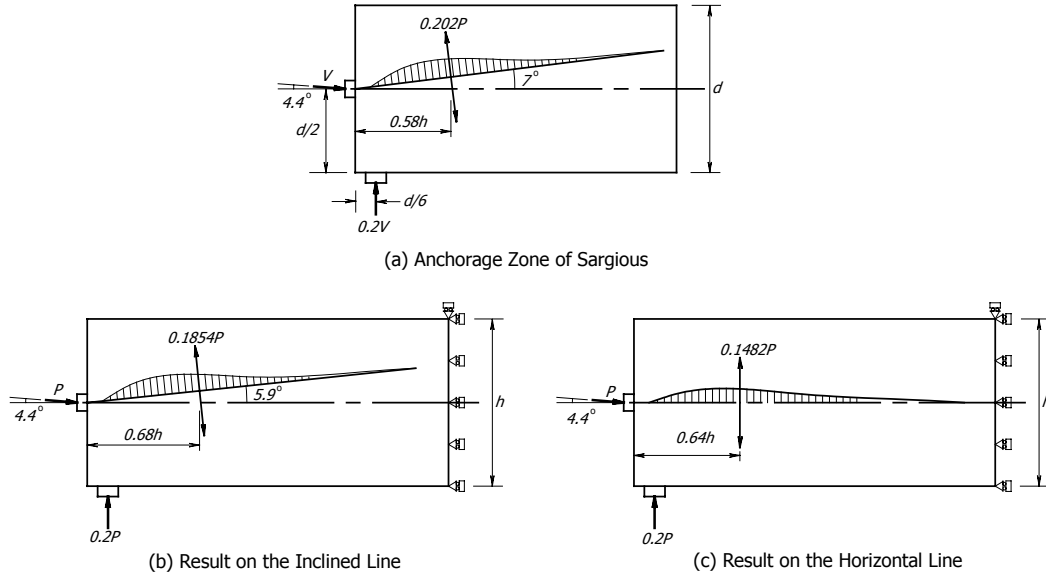
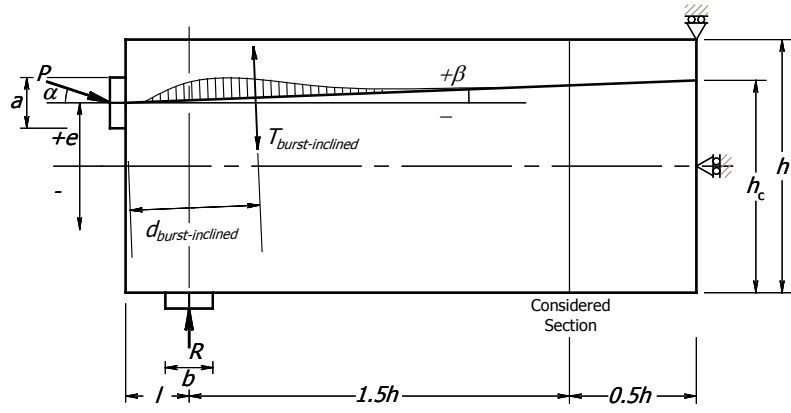
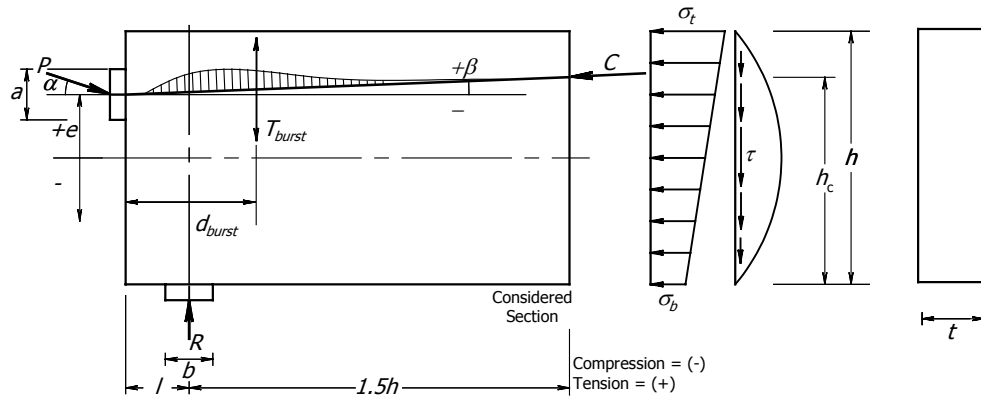


Fig. 3.8 COMPARISON OF MODEL WITH INCLINED STRUT LINE

Compared to the bursting force obtained from the integration of stresses on a horizontal line passing through the center of the anchorage plate (see Fig. 3.8c), the bursting force on the inclined line is obviously larger, with a 20.1 percent difference. It can be concluded that using the bursting force obtained from the integration of stresses along a horizontal strut line is unconservative for the design of anchorage zones with a support reaction. The finite element method with linear elastic approach is known to be a conservative method in the prediction of stresses or forces for the study of reinforced concrete structures compared to a nonlinear approach (see section 1.4.2.6). It can be stated that the less conservative result compared to that from the photo-elastic study does not mean the finite element analysis provides the user with inaccurate information. It may be that the photo-elastic study provides a more conservative outcome. Based on the comparison of bursting force on both horizontal and inclined compressive strut, it is considered a better approach in finite element modeling to construct a predefined compressive strut in order to obtain the most precise results for an anchorage zone with a support reaction. Fig. 3.9 shows a picture of a typical model used for the present study.



(a) Full Model



(b) Free Body Diagram

Fig. 3.9 TYPICAL MODEL FOR THE STUDY OF ANCHORAGE ZONE WITH SUPPORT REACTION

In Fig. 3.9b, the stress on the extreme fibers (σ_t and σ_b) of the considered section is negative in compression and positive in tension. The values of both σ_t and σ_b are based on simple beam theory and can be calculated from the following equations:

$$\sigma_t = -\frac{P}{A} - \frac{R \times 1.5h + P \cos \alpha \times e - P \sin \alpha \times (l + 1.5h)}{th^2 / 6} \quad (3.1a)$$

$$\sigma_b = -\frac{P}{A} + \frac{R \times 1.5h + P \cos \alpha \times e - P \sin \alpha \times (l + 1.5h)}{th^2 / 6} \quad (3.1b)$$

The location of the centroid of the main compressive strut at the considered section (h_c) is generally based on the geometry of the stress diagram and can be calculated using

formulations given in Appendix A. The angle of the main compressive strut β used in the modeling of anchorage zones in this study can be determined using the equation below:

$$\beta = \arctan \left[\frac{h_c - h/2 - e}{l + 1.5h} \right] \quad (3.2)$$

Since the configuration of the typical model has been defined, the verification of the location of the main compressive strut should be performed. Therefore, a series of finite element models was constructed with various dimensioning and load parameters. The goal was to compare the angles of the strut resulting from using both finite element result and the presented equations. The compared results are presented using percent difference between them in Table 3.1. As shown, all the models can be categorized into six groups including concentric, inclined concentric, two groups of eccentric with different location of support reaction, and the other two groups of inclined eccentric with different support reaction locations. The height and thickness of all models remain as 16 in. and 1 in., respectively. The inclination angle of the prestressing load was selected as 6 degrees for all models subjected to inclined load. The values of the eccentricity ratio for eccentrically loaded anchors were chosen to cover all possible locations on the beam. More explanation of the selection of the eccentricity ratio is given in section 3.3.3. Different magnitudes of support reaction were also applied for concentric and inclined concentric load categories.

The calculated stress values at top and bottom fiber of the beam based on equation (3.1) are shown in the columns σ_t and σ_b in the table. They were used to determine the values of h_c and β . The results from finite element analyses are presented in the β -*fem* column and the percent difference between these values and those from equation (3.2) are shown in the next column. A negative angle indicates downward rotation of the strut. As can be seen, although the percent difference may indicate values as large as 15.19 percent in the case of inclined eccentric load with location of support reaction at 2 in. and an eccentricity ratio of +0.25, the magnitude of the angle is, however, very small and has a minimal effect on the behavior of the stresses in the anchorage zone.

Additional information is given in the last two columns of Table 3.1. The β -vector column presents the angle of the resultant vector of the two forces, P and R . The percent difference shown in the adjacent column indicates the difference between the angle provided by the finite element result and that of the resultant vector. The comparison in Table 3.1 verifies that using equations (3.1) and (3.2) to determine the location of main compressive strut is acceptable.

Table 3.1 COMPARISON OF ANGLE OF MAIN COMPRESSIVE STRUT

	P	h	t	α	e/h	e	R/P	l	$1.5h$	σ_t	σ_b	h_c	β				β -vector	
													-1-	-2-	-1&2-	% Diff.	-3-	% Diff.
Concentric	1	16	1	0	0	0	0.05	2	24	-0.0906	-0.0344	9.20	2.64	2.65	0.43	2.86	7.28	
	1	16	1	0	0	0	0.10	2	24	-0.1188	-0.0062	10.40	5.27	5.30	0.43	5.71	7.25	
	1	16	1	0	0	0	0.15	2	24	-0.1469	0.0219	11.36	7.36	7.17	2.58	8.53	15.96	
	1	16	1	0	0	0	0.05	4	24	-0.0906	-0.0344	9.20	2.45	2.48	1.22	2.86	13.21	
	1	16	1	0	0	0	0.10	4	24	-0.1188	-0.0062	10.40	4.90	4.96	1.17	5.71	13.19	
	1	16	1	0	0	0	0.15	4	24	-0.1469	0.0219	11.36	6.84	6.59	3.67	8.53	22.78	
Inc. Concentric	1	16	1	6	0	0	0.05	2	24	-0.0266	-0.0977	6.47	-3.36	-3.36	0.12	-3.12	6.97	
	1	16	1	6	0	0	0.10	2	24	-0.0547	-0.0696	7.68	-0.70	-0.69	2.21	-0.26	62.31	
	1	16	1	6	0	0	0.15	2	24	-0.0828	-0.0415	8.89	1.95	1.98	1.37	2.60	23.90	
	1	16	1	6	0	0	0.05	4	24	-0.0217	-0.1026	6.26	-3.55	-3.53	0.65	-3.12	11.47	
	1	16	1	6	0	0	0.10	4	24	-0.0498	-0.0745	7.47	-1.08	-1.03	4.95	-0.26	74.81	
	1	16	1	6	0	0	0.15	4	24	-0.0779	-0.0464	8.68	1.38	1.47	5.72	2.60	43.58	
Eccentric	1	16	1	0	0.40	6.40	0.15	2	24	-0.2969	0.1719	12.62	-3.91	-3.81	2.53	8.53	55.31	
	1	16	1	0	0.25	4.00	0.15	2	24	-0.2406	0.1156	12.40	0.88	0.81	7.80	8.53	90.53	
	1	16	1	0	0.10	1.60	0.15	2	24	-0.1844	0.0594	11.97	5.20	5.00	3.82	8.53	41.38	
	1	16	1	0	-0.10	-1.60	0.15	2	24	-0.1094	-0.0156	10.00	7.88	7.91	0.37	8.53	7.25	
	1	16	1	0	-0.25	-4.00	0.15	2	24	-0.0531	-0.0719	7.60	7.88	7.91	0.29	8.53	7.32	
	1	16	1	0	-0.40	-6.40	0.15	2	24	0.0031	-0.1281	5.21	7.90	7.90	0.04	8.53	7.39	
Eccentric	1	16	1	0	0.40	6.40	0.15	4	24	-0.2969	0.1719	12.62	-3.63	-3.67	1.02	8.53	56.97	
	1	16	1	0	0.25	4.00	0.15	4	24	-0.2406	0.1156	12.40	0.81	0.76	6.73	8.53	91.10	
	1	16	1	0	0.10	1.60	0.15	4	24	-0.1844	0.0594	11.97	4.83	4.57	5.45	8.53	46.47	
	1	16	1	0	-0.10	-1.60	0.15	4	24	-0.1094	-0.0156	10.00	7.33	7.41	1.16	8.53	13.11	
	1	16	1	0	-0.25	-4.00	0.15	4	24	-0.0531	-0.0719	7.60	7.33	7.41	1.08	8.53	13.18	
	1	16	1	0	-0.40	-6.40	0.15	4	24	0.0031	-0.1281	5.21	7.34	7.41	0.91	8.53	13.18	
Inc Eccentric	1	16	1	6	0.40	6.40	0.15	2	24	-0.2320	0.1077	12.36	-4.49	-4.34	3.39	2.60	40.00	
	1	16	1	6	0.25	4.00	0.15	2	24	-0.1761	0.0518	11.88	-0.27	-0.25	5.35	2.60	90.25	
	1	16	1	6	0.10	1.60	0.15	2	24	-0.1201	-0.0042	10.49	1.95	1.99	1.57	2.60	23.74	
	1	16	1	6	-0.10	-1.60	0.15	2	24	-0.0455	-0.0788	7.29	1.95	1.98	1.15	2.60	24.07	
	1	16	1	6	-0.25	-4.00	0.15	2	24	0.0104	-0.1347	4.95	2.09	2.11	0.88	2.60	18.82	
	1	16	1	6	-0.40	-6.40	0.15	2	24	0.0663	-0.1907	3.96	5.18	5.05	2.52	2.60	48.43	
Inc Eccentric	1	16	1	6	0.40	6.40	0.15	4	24	-0.2271	0.1028	12.33	-4.23	-3.95	6.69	2.60	34.05	
	1	16	1	6	0.25	4.00	0.15	4	24	-0.1712	0.0469	11.81	-0.38	-0.32	15.19	2.60	87.53	
	1	16	1	6	0.10	1.60	0.15	4	24	-0.1152	-0.0091	10.28	1.38	1.47	5.96	2.60	43.43	
	1	16	1	6	-0.10	-1.60	0.15	4	24	-0.0406	-0.0837	7.08	1.38	1.47	5.48	2.60	43.73	
	1	16	1	6	-0.25	-4.00	0.15	4	24	0.0153	-0.1396	4.81	1.65	1.68	2.00	2.60	35.33	
	1	16	1	6	-0.40	-6.40	0.15	4	24	0.0712	-0.1956	3.91	4.71	4.47	5.16	2.60	41.77	

Besides the comparison of the strut angle in Table 3.1, a series of models with the same parameters was also used for the comparison of the bursting force on a horizontal strut passing through the center of the anchorage plate. All results are given in Appendix B.

3.3 Parameters

With the presence of a support reaction, the pattern and magnitude of the stresses in the anchorage zone change with the magnitude of the reaction force. Several parameters related to the reaction force can be varied. Besides parameters that were previously investigated in the other studies of anchorage zones, the support bearing plate width (b) and the location of the support reaction (l) were suspected to influence the magnitude or the location of the bursting force. In this section, important parameters are discussed and specified for further investigation.

3.3.1 Anchorage Ratio (a/h)

As shown in the study of Guyon (1953) and also illustrated in equation (1.5) in the AASHTO Standard Specifications (2002), the anchorage ratio has a major influence on the magnitude of the bursting force. The most frequently discussed load configuration in anchorage zone studies is a concentric load. Many researchers published their own proposed formulation to evaluate the magnitude of bursting stress. But eventually it was found that the simple linear equation is the best formulation to describe the relation between bursting force and anchorage ratio with a satisfactory level of conservatism. The first term on the right side of equation (1.5) accounts for the effect of the anchorage ratio. However, it is known that the first term of equation (1.5) results in unconservative predictions for anchorage ratios of less than 0.15, as can be seen from Fig. 3.10.

Based on intensive reviews of many published researches, the anchorage ratios used for the present study were chosen to be 0.10, 0.20, 0.35, and 0.50. An additional ratio of 0.00 was inserted into the study to complete the characteristic plot of magnitude of bursting force versus anchorage ratio. The development of the formulation derived in this study took advantage of equation (1.5) as a reference. The relation between the magnitude of the bursting force and the anchorage ratio is the first topic studied in every load configuration.

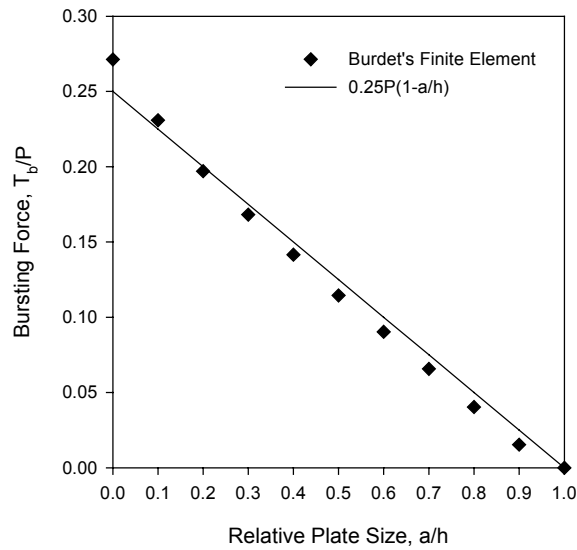


Fig. 3.10 COMPARISON OF FINITE ELEMENT RESULTS PRESENTED BY BURDET (1990)

3.3.2 Inclination Angle of Prestressing Force (α)

In reality, there is rarely a case in which a prestressing force is applied horizontally for post-tensioned structures. The angle of inclination has an extremely significant effect which cannot be neglected in the formulation. The bursting force can increase almost 25 percent of its magnitude if the inclination angle of the prestressing force changes from zero degrees to a 6 degree angle with an anchorage ratio of 0.20 according to equation (1.5). The second term of the equation accounts for the inclination effect. The term can be explained as 50 percent of the total shear force resulting from the vertical component of the inclined load. Fig. 3.11 illustrates a free body of an anchorage zone subjected to an inclined load, transformed into horizontal and vertical components.

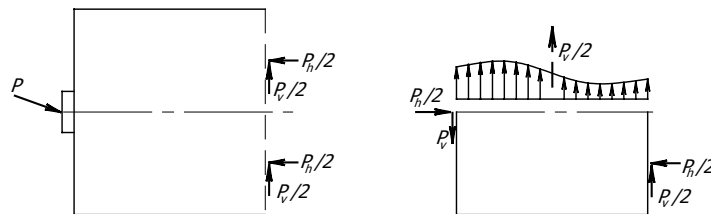


Fig. 3.11 EFFECT OF INCLINED PRESTRESSING FORCE ON ANCHORAGE ZONE

According to Fig. 3.11, tensile stresses occur at the centerline of the anchorage zone due to the vertical component of the inclined force. Fifty percent of the force is resisted by shear at the end of the beam. If this anchorage zone is subjected to an additional vertical reaction, certainly it will reduce the magnitude of the tensile stresses at the horizontal cut line. Since the maximum bursting force does not occur perpendicular to the horizontal line if a support reaction is present, an expression which is developed from the result on a horizontal line becomes less accurate. The effect of the support reaction needs to be included in the calculation of the bursting force.

Generally, the angle of inclination is smaller than 10 degrees. The present study investigated the effect of inclination of prestressing load with two selected angles consisting of 6 degrees and 9 degrees. At the beginning of the research, only the 6 degree angle was chosen for the study of the behavior of inclined loaded anchorage zone. During the course of the study, adding one more angle parameter to verify the formulation was found to be essential. The angle of 9 degrees was selected based on information discovered in some publications (Abeles et al., 1981; Leonhardt, 1964; Post-Tensioning Institute, 1999). It could be possible that a single anchor within a group of anchors has a larger inclination angle than 9 degrees. However, the angle of a group of anchors is measured from the centroidal axis of all anchors in that group, which rarely exceeds 9 degrees.

3.3.3 Eccentricity (e)

One of the most important parameters of anchorage zone design is eccentricity. Eccentrically loaded anchorage zones without a support reaction can be conveniently designed using the symmetric prism approach presented by Guyon (1953). The behavior of the bursting stresses within the prism is assumed to be similar to a concentrically loaded anchorage zone occurring within a smaller region. The magnitude and the location of bursting force can be determined using equations (1.5) and (1.6). By replacing the full height of the section (h) with the height of the symmetric prism ($h-2e$), the magnitude of the bursting force of an anchorage zone with eccentricity can be estimated (see Fig. 3.12).

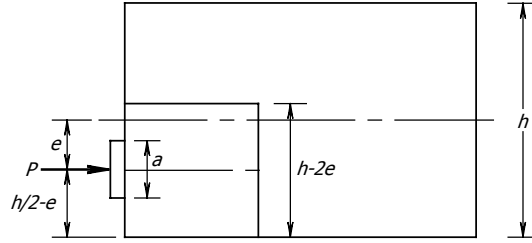


Fig. 3.12 ECCENTRICALLY LOADED ANCHORAGE ZONE

By substituting the height of the symmetric prism, equation (1.5) can be rewritten as shown below:

$$T_{burst} = 0.25 \Sigma P_u \left(1 - \frac{a}{h - 2e}\right) + 0.5 / \Sigma(P_u \sin \alpha) / \quad (3.3)$$

As mentioned earlier, the location of an eccentric prestressing load on an anchorage zone with a support reaction can be located in either the upper or the lower portion of the element (see Fig. 3.2). Furthermore, since the presence of a support reaction influences the displacement of the structure vertically, this behavior affects the strain compatibility of structure. The longitudinal edge tensile stresses may not occur normally even though the prestressing load is applied outside the kern of section. As a result, the parameter herein is not assigned by the location of the kern. Instead there are six values designed for the parameter of eccentricity ratio (e/h) consisting of 0.10, 0.25, and 0.40 located in both directions: upward and downward with respect to the centerline of the beam. Following the sign convention of Fig. 3.9, positive eccentricity means an anchor is located above the centroid of the section and negative if otherwise. Eccentricity also plays an important role in the alignment of the main compressive strut.

3.3.4 Magnitude of Reaction Force (R)

Since the present study is directly related to the effect of a support reaction in an anchorage zone, the magnitude of the reaction force becomes one of the most important parameters. In post-tensioned girders, the tendon is usually jacked with a high level of the force. The reaction force can be estimated as a proportion of the force. In the experimental study of Wollmann (1992), specimens Beam2 and Beam3 were designed to have a vertical

support reaction equal to 10 percent of the applied prestressing load on each side of the beam. Based on engineering experience, the magnitude of the support reaction on one side of a girder can rise above 10 percent of the prestressing force. Therefore, the parameter of the magnitude of the reaction force consists of four numbers: 0.00 (no reaction applied), 0.05, 0.10, and 0.15 times prestressing force. Since the two selected inclination angles were 6 degrees and 9 degrees, the vertical component of each inclined load is very close to 10 percent and 15 percent of prestressing load, respectively. This results in the cancellation of the vertical forces within the free body of the anchorage zone and leaves an insignificant effect in the determination of the main compressive strut alignment. However, the stress distribution in this case is still an interesting issue.

3.3.5 Bearing Support Ratio (b/h)

Besides the magnitude of support reaction, the bearing plate width of the support reaction was suspected to have a significant effect on the behavior of the anchorage zone as well. In many typical configurations, the width of the bearing plate is not as large as the width of anchorage plate since the reaction force has a smaller magnitude. However, when neoprene pads are used, the size of the bearing plate is not necessarily smaller than that of anchorage plate. The parameter of the bearing support ratio was divided into three cases comprising the ratios of 0.0 (simple concentrated load), 0.125, and 0.250. The values of the bearing support ratio were set to monitor the behavior of stresses from immediately above the bearing region to the extreme top fiber of the beam.

3.3.6 Location of Support Reaction (l)

The location of the support reaction is also significant. Based on simple beam theory, it can change the alignment of the main compressive strut. The parameter of the location of the support reaction consists of three values relative to the width of the beam section (h): $0.125h$, $0.25h$, and $0.5h$. The first value represents the case of a support reaction placed relatively close to the anchorage surface. The largest value illustrates the effect of a support reaction located at a distance equal to half of the section width (the location of d_{burst} if the inclination

angle and eccentricity are invalid according to equation (1.6) presented in the AASHTO Standard Specifications 2002).

3.3.7 Summary

All parameters used in this chapter are summarized in Table 3.2. A list of all finite element model which were constructed for the study, along with all dimensions and modeling details, is given in Appendix C.

Table 3.2 SUMMARY OF PARAMETERS

a/h	$\alpha (^{\circ})$	e/h	R/P	b/h	l/h
0.00	0	0.10	0.00	0.000	0.125
0.10	6	0.25	0.05	0.125	0.250
0.20	9	0.40	0.10	0.250	0.500
0.35		-0.10	0.15		
0.50		-0.25			
		-0.40			

3.4 Load Configurations

The following sections present the behavior of anchorage zones with the presence of a support reaction subjected to various load configurations consisting of concentric, inclined concentric, eccentric, and inclined eccentric. The presentation begins with the most basic configuration and continues with the more complex ones. For concentrically loaded anchorage zones, the results of both directly concentric and inclined concentric are discussed separately and then together at the end. A similar method of presentation is applied to eccentrically loaded anchorage zones. All results are brought together to develop the best methodology for anchorage zone design.

3.4.1 Concentrically Loaded Anchor Configuration

3.4.1.1 Elastic Stress Distribution

Figure 3.13 shows contour plots of stresses in the y-y and x-x direction and shear on the x-y plane, of a concentrically loaded anchorage zone with an anchorage ratio of 0.20. As can be seen, the stress distribution is symmetric along the horizontal axis. A similar behavior occurs in the same load configuration with other anchorage ratios. The stress value in the pictures is presented as a factor of average stress $\sigma_o (= P/(h \times t))$.

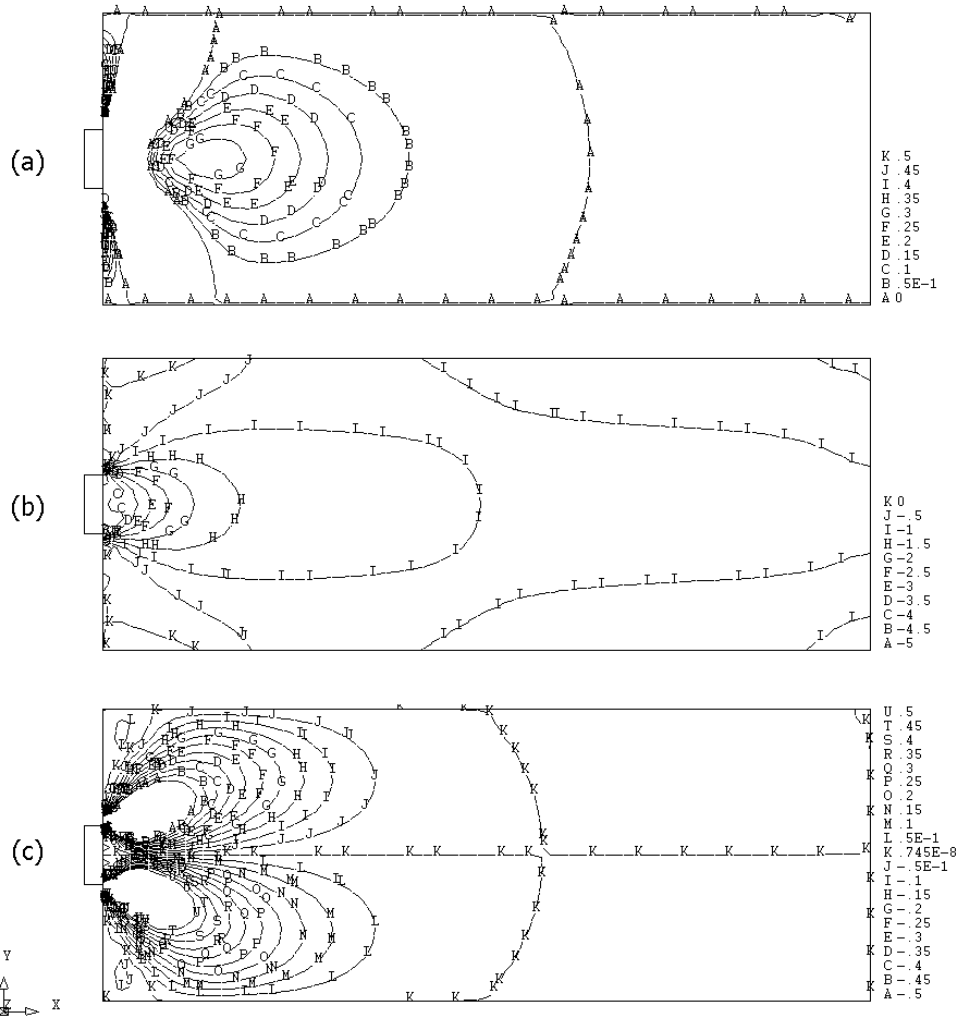


Fig. 3.13 CONCENTRIC LOAD WITH $a/h = 0.20$ AND $R/P = 0.00$
a) S_{yy} , b) S_{xx} , AND c) S_{xy} (Stress multiplied by σ_o)

Similarly Fig. 3.14 shows contour plots of a concentrically loaded anchorage zone with a support reaction with the R/P ratio equal to 0.05. The stress contours are no longer symmetric about the horizontal centerline. The symmetry is disrupted by the effect of the reaction force. In Fig. 3.14, the stress concentration near the top surface is caused by the presence of the vertical boundary support restraint at the top surface, which should be ignored since the study focuses on the bursting region ahead of the anchor to the position of $1.5h$ from the center of support reaction.

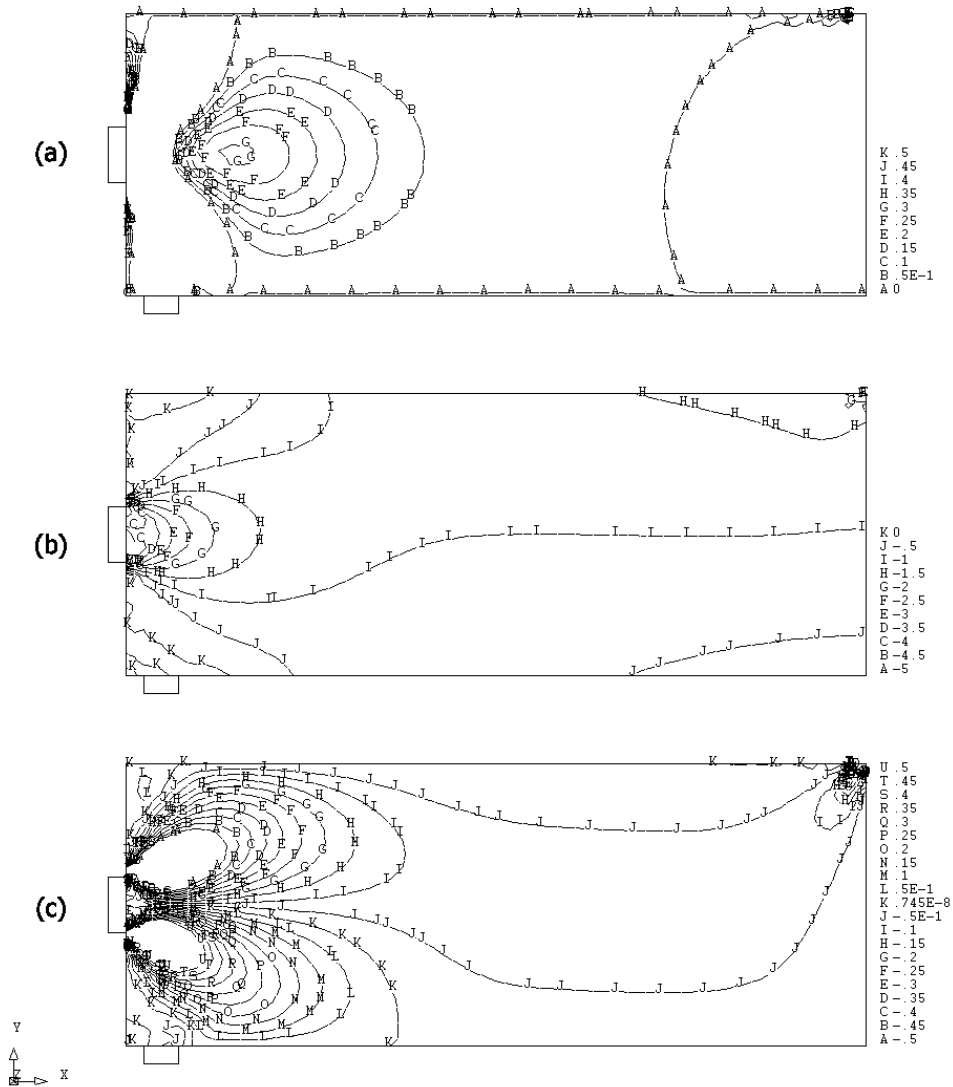


Fig. 3.14 CONCENTRIC LOAD WITH $a/h = 0.20$, $l/h = 0.125$, AND $R/P = 0.05$
 a) S_y , b) S_{xx} , AND c) S_{xy} (Stress multiplied by σ_o)

Another figure is given for comparison with Figs. 3.13 and 3.14. Fig. 3.15 shows contour plots of an anchorage zone subjected to concentric and support reaction with the ratio of R/P equal to 0.15, which is the highest magnitude of the reaction force in this study. As can be seen, the stress contours in each figure are quite different from those in Fig. 3.13. The bursting region in Fig. 3.15a shows that the maximum tensile stresses are still close to the line passing through the center of the anchor, but the contours are not symmetric about the horizontal line.

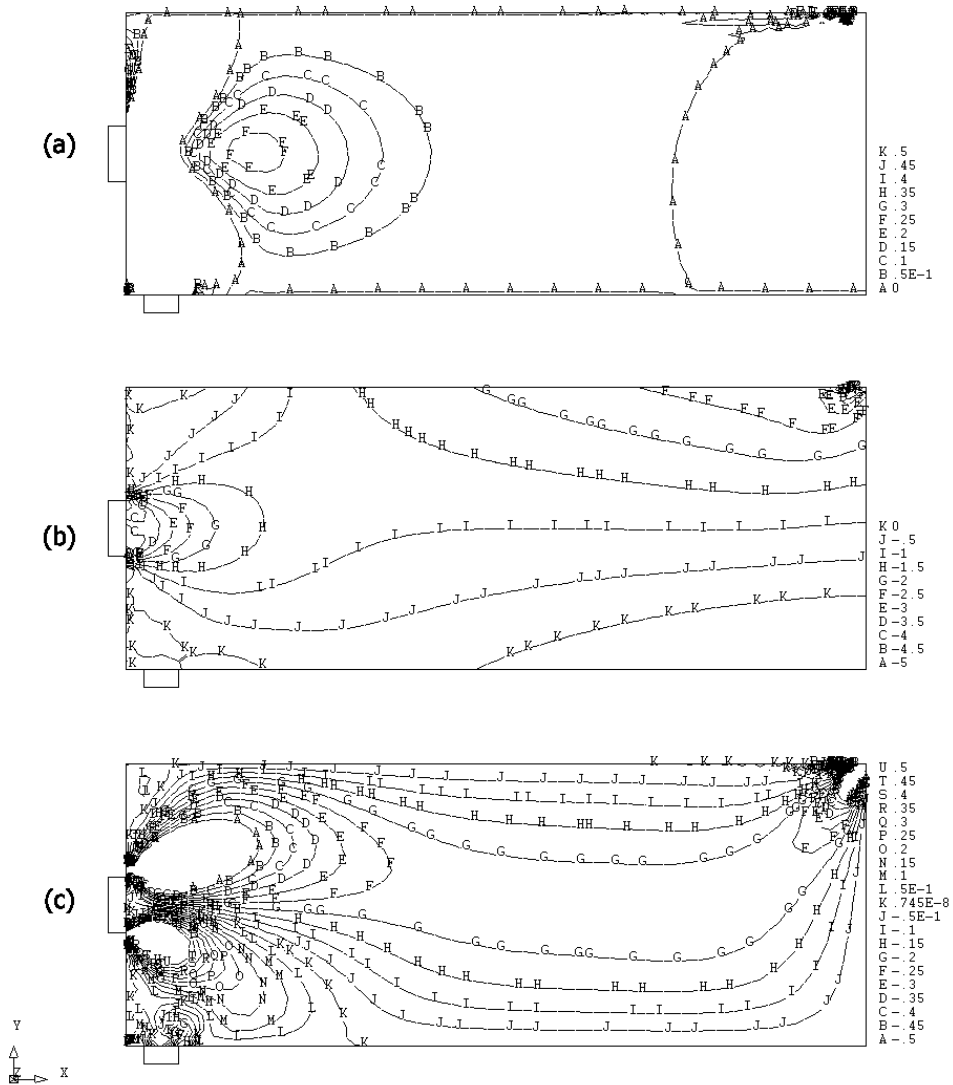


Fig. 3.15 CONCENTRIC LOAD WITH $a/h = 0.20$, $l/h = 0.125$, AND $R/P = 0.15$
 a) S_{yy} , b) S_{xx} , AND c) S_{xy} (Stress multiplied by σ_0)

Based on Figs. 3.13 through 3.15, it can be seen that a support reaction causes a change of the stress distribution within an anchorage zone. The magnitude of the reaction force also has a major effect on the behavior of the bursting stresses. Graphically the contour stress region within line B in part (a) of each figure does not reduce in size, but instead deviates slightly upward according to the direction of reaction force. It can also be seen in Fig. 3.15 that the spalling stress at the prestressing surface on the lower portion of the beam almost vanishes. This is caused by the rise of compressive stresses in the y-y direction which results in cancellation of the tensile stress. Fig. 3.16 shows the behavior of y-y stresses due to two different magnitudes of support reaction and without an applied prestressing force.

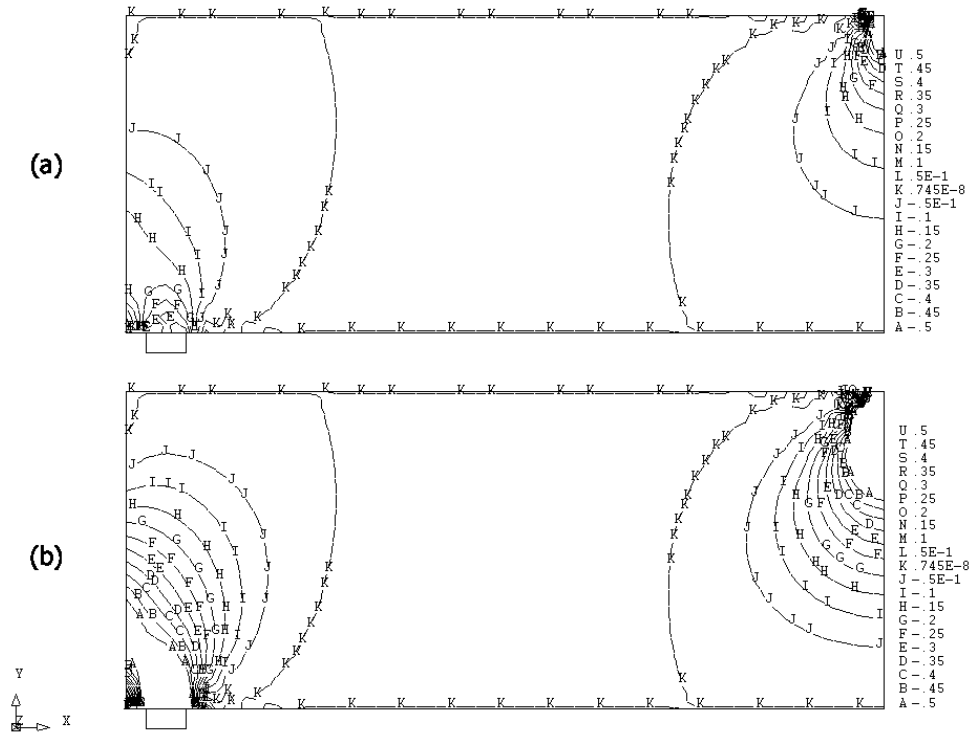


Fig. 3.16 Y-Y STRESSES DUE TO REACTION LOAD WITH $l/h = 0.125$, $R/P =$ a) 0.05 AND b) 0.15
(Stress multiplied by σ_0)

3.4.1.2 Bursting Force

As previously stated, the most general parameter that should be addressed is the anchorage ratio. The effect of the anchor plate size to the bursting force is considered along with the application of reaction force. Fig. 3.17 shows the relation between the anchorage ratio and the bursting force with three different reaction load parameters. In the figure, the solid lines with markers are used for finite element results and the dash-dot line is used for approximate equations. The bursting force is measured in the vertical direction and is presented in dimensionless form. The model has the same parameters of b/h and l/h equal to 0.00 and 0.125, respectively. It is shown that the bursting force of anchorage zone with R/P equal to zero and 0.05 almost share the same plot. When the R/P value increases, the bursting force also increases correspondingly. The magnitude of the force is larger than that provided by equation (1.5). All plots were determined based on the same direction in order to be able to compare to equation (1.5). As shown in the figure, the slopes of all plots are mostly parallel to one another for values of a/h larger than 0.20. This implies that the coefficient of 0.25 in the first term of equation (1.5) is still applicable in the bursting force formulation.

Figures 3.18 and 3.19 show similar plots of bursting force versus anchorage ratio to those in Fig. 3.17, but for different locations of reaction force, namely $0.25h$ and $0.50h$. The bearing ratio remains zero. According to these figures, as the reaction load is positioned further away from the anchor surface, the magnitude of the bursting force becomes smaller. In Fig. 3.18, the magnitude of the plot for R/P equal to 0.10 is slightly less than that using the equation. In Fig. 3.19, all plots from the finite element results now lie below the plot from the equation. Note that in the plots with the R/P ratio equal to 0.05 in Figs. 3.18 and 3.19, the magnitude of the bursting force is a little smaller than that with zero R/P . However, they are very close to each other. This may be resulted from computational manipulation of models with different node positions in the finite element method. Conclusively, for concentrically loaded anchorage zones, the first term of equation (1.5) gives a conservative value for anchorage zones which have the position of the reaction force placed furthest away from the anchorage surface. However, it is shown that equation (1.5) is no longer conservative for the design of anchorage zones with a support reaction based on the results in Figs. 3.17 and 3.18.

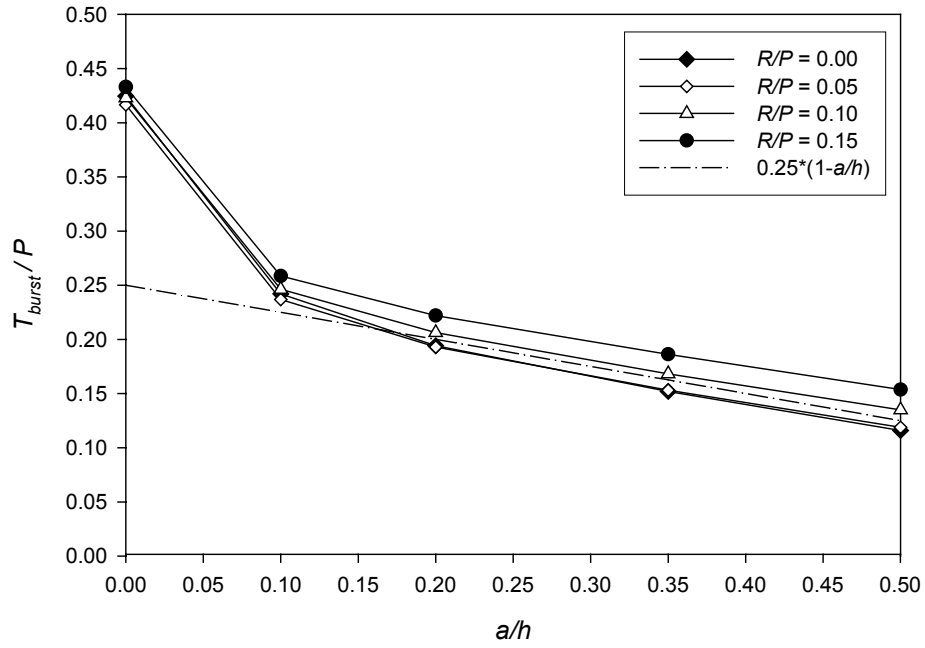


Fig. 3.17 BURSTING FORCE vs. ANCHORAGE RATIO ($b/h = 0.0, l/h = 0.125$)

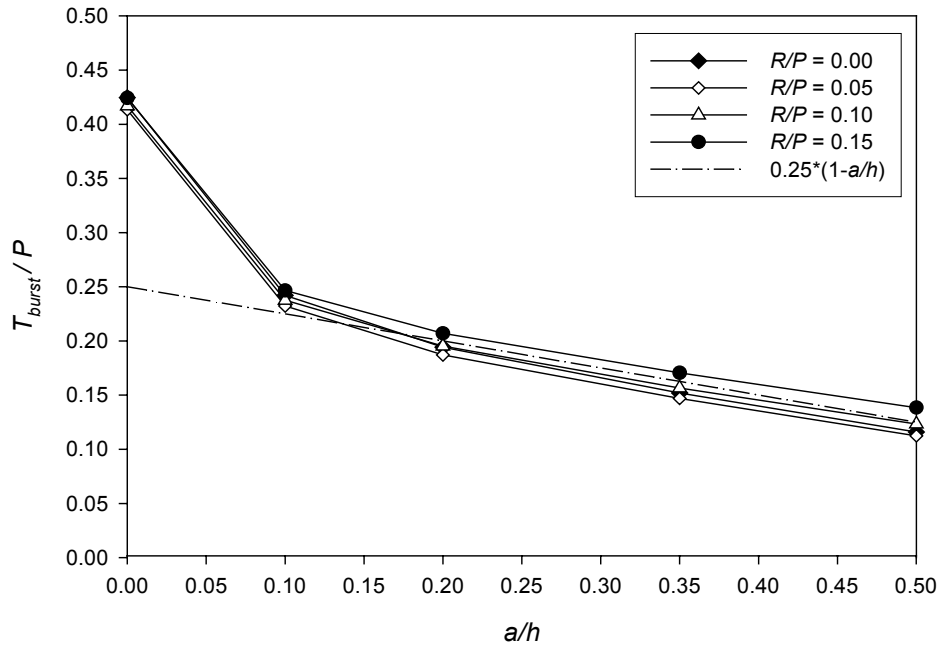


Fig. 3.18 BURSTING FORCE vs. ANCHORAGE RATIO ($b/h = 0.0, l/h = 0.25$)

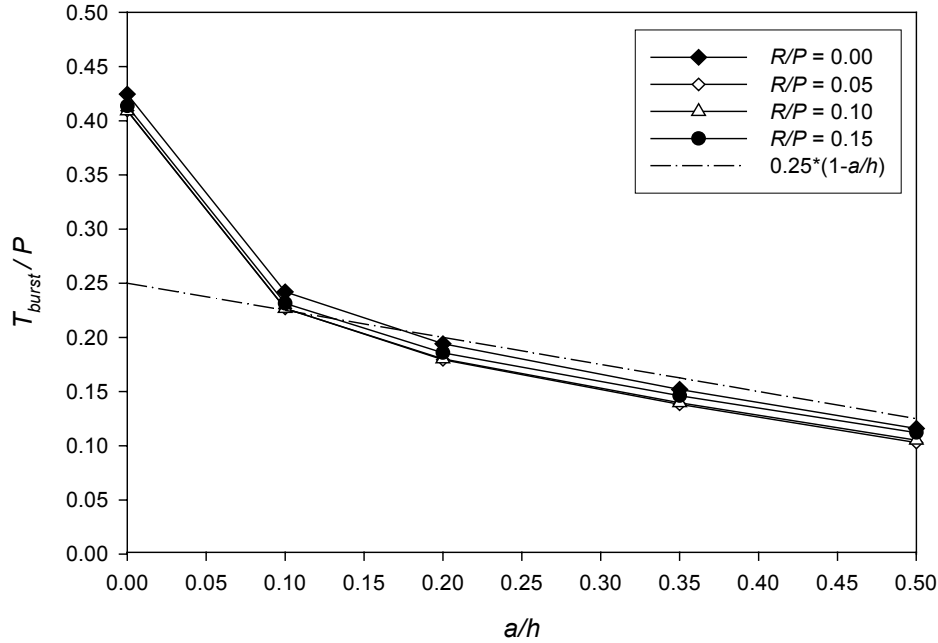


Fig. 3.19 BURSTING FORCE vs. ANCHORAGE RATIO ($b/h = 0.0$, $l/h = 0.50$)

Figure 3.20 shows the relation between bursting force and location of the support reaction for all values of a/h and R/P . The bearing plate ratio remains zero. The characteristics of the plots are similar for each a/h . When the reaction force is applied close to the anchorage surface, the bursting force from each value of R/P is obviously different for each a/h ratio. When the force is further away, approaching the position of l/h equal to 0.50, the bursting force from each plot converges to the lowest value. An observation can be made from the plots with the R/P ratio equal to 0.05. The plots seem to be nearly parallel to a horizontal line. Fig. 3.20 leads to the conclusion that the largest bursting force with respect to the location of the reaction force can be determined from the load configuration with the closest location of the support reaction to the surface of the anchorage zone. The furthest position of support reaction results in the smallest bursting force magnitude for concentrically loaded anchors with support reaction. Fig. 3.21 shows the stress contours of an anchorage zone subjected to a support reaction located at the l/h value 0.50. Compared to Fig. 3.16b, the contours of stresses in Fig. 3.21 are farther from the anchorage surface and distributed freely within the body of anchorage zone. The position of the support reaction results in stress propagating into the region of the bursting stresses presented in Fig. 3.13a.

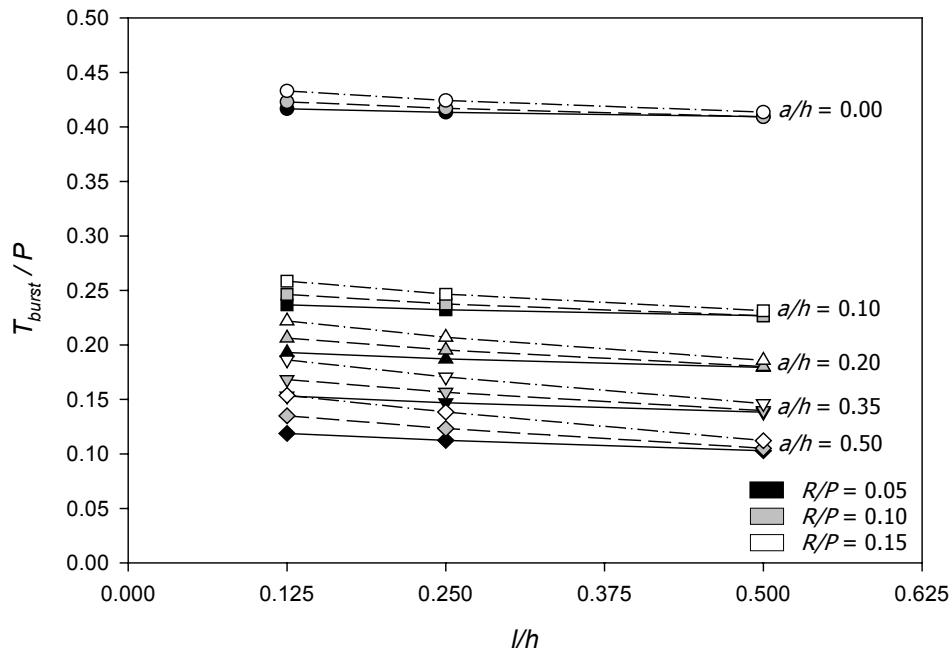


Fig. 3.20 BURSTING FORCE vs. LOCATION OF SUPPORT REACTION ($b/h = 0.0$)

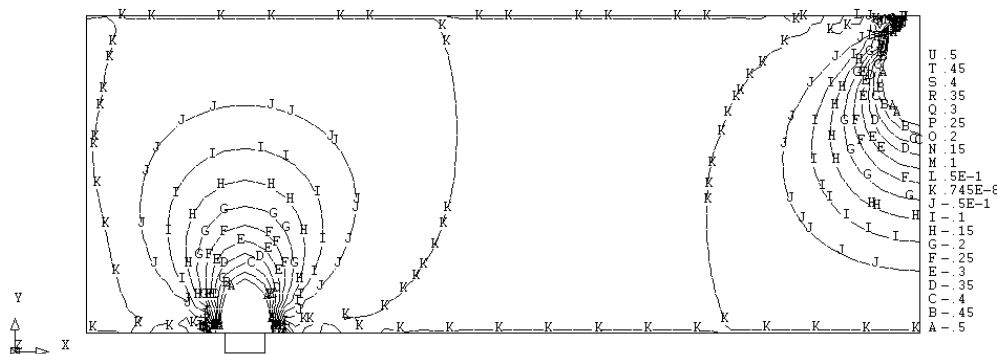


Fig. 3.21 STRESSES DUE TO REACTION LOAD WITH $R/P = 0.15$ AND $l/h = 0.50$
(Stress multiplied by σ_0)

Figures 3.22 through 3.24 show the relation between the bursting force and the bearing support ratio for three different support locations. As can be seen, the plots of all cases are similar in that they are almost parallel to a horizontal line. This indicates that the b/h ratio has a very slight effect on the magnitude of the bursting force for the case of concentrically loaded anchorage zones without inclination. Therefore, the bearing support term can be neglected in the formulation of the bursting force.

Figure 3.25 shows stress contours on a rectangular body subjected to a support reaction with three different bearing plate ratios: 0, 0.125, and 0.25. The only difference among these contour plots is the stress concentration immediately above the bearing support. If the line of the main compressive strut is assumed to be located in the upper half of the anchorage zone, the stress distribution in each picture at this level shows a similar contour shape. Based on linear elastic analysis, the stress values at a given node resulting from two models with exactly the same configuration but different load application can be combined together. In other words, the law of superposition can be applied to linear elastic finite element method. This explains how the bursting force in anchorage zones subjected to the same magnitude of reaction force but with different bearing plate size retains the same magnitude if the main compressive strut is located far away from the support reaction as shown in Figs. 3.22 to 3.24.

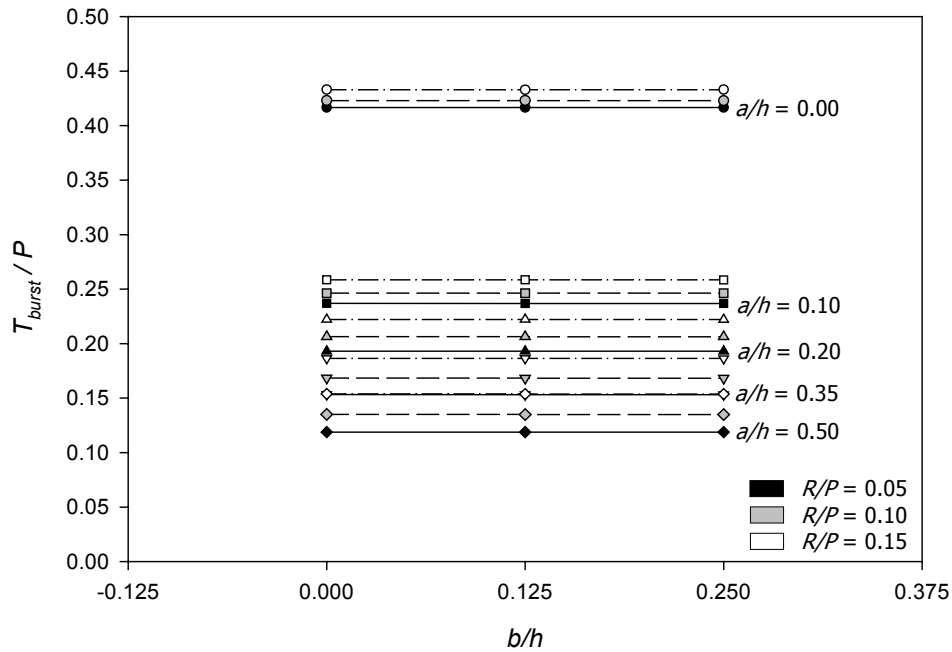


Fig. 3.22 BURSTING FORCE vs. BEARING PLATE RATIO ($l/h = 0.125$)

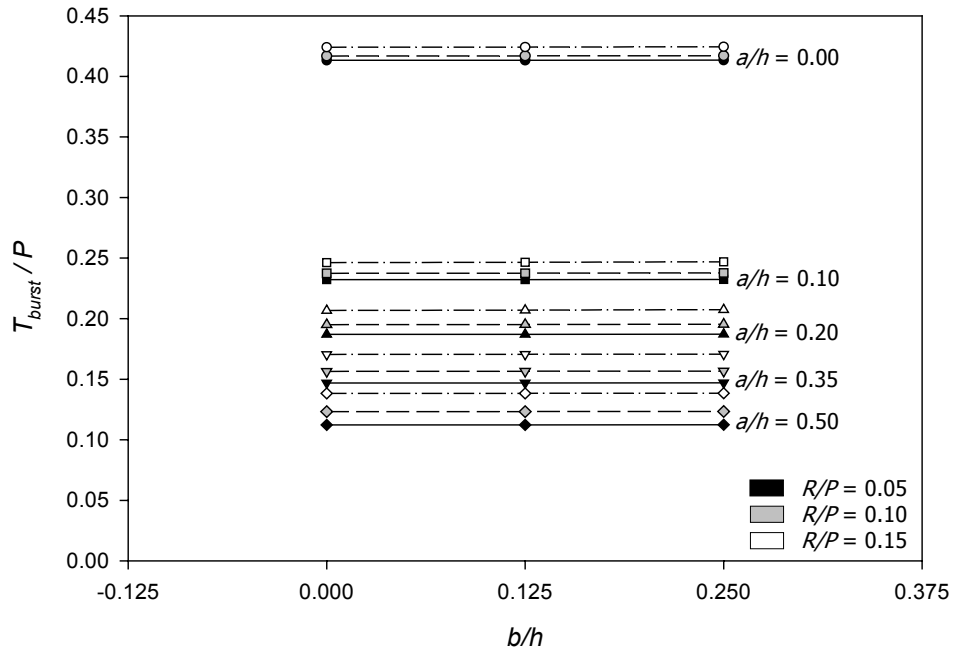


Fig. 3.23 BURSTING FORCE vs. BEARING PLATE RATIO ($l/h = 0.25$)

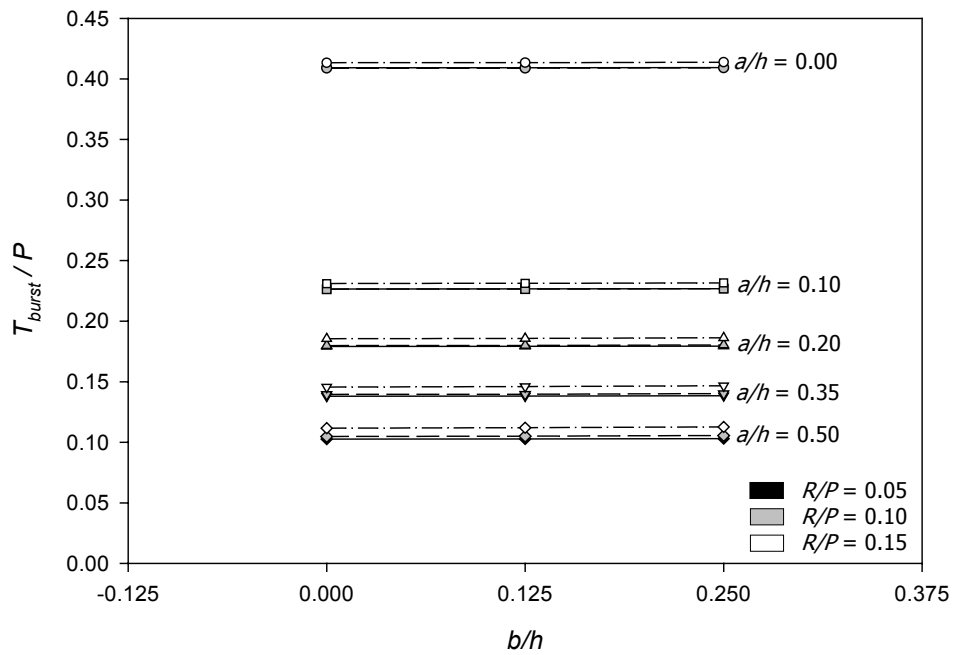


Fig. 3.24 BURSTING FORCE vs. BEARING PLATE RATIO ($l/h = 0.50$)

In Fig. 3.25, an observation can be made about the region between the two vertical supports: almost zero stress was detected in this region. This confirms that the full effect of the reaction force is seen in the vertical tensile stress in the bursting region. On a horizontal line, the reaction force decreases the magnitude of the tensile stress. However, the bursting stresses are not reduced in magnitude; instead they are rotated up in the direction of the resultant vector of the forces. But the angle of the vector is bounded and relocated by the edge of the structure.

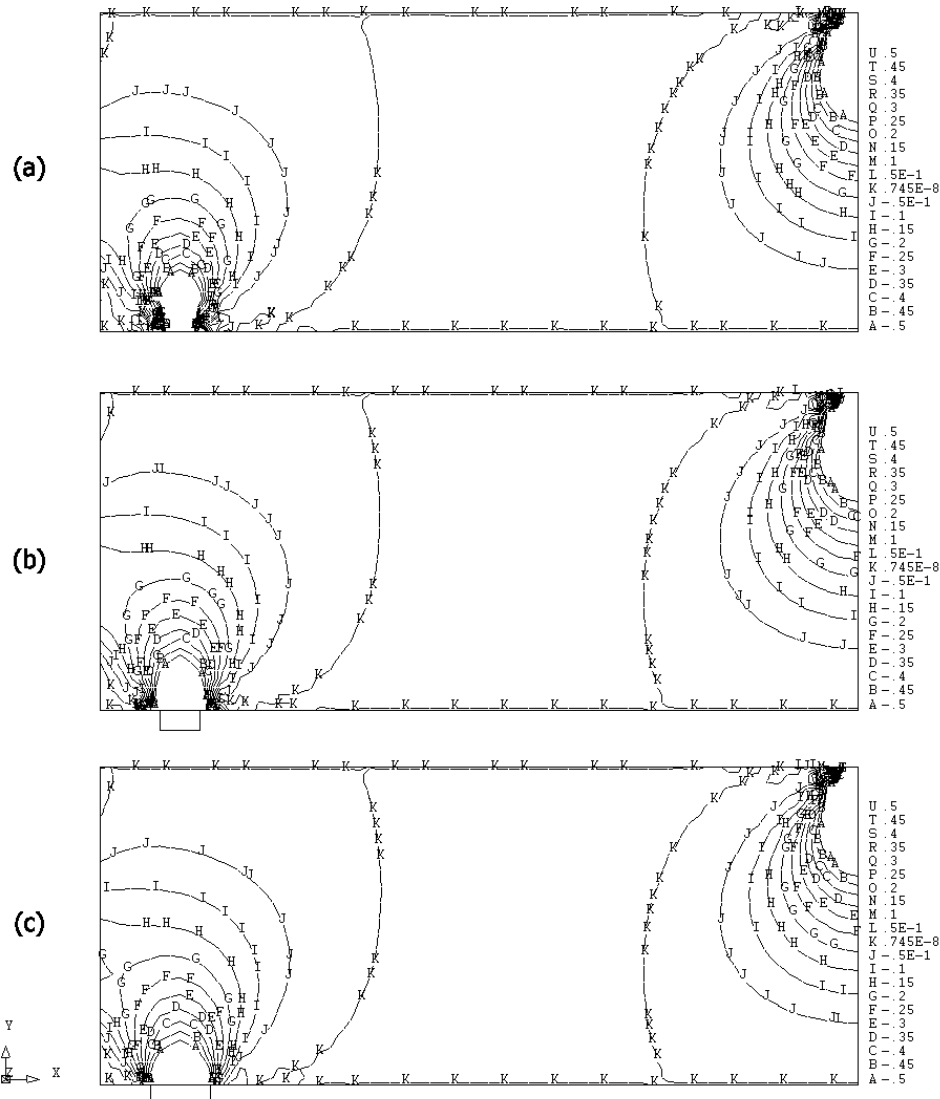


Fig. 3.25 Y-Y STRESSES DUE TO REACTION LOAD WITH $R/P = 0.15$, $l/h = 0.25$, AND $b/h =$
a) 0.0, b) 0.125, AND c) 0.25 (Stress multiplied by σ_0)

Since the bearing ratio can be neglected and the position of the support reaction which can produce a conservative result is determined, the next task is to investigate the effect of the magnitude of the reaction force. Figs. 3.26 through 3.28 show the relation between the bursting force and the reaction force with different support location. As can be seen, the plots do not vary linearly as the magnitude of the reaction force increases. The slopes vary as the R/P value increases. A unique characteristic detected from all plots is that they vary in a concave upward manner. Therefore, a conservative equation for determining a bursting force can be found by using a line drawn from one end of the plot to the other end (see Fig. 3.26). To achieve the most conservative equation to determine the bursting force for the concentric load configuration, the equation must be developed from the line which contains the largest increasing slope.

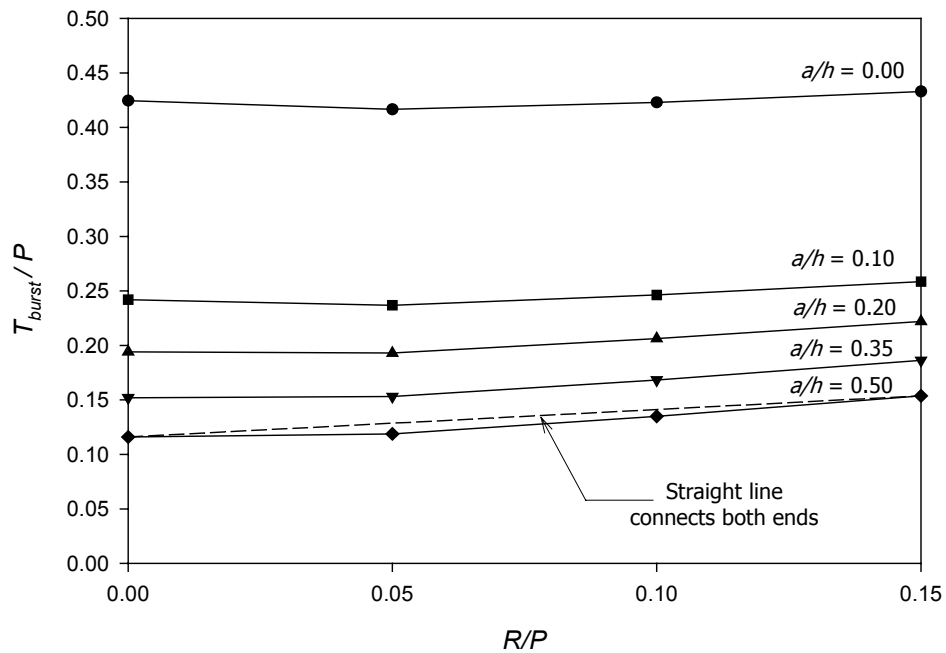


Fig. 3.26 BURSTING FORCE vs. REACTION RATIO ($l/h = 0.125$, $b/h = 0.0$)

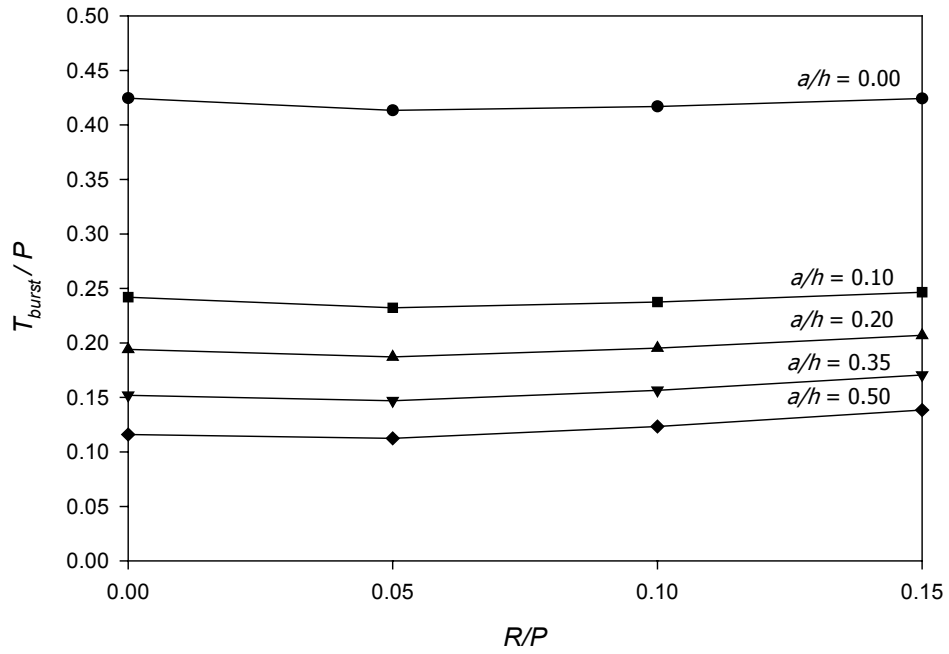


Fig. 3.27 BURSTING FORCE vs. REACTION RATIO ($l/h = 0.25$, $b/h = 0.0$)

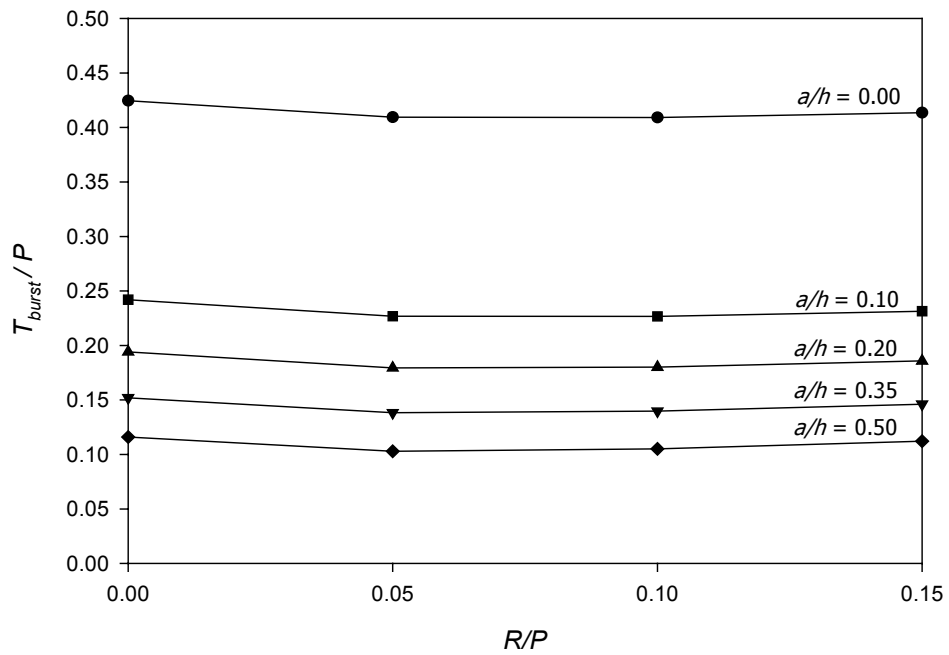


Fig. 3.28 BURSTING FORCE vs. REACTION RATIO ($l/h = 0.50$, $b/h = 0.0$)

Table 3.3 presents the values of the slopes of the straight lines that connect the ends of each plot in Figs. 3.26 through 3.28. The plot of anchorage ratio of 0.50 in Fig. 3.26 has the largest increasing slope of the straight line. Since the first term of equation (1.5) is used for the calculation of bursting force with zero support reaction, an additional term can be added to the equation to take the magnitude of the support reaction into account. The new term can be evaluated by using the value of largest slope, 0.25, multiplied by the reaction term, which is presented by the R/P ratio. An example comparison of finite element result and the modified equation is shown in Fig. 3.29.

Table 3.3 SLOPES OF STRAIGHT LINE FOR T_{burst}

a/h	Fig. 3.26	Fig. 3.27	Fig. 3.28
0.00	0.0555	-0.0022	-0.0735
0.10	0.1105	0.0311	-0.0705
0.20	0.1860	0.0857	-0.0553
0.35	0.2288	0.1239	-0.0395
0.50	0.2514	0.1492	-0.0255

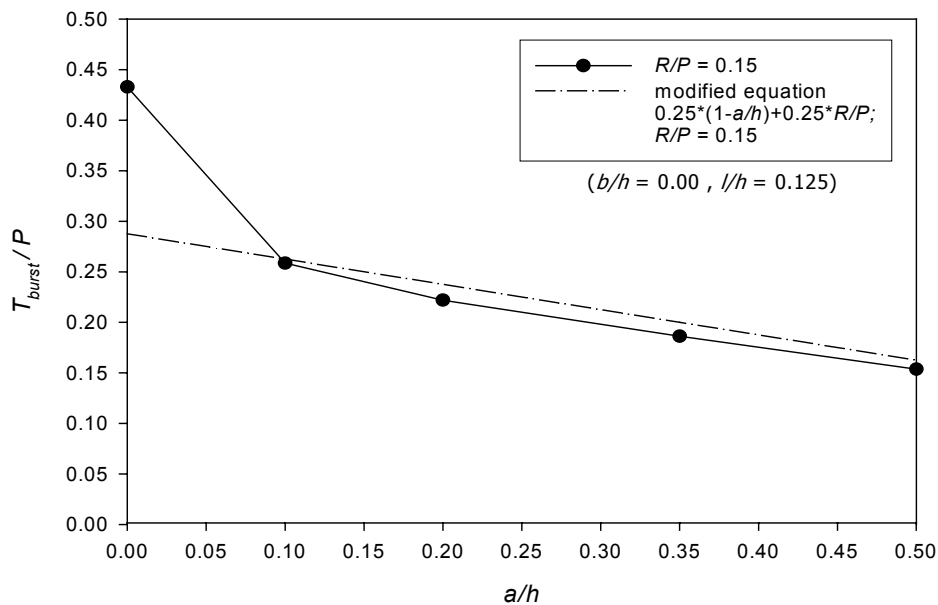


Fig. 3.29 COMPARISON OF FINITE ELEMENT RESULT AND MODIFIED EQUATION

Figure 3.29 presents the finite element result of an anchorage zone with 15 percent of prestressing load applied as a support reaction, which is considered to have the highest bursting force from all plots previously presented and the result from using the modified equation. The equation gives a conservative result compared to finite element analysis. This equation is applicable for the design of concentrically loaded anchorage zones with the magnitude of reaction force falling within the range of zero to 15 percent of the prestressing load.

3.4.1.3 Location of Bursting Force

This section illustrates the study of the location of the bursting force (d_{burst}). The location of bursting force discussed in the present study means the location of the centroid of the bursting stresses normal to the centerline of the anchorage zone (see Fig. 3.9). The position of the bursting force is as important as the magnitude of the bursting force. If reinforcing steel is not located properly, cracks in the concrete within the bursting region will develop and diminish the strength of the anchorage zone. As previously mentioned in Chapter 1, the AASHTO method allows the d_{burst} value to be determined from equation (1.6). A physical explanation of the expression is that the reinforcement must have a centroid equal to the distance of half of the section width ($h/2$) plus the term resulting from an inclination effect and eccentricity if both are present ($5e \sin \alpha$) with a consideration of the direction of the force relative to a horizontal axis passing through the anchor plate center.

In anchorage zone design, a conservative practice is to use a value of d_{burst} close to or slightly larger than the result determined by finite element analysis combined with a safe bursting force magnitude. Figs. 3.30 through 3.32 present the relation between d_{burst} and anchorage ratio (a/h) with different reaction location. The d_{burst} value is presented by dividing by the section width (h). As seen from the figures, the d_{burst}/h value on each plot approaches a straight line at the values of a/h from 0.20 to 0.50. The larger magnitudes of R/P result in larger distances of the bursting force from the anchor surface for the concentric load case. A plot of d_{burst}/h from the first term of equation (1.6) is also presented in Figs. 3.30 through 3.32. The equation gives a much smaller value of d_{burst}/h for a/h values of 0.20

to 0.50 compared to finite element results and shows no variation due to the change of the anchorage ratio.

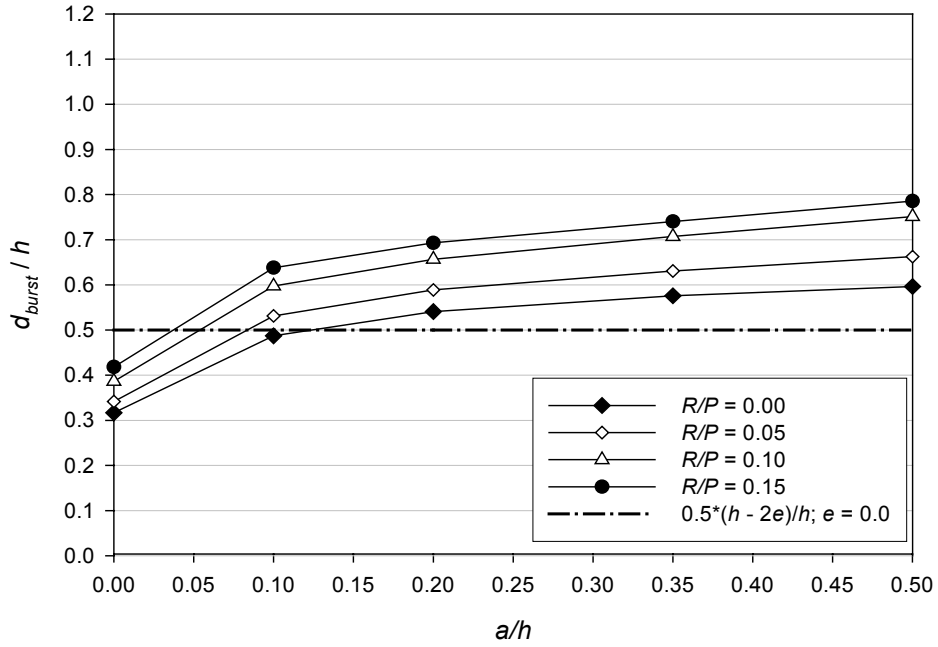


Fig. 3.30 BURSTING FORCE LOCATION vs. ANCHORAGE RATIO ($b/h = 0.0, l/h = 0.125$)

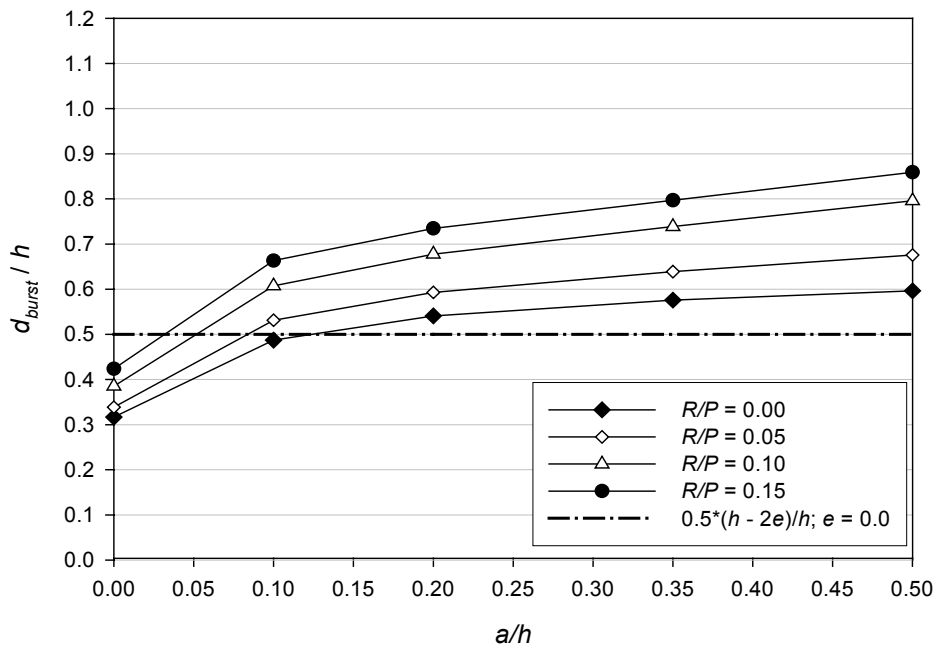


Fig. 3.31 BURSTING FORCE LOCATION vs. ANCHORAGE RATIO ($b/h = 0.0, l/h = 0.25$)

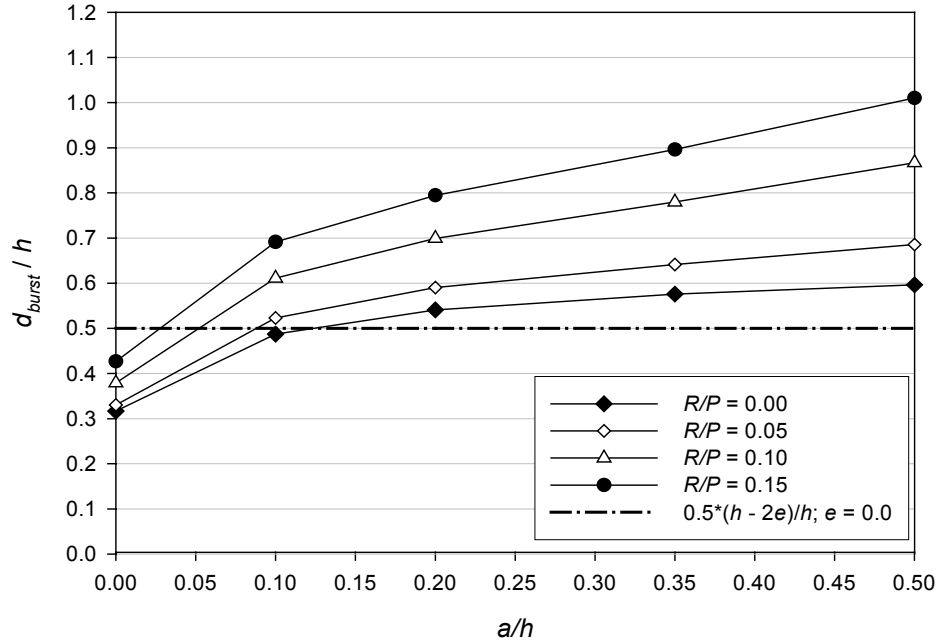


Fig. 3.32 BURSTING FORCE LOCATION vs. ANCHORAGE RATIO ($b/h = 0.0$, $l/h = 0.50$)

Figure 3.33 shows the comparison of the plots of d_{burst} from three different methods consisting of finite element method, the first term of equation (1.6), and a modification of the term. By including the anchorage ratio (as the second term of the modified equation shown in Fig. 3.33), a better agreement is produced in which the new plot more closely parallels the plot from the finite element method. A physical explanation of the modified term is that the distance of the bursting force extends from the anchorage surface for a distance of half of its section width plus a quarter of the anchorage plate width. This modified equation needs to be further developed to include the effect of the support reaction. Figs. 3.34 and 3.35 present the relation between d_{burst} and support reaction location (l/h) for the magnitude of reaction of 5 percent and 15 percent of prestressing force, respectively. As can be seen, the variation of the plots with the smaller magnitude of reaction is not as obvious as that with the larger one. This indicates that for an anchorage zone with a large reaction force, as the distance from the reaction to the prestressing surface increases, the location of the bursting force moves further away. With the same magnitude of bursting force while the reinforcement is located closer to anchor surface, anchorage zone remains conservative in design. The cracks usually originate at the position of maximum tensile stress, which is located closer to the anchorage

surface than the location of the bursting stress centroid. As the magnitude of the prestressing force reaches the first cracking load level of the structure, the reinforcement helps to withstand the maximum tensile stress and results in an increasing of strength of the structure. Therefore neglecting the parameter of support location in the formulation of d_{burst} is acceptable.

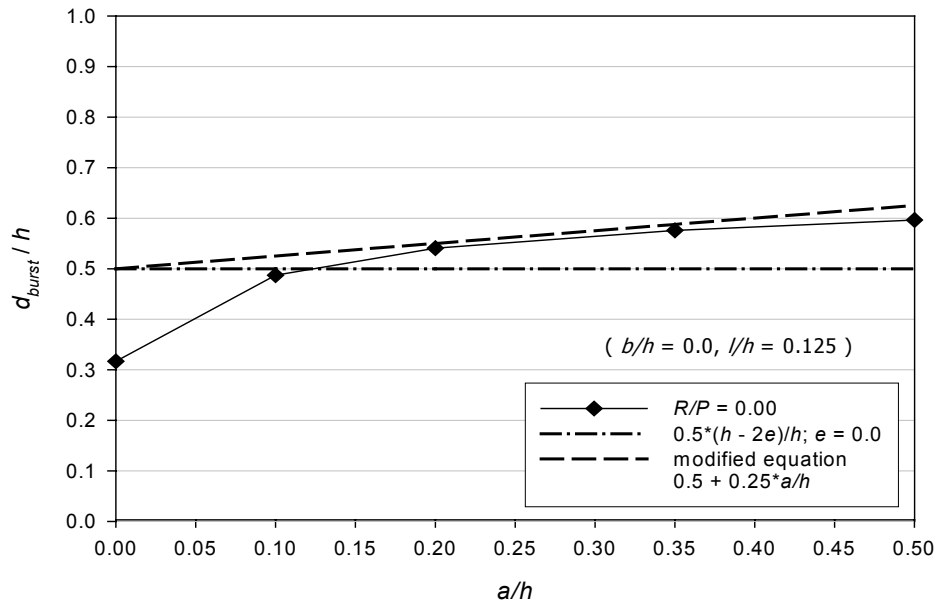


Fig. 3.33 COMPARISON OF d_{burst} WITH MODIFIED EQUATION

The bearing plate ratio has the same effect on the location of the bursting force as on the magnitude of the bursting force. The distance d_{burst} does not vary with the change of the bearing support width. Fig. 3.36 shows an example of the relation between the distance of the bursting force and the bearing plate ratio for the ratio of support location to section width (l/h) equal to 0.50. Similar plots result from different values of l/h . Therefore, based on the study of concentrically loaded anchors, the parameter b/h is not considered in the formulation of bursting force and its location.

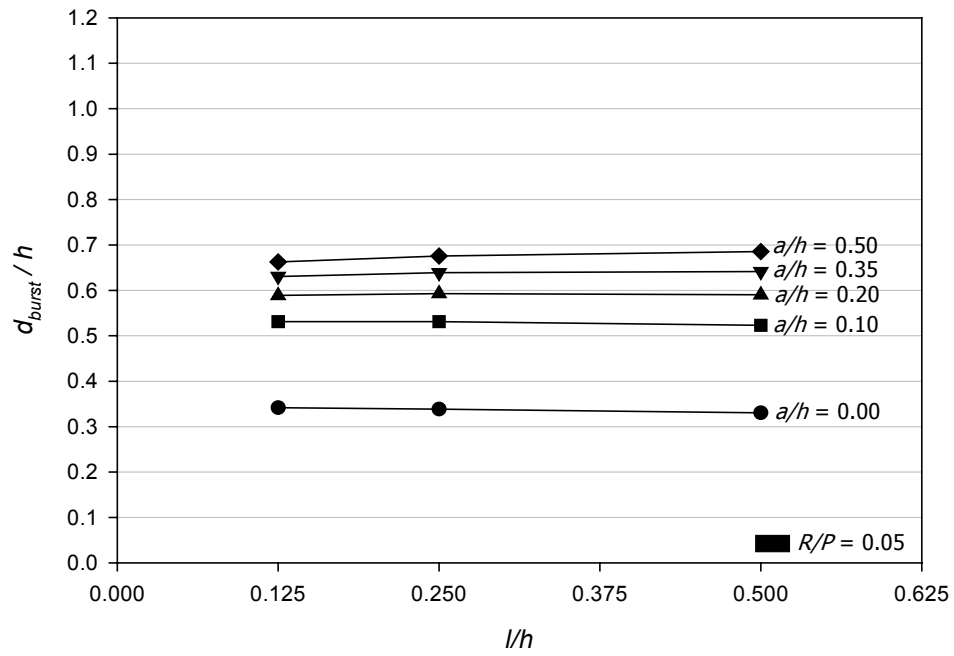


Fig. 3.34 BURSTING FORCE LOCATION vs. LOCATION OF SUPPORT REACTION ($R/P = 0.05$)

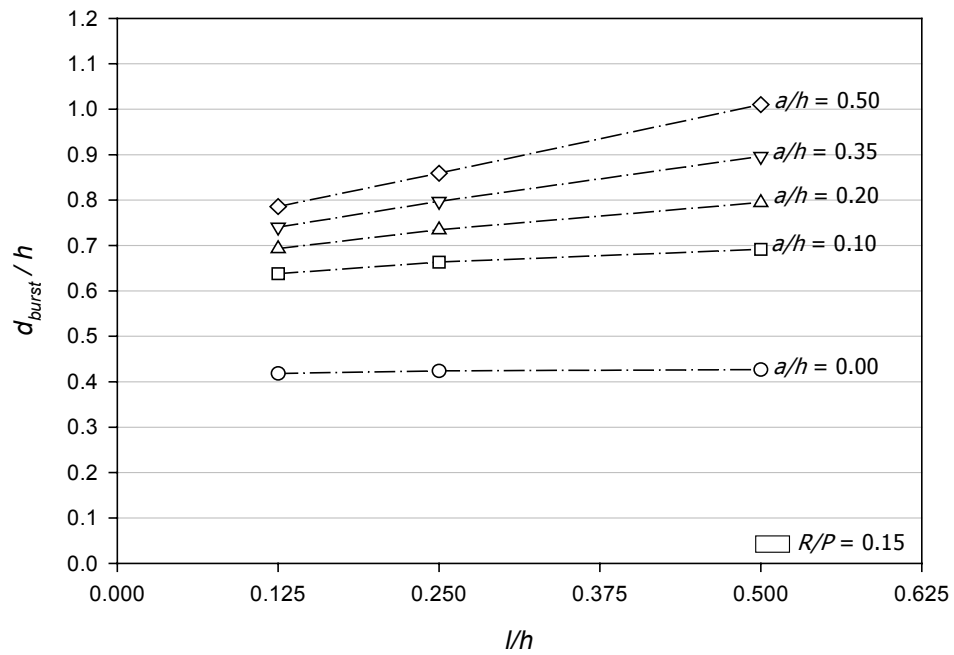


Fig. 3.35 BURSTING FORCE LOCATION vs. LOCATION OF SUPPORT REACTION ($R/P = 0.15$)

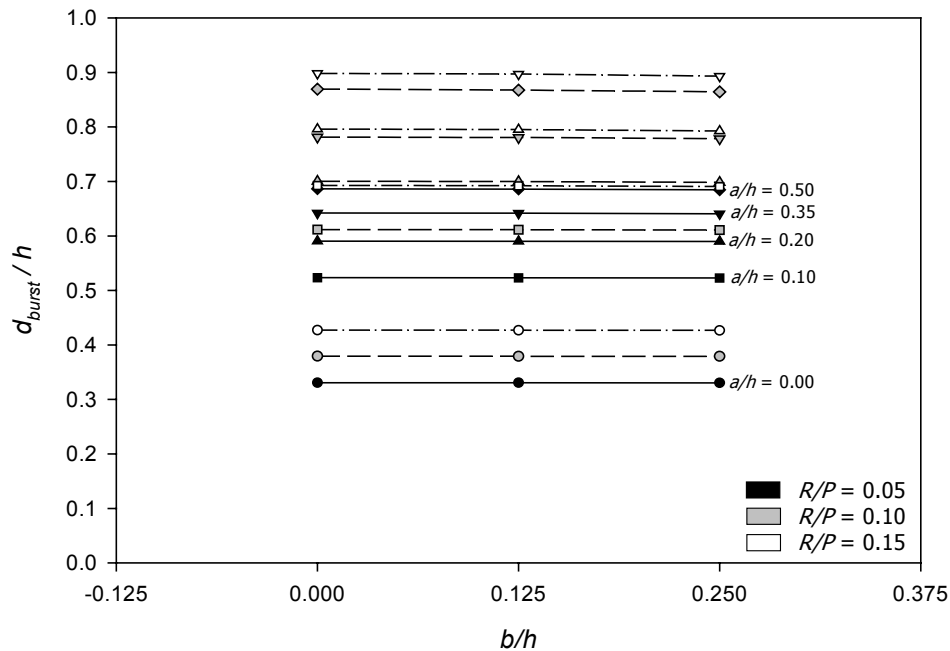


Fig. 3.36 BURSTING FORCE LOCATION vs. BEARING PLATE RATIO ($l/h = 0.50$)

The magnitude of the reaction force (R/P) is significant for the location of the bursting force. As previously stated, a good prediction of the distance of the bursting force results in a value close to or larger than what finite element analysis provides. In other words, if the predicted result establishes the smallest absolute value of percent difference compared to the result from finite element analysis, it is acceptable. As shown in Fig. 3.33, the modified equation produces a closer value of d_{burst} than that from equation (1.6). But it is only for the case of concentric load with no support reaction. To include the magnitude of the reaction force, the relation between the bursting force location and the magnitude of the reaction must be investigated thoroughly.

As shown in Figs. 3.37 through 3.39, a method similar to that illustrated in section 3.4.1.2 was used for finding an equation for estimating the bursting force location. A straight line connecting the ends of each plot (an example is shown in Fig. 3.37) is used for determining the slope. Instead of using the largest increasing slope, the expression for determining the location of bursting force is formulated using the average of slopes from all straight lines. Slopes of each straight line from Figs. 3.37 through 3.39 are listed in Table 3.4 along with the resulting of average slope.

By neglecting the effect of reaction location (l/h), the modified equation for the calculation of d_{burst} can be formulated. The value of 1.34 multiplied by the ratio of support reaction to prestressing load is included in the modified expression shown in Fig. 3.33. Fig. 3.40 presents an example plot comparing the result from the finite element method with the latest modified equation.

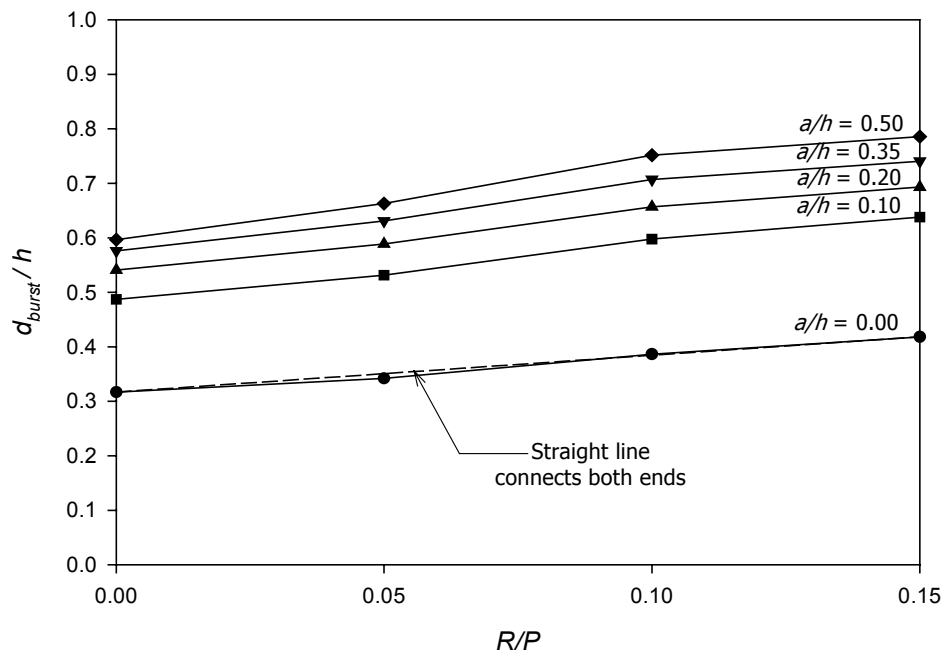


Fig. 3.37 BURSTING FORCE LOCATION vs. REACTION RATIO ($l/h = 0.125$, $b/h = 0.0$)

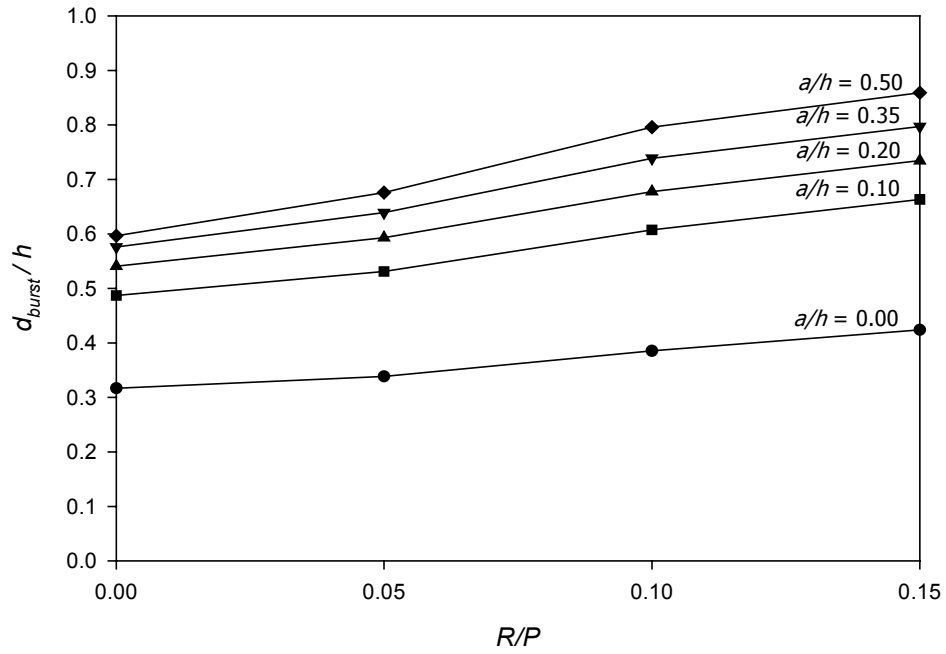


Fig. 3.38 BURSTING FORCE LOCATION vs. REACTION RATIO ($l/h = 0.25, b/h = 0.0$)

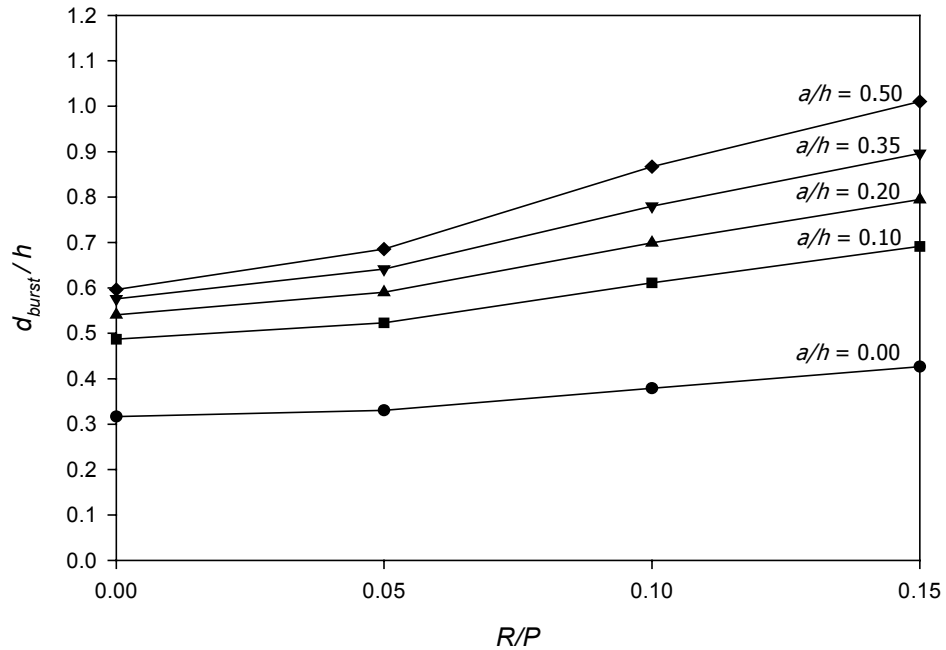


Fig. 3.39 BURSTING FORCE LOCATION vs. REACTION RATIO ($l/h = 0.50, b/h = 0.0$)

Table 3.4 SLOPES OF STRAIGHT LINE FOR THE PREDICTION OF d_{burst}

a/h	Fig. 3.37	Fig. 3.38	Fig. 3.39
0.00	0.6767	0.7138	0.7337
0.10	1.0058	1.1738	1.3631
0.20	1.0151	1.2915	1.6913
0.35	1.0987	1.4759	2.1348
0.50	1.2620	1.7501	2.7582
Average =		1.3430	

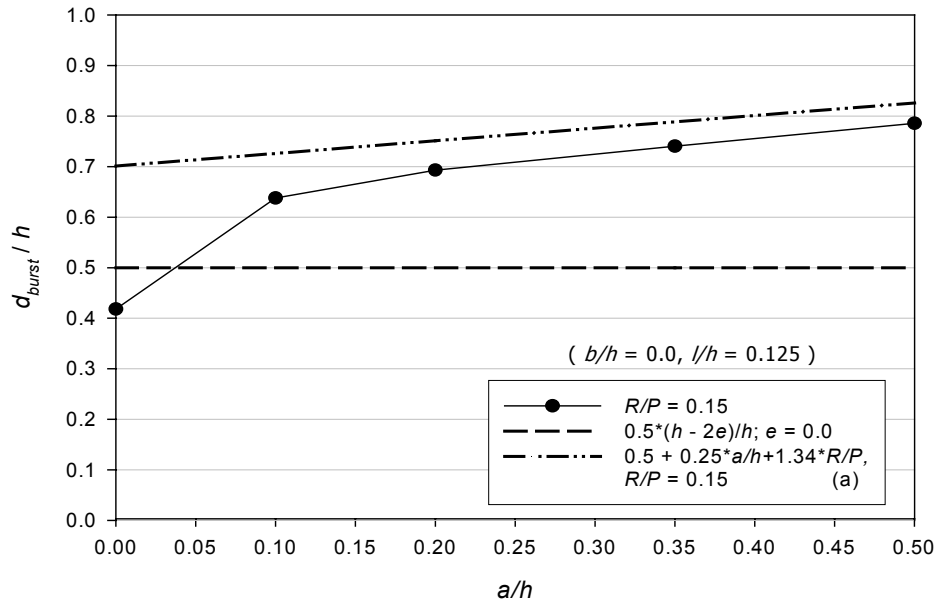


Fig. 3.40 MODIFIED EQUATION OF d_{burst} FOR CONCENTRIC LOAD CONFIGURATION

As can be seen, the modified equation with a coefficient of 1.34 multiplied by R/P (modified equation) gives a close prediction to the finite element result. The predicted result is slightly higher than that of the finite element analysis and it gives a closer approximation to the result from the finite element method than that given by equation (1.6). The equation performs best in the range of a/h from 0.20 to 0.50. Therefore, this confirms the applicability of using the modified equation to estimate a close value of d_{burst} to that given from the finite element prediction.

3.4.2 Inclined Concentrically Loaded Anchor Configuration

3.4.2.1 Elastic Stress Distribution

This section presents the study of inclined concentrically loaded anchorage zones with two inclination angles consisting of 6 and 9 degrees. With the unsymmetrical nature of typical structures and based on general configurations of inclined loaded anchorage zones, the selected angles in the present study are located in only the downward direction as shown in Fig. 3.9. Since there is only one case for the direction of inclination, the angle α always remains positive. The study presented herein is used for comparison with those in the previous section after all parametric studies are presented.

Figure 3.41 shows the contour plots of an anchorage zone subjected to a 6 degree inclined concentric load. As can be seen, the stress distribution deviates from the centerline of the anchorage zone in the direction of the inclination angle. With a deviation of 6 degrees downward in the figure, the bursting stress contour in Fig. 3.41a does not remain symmetric about the horizontal centerline. Although the contour plots may look only slightly different graphically compared to Fig. 3.13, the integration of stresses along the line of the inclined axis give an obvious difference numerically. Fig. 3.42 presents the contour plots of another anchorage zone with the application of a 9 degree inclined prestressing load. The contour plots in Fig. 3.42 show a larger deviation from horizontal symmetry than those in Fig. 3.41 based on Fig. 3.13.

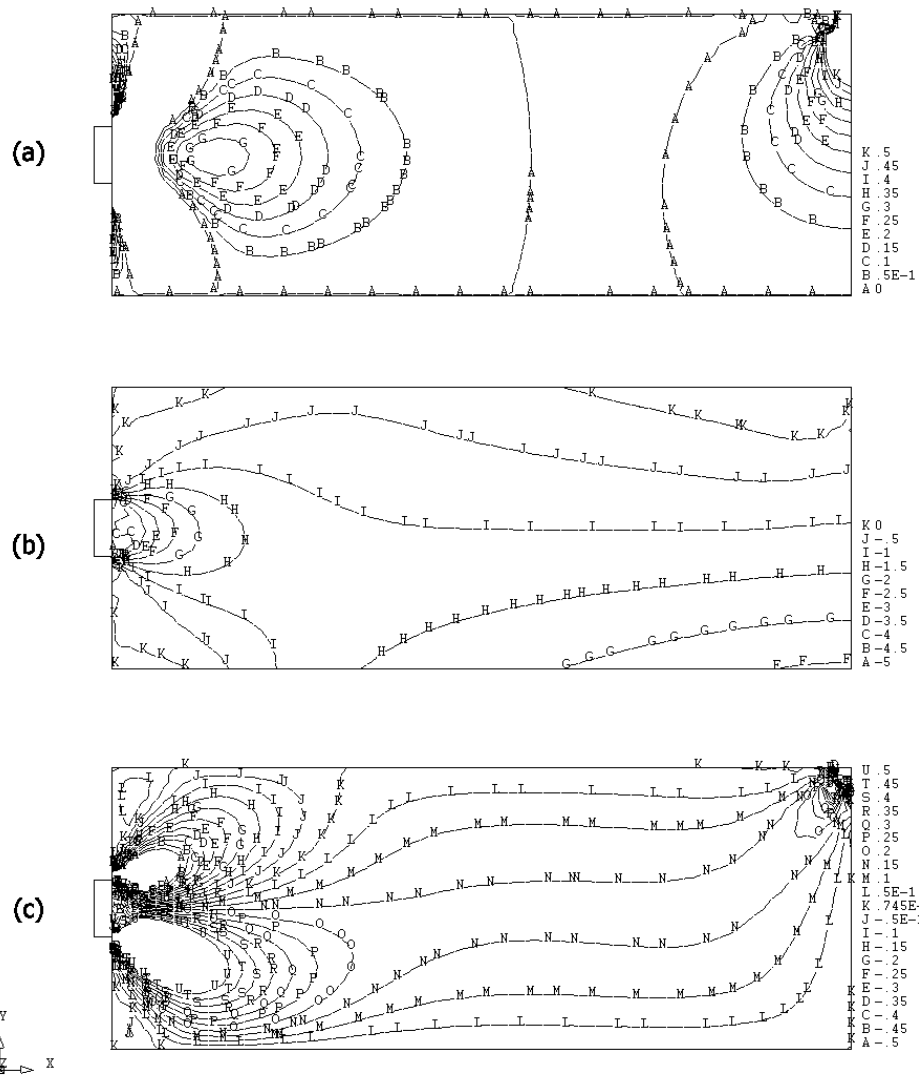


Fig. 3.41 6 DEGREE INCLINED CONCENTRIC LOAD WITH $a/h = 0.20$, $R/P = 0.00$
 a) S_{yy} , b) S_{xx} , AND c) S_{xy} (Stress multiplied by σ_0)

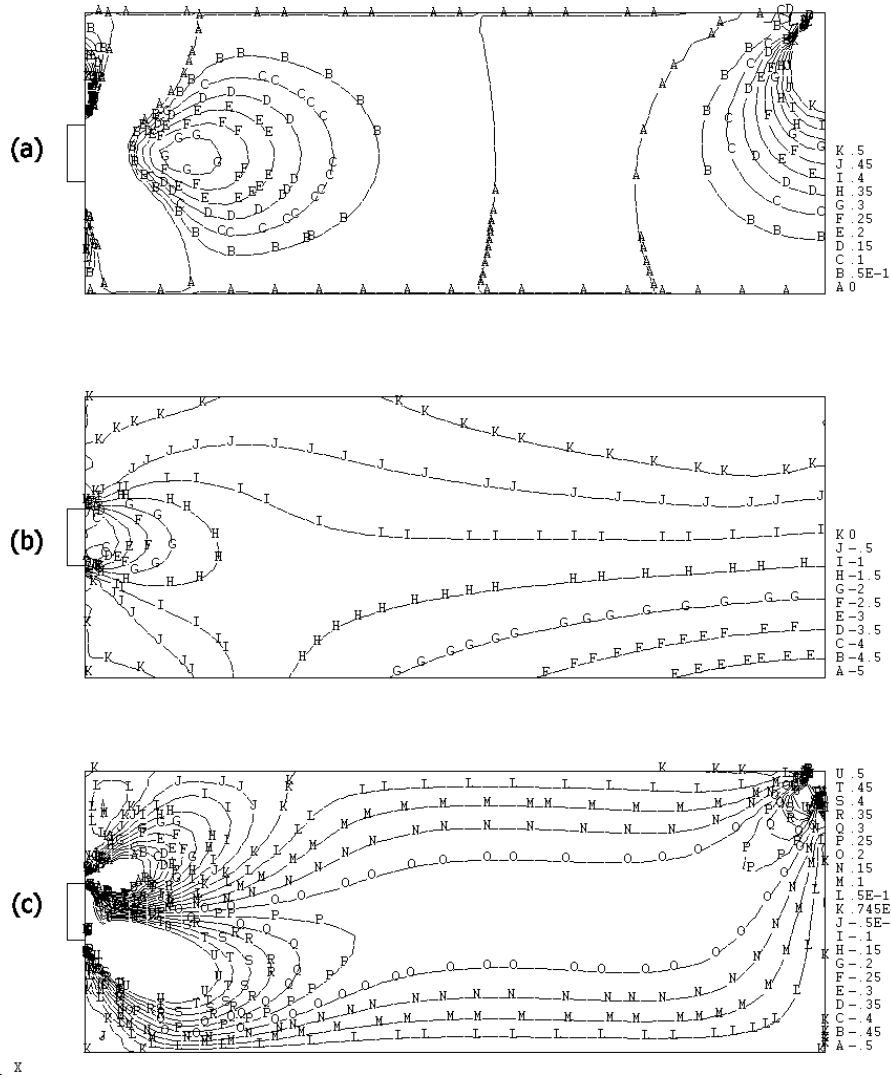


Fig. 3.42 9 DEGREE INCLINED CONCENTRIC LOAD WITH $a/h = 0.20$, $R/P = 0.00$
 a) S_{yy} , b) S_{xx} , AND c) S_{xy} (Stress multiplied by σ_0)

Another contour stress behavior is illustrated in Fig. 3.43. The anchorage zone is subjected to both an inclined prestressing load and a support reaction with a magnitude of 15 percent of the prestressing load. The stress distribution now deviates upward due to the larger reaction force acting at the lower bottom surface. The main compressive strut of this anchorage zone is located in the upper region with respect to the centerline. The maximum bursting stress now does not occur in the direction of the prestressing load. Similarly, the

integration of the bursting stress must be calculated along the main compressive strut direction.

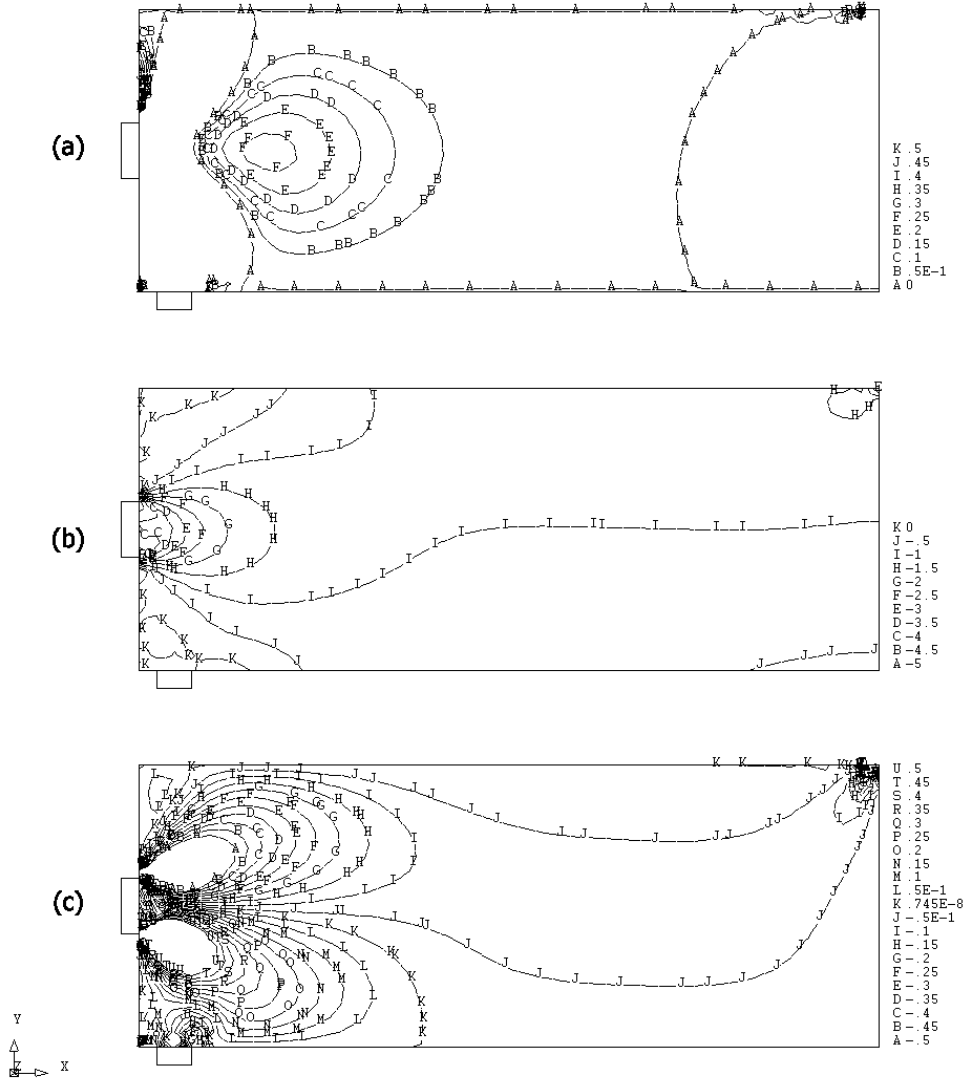


Fig. 3.43 6 DEGREE INCLINED CONCENTRIC LOAD WITH $a/h = 0.20$, $R/P = 0.15$
a) S_{yy} , b) S_{xx} , AND c) S_{xy} (Stress multiplied by σ_o)

As stated in section 3.3.2, the effect of inclination can be generally described as 50 percent of the vertical component of the inclined prestressing load. Fig. 3.44 shows the relation between the bursting force and the inclination angle for a concentrically loaded anchorage zone. The plots from the finite element results for each anchorage ratio are almost parallel to one another. As a result, it can be considered to use only one term, independent of

other parameters, to present the inclination effect. In Fig. 3.44, the comparison of the plot of the anchorage ratio of 0.20 with the plot using equation (1.5) is given. The plot from the equation is a straight line with a steeper slope compared to those from the finite element method. As the angle increases, the difference between the bursting force from the finite element method and the equation becomes larger. A closer prediction of the bursting force due to the inclination angle can be formulated by decreasing the value of the coefficient 0.50 in the second term of equation (1.5).

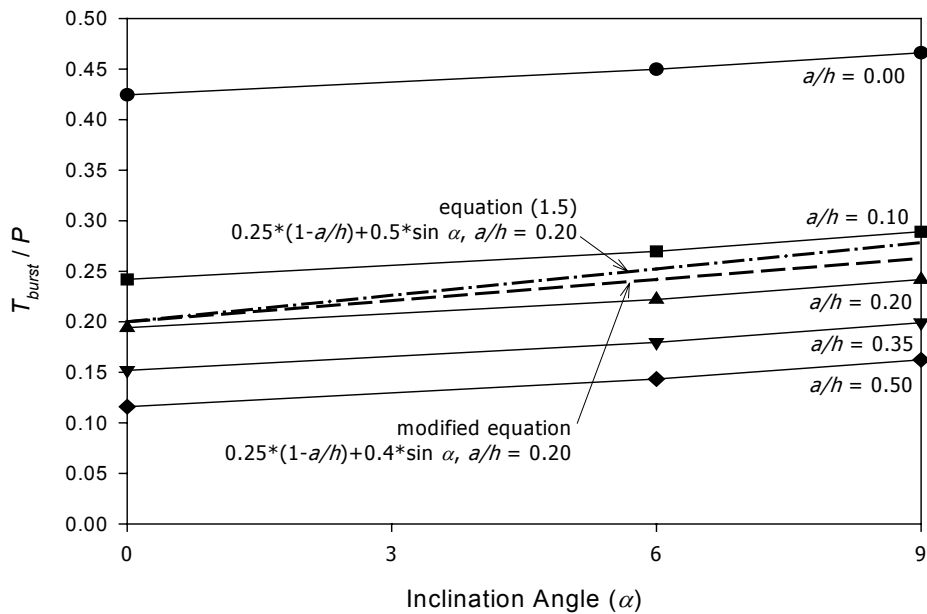


Fig. 3.44 BURSTING FORCE vs. INCLINATION ANGLE FOR CONCENTRIC LOAD

Considering a portion cut from a full structure of an anchorage zone subjected to an inclined concentric load as shown in Fig. 3.45, if the considered portion includes the region of the anchor, the integration of tensile stresses along the cut line does not equal 50 percent of the vertical component of the load. Instead it can be determined based on the shearing stress diagram at the end of the body. From the free body of the considered portion, the magnitude of P_{vl} is the resultant shear force occurring at the cutting edge of the considered portion. Based on the study of the basic concentric load configuration, it has been recognized that if equation (1.5) is used to predict the bursting force, the result is conservative for anchorage ratios larger than 0.15 (see section 3.3.1). By substituting 0.15

for the a/h value, the magnitude of P_{v1} becomes 0.3883 times total shear force or approximately 39 percent of the vertical component of the prestressing load. Therefore, the coefficient of 0.5 in the second term of equation (1.5) can be replaced with a more accurate number. A comparison of a modified equation using the coefficient of 0.40 is presented in Fig. 3.44. As can be seen, the modified equation produces a better agreement with the finite element results. However, equation (1.5) is more conservative.

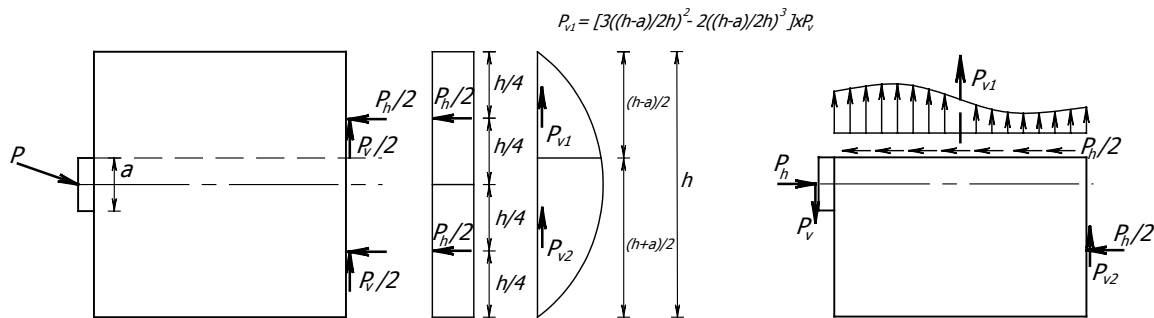


Fig. 3.45 VERTICAL STRESSES ON INCLINED CONCENTRICALLY LOADED ANCHORAGE ZONE

3.4.2.2 Bursting Force

Figures 3.46 through 3.51 show the relation between bursting force and anchorage ratio with six different load configurations consisting of 6 degree and 9 degree inclined concentric load combined with three different magnitudes of support reaction for each of the loads. Based on the overall characteristics of the plots, each plot has the same variation of bursting force with respect to the anchorage ratio as the plots for the concentric load configuration. Each plot begins to approach a straight line at the value of the anchorage ratio of 0.20. The influence of the R/P ratio is similar in the figures. The bursting force with a zero reaction force has the highest magnitude of all reaction forces. The next highest bursting force is with a reaction ratio (R/P) of 0.05. The lowest bursting force occurs with R/P of 0.15, which is the largest in the series. This indicates that for the inclined concentric load configuration, the maximum bursting force occurs in the configuration without a support reaction.

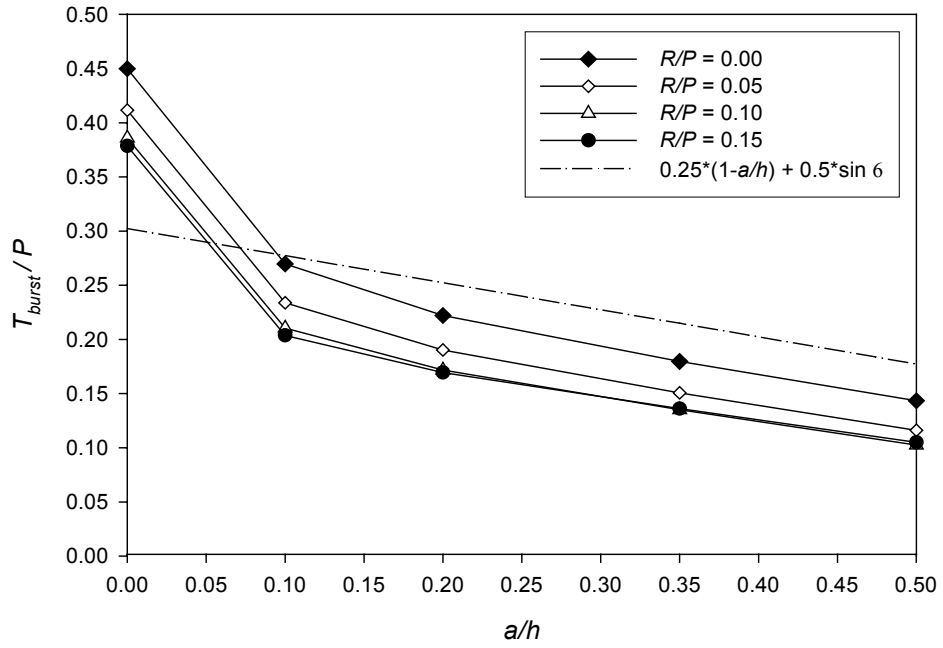


Fig. 3.46 BURSTING FORCE vs. ANCHORAGE RATIO FOR 6 DEGREE INCLINED CONCENTRIC LOAD
($b/h = 0.0$, $l/h = 0.125$)

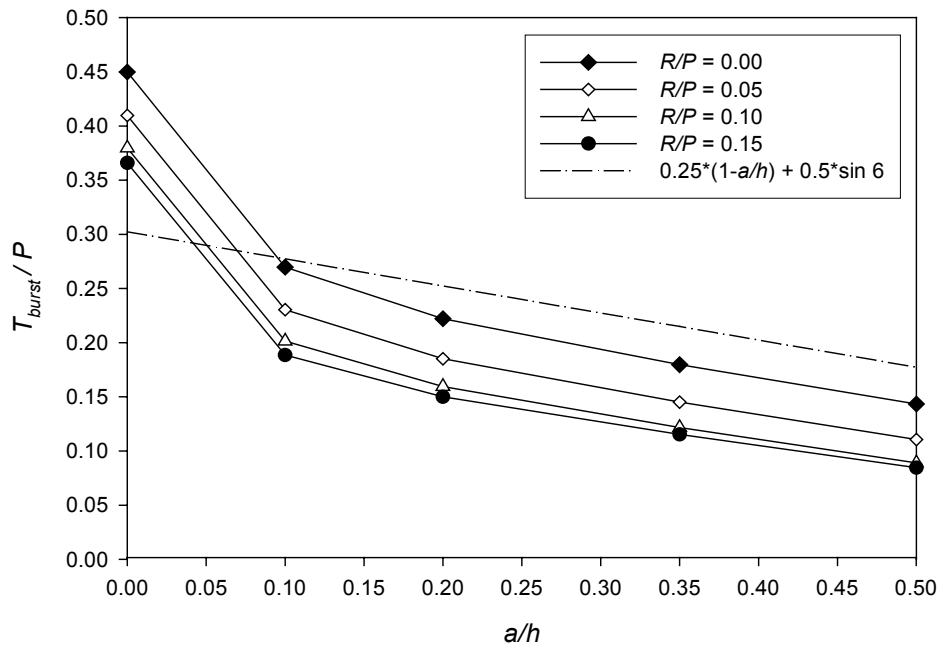


Fig. 3.47 BURSTING FORCE vs. ANCHORAGE RATIO FOR 6 DEGREE INCLINED CONCENTRIC LOAD
($b/h = 0.0$, $l/h = 0.25$)

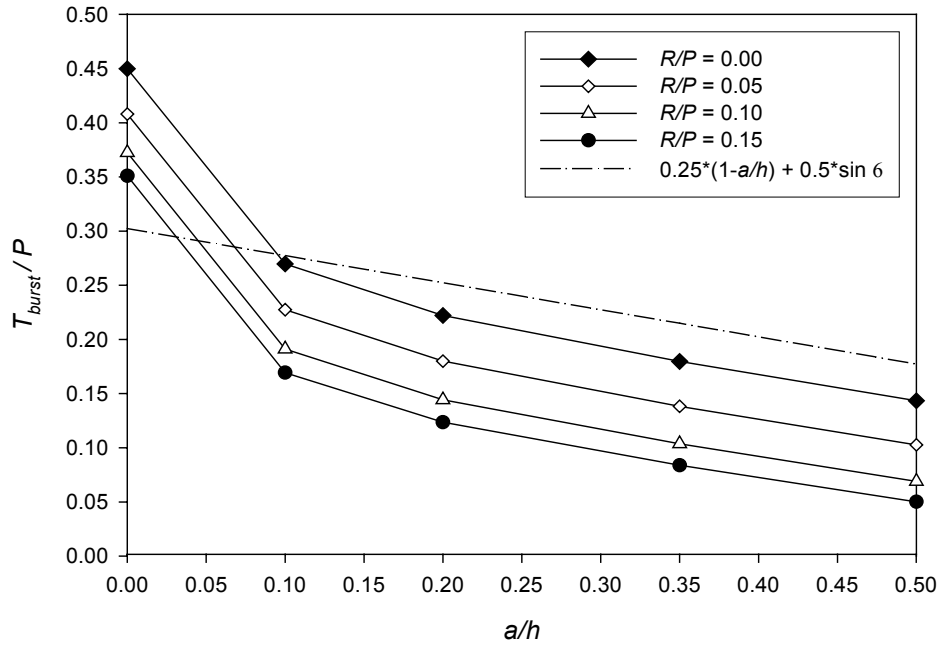


Fig. 3.48 BURSTING FORCE vs. ANCHORAGE RATIO FOR 6 DEGREE INCLINED CONCENTRIC LOAD
($b/h = 0.0$, $l/h = 0.50$)

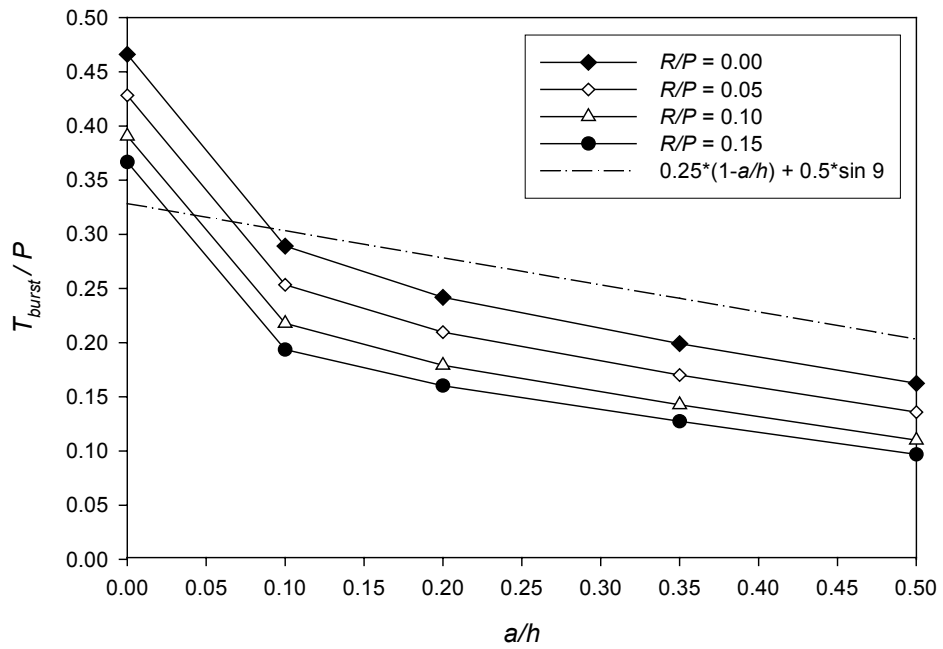


Fig. 3.49 BURSTING FORCE vs. ANCHORAGE RATIO FOR 9 DEGREE INCLINED CONCENTRIC LOAD
($b/h = 0.0$, $l/h = 0.125$)

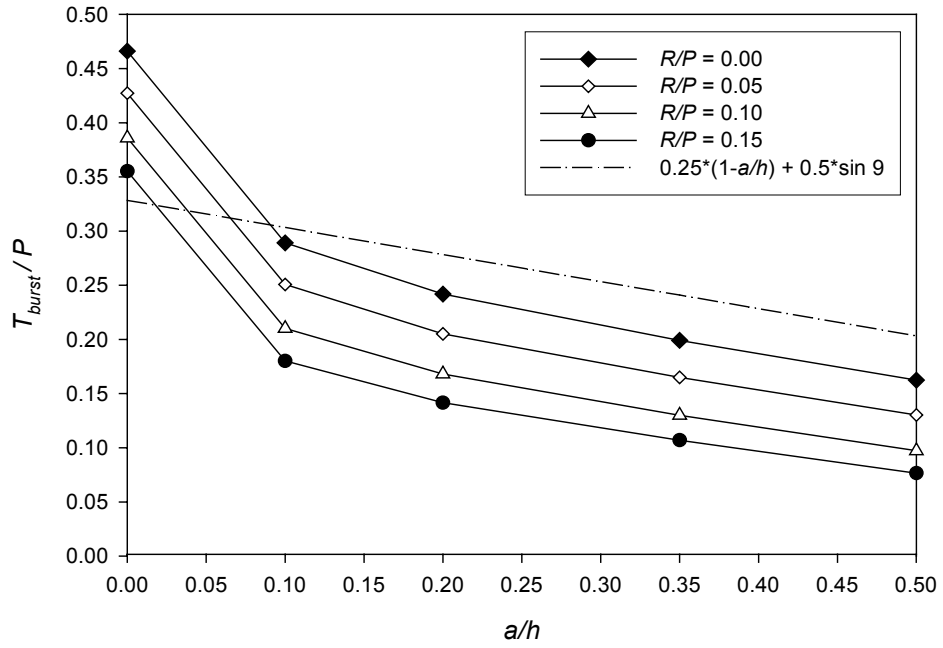


Fig. 3.50 BURSTING FORCE vs. ANCHORAGE RATIO FOR 9 DEGREE INCLINED CONCENTRIC LOAD ($b/h = 0.0, l/h = 0.25$)

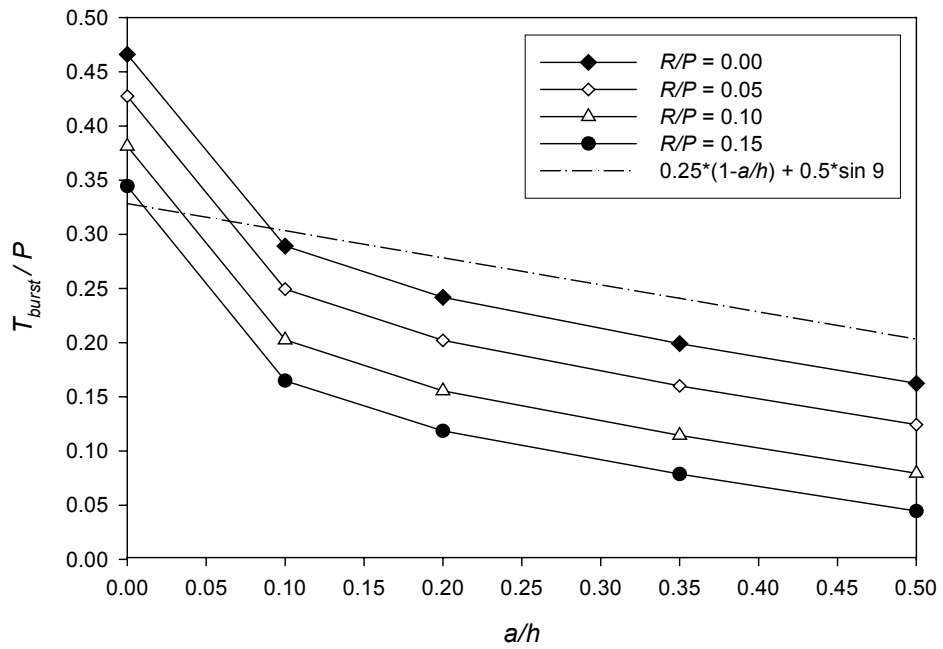


Fig. 3.51 BURSTING FORCE vs. ANCHORAGE RATIO FOR 9 DEGREE INCLINED CONCENTRIC LOAD ($b/h = 0.0, l/h = 0.50$)

In Figs. 3.46 through 3.51, the plot from equation (1.5) is also presented for comparison. As can be seen, the result given by the equation shows a conservative bursting force in every case. Based on the finite element results, the presence of a support reaction seems to reduce the magnitude of the bursting force for both inclination angles. The bursting force prediction given by equation (1.5) gives a very conservative result for anchorage zones with support reaction, especially in the case of a large reaction force. This may be reduced by adding the effect of support reaction into the calculation of the bursting force. According to all the figures discussed, no significant change in sequence of the plots due to the effect of the location of support reaction (l) is observed in each figure.

Figures 3.52 and 3.53 present the relation between the bursting force and the location of the support reaction for the inclination angles of 6 degrees and 9 degrees, respectively. As can be seen, the bursting force is reduced in magnitude as the distance from the reaction force to the anchor surface increases.

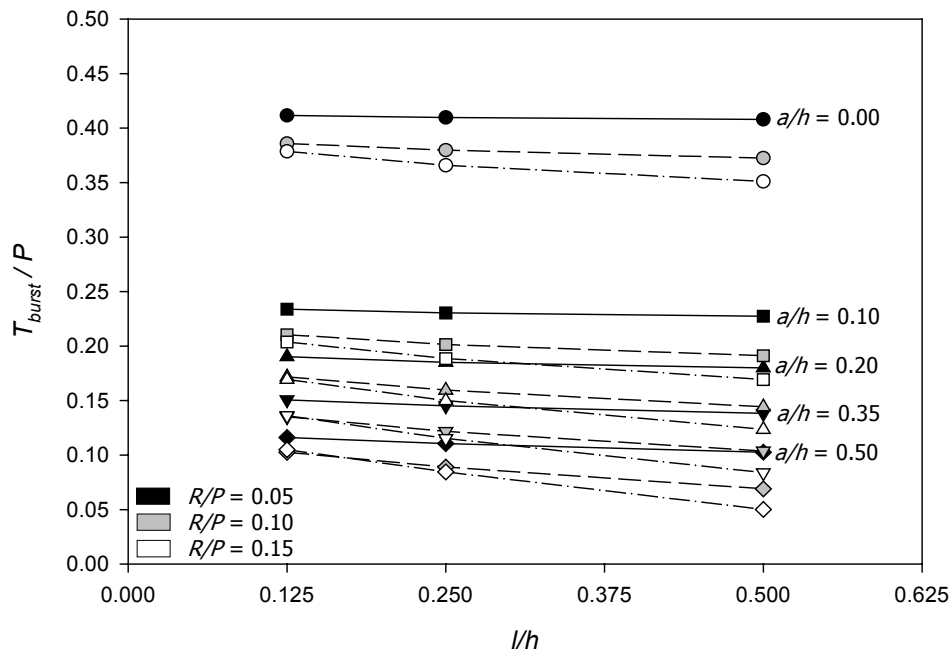


Fig. 3.52 BURSTING FORCE vs. LOCATION OF SUPPORT REACTION FOR 6 DEGREE INCLINED CONCENTRIC LOAD ($b/h = 0.0$)

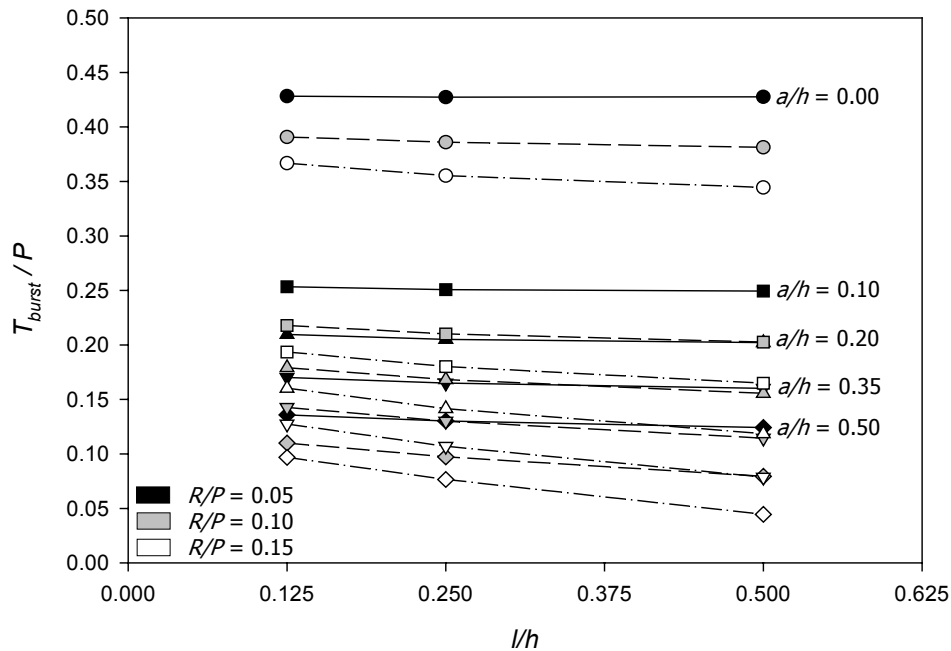


Fig. 3.53 BURSTING FORCE vs. LOCATION OF SUPPORT REACTION FOR 9 DEGREE INCLINED CONCENTRIC LOAD ($b/h = 0.0$)

The largest bursting force in each anchorage ratio and reaction magnitude also occurs in the anchorage zone with support reaction closest to the surface. This is similar to the results from the study of the concentric load configuration. The closest location of the reaction force to the surface may result in the deviation of the resultant force without disturbing the tensile stresses, which occur along the main compressive strut line. On the other hand, the farthest position of the reaction force in this study ($l/h = 0.50$), which is closer to the centroid of the bursting force than other l/h values, results in cancellation of the tensile stresses. Similar to the former study, neglecting the effect of the reaction location results in a conservative estimation of the bursting force.

The bearing plate ratio (b/h) also has no significant effect on inclined concentrically loaded anchorage zones. Figs. 3.54 and 3.55 show the relation of the bursting force and the bearing plate ratio for 6 degree and 9 degree inclined concentric loads, respectively. All plots are essentially horizontal lines, which leads to the conclusion that the bearing plate width has no effect on the bursting force.

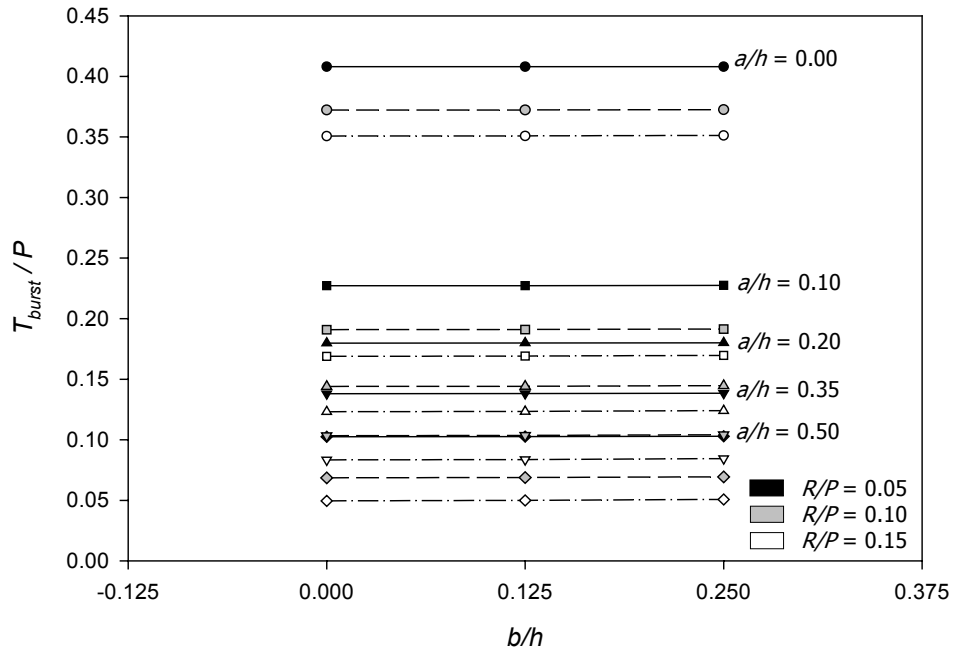


Fig. 3.54 BURSTING FORCE vs. BEARING PLATE RATIO FOR 6 DEGREE INCLINED CONCENTRIC LOAD ($l/h = 0.50$)

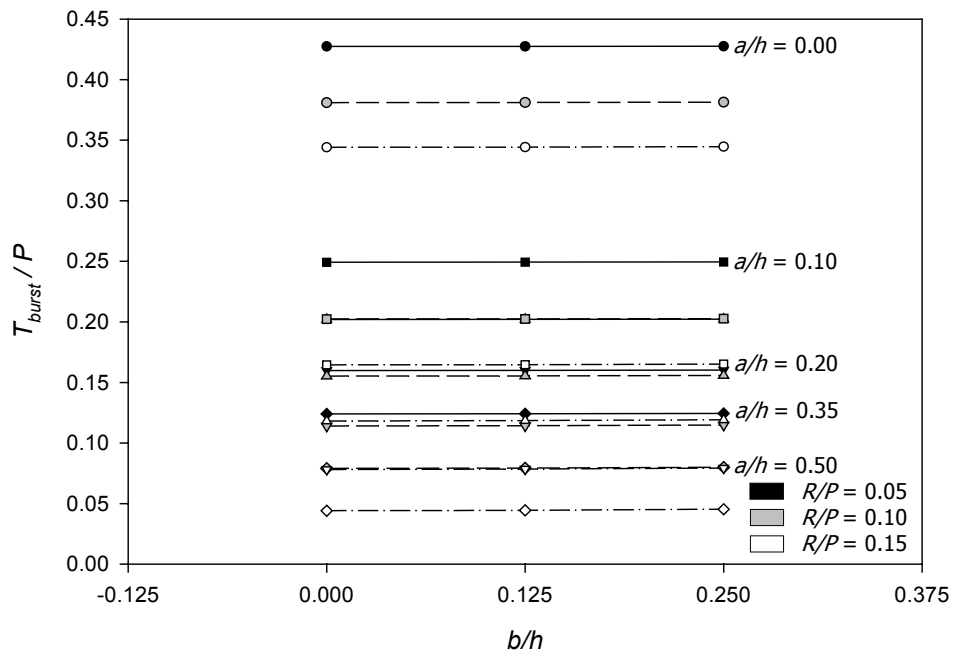


Fig. 3.55 BURSTING FORCE vs. BEARING PLATE RATIO FOR 9 DEGREE INCLINED CONCENTRIC LOAD ($l/h = 0.50$)

The effect of the magnitude of the reaction force in inclined concentrically loaded anchorage zones is presented in Figs. 3.56 through 3.61 for both inclination angles. As can be seen, the shape of each plot is concave upward. Figs. 3.59 and 3.61 indicate that with an inclination angle of 9 degrees the plots slope downward with the smallest bursting force at the R/P ratio of 0.15. To arrive at a conservative method to calculate the bursting force, the method illustrated earlier for the formulation of the bursting force in the concentric load configuration is applied to establish the term representing the influence of the reaction force due to the inclination of the prestressing force. A straight line was drawn to connect the bursting force of the R/P ratio of 0.00 and 0.15 in order to find the maximum slope for all load configurations. A summary of all slope values is listed in Table 3.5. Because of the relation with the inclination angle, the maximum slopes in all the load configurations including concentric with zero, 6, and 9 degrees are plotted relative to the inclination angles. The plot is shown in Fig. 3.62 together with the approximate equation.

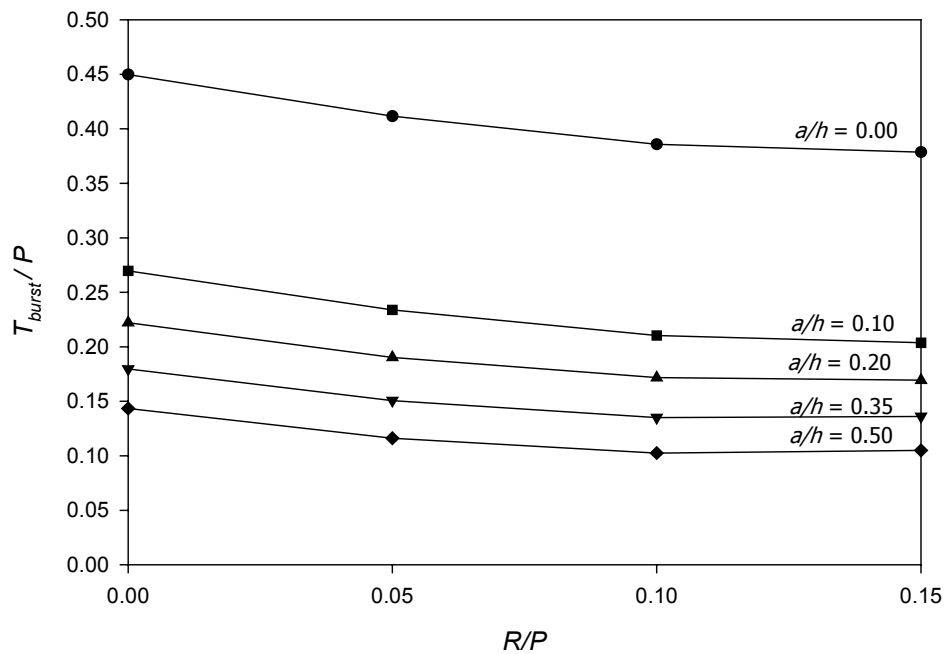


Fig. 3.56 BURSTING FORCE vs. REACTION RATIO FOR 6 DEGREE INCLINED CONCENTRIC LOAD ($l/h = 0.125, b/h = 0.0$)

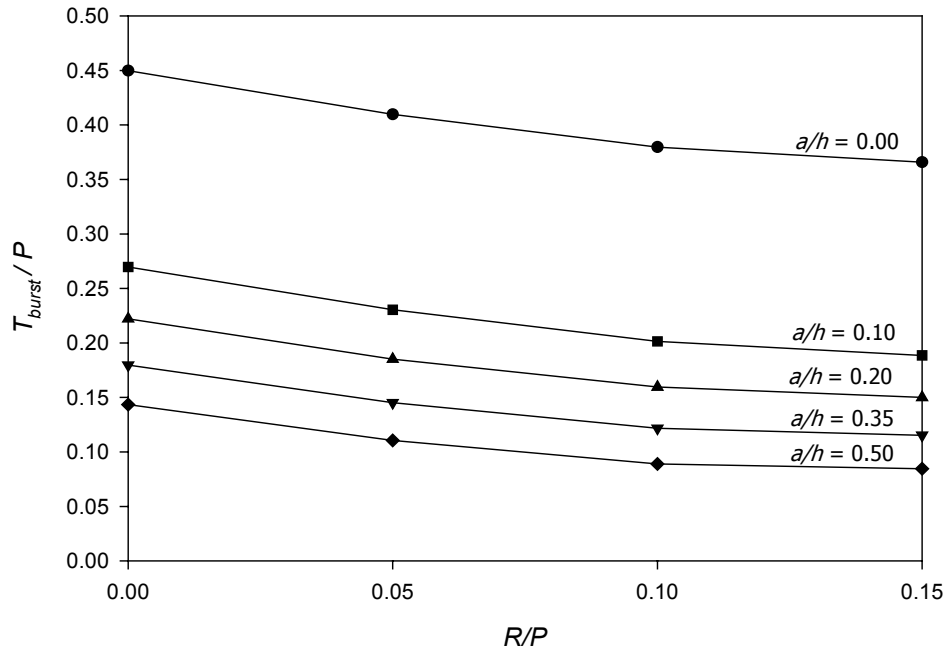


Fig. 3.57 BURSTING FORCE vs. REACTION RATIO FOR 6 DEGREE INCLINED CONCENTRIC LOAD ($l/h = 0.25, b/h = 0.0$)

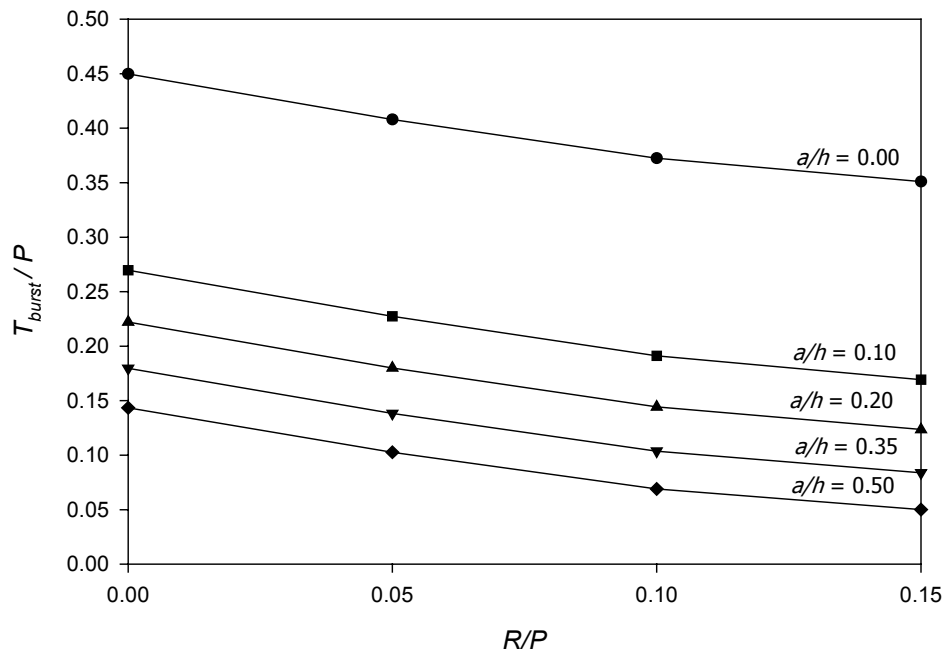


Fig. 3.58 BURSTING FORCE vs. REACTION RATIO FOR 6 DEGREE INCLINED CONCENTRIC LOAD ($l/h = 0.50, b/h = 0.0$)

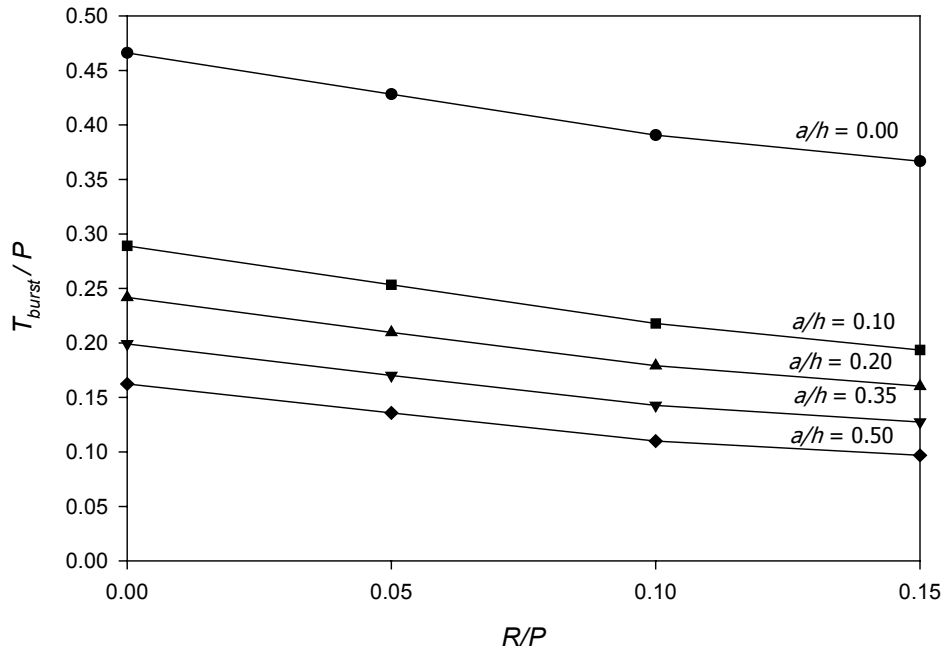


Fig. 3.59 BURSTING FORCE vs. REACTION RATIO FOR 9 DEGREE INCLINED CONCENTRIC LOAD ($l/h = 0.125, b/h = 0.0$)

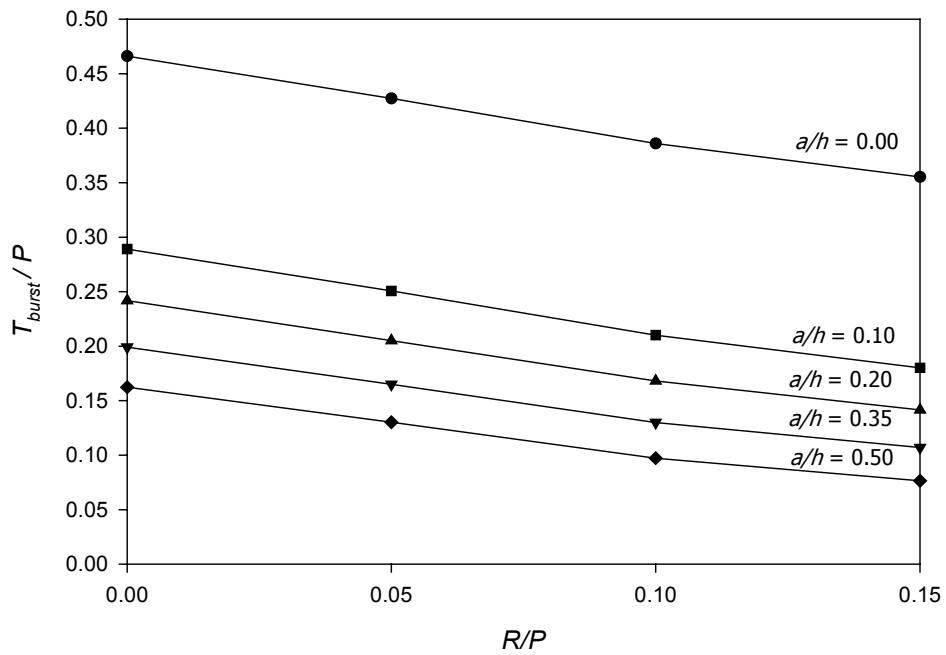


Fig. 3.60 BURSTING FORCE vs. REACTION RATIO FOR 9 DEGREE INCLINED CONCENTRIC LOAD ($l/h = 0.25, b/h = 0.0$)

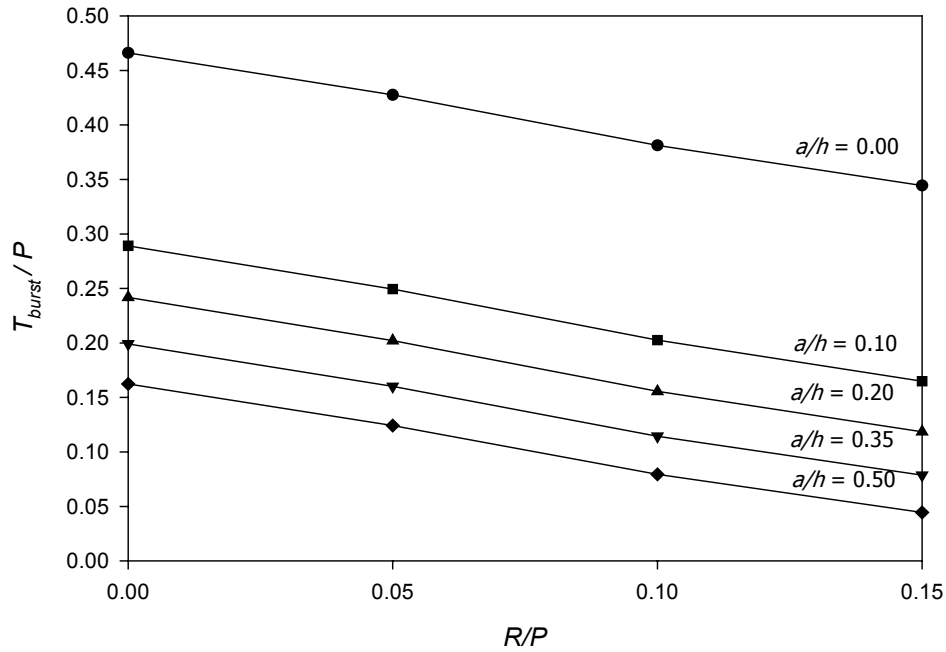


Fig. 3.61 BURSTING FORCE vs. REACTION RATIO FOR 9 DEGREE INCLINED CONCENTRIC LOAD ($l/h = 0.50, b/h = 0.0$)

Table 3.5 SLOPES OF STRAIGHT LINE FOR T_{burst} OF INCLINED CONCENTRIC LOAD

a/h	Fig. 3.56	Fig. 3.57	Fig. 3.58	Fig. 3.59	Fig. 3.60	Fig. 3.61
0.00	-0.4746	-0.5593	-0.6587	-0.6626	-0.7382	-0.8112
0.10	-0.4403	-0.5409	-0.6696	-0.6373	-0.7270	-0.8289
0.20	-0.3514	-0.4811	-0.6570	-0.5433	-0.6681	-0.8212
0.35	-0.2910	-0.4300	-0.6392	-0.4784	-0.6142	-0.8032
0.50	-0.2567	-0.3925	-0.6222	-0.4373	-0.5724	-0.7857

As shown in Fig. 3.62, the plot of inclination angle and maximum increasing slope resulting from all concentric load studies decreases as the inclination angle increases. This relationship can be approximated using a linear equation which is plotted presented in the figure.

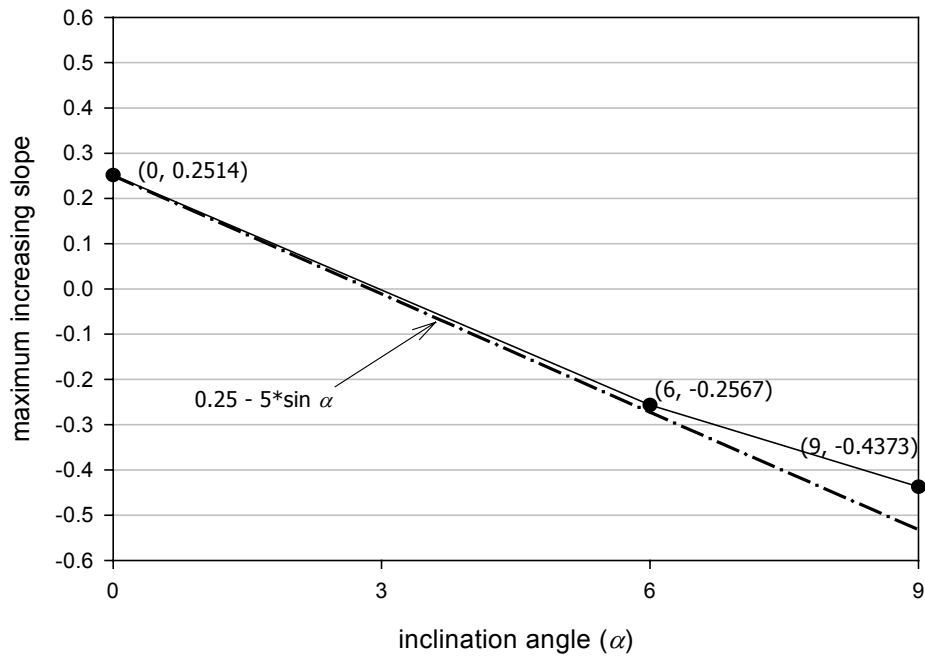


Fig. 3.62 EQUATION FOR BURSTING FORCE PREDICTION

By adding this approximate equation to the modified equation stated in section 3.4.2.1, the new expression for the determination of the bursting force for all concentrically loaded anchorage zones can be written as shown below:

$$T_{burst} = 0.25 P \left(1 - \frac{a}{h}\right) + 0.4 P \sin \alpha + R (0.25 - 5 \sin \alpha) \quad (3.4)$$

where α is always positive if the inclination angle points downward. Equation (3.4) is based on parametric studies within the limitation of parameters α and R/P presented in Table 3.2. To verify the applicability of equation (3.4), the results achieved by using the equation were compared with the results given by finite element analysis.

Tables 3.6, 3.7, and 3.8 present two sets of comparisons of equations (1.5) and (3.4), with the finite element results for concentrically loaded anchorage zones with all inclinations. As shown, the first six columns list the values of parameters used in the models. The column $T_{burst-fem}$ presents the finite element results achieved by using the vertical component of bursting force on the main compressive strut. The next four columns from the column T_{burst-}

f_{em} show the values from equation (1.5) and those from using the newly formulated equation with percent difference compared to finite element results.

According to all Tables, equation (3.4) predicts poorly for the case of anchorage ratio equal to zero, which is considered to be an unrealistic case. For the anchorage ratio of 0.10, it is found to be unconservative (negative percent difference) in some cases with zero reaction force applied. In Table 3.6, for a concentric load with no inclination, equation (1.5) predicts poorly in the case in which the reaction force with the largest magnitude is applied near the anchor surface. As the reaction force is placed further away from the surface, the prediction becomes conservative. Contrary to equation (1.5), equation (3.4) gives a good prediction for a concentric load with no inclination for all anchorage ratios bigger than 0.10.

When the inclination of the prestressing load is considered (see Tables 3.7 and 3.8), equation (1.5) gives very conservative results compared to those using the finite element method, especially for the case with the largest magnitude of reaction force. The results from using equation (3.4) provide a smaller positive percent difference, which indicates a better prediction. In reality, the degree of conservatism may lead to problems with steel congestion during the casting process, which is considered as one of the leading problems in anchorage zone construction. If the bursting force predicted is much larger than reality, a large amount of reinforcement may be unnecessarily required. Therefore, a closer prediction is better in terms of both economy and constructability than one with excessive conservativeness.

Note the value of the bursting force in the case of anchorage ratio of 0.5 with the largest magnitude of reaction force in Table 3.8. The bursting force from the finite element analysis for a large anchor width becomes rather small as the large reaction force is applied. This results in the percent difference of 78.07 compared to that from equation (1.5), and 58.64 compared with that of equation (3.4). This level of conservativeness may be acceptable since the magnitude of the bursting force from the finite element analysis is quite small.

Table 3.6 COMPARISON OF THE RESULTS FOR CONCENTRIC LOAD WITH NO INCLINATION ANGLE

<i>h</i>	<i>a/h</i>	<i>R/P</i>	<i>l/h</i>	α	β	<i>T_{burst-fem}/P</i>			<i>Eqn (3.4)</i>	
						-1-	-2-	-1 & 2-	-3-	-1 & 3-
16	0.00	0.00	0.125	0	0.00	0.4246	0.2500	-69.82	0.2500	-69.82
16	0.10	0.00	0.125	0	0.00	0.2419	0.2250	-7.51	0.2250	-7.51
16	0.20	0.00	0.125	0	0.00	0.1941	0.2000	2.95	0.2000	2.95
16	0.35	0.00	0.125	0	0.00	0.1520	0.1625	6.48	0.1625	6.48
16	0.50	0.00	0.125	0	0.00	0.1160	0.1250	7.24	0.1250	7.24
16	0.00	0.05	0.125	0	2.64	0.4165	0.2500	-66.59	0.2625	-58.66
16	0.10	0.05	0.125	0	2.64	0.2368	0.2250	-5.26	0.2375	0.28
16	0.20	0.05	0.125	0	2.64	0.1929	0.2000	3.54	0.2125	9.21
16	0.35	0.05	0.125	0	2.64	0.1531	0.1625	5.77	0.1750	12.50
16	0.50	0.05	0.125	0	2.64	0.1188	0.1250	5.00	0.1375	13.64
16	0.00	0.10	0.125	0	5.27	0.4229	0.2500	-69.15	0.2750	-53.77
16	0.10	0.10	0.125	0	5.27	0.2462	0.2250	-9.43	0.2500	1.51
16	0.20	0.10	0.125	0	5.27	0.2062	0.2000	-3.12	0.2250	8.33
16	0.35	0.10	0.125	0	5.27	0.1682	0.1625	-3.53	0.1875	10.27
16	0.50	0.10	0.125	0	5.27	0.1349	0.1250	-7.96	0.1500	10.03
16	0.00	0.15	0.125	0	7.36	0.4329	0.2500	-73.15	0.2875	-50.57
16	0.10	0.15	0.125	0	7.36	0.2585	0.2250	-14.88	0.2625	1.53
16	0.20	0.15	0.125	0	7.36	0.2220	0.2000	-11.00	0.2375	6.53
16	0.35	0.15	0.125	0	7.36	0.1863	0.1625	-14.64	0.2000	6.86
16	0.50	0.15	0.125	0	7.36	0.1537	0.1250	-22.93	0.1625	5.43
16	0.00	0.00	0.25	0	0.00	0.4246	0.2500	-69.82	0.2500	-69.82
16	0.10	0.00	0.25	0	0.00	0.2419	0.2250	-7.51	0.2250	-7.51
16	0.20	0.00	0.25	0	0.00	0.1941	0.2000	2.95	0.2000	2.95
16	0.35	0.00	0.25	0	0.00	0.1520	0.1625	6.48	0.1625	6.48
16	0.50	0.00	0.25	0	0.00	0.1160	0.1250	7.24	0.1250	7.24
16	0.00	0.05	0.25	0	2.45	0.4133	0.2500	-65.33	0.2625	-57.46
16	0.10	0.05	0.25	0	2.45	0.2323	0.2250	-3.24	0.2375	2.20
16	0.20	0.05	0.25	0	2.45	0.1870	0.2000	6.49	0.2125	11.99
16	0.35	0.05	0.25	0	2.45	0.1469	0.1625	9.60	0.1750	16.05
16	0.50	0.05	0.25	0	2.45	0.1124	0.1250	10.10	0.1375	18.27
16	0.00	0.10	0.25	0	4.90	0.4169	0.2500	-66.76	0.2750	-51.60
16	0.10	0.10	0.25	0	4.90	0.2375	0.2250	-5.57	0.2500	4.99
16	0.20	0.10	0.25	0	4.90	0.1952	0.2000	2.40	0.2250	13.24
16	0.35	0.10	0.25	0	4.90	0.1565	0.1625	3.69	0.1875	16.53
16	0.50	0.10	0.25	0	4.90	0.1233	0.1250	1.40	0.1500	17.83
16	0.00	0.15	0.25	0	6.84	0.4242	0.2500	-69.69	0.2875	-47.56
16	0.10	0.15	0.25	0	6.84	0.2466	0.2250	-9.58	0.2625	6.07
16	0.20	0.15	0.25	0	6.84	0.2070	0.2000	-3.48	0.2375	12.86
16	0.35	0.15	0.25	0	6.84	0.1706	0.1625	-4.96	0.2000	14.72
16	0.50	0.15	0.25	0	6.84	0.1383	0.1250	-10.66	0.1625	14.88
16	0.00	0.00	0.5	0	0.00	0.4246	0.2500	-69.82	0.2500	-69.82
16	0.10	0.00	0.5	0	0.00	0.2419	0.2250	-7.51	0.2250	-7.51
16	0.20	0.00	0.5	0	0.00	0.1941	0.2000	2.95	0.2000	2.95
16	0.35	0.00	0.5	0	0.00	0.1520	0.1625	6.48	0.1625	6.48
16	0.50	0.00	0.5	0	0.00	0.1160	0.1250	7.24	0.1250	7.24
16	0.00	0.05	0.5	0	2.15	0.4093	0.2500	-63.73	0.2625	-55.93
16	0.10	0.05	0.5	0	2.15	0.2267	0.2250	-0.77	0.2375	4.53
16	0.20	0.05	0.5	0	2.15	0.1793	0.2000	10.33	0.2125	15.61
16	0.35	0.05	0.5	0	2.15	0.1382	0.1625	14.96	0.1750	21.03
16	0.50	0.05	0.5	0	2.15	0.1029	0.1250	17.69	0.1375	25.18
16	0.00	0.10	0.5	0	4.29	0.4090	0.2500	-63.60	0.2750	-48.73
16	0.10	0.10	0.5	0	4.29	0.2266	0.2250	-0.70	0.2500	9.37
16	0.20	0.10	0.5	0	4.29	0.1801	0.2000	9.97	0.2250	19.98
16	0.35	0.10	0.5	0	4.29	0.1397	0.1625	14.06	0.1875	25.52
16	0.50	0.10	0.5	0	4.29	0.1050	0.1250	15.96	0.1500	29.97
16	0.00	0.15	0.5	0	5.99	0.4135	0.2500	-65.41	0.2875	-43.83
16	0.10	0.15	0.5	0	5.99	0.2313	0.2250	-2.81	0.2625	11.88
16	0.20	0.15	0.5	0	5.99	0.1858	0.2000	7.10	0.2375	21.77
16	0.35	0.15	0.5	0	5.99	0.1460	0.1625	10.12	0.2000	26.98
16	0.50	0.15	0.5	0	5.99	0.1121	0.1250	10.29	0.1625	31.00

Table 3.7 COMPARISON OF THE RESULTS FOR CONCENTRIC LOAD WITH 6 DEGREE INCLINATION ANGLE

<i>h</i>	<i>a/h</i>	<i>R/P</i>	<i>l/h</i>	α	β	<i>T_{burst-fem}/P</i>			<i>Eqn (3.4)</i>	
						-1-	-2-	-1 & 2-	-3-	-1 & 3-
16	0.00	0.00	0.125	6	-6.00	0.4497	0.3023	-48.79	0.2918	-54.12
16	0.10	0.00	0.125	6	-6.00	0.2697	0.2773	2.74	0.2668	-1.07
16	0.20	0.00	0.125	6	-6.00	0.2220	0.2523	11.98	0.2418	8.17
16	0.35	0.00	0.125	6	-6.00	0.1797	0.2148	16.33	0.2043	12.05
16	0.50	0.00	0.125	6	-6.00	0.1434	0.1773	19.12	0.1668	14.05
16	0.00	0.05	0.125	6	-3.36	0.4116	0.3023	-36.16	0.2782	-47.95
16	0.10	0.05	0.125	6	-3.36	0.2338	0.2773	15.68	0.2532	7.66
16	0.20	0.05	0.125	6	-3.36	0.1902	0.2523	24.59	0.2282	16.63
16	0.35	0.05	0.125	6	-3.36	0.1507	0.2148	29.84	0.1907	20.97
16	0.50	0.05	0.125	6	-3.36	0.1160	0.1773	34.54	0.1532	24.24
16	0.00	0.10	0.125	6	-0.70	0.3858	0.3023	-27.63	0.2645	-45.83
16	0.10	0.10	0.125	6	-0.70	0.2104	0.2773	24.12	0.2395	12.18
16	0.20	0.10	0.125	6	-0.70	0.1716	0.2523	31.98	0.2145	20.02
16	0.35	0.10	0.125	6	-0.70	0.1351	0.2148	37.10	0.1770	23.70
16	0.50	0.10	0.125	6	-0.70	0.1025	0.1773	42.19	0.1395	26.57
16	0.00	0.15	0.125	6	1.95	0.3785	0.3023	-25.23	0.2509	-50.86
16	0.10	0.15	0.125	6	1.95	0.2036	0.2773	26.56	0.2259	9.87
16	0.20	0.15	0.125	6	1.95	0.1693	0.2523	32.87	0.2009	15.71
16	0.35	0.15	0.125	6	1.95	0.1360	0.2148	36.66	0.1634	16.76
16	0.50	0.15	0.125	6	1.95	0.1049	0.1773	40.84	0.1259	16.72
16	0.00	0.00	0.25	6	-6.00	0.4497	0.3023	-48.79	0.2918	-54.12
16	0.10	0.00	0.25	6	-6.00	0.2697	0.2773	2.74	0.2668	-1.07
16	0.20	0.00	0.25	6	-6.00	0.2220	0.2523	11.98	0.2418	8.17
16	0.35	0.00	0.25	6	-6.00	0.1797	0.2148	16.33	0.2043	12.05
16	0.50	0.00	0.25	6	-6.00	0.1434	0.1773	19.12	0.1668	14.05
16	0.00	0.05	0.25	6	-3.55	0.4096	0.3023	-35.50	0.2782	-47.24
16	0.10	0.05	0.25	6	-3.55	0.2304	0.2773	16.92	0.2532	9.01
16	0.20	0.05	0.25	6	-3.55	0.1851	0.2523	26.62	0.2282	18.88
16	0.35	0.05	0.25	6	-3.55	0.1450	0.2148	32.47	0.1907	23.94
16	0.50	0.05	0.25	6	-3.55	0.1106	0.1773	37.64	0.1532	27.83
16	0.00	0.10	0.25	6	-1.08	0.3797	0.3023	-25.62	0.2645	-43.53
16	0.10	0.10	0.25	6	-1.08	0.2014	0.2773	27.36	0.2395	15.92
16	0.20	0.10	0.25	6	-1.08	0.1595	0.2523	36.77	0.2145	25.66
16	0.35	0.10	0.25	6	-1.08	0.1216	0.2148	43.38	0.1770	31.31
16	0.50	0.10	0.25	6	-1.08	0.0889	0.1773	49.85	0.1395	36.30
16	0.00	0.15	0.25	6	1.38	0.3658	0.3023	-21.03	0.2509	-45.80
16	0.10	0.15	0.25	6	1.38	0.1885	0.2773	32.00	0.2259	16.55
16	0.20	0.15	0.25	6	1.38	0.1499	0.2523	40.58	0.2009	25.40
16	0.35	0.15	0.25	6	1.38	0.1152	0.2148	46.37	0.1634	29.52
16	0.50	0.15	0.25	6	1.38	0.0845	0.1773	52.33	0.1259	32.89
16	0.00	0.00	0.5	6	-6.00	0.4497	0.3023	-48.79	0.2918	-54.12
16	0.10	0.00	0.5	6	-6.00	0.2697	0.2773	2.74	0.2668	-1.07
16	0.20	0.00	0.5	6	-6.00	0.2220	0.2523	11.98	0.2418	8.17
16	0.35	0.00	0.5	6	-6.00	0.1797	0.2148	16.33	0.2043	12.05
16	0.50	0.00	0.5	6	-6.00	0.1434	0.1773	19.12	0.1668	14.05
16	0.00	0.05	0.5	6	-3.86	0.4080	0.3023	-34.98	0.2782	-46.66
16	0.10	0.05	0.5	6	-3.86	0.2273	0.2773	18.01	0.2532	10.21
16	0.20	0.05	0.5	6	-3.86	0.1799	0.2523	28.67	0.2282	21.14
16	0.35	0.05	0.5	6	-3.86	0.1382	0.2148	35.64	0.1907	27.51
16	0.50	0.05	0.5	6	-3.86	0.1027	0.1773	42.07	0.1532	32.96
16	0.00	0.10	0.5	6	-1.70	0.3724	0.3023	-23.19	0.2645	-40.76
16	0.10	0.10	0.5	6	-1.70	0.1911	0.2773	31.07	0.2395	20.22
16	0.20	0.10	0.5	6	-1.70	0.1442	0.2523	42.83	0.2145	32.78
16	0.35	0.10	0.5	6	-1.70	0.1037	0.2148	51.73	0.1770	41.44
16	0.50	0.10	0.5	6	-1.70	0.0690	0.1773	61.09	0.1395	50.58
16	0.00	0.15	0.5	6	0.46	0.3509	0.3023	-16.10	0.2509	-39.86
16	0.10	0.15	0.5	6	0.46	0.1692	0.2773	38.97	0.2259	25.09
16	0.20	0.15	0.5	6	0.46	0.1235	0.2523	51.05	0.2009	38.53
16	0.35	0.15	0.5	6	0.46	0.0838	0.2148	60.98	0.1634	48.72
16	0.50	0.15	0.5	6	0.46	0.0500	0.1773	71.77	0.1259	60.26

Table 3.8 COMPARISON OF THE RESULTS FOR CONCENTRIC LOAD WITH 9 DEGREE INCLINATION ANGLE

<i>h</i>	<i>a/h</i>	<i>R/P</i>	<i>l/h</i>	α	β	<i>T_{burst-fem}/P</i>			<i>Eqn (3.4)</i>	
						-1-	-2-	-1 & 2-	-3-	-1 & 3-
16	0.00	0.00	0.125	9	-9.00	0.4660	0.3282	-41.98	0.3126	-49.09
16	0.10	0.00	0.125	9	-9.00	0.2891	0.3032	4.65	0.2876	-0.54
16	0.20	0.00	0.125	9	-9.00	0.2417	0.2782	13.11	0.2626	7.93
16	0.35	0.00	0.125	9	-9.00	0.1991	0.2407	17.29	0.2251	11.54
16	0.50	0.00	0.125	9	-9.00	0.1624	0.2032	20.07	0.1876	13.41
16	0.00	0.05	0.125	9	-6.33	0.4283	0.3282	-30.49	0.2860	-49.77
16	0.10	0.05	0.125	9	-6.33	0.2533	0.3032	16.45	0.2610	2.92
16	0.20	0.05	0.125	9	-6.33	0.2097	0.2782	24.62	0.2360	11.13
16	0.35	0.05	0.125	9	-6.33	0.1701	0.2407	29.34	0.1985	14.30
16	0.50	0.05	0.125	9	-6.33	0.1358	0.2032	33.19	0.1610	15.65
16	0.00	0.10	0.125	9	-3.71	0.3907	0.3282	-19.04	0.2594	-50.65
16	0.10	0.10	0.125	9	-3.71	0.2178	0.3032	28.18	0.2344	7.08
16	0.20	0.10	0.125	9	-3.71	0.1791	0.2782	35.64	0.2094	14.46
16	0.35	0.10	0.125	9	-3.71	0.1426	0.2407	40.75	0.1719	17.00
16	0.50	0.10	0.125	9	-3.71	0.1099	0.2032	45.92	0.1344	18.20
16	0.00	0.15	0.125	9	-1.04	0.3666	0.3282	-11.70	0.2327	-57.52
16	0.10	0.15	0.125	9	-1.04	0.1935	0.3032	36.18	0.2077	6.85
16	0.20	0.15	0.125	9	-1.04	0.1602	0.2782	42.40	0.1827	12.31
16	0.35	0.15	0.125	9	-1.04	0.1273	0.2407	47.11	0.1452	12.34
16	0.50	0.15	0.125	9	-1.04	0.0968	0.2032	52.35	0.1077	10.14
16	0.00	0.00	0.25	9	-9.00	0.4660	0.3282	-41.98	0.3126	-49.09
16	0.10	0.00	0.25	9	-9.00	0.2891	0.3032	4.65	0.2876	-0.54
16	0.20	0.00	0.25	9	-9.00	0.2417	0.2782	13.11	0.2626	7.93
16	0.35	0.00	0.25	9	-9.00	0.1991	0.2407	17.29	0.2251	11.54
16	0.50	0.00	0.25	9	-9.00	0.1624	0.2032	20.07	0.1876	13.41
16	0.00	0.05	0.25	9	-6.37	0.4272	0.3282	-30.14	0.2860	-49.37
16	0.10	0.05	0.25	9	-6.37	0.2507	0.3032	17.33	0.2610	3.94
16	0.20	0.05	0.25	9	-6.37	0.2051	0.2782	26.27	0.2360	13.06
16	0.35	0.05	0.25	9	-6.37	0.1649	0.2407	31.49	0.1985	16.91
16	0.50	0.05	0.25	9	-6.37	0.1302	0.2032	35.94	0.1610	19.12
16	0.00	0.10	0.25	9	-4.10	0.3859	0.3282	-17.58	0.2594	-48.80
16	0.10	0.10	0.25	9	-4.10	0.2101	0.3032	30.71	0.2344	10.35
16	0.20	0.10	0.25	9	-4.10	0.1681	0.2782	39.58	0.2094	19.71
16	0.35	0.10	0.25	9	-4.10	0.1299	0.2407	46.03	0.1719	24.40
16	0.50	0.10	0.25	9	-4.10	0.0972	0.2032	52.18	0.1344	27.67
16	0.00	0.15	0.25	9	-1.62	0.3553	0.3282	-8.24	0.2327	-52.64
16	0.10	0.15	0.25	9	-1.62	0.1801	0.3032	40.61	0.2077	13.32
16	0.20	0.15	0.25	9	-1.62	0.1415	0.2782	49.13	0.1827	22.56
16	0.35	0.15	0.25	9	-1.62	0.1070	0.2407	55.57	0.1452	26.36
16	0.50	0.15	0.25	9	-1.62	0.0766	0.2032	62.33	0.1077	28.95
16	0.00	0.00	0.5	9	-9.00	0.4660	0.3282	-41.98	0.3126	-49.09
16	0.10	0.00	0.5	9	-9.00	0.2891	0.3032	4.65	0.2876	-0.54
16	0.20	0.00	0.5	9	-9.00	0.2417	0.2782	13.11	0.2626	7.93
16	0.35	0.00	0.5	9	-9.00	0.1991	0.2407	17.29	0.2251	11.54
16	0.50	0.00	0.5	9	-9.00	0.1624	0.2032	20.07	0.1876	13.41
16	0.00	0.05	0.5	9	-6.22	0.4275	0.3282	-30.24	0.2860	-49.48
16	0.10	0.05	0.5	9	-6.22	0.2494	0.3032	17.76	0.2610	4.45
16	0.20	0.05	0.5	9	-6.22	0.2021	0.2782	27.37	0.2360	14.37
16	0.35	0.05	0.5	9	-6.22	0.1601	0.2407	33.50	0.1985	19.34
16	0.50	0.05	0.5	9	-6.22	0.1242	0.2032	38.88	0.1610	22.84
16	0.00	0.10	0.5	9	-4.71	0.3812	0.3282	-16.14	0.2594	-46.98
16	0.10	0.10	0.5	9	-4.71	0.2025	0.3032	33.22	0.2344	13.60
16	0.20	0.10	0.5	9	-4.71	0.1555	0.2782	44.11	0.2094	25.73
16	0.35	0.10	0.5	9	-4.71	0.1144	0.2407	52.49	0.1719	33.46
16	0.50	0.10	0.5	9	-4.71	0.0794	0.2032	60.95	0.1344	40.94
16	0.00	0.15	0.5	9	-2.55	0.3443	0.3282	-4.91	0.2327	-47.94
16	0.10	0.15	0.5	9	-2.55	0.1648	0.3032	45.65	0.2077	20.68
16	0.20	0.15	0.5	9	-2.55	0.1186	0.2782	57.38	0.1827	35.12
16	0.35	0.15	0.5	9	-2.55	0.0786	0.2407	67.34	0.1452	45.88
16	0.50	0.15	0.5	9	-2.55	0.0446	0.2032	78.07	0.1077	58.64

3.4.2.3 Location of Bursting Force

For an inclined concentrically loaded anchorage zone, the calculation of the distance to the bursting force should include the effect of the inclination angle. Based on the study of Burdet (1990) which was adopted into the AASHTO Standard Specifications (1994), the equation as presented in equation (1.6) stated that the inclination effect of the force is taken into account in the calculation of d_{burst} if eccentricity is also present. Furthermore, the sign of the inclination angle is considered with respect to its direction. If the direction of load points toward the centerline of anchorage zone, a positive value is used. If the load points otherwise, a negative value is considered. The results of the finite element analysis in the present study show that the effect of the inclination of the prestressing load does not necessarily depend on the eccentricity. Instead, the results show that the inclination of the load alone has some effect on the distance of the bursting force.

Figure 3.63 shows the relation between d_{burst} and three inclination angles: 0, 6, and 9 degrees. As previously presented, d_{burst} for a prestressing load with no inclination can be better predicted compared to the finite element results if an additional term involving the anchorage ratio (a/h) is introduced (see Fig. 3.33). As can be seen in Fig. 3.63, all plots for each anchorage ratio are essentially parallel lines. A single slope can be used in a linear equation to establish the behavior of d_{burst} with respect to the inclination angle. Therefore, a modified equation can be formulated by adding a term representing the effect of the inclination angle. As shown in Fig. 3.63, a result from using the modified equation is compared for the case of a/h equals to 0.20. In the equation, the value 0.25 was selected as a multiplier for the angle term, similar to that used in the bursting force formulation.

According to the plots, the modified equation gives good agreement with the finite element result with the same anchorage ratio. With the addition of the anchorage ratio and inclination angle terms to the equation, the prediction of d_{burst} is much improved. However, the presence of the support reaction is expected to have a significant effect on the calculation of d_{burst} for the inclined concentric load configuration, as will be illustrated in the following sections.

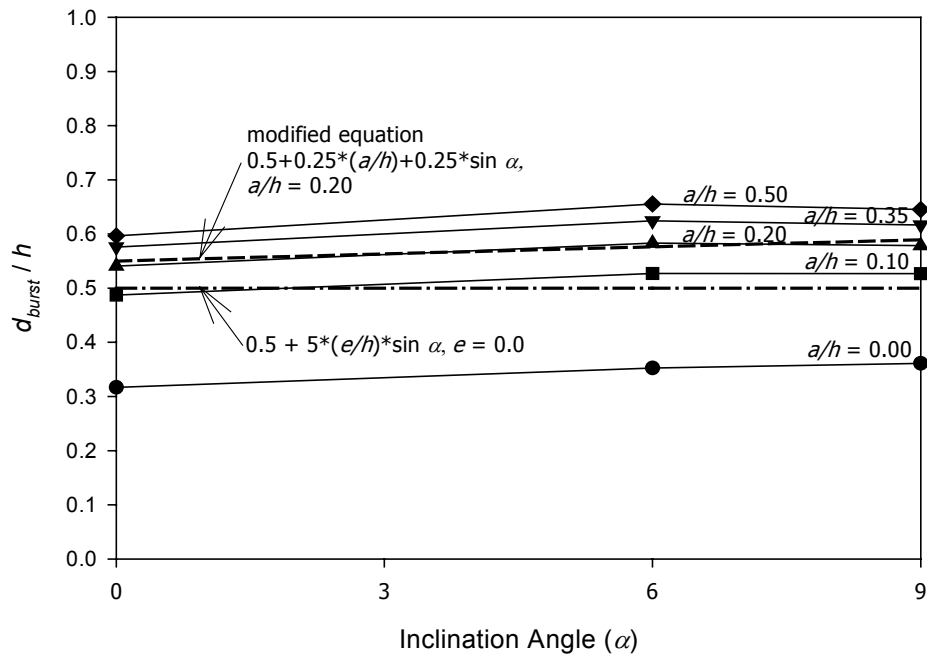


Fig. 3.63 BURSTING FORCE LOCATION vs. INCLINATION ANGLE FOR CONCENTRIC LOAD (NO REACTION)

Similarly to the illustration given in section 3.4.1.3, the first parametric study for the location of the bursting force of inclined concentrically loaded anchorage zones is the anchorage ratio (a/h). Figs. 3.64 through 3.69 present the relation between the location of the bursting force and the anchorage ratio for 6 degree and 9 degree inclined concentric load with three different reaction locations. The modified equation developed previously is added into each figure for comparison. As can be seen, the slope from the plot of the modified equation is almost parallel to the plots of the finite element results with the range of a/h from 0.20 to 0.50. Note that the plot of equation (1.6) is a horizontal line. In Figs. 3.64 to 3.66, the finite element result of the case with the largest reaction force ($R/P = 0.15$) gives the largest d_{burst} value, while other cases with smaller reaction force provide the magnitude of d_{burst} similar to or less than that of the modified equation. Figs. 3.67 to 3.69 show similar trends of behavior in that the largest R/P magnitude results in the largest d_{burst} except in Fig. 3.69. The plots indicate that the d_{burst} value corresponding to each R/P does not vary in sequence from the smallest value to the largest one. However, as can be observed, the magnitude of R/P has a significant effect on d_{burst} .

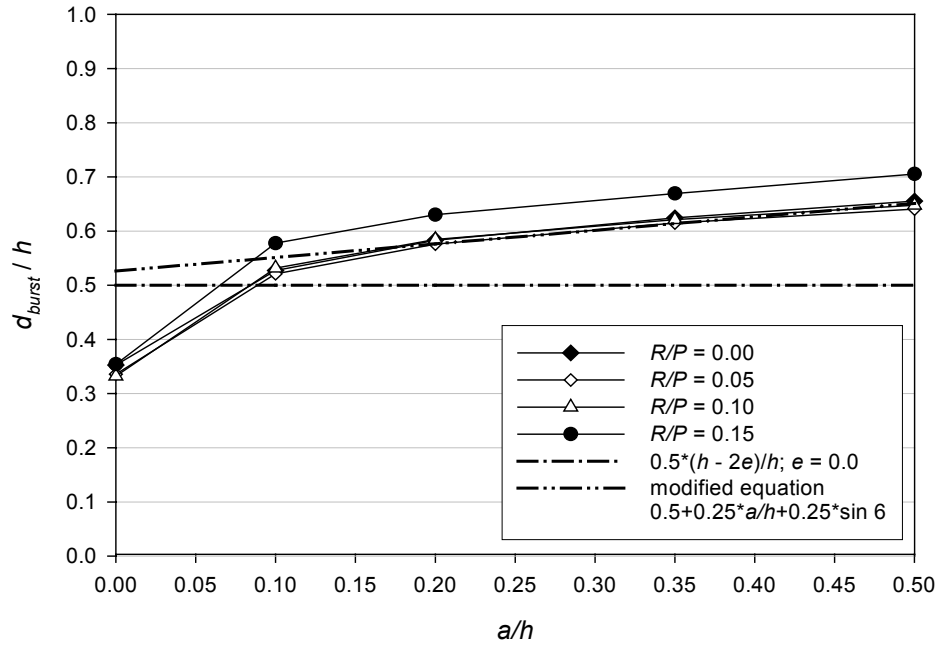


Fig. 3.64 BURSTING FORCE LOCATION vs. ANCHORAGE RATIO FOR 6 DEGREE INCLINED CONCENTRIC LOAD ($b/h = 0.0$, $l/h = 0.125$)

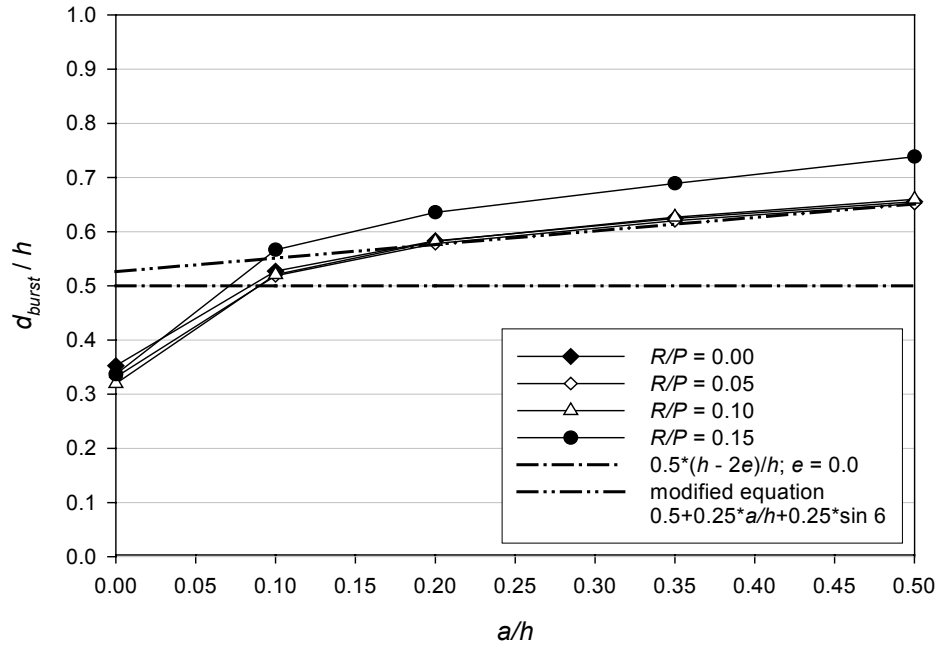


Fig. 3.65 BURSTING FORCE LOCATION vs. ANCHORAGE RATIO FOR 6 DEGREE INCLINED CONCENTRIC LOAD ($b/h = 0.0$, $l/h = 0.25$)

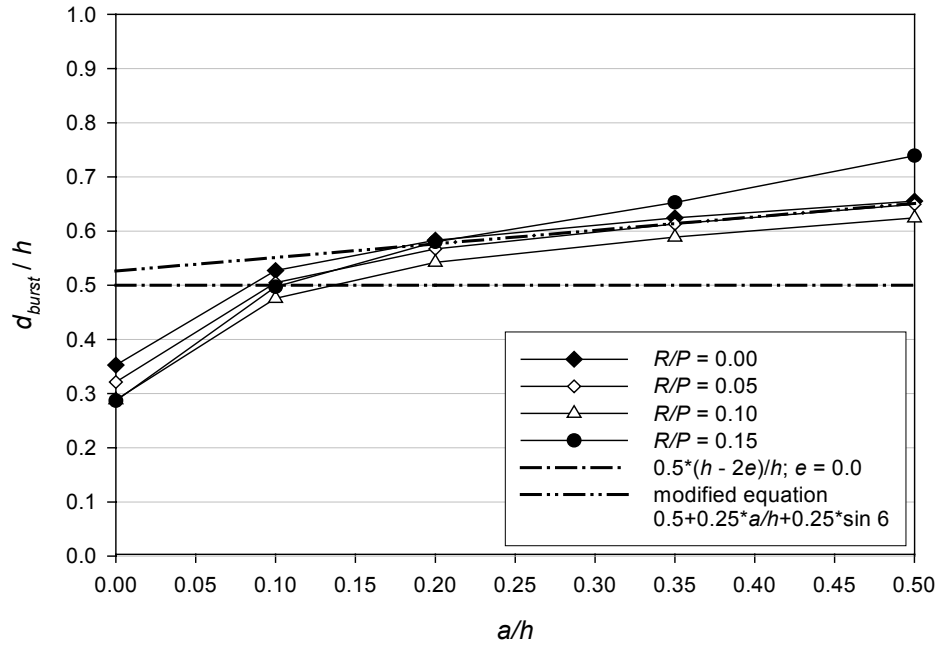


Fig. 3.66 BURSTING FORCE LOCATION vs. ANCHORAGE RATIO FOR 6 DEGREE INCLINED CONCENTRIC LOAD ($b/h = 0.0$, $l/h = 0.50$)

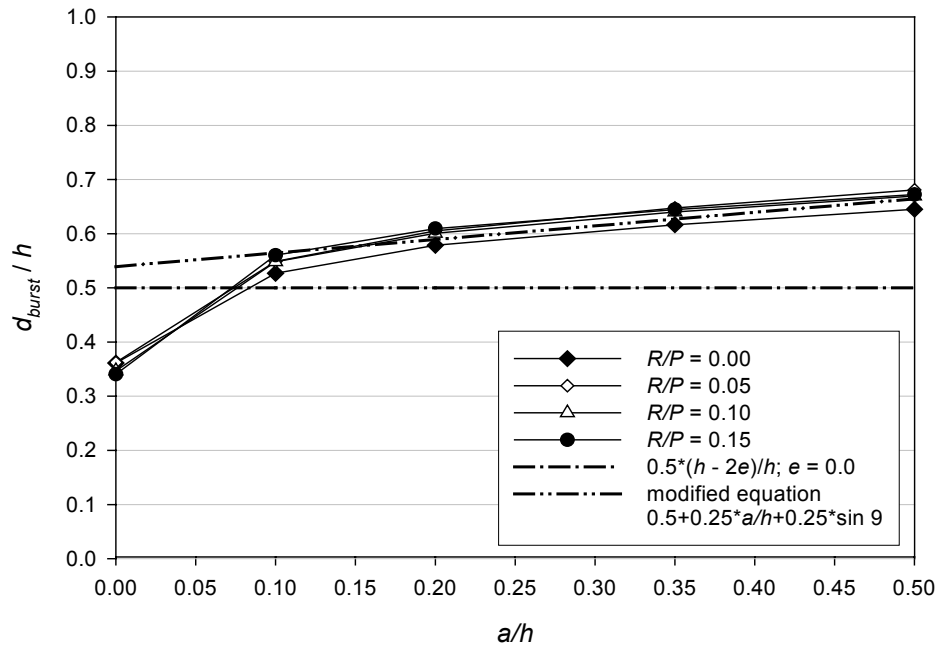


Fig. 3.67 BURSTING FORCE LOCATION vs. ANCHORAGE RATIO FOR 9 DEGREE INCLINED CONCENTRIC LOAD ($b/h = 0.0$, $l/h = 0.125$)

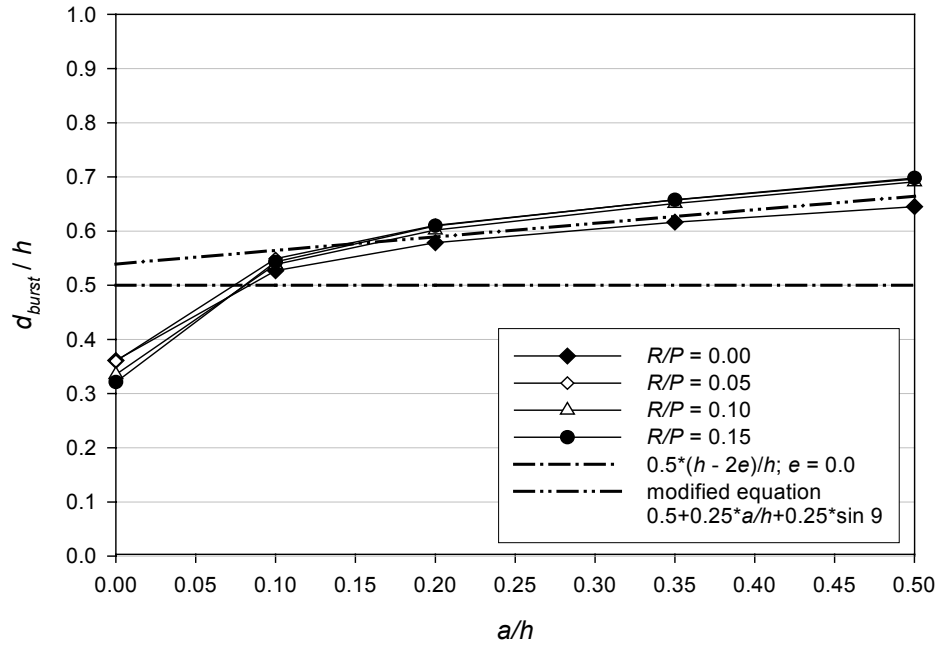


Fig. 3.68 BURSTING FORCE LOCATION vs. ANCHORAGE RATIO FOR 9 DEGREE INCLINED CONCENTRIC LOAD ($b/h = 0.0$, $l/h = 0.25$)

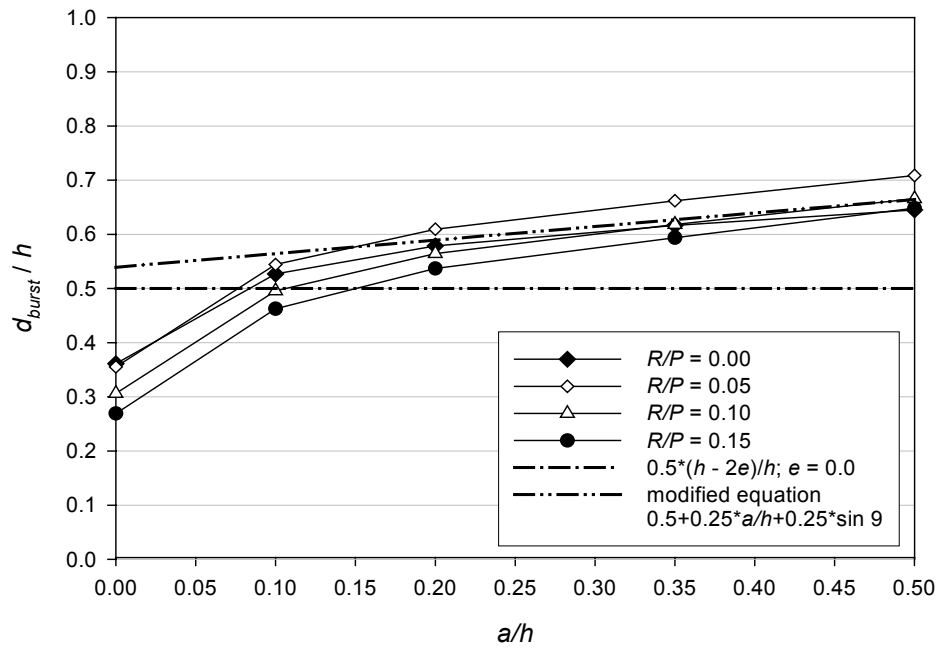


Fig. 3.69 BURSTING FORCE LOCATION vs. ANCHORAGE RATIO FOR 9 DEGREE INCLINED CONCENTRIC LOAD ($b/h = 0.0$, $l/h = 0.50$)

Figures 3.70 and 3.71 show examples of the relation between the location of the bursting force (d_{burst}) and the location of the reaction force (l/h) for both inclination angles. Fig. 3.70 presents the results for the reaction ratio of 0.05 while Fig. 3.71 presents for the largest reaction ratio. As can be seen, all plots illustrate the same characteristic as those which appeared in the previous study for the case of a small reaction force (Fig. 3.34). However, as the reaction force becomes larger, unlike the plots in Fig. 3.35, the plots for R/P of 0.15 show decreasing d_{burst} values as the l/h value approaches 0.50.

Both inclination angles exhibit a similar trend. It can be noted that when the prestressing load points down toward the position of the vertical reaction force, it results in the cancellation of stresses due to the forces acting in opposite directions. The prestressing force is trying to generate bursting stresses downward in the region ahead of the load, while the reaction force creates compressive stresses upward and distributes them into the bursting region. The results of d_{burst} for the largest R/P ratio are related to the behavior of the bursting force in the case of an inclined load configuration with the largest reaction magnitude (see Tables 3.7 and 3.8). Since the prediction of the bursting force for the inclined concentric load with the largest magnitude of reaction force is quite conservative, the location of the bursting steel may be able to be located at a position further than the location specified by the finite element results because the distribution of the excessive amount of reinforcement will compensate for incorrect location of the force.

Referring to Figs. 3.66 and 3.69, the position of the reaction force in both figures is located at l/h equal to 0.50. The line presenting the result from the modified equation lies in between the scattered region of the plots from the finite element results. This indicates the closeness of the prediction using the modified equation for determining the location of d_{burst} . However, the conclusion of the applicability of the modified equation cannot be made if a study of all parameters related to the support reaction has not yet been performed.

Figure 3.72 presents an example of the plots examining the relation of the location of the bursting force (d_{burst}) and the bearing plate ratio (b/h). Once again b/h does not have any effect on the location of the bursting force. This behavior occurs in other inclined concentric load configurations as well. Therefore, the b/h ratio can be neglected.

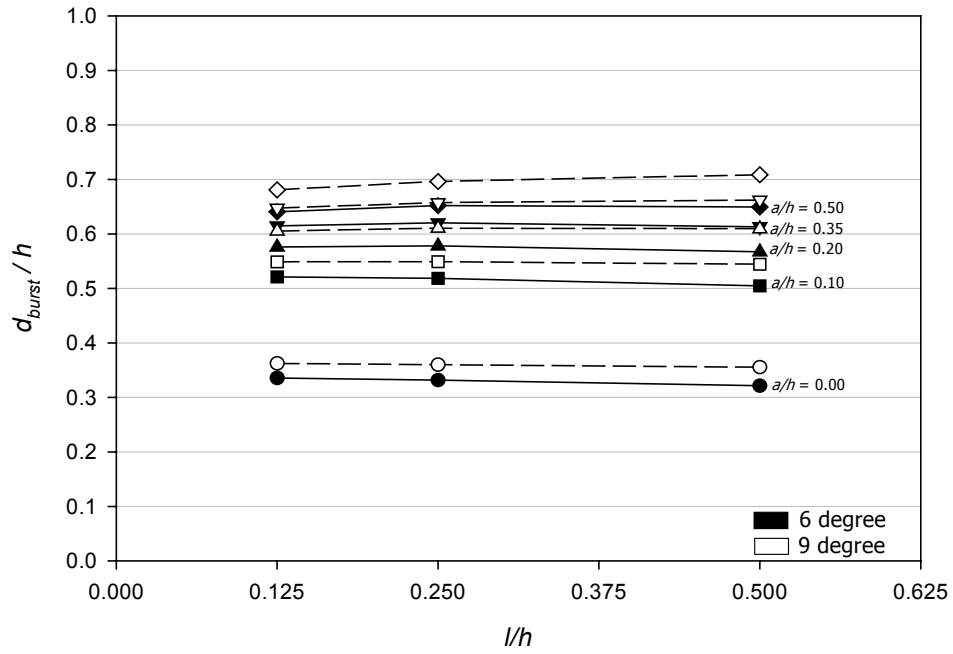


Fig. 3.70 BURSTING FORCE LOCATION vs. LOCATION OF SUPPORT REACTION FOR 6 AND 9 DEGREE INCLINED CONCENTRIC LOADS AND $R/P = 0.05$

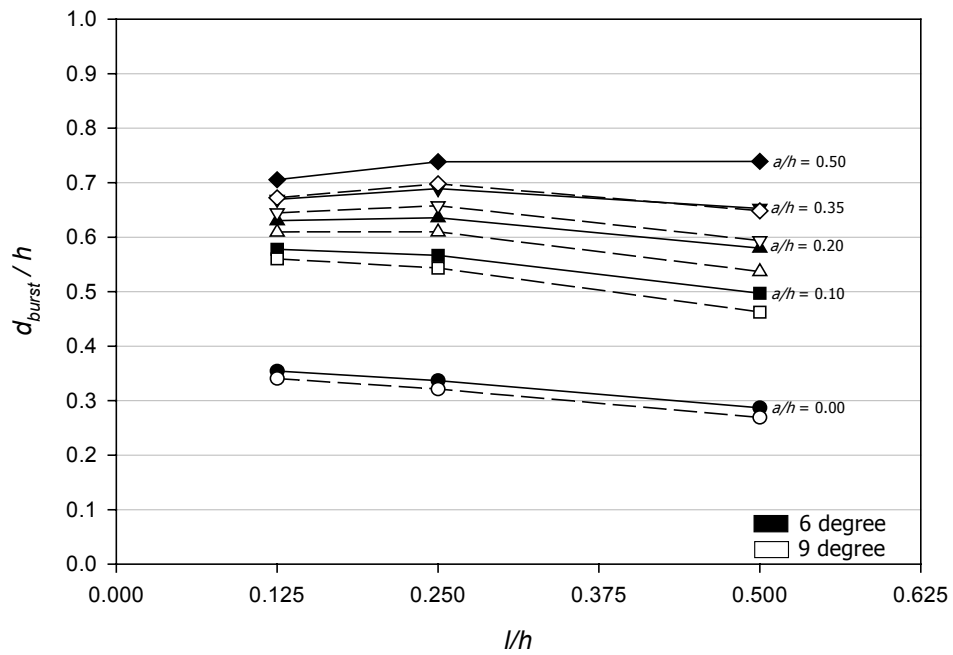


Fig. 3.71 BURSTING FORCE LOCATION vs. LOCATION OF SUPPORT REACTION FOR 6 AND 9 DEGREE INCLINED CONCENTRIC LOADS AND $R/P = 0.15$

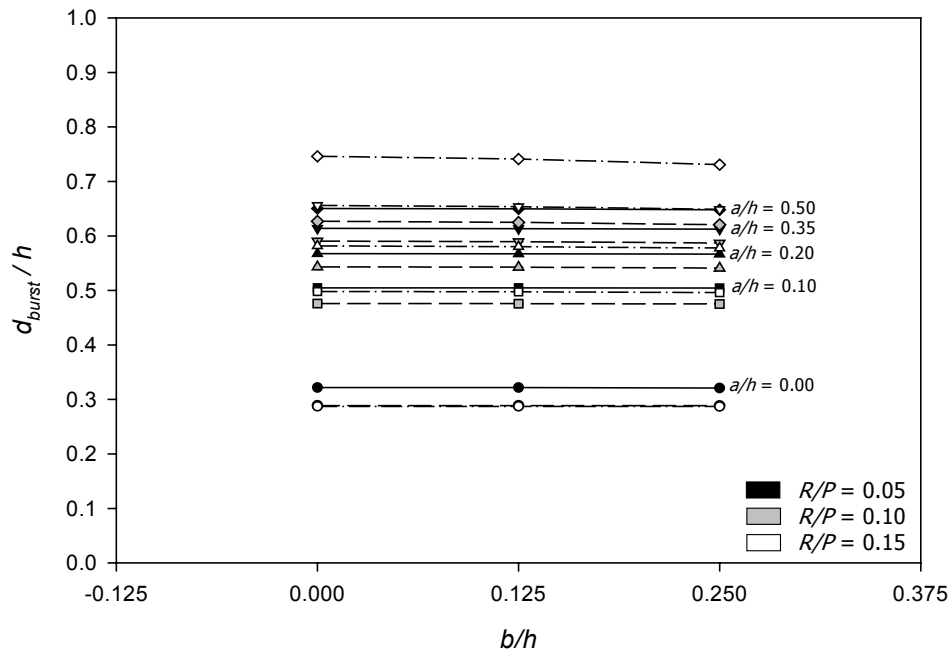


Fig. 3.72 BURSTING FORCE LOCATION vs. BEARING PLATE RATIO FOR 6 DEGREE INCLINED CONCENTRIC LOAD ($l/h = 0.50$)

The final parametric study of inclined concentrically loaded anchorage zones is the reaction ratio (R/P). Figs. 3.73 through 3.78 present the relation between the location of the bursting force (d_{burst}) and the reaction ratio (R/P) for two inclined concentric load configurations with three different reaction locations (l/h) for each inclination angle. Similar to those developed in the study of concentric loads, the plots are not linear with respect to the variation of R/P ratio. Therefore, a similar method is used to find the average slope in order to create an equation to predict the d_{burst} value.

As presented earlier in section 3.4.1.3, a straight line is constructed by connecting the ends of each plot. The slopes of all straight lines in Figs. 3.73 to 3.78 are listed in Table 3.9. After determining the average values of each inclination angle, a term representing the effect of the R/P ratio on an inclined load configuration can be estimated. Fig. 3.79 shows the estimation plot. As can be seen, a linear equation can be applied to approximate the plot of the average slopes. Equation (a) is developed from the numbers given in Table 3.4 and 3.9. Equation (b) is a simplified form of equation (a), which provides an acceptable estimation.

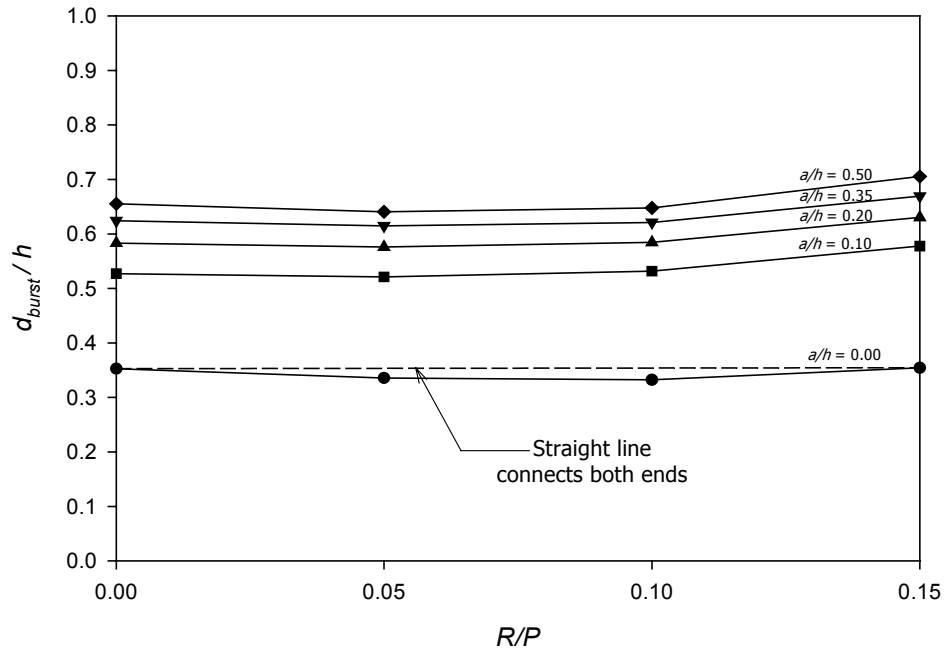


Fig. 3.73 BURSTING FORCE LOCATION vs. REACTION RATIO FOR 6 DEGREE INCLINED CONCENTRIC LOAD ($l/h = 0.125$, $b/h = 0.0$)

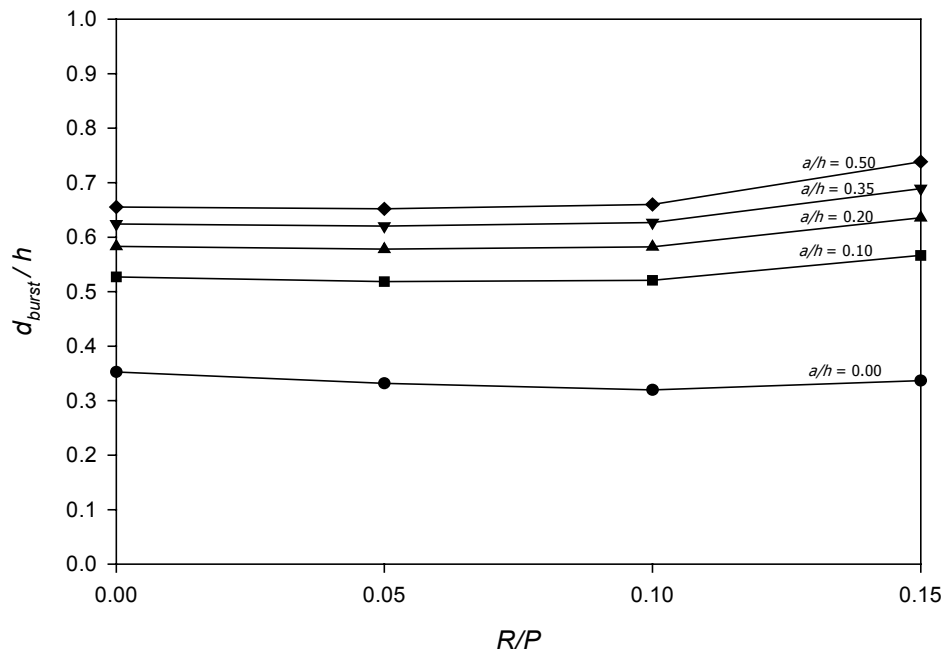


Fig. 3.74 BURSTING FORCE LOCATION vs. REACTION RATIO FOR 6 DEGREE INCLINED CONCENTRIC LOAD ($l/h = 0.25$, $b/h = 0.0$)

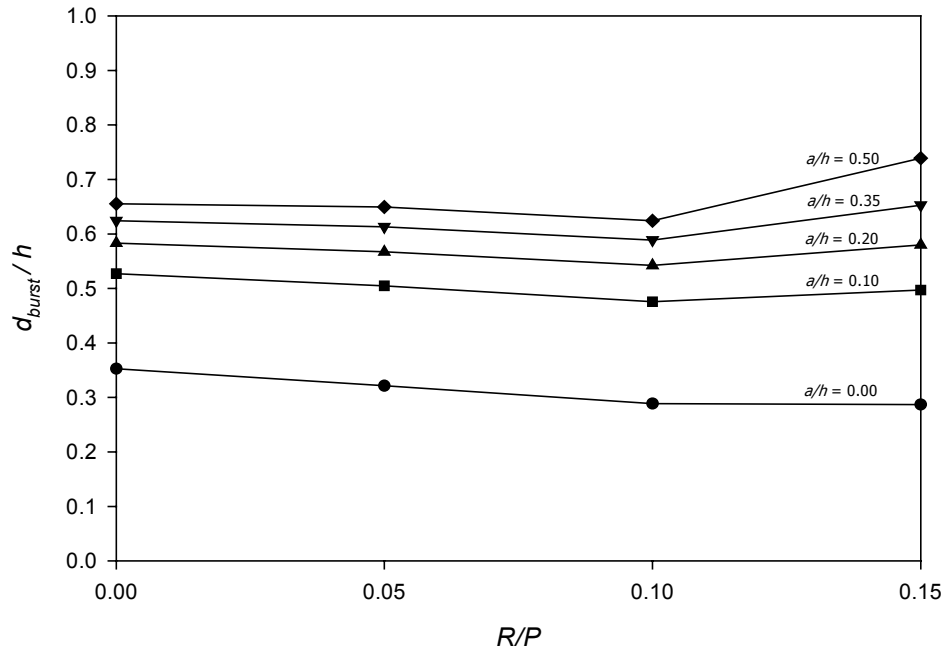


Fig. 3.75 BURSTING FORCE LOCATION vs. REACTION RATIO FOR 6 DEGREE INCLINED CONCENTRIC LOAD ($l/h = 0.50$, $b/h = 0.0$)

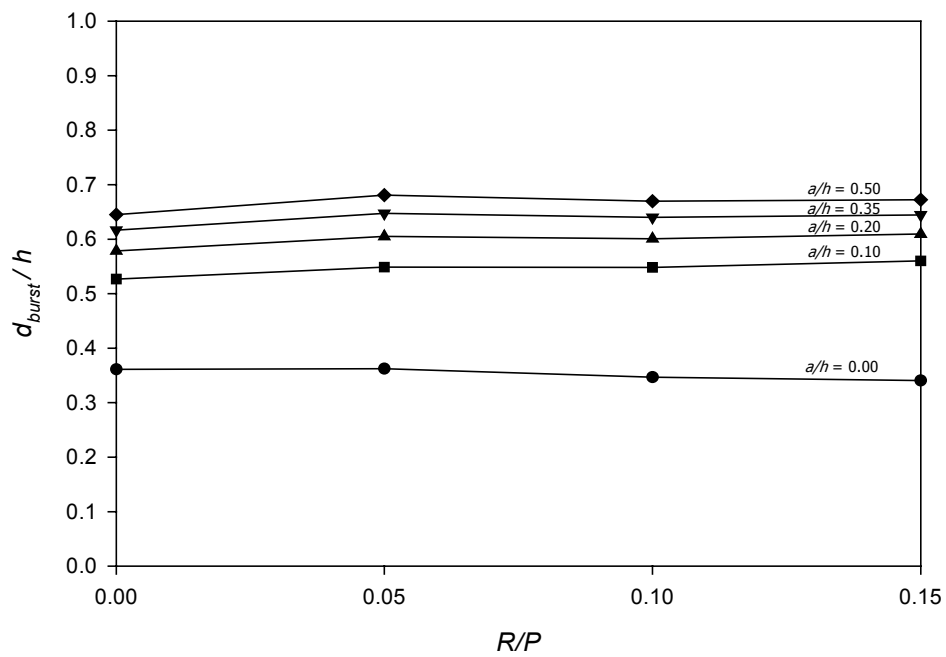


Fig. 3.76 BURSTING FORCE LOCATION vs. REACTION RATIO FOR 9 DEGREE INCLINED CONCENTRIC LOAD ($l/h = 0.125$, $b/h = 0.0$)

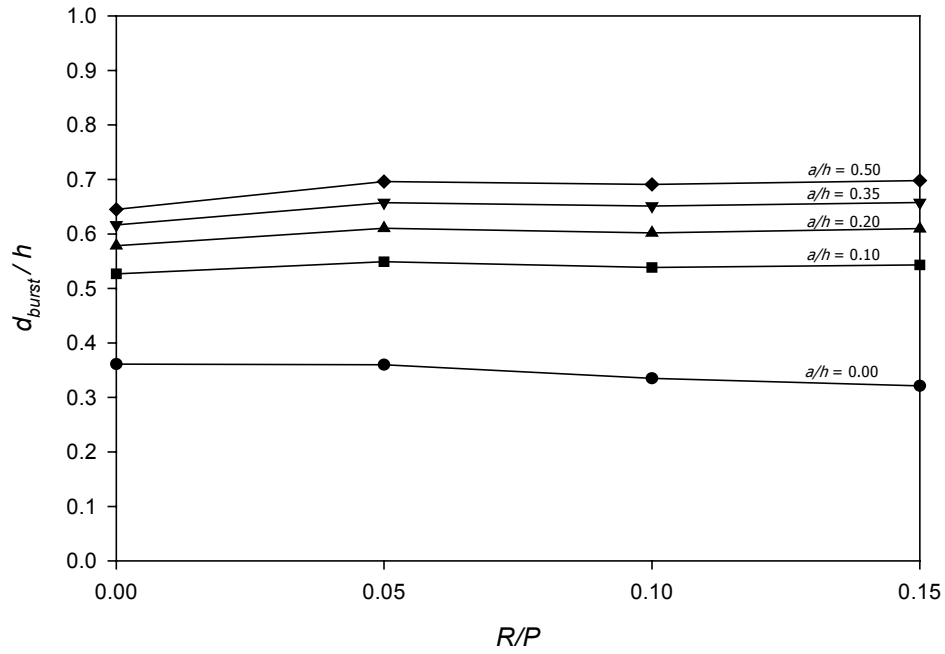


Fig. 3.77 BURSTING FORCE LOCATION vs. REACTION RATIO FOR 9 DEGREE INCLINED CONCENTRIC LOAD ($l/h = 0.25$, $b/h = 0.0$)

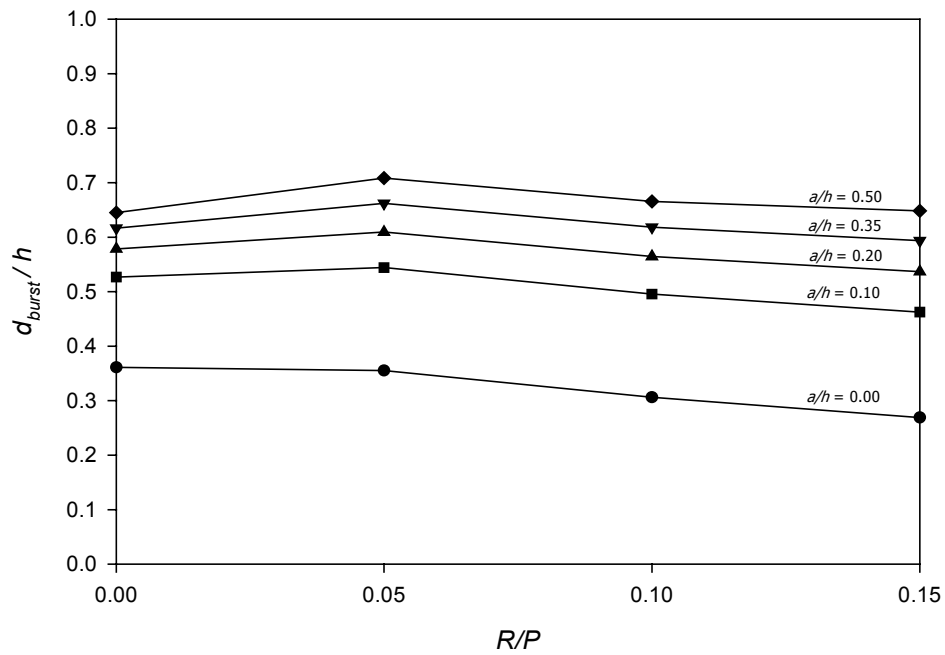


Fig. 3.78 BURSTING FORCE LOCATION vs. REACTION RATIO FOR 9 DEGREE INCLINED CONCENTRIC LOAD ($l/h = 0.50$, $b/h = 0.0$)

Table 3.9 SLOPES OF STRAIGHT LINE FOR THE PREDICTION OF d_{burst}
INCLINED CONCENTRIC LOAD CASE

a/h	Fig. 3.73	Fig. 3.74	Fig. 3.75	Fig. 3.76	Fig. 3.77	Fig. 3.78
0.00	0.0121	-0.1043	-0.44	-0.1382	-0.2674	-0.6142
0.10	0.3376	0.2629	-0.20	0.2231	0.1088	-0.4281
0.20	0.3151	0.3515	-0.02	0.2063	0.2080	-0.2776
0.35	0.3023	0.4322	0.19	0.1859	0.2750	-0.1516
0.50	0.3333	0.5539	0.56	0.1814	0.3533	0.0217
Average =	0.1926			-0.0076		

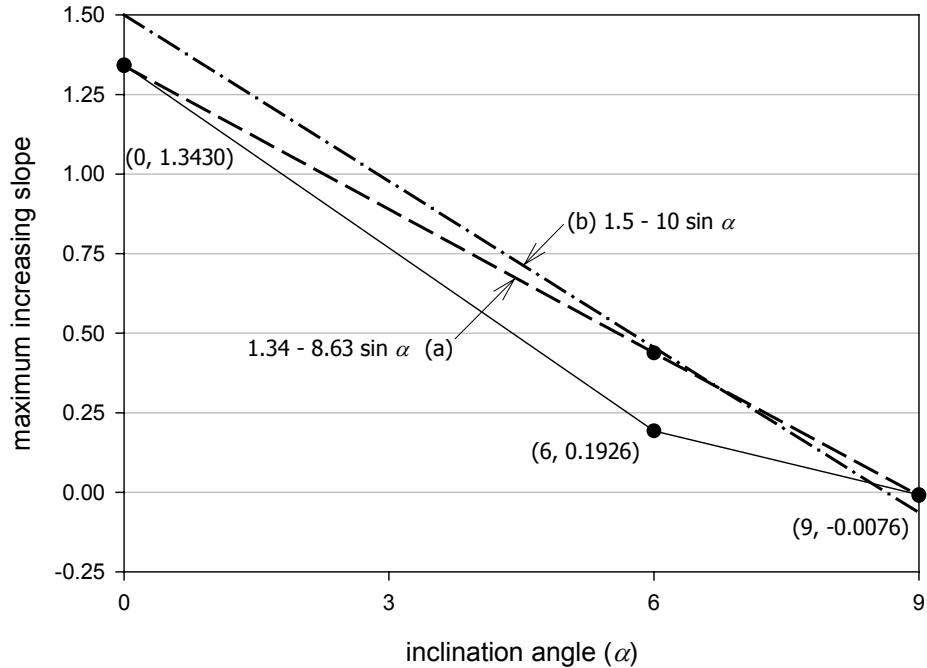


Fig. 3.79 EQUATION FOR THE PREDICTION OF BURSTING FORCE LOCATION

Since all parametric studies for horizontal and inclined concentrically loaded anchorage zone with support reaction have been conducted, the final equation for determining the location of bursting force can be established as shown below:

$$d_{burst} = 0.5 h + 0.25 a + 0.25 h \sin \alpha + \frac{R}{P} h (1.5 - 10 \sin \alpha) \quad (3.5)$$

Equation (3.5) accounts for the effects due to anchorage plate width (a), inclination angle (α), and magnitude of reaction (R).

Tables 3.10 through 3.12 provide a comparison of all results determined from three different methods: finite element analysis, equation (1.6), and equation (3.5). Similarly to Tables 3.6 through 3.8, the first six columns present the parameters used in all models. The last five columns show the results from those methods described and their percent differences. As usual, the column $d_{burst-fem}$ stands for the location of the bursting force from finite element results, which is determined along a horizontal line. The column *Eqn (1.6)* and *Eqn (3.5)* present the results using equations (1.6) and (3.5), respectively, with their percent difference compared to that in column $d_{burst-fem}$ presented next to each of them.

Equation (3.5) predicts d_{burst} best for anchorage ratios larger than 0.10. The percent difference between the results of the finite element method and equation (3.5) becomes very large for a/h equal to zero and relatively high for a/h of 0.10. However, for those a/h values larger than 0.10, equation (3.5) provides a smaller absolute percent difference compared to that determined using equation (1.6). The d_{burst} values predicted using equation (1.6) are mostly lower in magnitude than those obtained from the finite element method. Some of them have values as high as almost 50 percent difference. For the results produced by using equation (3.5), the highest absolute percent difference detected is 15.85. Generally, the percent difference given for almost every model with a/h larger than 0.10 has an absolute percent difference of less than 10 percent. Based on the comparisons given in Tables 3.10 to 3.12, it can be concluded that the newly developed equation predicts the bursting force location quite well.

Note in Table 3.12, with 9 degree inclination, the d_{burst} value is smaller in magnitude for the case of the furthest position and largest magnitude of reaction force ($l/h = 0.50$ and $R/P = 0.15$) compared to those with flatter angles. However, the percent difference obtained is rather small. This may be a result of the simplification of the equation in Fig. 3.79. Therefore, neglecting the l/h variable from the equation remains acceptable.

Table 3.10 COMPARISON OF d_{burst} FOR CONCENTRIC LOAD WITH NO INCLINATION ANGLE

h	a/h	R/P	l/h	α	β	$d_{burst-fem}/h$	$Eqn (1.6)$	$\%diff$	$Eqn (3.5)$	$\%diff$
						-1-	-2-	-1 & 2-	-3-	-1 & 3-
16	0.00	0.00	0.125	0	0.00	0.3167	0.5000	36.67	0.5000	36.67
16	0.10	0.00	0.125	0	0.00	0.4871	0.5000	2.58	0.5250	7.22
16	0.20	0.00	0.125	0	0.00	0.5408	0.5000	-7.54	0.5500	1.68
16	0.35	0.00	0.125	0	0.00	0.5757	0.5000	-13.15	0.5875	2.00
16	0.50	0.00	0.125	0	0.00	0.5964	0.5000	-16.16	0.6250	4.58
16	0.00	0.05	0.125	0	2.64	0.3417	0.5000	31.65	0.5750	40.57
16	0.10	0.05	0.125	0	2.64	0.5314	0.5000	-5.91	0.6000	11.43
16	0.20	0.05	0.125	0	2.64	0.5887	0.5000	-15.07	0.6250	5.81
16	0.35	0.05	0.125	0	2.64	0.6308	0.5000	-20.73	0.6625	4.79
16	0.50	0.05	0.125	0	2.64	0.6626	0.5000	-24.54	0.7000	5.34
16	0.00	0.10	0.125	0	5.27	0.3863	0.5000	22.74	0.6500	40.57
16	0.10	0.10	0.125	0	5.27	0.5974	0.5000	-16.31	0.6750	11.49
16	0.20	0.10	0.125	0	5.27	0.6568	0.5000	-23.87	0.7000	6.17
16	0.35	0.10	0.125	0	5.27	0.7070	0.5000	-29.28	0.7375	4.14
16	0.50	0.10	0.125	0	5.27	0.7514	0.5000	-33.46	0.7750	3.04
16	0.00	0.15	0.125	0	7.36	0.4182	0.5000	16.36	0.7250	42.32
16	0.10	0.15	0.125	0	7.36	0.6380	0.5000	-21.63	0.7500	14.94
16	0.20	0.15	0.125	0	7.36	0.6930	0.5000	-27.85	0.7750	10.58
16	0.35	0.15	0.125	0	7.36	0.7405	0.5000	-32.48	0.8125	8.86
16	0.50	0.15	0.125	0	7.36	0.7857	0.5000	-36.36	0.8500	7.57
16	0.00	0.00	0.25	0	0.00	0.3167	0.5000	36.67	0.5000	36.67
16	0.10	0.00	0.25	0	0.00	0.4871	0.5000	2.58	0.5250	7.22
16	0.20	0.00	0.25	0	0.00	0.5408	0.5000	-7.54	0.5500	1.68
16	0.35	0.00	0.25	0	0.00	0.5757	0.5000	-13.15	0.5875	2.00
16	0.50	0.00	0.25	0	0.00	0.5964	0.5000	-16.16	0.6250	4.58
16	0.00	0.05	0.25	0	2.45	0.3385	0.5000	32.30	0.5750	41.13
16	0.10	0.05	0.25	0	2.45	0.5311	0.5000	-5.86	0.6000	11.48
16	0.20	0.05	0.25	0	2.45	0.5930	0.5000	-15.68	0.6250	5.13
16	0.35	0.05	0.25	0	2.45	0.6390	0.5000	-21.75	0.6625	3.55
16	0.50	0.05	0.25	0	2.45	0.6758	0.5000	-26.01	0.7000	3.46
16	0.00	0.10	0.25	0	4.90	0.3854	0.5000	22.93	0.6500	40.71
16	0.10	0.10	0.25	0	4.90	0.6073	0.5000	-17.67	0.6750	10.03
16	0.20	0.10	0.25	0	4.90	0.6776	0.5000	-26.21	0.7000	3.20
16	0.35	0.10	0.25	0	4.90	0.7387	0.5000	-32.32	0.7375	-0.17
16	0.50	0.10	0.25	0	4.90	0.7958	0.5000	-37.17	0.7750	-2.61
16	0.00	0.15	0.25	0	6.84	0.4237	0.5000	15.25	0.7250	41.55
16	0.10	0.15	0.25	0	6.84	0.6632	0.5000	-24.60	0.7500	11.58
16	0.20	0.15	0.25	0	6.84	0.7345	0.5000	-31.93	0.7750	5.23
16	0.35	0.15	0.25	0	6.84	0.7971	0.5000	-37.27	0.8125	1.89
16	0.50	0.15	0.25	0	6.84	0.8589	0.5000	-41.79	0.8500	-1.04
16	0.00	0.00	0.5	0	0.00	0.3167	0.5000	36.67	0.5000	36.67
16	0.10	0.00	0.5	0	0.00	0.4871	0.5000	2.58	0.5250	7.22
16	0.20	0.00	0.5	0	0.00	0.5408	0.5000	-7.54	0.5500	1.68
16	0.35	0.00	0.5	0	0.00	0.5757	0.5000	-13.15	0.5875	2.00
16	0.50	0.00	0.5	0	0.00	0.5964	0.5000	-16.16	0.6250	4.58
16	0.00	0.05	0.5	0	2.15	0.3303	0.5000	33.94	0.5750	42.56
16	0.10	0.05	0.5	0	2.15	0.5231	0.5000	-4.41	0.6000	12.82
16	0.20	0.05	0.5	0	2.15	0.5901	0.5000	-15.27	0.6250	5.58
16	0.35	0.05	0.5	0	2.15	0.6413	0.5000	-22.03	0.6625	3.20
16	0.50	0.05	0.5	0	2.15	0.6856	0.5000	-27.08	0.7000	2.05
16	0.00	0.10	0.5	0	4.29	0.3791	0.5000	24.19	0.6500	41.68
16	0.10	0.10	0.5	0	4.29	0.6112	0.5000	-18.19	0.6750	9.46
16	0.20	0.10	0.5	0	4.29	0.6993	0.5000	-28.50	0.7000	0.11
16	0.35	0.10	0.5	0	4.29	0.7799	0.5000	-35.89	0.7375	-5.44
16	0.50	0.10	0.5	0	4.29	0.8670	0.5000	-42.33	0.7750	-10.61
16	0.00	0.15	0.5	0	5.99	0.4267	0.5000	14.66	0.7250	41.14
16	0.10	0.15	0.5	0	5.99	0.6915	0.5000	-27.70	0.7500	7.79
16	0.20	0.15	0.5	0	5.99	0.7945	0.5000	-37.06	0.7750	-2.45
16	0.35	0.15	0.5	0	5.99	0.8959	0.5000	-44.19	0.8125	-9.31
16	0.50	0.15	0.5	0	5.99	1.0101	0.5000	-50.50	0.8500	-15.85

Table 3.11 COMPARISON OF d_{burst} FOR CONCENTRIC LOAD WITH 6 DEGREE INCLINATION ANGLE

h	a/h	R/P	l/h	α	β	$d_{burst-fem}/h$	$Eqn (1.6)$	$\%diff$	$Eqn (3.5)$	$\%diff$
						-1-	-2-	-1 & 2-	-3-	-1 & 3-
16	0.00	0.00	0.125	6	-6.00	0.3523	0.5000	29.54	0.5261	33.04
16	0.10	0.00	0.125	6	-6.00	0.5270	0.5000	-5.12	0.5511	4.39
16	0.20	0.00	0.125	6	-6.00	0.5829	0.5000	-14.22	0.5761	-1.16
16	0.35	0.00	0.125	6	-6.00	0.6241	0.5000	-19.88	0.6136	-1.67
16	0.50	0.00	0.125	6	-6.00	0.6554	0.5000	-23.71	0.6511	-0.65
16	0.00	0.05	0.125	6	-3.36	0.3356	0.5000	32.87	0.5489	38.85
16	0.10	0.05	0.125	6	-3.36	0.5209	0.5000	-4.01	0.5739	9.23
16	0.20	0.05	0.125	6	-3.36	0.5759	0.5000	-13.18	0.5989	3.83
16	0.35	0.05	0.125	6	-3.36	0.6147	0.5000	-18.66	0.6364	3.40
16	0.50	0.05	0.125	6	-3.36	0.6405	0.5000	-21.93	0.6739	4.96
16	0.00	0.10	0.125	6	-0.70	0.3321	0.5000	33.57	0.5716	41.89
16	0.10	0.10	0.125	6	-0.70	0.5317	0.5000	-5.96	0.5966	10.88
16	0.20	0.10	0.125	6	-0.70	0.5844	0.5000	-14.44	0.6216	5.99
16	0.35	0.10	0.125	6	-0.70	0.6211	0.5000	-19.50	0.6591	5.77
16	0.50	0.10	0.125	6	-0.70	0.6476	0.5000	-22.79	0.6966	7.04
16	0.00	0.15	0.125	6	1.95	0.3541	0.5000	29.17	0.5943	40.42
16	0.10	0.15	0.125	6	1.95	0.5776	0.5000	-13.44	0.6193	6.74
16	0.20	0.15	0.125	6	1.95	0.6301	0.5000	-20.65	0.6443	2.20
16	0.35	0.15	0.125	6	1.95	0.6694	0.5000	-25.31	0.6818	1.82
16	0.50	0.15	0.125	6	1.95	0.7054	0.5000	-29.11	0.7193	1.94
16	0.00	0.00	0.25	6	-6.00	0.3523	0.5000	29.54	0.5261	33.04
16	0.10	0.00	0.25	6	-6.00	0.5270	0.5000	-5.12	0.5511	4.39
16	0.20	0.00	0.25	6	-6.00	0.5829	0.5000	-14.22	0.5761	-1.16
16	0.35	0.00	0.25	6	-6.00	0.6241	0.5000	-19.88	0.6136	-1.67
16	0.50	0.00	0.25	6	-6.00	0.6554	0.5000	-23.71	0.6511	-0.65
16	0.00	0.05	0.25	6	-3.55	0.3316	0.5000	33.68	0.5489	39.59
16	0.10	0.05	0.25	6	-3.55	0.5184	0.5000	-3.54	0.5739	9.67
16	0.20	0.05	0.25	6	-3.55	0.5778	0.5000	-13.47	0.5989	3.51
16	0.35	0.05	0.25	6	-3.55	0.6203	0.5000	-19.39	0.6364	2.53
16	0.50	0.05	0.25	6	-3.55	0.6518	0.5000	-23.29	0.6739	3.28
16	0.00	0.10	0.25	6	-1.08	0.3195	0.5000	36.11	0.5716	44.11
16	0.10	0.10	0.25	6	-1.08	0.5207	0.5000	-3.98	0.5966	12.72
16	0.20	0.10	0.25	6	-1.08	0.5822	0.5000	-14.12	0.6216	6.34
16	0.35	0.10	0.25	6	-1.08	0.6268	0.5000	-20.23	0.6591	4.90
16	0.50	0.10	0.25	6	-1.08	0.6599	0.5000	-24.23	0.6966	5.27
16	0.00	0.15	0.25	6	1.38	0.3367	0.5000	32.67	0.5943	43.35
16	0.10	0.15	0.25	6	1.38	0.5664	0.5000	-11.72	0.6193	8.55
16	0.20	0.15	0.25	6	1.38	0.6356	0.5000	-21.33	0.6443	1.36
16	0.35	0.15	0.25	6	1.38	0.6889	0.5000	-27.42	0.6818	-1.02
16	0.50	0.15	0.25	6	1.38	0.7384	0.5000	-32.29	0.7193	-2.59
16	0.00	0.00	0.5	6	-6.00	0.3523	0.5000	29.54	0.5261	33.04
16	0.10	0.00	0.5	6	-6.00	0.5270	0.5000	-5.12	0.5511	4.39
16	0.20	0.00	0.5	6	-6.00	0.5829	0.5000	-14.22	0.5761	-1.16
16	0.35	0.00	0.5	6	-6.00	0.6241	0.5000	-19.88	0.6136	-1.67
16	0.50	0.00	0.5	6	-6.00	0.6554	0.5000	-23.71	0.6511	-0.65
16	0.00	0.05	0.5	6	-3.86	0.3212	0.5000	35.75	0.5489	41.47
16	0.10	0.05	0.5	6	-3.86	0.5046	0.5000	-0.92	0.5739	12.06
16	0.20	0.05	0.5	6	-3.86	0.5669	0.5000	-11.80	0.5989	5.34
16	0.35	0.05	0.5	6	-3.86	0.6131	0.5000	-18.45	0.6364	3.65
16	0.50	0.05	0.5	6	-3.86	0.6493	0.5000	-22.99	0.6739	3.65
16	0.00	0.10	0.5	6	-1.70	0.2884	0.5000	42.31	0.5716	49.54
16	0.10	0.10	0.5	6	-1.70	0.4755	0.5000	4.90	0.5966	20.30
16	0.20	0.10	0.5	6	-1.70	0.5421	0.5000	-7.76	0.6216	12.80
16	0.35	0.10	0.5	6	-1.70	0.5887	0.5000	-15.07	0.6591	10.68
16	0.50	0.10	0.5	6	-1.70	0.6240	0.5000	-19.87	0.6966	10.42
16	0.00	0.15	0.5	6	0.46	0.2868	0.5000	42.63	0.5943	51.74
16	0.10	0.15	0.5	6	0.46	0.4970	0.5000	0.60	0.6193	19.76
16	0.20	0.15	0.5	6	0.46	0.5798	0.5000	-13.76	0.6443	10.02
16	0.35	0.15	0.5	6	0.46	0.6526	0.5000	-23.39	0.6818	4.28
16	0.50	0.15	0.5	6	0.46	0.7391	0.5000	-32.35	0.7193	-2.68

Table 3.12 COMPARISON OF d_{burst} FOR CONCENTRIC LOAD WITH 9 DEGREE INCLINATION ANGLE

h	a/h	R/P	l/h	α	β	$d_{burst-fem}/h$			$Eqn (3.5)$	
						-1-	-2-	-1 & 2-	-3-	-1 & 3-
16	0.00	0.00	0.125	9	-9.00	0.3610	0.5000	27.79	0.5391	33.03
16	0.10	0.00	0.125	9	-9.00	0.5266	0.5000	-5.05	0.5641	6.65
16	0.20	0.00	0.125	9	-9.00	0.5783	0.5000	-13.54	0.5891	1.84
16	0.35	0.00	0.125	9	-9.00	0.6164	0.5000	-18.89	0.6266	1.62
16	0.50	0.00	0.125	9	-9.00	0.6450	0.5000	-22.48	0.6641	2.88
16	0.00	0.05	0.125	9	-6.33	0.3621	0.5000	27.58	0.5359	32.43
16	0.10	0.05	0.125	9	-6.33	0.5487	0.5000	-8.87	0.5609	2.18
16	0.20	0.05	0.125	9	-6.33	0.6051	0.5000	-17.37	0.5859	-3.17
16	0.35	0.05	0.125	9	-6.33	0.6474	0.5000	-22.77	0.6234	-3.71
16	0.50	0.05	0.125	9	-6.33	0.6807	0.5000	-26.54	0.6609	-2.91
16	0.00	0.10	0.125	9	-3.71	0.3467	0.5000	30.66	0.5327	34.91
16	0.10	0.10	0.125	9	-3.71	0.5482	0.5000	-8.79	0.5577	1.71
16	0.20	0.10	0.125	9	-3.71	0.6007	0.5000	-16.77	0.5827	-3.01
16	0.35	0.10	0.125	9	-3.71	0.6397	0.5000	-21.84	0.6202	-3.06
16	0.50	0.10	0.125	9	-3.71	0.6697	0.5000	-25.34	0.6577	-1.80
16	0.00	0.15	0.125	9	-1.04	0.3403	0.5000	31.94	0.5295	35.73
16	0.10	0.15	0.125	9	-1.04	0.5601	0.5000	-10.72	0.5545	-1.00
16	0.20	0.15	0.125	9	-1.04	0.6092	0.5000	-17.93	0.5795	-4.89
16	0.35	0.15	0.125	9	-1.04	0.6443	0.5000	-22.40	0.6170	-4.25
16	0.50	0.15	0.125	9	-1.04	0.6722	0.5000	-25.62	0.6545	-2.64
16	0.00	0.00	0.25	9	-9.00	0.3610	0.5000	27.79	0.5391	33.03
16	0.10	0.00	0.25	9	-9.00	0.5266	0.5000	-5.05	0.5641	6.65
16	0.20	0.00	0.25	9	-9.00	0.5783	0.5000	-13.54	0.5891	1.84
16	0.35	0.00	0.25	9	-9.00	0.6164	0.5000	-18.89	0.6266	1.62
16	0.50	0.00	0.25	9	-9.00	0.6450	0.5000	-22.48	0.6641	2.88
16	0.00	0.05	0.25	9	-6.37	0.3599	0.5000	28.01	0.5359	32.83
16	0.10	0.05	0.25	9	-6.37	0.5489	0.5000	-8.92	0.5609	2.13
16	0.20	0.05	0.25	9	-6.37	0.6106	0.5000	-18.11	0.5859	-4.04
16	0.35	0.05	0.25	9	-6.37	0.6572	0.5000	-23.92	0.6234	-5.15
16	0.50	0.05	0.25	9	-6.37	0.6960	0.5000	-28.16	0.6609	-5.05
16	0.00	0.10	0.25	9	-4.10	0.3351	0.5000	32.98	0.5327	37.09
16	0.10	0.10	0.25	9	-4.10	0.5383	0.5000	-7.12	0.5577	3.47
16	0.20	0.10	0.25	9	-4.10	0.6018	0.5000	-16.91	0.5827	-3.17
16	0.35	0.10	0.25	9	-4.10	0.6509	0.5000	-23.18	0.6202	-4.72
16	0.50	0.10	0.25	9	-4.10	0.6906	0.5000	-27.60	0.6577	-4.77
16	0.00	0.15	0.25	9	-1.62	0.3209	0.5000	35.82	0.5295	39.39
16	0.10	0.15	0.25	9	-1.62	0.5429	0.5000	-7.90	0.5545	2.08
16	0.20	0.15	0.25	9	-1.62	0.6095	0.5000	-17.97	0.5795	-4.93
16	0.35	0.15	0.25	9	-1.62	0.6577	0.5000	-23.98	0.6170	-6.19
16	0.50	0.15	0.25	9	-1.62	0.6980	0.5000	-28.37	0.6545	-6.24
16	0.00	0.00	0.5	9	-9.00	0.3610	0.5000	27.79	0.5391	33.03
16	0.10	0.00	0.5	9	-9.00	0.5266	0.5000	-5.05	0.5641	6.65
16	0.20	0.00	0.5	9	-9.00	0.5783	0.5000	-13.54	0.5891	1.84
16	0.35	0.00	0.5	9	-9.00	0.6164	0.5000	-18.89	0.6266	1.62
16	0.50	0.00	0.5	9	-9.00	0.6450	0.5000	-22.48	0.6641	2.88
16	0.00	0.05	0.5	9	-6.22	0.3553	0.5000	28.93	0.5359	33.69
16	0.10	0.05	0.5	9	-6.22	0.5442	0.5000	-8.11	0.5609	2.98
16	0.20	0.05	0.5	9	-6.22	0.6092	0.5000	-17.93	0.5859	-3.83
16	0.35	0.05	0.5	9	-6.22	0.6619	0.5000	-24.47	0.6234	-5.82
16	0.50	0.05	0.5	9	-6.22	0.7084	0.5000	-29.42	0.6609	-6.70
16	0.00	0.10	0.5	9	-4.71	0.3061	0.5000	38.79	0.5327	42.54
16	0.10	0.10	0.5	9	-4.71	0.4957	0.5000	0.86	0.5577	11.11
16	0.20	0.10	0.5	9	-4.71	0.5645	0.5000	-11.42	0.5827	3.13
16	0.35	0.10	0.5	9	-4.71	0.6181	0.5000	-19.11	0.6202	0.33
16	0.50	0.10	0.5	9	-4.71	0.6655	0.5000	-24.86	0.6577	-1.17
16	0.00	0.15	0.5	9	-2.55	0.2689	0.5000	46.22	0.5295	49.21
16	0.10	0.15	0.5	9	-2.55	0.4624	0.5000	7.53	0.5545	16.61
16	0.20	0.15	0.5	9	-2.55	0.5367	0.5000	-6.83	0.5795	7.39
16	0.35	0.15	0.5	9	-2.55	0.5937	0.5000	-15.78	0.6170	3.77
16	0.50	0.15	0.5	9	-2.55	0.6483	0.5000	-22.87	0.6545	0.95

3.4.3 Eccentrically Loaded Anchor Configuration

Quite often anchor in post-tensioned rectangular girders are not located exactly at the center of the section. In common cases in post-tensioned concrete beams, the prestressing force is applied eccentrically. The eccentricity of an anchorage zone without support reaction can be categorized into two major groups: eccentric within and outside the kern of the section. The kern of a rectangular section is located at a distance of $0.167h$ from the center of girder section. If a prestressing load acts within the kern, the behavior of stresses in the bursting region is similar to that for a concentric load configuration. If the load is applied outside the kern, the determination of the bursting force and its location becomes more complicated. With a high eccentricity resulting from the load applied outside the kern, longitudinal edge tensile stresses occur at the farthest edge of the girder from the load and can produce cracks in the concrete which requires reinforcement for crack controlling.

The AASHTO Standard Specifications 2002 present a method for the calculation of the forces resulting from an eccentric prestressing load. As presented in section 3.3.3, the bursting force in an anchorage zone can be determined using a symmetric prism approach. The approach has proven to be applicable for anchorage zones without support reactions. Equations (3.3) and (1.6) calculate T_{burst} including the presence of an eccentricity term. The longitudinal edge tension can be calculated using axial-flexural beam theory. However, these methods of determining the effect of the prestressing force related to the position of the kern are effective only for anchorage zones without support reactions. When a reaction force is present, longitudinal edge tension does not necessarily occur even though the prestressing force is applied outside of the kern. Therefore, the kern of the section is no longer a criterion for categorizing the cases of eccentric load configurations with support reaction.

Values used for the parametric study of the eccentric load configuration, as previously stated, consist of six eccentricity ratios (e/h): +0.10, +0.25, +0.40, -0.10, -0.25, and -0.40. From Fig. 3.9, positive sign indicates an upward direction of eccentricity and negative sign indicates otherwise. The largest e/h value in the series is the one with a magnitude of 0.40. This number is the maximum eccentricity for the a/h ratio of 0.20. In the finite element analysis of the present study, only two a/h values were selected, including 0.10 and 0.20.

Although the a/h value of 0.10 is not a typical case in the equations that have been developed so far, it was found to be useful for the present parametric study such as the bearing plate ratio (b/h). If an anchor plate with the size of $0.20h$ is located with the largest eccentricity of $0.40h$, the edge of the plate reaches the outmost fiber of the anchorage zone (see Fig. 3.80a). If a smaller plate size is used as shown in Fig. 3.80b, the region around the edge of the plate and anchorage body will have some space for the propagation of stresses from a support reaction. Therefore, the a/h value of 0.10 is appropriate.

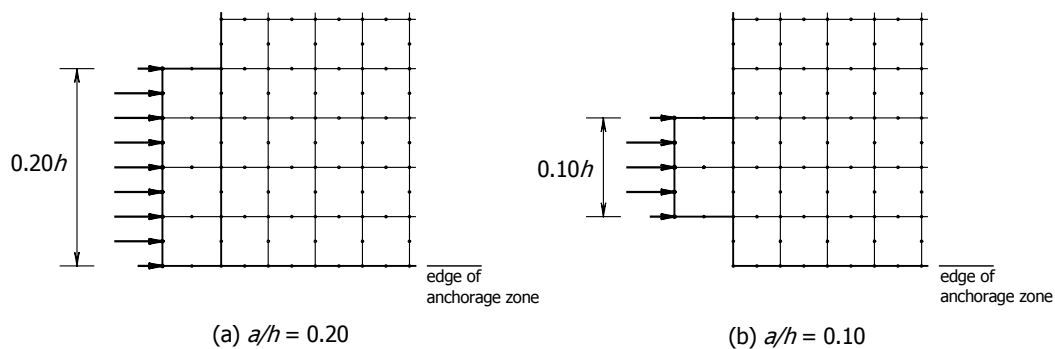


Fig. 3.80 ANCHOR PLATES AT THE HIGHEST ECCENTRIC LOCATION

The spalling force is also a part of the behavior of stresses in eccentrically loaded anchorage zone. The force is large in the case of large eccentricity. The AASHTO Standard Specifications 2002 address the reinforcement for spalling force by requiring it to resist a minimum of 2 percent of the prestressing force. If the prestressing force is located outside the kern of the section, special consideration using axial-flexural beam theory must be taken for determining the longitudinal edge tensile force. The reinforcement to resist the force can be applied for both longitudinal edge tension and spalling force reinforcement. This method is quite conservative for the resistance of the spalling effect. Although a reaction force is introduced into a structure, the axial-flexural beam theory remains effectively useful. The present study comments on some parts of the investigation in which the spalling force is found to possibly produce an effect for the design of anchorage zone. However, the spalling force is not the major focus of the present study. Therefore, it will not be investigated in much detail.

3.4.3.1 Elastic Stress Distribution

The concentration of the bursting stresses usually occurs around the region immediately ahead of the anchor plate, as has been illustrated in the previous two sections. The bursting stresses are bounded by the shape of the anchorage zone and affected directly by the distance between the anchor and the edge of the body. If the distance is reduced due to the change in position of the anchor plate, the stress distribution certainly differs from that which appears in a concentric load configuration, and results in a different magnitude of bursting force. Fig. 3.81 shows contour plots of normal stresses in two directions, y - y and x - x , and shearing stresses on the x - y plane for an anchorage zone with anchorage ratio of 0.10 and a load configuration with eccentricity of $0.10h$. The stress contours move according to the direction of eccentricity. Since the a/h value in the figure is 0.10, the maximum bursting stress region is obviously occurred. The spalling stresses appear on both sides of the anchor plate.

Another eccentrically loaded anchorage zone is given in Fig. 3.82. The anchorage zone now is subjected to a prestressing force with a high eccentricity. The bursting stress region still occurs ahead of the position of the anchor plate but within a smaller region than that in Fig. 3.81. Considering the spalling region in the figure, the largest spalling stress occurs over the upper surface above the anchor, and has a magnitude over $2.75 \sigma_o$. This is caused by the application of the load outside the kern of the section including the effect of a small anchorage plate. In Fig. 3.82b, the stress contours in the x - x direction are almost straight lines parallel to the axis of the beam. The zero stress contour line occurs in the upper part with respect to the center of the anchor plate. This indicates that the longitudinal tensile stresses are developed above the line. The general behavior of an eccentrically loaded anchorage zone without a support reaction has similar characteristics in both figures.

Since the study is focusing on the behavior of tensile stresses in the y - y direction, Fig. 3.83 shows the comparison between the y - y stress contours in eccentrically loaded anchorage zones with support reaction for four different e/h values: +0.40, +0.10, -0.10, and -0.40 (see Figs. 3.83a to 3.83d). As can be seen, the reaction force has a significant effect on the stress contours in all figures. The bursting stress region is still located at the position ahead of anchor plate and varies in size corresponding to the distance between the anchor and the edge

surface. The anchorage zones with the highest eccentricity (Figs. 3.83a and 3.83d) contain a small region of bursting stresses. Note in Figs. 3.83a to 3.83c that the presence of the reaction has a major influence on the spalling stresses at the anchorage surface. The spalling stress almost vanishes in the region between the anchor and the lowest surface of the anchorage zone in Figs. 3.83b and 3.83c. In Fig. 3.83d, the spalling stresses occur at the surface above the anchor plate, which is located near the unstressed corner region of the anchorage zone.

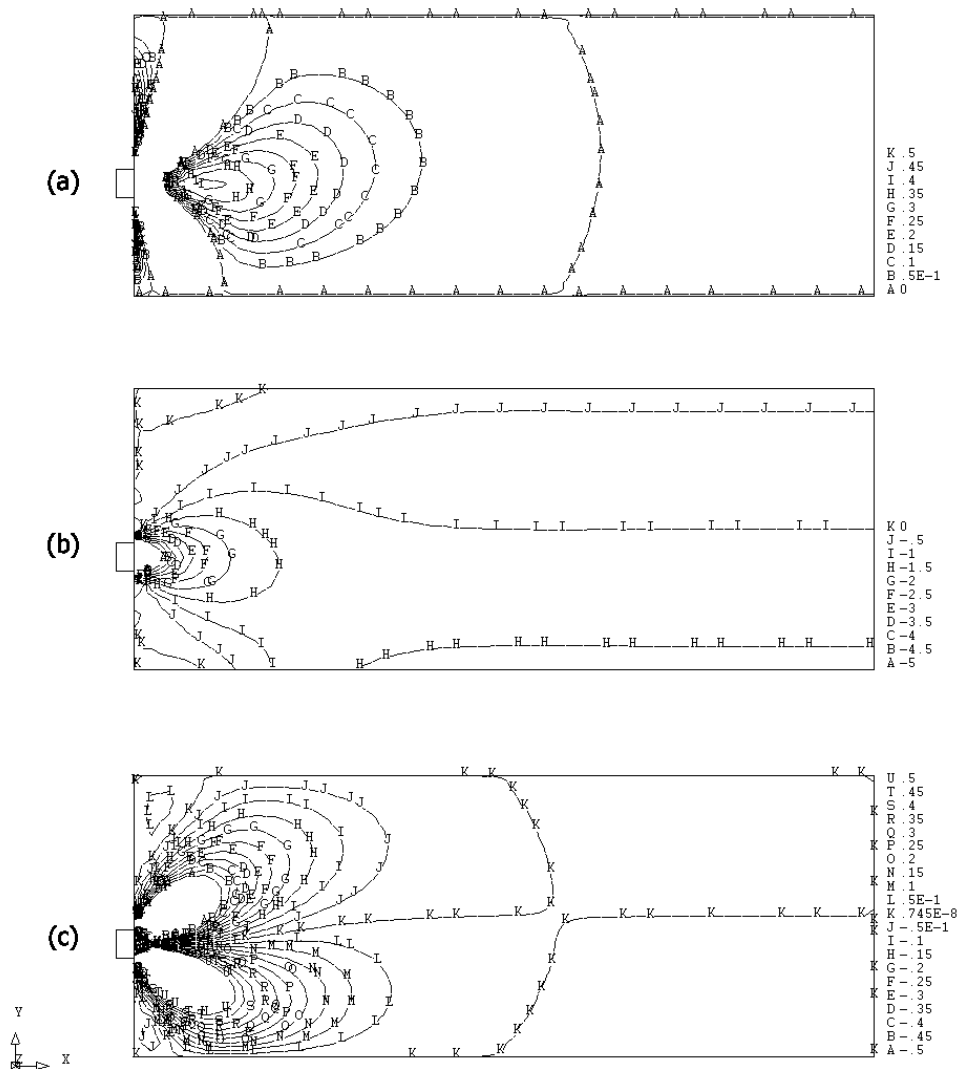


Fig. 3.81 ECCENTRIC LOAD WITH $e/h = 0.10$, $a/h = 0.10$, $R/P = 0.00$
 a) S_{yy} , b) S_{xx} , AND c) S_{xy} (Stress multiplied by σ_o)

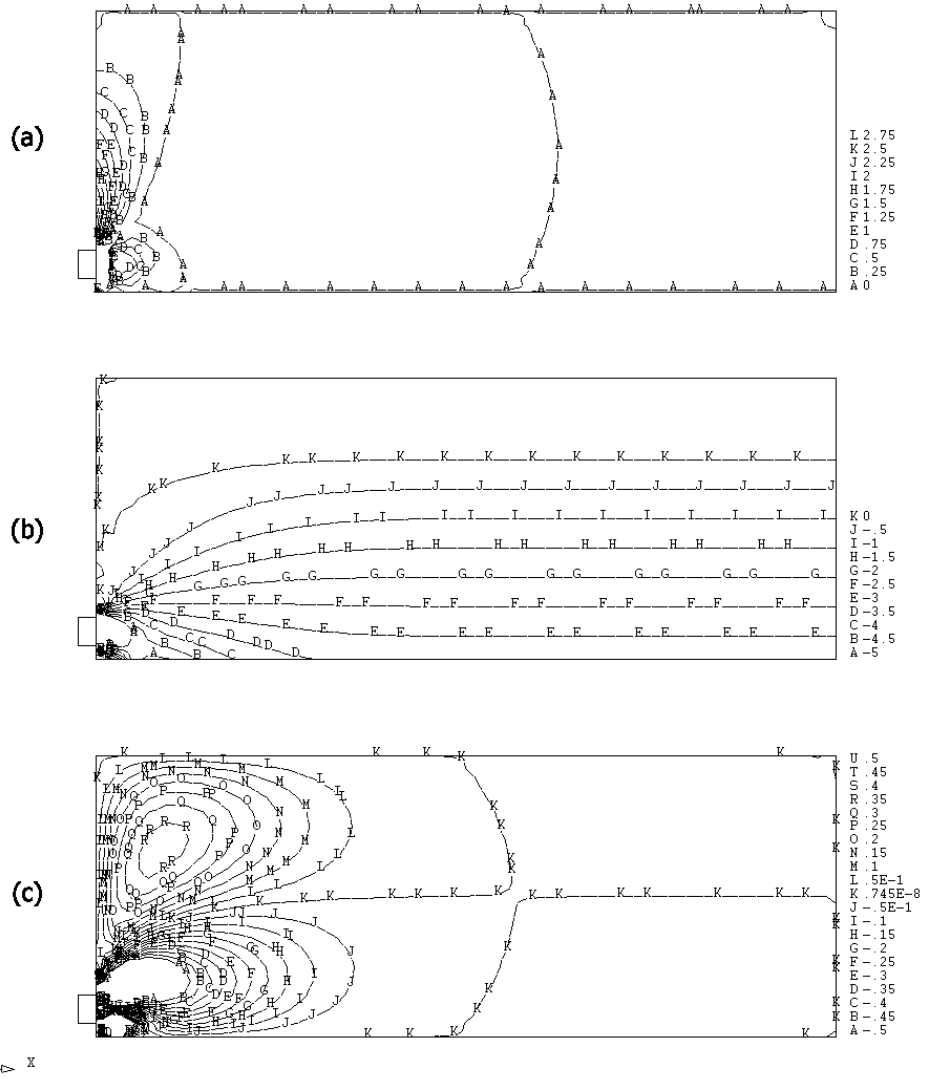


Fig. 3.82 ECCENTRIC LOAD WITH $e/h = 0.40$, $a/h = 0.10$, $R/P = 0.00$
 a) S_{yy} , b) S_{xx} , AND c) S_{xy} (Stress multiplied by σ_0)

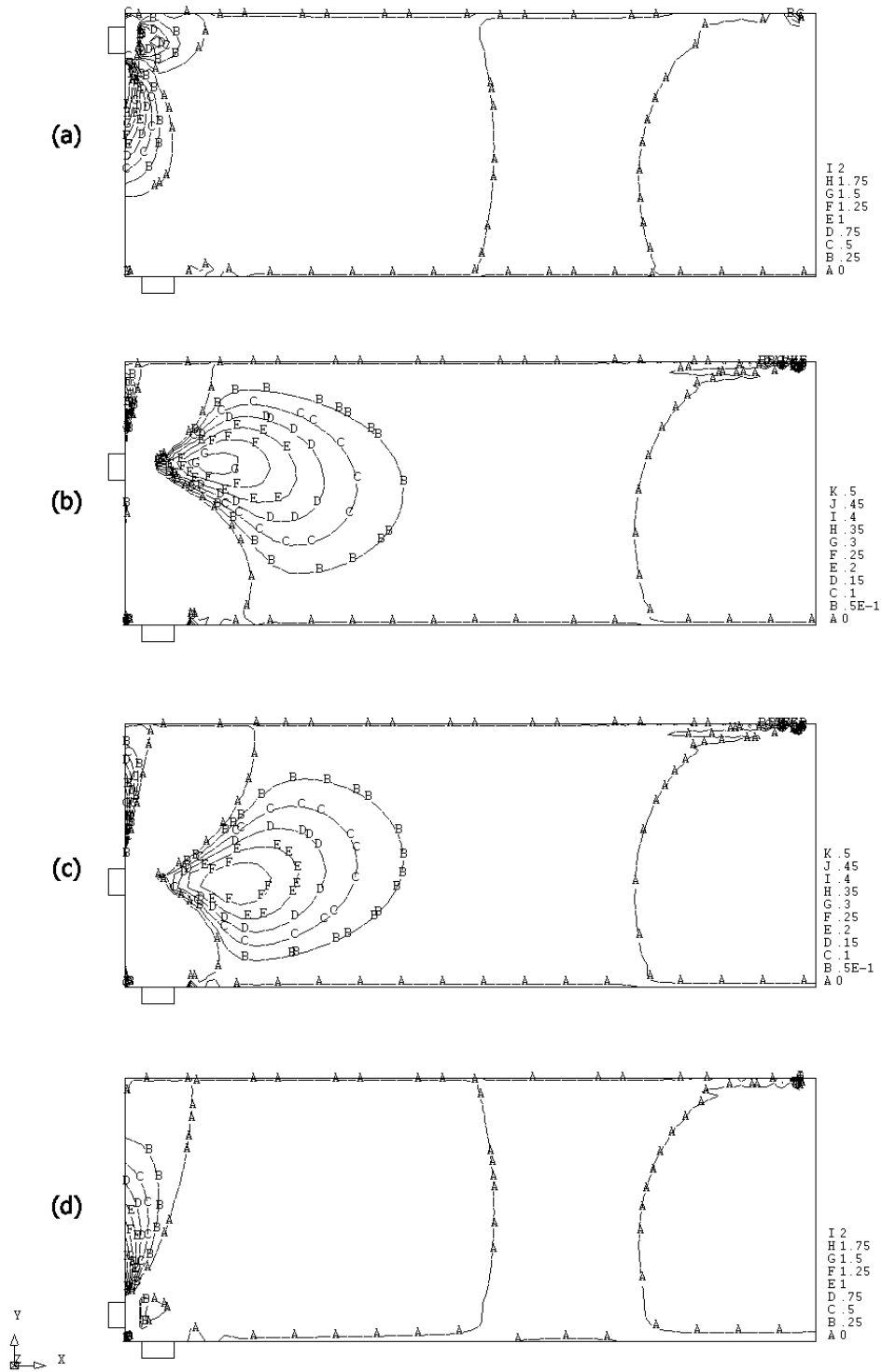


Fig. 3.83 STRESS IN Y-Y DIRECTION OF ECCENTRIC LOAD WITH e/h EQUAL TO
 a) +0.40, b) +0.10, c) -0.10, AND d) -0.40 (Stress multiplied by σ_0)
 ($l/h = 0.125$, $b/h = 0.125$, and $R/P = 0.15$)

The unstressed corner is the region divided by the boundaries of highly stressed and lightly stressed regions in anchorage zones (Wollmann et al., 2000). Fig. 3.84 shows the other stress contours for the anchorage zone in Fig. 3.83d. The stress in the x-x direction and the shear stress in the x-y plane are presented. In Fig. 3.84a, the upper corner of the anchorage zone has a triangular shaped zone of zero stress. This indicates that the alignment of the main compressive strut runs from the bottom left corner diagonally to the upper right corner of the picture. In Fig. 3.84b, the shear stress contours look different from those in Fig. 3.82c in that the stresses deviate in the direction toward the top vertical boundary support.

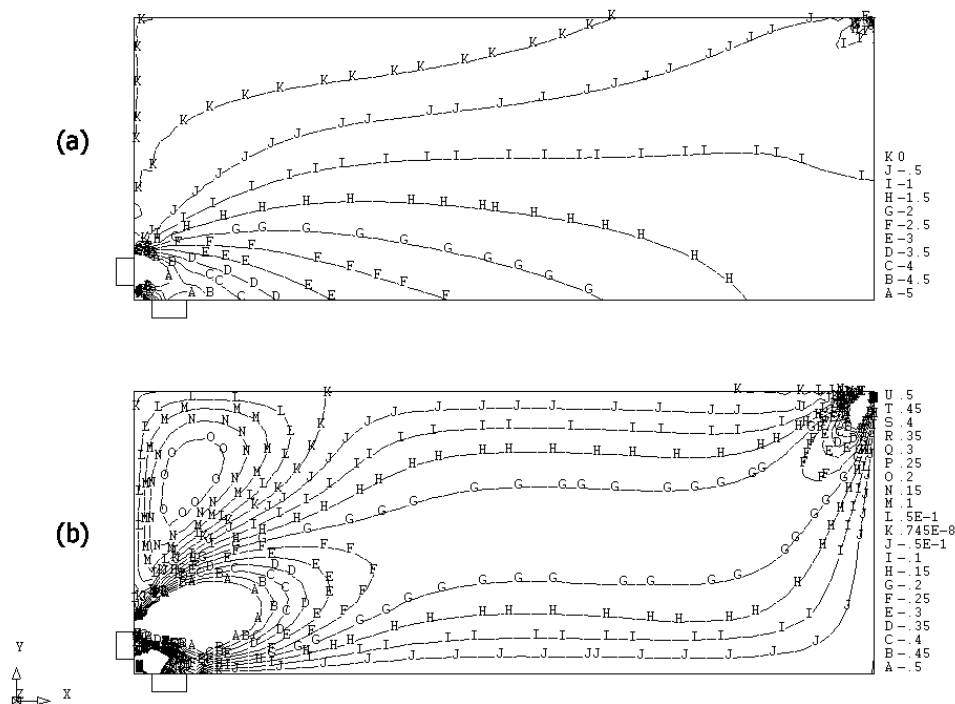


Fig. 3.84 ECCENTRIC LOAD WITH $e/h = -0.40$, $a/h = 0.10$, $R/P = 0.15$

a) S_{xx} AND b) S_{xy} (Stress multiplied by σ_o)
 $(l/h = 0.125$, $b/h = 0.125$, and $R/P = 0.15)$

3.4.3.2 Bursting Force

Based on the results presented in the last two sections, several parameters can be eliminated by selecting the most applicable parameters used in the investigation in order to give the most effective results. In the present study, as previously stated, two anchorage

ratios are chosen to illustrate the general behavior of eccentrically loaded anchorage zones with support reaction. The first parameter with a/h equal to 0.10 is used for the study of the bearing plate size effect, while the second with a/h equal to 0.20 is for the investigation of reaction force location and magnitude. The magnitude of the reaction force is also limited to two numbers consisting of 5 and 15 percent of the prestressing force. After the improved design formulation is constructed, a comparison to the result given by equation (1.5) is performed and discussed.

As graphically illustrated in Fig. 3.83, the bursting regions which develop are a function of the distance between the center of the anchor plate and the closest edge of the anchorage body. This implies that the symmetric prism approach is still applicable to the prediction of the bursting force in eccentrically loaded anchorage zones with support reaction. The results from other parametric studies investigating the effect of the reaction force will provide supportive information.

The first parametric study is the effect of the reaction location. Figs. 3.85 and 3.86 show the relation between the bursting force and the location of the reaction force for the R/P ratio of 0.05 and 0.15, respectively. These figures are for the structures with a/h equal to 0.20. As shown, the behaviors of the plots in both figures are similar to the case in which the eccentricity is above the centerline of the anchorage zone. For the eccentricity close to the centerline, the behavior of each plot is slightly different but exhibits the same characteristics for the bursting force as for the cases with eccentricities of +0.25, +0.10, 0.00, -0.10, and -0.25. For the largest eccentricity, the largest bursting force occurs when the reaction force is furthest from the anchor surface. The bursting force with an eccentricity of +0.40 has a slightly larger magnitude compared to the anchor with a negative eccentric direction.

When the location of the prestressing load is closest to the edge of the anchorage zone, the symmetric prism becomes smallest. Since the prism is very small, the bursting region appears quite close to the anchor plate. These stresses counteract the compressive stresses due to the application of the reaction force. When the reaction force is located closest to the anchor, a direct cancellation of stresses within the region occurs. When the reaction force is

located further away, the stresses from the two forces are farther from each other and a larger magnitude of bursting force occurs.

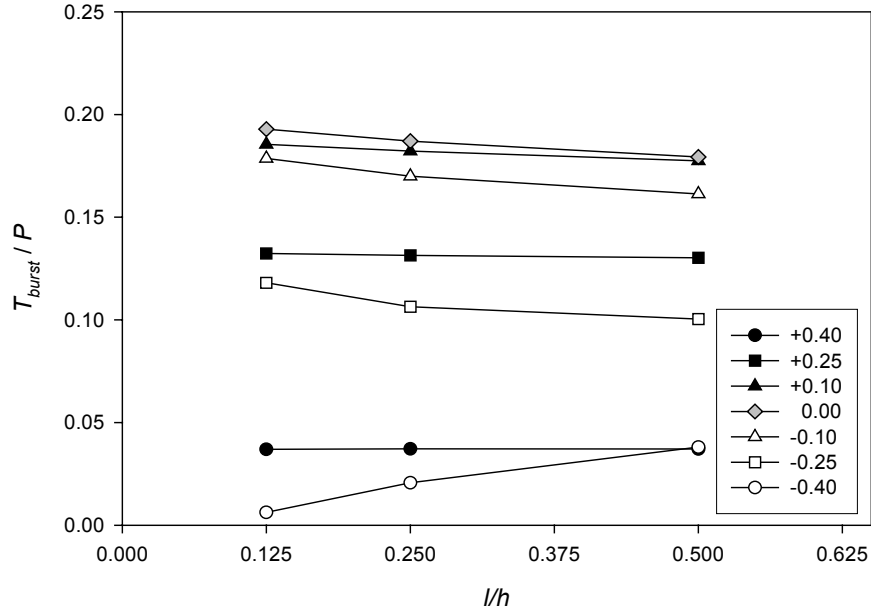


Fig. 3.85 BURSTING FORCE vs. LOCATION OF SUPPORT REACTION FOR ECCENTRIC LOAD AND $R/P = 0.05$ ($a/h = 0.20$, $b/h = 0.125$)

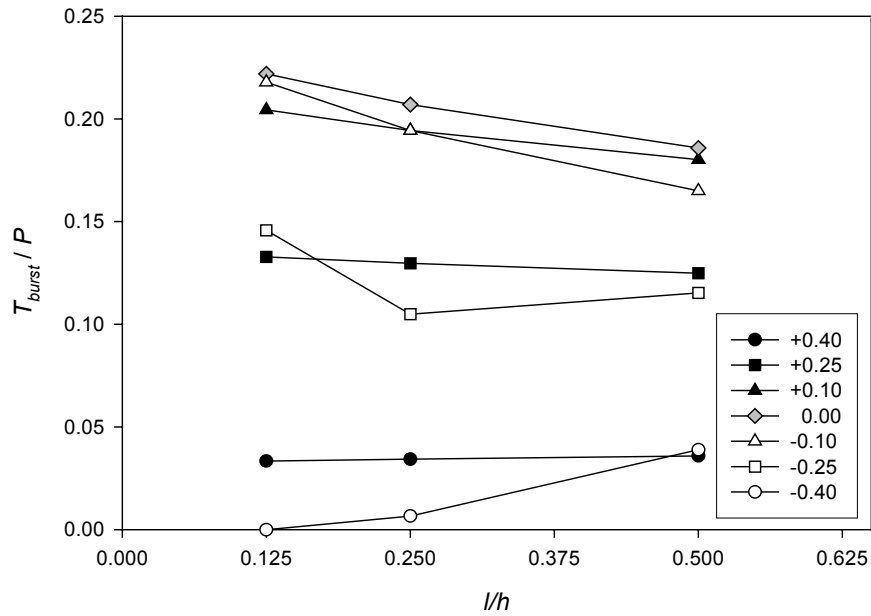


Fig. 3.86 BURSTING FORCE vs. LOCATION OF SUPPORT REACTION FOR ECCENTRIC LOAD AND $R/P = 0.15$ ($a/h = 0.20$, $b/h = 0.125$)

Fig. 3.87 illustrates the effect of the bearing plate width on the behavior of the bursting force for an anchorage zone with an a/h value of 0.10. As can be seen, the plots are very similar to those presented previously. The effect of the bearing plate width does not influence the magnitude of the bursting force for eccentricities vertically distant from the support reaction. The plot for the eccentricity ratio of -0.40 shows a variation with respect to the bearing plate ratio. The magnitude of the prestressing force in this case slightly decreases as the bearing plate ratio increases. Since the bearing plate size of zero is not realistic in practice, the considered bursting force should be taken at the bearing plate ratio of 0.125. Therefore neglecting the effect of the bearing support plate in the formulation to predict bursting force is acceptable.

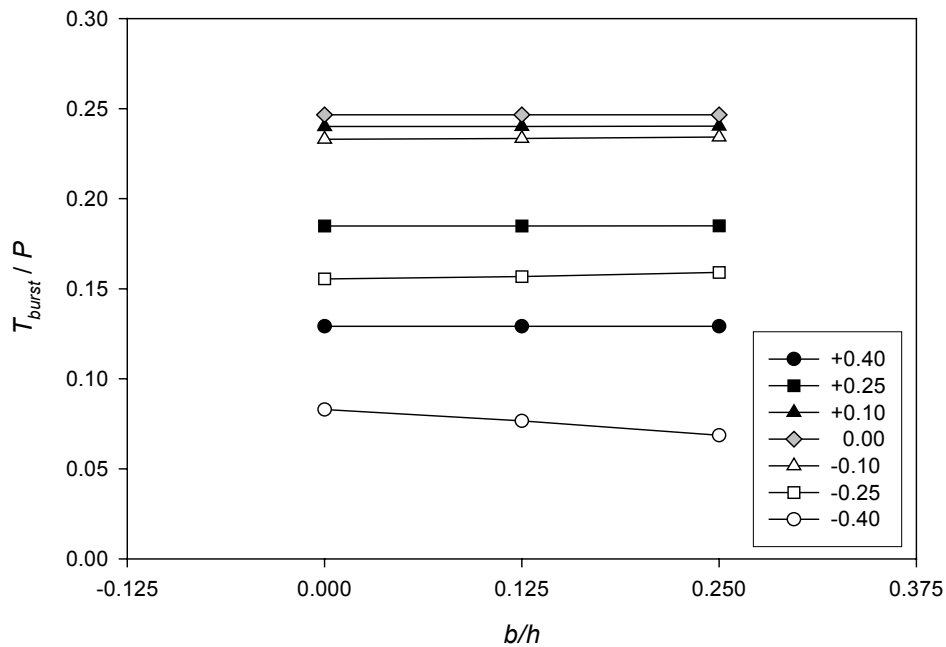


Fig. 3.87 BURSTING FORCE vs. BEARING PLATE RATIO FOR ECCENTRIC LOAD AND $R/P = 0.15$
($a/h = 0.10$, $l/h = 0.25$)

Figure 3.88 shows an example of the comparison of the bursting force between two magnitudes of reaction force: 5 and 15 percent of prestressing force. The parameters of a/h , l/h , and b/h are indicated beneath the figure. The bursting forces for eccentricities of $+0.10$, -0.10 , and -0.25 have a larger magnitude with the R/P ratio equal to 0.15 similar to that of the non-eccentric case. The others with larger eccentricity have the opposite result. Since

equation (3.4) was developed based on an increase of the bursting force relative to the rise of reaction magnitude, the equation provides a conservative method to predict the bursting force with various reaction forces. However, it has not yet been proven that the equation can provide a good result for all eccentric load configurations.

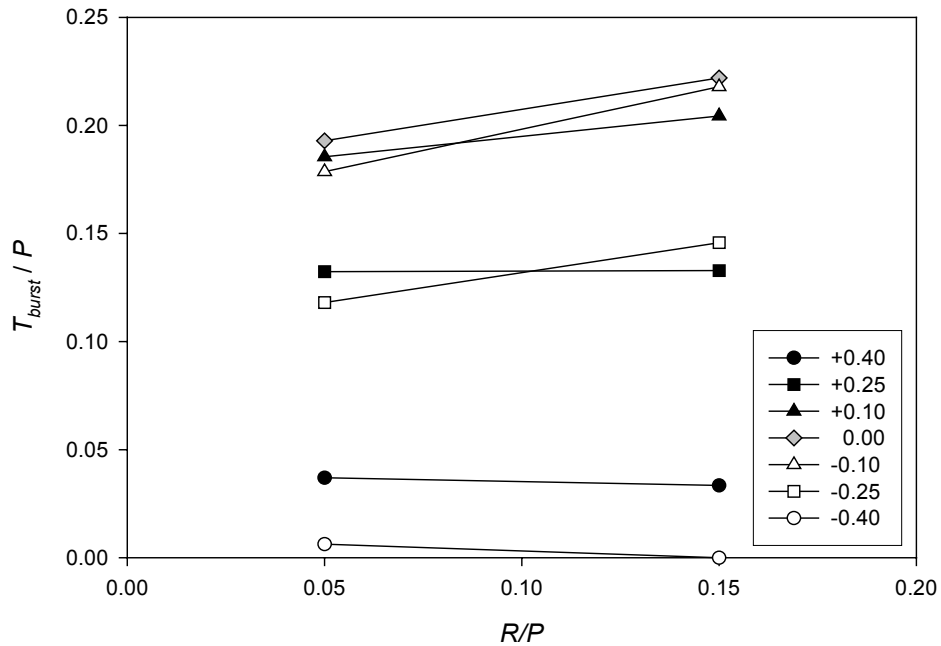


Fig. 3.88 BURSTING FORCE vs. REACTION FOR ECCENTRIC LOAD
($a/h = 0.20$, $l/h = 0.125$, and $b/h = 0.125$)

Figures 3.89 and 3.90 show the effect of the reaction force on all eccentricity ratios for reaction ratios of 0.05 and 0.15, respectively. Two additional plots given by equation (1.5) and a modified version of equation (3.4) are also presented. As mentioned earlier, the estimation of the bursting force for eccentrically loaded anchorage zones with support reactions may be determined with the symmetric prism approach. The section width (h) in equation (3.4) is replaced by the width of the symmetric prism ($h-2e$). As a result, the modified equation is shown below:

$$T_{burst} = 0.25 P \left(1 - \frac{a}{h-2e}\right) + 0.4 P \sin \alpha + R (0.25 - 5 \sin \alpha) \quad (3.6)$$

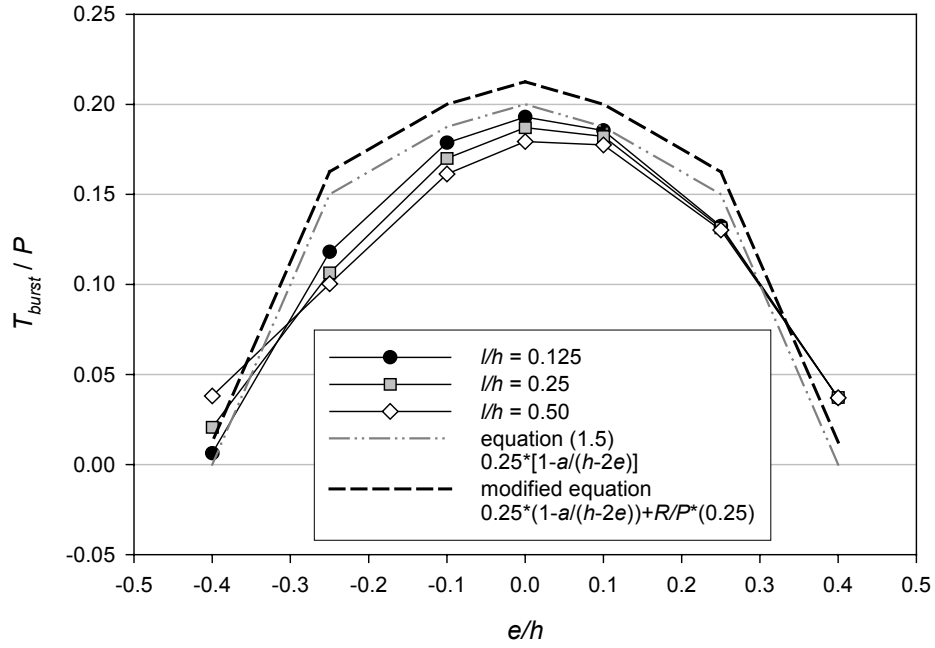


Fig. 3.89 BURSTING FORCE vs. ECCENTRICITY RATIO FOR $R/P = 0.05$
 $(a/h = 0.20$ and $b/h = 0.125)$

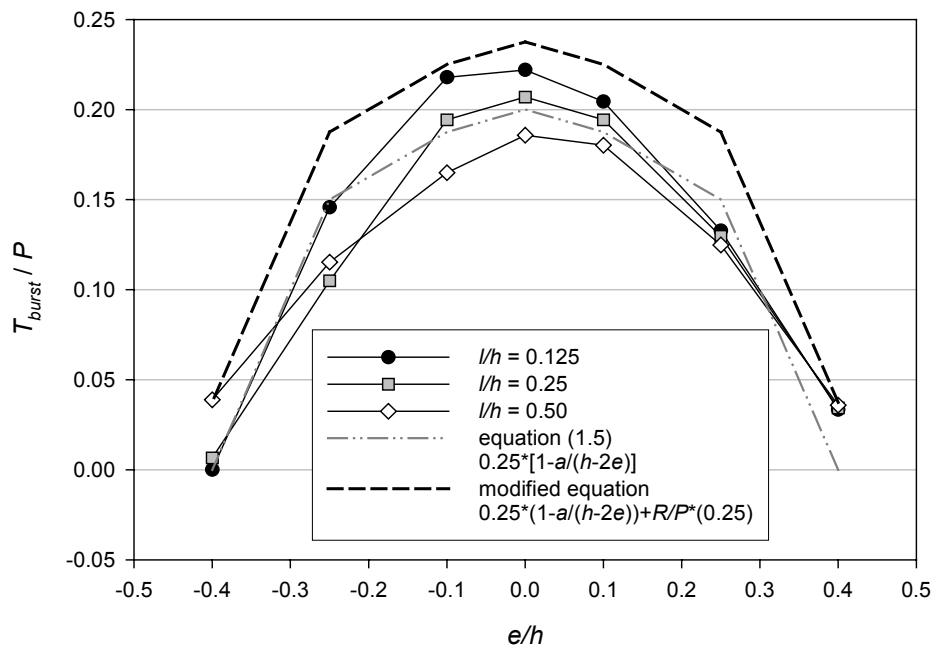


Fig. 3.90 BURSTING FORCE vs. ECCENTRICITY RATIO FOR $R/P = 0.15$
 $(a/h = 0.20$ and $b/h = 0.125)$

As can be seen, the plots from the finite element analysis are not symmetric due to the application of the support reaction. On the left side of the plots, the bursting force for the largest eccentricity ratio (-0.40) has a smaller magnitude compared to that of the right side. For the range of e/h from +0.25 to -0.25, equation (1.5) gives a conservative result for the case with small reaction force but does not predict as well when the reaction force becomes higher (see Fig. 3.90). The modified equation provides a conservative result for all magnitudes of the reaction force. For the largest eccentricities ($e/h = +0.40$ and -0.40), both equations result in bursting forces smaller than those from the finite element analysis. Therefore, to find the most effective method for the design of anchorage zones with eccentric load configurations, a special consideration for a high eccentricity must be made along with the use of the modified equation.

3.4.3.3 Location of Bursting Force

Since the symmetric prism approach can be used for the determination of the bursting force, the same method is investigated to determine the location of the bursting force for the eccentric load configuration. First of all, parametric studies for all effects related to support reaction must be conducted in order to monitor the variation of d_{burst} , which is caused by the presence of the support reaction.

Figures 3.91 and 3.92 show the relation between d_{burst} and the reaction location (l/h). The plots in both figures are not parallel to one another. For eccentricities of -0.25 and -0.40, the plots are even more unpredictable since the d_{burst} value does not vary linearly from the smallest distance of the reaction force to the largest one. However, using one value of d_{burst} to present for each plot can provide an acceptable result without causing excessive complexity in the modified equation.

Figure 3.93 presents the relation between d_{burst} and the b/h ratio. The plots are similar to those shown previously. There is no significant effect due to the change of bearing plate width. This indicates the negligibility of the bearing plate ratio in the formulation of d_{burst} for the eccentric load configuration.

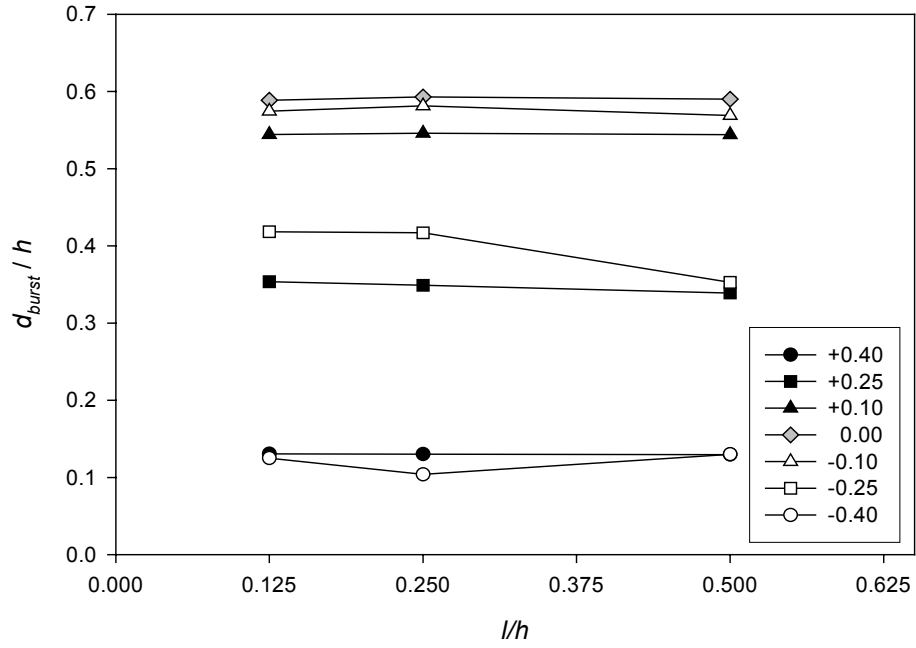


Fig. 3.91 BURSTING FORCE LOCATION vs. LOCATION OF SUPPORT REACTION FOR ECCENTRIC LOAD AND $R/P = 0.05$ ($a/h = 0.20$, $b/h = 0.125$)

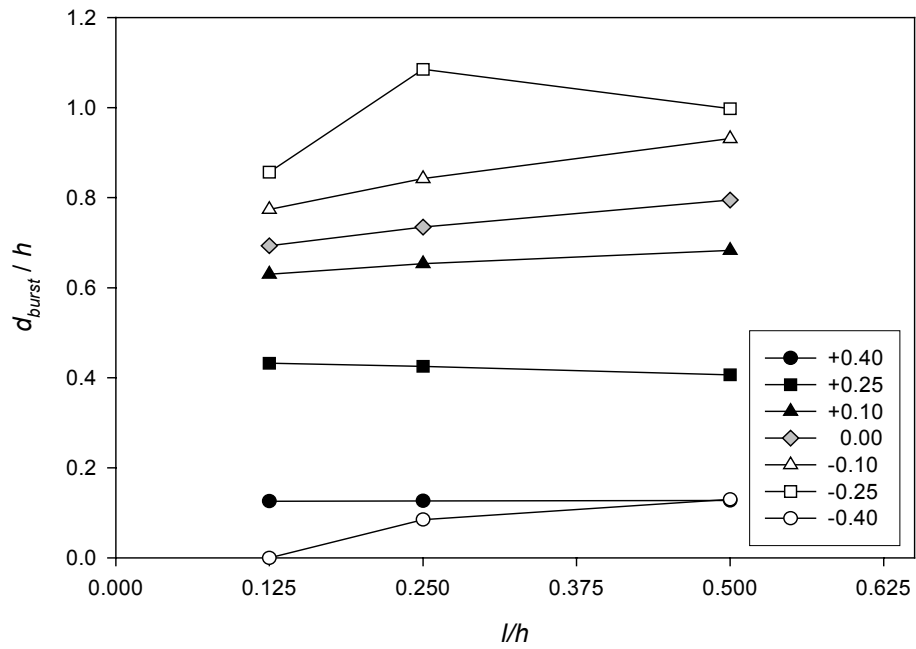


Fig. 3.92 BURSTING FORCE LOCATION vs. LOCATION OF SUPPORT REACTION FOR ECCENTRIC LOAD AND $R/P = 0.15$ ($a/h = 0.20$, $b/h = 0.125$)

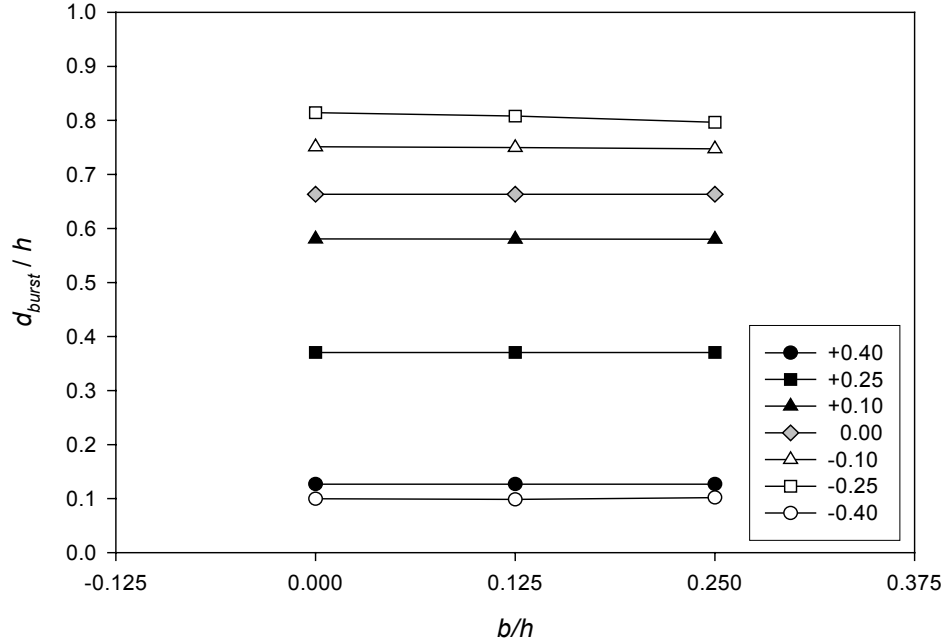


Fig. 3.93 BURSTING FORCE LOCATION vs. BEARING PLATE RATIO FOR ECCENTRIC LOAD
($a/h = 0.10$, $l/h = 0.25$)

Since the application of the symmetric prism approach is effective for the estimation of the bursting force, it is also adopted into the formulation of d_{burst} . Based on equation (3.5) in section 3.4.2.3, the variable of section width (h) can be replaced by the width of the symmetric prism ($h-2e$) as shown in equation (3.7):

$$d_{burst} = 0.5 (h-2e) + 0.25 a + 0.25 (h-2e) \sin \alpha + \frac{R}{P} (h-2e) (1.5-10 \sin \alpha) \quad (3.7)$$

The results using this equation are compared to the finite element results and those obtained using equation (1.6) as shown in Figs. 3.94 and 3.95. The figures present the comparison of the plot of d_{burst} versus the e/h ratio for two different reaction force magnitudes: 5 and 15 percent of prestressing force.

In Fig. 3.94, the smaller reaction force slightly influences the behavior of the finite element plots, resulting in an almost symmetrical shape. The plot from equation (1.6) is below all the finite element plots except for one point at the left end, which matches well with one of the finite element results. The plot from equation (3.7) (modified equation in the

figures) corresponds more closely with the finite element plots with a small difference of d_{burst} value for each e/h . When the magnitude of the reaction force becomes higher, the finite element analysis indicates values of d_{burst} for eccentricity ratios of -0.10 and -0.25 larger than that for the concentric load. The value of d_{burst} rapidly drops when the eccentricity ratio reaches the value of -0.40 . Although the prediction of equation (3.7) cannot match this behavior, it produces a good agreement for all positive eccentricity ratios, while equation (1.6) provides a much lower result compared to those from finite element analysis.

Although the prediction of equation (3.7) provides a relatively large value of d_{burst} for the eccentricity ratios of $+0.40$ and -0.40 , the bursting forces for these eccentricity ratios are very small due to the small dimensions of the symmetric prism. This can be considered as a non-critical case for the design of an anchorage zone with support reaction. However, equations (3.6) and (3.7) are not yet completed since the effect of inclined eccentric load configuration still must be considered.

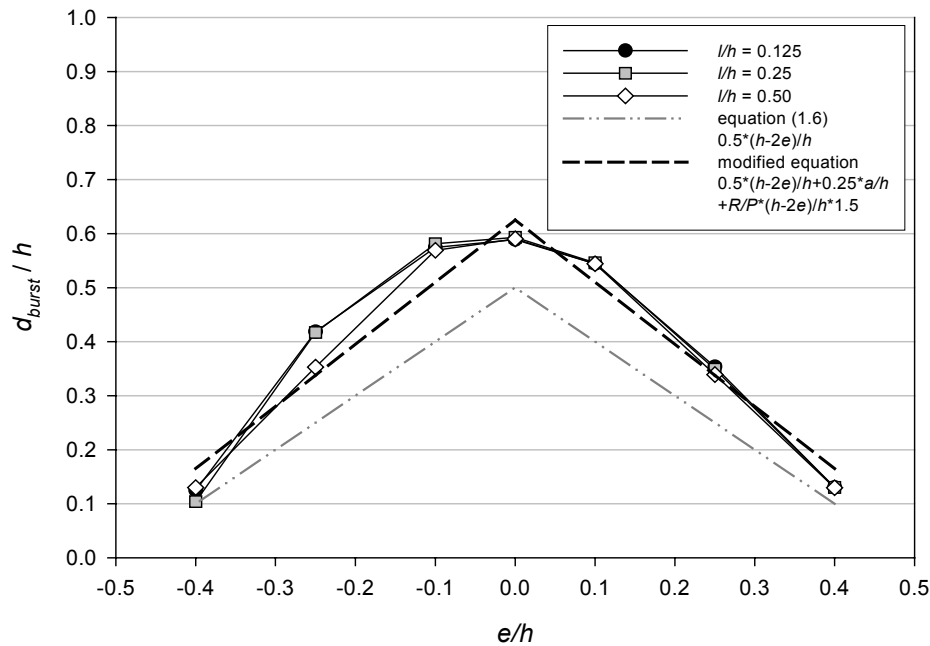


Fig. 3.94 BURSTING FORCE LOCATION vs. ECCENTRICITY RATIO FOR $R/P = 0.05$
($a/h = 0.20$, $b/h = 0.125$)

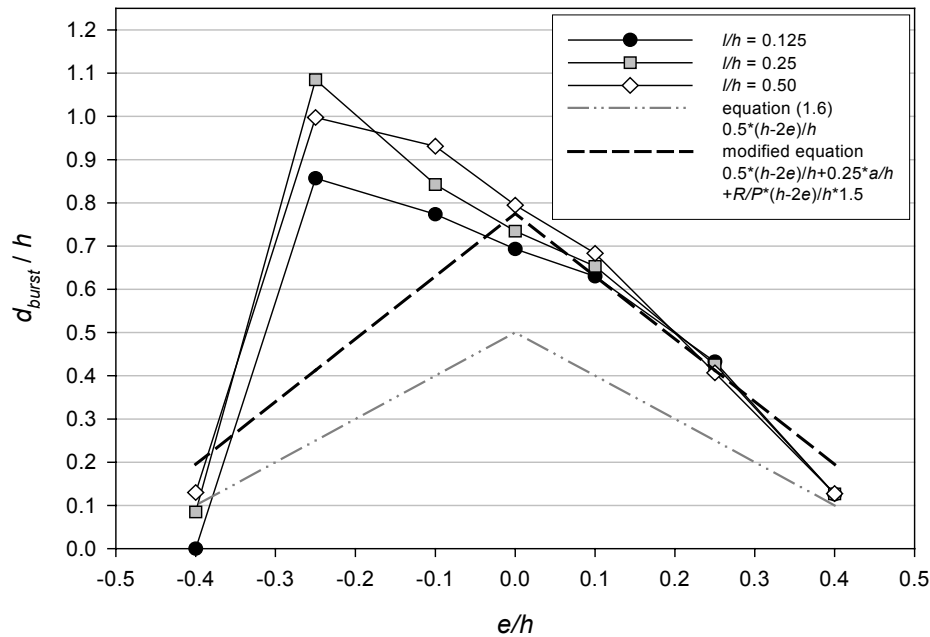


Fig. 3.95 BURSTING FORCE LOCATION vs. ECCENTRICITY RATIO FOR $R/P = 0.15$
 $(a/h = 0.20, b/h = 0.125)$

3.4.4 Inclined Eccentrically Loaded Anchor Configuration

Before equations (3.6) and (3.7) can be used for the estimation of the bursting force and its location for all load configurations, one of the most generally used configurations must be investigated. In reality, a prestressing force may not be located exactly at the centroid of the section and the tendon may not be stressed in the horizontal direction. The investigation of inclined eccentric load is the most applicable of all. However, it requires all studies of basic configurations from previous sections be considered as they apply to the most complicated configuration. This section benefits from the previous sections in that not all parametric studies need to be performed. Similar models to those presented in section 3.4.3 with the addition of inclination to the prestressing load are analyzed. Two inclination angles consisting of 6 and 9 degrees are still applied. The most critical cases found in the study are selected for the following presentation.

3.4.4.1 Elastic Stress Distribution

Figures 3.96 and 3.97 present contour plots of inclined eccentrically loaded anchorage zones without and with the presence of a support reaction. The anchorage and bearing support ratios are similar to those presented in Figs. 3.81 through 3.83. Only the y-y stress contour plots and the inclination angle of 6 degrees were selected for illustration. Both Figs. 3.96 and 3.97 show four eccentricity ratios consisting of +0.40, +0.10, -0.10, and -0.40.

In Fig. 3.96, all stress distributions show the typical pattern of bursting stresses, which always occur ahead of the anchor plate. The comparison of the stress distribution in Figs. 3.96c and d to those in Figs. 3.81a and 3.82a indicates a slightly different distribution except in the region close to the right end of the model, in which the stress contours in Figs. 3.96c and d are caused by the vertical boundary support at the top surface. When the reaction force is introduced into the models (Fig. 3.97), an important effect caused by the force is the vanishing of the spalling stresses in the region between the anchor and the lowest surface of the anchorage zone. This behavior is similar to that which occurs in the eccentric load configuration with support reaction as presented in Fig. 3.83. This suggests that there is no spalling reinforcement required in this region. However, a minimum amount of reinforcing steel should be provided.

The bursting regions in Fig. 3.97 look slightly different from those presented in Fig. 3.83. In Fig. 3.97d, the bursting region is joined to the tensile stresses of the spalling region. This is caused by the downward inclination of the prestressing force, which results in the transfer of the vertical compressive stress directly to the support reaction and creates the tensile stresses above the centerline of the anchor. Fig. 3.97d also shows another example of unstressed corner with spalling stresses occurring on the anchor surface caused by strain compatibility of the structure. As can be seen, the bursting region seems to have a little deviation in the upward direction. This is because the main compressive strut lies in the direction from the plate diagonally toward the centroid of the compressive stresses at the end section as already mentioned at the beginning of this study.

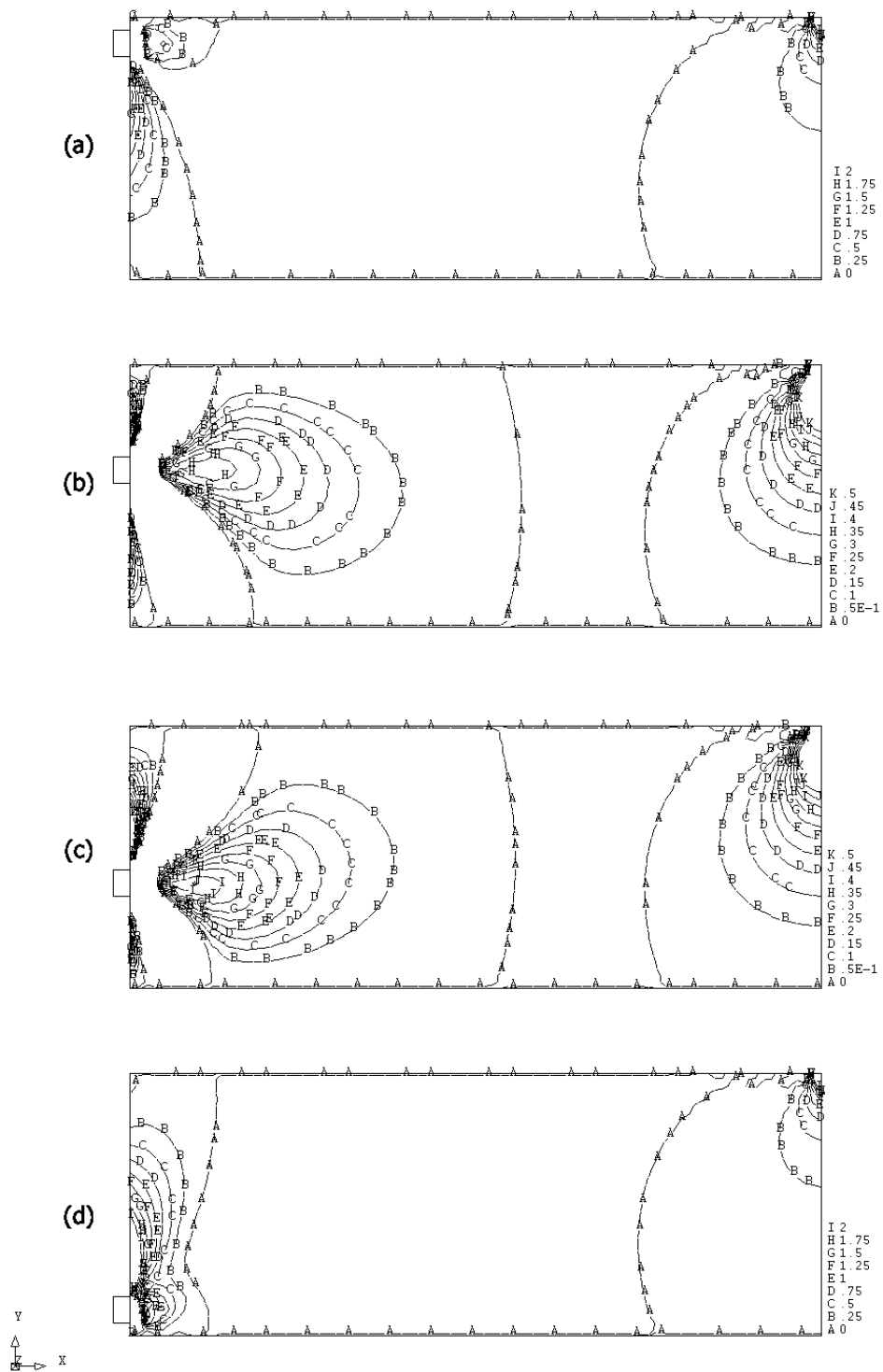


Fig. 3.96 STRESS IN Y-Y DIRECTION OF 6 DEGREE INCLINED ECCENTRIC LOAD WITH e/h EQUAL TO a) +0.40, b) +0.10, c) -0.10, AND d) -0.40 ($R/P = 0.0$) (Stress multiplied by σ_O)

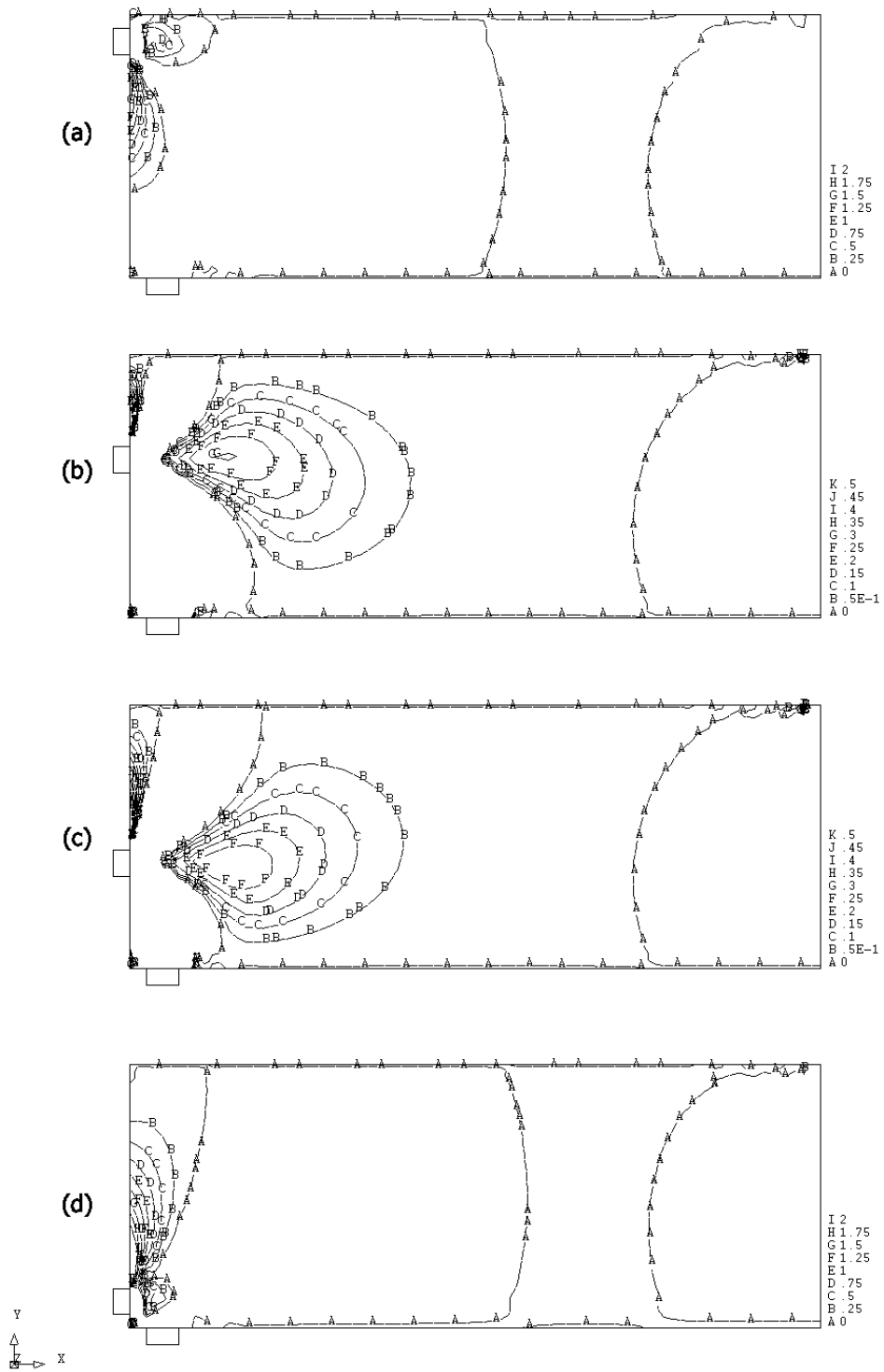


Fig. 3.97 STRESS IN Y-Y DIRECTION OF 6 DEGREE INCLINED ECCENTRIC LOAD WITH e/h EQUAL TO a) +0.40, b) +0.10, c) -0.10, AND d) -0.40 ($l/h = 0.125$, $b/h = 0.125$, and $R/P = 0.15$) (Stress multiplied by σ_0)

3.4.4.2 Bursting Force

Since the previous presentations gave considerable information on each parameter studied, this present section provides a few examples of each parameter along with a discussion. Two inclination parameters, 6 and 9 degree angles, are still chosen for the illustration and comparison. The effects of the location of the reaction force and the bearing support plate are the first two topics to be discussed. Information about the influence of the reaction magnitude is given in a similar manner as in section 3.4.3.2.

Figures 3.98 and 3.99 show the relation of the bursting force and the location of the support reaction for 6 and 9 degree inclined prestressing load, respectively, with 5 percent of the load as a reaction force. As can be seen, the plots in both figures are similar in characteristics for each eccentricity ratio. The bursting force for the anchorage zone with the closest location of the reaction force to anchor surface still has the largest magnitude except for the eccentricity of -0.40 , which is the eccentric location nearest to the support bearing plate. In Fig. 3.99, the plot for the eccentricity of $+0.25$ also has its largest magnitude of bursting force corresponding to the furthest location of bearing support.

For a larger magnitude of the reaction force, the characteristics of some of the plots are quite different. Figs. 3.100 and 3.101 show the relation of the bursting force and the support location for the R/P ratio of 0.15. The bursting force magnitudes for the eccentricity ratios of $+0.40$ to $+0.25$ are relatively unchanged with varying l/h . However, the magnitudes for the eccentricity ratios of $+0.10$ to -0.10 drop with increasing l/h . For the e/h ratio of -0.25 , the magnitude drops and rises unpredictably while that of -0.40 steeply increases in magnitude with increase in l/h . These inconsistencies indicate complexity if the formulation accounts for all behaviors in the plots. A simplified formulation should be selected to result in an effective estimation of bursting force for the inclined eccentric with reaction load configuration. Since the behavior of the bursting force for the largest eccentricity in the negative direction is obviously different from the others, a special consideration should be taken to account for this unique characteristic.

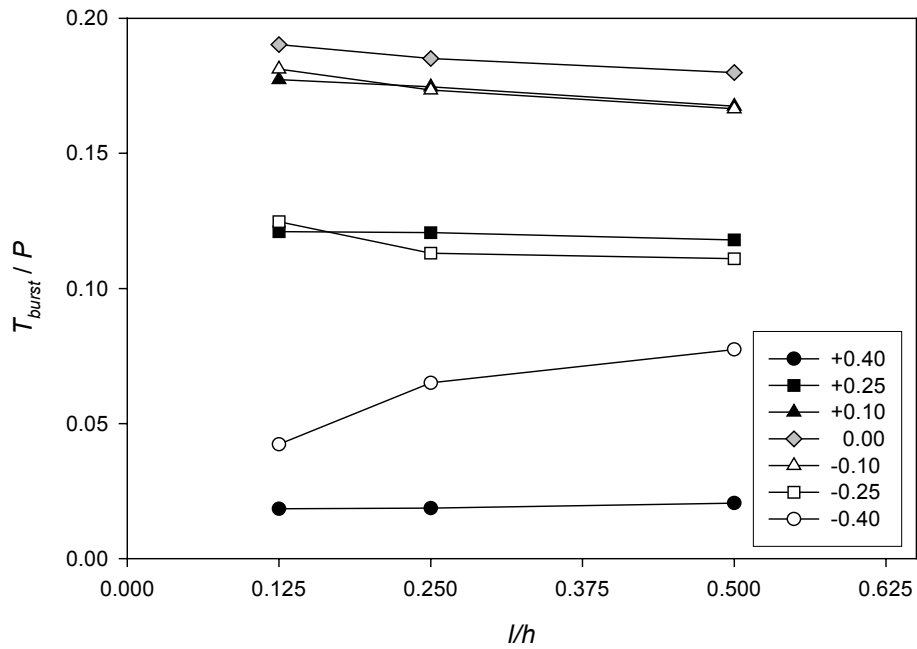


Fig. 3.98 BURSTING FORCE vs. LOCATION OF SUPPORT REACTION FOR 6 DEGREE INCLINED ECCENTRIC LOAD AND $R/P = 0.05$ ($a/h = 0.20$, $b/h = 0.125$)

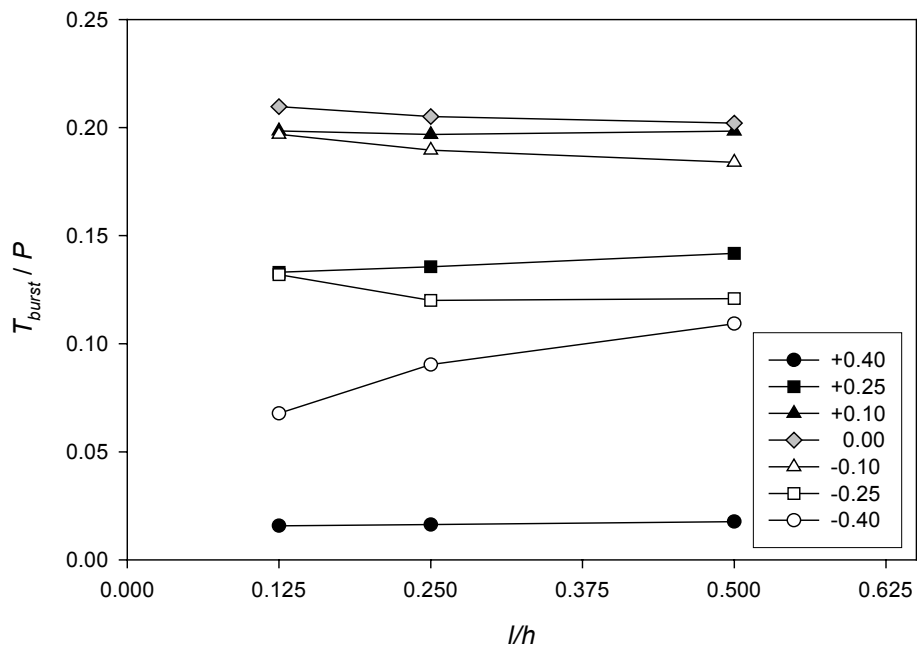


Fig. 3.99 BURSTING FORCE vs. LOCATION OF SUPPORT REACTION FOR 9 DEGREE INCLINED ECCENTRIC LOAD AND $R/P = 0.05$ ($a/h = 0.20$, $b/h = 0.125$)

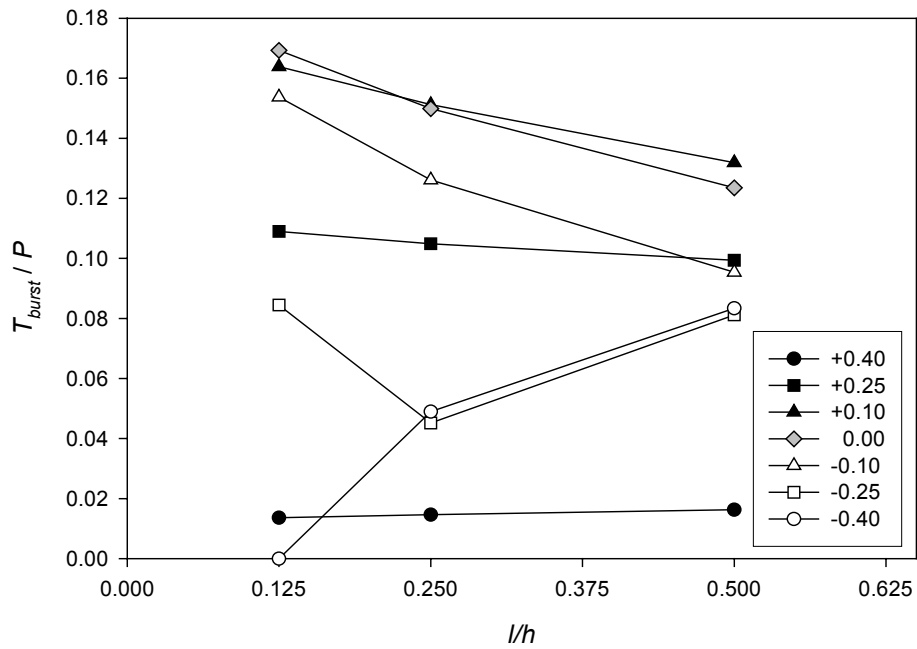


Fig. 3.100 BURSTING FORCE vs. LOCATION OF SUPPORT REACTION FOR 6 DEGREE INCLINED ECCENTRIC LOAD AND $R/P = 0.15$ ($a/h = 0.20$, $b/h = 0.125$)

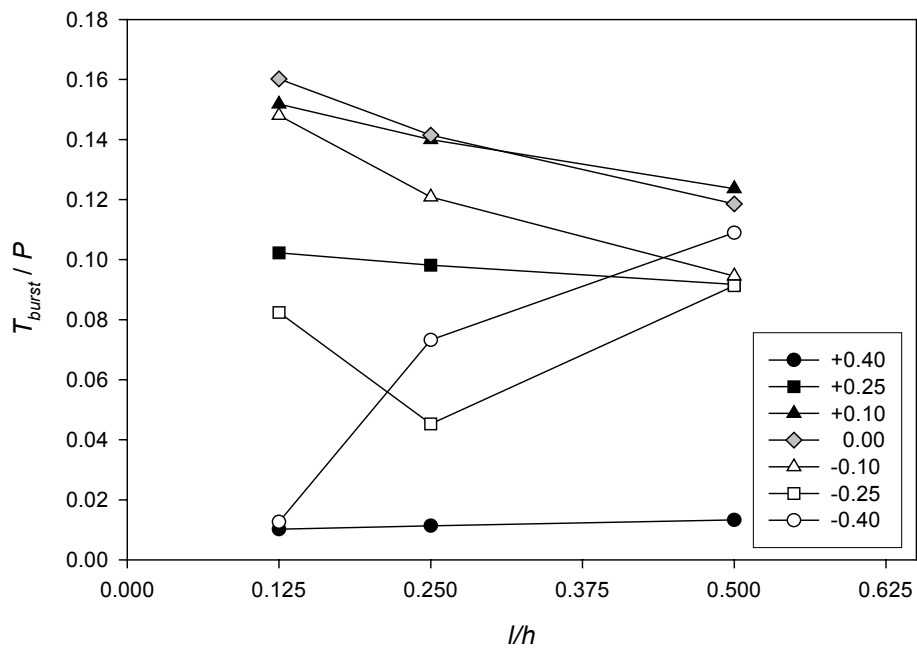


Fig. 3.101 BURSTING FORCE vs. LOCATION OF SUPPORT REACTION FOR 9 DEGREE INCLINED ECCENTRIC LOAD AND $R/P = 0.15$ ($a/h = 0.20$, $b/h = 0.125$)

Figures 3.102 and 3.103 show the relation of the bursting force and the bearing plate ratio for 6 and 9 degree inclined eccentric load, respectively. The plots are once again similar to those occurring in previous sections. The bursting force for the case in which the prestressing load is placed close to the support reaction illustrates the effect of the bearing plate size. However, the effect of the bearing plate ratio can be considered negligible.

Based on the parametric studies of the reaction location and the bearing support plate, it is found that an inclined eccentrically loaded anchorage zone has a similar behavior in terms of the magnitude of the bursting force as that with an eccentric load, but no inclination. The inclination angle causes an obvious change in the plots of the bursting force and the support location with a reaction ratio of 0.15. The inclined prestressing load and large reaction force counteraction was addressed in section 3.4.2.2. The position of the reaction force close to the location of the bursting region from an inclined prestressing load results in a counteraction of the stresses and then results in a small bursting force.

Figures 3.104 through 3.107 show the comparison of the bursting force from the finite element analyses and those from equation (1.5) and equation (3.6), which is called the modified equation in the figures. Both equations provide a conservative estimation of the bursting force for all eccentricity ratios except for those with largest eccentricities, +0.40 and -0.40. According to the plots, the results from equation (1.5) produce a higher estimation than the results from finite element analysis and from equation (3.6). Although it is considered as a safe design, this may lead to difficulties consolidating concrete in structures with unnecessarily excessive amounts of reinforcing steel.

For the eccentricity ratio of -0.40, the finite element analysis provides three distinct magnitudes of bursting force with respect to the location of the reaction load. It is noted that the largest bursting force for the eccentricity ratio of -0.40 occurs in the case where the reaction force is located at $0.50h$ from the anchor surface. Based on Figs. 3.89, 3.90, and 3.104 to 3.107, the highest bursting force detected in all six figures appears in Fig. 3.105 with a magnitude of approximately 0.11 times the prestressing force. This number can be used as a lower bound for the prediction of the bursting force for anchorage zones with eccentric loads.

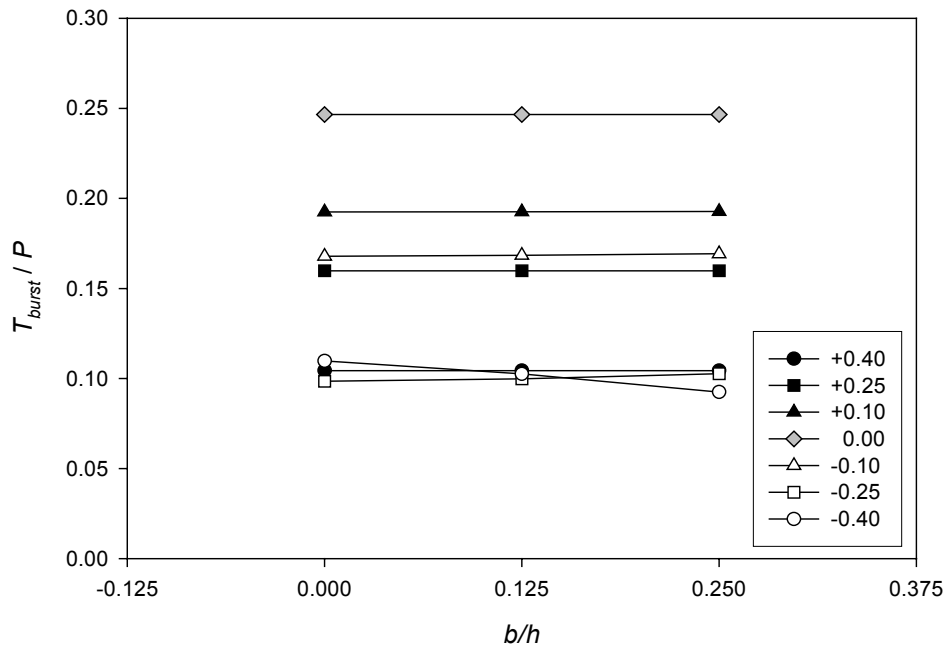


Fig. 3.102 BURSTING FORCE vs. BEARING PLATE RATIO FOR 6 DEGREE INCLINED ECCENTRIC LOAD AND $R/P = 0.15$ ($a/h = 0.10$, $l/h = 0.25$)

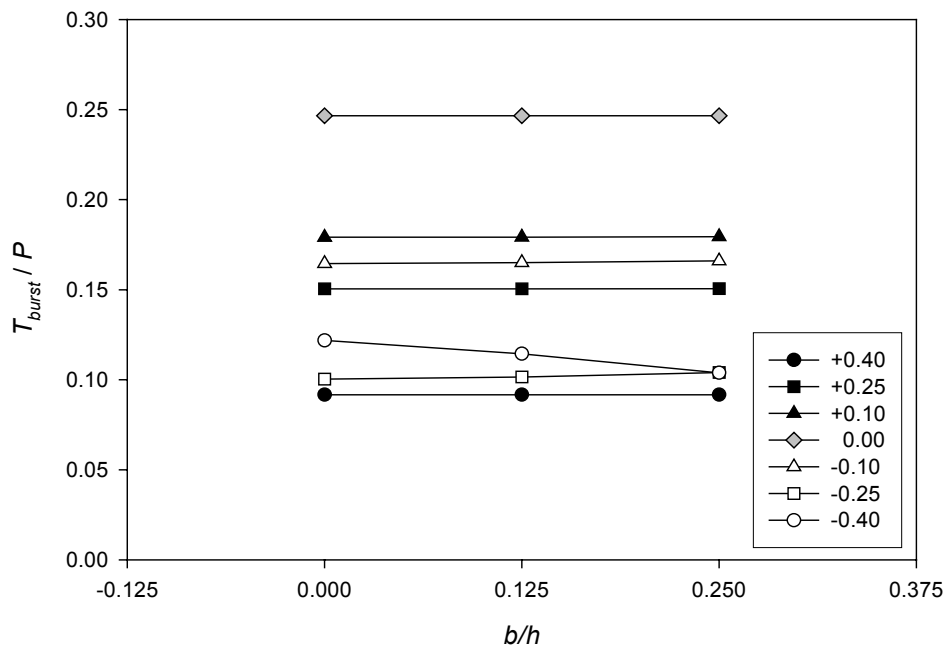


Fig. 3.103 BURSTING FORCE vs. BEARING PLATE RATIO FOR 9 DEGREE INCLINED ECCENTRIC LOAD AND $R/P = 0.15$ ($a/h = 0.10$, $l/h = 0.25$)

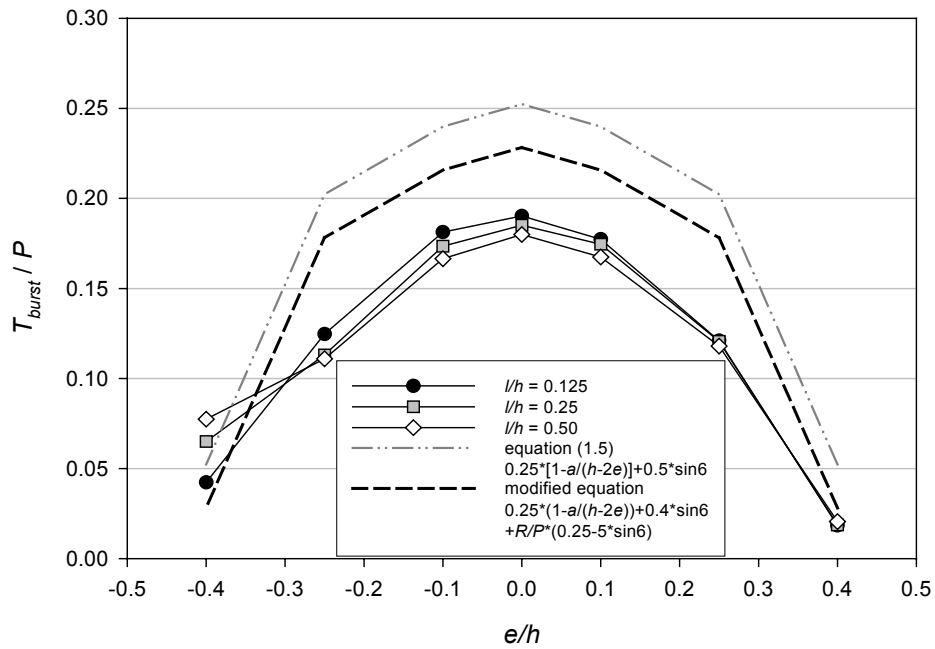


Fig. 3.104 BURSTING FORCE vs. ECCENTRICITY RATIO FOR 6 DEGREE INCLINED ECCENTRIC LOAD AND $R/P = 0.05$ ($a/h = 0.20$, $b/h = 0.125$)

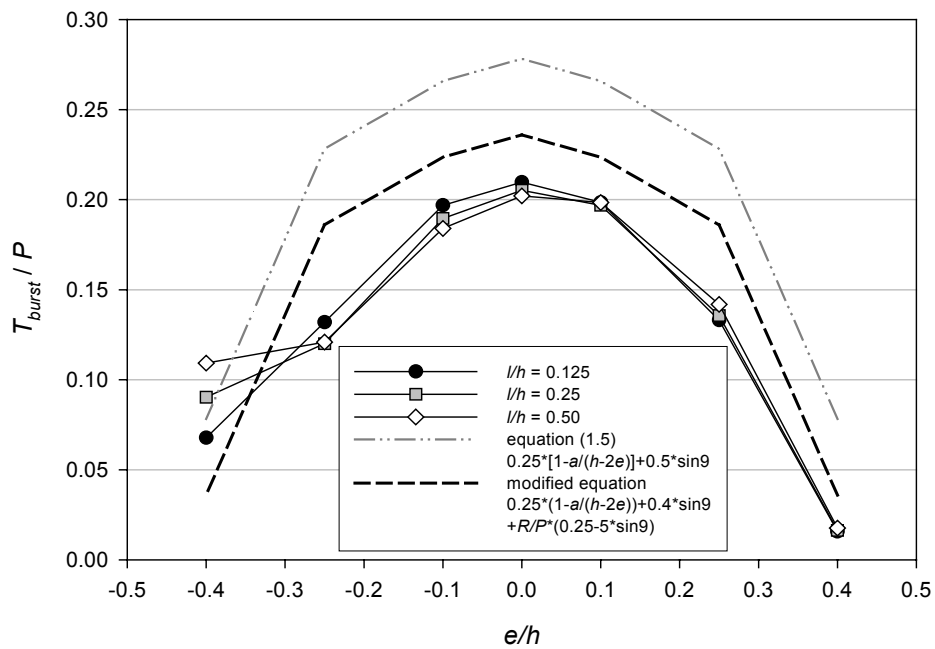


Fig. 3.105 BURSTING FORCE vs. ECCENTRICITY RATIO FOR 9 DEGREE INCLINED ECCENTRIC LOAD AND $R/P = 0.05$ ($a/h = 0.20$, $b/h = 0.125$)

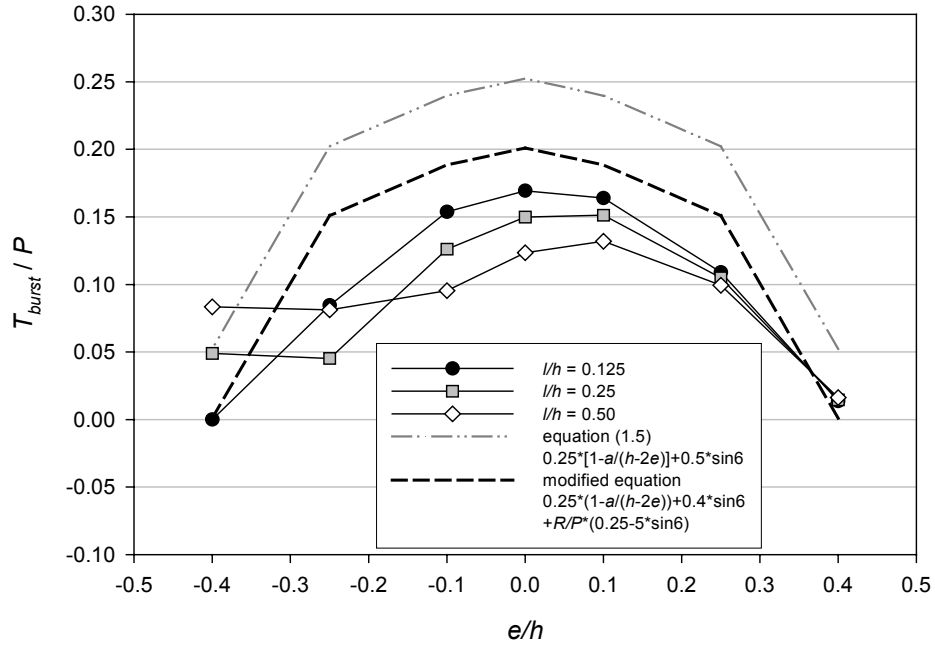


Fig. 3.106 BURSTING FORCE vs. ECCENTRICITY RATIO FOR 6 DEGREE INCLINED ECCENTRIC LOAD AND $R/P = 0.15$ ($a/h = 0.20$, $b/h = 0.125$)

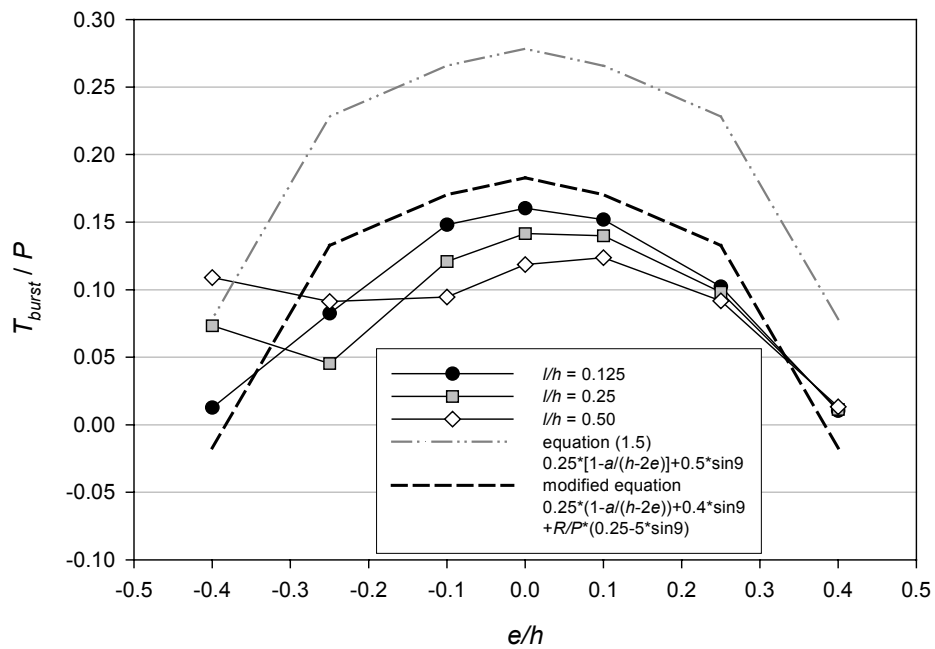


Fig. 3.107 BURSTING FORCE vs. ECCENTRICITY RATIO FOR 9 DEGREE INCLINED ECCENTRIC LOAD AND $R/P = 0.15$ ($a/h = 0.20$, $b/h = 0.125$)

Equation (3.6) provides a better estimation than equation (1.5) with a more reasonable level of conservatism except for anchorage zones with 9 degree inclined prestressing load applied eccentrically at $0.40h$ below the center of the section. The equation can be modified to provide the most effective prediction for all cases. A number of 12.5 percent of prestressing load can be used as a lower bound for the determination of the bursting force. Therefore, equation (3.6) can be rewritten as shown below:

$$T_{burst} = 0.25 P \left(1 - \frac{a}{h - 2e}\right) + 0.4 P \sin \alpha + R (0.25 - 5 \sin \alpha) \geq 0.125P \quad (3.8)$$

The number 0.125 is selected based on the highest bursting force for an eccentricity ratio of -0.40 in Fig. 3.105. An example of the comparison of the finite element results and the latest modified equation is given in Fig. 3.108. The plot from equation (3.8) is now above all finite element plots, which represents a conservative approach in the design of anchorage zones with a support reaction and an inclined eccentric load configuration.

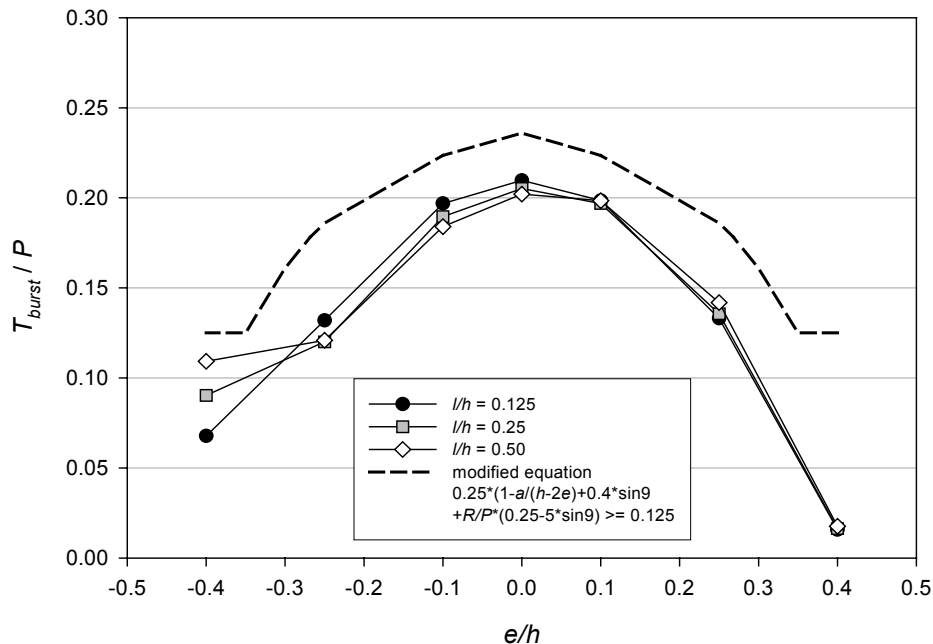


Fig. 3.108 EXAMPLE OF COMPARISON OF MODIFIED EQUATION FOR 9 DEGREE INCLINED ECCENTRIC LOAD AND $R/P = 0.05$ ($a/h = 0.20$, $b/h = 0.125$)

Referring to Tables 3.6 through 3.8, the selected number $0.125P$ can be compared to the bursting force prediction in every case presented. It can be seen that the selected number does not affect the predictions for almost all cases except the case of 9 degree inclined concentric load applied on anchorage size of $0.50h$ with a support reaction of 15 percent of prestressing load. With the magnitude of $0.1077P$, the estimation of this case is approximately 13.84 percent lower than the selected number. However, the number of $0.1077P$ is the smallest bursting force from every case presented in Tables 3.6 through 3.8.

Tables 3.13 through 3.15 present the numerical comparison of all models created for the study of horizontal and inclined eccentrically loaded anchorage zones with support reaction. All models listed in each table consist of two different anchorage ratios. The anchorage ratio of 0.10 was used with the R/P value of 0.15 while the anchorage ratio of 0.20 was used with two R/P values: 0.05 and 0.15. Three different locations of reaction force were applied. Tables 3.13, 3.14, and 3.15 show the results for three different inclination angles: 0, 6, and 9 degrees, respectively. Equation (3.8) provides a conservative estimation of the bursting force in the case of a/h ratio equal to 0.20 as can be seen from the positive percent differences shown in the last column.

For inclined eccentric load configurations with the eccentricity ratios between +0.25 to -0.25, the bursting force given by equation (3.8) produces a smaller positive percent difference than that given by equation (1.5). It results in a smaller amount of reinforcing steel required based on the smaller magnitude of the bursting force while the structure remains in a safe condition. In the case of the largest eccentricity, equation (3.8) may give a rather high level of conservatism, however the force is relatively small and the amount of reinforcing steel will not be excessive. The largest eccentricity may cause longitudinal tensile stresses at the edge of the section. The code provisions require that the longitudinal edge tension reinforcement be continuous and extended to cover the anchorage surface. This amount of steel may even be larger than the amount required to resist 12.5 percent of the prestressing force. One additional finding from the study is that the influence of the spalling force at the surface of the anchorage zone diminishes due to the presence of a support reaction.

Table 3.13 COMPARISON OF THE RESULTS FOR ECCENTRIC LOAD WITH NO INCLINATION ANGLE

h	a/h	R/P	l/h	α	e/h	β	$T_{burst-fem}/P$	Eqn (1.5)	%diff	Eqn (3.8)	%diff
							-1-	-2-	-1 & 2-	-3-	-1 & 3-
16	0.10	0.15	0.125	0	0.4	-3.91	0.1280	0.1250	-2.38	0.1625	21.24
16	0.10	0.15	0.125	0	0.25	0.88	0.1880	0.2000	6.01	0.2375	20.85
16	0.10	0.15	0.125	0	0.1	5.20	0.2478	0.2188	-13.30	0.2563	3.28
16	0.10	0.15	0.125	0	0	7.36	0.2585	0.2250	-14.88	0.2625	1.53
16	0.10	0.15	0.125	0	-0.1	7.88	0.2529	0.2188	-15.63	0.2563	1.29
16	0.10	0.15	0.125	0	-0.25	7.88	0.1916	0.2000	4.20	0.2375	19.33
16	0.10	0.15	0.125	0	-0.4	7.90	0.0274	0.1250	78.10	0.1625	83.15
16	0.10	0.15	0.25	0	0.4	-3.63	0.1292	0.1250	-3.32	0.1625	20.52
16	0.10	0.15	0.25	0	0.25	0.81	0.1849	0.2000	7.56	0.2375	22.16
16	0.10	0.15	0.25	0	0.1	4.83	0.2401	0.2188	-9.77	0.2563	6.29
16	0.10	0.15	0.25	0	0	6.84	0.2466	0.2250	-9.58	0.2625	6.07
16	0.10	0.15	0.25	0	-0.1	7.33	0.2336	0.2188	-6.77	0.2563	8.85
16	0.10	0.15	0.25	0	-0.25	7.33	0.1571	0.2000	21.47	0.2375	33.87
16	0.10	0.15	0.25	0	-0.4	7.34	0.0761	0.1250	39.16	0.1625	53.20
16	0.10	0.15	0.5	0	0.4	-3.18	0.1312	0.1250	-4.99	0.1625	19.24
16	0.10	0.15	0.5	0	0.25	0.71	0.1801	0.2000	9.94	0.2375	24.16
16	0.10	0.15	0.5	0	0.1	4.23	0.2290	0.2188	-4.68	0.2563	10.64
16	0.10	0.15	0.5	0	0	5.99	0.2313	0.2250	-2.81	0.2625	11.88
16	0.10	0.15	0.5	0	-0.1	6.42	0.2128	0.2188	2.74	0.2563	16.97
16	0.10	0.15	0.5	0	-0.25	6.42	0.1625	0.2000	18.77	0.2375	31.59
16	0.10	0.15	0.5	0	-0.4	6.43	0.1311	0.1250	-4.90	0.1625	19.31
16	0.20	0.05	0.125	0	0.4	-4.40	0.0370	0.0000	N/A	0.1250	70.43
16	0.20	0.05	0.125	0	0.25	-0.08	0.1324	0.1500	11.76	0.1625	18.55
16	0.20	0.05	0.125	0	0.1	2.63	0.1855	0.1875	1.07	0.2000	7.25
16	0.20	0.05	0.125	0	0	2.64	0.1929	0.2000	3.54	0.2125	9.21
16	0.20	0.05	0.125	0	-0.1	2.64	0.1786	0.1875	4.74	0.2000	10.70
16	0.20	0.05	0.125	0	-0.25	2.66	0.1180	0.1500	21.30	0.1625	27.36
16	0.20	0.05	0.125	0	-0.4	5.35	0.0063	0.0000	N/A	0.1250	94.97
16	0.20	0.05	0.25	0	0.4	-4.09	0.0372	0.0000	N/A	0.1250	70.26
16	0.20	0.05	0.25	0	0.25	-0.07	0.1314	0.1500	12.39	0.1625	19.13
16	0.20	0.05	0.25	0	0.1	2.44	0.1822	0.1875	2.84	0.2000	8.91
16	0.20	0.05	0.25	0	0	2.45	0.1870	0.2000	6.49	0.2125	11.99
16	0.20	0.05	0.25	0	-0.1	2.45	0.1699	0.1875	9.36	0.2000	15.03
16	0.20	0.05	0.25	0	-0.25	2.47	0.1064	0.1500	29.07	0.1625	34.53
16	0.20	0.05	0.25	0	-0.4	4.97	0.0207	0.0000	N/A	0.1250	83.44
16	0.20	0.05	0.5	0	0.4	-3.58	0.0371	0.0000	N/A	0.1250	70.34
16	0.20	0.05	0.5	0	0.25	-0.06	0.1302	0.1500	13.19	0.1625	19.86
16	0.20	0.05	0.5	0	0.1	2.14	0.1775	0.1875	5.34	0.2000	11.26
16	0.20	0.05	0.5	0	0	2.15	0.1793	0.2000	10.33	0.2125	15.61
16	0.20	0.05	0.5	0	-0.1	2.15	0.1613	0.1875	13.95	0.2000	19.33
16	0.20	0.05	0.5	0	-0.25	2.16	0.1004	0.1500	33.05	0.1625	38.20
16	0.20	0.05	0.5	0	-0.4	4.35	0.0380	0.0000	N/A	0.1250	69.57
16	0.20	0.15	0.125	0	0.4	-3.91	0.0334	0.0000	N/A	0.1250	73.29
16	0.20	0.15	0.125	0	0.25	0.88	0.1328	0.1500	11.46	0.1875	29.17
16	0.20	0.15	0.125	0	0.1	5.20	0.2044	0.1875	-9.03	0.2250	9.14
16	0.20	0.15	0.125	0	0	7.36	0.2220	0.2000	-11.00	0.2375	6.53
16	0.20	0.15	0.125	0	-0.1	7.88	0.2179	0.1875	-16.20	0.2250	3.17
16	0.20	0.15	0.125	0	-0.25	7.88	0.1458	0.1500	2.82	0.1875	22.26
16	0.20	0.15	0.125	0	-0.4	7.90	0.0000	0.0000	100.00	0.1250	100.00
16	0.20	0.15	0.25	0	0.4	-3.63	0.0343	0.0000	N/A	0.1250	72.54
16	0.20	0.15	0.25	0	0.25	0.81	0.1297	0.1500	13.56	0.1875	30.85
16	0.20	0.15	0.25	0	0.1	4.83	0.1943	0.1875	-3.62	0.2250	13.65
16	0.20	0.15	0.25	0	0	6.84	0.2070	0.2000	-3.48	0.2375	12.86
16	0.20	0.15	0.25	0	-0.1	7.33	0.1943	0.1875	-3.62	0.2250	13.65
16	0.20	0.15	0.25	0	-0.25	7.33	0.1049	0.1500	30.05	0.1875	44.04
16	0.20	0.15	0.25	0	-0.4	7.34	0.0066	0.0000	N/A	0.1250	94.71
16	0.20	0.15	0.5	0	0.4	-3.18	0.0359	0.0000	N/A	0.1250	71.31
16	0.20	0.15	0.5	0	0.25	0.71	0.1248	0.1500	16.79	0.1875	33.43
16	0.20	0.15	0.5	0	0.1	4.23	0.1802	0.1875	3.92	0.2250	19.93
16	0.20	0.15	0.5	0	0	5.99	0.1858	0.2000	7.10	0.2375	21.77
16	0.20	0.15	0.5	0	-0.1	6.42	0.1649	0.1875	12.03	0.2250	26.69
16	0.20	0.15	0.5	0	-0.25	6.42	0.1153	0.1500	23.15	0.1875	38.52
16	0.20	0.15	0.5	0	-0.4	6.43	0.0389	0.0000	N/A	0.1250	68.90

Table 3.14 COMPARISON OF THE RESULTS FOR ECCENTRIC LOAD WITH 6 DEGREE INCLINATION ANGLE

<i>h</i>	<i>a/h</i>	<i>R/P</i>	<i>l/h</i>	α	<i>e/h</i>	β	<i>T_{burst-fem}/P</i>	<i>Eqn (1.5)</i>	%diff	<i>Eqn (3.8)</i>	%diff
							-1-	-2-	-1 & 2-	-3-	-1 & 3-
16	0.10	0.15	0.125	6	0.4	-4.49	0.1027	0.1773	42.07	0.1259	18.44
16	0.10	0.15	0.125	6	0.25	-0.27	0.1632	0.2523	35.30	0.2009	18.77
16	0.10	0.15	0.125	6	0.1	1.95	0.2023	0.2710	25.35	0.2197	7.90
16	0.10	0.15	0.125	6	0	1.95	0.2036	0.2773	26.56	0.2259	9.87
16	0.10	0.15	0.125	6	-0.1	1.95	0.1905	0.2710	29.72	0.2197	13.29
16	0.10	0.15	0.125	6	-0.25	2.09	0.1367	0.2523	45.82	0.2009	31.97
16	0.10	0.15	0.125	6	-0.4	5.18	0.0510	0.1773	71.25	0.1259	59.53
16	0.10	0.15	0.25	6	0.4	-4.23	0.1043	0.1773	41.14	0.1259	17.14
16	0.10	0.15	0.25	6	0.25	-0.38	0.1598	0.2523	36.65	0.2009	20.46
16	0.10	0.15	0.25	6	0.1	1.38	0.1926	0.2710	28.95	0.2197	12.34
16	0.10	0.15	0.25	6	0	1.38	0.1885	0.2773	32.00	0.2259	16.55
16	0.10	0.15	0.25	6	-0.1	1.38	0.1685	0.2710	37.82	0.2197	23.28
16	0.10	0.15	0.25	6	-0.25	1.65	0.1003	0.2523	60.24	0.2009	50.08
16	0.10	0.15	0.25	6	-0.4	4.71	0.1016	0.1773	42.69	0.1259	19.32
16	0.10	0.15	0.5	6	0.4	-3.82	0.1069	0.1773	39.70	0.1259	15.11
16	0.10	0.15	0.5	6	0.25	-0.60	0.1543	0.2523	38.82	0.2009	23.19
16	0.10	0.15	0.5	6	0.1	0.46	0.1781	0.2710	34.29	0.2197	18.93
16	0.10	0.15	0.5	6	0	0.46	0.1692	0.2773	38.97	0.2259	25.09
16	0.10	0.15	0.5	6	-0.1	0.46	0.1457	0.2710	46.26	0.2197	33.69
16	0.10	0.15	0.5	6	-0.25	1.01	0.1338	0.2523	46.96	0.2009	33.40
16	0.10	0.15	0.5	6	-0.4	3.98	0.1544	0.1773	12.92	0.1259	-22.60
16	0.20	0.05	0.125	6	0.4	-5.55	0.0184	0.0523	64.78	0.1250	85.27
16	0.20	0.05	0.125	6	0.25	-3.36	0.1210	0.2023	40.18	0.1782	32.09
16	0.20	0.05	0.125	6	0.1	-3.36	0.1773	0.2398	26.07	0.2157	17.81
16	0.20	0.05	0.125	6	0	-3.36	0.1902	0.2523	24.59	0.2282	16.63
16	0.20	0.05	0.125	6	-0.1	-3.21	0.1812	0.2398	24.41	0.2157	15.97
16	0.20	0.05	0.125	6	-0.25	-0.10	0.1247	0.2023	38.34	0.1782	30.01
16	0.20	0.05	0.125	6	-0.4	4.32	0.0423	0.0523	18.99	0.1250	66.13
16	0.20	0.05	0.25	6	0.4	-5.29	0.0187	0.0523	64.28	0.1250	85.07
16	0.20	0.05	0.25	6	0.25	-3.55	0.1207	0.2023	40.33	0.1782	32.27
16	0.20	0.05	0.25	6	0.1	-3.55	0.1746	0.2398	27.19	0.2157	19.06
16	0.20	0.05	0.25	6	0	-3.55	0.1851	0.2523	26.62	0.2282	18.88
16	0.20	0.05	0.25	6	-0.1	-3.27	0.1735	0.2398	27.64	0.2157	19.56
16	0.20	0.05	0.25	6	-0.25	-0.19	0.1131	0.2023	44.10	0.1782	36.54
16	0.20	0.05	0.25	6	-0.4	3.96	0.0650	0.0523	-24.46	0.1250	47.96
16	0.20	0.05	0.5	6	0.4	-4.90	0.0205	0.0523	60.70	0.1250	83.57
16	0.20	0.05	0.5	6	0.25	-3.86	0.1180	0.2023	41.66	0.1782	33.78
16	0.20	0.05	0.5	6	0.1	-3.86	0.1675	0.2398	30.15	0.2157	22.35
16	0.20	0.05	0.5	6	0	-3.86	0.1799	0.2523	28.67	0.2282	21.14
16	0.20	0.05	0.5	6	-0.1	-3.29	0.1665	0.2398	30.57	0.2157	22.82
16	0.20	0.05	0.5	6	-0.25	-0.32	0.1110	0.2023	45.13	0.1782	37.72
16	0.20	0.05	0.5	6	-0.4	3.39	0.0774	0.0523	-48.11	0.1250	38.07
16	0.20	0.15	0.125	6	0.4	-4.49	0.0136	0.0523	73.95	0.1250	89.11
16	0.20	0.15	0.125	6	0.25	-0.27	0.1090	0.2023	46.10	0.1509	27.76
16	0.20	0.15	0.125	6	0.1	1.95	0.1639	0.2398	31.64	0.1884	13.01
16	0.20	0.15	0.125	6	0	1.95	0.1693	0.2523	32.87	0.2009	15.71
16	0.20	0.15	0.125	6	-0.1	1.95	0.1537	0.2398	35.88	0.1884	18.41
16	0.20	0.15	0.125	6	-0.25	2.09	0.0845	0.2023	58.23	0.1509	44.02
16	0.20	0.15	0.125	6	-0.4	5.18	0.0000	0.0523	100.00	0.1250	100.00
16	0.20	0.15	0.25	6	0.4	-4.23	0.0146	0.0523	72.02	0.1250	88.30
16	0.20	0.15	0.25	6	0.25	-0.38	0.1049	0.2023	48.13	0.1509	30.48
16	0.20	0.15	0.25	6	0.1	1.38	0.1513	0.2398	36.92	0.1884	19.72
16	0.20	0.15	0.25	6	0	1.38	0.1499	0.2523	40.58	0.2009	25.40
16	0.20	0.15	0.25	6	-0.1	1.38	0.1261	0.2398	47.40	0.1884	33.07
16	0.20	0.15	0.25	6	-0.25	1.65	0.0452	0.2023	77.67	0.1509	70.07
16	0.20	0.15	0.25	6	-0.4	4.71	0.0489	0.0523	6.41	0.1250	60.87
16	0.20	0.15	0.5	6	0.4	-3.82	0.0163	0.0523	68.83	0.1250	86.97
16	0.20	0.15	0.5	6	0.25	-0.60	0.0994	0.2023	50.86	0.1509	34.14
16	0.20	0.15	0.5	6	0.1	0.46	0.1319	0.2398	44.99	0.1884	30.00
16	0.20	0.15	0.5	6	0	0.46	0.1235	0.2523	51.05	0.2009	38.53
16	0.20	0.15	0.5	6	-0.1	0.46	0.0954	0.2398	60.21	0.1884	49.37
16	0.20	0.15	0.5	6	-0.25	1.01	0.0812	0.2023	59.87	0.1509	46.22
16	0.20	0.15	0.5	6	-0.4	3.98	0.0834	0.0523	-59.54	0.1250	33.29

Table 3.15 COMPARISON OF THE RESULTS FOR ECCENTRIC LOAD WITH 9 DEGREE INCLINATION ANGLE

h	a/h	R/P	l/h	α	e/h	β	$T_{burst-fem}/P$	Eqn (1.5)	%diff	Eqn (3.8)	%diff
							-1-	-2-	-1 & 2-	-3-	-1 & 3-
16	0.10	0.15	0.125	9	0.4	-4.98	0.0897	0.2032	55.86	0.1250	28.23
16	0.10	0.15	0.125	9	0.25	-1.50	0.1537	0.2782	44.75	0.1827	15.88
16	0.10	0.15	0.125	9	0.1	-1.04	0.1878	0.2970	36.77	0.2015	6.82
16	0.10	0.15	0.125	9	0	-1.04	0.1935	0.3032	36.18	0.2077	6.85
16	0.10	0.15	0.125	9	-0.1	-1.04	0.1859	0.2970	37.39	0.2015	7.72
16	0.10	0.15	0.125	9	-0.25	0.57	0.1365	0.2782	50.93	0.1827	25.30
16	0.10	0.15	0.125	9	-0.4	4.62	0.0631	0.2032	68.94	0.1250	49.50
16	0.10	0.15	0.25	9	0.4	-4.77	0.0917	0.2032	54.89	0.1250	26.66
16	0.10	0.15	0.25	9	0.25	-1.80	0.1505	0.2782	45.90	0.1827	17.64
16	0.10	0.15	0.25	9	0.1	-1.62	0.1792	0.2970	39.64	0.2015	11.05
16	0.10	0.15	0.25	9	0	-1.62	0.1801	0.3032	40.61	0.2077	13.32
16	0.10	0.15	0.25	9	-0.1	-1.62	0.1652	0.2970	44.38	0.2015	18.03
16	0.10	0.15	0.25	9	-0.25	0.31	0.1020	0.2782	63.35	0.1827	44.20
16	0.10	0.15	0.25	9	-0.4	4.20	0.1134	0.2032	44.21	0.1250	9.29
16	0.10	0.15	0.5	9	0.4	-4.46	0.0950	0.2032	53.25	0.1250	24.00
16	0.10	0.15	0.5	9	0.25	-2.55	0.1455	0.2782	47.70	0.1827	20.37
16	0.10	0.15	0.5	9	0.1	-2.55	0.1683	0.2970	43.32	0.2015	16.46
16	0.10	0.15	0.5	9	0	-2.55	0.1648	0.3032	45.65	0.2077	20.68
16	0.10	0.15	0.5	9	-0.1	-2.47	0.1459	0.2970	50.88	0.2015	27.61
16	0.10	0.15	0.5	9	-0.25	-0.04	0.1497	0.2782	46.18	0.1827	18.07
16	0.10	0.15	0.5	9	-0.4	3.53	0.1656	0.2032	18.52	0.1250	-32.47
16	0.20	0.15	0.125	9	0.4	-4.98	0.0102	0.0782	86.95	0.1250	91.83
16	0.20	0.15	0.125	9	0.25	-1.50	0.1022	0.2282	55.20	0.1327	22.98
16	0.20	0.15	0.125	9	0.1	-1.04	0.1519	0.2657	42.85	0.1702	10.80
16	0.20	0.15	0.125	9	0	-1.04	0.1602	0.2782	42.40	0.1827	12.31
16	0.20	0.15	0.125	9	-0.1	-1.04	0.1481	0.2657	44.28	0.1702	13.04
16	0.20	0.15	0.125	9	-0.25	0.57	0.0824	0.2282	63.88	0.1327	37.91
16	0.20	0.15	0.125	9	-0.4	4.62	0.0126	0.0782	83.89	0.1250	89.92
16	0.20	0.15	0.25	9	0.4	-4.77	0.0113	0.0782	85.52	0.1250	90.94
16	0.20	0.15	0.25	9	0.25	-1.80	0.0982	0.2282	56.99	0.1327	26.06
16	0.20	0.15	0.25	9	0.1	-1.62	0.1400	0.2657	47.31	0.1702	17.77
16	0.20	0.15	0.25	9	0	-1.62	0.1415	0.2782	49.13	0.1827	22.56
16	0.20	0.15	0.25	9	-0.1	-1.62	0.1209	0.2657	54.51	0.1702	29.01
16	0.20	0.15	0.25	9	-0.25	0.31	0.0453	0.2282	80.15	0.1327	65.88
16	0.20	0.15	0.25	9	-0.4	4.20	0.0733	0.0782	6.33	0.1250	41.39
16	0.20	0.15	0.5	9	0.4	-4.46	0.0133	0.0782	83.02	0.1250	89.38
16	0.20	0.15	0.5	9	0.25	-2.55	0.0918	0.2282	59.79	0.1327	30.87
16	0.20	0.15	0.5	9	0.1	-2.55	0.1237	0.2657	53.46	0.1702	27.36
16	0.20	0.15	0.5	9	0	-2.55	0.1186	0.2782	57.38	0.1827	35.12
16	0.20	0.15	0.5	9	-0.1	-2.47	0.0946	0.2657	64.41	0.1702	44.46
16	0.20	0.15	0.5	9	-0.25	-0.04	0.0913	0.2282	59.99	0.1327	31.22
16	0.20	0.15	0.5	9	-0.4	3.53	0.1089	0.0782	-39.27	0.1250	12.85
16	0.20	0.05	0.125	9	0.4	-6.80	0.0157	0.0782	79.90	0.1250	87.42
16	0.20	0.05	0.125	9	0.25	-6.37	0.1330	0.2282	41.71	0.1860	28.46
16	0.20	0.05	0.125	9	0.1	-6.37	0.1985	0.2657	25.31	0.2235	11.19
16	0.20	0.05	0.125	9	0	-6.33	0.2097	0.2782	24.62	0.2360	11.13
16	0.20	0.05	0.125	9	-0.1	-4.74	0.1969	0.2657	25.90	0.2235	11.89
16	0.20	0.05	0.125	9	-0.25	-0.67	0.1320	0.2282	42.16	0.1860	29.02
16	0.20	0.05	0.125	9	-0.4	4.03	0.0678	0.0782	13.37	0.1250	45.79
16	0.20	0.05	0.25	9	0.4	-6.73	0.0163	0.0782	79.17	0.1250	86.96
16	0.20	0.05	0.25	9	0.25	-6.56	0.1356	0.2282	40.57	0.1860	27.07
16	0.20	0.05	0.25	9	0.1	-6.56	0.1968	0.2657	25.93	0.2235	11.92
16	0.20	0.05	0.25	9	0	-6.37	0.2051	0.2782	26.27	0.2360	13.06
16	0.20	0.05	0.25	9	-0.1	-4.61	0.1896	0.2657	28.66	0.2235	15.17
16	0.20	0.05	0.25	9	-0.25	-0.71	0.1200	0.2282	47.40	0.1860	35.45
16	0.20	0.05	0.25	9	-0.4	3.69	0.0903	0.0782	-15.50	0.1250	27.73
16	0.20	0.05	0.5	9	0.4	-6.87	0.0177	0.0782	77.43	0.1250	85.88
16	0.20	0.05	0.5	9	0.25	-6.87	0.1418	0.2282	37.85	0.1860	23.72
16	0.20	0.05	0.5	9	0.1	-6.87	0.1984	0.2657	25.33	0.2235	11.21
16	0.20	0.05	0.5	9	0	-6.22	0.2021	0.2782	27.37	0.2360	14.37
16	0.20	0.05	0.5	9	-0.1	-4.34	0.1840	0.2657	30.76	0.2235	17.67
16	0.20	0.05	0.5	9	-0.25	-0.77	0.1209	0.2282	47.02	0.1860	34.99
16	0.20	0.05	0.5	9	-0.4	3.15	0.1092	0.0782	-39.63	0.1250	12.63

3.4.4.3 Location of Bursting Force

The symmetric prism approach performed well to determine the location of the bursting force as illustrated in section 3.4.3.3. It is assumed that it will also provide acceptable predictions of d_{burst} for an inclined eccentric prestressing load applied to a structure with a support reaction. Fig. 3.109 shows an example of the relation between d_{burst} and the reaction location for an eccentric prestressing load with 9 degree angle. As can be seen, all plots vary with different characteristics with respect to increasing values of the l/h ratio. Similar plot characteristics appear for all other inclined eccentric load configurations.

Figure 3.110 shows the effect of the bearing support ratio of 9 degree inclined eccentric load configuration. Once again, there is no indication of a significant effect due to the size of the support bearing plate. Therefore, equation (3.7) is still valid without the b/h term in the formulation. Based on the studies of all load configurations, it can be concluded that the support bearing plate size does not have an important influence on bursting force magnitude or location. It is the magnitude and location of the reaction force that affects the design methodology. However, as has been shown in the development of the equations, neglecting the l/h ratio leads to less complicated expressions, without sacrificing accuracy significantly.

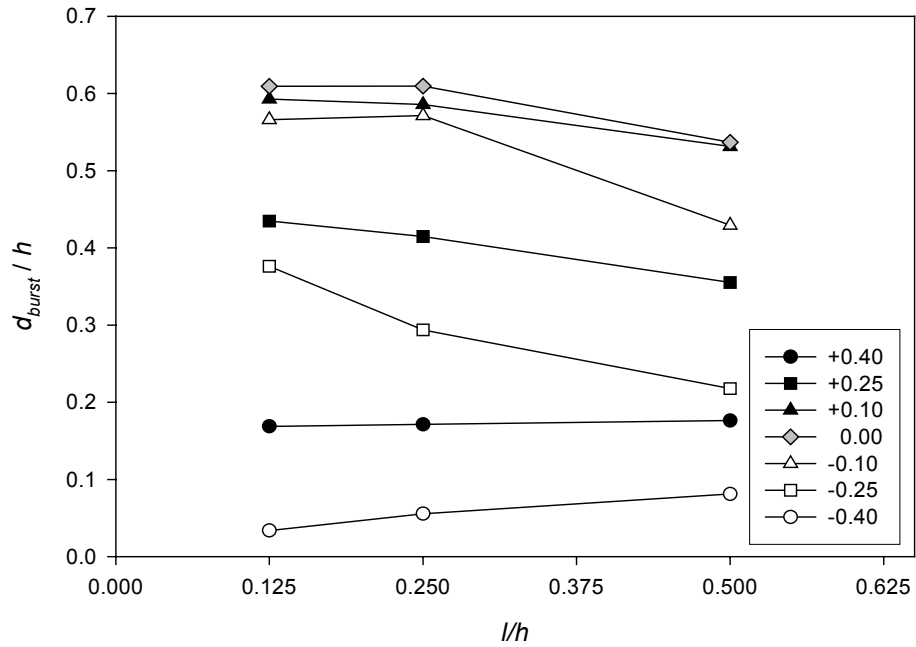


Fig. 3.109 BURSTING FORCE LOCATION vs. LOCATION OF SUPPORT REACTION FOR 9 DEGREE INCLINED ECCENTRIC LOAD AND $R/P = 0.15$ ($a/h = 0.20$, $b/h = 0.125$)

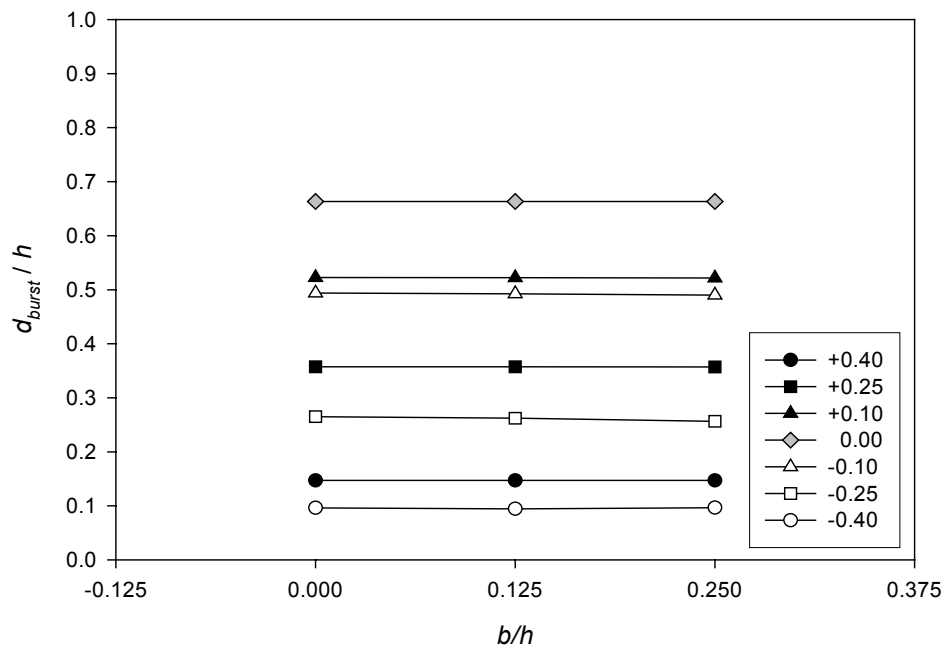


Fig. 3.110 BURSTING FORCE LOCATION vs. BEARING PLATE RATIO FOR 9 DEGREE INCLINED ECCENTRIC LOAD ($a/h = 0.10$, $l/h = 0.25$)

Figures 3.111 through 3.114 show the comparison of all results using three different methods consisting of finite element analysis, equation (1.6), and equation (3.7) as previously presented in section 3.4.3.3. The second term of equation (1.6) accounts for the effect of inclination by considering the sign of the angle. When the inclined prestressing load points in the direction outward from the centerline of the anchorage zone, such as an inclined load acting downward in the lower portion of the anchorage zone in this study, a negative sign is applied to the second term of the equation. As a result, the plot from equation (1.6) has a steeper slope on the left side than on the right side. The plots from the finite element analysis do not show the same steep line. Instead, the results of the finite element analysis have a larger d_{burst} on the left side than that of equation (1.6). On the right side of finite element plots, the d_{burst} values that occur in the case of a small magnitude of reaction force ($R/P = 0.05$) are larger than those on the left. This may be affected by the tensile stresses resulting from the downwardly inclined prestressing force.

The plot from the newly developed equation provides a better estimation for the d_{burst} value than that from equation (1.6). As can be seen, the plot from equation (3.7) is quite similar to the plots from the finite element analysis. On the left side of all figures, the prediction from equation (3.7) may provide a slightly larger d_{burst} than that from finite element analysis. In Fig. 3.113, the difference between the plot from equation (3.7) and that from the finite element analysis at an eccentricity ratio of -0.40 is as high as $0.20h$. With this load configuration, the anchorage zone may not require any reinforcement because the finite element analysis indicates the bursting force has a zero magnitude. However, for good practice a minimum reinforcement should be provided.

Tables 3.16 through 3.18 show the numerical comparison between the results from finite element analysis and those using equations (1.6) and (3.7) for the same models presented in the previous section. Similarly to the graphic presentation in Figs. 3.111 through 3.114, the percent differences between the finite element results and those of equation (3.7) indicate better estimation of d_{burst} than those using equation (1.7). The largest positive percent difference may be detected at the eccentricity of $0.40h$. Since the bursting force is not critical and the d_{burst} is relatively small compared to the section width (h), good detailing practice will result in a safe and serviceable anchorage zone.

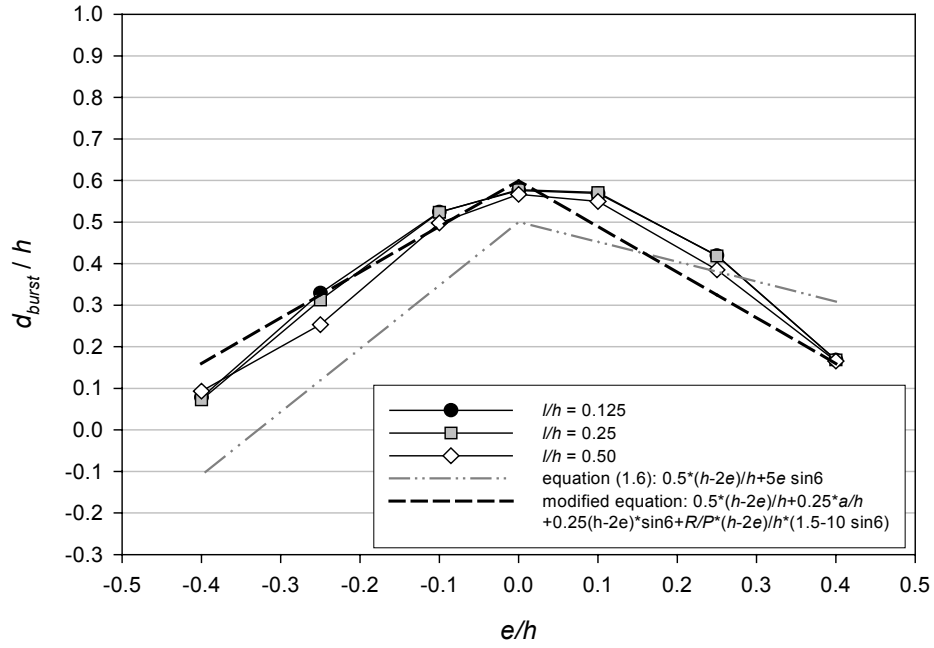


Fig. 3.111 BURSTING FORCE LOCATION vs. ECCENTRICITY RATIO FOR 6 DEGREE INCLINED ECCENTRIC LOAD AND $R/P = 0.05$ ($a/h = 0.20$, $b/h = 0.125$)

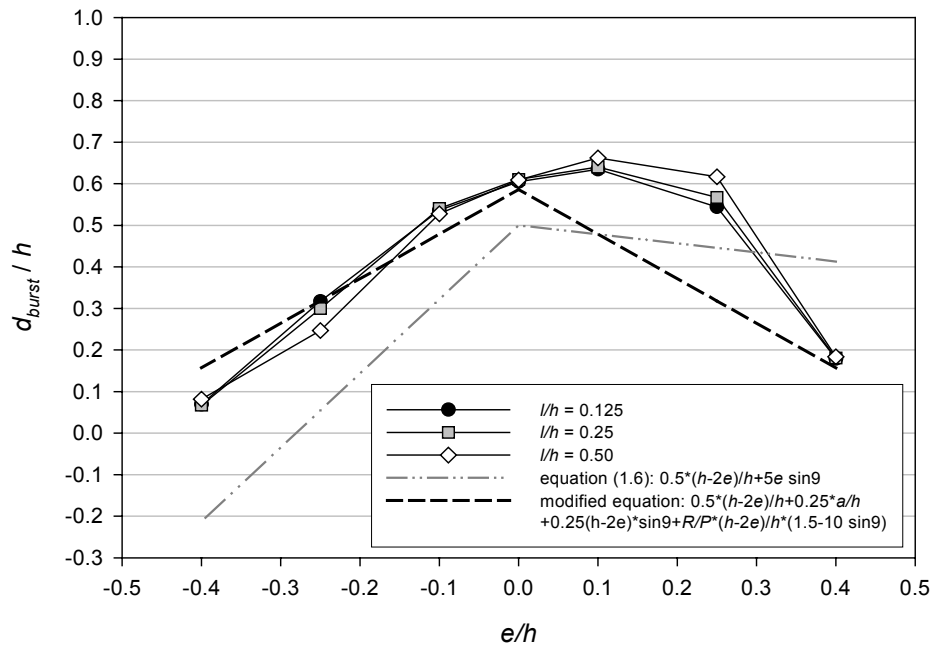


Fig. 3.112 BURSTING FORCE LOCATION vs. ECCENTRICITY RATIO FOR 9 DEGREE INCLINED ECCENTRIC LOAD AND $R/P = 0.05$ ($a/h = 0.20$, $b/h = 0.125$)

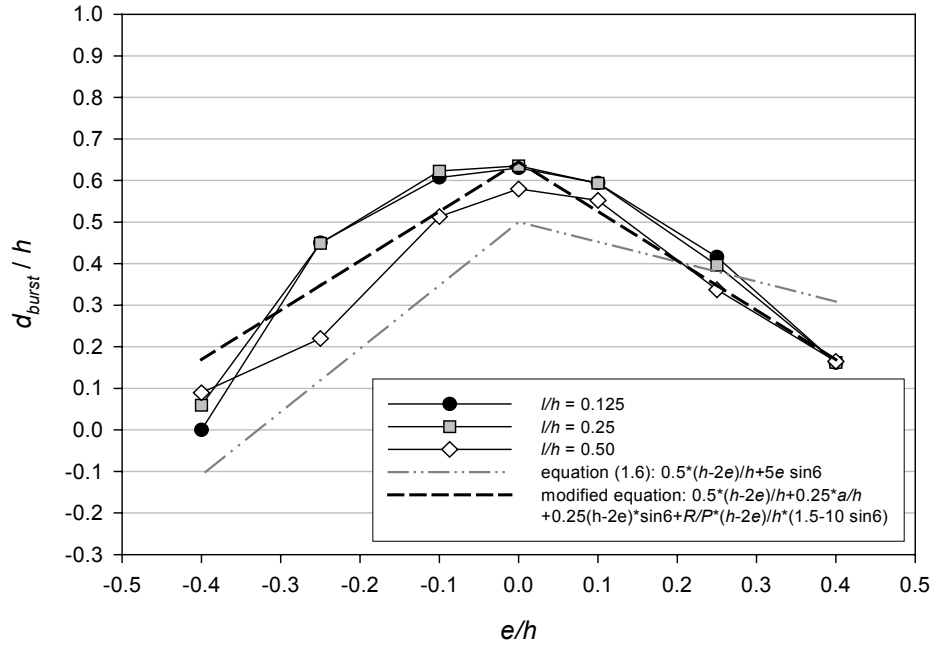


Fig. 3.113 BURSTING FORCE LOCATION vs. ECCENTRICITY RATIO FOR 6 DEGREE INCLINED ECCENTRIC LOAD AND $R/P = 0.15$ ($a/h = 0.20$, $b/h = 0.125$)

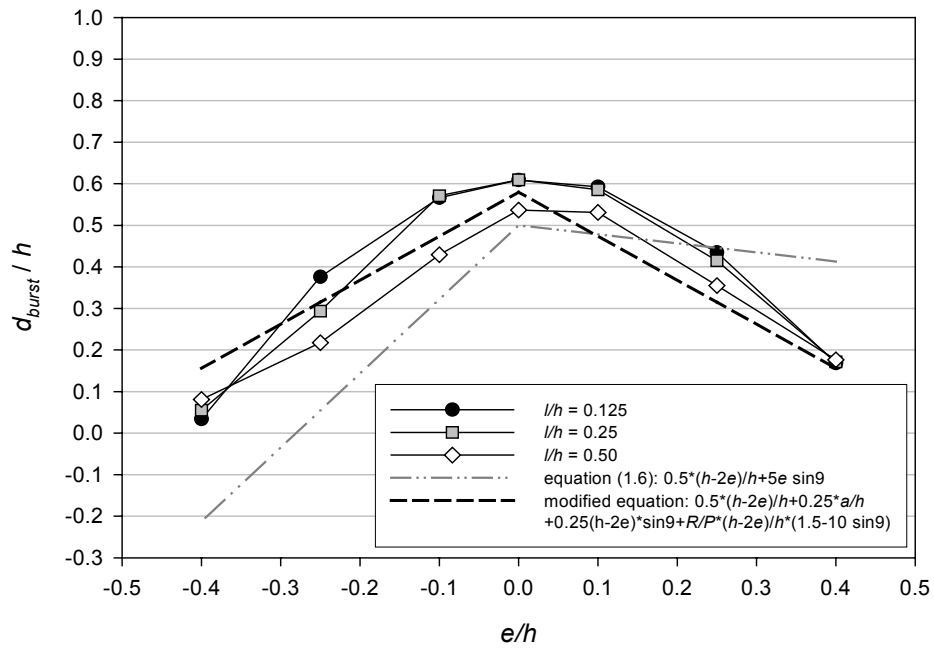


Fig. 3.114 BURSTING FORCE LOCATION vs. ECCENTRICITY RATIO FOR 9 DEGREE INCLINED ECCENTRIC LOAD AND $R/P = 0.15$ ($a/h = 0.20$, $b/h = 0.125$)

Table 3.16 COMPARISON OF d_{burst} FOR ECCENTRIC LOAD WITH NO INCLINATION ANGLE

h	a/h	R/P	l/h	α	e/h	β	$d_{burst-fem}/h$	Eqn (1.6)	%diff	Eqn (3.7)	%diff
							-1-	-2-	-1 & 2-	-3-	-1 & 3-
16	0.10	0.15	0.125	0	0.4	-3.91	0.1264	0.1000	-20.89	0.1700	25.64
16	0.10	0.15	0.125	0	0.25	0.88	0.3763	0.2500	-33.57	0.3875	2.88
16	0.10	0.15	0.125	0	0.1	5.20	0.5682	0.4000	-29.60	0.6050	6.08
16	0.10	0.15	0.125	0	0	7.36	0.6380	0.5000	-21.63	0.7500	14.94
16	0.10	0.15	0.125	0	-0.1	7.88	0.7089	0.4000	-43.58	0.6050	-14.66
16	0.10	0.15	0.125	0	-0.25	7.88	0.7140	0.2500	-64.99	0.3875	-45.73
16	0.10	0.15	0.125	0	-0.4	7.90	0.1048	0.1000	-4.57	0.1700	38.36
16	0.10	0.15	0.25	0	0.4	-3.63	0.1268	0.1000	-21.13	0.1700	25.42
16	0.10	0.15	0.25	0	0.25	0.81	0.3705	0.2500	-32.52	0.3875	4.39
16	0.10	0.15	0.25	0	0.1	4.83	0.5802	0.4000	-31.06	0.6050	4.10
16	0.10	0.15	0.25	0	0	6.84	0.6632	0.5000	-24.60	0.7500	11.58
16	0.10	0.15	0.25	0	-0.1	7.33	0.7493	0.4000	-46.62	0.6050	-19.26
16	0.10	0.15	0.25	0	-0.25	7.33	0.8061	0.2500	-68.98	0.3875	-51.93
16	0.10	0.15	0.25	0	-0.4	7.34	0.0999	0.1000	0.07	0.1700	41.22
16	0.10	0.15	0.5	0	0.4	-3.18	0.1276	0.1000	-21.61	0.1700	24.96
16	0.10	0.15	0.5	0	0.25	0.71	0.3559	0.2500	-29.75	0.3875	8.17
16	0.10	0.15	0.5	0	0.1	4.23	0.5933	0.4000	-32.58	0.6050	1.93
16	0.10	0.15	0.5	0	0	5.99	0.6915	0.5000	-27.70	0.7500	7.79
16	0.10	0.15	0.5	0	-0.1	6.42	0.7810	0.4000	-48.79	0.6050	-22.54
16	0.10	0.15	0.5	0	-0.25	6.42	0.7650	0.2500	-67.32	0.3875	-49.35
16	0.10	0.15	0.5	0	-0.4	6.43	0.1255	0.1000	-20.30	0.1700	26.19
16	0.20	0.05	0.125	0	0.4	-4.40	0.1305	0.1000	-23.35	0.1650	20.94
16	0.20	0.05	0.125	0	0.25	-0.08	0.3535	0.2500	-29.28	0.3375	-4.53
16	0.20	0.05	0.125	0	0.1	2.63	0.5443	0.4000	-26.51	0.5100	-6.30
16	0.20	0.05	0.125	0	0	2.64	0.5887	0.5000	-15.07	0.6250	5.81
16	0.20	0.05	0.125	0	-0.1	2.64	0.5744	0.4000	-30.37	0.5100	-11.22
16	0.20	0.05	0.125	0	-0.25	2.66	0.4183	0.2500	-40.23	0.3375	-19.31
16	0.20	0.05	0.125	0	-0.4	5.35	0.1248	0.1000	-19.89	0.1650	24.35
16	0.20	0.05	0.25	0	0.4	-4.09	0.1301	0.1000	-23.13	0.1650	21.16
16	0.20	0.05	0.25	0	0.25	-0.07	0.3490	0.2500	-28.36	0.3375	-3.29
16	0.20	0.05	0.25	0	0.1	2.44	0.5459	0.4000	-26.73	0.5100	-6.58
16	0.20	0.05	0.25	0	0	2.45	0.5930	0.5000	-15.68	0.6250	5.13
16	0.20	0.05	0.25	0	-0.1	2.45	0.5813	0.4000	-31.19	0.5100	-12.27
16	0.20	0.05	0.25	0	-0.25	2.47	0.4169	0.2500	-40.03	0.3375	-19.04
16	0.20	0.05	0.25	0	-0.4	4.97	0.1038	0.1000	-3.70	0.1650	37.06
16	0.20	0.05	0.5	0	0.4	-3.58	0.1296	0.1000	-22.82	0.1650	21.47
16	0.20	0.05	0.5	0	0.25	-0.06	0.3389	0.2500	-26.24	0.3375	-0.42
16	0.20	0.05	0.5	0	0.1	2.14	0.5440	0.4000	-26.47	0.5100	-6.25
16	0.20	0.05	0.5	0	0	2.15	0.5901	0.5000	-15.27	0.6250	5.58
16	0.20	0.05	0.5	0	-0.1	2.15	0.5690	0.4000	-29.70	0.5100	-10.37
16	0.20	0.05	0.5	0	-0.25	2.16	0.3527	0.2500	-29.11	0.3375	-4.30
16	0.20	0.05	0.5	0	-0.4	4.35	0.1300	0.1000	-23.06	0.1650	21.23
16	0.20	0.15	0.125	0	0.4	-3.91	0.1257	0.1000	-20.44	0.1950	35.54
16	0.20	0.15	0.125	0	0.25	0.88	0.4322	0.2500	-42.16	0.4125	-4.56
16	0.20	0.15	0.125	0	0.1	5.20	0.6298	0.4000	-36.49	0.6300	0.03
16	0.20	0.15	0.125	0	0	7.36	0.6930	0.5000	-27.85	0.7750	10.58
16	0.20	0.15	0.125	0	-0.1	7.88	0.7735	0.4000	-48.29	0.6300	-18.55
16	0.20	0.15	0.125	0	-0.25	7.88	0.8566	0.2500	-70.81	0.4125	-51.84
16	0.20	0.15	0.125	0	-0.4	7.90	0.0000	0.1000	100.00	0.1950	100.00
16	0.20	0.15	0.25	0	0.4	-3.63	0.1265	0.1000	-20.92	0.1950	35.15
16	0.20	0.15	0.25	0	0.25	0.81	0.4253	0.2500	-41.22	0.4125	-3.01
16	0.20	0.15	0.25	0	0.1	4.83	0.6532	0.4000	-38.76	0.6300	-3.55
16	0.20	0.15	0.25	0	0	6.84	0.7345	0.5000	-31.93	0.7750	5.23
16	0.20	0.15	0.25	0	-0.1	7.33	0.8423	0.4000	-52.51	0.6300	-25.20
16	0.20	0.15	0.25	0	-0.25	7.33	1.0850	0.2500	-76.96	0.4125	-61.98
16	0.20	0.15	0.25	0	-0.4	7.34	0.0850	0.1000	15.01	0.1950	56.41
16	0.20	0.15	0.5	0	0.4	-3.18	0.1275	0.1000	-21.56	0.1950	34.63
16	0.20	0.15	0.5	0	0.25	0.71	0.4065	0.2500	-38.49	0.4125	1.46
16	0.20	0.15	0.5	0	0.1	4.23	0.6830	0.4000	-41.43	0.6300	-7.76
16	0.20	0.15	0.5	0	0	5.99	0.7945	0.5000	-37.06	0.7750	-2.45
16	0.20	0.15	0.5	0	-0.1	6.42	0.9310	0.4000	-57.04	0.6300	-32.33
16	0.20	0.15	0.5	0	-0.25	6.42	0.9974	0.2500	-74.94	0.4125	-58.64
16	0.20	0.15	0.5	0	-0.4	6.43	0.1297	0.1000	-22.92	0.1950	33.47

Table 3.17 COMPARISON OF d_{burst} FOR ECCENTRIC LOAD WITH 6 DEGREE INCLINATION ANGLE

h	a/h	R/P	l/h	α	e/h	β	$d_{burst-fem}/h$	Eqn (1.6)	%diff	Eqn (3.7)	%diff
							-1-	-2-	-1 & 2-	-3-	-1 & 3-
16	0.10	0.15	0.125	6	0.4	-4.49	0.1376	0.3091	55.46	0.1439	4.33
16	0.10	0.15	0.125	6	0.25	-0.27	0.3588	0.3807	5.75	0.3222	-10.20
16	0.10	0.15	0.125	6	0.1	1.95	0.5378	0.4523	-15.90	0.5005	-6.94
16	0.10	0.15	0.125	6	0	1.95	0.5776	0.5000	-13.44	0.6193	6.74
16	0.10	0.15	0.125	6	-0.1	1.95	0.5490	0.3477	-36.66	0.5005	-8.85
16	0.10	0.15	0.125	6	-0.25	2.09	0.3729	0.1193	-67.99	0.3222	-13.60
16	0.10	0.15	0.125	6	-0.4	5.18	0.0943	-0.1091	-215.65	0.1439	34.46
16	0.10	0.15	0.25	6	0.4	-4.23	0.1383	0.3091	55.25	0.1439	3.88
16	0.10	0.15	0.25	6	0.25	-0.38	0.3435	0.3807	9.75	0.3222	-6.22
16	0.10	0.15	0.25	6	0.1	1.38	0.5276	0.4523	-14.27	0.5005	-5.14
16	0.10	0.15	0.25	6	0	1.38	0.5664	0.5000	-11.72	0.6193	8.55
16	0.10	0.15	0.25	6	-0.1	1.38	0.5371	0.3477	-35.25	0.5005	-6.81
16	0.10	0.15	0.25	6	-0.25	1.65	0.3339	0.1193	-64.26	0.3222	-3.52
16	0.10	0.15	0.25	6	-0.4	4.71	0.0967	-0.1091	-212.77	0.1439	32.78
16	0.10	0.15	0.5	6	0.4	-3.82	0.1394	0.3091	54.88	0.1439	3.07
16	0.10	0.15	0.5	6	0.25	-0.60	0.3039	0.3807	20.18	0.3222	5.68
16	0.10	0.15	0.5	6	0.1	0.46	0.4795	0.4523	-5.68	0.5005	4.19
16	0.10	0.15	0.5	6	0	0.46	0.4970	0.5000	0.60	0.6193	19.76
16	0.10	0.15	0.5	6	-0.1	0.46	0.4257	0.3477	-18.31	0.5005	14.94
16	0.10	0.15	0.5	6	-0.25	1.01	0.2061	0.1193	-42.08	0.3222	36.04
16	0.10	0.15	0.5	6	-0.4	3.98	0.1183	-0.1091	-192.18	0.1439	17.77
16	0.20	0.05	0.125	6	0.4	-5.55	0.1683	0.3091	45.54	0.1598	-5.08
16	0.20	0.05	0.125	6	0.25	-3.36	0.4196	0.3807	-9.29	0.3244	-22.69
16	0.20	0.05	0.125	6	0.1	-3.36	0.5689	0.4523	-20.50	0.4891	-14.02
16	0.20	0.05	0.125	6	0	-3.36	0.5759	0.5000	-13.18	0.5989	3.83
16	0.20	0.05	0.125	6	-0.1	-3.21	0.5243	0.3477	-33.68	0.4891	-6.72
16	0.20	0.05	0.125	6	-0.25	-0.10	0.3294	0.1193	-63.77	0.3244	-1.51
16	0.20	0.05	0.125	6	-0.4	4.32	0.0780	-0.1091	-239.84	0.1598	51.19
16	0.20	0.05	0.25	6	0.4	-5.29	0.1684	0.3091	45.50	0.1598	-5.15
16	0.20	0.05	0.25	6	0.25	-3.55	0.4184	0.3807	-9.02	0.3244	-22.46
16	0.20	0.05	0.25	6	0.1	-3.55	0.5712	0.4523	-20.82	0.4891	-14.37
16	0.20	0.05	0.25	6	0	-3.55	0.5778	0.5000	-13.47	0.5989	3.51
16	0.20	0.05	0.25	6	-0.1	-3.27	0.5235	0.3477	-33.58	0.4891	-6.58
16	0.20	0.05	0.25	6	-0.25	-0.19	0.3125	0.1193	-61.81	0.3244	3.68
16	0.20	0.05	0.25	6	-0.4	3.96	0.0724	-0.1091	-250.56	0.1598	54.67
16	0.20	0.05	0.5	6	0.4	-4.90	0.1655	0.3091	46.44	0.1598	-3.48
16	0.20	0.05	0.5	6	0.25	-3.86	0.3850	0.3807	-1.14	0.3244	-15.74
16	0.20	0.05	0.5	6	0.1	-3.86	0.5498	0.4523	-17.74	0.4891	-11.04
16	0.20	0.05	0.5	6	0	-3.86	0.5669	0.5000	-11.80	0.5989	5.34
16	0.20	0.05	0.5	6	-0.1	-3.29	0.4981	0.3477	-30.19	0.4891	-1.82
16	0.20	0.05	0.5	6	-0.25	-0.32	0.2533	0.1193	-52.88	0.3244	21.94
16	0.20	0.05	0.5	6	-0.4	3.39	0.0932	-0.1091	-217.00	0.1598	41.66
16	0.20	0.15	0.125	6	0.4	-4.49	0.1615	0.3091	47.75	0.1689	4.38
16	0.20	0.15	0.125	6	0.25	-0.27	0.4158	0.3807	-8.44	0.3472	-16.50
16	0.20	0.15	0.125	6	0.1	1.95	0.5940	0.4523	-23.86	0.5255	-11.53
16	0.20	0.15	0.125	6	0	1.95	0.6301	0.5000	-20.65	0.6443	2.20
16	0.20	0.15	0.125	6	-0.1	1.95	0.6073	0.3477	-42.74	0.5255	-13.48
16	0.20	0.15	0.125	6	-0.25	2.09	0.4503	0.1193	-73.50	0.3472	-22.90
16	0.20	0.15	0.125	6	-0.4	5.18	0.0000	-0.1091	N/A	0.1689	100.00
16	0.20	0.15	0.25	6	0.4	-4.23	0.1622	0.3091	47.51	0.1689	3.93
16	0.20	0.15	0.25	6	0.25	-0.38	0.3961	0.3807	-3.89	0.3472	-12.35
16	0.20	0.15	0.25	6	0.1	1.38	0.5933	0.4523	-23.77	0.5255	-11.43
16	0.20	0.15	0.25	6	0	1.38	0.6356	0.5000	-21.33	0.6443	1.36
16	0.20	0.15	0.25	6	-0.1	1.38	0.6228	0.3477	-44.16	0.5255	-15.62
16	0.20	0.15	0.25	6	-0.25	1.65	0.4490	0.1193	-73.42	0.3472	-22.67
16	0.20	0.15	0.25	6	-0.4	4.71	0.0592	-0.1091	-284.22	0.1689	64.94
16	0.20	0.15	0.5	6	0.4	-3.82	0.1648	0.3091	46.68	0.1689	2.41
16	0.20	0.15	0.5	6	0.25	-0.60	0.3373	0.3807	11.39	0.3472	2.84
16	0.20	0.15	0.5	6	0.1	0.46	0.5524	0.4523	-18.12	0.5255	-4.87
16	0.20	0.15	0.5	6	0	0.46	0.5798	0.5000	-13.76	0.6443	10.02
16	0.20	0.15	0.5	6	-0.1	0.46	0.5133	0.3477	-32.26	0.5255	2.31
16	0.20	0.15	0.5	6	-0.25	1.01	0.2198	0.1193	-45.71	0.3472	36.68
16	0.20	0.15	0.5	6	-0.4	3.98	0.0895	-0.1091	-221.80	0.1689	46.98

Table 3.18 COMPARISON OF d_{burst} FOR ECCENTRIC LOAD WITH 9 DEGREE INCLINATION ANGLE

h	a/h	R/P	l/h	α	e/h	β	$d_{burst-fem}/h$	$Eqn (1.6)$	$\%diff$	$Eqn (3.7)$	$\%diff$
							-1-	-2-	-1 & 2-	-3-	-1 & 3-
16	0.10	0.15	0.125	9	0.4	-4.98	0.1460	0.4129	64.63	0.1309	-10.36
16	0.10	0.15	0.125	9	0.25	-1.50	0.3733	0.4455	16.22	0.2897	-22.38
16	0.10	0.15	0.125	9	0.1	-1.04	0.5386	0.4782	-11.20	0.4486	-16.71
16	0.10	0.15	0.125	9	0	-1.04	0.5601	0.5000	-10.72	0.5545	-1.00
16	0.10	0.15	0.125	9	-0.1	-1.04	0.5120	0.3218	-37.15	0.4486	-12.38
16	0.10	0.15	0.125	9	-0.25	0.57	0.3234	0.0545	-83.16	0.2897	-10.40
16	0.10	0.15	0.125	9	-0.4	4.62	0.0929	-0.2129	-329.22	0.1309	29.05
16	0.10	0.15	0.25	9	0.4	-4.77	0.1469	0.4129	64.42	0.1309	-10.91
16	0.10	0.15	0.25	9	0.25	-1.80	0.3572	0.4455	19.83	0.2897	-18.89
16	0.10	0.15	0.25	9	0.1	-1.62	0.5220	0.4782	-8.39	0.4486	-14.07
16	0.10	0.15	0.25	9	0	-1.62	0.5429	0.5000	-7.90	0.5545	2.08
16	0.10	0.15	0.25	9	-0.1	-1.62	0.4921	0.3218	-34.60	0.4486	-8.84
16	0.10	0.15	0.25	9	-0.25	0.31	0.2611	0.0545	-79.15	0.2897	9.87
16	0.10	0.15	0.25	9	-0.4	4.20	0.0957	-0.2129	-322.47	0.1309	26.90
16	0.10	0.15	0.5	9	0.4	-4.46	0.1488	0.4129	63.95	0.1309	-12.06
16	0.10	0.15	0.5	9	0.25	-2.55	0.3148	0.4455	29.34	0.2897	-7.97
16	0.10	0.15	0.5	9	0.1	-2.55	0.4635	0.4782	3.08	0.4486	-3.22
16	0.10	0.15	0.5	9	0	-2.55	0.4624	0.5000	7.53	0.5545	16.61
16	0.10	0.15	0.5	9	-0.1	-2.47	0.3683	0.3218	-12.62	0.4486	17.90
16	0.10	0.15	0.5	9	-0.25	-0.04	0.2007	0.0545	-72.86	0.2897	30.75
16	0.10	0.15	0.5	9	-0.4	3.53	0.1156	-0.2129	-284.13	0.1309	11.68
16	0.20	0.05	0.125	9	0.4	-6.80	0.1794	0.4129	56.56	0.1572	-12.36
16	0.20	0.05	0.125	9	0.25	-6.37	0.5442	0.4455	-18.13	0.3179	-41.57
16	0.20	0.05	0.125	9	0.1	-6.37	0.6346	0.4782	-24.64	0.4787	-24.56
16	0.20	0.05	0.125	9	0	-6.33	0.6051	0.5000	-17.37	0.5859	-3.17
16	0.20	0.05	0.125	9	-0.1	-4.74	0.5364	0.3218	-40.01	0.4787	-10.75
16	0.20	0.05	0.125	9	-0.25	-0.67	0.3170	0.0545	-82.82	0.3179	0.30
16	0.20	0.05	0.125	9	-0.4	4.03	0.0695	-0.2129	-406.11	0.1572	55.76
16	0.20	0.05	0.25	9	0.4	-6.73	0.1808	0.4129	56.21	0.1572	-13.07
16	0.20	0.05	0.25	9	0.25	-6.56	0.5671	0.4455	-21.43	0.3179	-43.93
16	0.20	0.05	0.25	9	0.1	-6.56	0.6402	0.4782	-25.30	0.4787	-25.23
16	0.20	0.05	0.25	9	0	-6.37	0.6106	0.5000	-18.11	0.5859	-4.04
16	0.20	0.05	0.25	9	-0.1	-4.61	0.5408	0.3218	-40.50	0.4787	-11.49
16	0.20	0.05	0.25	9	-0.25	-0.71	0.2996	0.0545	-81.83	0.3179	5.75
16	0.20	0.05	0.25	9	-0.4	3.69	0.0671	-0.2129	-417.01	0.1572	57.28
16	0.20	0.05	0.5	9	0.4	-6.87	0.1837	0.4129	55.52	0.1572	-14.42
16	0.20	0.05	0.5	9	0.25	-6.87	0.6168	0.4455	-27.76	0.3179	-48.45
16	0.20	0.05	0.5	9	0.1	-6.87	0.6621	0.4782	-27.77	0.4787	-27.70
16	0.20	0.05	0.5	9	0	-6.22	0.6092	0.5000	-17.93	0.5859	-3.83
16	0.20	0.05	0.5	9	-0.1	-4.34	0.5277	0.3218	-39.03	0.4787	-9.29
16	0.20	0.05	0.5	9	-0.25	-0.77	0.2471	0.0545	-77.96	0.3179	22.29
16	0.20	0.05	0.5	9	-0.4	3.15	0.0816	-0.2129	-361.01	0.1572	48.11
16	0.20	0.15	0.125	9	0.4	-4.98	0.1687	0.4129	59.15	0.1559	-7.58
16	0.20	0.15	0.125	9	0.25	-1.50	0.4347	0.4455	2.43	0.3147	-27.60
16	0.20	0.15	0.125	9	0.1	-1.04	0.5927	0.4782	-19.31	0.4736	-20.10
16	0.20	0.15	0.125	9	0	-1.04	0.6092	0.5000	-17.93	0.5795	-4.89
16	0.20	0.15	0.125	9	-0.1	-1.04	0.5662	0.3218	-43.17	0.4736	-16.36
16	0.20	0.15	0.125	9	-0.25	0.57	0.3761	0.0545	-85.52	0.3147	-16.32
16	0.20	0.15	0.125	9	-0.4	4.62	0.0337	-0.2129	-731.58	0.1559	78.38
16	0.20	0.15	0.25	9	0.4	-4.77	0.1714	0.4129	58.49	0.1559	-9.05
16	0.20	0.15	0.25	9	0.25	-1.80	0.4148	0.4455	6.90	0.3147	-24.12
16	0.20	0.15	0.25	9	0.1	-1.62	0.5856	0.4782	-18.34	0.4736	-19.13
16	0.20	0.15	0.25	9	0	-1.62	0.6095	0.5000	-17.97	0.5795	-4.93
16	0.20	0.15	0.25	9	-0.1	-1.62	0.5713	0.3218	-43.68	0.4736	-17.11
16	0.20	0.15	0.25	9	-0.25	0.31	0.2936	0.0545	-81.45	0.3147	6.71
16	0.20	0.15	0.25	9	-0.4	4.20	0.0554	-0.2129	-484.00	0.1559	64.44
16	0.20	0.15	0.5	9	0.4	-4.46	0.1764	0.4129	57.28	0.1559	-11.62
16	0.20	0.15	0.5	9	0.25	-2.55	0.3551	0.4455	20.30	0.3147	-11.37
16	0.20	0.15	0.5	9	0.1	-2.55	0.5312	0.4782	-9.98	0.4736	-10.86
16	0.20	0.15	0.5	9	0	-2.55	0.5367	0.5000	-6.83	0.5795	7.39
16	0.20	0.15	0.5	9	-0.1	-2.47	0.4293	0.3218	-25.04	0.4736	9.35
16	0.20	0.15	0.5	9	-0.25	-0.04	0.2177	0.0545	-74.99	0.3147	30.82
16	0.20	0.15	0.5	9	-0.4	3.53	0.0810	-0.2129	-362.75	0.1559	48.03

3.5 Examples Using Nonlinear Analysis

With the equations for determining the bursting force magnitude and location established, an investigation using a more sophisticated method is conducted. A nonlinear finite element analysis is used as a tool to evaluate the applicability of the design equations. As mentioned in the previous chapter, the best way to conduct a nonlinear finite element analysis for the case in which many parameters are unknown is to use simple assumptions in constitutive modeling. In the following examples, constitutive material properties used are constructed from available information on material properties. Two examples using nonlinear analysis are presented in this chapter. They consist of one beam from Wollmann's research (1992) and a selected example from the PTI Anchorage Zone Design Manual (2000). The first example is chosen for the purpose of investigating the method to model a rectangular post-tensioned beam with a support reaction. The second one is for the comparison of three methods used in the design of anchorage zones with support reaction, which consist of the AASHTO Specifications, the STM method, and the newly developed approach. In an enhancement of the second example, several patterns of reinforcement are used in the model to study the efficiency of steel arrangement methods.

According to the AASHTO Standard Specifications (2002), the method of detailing bursting reinforcement is related to the section width (h) and the location of bursting force (d_{burst}) as previously stated in section 1.3.2. To achieve the most effective arrangement of bursting steel, the method strictly follows the distribution of bursting stresses occurring in the anchorage zone. The steel is to be distributed over the smaller distance of either $2.5d_{burst}$ or $1.5h$ and the position of the centroid of the bursting steel must be at the distance d_{burst} . This results in unequal reinforcement spacing within the anchorage zone. This may require more effort for engineer to arrive at an acceptable arrangement according to the code. Therefore, based on the distribution of the bursting stresses, other possible patterns of bursting reinforcement are investigated using the same model configuration as that for the second example. It is expected to provide a suitable bursting steel arrangement with a less complicated design.

3.5.1 Example Based on Wollmann's Experimental Specimen

3.5.1.1 Problem Illustration

The initial evaluation of the program DIANA proved its efficiency in conducting nonlinear analyses. The reliability of using a nonlinear finite element method now depends on the physical modeling method and constitutive material assumptions. A good practice before conducting a nonlinear analysis is to calibrate the modeling method to available experimental information. As introduced in Chapter 1, the specimens Beam2 and Beam3 in the experimental work conducted by Wollmann (1992) are an appropriate selection. Beam3, which contains a normal weight concrete, is chosen for this example. A picture of the Beam3 specimen used in the experiment is shown in Fig. 1.12. The properties of concrete and reinforcing steel are listed in Table 3.19 along with all other information such as design forces, locations of the forces, and test results.

Table 3.19 EXPERIMENTAL DATA OF Beam3 FROM WOLLMANN'S RESEARCH (1992)

Specimen : Beam3			
Concrete Strength (f_c'), psi :	5100	Duct Diameter, in. :	2 5/8
Reinforcement,		Design Parameters,	
Bar #2:		Live End :	
Yield Strength (f_y), psi :	72000	T_{burst} , kips :	44.4
Area, sq.in. :	0.044	d_{burst} , in. :	12
Bar #3:		Dead End :	
Yield Strength (f_y), psi :	60000	T_{burst} , kips :	50.7
Area, sq.in. :	0.11	d_{burst} , in. :	10.5
Bar #5:			
Yield Strength (f_y), psi :	60000		
Area, sq.in. :	0.31		
		Load Capacity,	
		Live End :	
		F_{pu} , kips :	284
		1st Cracking Load/ F_{pu} :	0.84
		1st Yield Load/ F_{pu} :	1.25
		Ultimate Load/ F_{pu} :	1.34
		Dead End :	
		F_{pu} , kips :	284
		1st Cracking Load/ F_{pu} :	0.99
		1st Yield Load/ F_{pu} :	N/A
		Ultimate Load/ F_{pu} :	N/A

Based on all available information, the model was constructed strictly reproducing all physical dimensions in the real specimen. The boundary condition of the model is an imitation of the bearing plate resting on top of a roller support. The plane stress element CQ16M and bar element as previously described in Chapter 1 were used in the model. Fig. 3.115 shows the finite element model of specimen Beam3. Besides the typical material properties of concrete and steel, special material properties were defined for the confining region of concrete in the local zone. The lateral stress of 1.2 ksi was used for the calculation of confined concrete strength based on Roberts' recommendation. The confined region has

the same dimensions as the steel bearing plate and it extends in the longitudinal direction for a length of 9 in. from the loaded surface. The tensile strength of the concrete was calculated from percent reduction of the whole width of the beam reduced by the duct diameter and multiplied by 10 percent of the compressive strength. The compressive and tensile strength of concrete have a linear relationship following the linear tension cut-off model. Linear tension softening and variable shear retention criteria were applied for the concrete cracking model.

For the steel properties, the Von Mises yield criterion was adopted and two yield strengths, 60 ksi and 72 ksi, were assigned to the corresponding steel bars. All steel plate models have a tensile strength of 60 ksi. The same iteration scheme as used in Chapter 2 was applied. The convergence criterion in this example was modified to increase the speed of computation by using all available convergence criteria including force, displacement, and internal energy for each iteration. As conducted in experimental work, the support reaction on each side of the beam was set to have the magnitude of 10 percent of the prestressing load. The vertical load then had magnitude of 20 percent of the prestressing load. Both prestressing and vertical loads were increased in magnitude in each load step simultaneously.

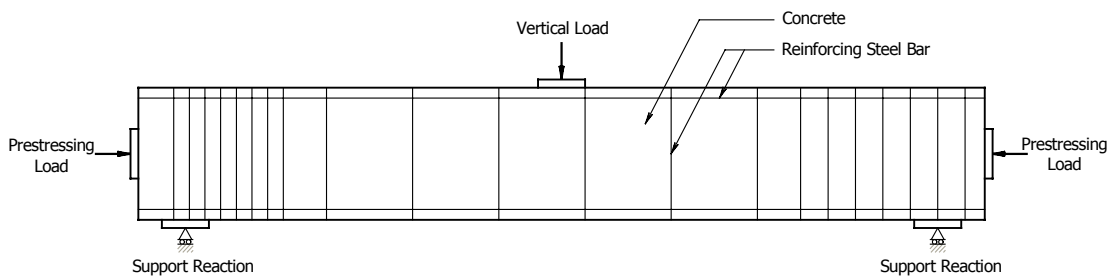


Fig. 3.115 STRUCTURE USED FOR MODELING OF Beam3

3.5.1.2 Nonlinear Analysis Result

Figure 3.116 shows the cracking strain vectors occurring in the finite element model at the ultimate load step. As can be seen, the cracking strains occur in three locations, at the bottom fiber at midspan and at the region near the anchorage zone on both sides of the beam. Based on numerical information, the strains on the live end side have larger magnitudes than those

on the dead end side. In other words, the live end of the beam appears to have larger tensile stresses than the dead end. This is consistent with the experimental result. The pattern of cracks near the anchorage region also coincides with those appearing in the experiment. However, the finite element analysis indicates the first cracking load occurring when the load reaches 0.74 of the prestressing force, which is a lower load than that observed in the experiment. The lower magnitude of the first cracking load could indicate when the cracking initiates inside the beam, which may not be detected visually.

The cracking pattern in the real specimen originated at the center of the anchor plate and propagated diagonally upward toward the location where the cracking strains in the finite element model occur. The finite element model cannot capture the same origin of cracking because of the difference between the finite element model and the real specimen in the local zone. The finite element model uses two-dimensional plane stress elements to model the confined region of concrete, while the real specimen has spiral reinforcement to increase bearing strength in the region. The lateral bulging effect caused by the displacement of the confined concrete cylinder in the direction of the prestressing force resulted in the cracking which was visually detected in the area close to the centerline of the beam.

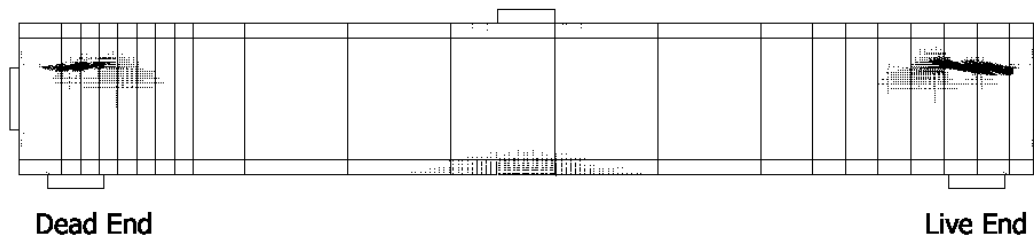


Fig. 3.116 CRACKING STRAIN VECTORS ON FINITE ELEMENT MODEL OF Beam3

Figures 3.117 and 3.118 show the vertical bar strains from the experimental and finite element analysis, respectively. Each point represents a strain gauge reading or a maximum bar strain from the finite element analysis. The plots are similar to each other. Because the analysis was terminated at a magnitude of prestressing load equal to 321 kips, which is close to the magnitude of 344 kips of the experimental plots, only two steps of the load can be used

for the comparison. However, the plots of these two load steps from the finite element result indicate the same trend of strain behavior as those occurring in the experiment.

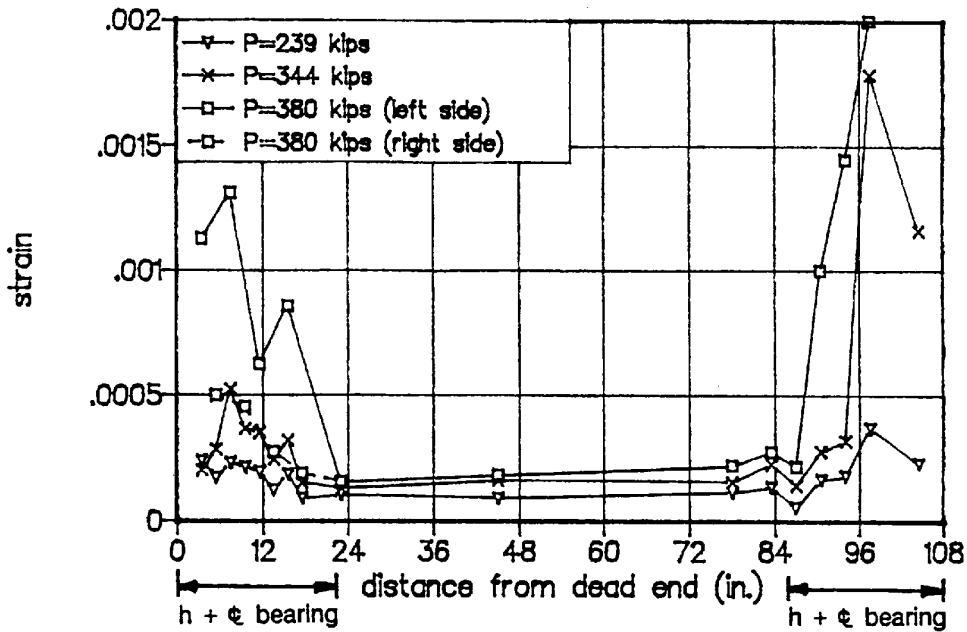


Fig. 3.117 VERTICAL BAR STRAINS IN SPECIMEN Beam3 FROM WOLLMAN'S STUDY (1992)

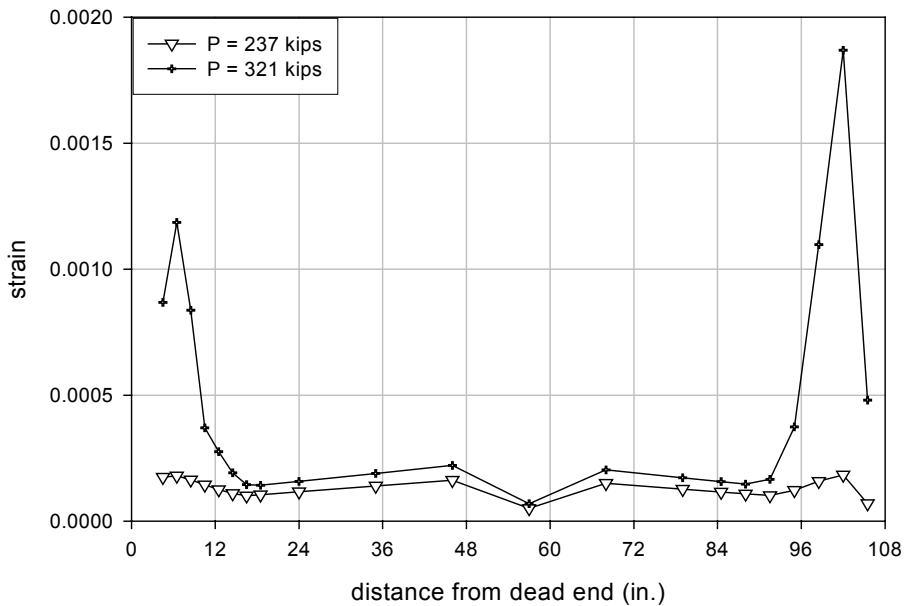


Fig. 3.118 VERTICAL BAR STRAINS IN SPECIMEN Beam3 FROM NONLINEAR ANALYSIS

3.5.2 Example Based on Precast Beam with Multi-Strand Tendon in PTI Manual

The following example illustrates the design of an anchorage zone with a support reaction using two recommended methodologies presented in the AASHTO Standard Specifications and one method from the newly developed expressions. The anchorage zone of the present example was modified from the example presented in section 6.5 in the PTI Anchorage Zone Design Manual (Wollmann et al., 2000). The two methodologies presented in the AASHTO Specifications are the approximate equations and the Strut-and-Tie Model (STM) method. For the STM method, a modified version of the method based on the present study is applied. The new approximate expressions, equations (3.8) and (3.7), are used for the design of the anchorage zone, and the result is compared to those using the existing methods. After the comparison is presented, several reinforcing steel arrangements are investigated to evaluate their efficiency

3.5.2.1 Problem Illustration

Figure 3.119 presents the details of the anchorage zone with a support reaction used for the present example. Fig. 3.119a shows the dimensions of the model, which were taken from the example in section 6.5 of the PTI manual with the modification of adding a support reaction at the bottom surface. The support reaction (R) has a magnitude of 5 percent of the prestressing load and it is applied to the anchorage zone at the position of 9 in. longitudinally from the centroid of the anchor plate (see Fig. 3.119a). The bearing plate size was chosen to have the same dimensions as those of the anchor plate. Fig. 3.119b presents the simplified model used in the nonlinear analysis. As can be seen, the inclined surface was replaced by a vertical surface. The inclined load was divided into vertical and horizontal components. The prestressing force is applied with a magnitude of 376 kips as indicated in Fig. 3.119a. The compressive strength of concrete is as shown in the figure.

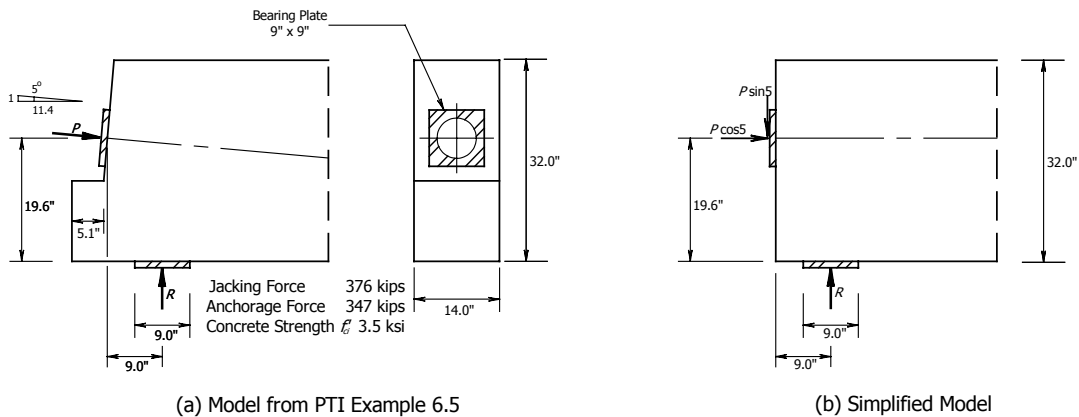


Fig. 3.119 TYPICAL DIMENSIONS OF THE MODEL

3.5.2.2 Design of the Bursting Reinforcement

Three design approaches for anchorage zones with support reactions are presented in the following subsections. The calculation of bursting force and location of bursting steel are illustrated step-by-step. The reinforcement arrangement is also shown.

3.5.2.2.1 Design Using Approximate Equations Presented in the AASHTO

Since the example is investigated using a two-dimensional finite element model, this example presents the design of the bursting steel only in one direction, which is parallel to the section width (h) and the bursting force in thin direction is ignored. In this subsection, the design using the equations (1.5) and (1.6) to calculate the bursting force and the location of the bursting steel is presented.

The anchorage zone of this example has an eccentricity e equal to $(19.6 - 32/2) = 3.6$ in. Based on the symmetric prism, the width of the prism can be calculated as $(h - 2e) = (32 - 2(3.6)) = 24.8$ in. Therefore, the bursting force can be calculated using equation (1.5) as

$$T_{burst} = P/4 \times (1 - a/(h - 2e)) + P/2 \times \sin \alpha = 376/4 \times (1 - 9/24.8) + 376/2 \times \sin 5$$

Therefore, $T_{burst} = 76.3$ kips.

Since the prestressing load points toward the centerline of the anchorage zone, the e value used in equation (1.6) is positive and the location of the bursting force can be determined as

$$d_{burst} = \frac{1}{2} \times (h - 2e) + 5e \sin \alpha = \frac{1}{2} \times 24.8 + 5(3.6) \sin 5$$

Therefore, $d_{burst} = 13.97$ in., use 14 in.

After calculating T_{burst} and d_{burst} , the amount of reinforcing steel and the pattern of its arrangement can be determined. The yield strength of reinforcing steel is 60 ksi, which is typical for a regular steel bar. AASHTO requires that a load factor of 1.2 be used on the jacking force and a strength reduction factor of 0.85 be used for anchorage zones. Therefore, the steel area A_s is

$$A_s = (T_{burst} \times 1.2)/(0.85 \times f_y) = (76.3 \times 1.2)/(0.85 \times 60) = 1.80 \text{ sq.in.}$$

The reinforcing steel, according to the AASHTO Specifications, must be distributed over a length equal to the smaller of $2.5d_{burst} = 2.5(14) = 35$ in. and $1.5h = 1.5(32) = 48$ in. Therefore, the steel will be distributed over 35 in. from the anchor surface with its centroid located at d_{burst} . The reinforcement can be three stirrups of No. 4 bar and four stirrups of No. 3 bar with a spacing of 3.5 in. and 7 in., respectively. The total area of steel is 2.08 sq.in. As for the spalling reinforcement, 2 percent of the prestressing load is used for spalling force (T_{spall}). Therefore, the required spalling reinforcement can be calculated as

$$A_s = (T_{spall} \times 1.2)/(0.85 \times f_y) = (0.02 \times 76.3 \times 1.2)/(0.85 \times 60) = 0.04 \text{ sq.in.}$$

This can be provided by using one stirrup of No. 3 bar at 1.5 in. from the loading surface. Fig. 3.120 shows the picture of the model with reinforcement. As shown in the figure, the centroid of the reinforcing bars is located at 14.4 in. from the anchor surface.

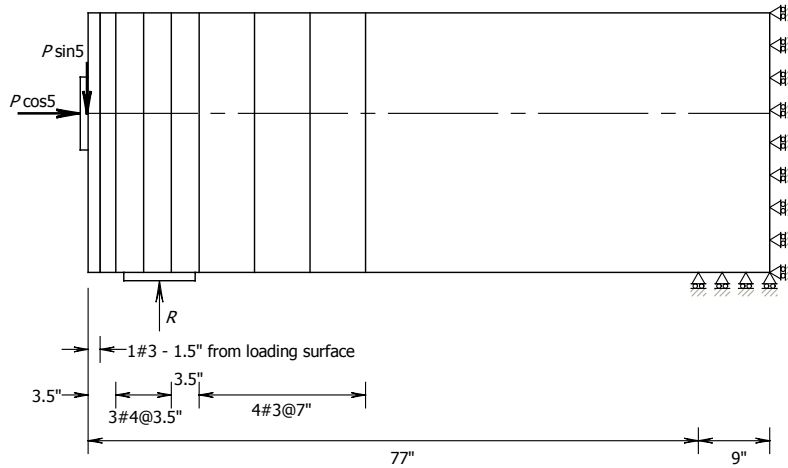


Fig. 3.120 MODEL FROM THE APPROXIMATE EQUATIONS

3.5.2.2.2 Design Using Strut-and-Tie Model Method

This subsection shows the design of the anchorage zone of the example using the STM method with a modification to the methodology based on the findings of this research. As has been shown in Fig. 1.13, the difference between a strut-and-tie model without and with a support reaction is the presence of a strut member from the application point of the reaction force vertically to the main compressive strut line (see Fig. 3.121a). This results in the deviation of the main compressive strut upward in the direction of the resultant vector. However, the angle of the main compressive strut is limited by the boundaries of the anchorage zone. The angle β (see Fig. 3.121) can be determined using equations (3.1) and (3.2). Because the alignment of the main compressive strut is quite important in the estimation of T_{burst} and d_{burst} , the methodology of anchorage zone design should be based on this alignment. In the STM method, the force path selected within the anchorage zone is significant to the determination of the bursting force. Based on the findings of the current study for anchorage zones with support reactions, a modification of the STM method is in order to arrive at an improved anchorage zone design.

Figure 3.121 shows a typical strut-and-tie model for an anchorage zone with a support reaction. Based on the main compressive strut line, the forces at the end of the anchorage zone are calculated by dividing the resultant stresses at the end region into sections. The normal forces at the end can be determined based on the geometry of the stress blocks as presented in Appendix A. The shear force can also be found using a shear stress diagram based on basic theory of elasticity (see Fig. 3.121b). The alignment of each divided strut is determined by the angle of the resultant vector of the forces. The position of the tie is also an important part of the strut-and-tie model. The magnitude of the bursting force depends on the location of the tie. With an appropriate location, the strut-and-tie model will lead to a reasonable amount of bursting steel.

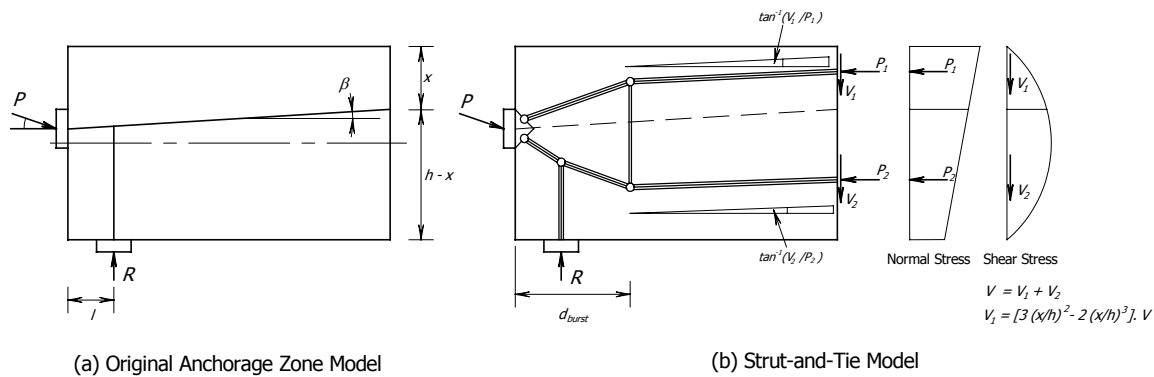


Fig. 3.121 STRUT-AND-TIE MODEL WITH A SUPPORT REACTION

The type of node used for the local zone affects the configuration of the strut-and-tie model. Fig. 3.122 shows two different typically used local zone node types for strut-and-tie models. In Fig. 3.122a, a hydrostatic node represents the condition of a node in which all applied stresses are normal to their corresponding surface of the node. The magnitudes of the stresses on each face are equal ($f_b = f_c$). The node results in smaller dimensions than those of the other node type. The depth of the node is adjustable as long as the strut-and-tie model remains in equilibrium. A non-hydrostatic node (see Fig. 3.122b), on the other hand, produces unequal stresses on all surfaces of the node. It is applicable for the case in which the node is designed to have a large depth relative to the anchorage dimension. The dispersion angle between a strut and the centerline of the node can be arbitrarily located based on equilibrium of the forces.

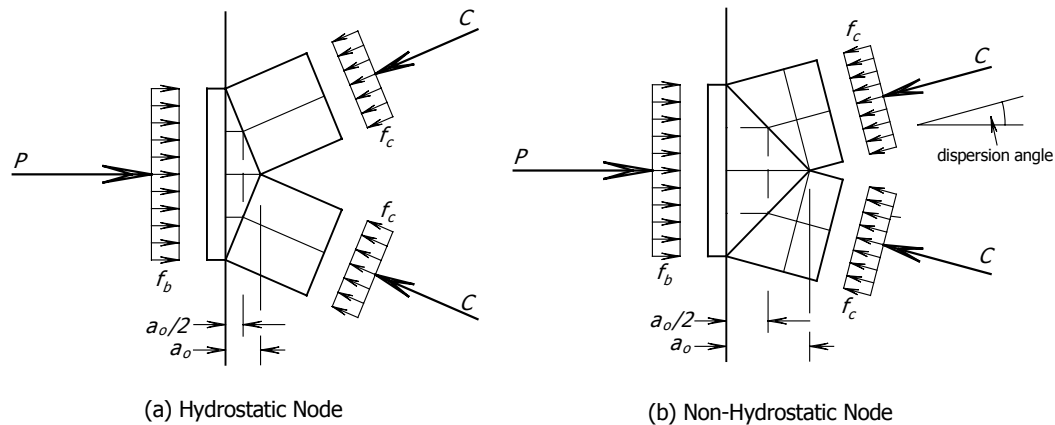


Fig. 3.122 LOCAL NODE IN STRUT-AND-TIE MODEL

A local zone node with fan-shaped struts is shown in Fig. 3.123. The unique characteristic of a fan-shaped strut is that it increases in width along the length of the strut. This characteristic becomes useful in the case in which a uniform-shaped strut is not applicable for the examination of compressive stress. Since the present research mainly focuses on the behavior of the general zone, it is assumed that the confined region of the local zone has enough capacity to withstand the bearing stress ahead of the anchor plate. The investigation of stress is mostly related to the general zone such as the local zone-general zone interface as presented in section 1.3.2.1. The design illustration for the anchorage zone of this example is given as follows, and additional guidance for anchorage zone design using the new STM method is presented in Chapter 5.

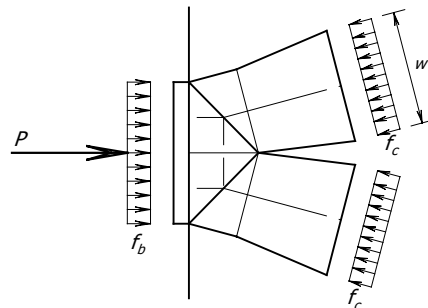


Fig. 3.123 LOCAL NODE AND FAN-SHAPED STRUTS

Generally in the STM method, the first task is to establish the external forces of the structure. For anchorage zone design, the considered length of the model and the position of boundary support reactions should be selected reasonably. Based on the present study, the length of the anchorage zone should be taken as $1.5h$ from the center of the bearing support plate. At the end section of the anchorage zone, which is labeled as a considered section in Fig. 3.9, the normal and shear stress diagram can be determined. Since the present study suggested that the maximum bursting force occurs on the main compressive strut of the anchorage zone, the alignment of the strut becomes significant for the magnitude of bursting force. Therefore, a strut-and-tie model configuration should be based on the main compressive strut alignment. The design of an anchorage zone using the STM method presented herein is based on the factored load design. The factored load used in the STM design is 452 kips, which is determined from the unfactored jacking load multiplied by 1.2. By using equations (3.1), (3.2) and those presented in Appendix A, the alignment of the main compressive strut can be determined as follows:

$$\begin{aligned}\sigma_t &= -\frac{P_u}{A} - \frac{R_u \times 1.5h + P_u \cos \alpha \times e - P_u \sin \alpha \times (l + 1.5h)}{th^2 / 6} \\ &= -\frac{(452) \cos 5}{14 \times 32} - \frac{0.05(452) \times 1.5(32) + (452) \cos 5 \times 3.6 - (452) \sin 5 \times (9 + 1.5(32))}{14 \times 32^2 / 6} \\ &= -1.198 \text{ ksi}\end{aligned}$$

$$\begin{aligned}\sigma_b &= -\frac{P_u}{A} + \frac{R_u \times 1.5h + P_u \cos \alpha \times e - P_u \sin \alpha \times (l + 1.5h)}{th^2 / 6} \\ &= -\frac{(452) \cos 5}{14 \times 32} + \frac{0.05(452) \times 1.5(32) + (452) \cos 5 \times 3.6 - (452) \sin 5 \times (9 + 1.5(32))}{14 \times 32^2 / 6} \\ &= -0.812 \text{ ksi}\end{aligned}$$

Since $s_1 = |\sigma_t|$ and $s_2 = |\sigma_b|$, the location of the centroid of the compressive stresses at the considered section can be determined using equation (A.2a) in Appendix A as shown below:

$$h_c = \left[\frac{2s_1 + s_2}{3(s_1 + s_2)} \right] h = \left[\frac{2(1.1977) + (0.8124)}{3(1.1977 + 0.8124)} \right] \times 32$$

$$= 17.02 \text{ in. (use 17 in.) from the bottom}$$

Therefore, the angle β of the main compressive strut can be determined as

$$\beta = \arctan\left[\frac{h_c - h/2 - e}{l + 1.5h}\right] = \tan^{-1}\left[\frac{17 - 16 - 3.6}{9 + 48}\right] = -2.61 \text{ degrees.}$$

Since the position of the centroid of the compressive stress at the considered section was set, the normal compressive and shear stresses can be divided into two forces at the end of the section. The normal compressive forces are also calculated using basic geometry and the equation presented in Appendix A. For the shear forces, the magnitudes can be calculated using an expression presented in Fig. 3.121. The total shear force (V) at the end section of the model is equal to $P \sin 5 - 0.05P = 16.8$ kips. All external forces of the anchorage zone are established as shown in Fig. 3.124.

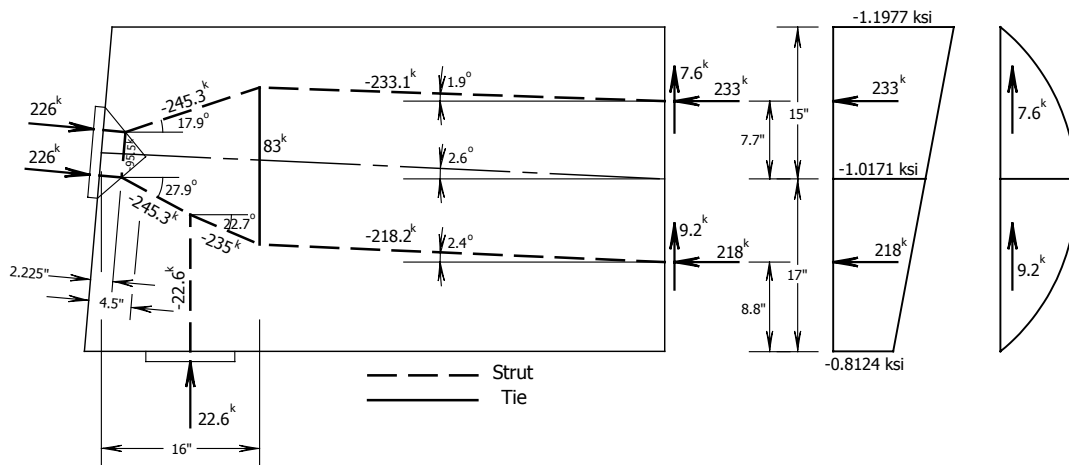


Fig. 3.124 FORCES IN STRUT-AND-TIE MODEL

The next step is to create the members within the anchorage zone body. All external forces are significant in determining the alignment of each strut. The resultant forces at the end section indicate the inclination angles of the struts from the end section toward the loading surface. Since the anchorage zone has an inclined loading surface, the local zone is located normal to the surface. The location of the tie is also established in this step. Based on the present research, the maximum bursting force is located at the distance of d_{burst} from the center of the anchor plate. Therefore, it is also chosen as the location of the tie in the present strut-and-tie model. Equation (3.7) is used to calculate d_{burst} as shown below:

$$\begin{aligned}
 d_{burst} &= 0.5 (h-2e) + 0.25 a + 0.25 (h-2e) \sin \alpha + \frac{R}{P} (h-2e) (1.5-10 \sin \alpha) \\
 &= 0.5(24.8) + 0.25(9) + 0.25(24.8) \times \sin 5 + 0.05(24.8)(1.5-10 \times \sin 5) \\
 &= 15.97 \text{ in. (use 16 in.)}
 \end{aligned}$$

A strut is connected from the bearing plate center to an arbitrary location vertically above the position of the bearing plate. This strut represents a compressive force resulting from the application of the reaction force. By using a non-hydrostatic local zone node with the depth equal to half the anchor plate width ($a/2$), the structure of the strut-and-tie model can be completed by connecting the nodes and determining all member forces using analytical or graphical methods. After all the forces are calculated, the tensile force in the tie, which is the bursting force, is known and the required cross-sectional area of steel can be determined. Fig. 3.124 shows the member forces in all struts and the tie in the structure.

The last step of the STM method is to examine the compression capacity of struts in the unconfined concrete region by using a limitation on design compressive strength of $\phi 0.7 f'_c$. The local zone-general zone interface is one of the most critical sections of the strut-and-tie model of the anchorage zone. Other critical sections are also investigated based on the designer's judgment. Since a uniform-shaped strut cannot provide a satisfactory condition for the model, a fan-shaped strut is used for the examination of the compression capacity of the concrete.

Figure 3.125 shows the strut-and-tie model with fan-shaped struts. The struts EF, HI, and IJ have the most critical sections since each member has a high magnitude of the force with a small section width. Note from Fig. 3.125 that the node I contains three compressive forces joining one another. The compressive stress can be checked on three different surfaces based on the direction perpendicular to the corresponding force. It is obvious that the most critical section occurs on the surface normal to strut HI. The width of the section is considered to be twice the distance in the direction normal to the member force from the intersection between the extreme fiber of the strut and the base of the local zone region to the centerline of the same strut (lines LM and NO in Fig. 3.125). The determination of the stress magnitude on LM and NO are as shown below:

$$f_{LM} = f_{NO} = (245.3)/(14 \times 9.26) = 1.89 \text{ ksi.}$$

The design compressive strength of concrete is equal to $0.7\phi f'_c = 0.7 \times 0.85 \times 3.5 = 2.08 \text{ ksi}$, which is larger than f_{LM} . Therefore, the strut-and-tie model has sufficient compressive strength.

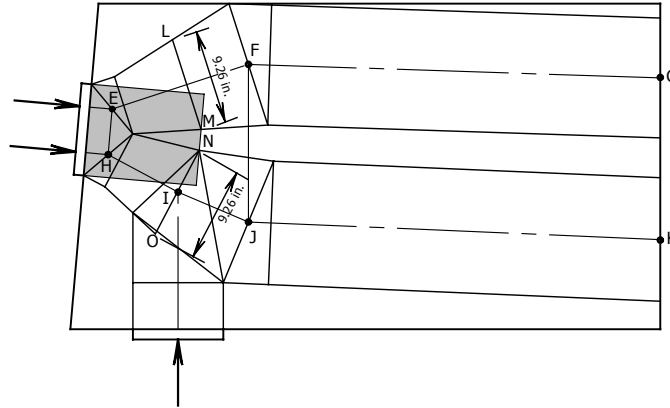


Fig. 3.125 STRUT-AND-TIE MODEL WITH FAN-SHAPED STRUTS

Since the bursting force from the strut-and-tie model has a magnitude of 83 kips (see Fig. 3.124), the required cross-sectional area of steel becomes $83/(0.85 \times 60) = 1.63 \text{ sq.in.}$ This can be reinforced by using eight stirrups of No. 3 bar, which provides a total area of steel equal to 1.76 sq.in. The reinforcement arrangement follows the requirements of the AASHTO Specifications. Therefore, the arrangement of the reinforcing steel is shown in Fig. 3.126. The centroid of the reinforcement is located at 15.9 in. from the loaded surface, which is close to the calculated d_{burst} . The spalling reinforcement is also determined based on 2 percent of the prestressing force. Except for the amount of reinforcing steel, all other aspects of the nonlinear finite model are identical to those used in the previous design.

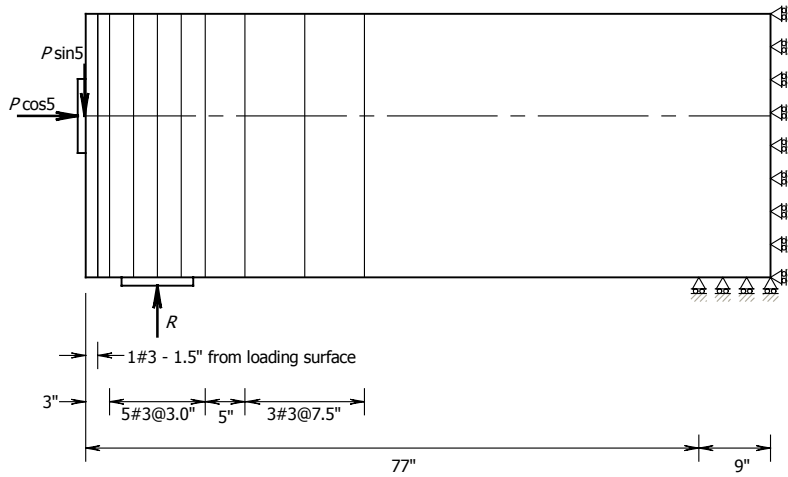


Fig. 3.126 MODEL FROM THE STM METHOD AND NEW APPROXIMATE EQUATIONS

3.5.2.2.3 Design Using New Approximate Equations

The following illustration shows the design of an anchorage zone with a support reaction using the new approximate equations for bursting force (T_{burst}) and location of bursting steel (d_{burst}) presented in equations (3.8) and (3.7), respectively. Since the calculation for d_{burst} has already been shown in the previous subsection, only the magnitude of T_{burst} needs to be determined. From equation (3.8), the bursting force can be found as follows:

$$\begin{aligned}
 T_{burst} &= 0.25 P \left(1 - \frac{a}{h - 2e}\right) + 0.4 P \sin \alpha + R (0.25 - 5 \sin \alpha), \text{ not less than } 0.125 P \\
 &= 0.25(376) \left(1 - \frac{9}{24.8}\right) + 0.4(376) \times \sin 5 + 0.05(376)(0.25 - 5 \times \sin 5) \\
 &= 69.5 \text{ kips, greater than } 0.125(376) = 47 \text{ kips}
 \end{aligned}$$

After being multiplied by a factor of 1.2, the magnitude of T_{burst} becomes 83.4 kips, which is very close to the T_{burst} determined using the STM method. Since both T_{burst} and d_{burst} values from both design methods are almost identical, the amount of bursting steel required and its arrangement from the former case can be applied to the design of this subsection.

3.5.2.3 Nonlinear Analysis Result

After all information required for a nonlinear finite element analysis is determined, the constitutive material properties are created. The confined concrete region is designed to have a width equal to the anchor plate and to extend for a length of 13 in. from the loaded surface. The compressive strength of confined concrete is determined using the expression suggested by Foster et al. (1996) as presented in equation (1.27). The tensile strength of concrete is chosen by applying a reduction factor of 10 percent of the compressive strength of the concrete. Therefore, the tensile strength used in the present example becomes 262.5 psi, which is about 7.5 percent of 3500 psi. The cracking property is assigned similarly to that in the former example. It consists of linear tension cut-off, linear tension softening, and variable shear retention. The steel property uses the same criterion as that in the former example as well. The yield strength of all steel elements is 60 ksi. The same iteration scheme and convergence criterion are applied.

Based on the nonlinear analyses, the first model (model 1) based on the AASHTO approximate equations resulted in a lower ultimate load than that of the second model based on the STM method and the new approach (model 2). The factor at ultimate load of model 1 is 2.47, while model 2 attained 2.54. The factor is the ultimate load divided by the jacking load of 376 kips. With a smaller amount of reinforcement, model 2 provides a higher load capacity than the first model. This might be caused by the pattern of reinforcement, which is different between these models. Model 2 has a narrower spacing of the reinforcement close to the loaded surface (within d_{burst}), but the bursting steel extends further than the first one. This indicates the significance of the reinforcement pattern. Additionally, it has been proven that, with the smaller amount of bursting steel, the structure can also produce a strength capacity as high as one with more reinforcement.

Figures 3.127 and 3.128 show the cracking strain vectors occurring in the two models at the ultimate load step. As can be seen, the cracking region propagates in the downward direction, which corresponds with the direction of main compressive strut. The cracks occur within the space between two bars and extend beyond the last bar. Since the ultimate factor is much higher than the factor of 1.2 used for general ultimate strength design, the

propagation of the cracks beyond the steel region is caused by a much greater load magnitude. Since the region ahead of the anchor plate is fully reinforced by 60 percent of the required amount of bursting steel, the tensile stresses occurring in this region are affected by the presence of steel. The strength of the structure increases due to the appropriate resistance provided. Cracks try to propagate into the weaker region and cause the cracking to extend beyond the reinforced area while the structure is not severely damaged. As can be noticed, the extended arrangement of the reinforcement with the length of $1.5d_{burst}$ from the centroid of bursting force is not as effective as had been expected. On the other hand, the closely spaced reinforcement in the region near the anchor plate seems to provide more strength to the structure.

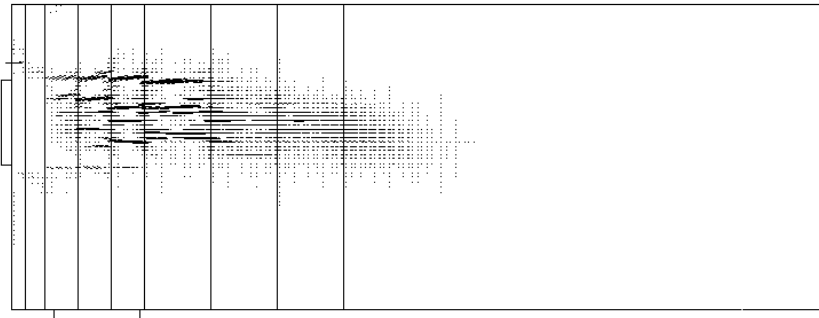


Fig. 3.127 CRACKING STRAIN VECTORS ON FINITE ELEMENT MODEL BASED ON APPROXIMATE EQUATIONS (MODEL 1)

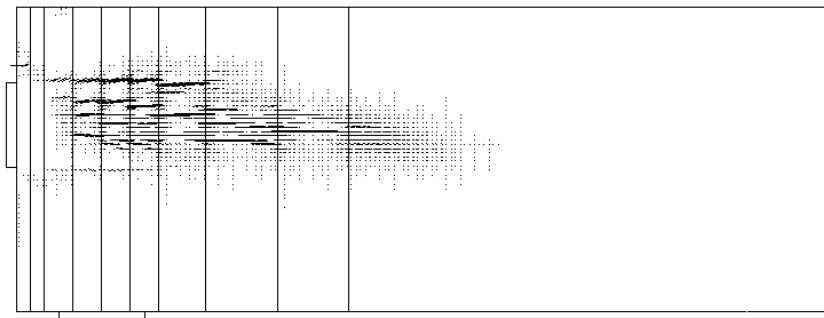


Fig. 3.128 CRACKING STRAIN VECTORS ON FINITE ELEMENT MODEL BASED ON STM AND NEW APPROACH (MODEL 2)

Figure 3.129 shows a comparison between tensile strains in reinforcing bars of the two models. Two different load steps are selected in the figure consisting of the ultimate and 1.2 times the jacking load, 452 kips. As can be seen, the strain plots at the factored load of 452 kips for both models have a similar magnitude. At ultimate load, model 1 has two bars yielded at the distance of 21 and 28 in. while model 2 has three steel bars yielded at the locations of 12, 15, and 20 in. The peaks of each strain plot occur at the first bar when the spacing between bars becomes larger. The first three bars in model 1 have a larger diameter, which may increase the stiffness within the region. However, the location of the yielded bars indicates the position at which the cracks are severely developed, which is caused by the large spacing of the steel bars. Using uniformly spaced reinforcing steel may result in a more uniform distribution of tensile stresses over the reinforced region.

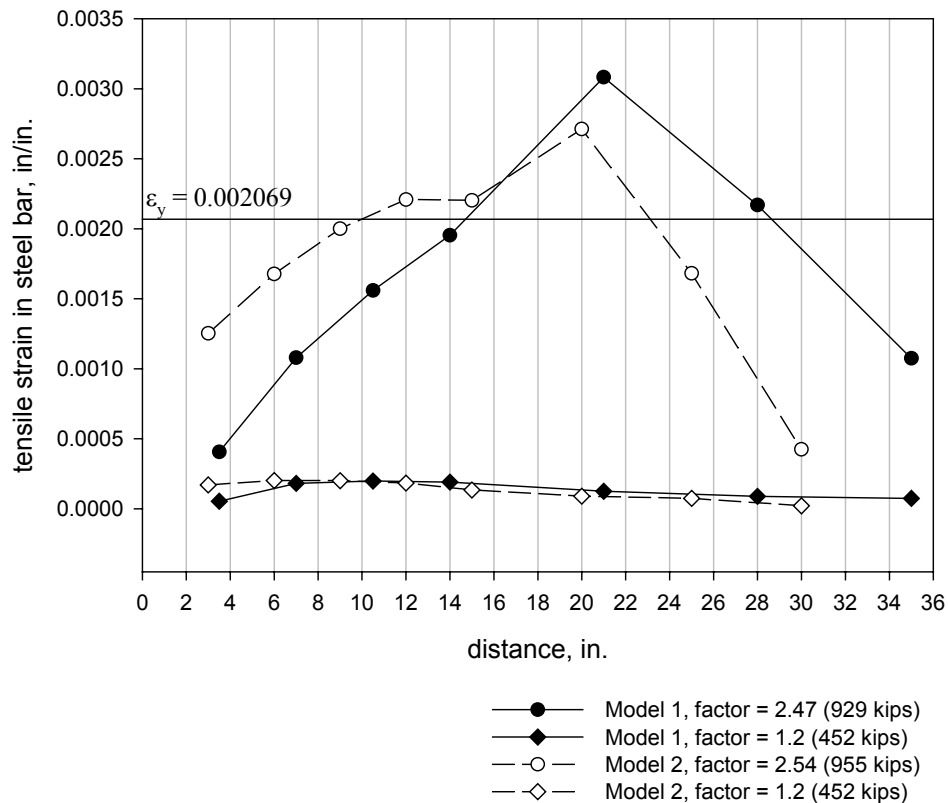


Fig. 3.129 TENSILE STRAIN IN BURSTING STEEL BARS OF MODEL 1 AND 2

3.5.2.4 Nonlinear Analysis to Investigate the Reinforcement Arrangement

To find an effective reinforcement arrangement which is less complicated than current methods, two additional models were created based on the present example. Two different reinforcement patterns were designed for the investigation of the effectiveness of reinforcement pattern. Based on the results from the previous subsection, a uniformly distributed pattern is used for the new arrangement of bursting steel. The two models are called model 3 and model 4 in this subsection. Model 3 contains reinforcing steel uniformly distributed over the distance of $2.5d_{burst}$. Based on the amount of bursting steel used in model 2, eight stirrups of No. 3 bar are distributed with a spacing of 5 in. The first bursting bar of model 3 is located at 5 in. from the loaded surface. Model 4 has its bursting steel uniformly distributed over the distance of $2d_{burst}$. Therefore, the spacing between each bar of model 4 becomes 4 in. and the first bar starts at 4 in. from the loaded surface. The centroid of the bursting steel in models 3 and 4 are positioned at 22.5 in. and 18 in. from the loaded surface, respectively. Fig. 3.130 shows the reinforcement patterns of both models.

After the nonlinear analyses were conducted, the tensile strains in the bursting bars were plotted similarly to those in Fig. 3.129. Fig. 3.131 shows the plots from models 3 and 4. As can be seen, the ultimate load of model 3 has the magnitude of 887 kips (a factor of 2.36), which is lower than those of models 1 and 2, while in model 4 the capacity of the load reaches 1008 kips (a factor of 2.68). It can be concluded that the reinforcement pattern with a larger spacing covering the region in which the bursting stresses occur ($2.5d_{burst}$) is not an effective arrangement. Based on the plot at the ultimate load of model 3, only two bars yield at the locations of 10 and 15 in. In model 4, the narrow spacing results in the higher strength of the anchorage zone. Three bursting bars yield at the locations of 8, 12, and 16 in. with a higher strain value compared to those of model 3. For a load factor equal to 1.2, both models have a similar magnitude of strain. Fig. 3.132 shows the cracking strain vectors for both models. The region close to the anchor plate contains a high density of cracking strain vectors while the cracks still propagate beyond the reinforced region of the anchorage zone. The difference between the models is that the model with a denser arrangement of reinforcing steel retains more strength after the cracks occur.

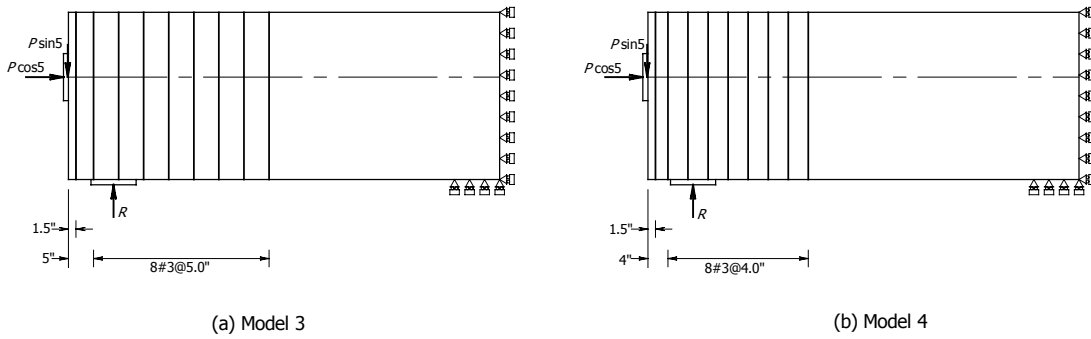


Fig. 3.130 MODELS FOR THE STUDY OF REINFORCEMENT ARRANGEMENT

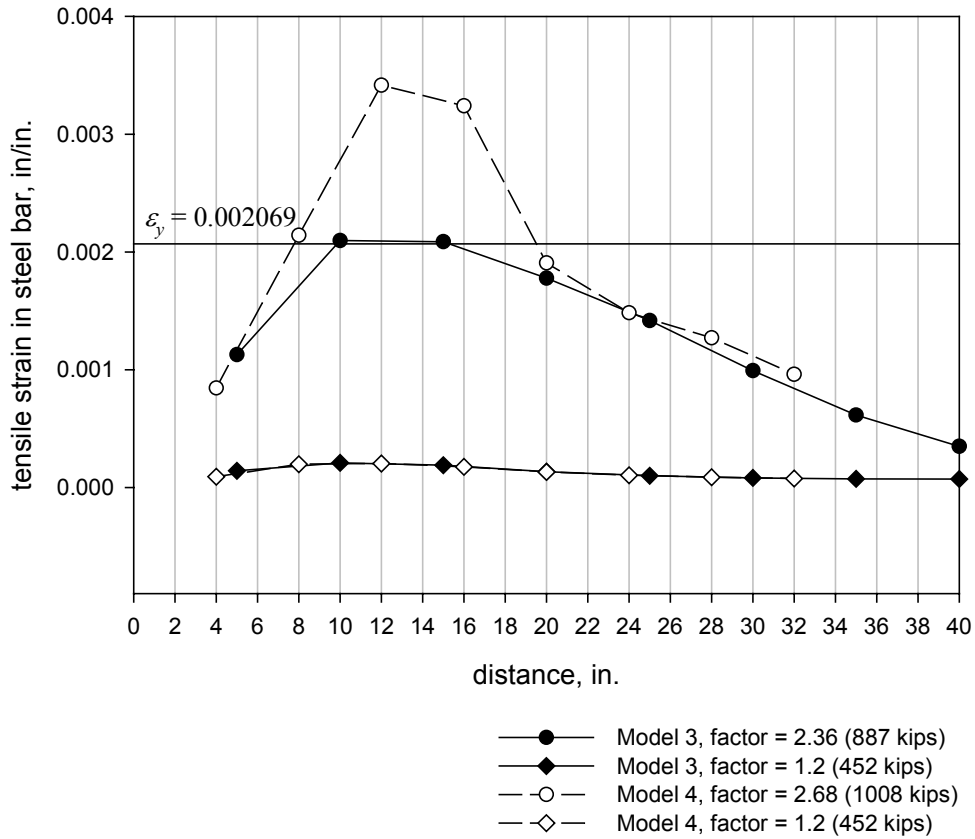


Fig. 3.131 TENSILE STRAIN IN BURSTING STEEL BARS OF MODELS 3 AND 4

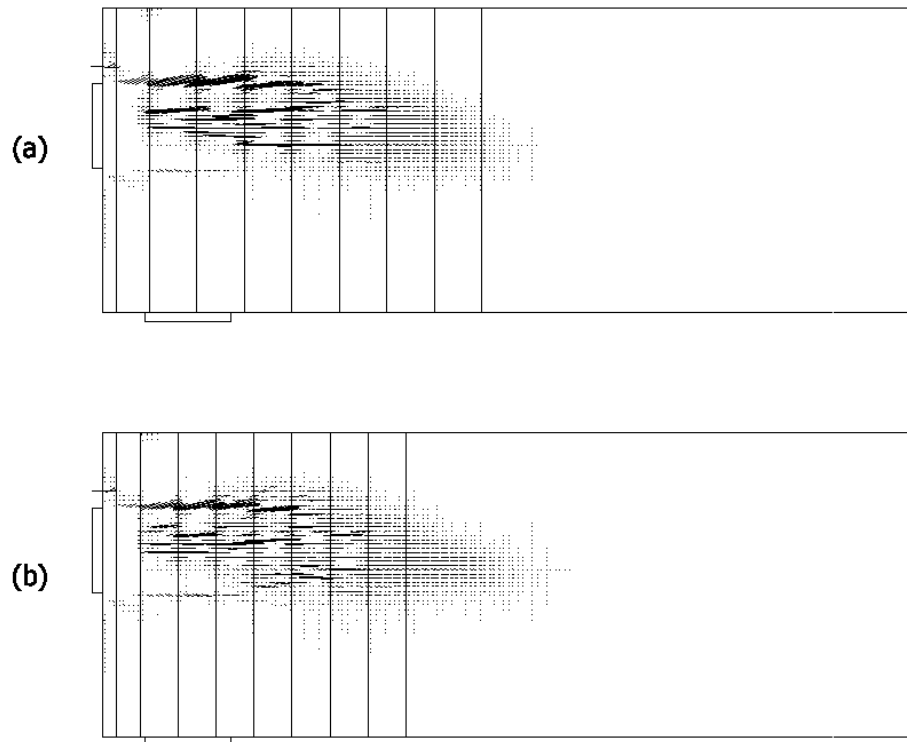


Fig. 3.132 CRACKING STRAIN VECTORS ON a) MODEL 3 AND b) MODEL 4

3.5.3 Summary

It was clearly illustrated that the arrangement of reinforcing steel in model 4 provides the most effective result. The uniform spacing of reinforcing steel is found to give a better resistance to the bursting force than bars with variable spacing. The strength of the anchorage zone with a support reaction is obviously improved when the reinforcement is distributed over the distance of $2d_{burst}$. In addition to the increased capacity that is achieved from using this arrangement, a more convenient method is also introduced. It is inconvenient to have to manipulate an amount of steel to fit into a specific distance with a non-uniform spacing or variable bar sizes in order to have the centroid placed over a required position. Distributed steel with both uniform spacing and cross-sectional area is a far more convenient detail. Therefore, the detail using uniform bursting steel in the anchorage zone design is recommended.

3.6 Discussions and Recommendations

As presented in this chapter, the study of rectangular sections in post-tensioned girder with a support reaction has been performed. A new approach has been established based on the results of the study. An improved design methodology has been presented. Examples were given for the verification of the revised methods of the design and specified reinforcement detailing has been investigated. The design guidelines are expected to give a more reasonable and economical result in the design of anchorage zone with support reaction with a more convenient reinforcement arrangement. The following subsections discuss the results from the study by categorizing into two major topics: the design of bursting reinforcement and its arrangement.

3.6.1 Design Recommendations

Four load configurations of rectangular sections in post-tensioned girders with a support reaction have been investigated. The presentation began with the study of concentrically loaded anchorage zones and continued to the most complex configuration, which is an inclined eccentrically loaded anchor. As has been illustrated, the results from finite element analysis indicated the necessity of modifying the design methods presented in the AASHTO Standard Specifications 2002 to achieve a conservative design. Furthermore, some parts of the present design guidelines were found to provide an excessive conservatism in the result, which is suspected to possibly cause problems of poor concrete consolidation due to the large amount of reinforcing steel required by the design. The improved methods were created to overcome this problem.

New formulations to determine the bursting force magnitude and location were proposed in equations (3.8) and (3.7), respectively. The bursting force estimated using equation (3.8) provides a reasonable level of conservatism, and the equation was developed to cover all possible load configurations that can occur in an anchorage zone in post-tensioned girders. Equation (3.7), used to determine the location of bursting force, was formulated to be a close approximation of the result from finite element analysis. Based on the design examples, the equations provide similar results to those of the new STM method. The STM method was

also developed based on the information given in the present study. Both newly found approximate equations and the STM approach are proven to provide a better design for anchorage zones with a presence of support reaction and should be adopted as new methodologies for a general anchorage zone design.

3.6.2 Detailing Recommendations

Based on the examples using nonlinear analysis, the most effective reinforcement arrangement was determined. The best pattern of reinforcement is a uniform distribution of bursting steel over a distance equal to twice d_{burst} from the prestressing surface. This was proven to be more effective in terms of the strength of the anchorage zone and it also reduces the effort required to detail the bursting steel. The new bursting steel arrangement can be used with both the approximate equations and the STM method proposed in this study. This arrangement is effective even if the location of d_{burst} is not accurately determined because the steel is distributed over twice the length of d_{burst} and it was designed to result in an efficient distribution of the tensile stresses within the reinforced region. It was confirmed from the illustrated example that the arrangement can withstand the prestressing load well past the conventional factored load used in the design of prestressed concrete structures. However, further investigation, such as experimental research, is recommended.

CHAPTER 4

NON-RECTANGULAR SECTIONS

4.1 Introduction

In typical concrete structures, rectangular sections are considered the most basic geometry which can be easily designed and constructed by a civil engineer. Commonly in the study of reinforced and prestressed concrete structures, a rectangular shape is the first configuration to be mastered. It exhibits the least complicated behavior, which can be easily described due to the small number of geometric parameters compared to other shapes such as a flanged section. In reality, structures in civil engineering construction do not contain only rectangular sections. In the construction of a prestressed concrete girder bridge, a deck is placed on top of a series of prestressed girders. Generally the girder cross-section is a non-rectangular shape (see Fig. 4.1), which consists of a web and two flanges. Another example is a post-tensioned box girder; the central section of the box girder can be considered to be a flanged section as shown in Fig. 4.1b. The design methods for a basic rectangular section are sometimes applied in design by simply considering the section to be made of individual rectangular sections. However, this may lead to an unrealistic design since several parameters which are related in a flanged section are ignored.

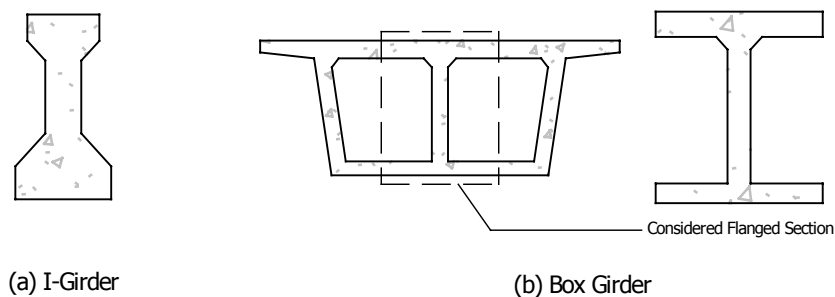


Fig. 4.1 FLANGED SECTIONS IN PRESTRESSED CONCRETE STRUCTURES

Flanged sections can be categorized into three major types: symmetrical I-section, T-section, and unsymmetrical I-section. Symmetrical I-sections are a doubly symmetric shape

with respect to the vertical and horizontal axes of the section, while an unsymmetrical I-section is only symmetric with respect to the vertical axis due to unequal sizes of the top and bottom flanges. The presence of the flange leads to the question of whether the behavior of the bursting stresses within an anchorage zone is changed compared to that which occurs in a rectangular section. Since the design of anchorage zones for flanged sections is not currently addressed in any code provisions, an investigation of flanged sections is important. In this chapter, an investigation of anchorage zones for flanged sections is described.

4.1.1 Objectives

The main objectives of this chapter are as follows:

1. To investigate the behavior of anchorage zones of non-rectangular post-tensioned girders under various load configurations consisting of concentric, eccentric, inclined concentric, and inclined eccentric.
2. To examine the influences of the presence of a flange by investigating several flange parameters.
3. To develop a method for anchorage zone design for post-tensioned girders with three types of non-rectangular sections, including symmetrical I-section, T-section, and unsymmetrical I-section, subjected to basic load configurations and investigate the applicability of the method to the design of more complex load configurations.
4. To investigate reinforcement detailing for anchorage zones in non-rectangular sections.

4.1.2 Scope

Since the design of anchorage zones in flanged sections is not currently addressed in any available code provisions, the present study begins with the most basic load configuration without additional applied force such as a support reaction. The load configurations used in the present study consist of concentric, eccentric, inclined concentric, and inclined eccentric. After the formulations to determine the bursting force magnitude and the location of the force

are developed, a verification of the formulations is conducted. Design examples are performed. Nonlinear finite element analysis examples are illustrated.

The parameters, which are related to the presence of the flange, can be determined using the available standard sections presented in the PCI Bridge Design Manual (1997). The values of important parameters related to the flange, which are used in the present study, are created based directly on the dimensions of the web. For this study, the height of the web for the models were defined and kept constant. Series of models were designed using relations between the dimensions of the web and the flange. For example, the height and the thickness of the web were 16 in. and 1.5 in. respectively, and the width and the thickness of the flanges were set based on the ratio of the flange width to the web height or the flange thickness to the web thickness.

The behaviors of bursting stresses in the web and the flanges of anchorage zones are the focus of this study. The bursting stresses in the web of flanged sections are investigated and compared to the stresses in rectangular sections. The stress distribution in each portion of the member is observed and used to develop a design formulation. Recommendations for anchorage zone design for non-rectangular post-tensioned girders are given.

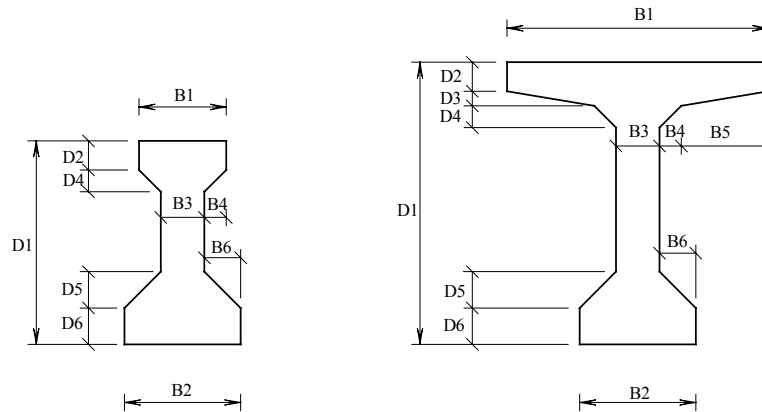
Besides the estimation of the bursting force magnitude and location, reinforcement detailing is also studied and a recommendation is provided. Since a flange is present, design of the bursting reinforcement in this part is also a goal of the study. By using a nonlinear example, an effective pattern of bursting steel in both web and flange can be determined. A recommendation for reinforcing steel arrangement is also provided.

4.2 Preparation of Work

4.2.1 Selection of Non-Rectangular Sections

A flanged section is created from the combination of a web and a flange. The standard I-sections presented in the PCI Bridge Design Manual (1997) are typically unsymmetrical sections. They are manufactured to create the most effective cross-sections for bridge construction. In addition to the standard precast sections presented in the manual, there are

occasions when cast-in-place post-tensioned structures contain a part that can be considered to be a flanged section. It will be useful for a structural engineer to have a design method for flanged section anchorage zones with complex shapes, especially if the design methodology is applicable for a wide variety of geometric configurations of flanged sections.



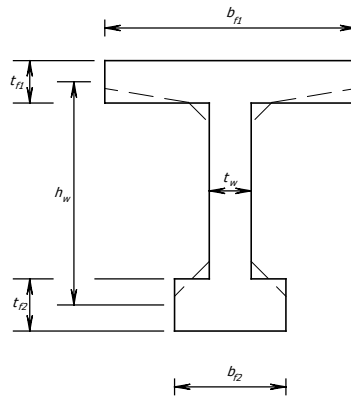
Dimensions (inches)

	Type	D1	D2	D3	D4	D5	D6	B1	B2	B3	B4	B5	B6
AASHTO/I-Beams	I	28.0	4.0	0.0	3.0	5.0	5.0	12.0	16.0	6.0	3.0	0.0	5.0
	II	36.0	6.0	0.0	3.0	6.0	6.0	12.0	18.0	6.0	3.0	0.0	6.0
	III	45.0	7.0	0.0	4.5	7.5	7.0	16.0	22.0	7.0	4.5	0.0	7.5
	IV	54.0	8.0	0.0	6.0	9.0	8.0	20.0	26.0	8.0	6.0	0.0	9.0
	V	63.0	5.0	3.0	4.0	10.0	8.0	42.0	28.0	8.0	4.0	13.0	10.0
	VI	72.0	5.0	3.0	4.0	10.0	8.0	42.0	28.0	8.0	4.0	13.0	10.0
AASHTO-PCI Bulb-Tees	BT-54	54.0	3.5	2.0	2.0	4.5	6.0	42.0	26.0	6.0	2.0	16.0	10.0
	BT-63	63.0	3.5	2.0	2.0	4.5	6.0	42.0	26.0	6.0	2.0	16.0	10.0
	BT-72	72.0	3.5	2.0	2.0	4.5	6.0	42.0	26.0	6.0	2.0	16.0	10.0
Deck Bulb-Tees	BT-35a	35.0	6.0	3.0	2.0	3.0	6.0	48.0	25.0	6.0	2.0	19.5	9.5
	BT-53a	53.0	6.0	3.0	2.0	3.0	6.0	48.0	25.0	6.0	2.0	19.5	9.5
	BT-65a	65.0	6.0	3.0	2.0	3.0	6.0	48.0	25.0	6.0	2.0	19.5	9.5
	BT-35b	35.0	6.0	3.0	2.0	3.0	6.0	72.0	25.0	6.0	2.0	19.5	9.5
	BT-53b	53.0	6.0	3.0	2.0	3.0	6.0	72.0	25.0	6.0	2.0	19.5	9.5
	BT-65b	65.0	6.0	3.0	2.0	3.0	6.0	72.0	25.0	6.0	2.0	19.5	9.5
	BT-35c	35.0	6.0	3.0	2.0	3.0	6.0	96.0	25.0	6.0	2.0	19.5	9.5
	BT-53c	53.0	6.0	3.0	2.0	3.0	6.0	96.0	25.0	6.0	2.0	19.5	9.5
	BT-65c	65.0	6.0	3.0	2.0	3.0	6.0	96.0	25.0	6.0	2.0	19.5	9.5

Fig. 4.2 STANDARD SECTIONS PRESENTED IN PCI BRIDGE DESIGN MANUAL (1997)

Based on the PCI Bridge Design Manual, the standard sections for prestressed girders can be categorized into three groups consisting of AASHTO I-beams, AASHTO-PCI bulb-tees, and deck bulb-tees. Fig. 4.2 presents the dimensions of the selected standard sections. Every section is a combination of rectangular and trapezoidal shapes. In order to create a shape with the exact dimensions using a finite element method, three-dimensional brick elements must be employed, which may result in a large amount of modeling time for the creation of one model. Furthermore, the interpretation of the result for one problem requires much more effort due to the complexity of a three-dimensional body.

Since a simple three-dimensional structure is needed for the present research, a flat shell element is chosen to simulate the concrete shapes in three-dimensional space. The flange of a standard section, which contains part of a trapezoidal shape, can be transformed into a rectangular shape to be able to use a shell element. Fig. 4.3 shows a transformed section used in the finite element modeling and for the parametric study of flanged sections. The table given in the figure presents the transformed dimensions of all selected standard sections. As can be seen, the first six columns indicate the dimensions of the modified section in Fig. 4.3. In addition to all dimensions, the next seven columns were created to show the relationship between each dimensioning parameter.



Dimensions (inches)

	Type	t_{f1}	t_{f2}	t_w	b_{f1}	b_{f2}	h_w	t_w/h_w	t_{f1}/t_w	t_{f2}/t_w	t_{f2}/t_{f1}	b_{f1}/h_w	b_{f2}/h_w	b_{f2}/b_{f1}
AASHTO/I-Beams	I	5.50	7.50	6.00	12.00	16.00	21.50	0.28	0.92	1.25	1.36	0.56	0.74	1.33
	II	7.50	9.00	6.00	12.00	18.00	27.75	0.22	1.25	1.50	1.20	0.43	0.65	1.50
	III	9.25	10.75	7.00	16.00	22.00	35.00	0.20	1.32	1.54	1.16	0.46	0.63	1.38
	IV	11.00	12.50	8.00	20.00	26.00	42.25	0.19	1.38	1.56	1.14	0.47	0.62	1.30
	V	7.32	13.00	8.00	42.00	28.00	52.84	0.15	0.92	1.63	1.78	0.79	0.53	0.67
	VI	7.32	13.00	8.00	42.00	28.00	61.84	0.13	0.92	1.63	1.78	0.68	0.45	0.67
AASHTO-PCI Bulb-Tees	BT-54	4.72	8.25	6.00	42.00	26.00	47.51	0.13	0.79	1.38	1.75	0.88	0.55	0.62
	BT-63	4.72	8.25	6.00	42.00	26.00	56.51	0.11	0.79	1.38	1.75	0.74	0.46	0.62
	BT-72	4.72	8.25	6.00	42.00	26.00	65.51	0.09	0.79	1.38	1.75	0.64	0.40	0.62
Deck Bulb-Tees	BT-35a	7.73	7.50	6.00	48.00	25.00	27.38	0.22	1.29	1.25	0.97	1.75	0.91	0.52
	BT-53a	7.73	7.50	6.00	48.00	25.00	45.38	0.13	1.29	1.25	0.97	1.06	0.55	0.52
	BT-65a	7.73	7.50	6.00	48.00	25.00	57.38	0.10	1.29	1.25	0.97	0.84	0.44	0.52
	BT-35b	7.73	7.50	6.00	72.00	25.00	27.38	0.22	1.29	1.25	0.97	2.63	0.91	0.35
	BT-53b	7.73	7.50	6.00	72.00	25.00	45.38	0.13	1.29	1.25	0.97	1.59	0.55	0.35
	BT-65b	7.73	7.50	6.00	72.00	25.00	57.38	0.10	1.29	1.25	0.97	1.25	0.44	0.35
	BT-35c	7.73	7.50	6.00	96.00	25.00	27.38	0.22	1.29	1.25	0.97	3.51	0.91	0.26
	BT-53c	7.73	7.50	6.00	96.00	25.00	45.38	0.13	1.29	1.25	0.97	2.12	0.55	0.26
	BT-65c	7.73	7.50	6.00	96.00	25.00	57.38	0.10	1.29	1.25	0.97	1.67	0.44	0.26
	min		4.72	7.50	6.00	12.00	16.00	21.50	0.09	0.79	1.25	0.97	0.43	0.40
max		11.00	13.00	8.00	96.00	28.00	65.51	0.28	1.38	1.63	1.78	3.51	0.91	1.50

Fig. 4.3 TRANSFORMED SECTIONS FOR THE PRESENT STUDY

The last two rows of the table in Fig. 4.3 present the minimum and maximum values of each column. Since the dimensions of the finite element model are based on the information

given in the table, these numbers are essential for setting the range of each parameter as will be described in the following section. In the present study, the height of a finite element model is set to have the same dimension as that used in the parametric study in Chapter 3. By using the height of the web equal to 16 in., other dimensions such as thickness of the web, thickness of the flange, and width of the flange are defined relative to it.

In the present study, a symmetrical I-section, which contains two absolutely identical flanges, is considered to be the most basic shape. The centroid of the symmetrical section is located exactly at the center of a flanged section, which is similar to the centroid of a rectangular section. As the study moves to an unsymmetrical shape, a more complex geometric configuration is investigated. The centroid of an unsymmetrical I-section is not located at the middle of the web, which results in an unequal distance from the center of each flange to the centroid. In order to create a concentric anchorage zone condition in an unsymmetrical I-section finite element model, the location of the centroid in the model must be predetermined.

4.2.2 Model Construction

As mentioned earlier, the height of all the models is set as 16 in., identical to that used in the parametric study in Chapter 3. Therefore, the element size in the web of the model remains the same as that used in a rectangular model. In the flanges, the size of the elements is the same as those in the web. If the width of the flange increases, the element size remains unchanged. Since the model has similar properties to those in the previous chapters, no convergence test is required.

The location of boundary support is also important. Since the model now exists in three-dimensional space, lateral support needs to be applied to the model. A lateral support is fixed on every node at the end of the model. The vertical boundary support can be arbitrarily positioned if the length of the model is adequately selected to avoid the stress disturbance from the supports. The length of the model is considered to extend directly from the prestressing surface to the distance not less than three times the height of the web (h_w) based on a test to find the appropriate length of the model.

A vertical support may influence the behavior of stresses within a flange if it is located on the surface of the flange. Therefore, the vertical support is located at the end of the web. The anchor plate is designed to be the same thickness as the web. It is connected to the concrete element by using a set of translation springs. Since the anchor plate is separated from the concrete in a three-dimensional space, a lateral boundary support is applied onto the plate body in order to fix the plate in a vertical plane. In the case of an inclined prestressing load, the vertical component of the load is applied directly onto the end of the spring elements on the surface of the concrete. Fig. 4.4 shows a typical model used in the present study.

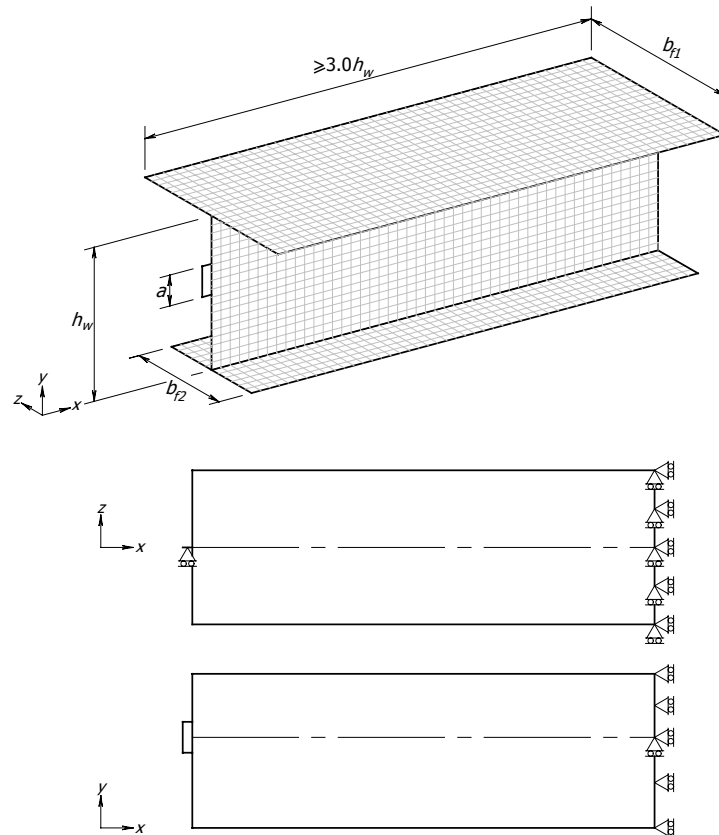


Fig. 4.4 TYPICAL MODEL USED IN THE STUDY OF ANCHORAGE ZONE WITH FLANGED SECTION

The eccentricity of the anchorage zone with a flanged section is limited by the geometric configuration of the section. If an unsymmetrical section is used, the centroid of the section may be located close to one of the flanges. The investigation of an eccentric load

configuration may not be performed as desired if the distance between the centroid and the center of the flange does not provide adequate space to model the anchor plate. Therefore, the present study considers only models that are physically possible.

4.2.3 Comparison of the Models

Since shell elements have been selected instead of brick elements, a comparison of the stress behavior occurring in models with two different types of element should be performed. Fig. 4.5 shows the picture of the anchorage zone with an I-shaped section used for comparison. The model is chosen from the models used in the present study. Both height and width of the model are equal to 16 in. The thickness of the web is 1.5 in. while the thickness of the flanges is 1.2 in. The thickness ratio of the flange to the web is 0.80. The length of the model is three times the height of the web. The anchorage plate has the length of $0.1h_w$.

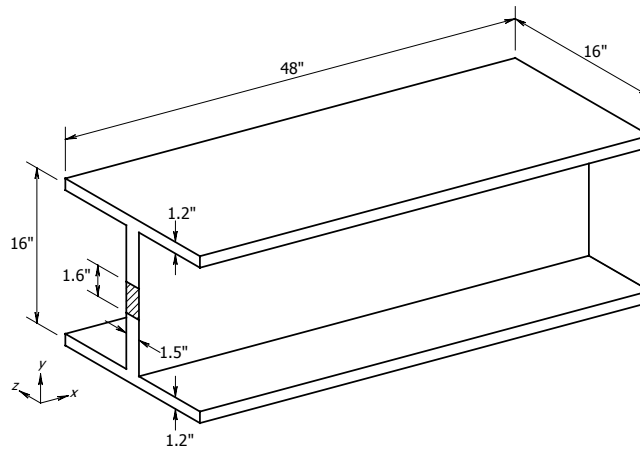


Fig. 4.5 ANCHORAGE ZONE USED FOR COMPARISON OF THE MODELS WITH DIFFERENT TYPE OF ELEMENT

Since the section is doubly symmetric, the model can be created by using only a quarter section of the structure. Fig. 4.6 shows the brick finite element model constructed for this study. A twenty-node solid brick element CHX60 was chosen for this model. Roller supports were used at all cut surfaces of the model. A quarter of the magnitude of the prestressing force is applied on the region of the anchorage surface. The dimensions of the

brick element are relatively close to those used in the model that is constructed from shell elements.

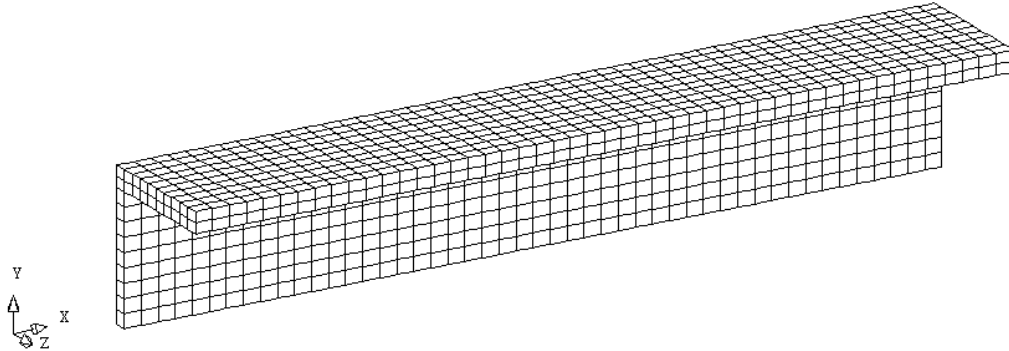


Fig. 4.6 FINITE ELEMENT MODEL USING BRICK ELEMENTS

Figure 4.7 shows the stress contour plot in the y-y direction on the web of the model. The stresses in the figure are presented as a factor of uniform stress σ_o , which is determined by dividing the prestressing load by the area of the section. As can be seen, the behavior of stresses in the bursting region of the web is similar to that in rectangular sections. The maximum tensile stress occurs in the region ahead of the anchorage surface. The region on the top of the web, which is the location of the flange, has a small magnitude of tensile stress due to the transfer of the forces into the plane of the flange.

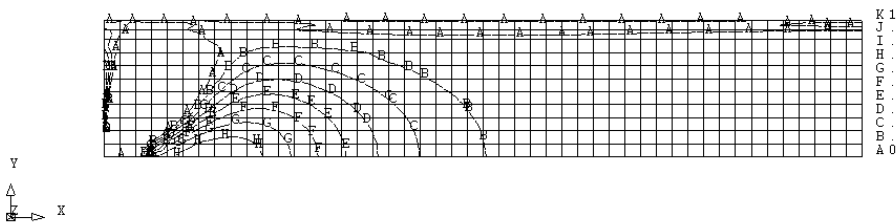


Fig. 4.7 Y-Y STRESSES IN THE WEB OF THE MODEL WITH BRICK ELEMENT
(Stress multiplied by σ_o)

Figure 4.8 shows the stress contour plots in the z-z direction for the flange, which represents the bursting stresses, in three layers consisting of top, middle, and bottom of the flange. As shown in the figure, the longest extension of tensile stresses occur at the centerline along the x-axis for the top and the middle layers of the flange, while the stresses

in the bottom layer extend further in the second row of finite element nodes adjacent to the centerline of the flange. The magnitude of the bursting force needs to be determined along the line that provides the highest value. The models contain several layers of elements, and the integration of stresses needs to be performed on every layer to arrive at the bursting force magnitude.

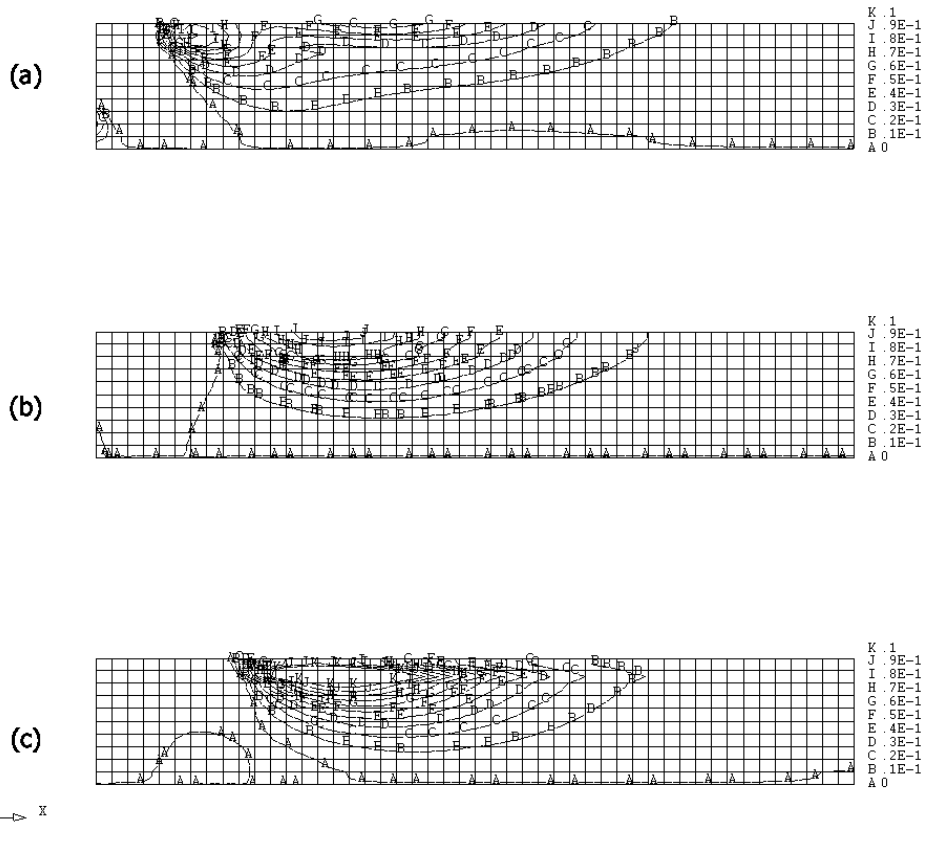


Fig. 4.8 Z-Z STRESSES IN THE FLANGE PRESENTED IN THREE LAYERS
a) TOP, b) MIDDLE, AND c) BOTTOM (Stress multiplied by σ_0)

Figure 4.9 presents the model constructed using shell elements. The full anchorage zone is modeled. The tensile stress plots in the lateral direction of each member are shown in Fig. 4.10. As can be seen from the figure, the tensile stress plots in the web look similar to those presented in the brick element model (see Fig. 4.7). The stress plot in the flange for the model with shell elements has characteristics like those of the three layers of the brick element model combined. It contains two separated regions with two different maximum

tensile stresses. At the centerline of the flange, which is the position of the interface between the web and the flange, the stress plots contain two sharp ends at line B and C in Fig. 4.10b. The bursting stresses in the flange extend for a longer distance than those in the web.

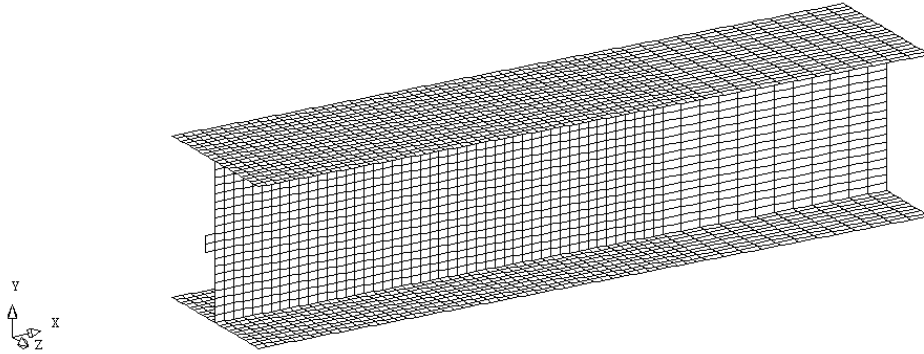


Fig. 4.9 FINITE ELEMENT MODEL USING SHELL ELEMENTS

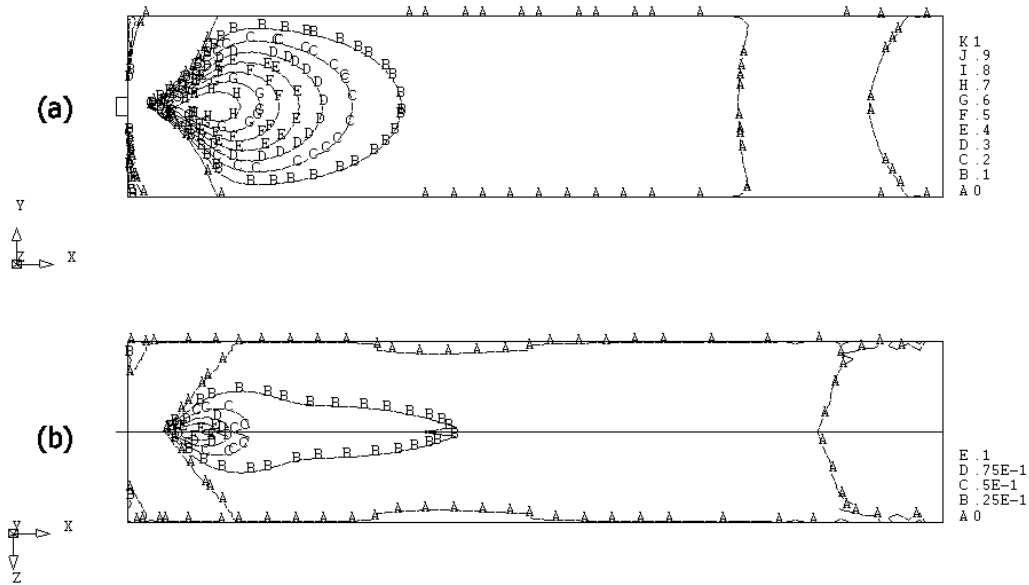


Fig. 4.10 TENSILE STRESSES IN EACH MEMBER a) WEB AND b) FLANGE
(Stress multiplied by σ_0)

Numerically, the magnitudes of the bursting force and the location of the force from both models are close to each other as can be seen in Table 4.1. The locations of the bursting force in the flanges of the two models are different by 10.26 percent. However, the

magnitude of the bursting force in the flange is very small compared to that in the web. The bursting force in the web of the shell element model is larger than that in the brick element model by 1.50 percent. As can be seen from the comparison, the results from the models are quite similar. Therefore, the model with shell elements can be used for the present study, which greatly simplifies the modeling and interpretation of the result. Two additional example models of flanged sections consisting of T-section model and unsymmetrical I-section model are shown in Fig. 4.11.

Table 4.1 COMPARISON OF THE RESULTS FROM TWO MODELS

<i>Model with Element Type</i>	<i>Web</i>		<i>Flange</i>	
	T_{burst}/P	D_{burst}/h_w	T_{burst}/P	D_{burst}/h_w
Brick Element	0.2691	0.72	0.0319	1.17
Shell Element	0.2732	0.71	0.0313	1.05

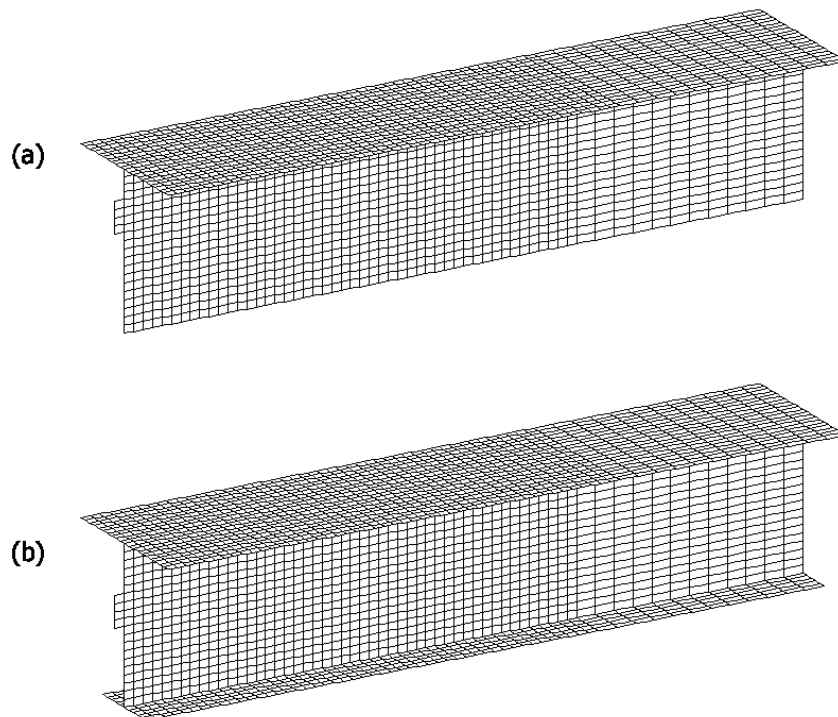


Fig. 4.11 MODELS OF a) T-SECTION AND b) UNSYMMETRICAL I-SECTION

4.3 Parameters

The study of an anchorage zone with a flanged section begins with the most basic load configuration, which is a horizontal concentric load. The parameters that relate to the concentric load configuration are investigated. These parameters consist of anchorage ratio and an inclination angle of the prestressing load. When the study continues to an eccentric load case, the eccentricity is the next parameter that needs to be considered. Besides load-related parameters, three geometry-related parameters are used to modify the geometric configuration of the model. They consist of a web thickness, the thickness ratio of the flange to the web, and a flange width. As previously stated, after the formulations have been developed, an additional parameter involving a support reaction is then added to investigate the use of the formulations. The parameters used in the present study can be described as follows:

4.3.1 Anchorage Ratio (a/h_w)

The anchorage ratios used in the present study were 0.10, 0.20, 0.35, and 0.50. The ratio of zero is not used. All four anchorage ratios are applied for the study of symmetrical I-section and T-section with the concentric load configuration. For the investigation of anchorage zones with an unsymmetrical I-section, the a/h_w ratio of 0.20 is the only one that is used. The ratio of 0.20 is also applied for the study of other load configurations consisting of eccentric, inclined concentric, and inclined eccentric.

4.3.2 Inclination Angle of Prestressing Force (α)

For the present study, only a 6 degree angle is selected. The equations developed in the previous chapter for determining the bursting force magnitude and location can be used as a starting point to develop the formulations for anchorage zones in a flanged section. Therefore, investigation of only one angle is considered sufficient to study the effect of an inclined load in flanged sections.

4.3.3 Eccentricity (e)

Since the present study focuses on the configuration with a prestressing load but with no support reaction, the eccentricity of the prestressing load can be divided into two groups: the load applied within and outside the kern of the section. For unsymmetrical sections, the application of the eccentric load is divided into eccentric loads in the upper portion and the lower portion of the anchorage zone with respect to the centroid of the section. The eccentricity is limited by the available space between the center of the anchor plate and the center of the flange. This limits the number of unsymmetrical section models which are possible. The method to locate the kern in each type of flanged section is given in Appendix A. Similar to those presented in Chapter 3, a positive eccentricity indicates the application of the prestressing load in the upper portion of the model with respect to the centroid of the section, while a negative sign indicates otherwise.

4.3.4 Web Thickness (t_w)

One of the geometry-related parameters of this study is the web thickness (t_w). Varying the thickness of the web will change the magnitudes of the internal forces that are transferred into the flange. The thicknesses of the web for this study were selected based on the geometric properties of the sections given in Fig. 4.3. The chosen values were based on the maximum and minimum values of the ratio of the thickness to the height of the web (t_w/h_w). Therefore, since the height of the model is 16 in., the minimum value becomes 1.47 in. while the maximum value of t_w equals 4.47 in. By approximation, the values of t_w used in the study were 1.5, 3.0, and 5.0 in.

4.3.5 Thickness Ratio of Flange and Web (t_f/t_w)

After the value of t_w was set, the ratio of the thickness of the flange to the thickness of the web (t_f/t_w) can be used to select the flange thicknesses. Three different thickness ratios were chosen based on the maximum and minimum values given in Fig. 4.3: 0.8, 1.1, and 1.4. These ratios will represent the behavior of typical flanged sections based on the information given in the PCI standard sections.

4.3.6 Flange Width (b_f)

In Fig. 4.3, the ratio of the flange width to the height of the web ranges from 0.43 to 3.51 for the top flange and 0.40 to 0.91 for the bottom flange. After they are multiplied by the height of web, which is set as 16 in., the flange width of the model will vary from 6.35 to 56.09 in. This range of flange width is designed to cover a wide variety of shapes of flanged sections, which is a combination of a web and either one of two flanges. For the study of symmetrical I-sections, widths of the flanges are 6.4, 16, and 56 in. For the study of T-sections, the same flange widths are used. For the unsymmetrical I-sections, the width of the bottom flange varies while the width of the top flange remains unchanged. Additional flange widths are used for some parts of the study to provide more detail on the magnitude of the bursting force or the location of the force.

4.3.7 Other Parameters

When the formulations to estimate the bursting force magnitude and location have been developed, a few models of flanged sections subjected to a support reaction are created to examine the formulations. The parameters related to reaction forces include the location and the magnitude of the force. The l/h_w ratio is chosen as 0.25 while the chosen magnitudes of the force are of 5, 10, and 15 percent of the prestressing load. The size of the support bearing plate is fixed as $0.10h_w$.

4.3.8 Summary

Table 4.2 lists all of the parameters related to the present study.

Table 4.2 SUMMARY OF PARAMETERS USED IN THE STUDY OF FLANGED SECTIONS

a/h_w	$\alpha (^{\circ})$	e/h_w	t_w (in.)	t_f/t_w	b_f (in.)	l/h_w	R/P	b/h_w
0.10	0	0.10	1.5	0.8	6.4	0.25	0.05	0.10
0.20	6	-0.10	3.0	1.1	16.0		0.10	
0.35		-0.40	5.0	1.4	56.0		0.15	
0.50		-0.45						

4.4 Load Configurations

Since the study begins with the most basic load configuration, which is applied to a symmetrical I-section and then to more complex sections, the results are presented based on the type of load configuration. It begins with the concentric load configuration and continues to other load configurations including eccentric, inclined concentric, and inclined eccentric. The most important information from all the results of finite element analysis are presented to demonstrate the behavior of a flanged section graphically and numerically. After the information from the finite element results for each load configuration is given, the formulations used for the design of the bursting steel are developed and compared to the finite element results.

4.4.1 Concentrically Loaded Anchor Configuration

4.4.1.1 Finite Element Results

4.4.1.1.1 Elastic Stress Distribution

The bursting stress contours for concentrically loaded anchorage zones in rectangular sections presented in Chapter 3 showed that the maximum bursting stresses occur in the region directly ahead of the anchorage plate and varied with the anchor plate size. When a flange is present at the edge of a rectangular beam, some of the anchorage force must be transferred from the web to the flange. A region of bursting stresses is generated in the flange. The flow of the forces in the flange is different from that in the web, because the loads are introduced gradually along the interface between the web and the flange.

Figure 4.12 shows the y-y stress contour plot for a rectangular section. The section has a height and a thickness equal to 16 and 1.5 in., respectively. Tensile stresses occur over a length roughly equal to the section height (h). The stresses are presented as a factor of the uniform stress on the section σ_o , which is calculated as the prestressing force divided by the area of the rectangular section.

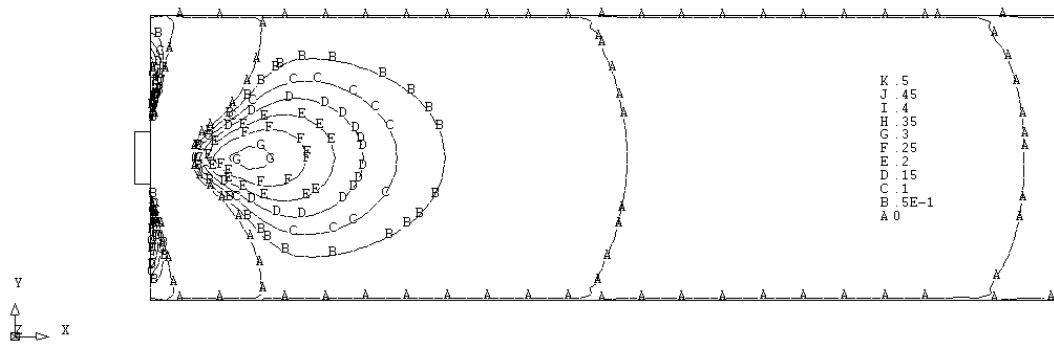


Fig. 4.12 TENSILE STRESSES IN THE MODEL WITH RECTANGULAR SECTION
 (Stress multiplied by σ_o , $A = 24.0$ sq.in.)

Figures 4.13 through 4.15 show stress contour plots of transverse tensile stresses in the planes of the web and the flanges from symmetrical I-section models with three different flange widths. The plots are also presented as a factor of σ_o , which equals the prestressing force divided by the area of the flanged section. All models have the same dimensions except the width of the flanges. The height and the thickness of web are 16 in. and 1.5 in., respectively, while the thickness of the flange is 1.65 in. based on the thickness ratio (t_f/t_w) of 1.1. Fig. 4.13 shows the model that has a flange width of 6.4 in. As can be seen, the bursting stresses in the web extend over a longer distance than those in Fig. 4.12, to approximately $1.5h_w$ from the prestressing surface. Since the presence of the flange results in the force flowing into a larger volume of concrete, the stresses take a longer distance to spread than those in a rectangular section. The bursting stresses in the flange are located close to the loaded surface and have a smaller magnitude compared to those in the web.

When the width of the flange increases, the distribution of stresses in the bursting region extends even longer as can be seen from Fig. 4.14. The size of the bursting region is directly related to the size of the flange. The bursting stresses in the flange are now located further from the prestressing surface compared to those in Fig. 4.13. It is noted that the shape of the bursting region in the flange of Figs. 4.13 and 4.14 can be separated as two regions with respect to the centerline of the flange. The largest tensile stress does not occur at the centerline of the flange. Instead the magnitude of the bursting force in the flange must be

determined from a row of finite element nodes parallel to the web line wherever the maximum value of the force is produced.

In Fig. 4.15, the model with the widest flange is presented. The bursting stresses in the web extend even further than those in two previous models, extending over a length approximately equal to $2h_w$. The model in Fig. 4.15 has a length of 72 in., which is set to equal the width of the flange plus the height of the web. This length is used to give more space, which allows the stresses to fully spread over the body of the flange. As can be seen from the figure, the tensile stresses occur over almost the whole flange body and extend to a distance approximately equal to the flange width. Similar to those occurring in the models with narrower flanges, the bursting region occurring in the flange has two separate regions with respect to the centerline of the flange. This also indicates that the maximum bursting force in the flange should be taken from the integration of the tensile stresses on the node row close to the web line. Since the bursting region in the flange occurs far from the loaded surface (see Fig. 4.15), the location of its centroid moves correspondingly to the width as well. As can be seen, flange width has a significant influence on the location of the bursting stresses in both the web and the flange. However, the magnitude of bursting force needs to be investigated numerically.

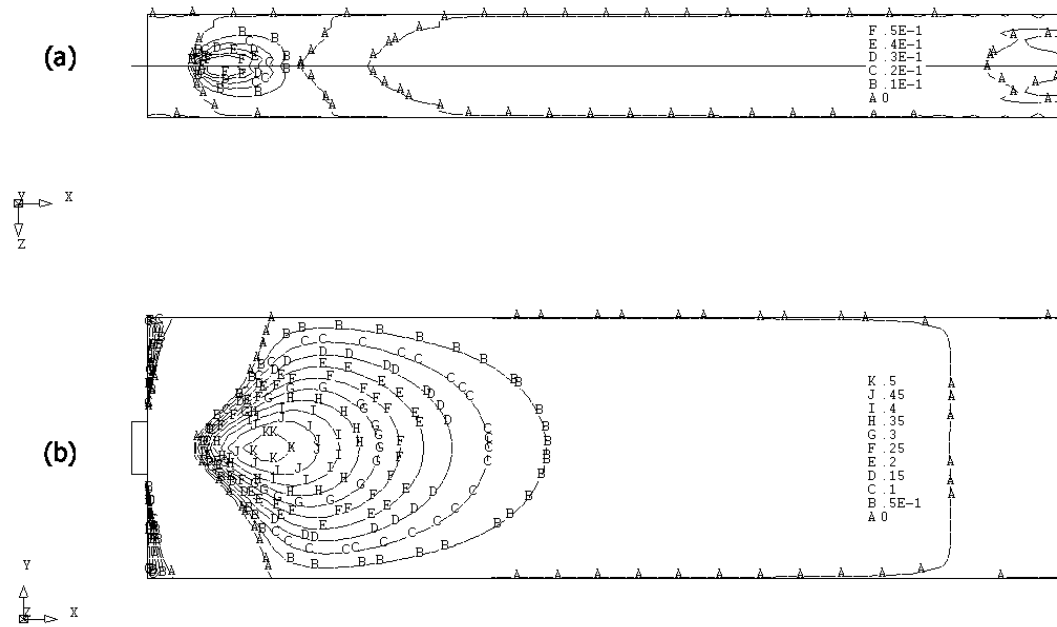


Fig. 4.13 TENSILE STRESSES IN EACH MEMBER OF SYMMETRICAL I-SECTION MODEL with $b_f = 6.4$ in.
 a) FLANGE AND b) WEB (Stress multiplied by σ_o , $A = 42.645$ sq.in.)

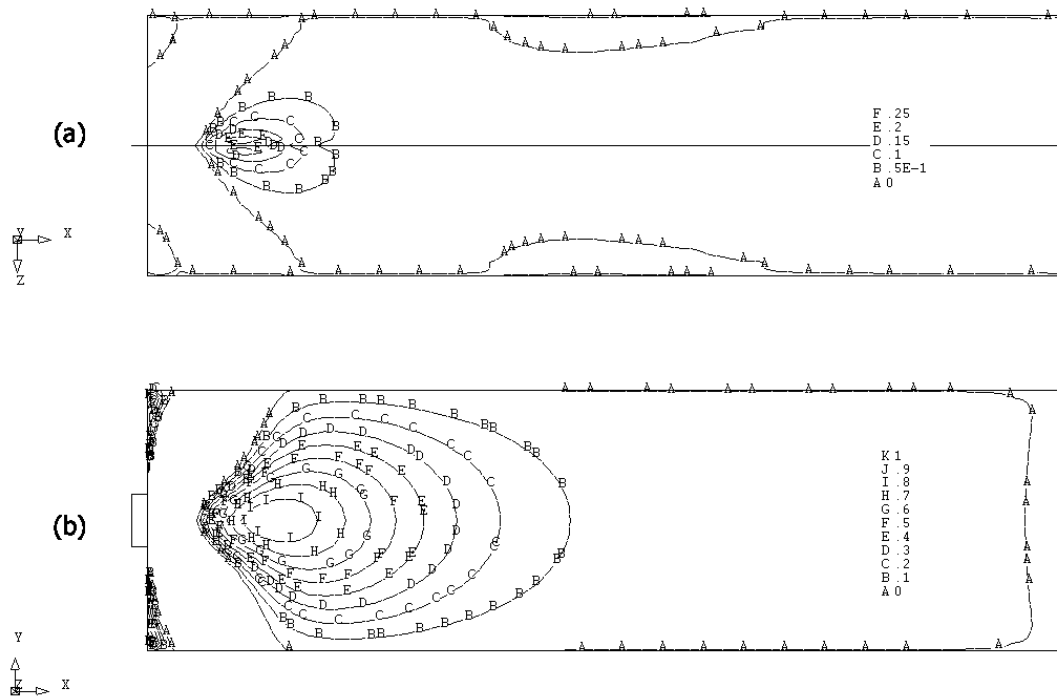


Fig. 4.14 TENSILE STRESSES IN EACH MEMBER OF SYMMETRICAL I-SECTION MODEL with $b_f = 16.0$ in.
 a) FLANGE AND b) WEB (Stress multiplied by σ_o , $A = 74.325$ sq.in.)

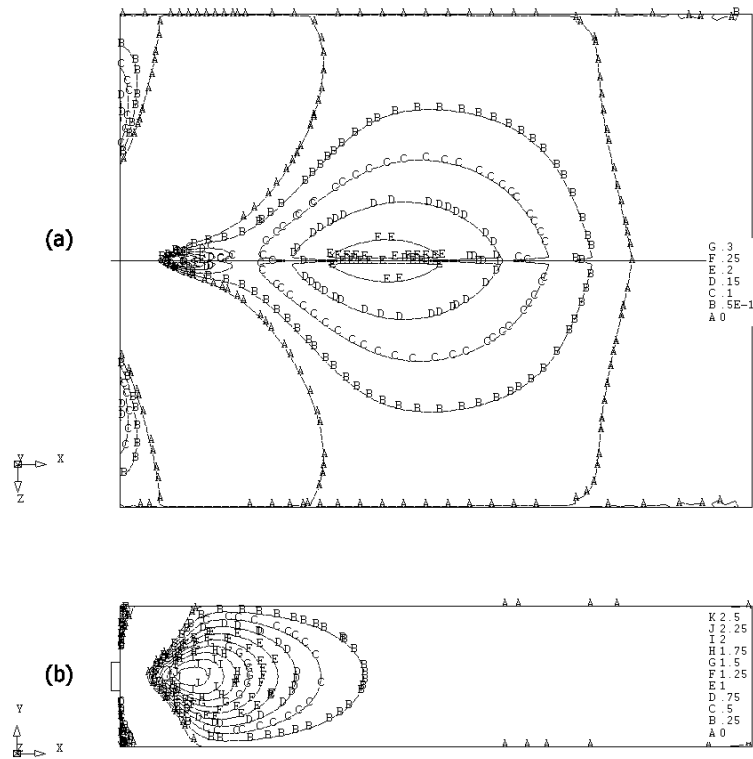


Fig. 4.15 TENSILE STRESSES IN EACH MEMBER OF SYMMETRICAL I-SECTION MODEL WITH $b_f = 56.0$ in.
a) FLANGE AND b) WEB (Stress multiplied by $\sigma_o, A = 206.325$ sq.in.)

Figure 4.16 shows an example of contour plots of principal compressive stresses from the model used in Fig. 4.15. As can be seen, the contours are concentrated in the direction that represents an inclined strut line toward the flange. Based on line A in the figure, which indicates the largest magnitude of stress among the contours, the main axis of the strut lies in a direction close to 45 degrees from the horizontal centerline of the anchor plate. The distribution of the principal stresses is located within a triangular shape at the corner region of the web. This information can be useful for the construction of a strut-and-tie model of a flanged section anchorage zone. It indicates the location of a compressive strut connecting from the local zone to the flange, which can be a starting point for the creation of a strut-and-tie model.

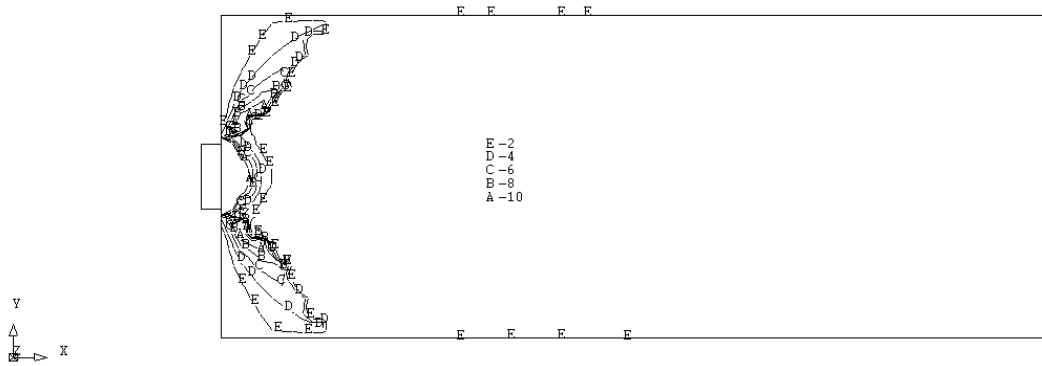


Fig. 4.16 PRINCIPAL COMPRESSIVE STRESSES OF SYMMETRICAL I-SECTION MODEL WITH $b_f = 56.0$ in.
(Stress multiplied by σ_o , $A = 206.325$ sq.in.)

In some cases, two peaks of bursting stresses within the flange may occur if the thickness of the flange is thin relative to the web thickness. Fig. 4.17 shows an example of a stress contour plot for a model that contains two bursting stress peaks. The thickness of the flange is 1.2 in while the thickness of the web is 1.5 in. As can be seen, two bursting regions occur on the flange body with one region having a larger magnitude than the other. Fig. 4.18 shows the tensile stress diagrams of two node rows, which are located at the centerline of the flange and at the row adjacent to the centerline. The integration of the area under the diagrams produces the magnitude of bursting force of the flange. The bursting force from the stresses at the centerline has a smaller magnitude than that from the nodes adjacent to the centerline. This characteristic is also seen in the integration of bursting stresses in other models as well.

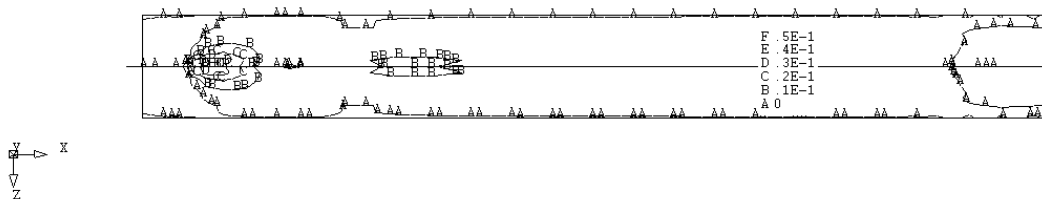


Fig. 4.17 TENSILE STRESSES IN FLANGE OF SYMMETRICAL I-SECTION MODEL
WITH $b_f = 6.4$ in. AND $t_f = 1.2$ in. (Stress multiplied by σ_o , $A = 37.56$ sq.in.)

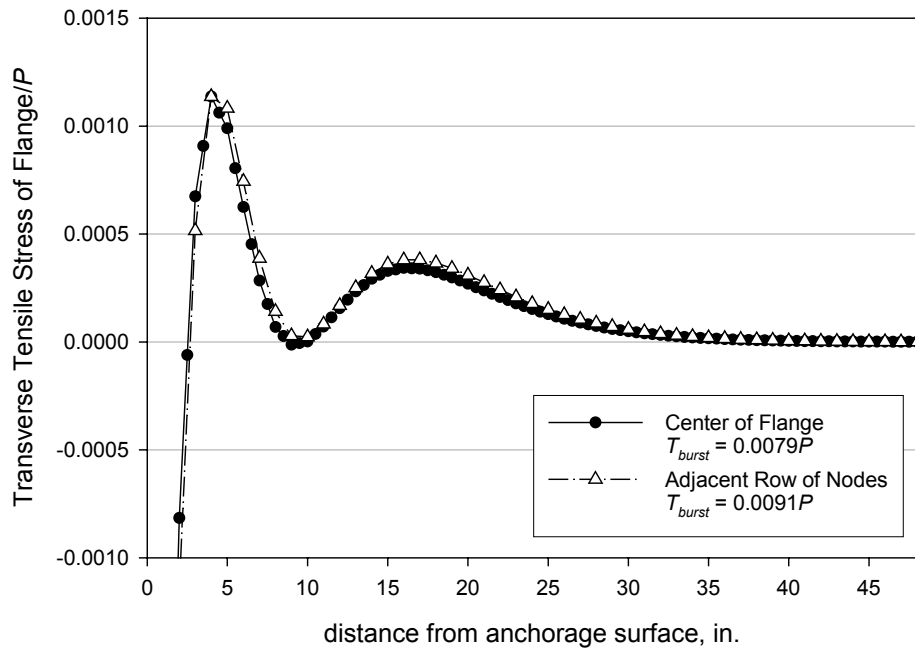


Fig. 4.18 TENSILE STRESS DIAGRAMS IN FLANGE OF SYMMETRICAL I-SECTION MODEL WITH $b_f = 6.4$ in. AND $t_f = 1.2$ in.

When there is no bottom flange, the section is T-shaped and is symmetric only with respect to the vertical axis. The internal forces now transfer into only the top flange. For a concentrically loaded anchorage zone, the prestressing load does not act at the center of the web due to an unsymmetrical shape of the section. Fig. 4.19 shows the stress contour plots for a T-section. The height and the thickness of the web are 16 in. and 1.5 in., respectively. The dimensions of top flange are 6.4 in. wide and 1.65 in. thick. As can be seen, the bursting region is distributed over a large portion of the web. The stresses are not limited by the edge of the web as occurs in a rectangular section. They propagate into the flange. Therefore, the symmetric prism approach is not applicable for the behavior of the stresses in the web of a T-section. In Fig. 4.19a, the tensile stress contours in the flange are similar to those presented in Fig. 4.13a.

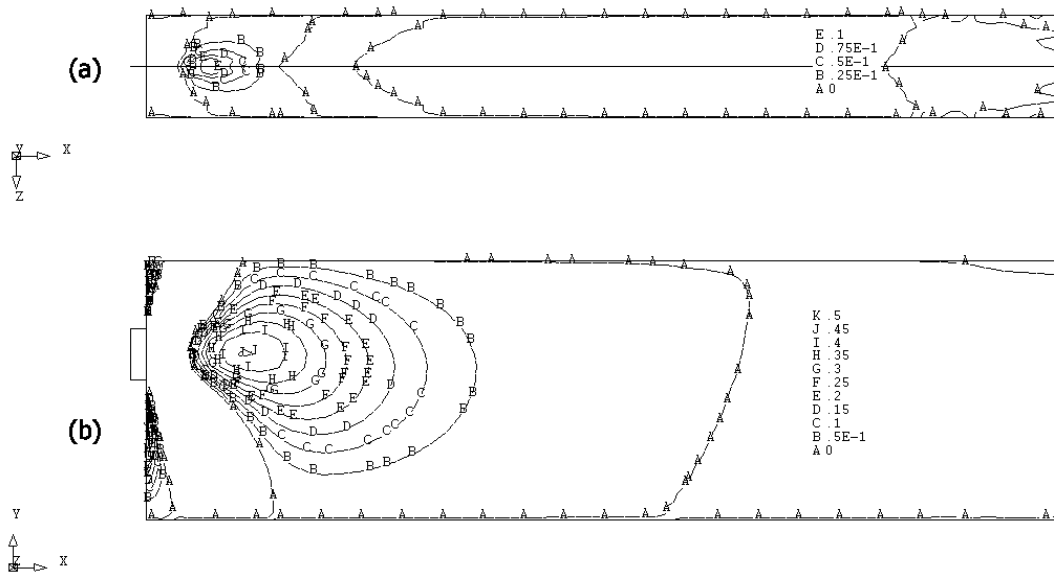


Fig. 4.19 TENSILE STRESSES IN EACH MEMBER OF T-SECTION MODEL WITH $b_f = 6.4$ in.
a) FLANGE AND b) WEB (Stress multiplied by σ_o , $A = 33.3225$ sq.in.)

Figures 4.20 and 4.21 present the contour plots for the T-section models with flange widths of 16 in. and 56 in., respectively. Because the centroid of the T-section is located closer to the flange than in the previous model, the bursting region in the web of each model is located very close to the interface line between the web and the flange. A larger fraction of the total prestressing force must transfer into the flange than the amount of the force that transfers in the model with the narrower flange. The tensile stress contours occurring in the flanges of both models are very similar to those presented earlier for the symmetrical I-section.

The center of the anchor plate is located very high above the centerline of the web in the model in Fig. 4.21. The distance between the center of the anchor plate and the centerline of the web is $0.40h_w$. Spalling stresses can be seen below the anchor plate. The spalling stresses are the result of strain compatibility. The primary difference between the stresses in the symmetrical I-section and T-section is the bursting stresses in the web.

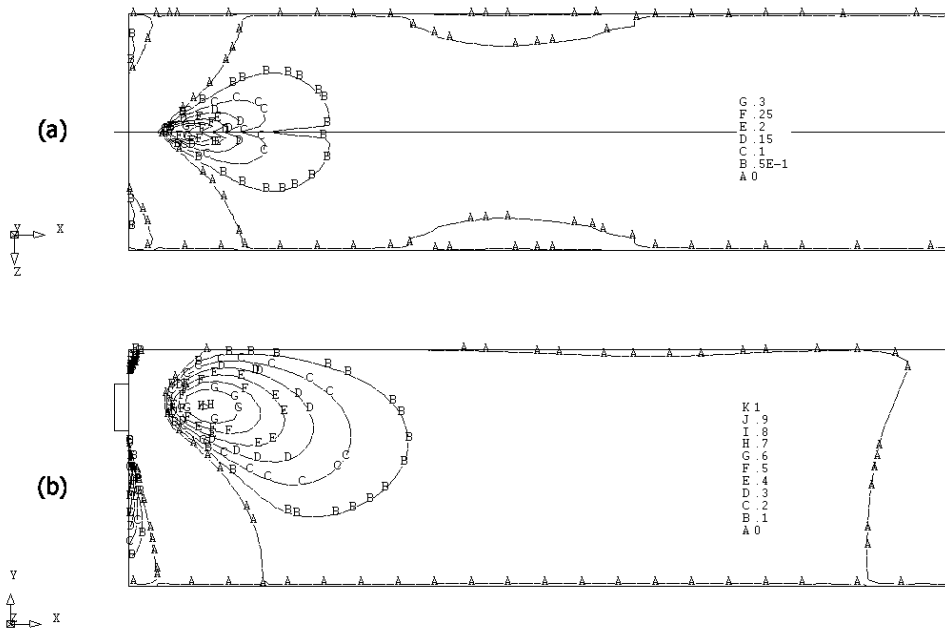


Fig. 4.20 TENSILE STRESSES IN EACH MEMBER OF T-SECTION MODEL WITH $b_f = 16.0$ in.
 a) FLANGE AND b) WEB (Stress multiplied by σ_o , $A = 49.1625$ sq.in.)

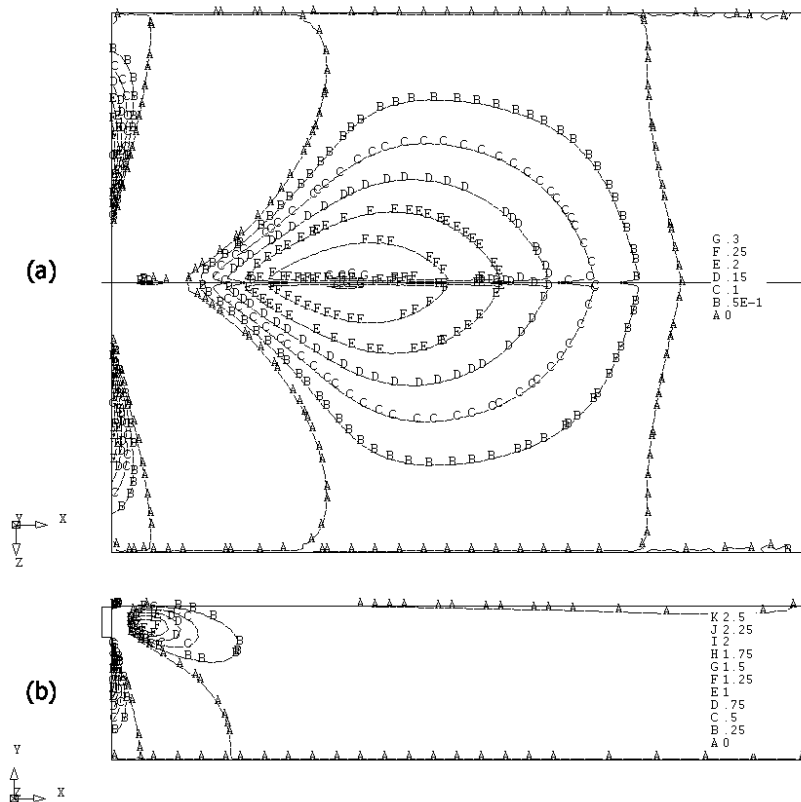


Fig. 4.21 TENSILE STRESSES IN EACH MEMBER OF T-SECTION MODEL WITH $b_f = 56.0$ in.
 a) FLANGE AND b) WEB (Stress multiplied by σ_o , $A = 115.1625$ sq.in.)

Figure 4.22 shows an example of the stress contour plots for an unsymmetrical I-section model with unequal flange widths. The height and the thickness of the web are equal to those used in the previous models. The thickness of both flanges is 1.65 in. The top and the bottom flange have widths of 16 and 8 in., respectively. According to Fig. 4.22, the tensile stress contours in the web are similar to those in the T-section models. The stresses deviate in the direction of the wider flange. The highest tensile stresses occur on the horizontal line passing through the center of the anchor plate. Figs. 4.22a and c show that the bursting stresses in the top flange are larger in magnitude than those in the bottom flange. It can be concluded that the width of the flange has a major influence on the behavior of the stresses. The larger the flange width is, the larger the bursting stresses are.

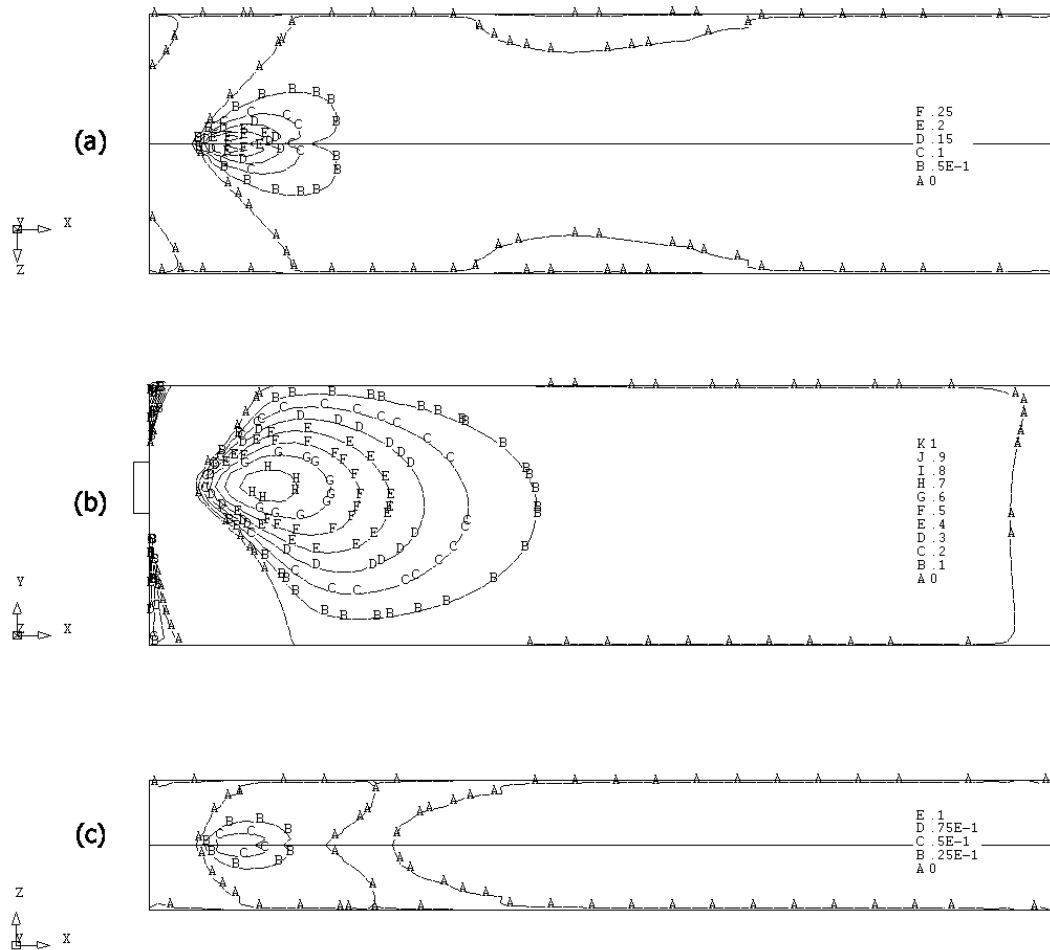


Fig. 4.22 TENSILE STRESSES IN EACH MEMBER OF UNSYMMETRICAL I-SECTION MODEL WITH $b_{f1} = 16.0$ in. AND $b_{f2} = 8.0$ in.

a) TOP FLANGE, b) WEB, AND c) BOTTOM FLANGE (Stress multiplied by σ_o , $A = 61.125$ sq.in.)

An appropriate method of integrating the bursting stresses is needed for the determination of the bursting force magnitude and location in the web. For the bursting force in a flange, the largest magnitude from the integration can be obtained at the first row of finite element nodes adjacent to the interface line of the web and the flange. It is found that there may be two peaks of bursting stresses in the flange as shown in Fig. 4.17. However, the centroid of the forces from the integration of these two stress regions is used to present the location of the total bursting force.

4.4.1.1.2 Bursting Force

In this section, the magnitude of the bursting force relative to each parameter stated in section 4.3 is investigated and discussed. The least influential parameters, which are found in the study, are given at the beginning. Then the most important parameter is presented.

4.4.1.1.2.1 Symmetrical I-Section

Figures 4.23 through 4.25 show the relation between the bursting force magnitude in the web, designated by $T_{burst-web}$, and the thickness ratio (t_f/t_w) for symmetric I-sections with three different flange widths consisting of 6.4, 16, and 56 in. The bursting force magnitude is presented by dividing by the magnitude of prestressing force P . The a/h_w characters indicate groups of the same anchorage ratio using the same symbol but different shading. As the thickness of the flange increases, the bursting force changes slightly in magnitude. It is noted that for the models with the thinnest web, the web bursting force magnitude always increases with respect to the thickness ratio. Therefore, it can be concluded that the symmetrical I-section with the thinnest web and the thickest flange results in the highest web bursting force for all cases.

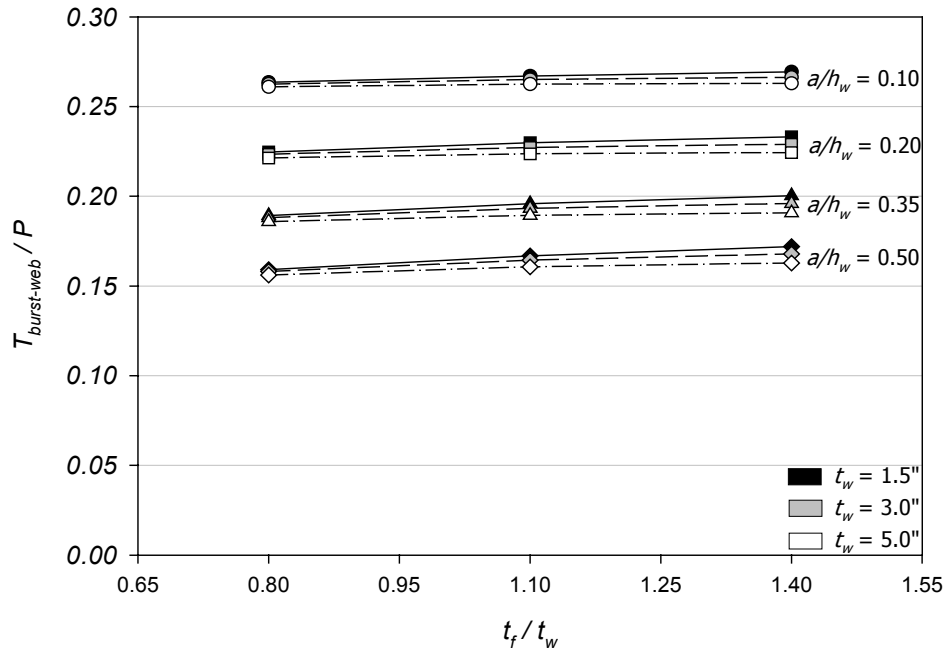


Fig. 4.23 WEB BURSTING FORCE vs. THICKNESS RATIO FOR SYMMETRICAL I-SECTION ($b_f = 6.4$ in.)

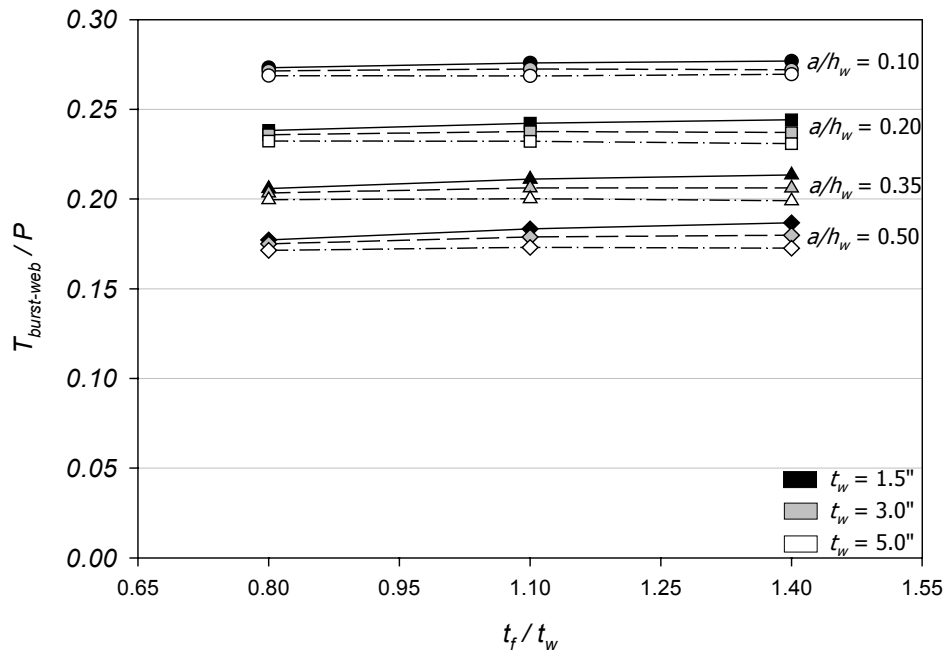


Fig. 4.24 WEB BURSTING FORCE vs. THICKNESS RATIO FOR SYMMETRICAL I-SECTION ($b_f = 16.0$ in.)

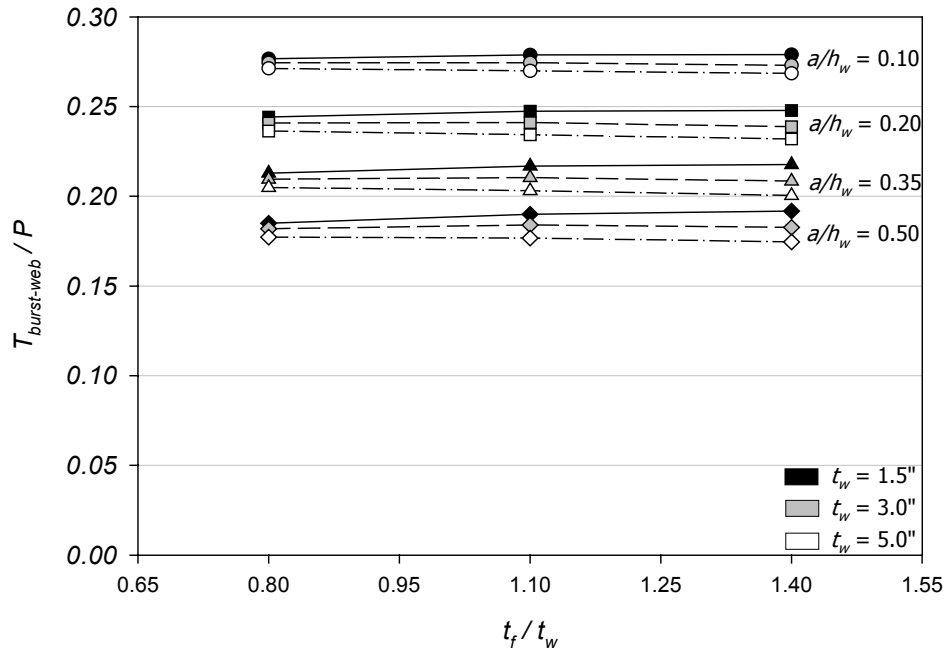


Fig. 4.25 WEB BURSTING FORCE vs. THICKNESS RATIO FOR SYMMETRICAL I-SECTION ($b_f = 56.0$ in.)

For the magnitude of bursting force in the flange, the thickness of the flange visibly affects the magnitude of bursting force. Figs. 4.26 to 4.28 present the relation between bursting force in the flange ($T_{burst-flg}$) and the thickness ratio. The characters of t_w indicated the plots of the model with the same thickness of the web using the same symbol but different shading. The plots shown in each figure can be classified into three groups based on the thickness of web. The models with the same web thickness have a similar variation of the plots, but are slightly different in magnitude within a group. As the thickness of the flange increases, the bursting force magnitude in the flange obviously increases. It is noticed that the magnitude of the flange bursting force is much smaller than that in the web. The highest bursting force magnitude in the flange is detected in Fig. 4.28, which contains the magnitude of $0.0884P$, occurs in the section with the largest flange. The same section produces the web bursting force with the magnitude of $0.2685P$, which is approximately three times the bursting force in the flange.

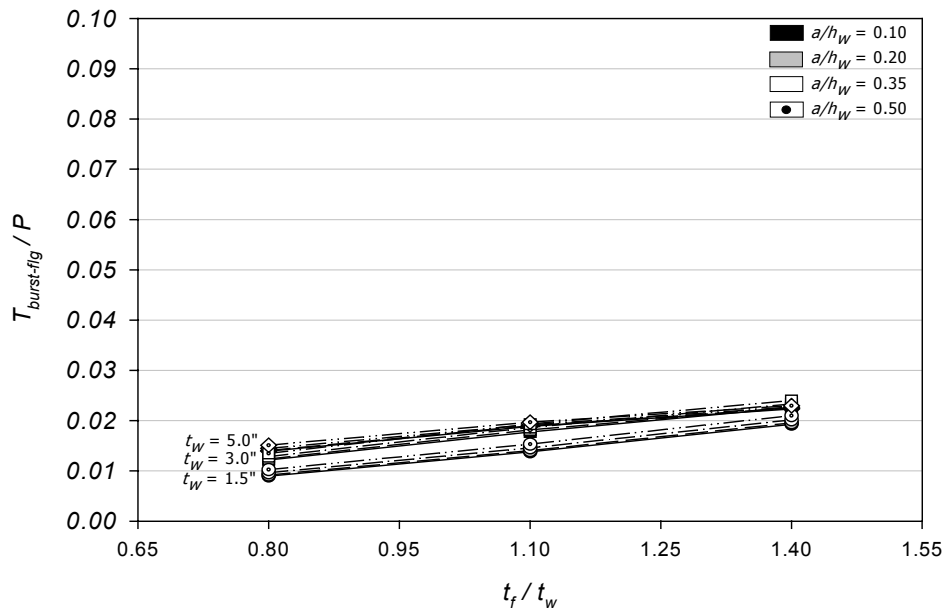


Fig. 4.26 FLANGE BURSTING FORCE vs. THICKNESS RATIO FOR SYMMETRICAL I-SECTION (b_f = 6.4 in.)

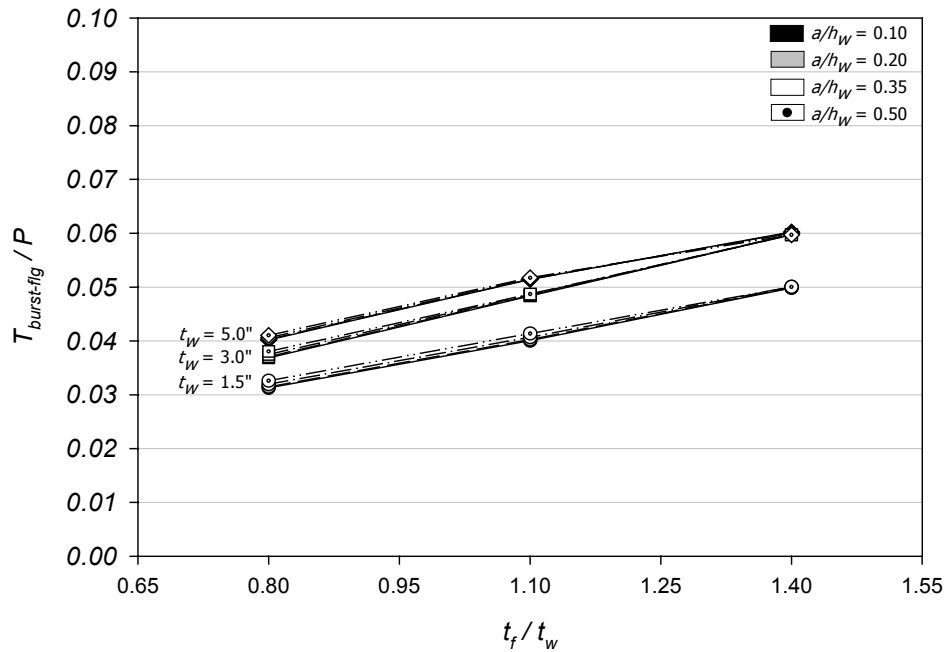


Fig. 4.27 FLANGE BURSTING FORCE vs. THICKNESS RATIO FOR SYMMETRICAL I-SECTION (b_f = 16.0 in.)

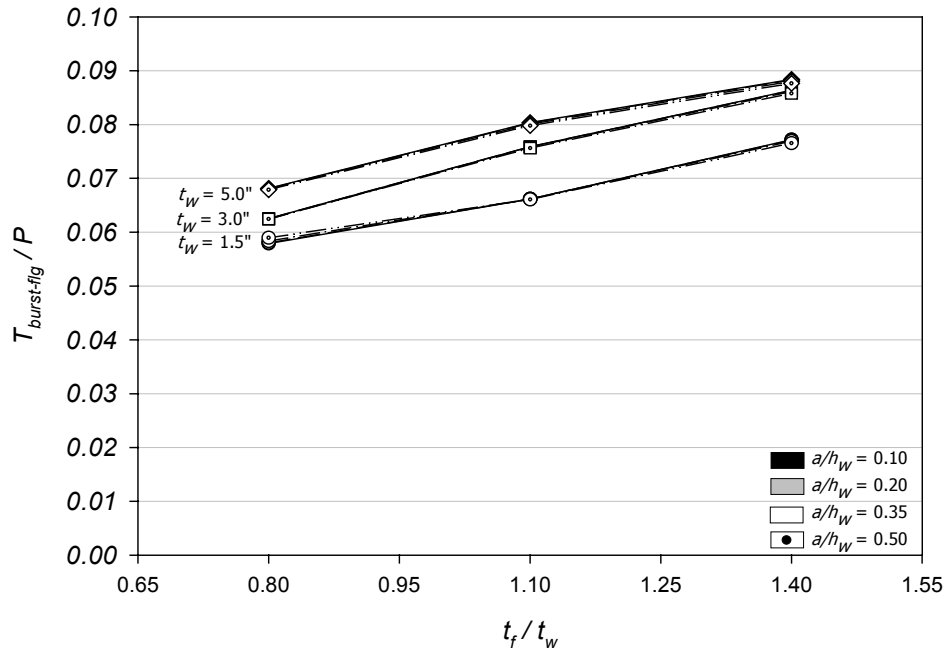


Fig. 4.28 FLANGE BURSTING FORCE vs. THICKNESS RATIO FOR SYMMETRICAL I-SECTION ($b_f = 56.0$ in.)

Based on all plots presented in Figs. 4.23 to 4.28, it can be stated that for symmetrical I-sections with different web thicknesses, the section with the thinnest web has the largest magnitude of web bursting force. If considering the same thickness of the web, the section with the thickest flange produces the highest flange bursting force. Fig. 4.29 shows an example of the relation between web bursting force and the thickness of the web for the sections with largest flange width (56 in.).

Figure 4.30 shows the relation between web bursting force and anchorage ratio for the models with a web thickness of 1.5 in. In the figure, a plot from the study of a rectangular section with a height equal to 16 in. is also given. Another plot drawn as a dash-dot line with no scattered symbol is added into the figure to illustrate the result from the approximate equation for bursting force magnitude in a rectangular section. As can be seen, finite element results from the models of a flanged section are obviously different from those of a rectangular section model. They are larger in magnitude than the bursting force from a rectangular model. This indicates that the equation used for the bursting force calculation of rectangular sections as proposed in Chapter 3 is no longer valid for the design of anchorage

zones in flanged sections. However, the plots have a similar trend. As the a/h_w ratio increases, the magnitude of the web bursting force decreases. It can be seen that the web bursting force of a flanged section depends on the dimensions of the flange.

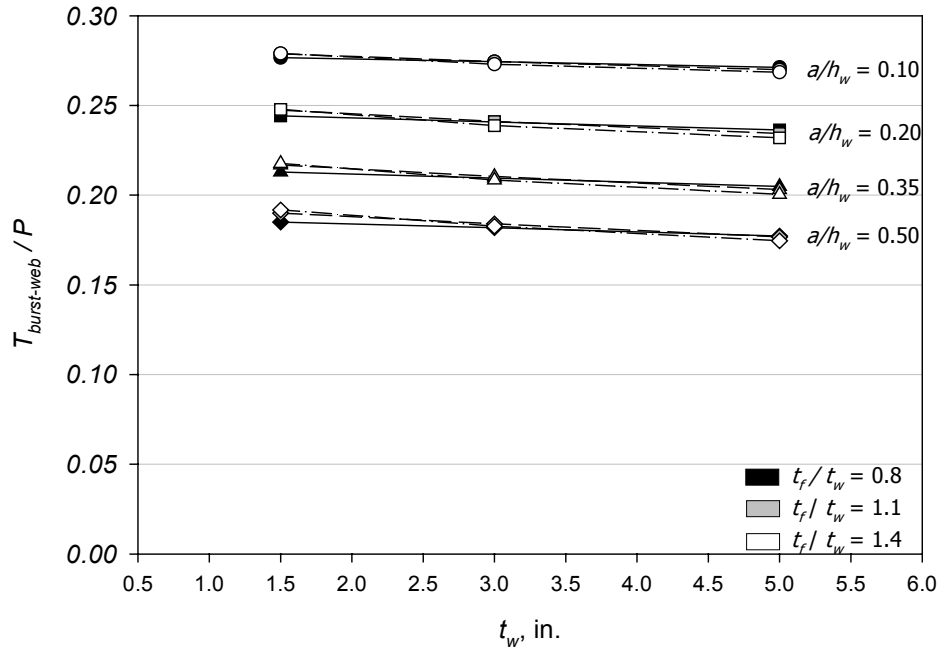


Fig. 4.29 WEB BURSTING FORCE vs. WEB THICKNESS FOR SYMMETRICAL I-SECTION ($b_f = 56.0$ in.)

Figure 4.31 shows the relation between the flange bursting force and anchorage ratio for the flanged sections of the models used in Fig. 4.30. The magnitude of the bursting force does not vary as the a/h_w ratio increases. Therefore, the anchor plate size does not have much influence on the magnitude of the flange bursting force of the section.

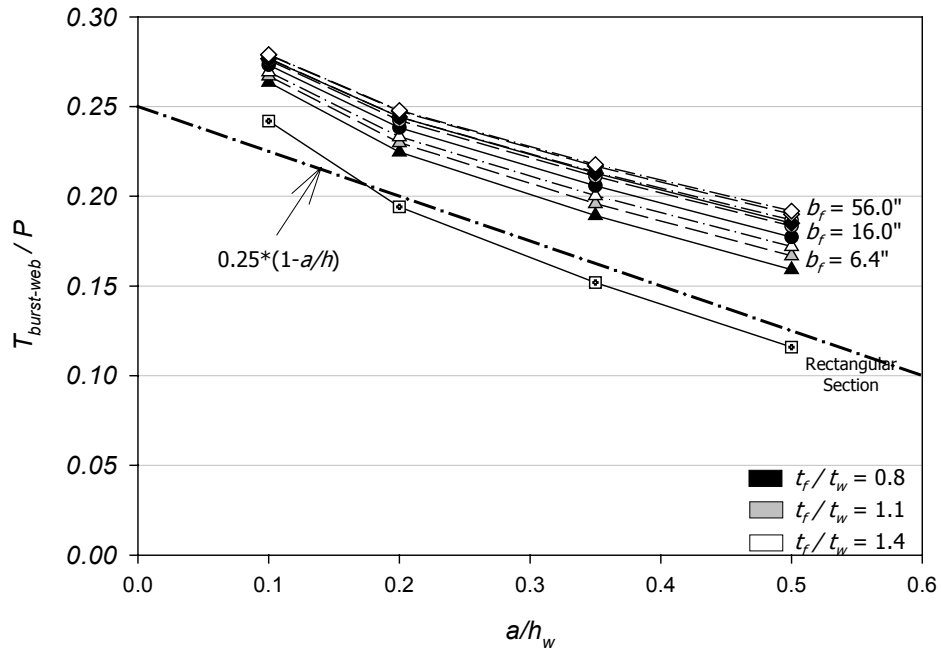


Fig. 4.30 WEB BURSTING FORCE vs. ANCHORAGE RATIO FOR SYMMETRICAL I-SECTION ($t_w = 1.5$ in.)

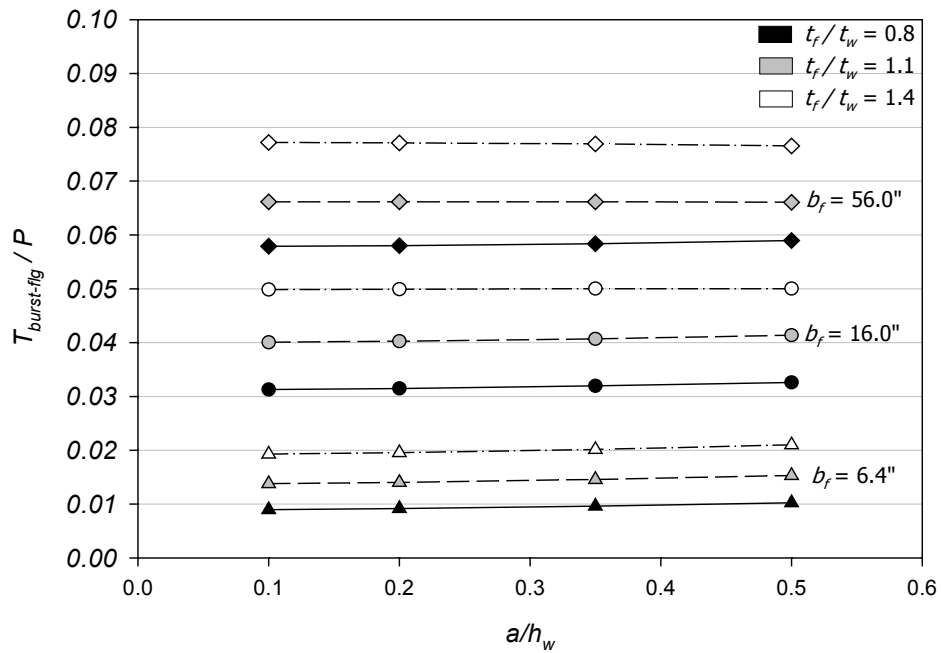


Fig. 4.31 FLANGE BURSTING FORCE vs. ANCHORAGE RATIO FOR SYMMETRICAL I-SECTION ($t_w = 1.5$ in.)

It can be seen that the magnitude of the bursting force in the web and flange are related to the flange width. As a flange width becomes larger, the magnitudes of bursting force in the web and flanges increase significantly. Fig. 4.32 shows the relation between web bursting force and flange width for the models with web thickness equal to 1.5 in. The characteristic of each plot is similar. The magnitude of the bursting force increases rapidly at the beginning and approaches a horizontal line as the flange width becomes larger. This characteristic of the plots occurs in other models with different web thicknesses as well. The tensile stress distributions in the webs of symmetrical I-sections with different flange width can be seen in Appendix C. Fig. 4.33 shows the relation of flange bursting force and flange width. As previously stated, the anchor plate size rarely has an influence on the magnitude of the flange bursting force. The plots in Fig. 4.33 are divided into three groups based on the thickness ratio. All groups exhibit the same trend. All groups exhibit the same trend.

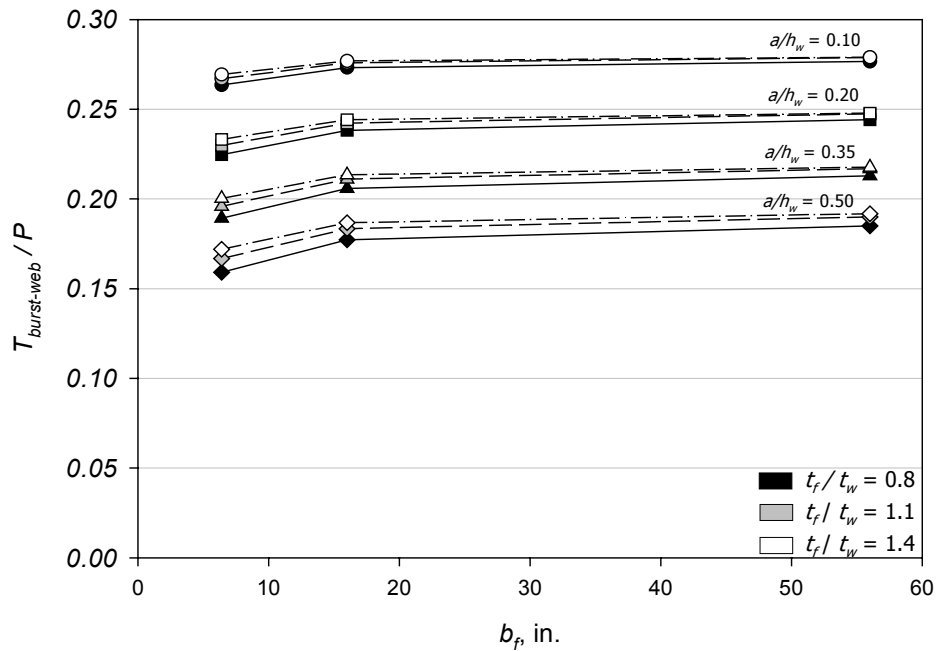


Fig. 4.32 WEB BURSTING FORCE vs. FLANGE WIDTH FOR SYMMETRICAL I-SECTION ($t_w = 1.5$ in.)

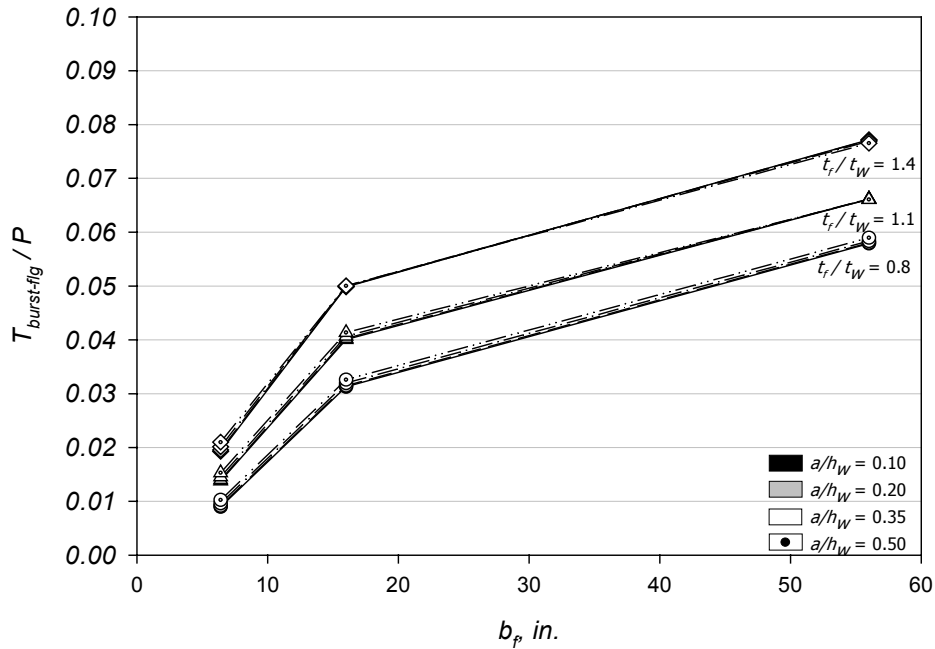


Fig. 4.33 FLANGE BURSTING FORCE vs. FLANGE WIDTH FOR SYMMETRICAL I-SECTION ($t_w = 1.5$ in.)

4.4.1.1.2.2 T-Section

In the investigation of T-section anchorage zones, the possibility of modeling a large anchor plate on the section with a wide flange is limited due to the available space between the center of the plate and the center of the flange, as stated earlier. The models of a T-section with the flange width larger than 16 in. cannot be loaded with an anchor plate larger than $0.35h_w$. However, for all available results from finite element analysis, the behavior of bursting forces in T-section models can be illustrated as follows.

Figure 4.34 shows the behavior of the bursting force magnitude in the web of T-sections relative to the thickness ratio t_f/t_w for a flange width equal to 6.4 in. As seen from the figure, flange thickness does not have a significant influence on the magnitude of the web bursting force, similar to symmetrical I-sections. It is again observed that the web bursting force of the model with the thickest flange and the thinnest web yields the largest magnitude among the models with the same anchorage ratio.

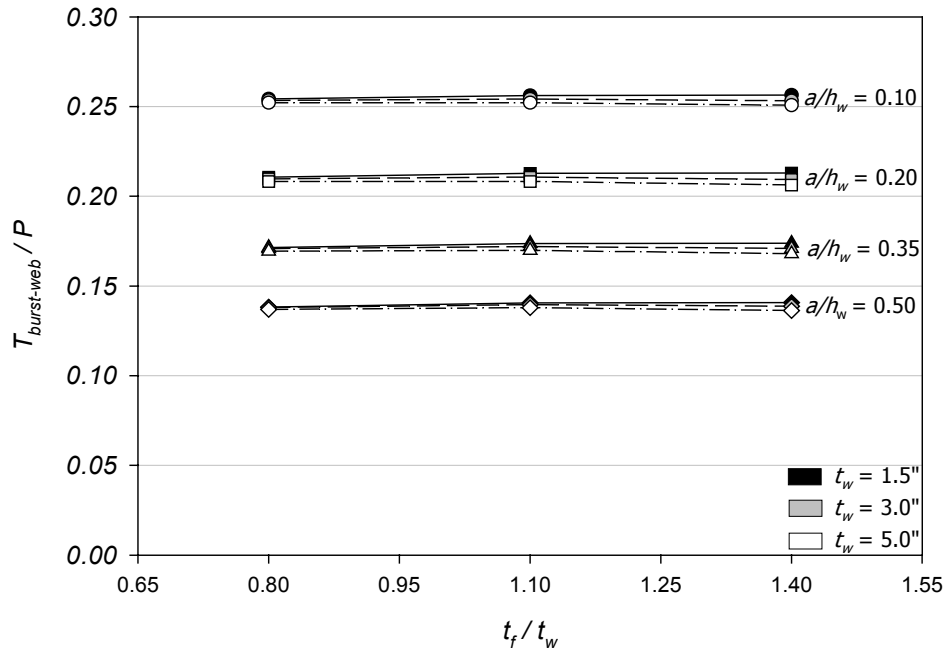


Fig. 4.34 WEB BURSTING FORCE vs. THICKNESS RATIO FOR T-SECTION ($b_f = 6.4$ in.)

Figure 4.35 presents the relation of the web bursting force magnitude and the thickness ratio for T-sections with three different flange widths consisting of 6.4, 16, and 56 in. The anchor plate size used in the models has a width of $0.20h_w$. As the thickness of the flange increases, the centroid of the T-section is pulled closer to the top flange. Because more of the internal forces flow out of the web, the magnitude of the web bursting force is smaller compared to those in the models with a thinner flange.

Figure 4.36 presents the magnitude of flange bursting force with respect to the thickness ratio. The plots are separated into three groups based on the flange width. The models in the group with the widest flange have the highest magnitude of bursting force. This trend is similar to that occurring in symmetrical I-section models. However, the comparison between the bursting force in the web and the flange indicates a different behavior in the T-section model. The largest magnitude of flange bursting force found in Fig. 4.36, which occurs in the model with the flange width of 56 in. and the flange thickness of 7 in., is $0.1465P$ while the magnitude of web bursting force of the same model has magnitude $0.1142P$. The ratio of web to flange bursting force is 0.78, which is much larger than the ratio from a symmetrical I-section with the same flange width. It can be stated that the flange dimension is very

significant in the behavior of bursting force in T-section anchorage zone, since it can cause a large magnitude of bursting force to occur in the flange.

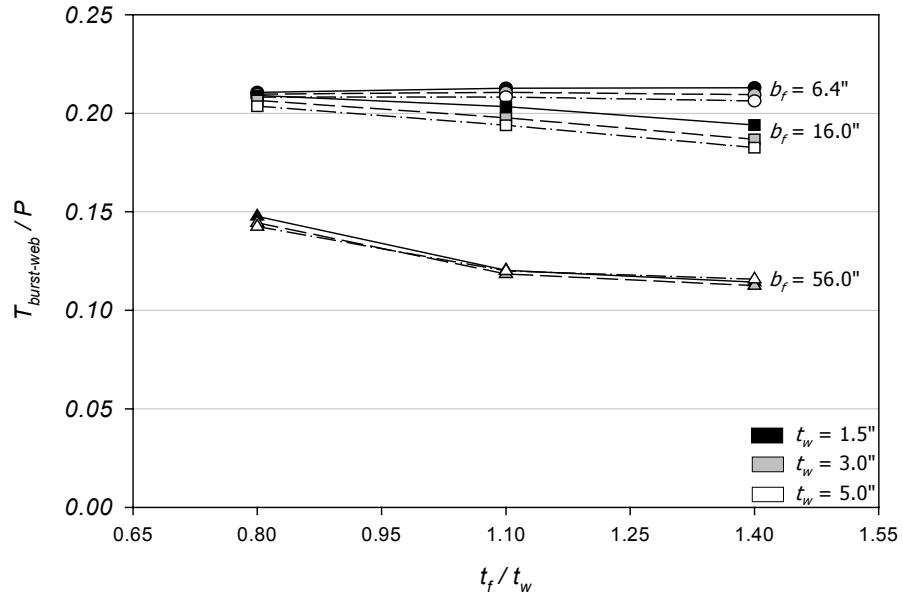


Fig. 4.35 WEB BURSTING FORCE vs. THICKNESS RATIO FOR T-SECTION ($a/h_w = 0.20$)

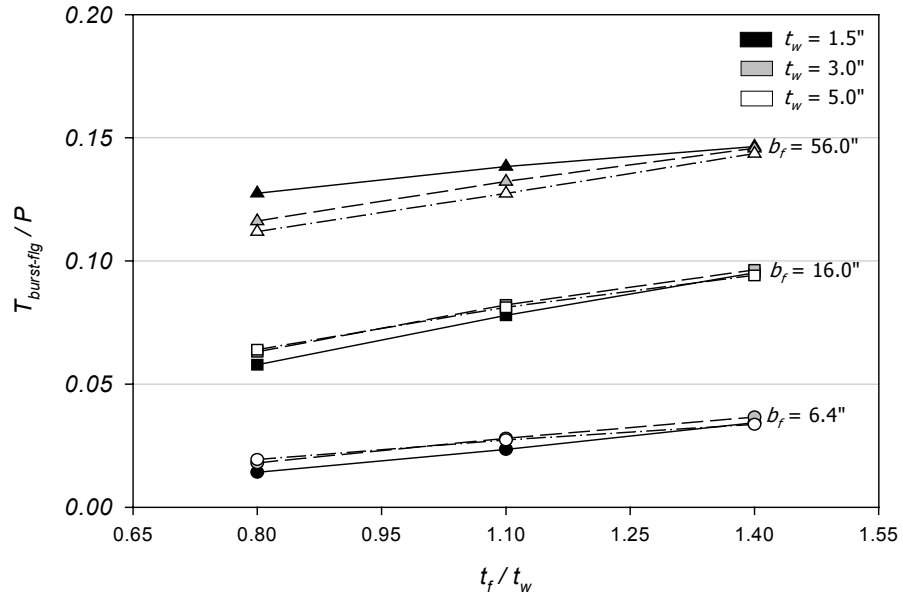


Fig. 4.36 FLANGE BURSTING FORCE vs. THICKNESS RATIO FOR T-SECTION ($a/h_w = 0.20$)

The effect of anchorage ratio on bursting force magnitude in T-sections is very similar to that in symmetrical I-sections. Fig. 4.37 shows an example of the relation between the magnitude of the bursting force in the web and the flange and anchorage ratio from T-section models. The models presented in Fig. 4.37 have a thickness ratio t_f/t_w of 1.4 and a flange width of 6.4 in. The models contain three different web thicknesses. Additional plots are given for a comparison between the models with symmetrical I-section and T-section. From the plots it can be seen that the magnitudes of web bursting force in T-section models are less than that of symmetrical I-sections, while the magnitudes of flange bursting force in T-section models are higher than those of the I-sections. Since a T-section model has its centroid close to the top flange, more of the prestressing load is distributed into the flange, which causes the bursting stresses within the flange to have a higher magnitude while the stresses in the web are reduced. For a symmetrical I-section, the prestressing load is distributed equally in two directions to the flanges, which causes a smaller magnitude of flange bursting force.

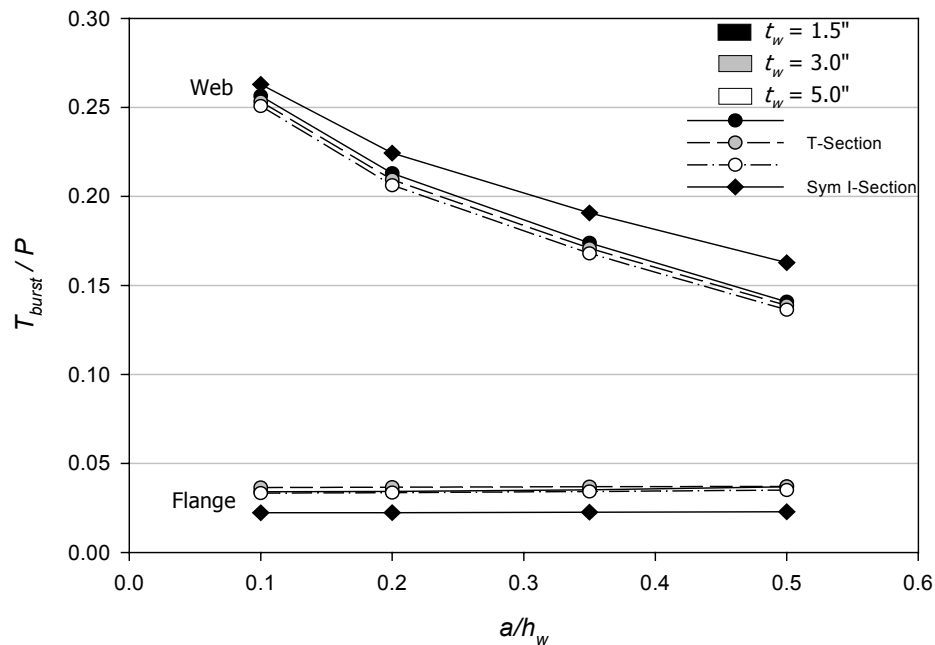


Fig. 4.37 BURSTING FORCE vs. ANCHORAGE RATIO FOR T-SECTION
($b_f = 6.4$ in. and $t_f/t_w = 1.4$)

Figure 4.38 shows the relation of the bursting force in the web and the flange of T-section models with two anchorage ratios. The web bursting force magnitude decreases as the flange width increases. In the models with the a/h_w ratio of 0.20, as the flange width approaches the value of 56 in. the magnitudes of bursting force in the web in some models are less than those in the flange. The flange bursting force magnitude increases at a faster rate as the flange width becomes larger compared to that in symmetrical I-section models. With both top and bottom flanges, the magnitude of the web bursting force is quite large compared to the flange bursting force in the same model. With no bottom flange, the centroid of the section shifts closer to the top flange and results in more force flowing into the flange and causes the magnitude of the flange bursting force to be larger.

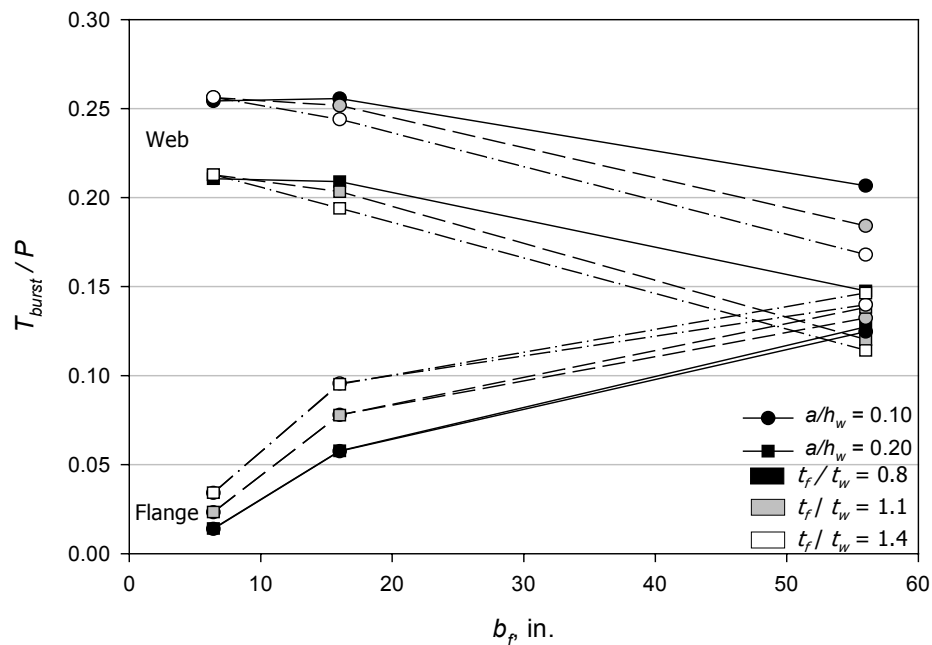


Fig. 4.38 BURSTING FORCE vs. FLANGE WIDTH FOR T-SECTION ($t_w = 1.5$ in.)

4.4.1.1.2.3 Unsymmetrical I-Section

For the previous two types of flanged sections, it was found that the flange size has a major influence on the magnitudes of the bursting force in the web and the flange. In the study of unsymmetrical I-sections, only the behavior of the bursting forces with changing flange width is presented. Because an unsymmetrical I-section contains two flanges, at the

top and the bottom of the web, the size of the bottom flange compared to that of the top flange can be presented as a ratio between two flanges. If the bottom flange is not present, as in the case of a T-section, the flange width ratio becomes zero. If the section contains two equal width flanges, as for a symmetrical I-section, the ratio for this case is presented as 1.0.

Figure 4.39 illustrates an example of the behavior of the web bursting force and the flange width ratio b_{f2}/b_{f1} . The subscript numbers 1 and 2 indicate the top and the bottom flange, respectively. Models with three different top flange widths are investigated. All models used in the investigation have thicknesses of web and flanges equal to 1.5 and 2.1 in., respectively. At the ratio of zero, the web bursting force in the model with largest top flange is the smallest among all three. As the ratio increases, the web bursting force magnitudes of each model increase. The plot of web bursting force in the model with largest top flange develops rapidly upward at the beginning and slowly approaches a flatter slope as the ratio increases to 1.0. Unlike the plot for the model with the largest top flange, the web bursting force of the model with the smallest top flange increases in magnitude at a slower rate relative to the others and approaches the flange width ratio of 1.0 with a very flat slope.

Figure 4.40 shows the relation between the flange bursting force and the flange width ratio for the same models used in Fig. 4.39. The magnitudes of the bursting force from both top and bottom flanges are presented in the figure. If the ratio is zero, the bursting force in the top flange contains the largest magnitude. With the bottom flange present, as the flange width ratio increases, the bursting force in the top flange reduces in magnitude while that of the bottom flange becomes larger. When both flanges have the same dimensions, the bursting forces in the flanges are exactly equal. This characteristic presents the transition of the flange bursting force from the section with T-shape to the section with symmetrical I-shape. It has been confirmed that the behavior of the bursting forces in both the web and the flange are related to the flange dimension. In some case of unsymmetrical I-section, besides having unequal widths of the two flanges, the thicknesses of the flanges may also be unequal. However, since the force depends on the size of each member of a flanged section, the estimation of the magnitude of the bursting force within each member can be formulated.

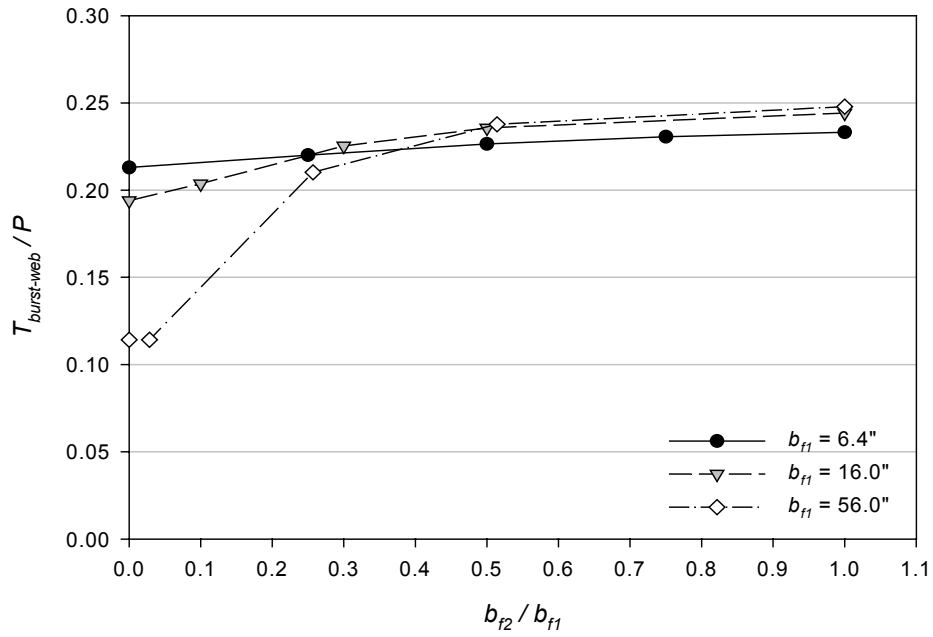


Fig. 4.39 WEB BURSTING FORCE vs. FLANGE WIDTH RATIO
 ($a/h_w = 0.20$, $t_w = 1.5$ in. and $t_f/t_w = 1.40$)

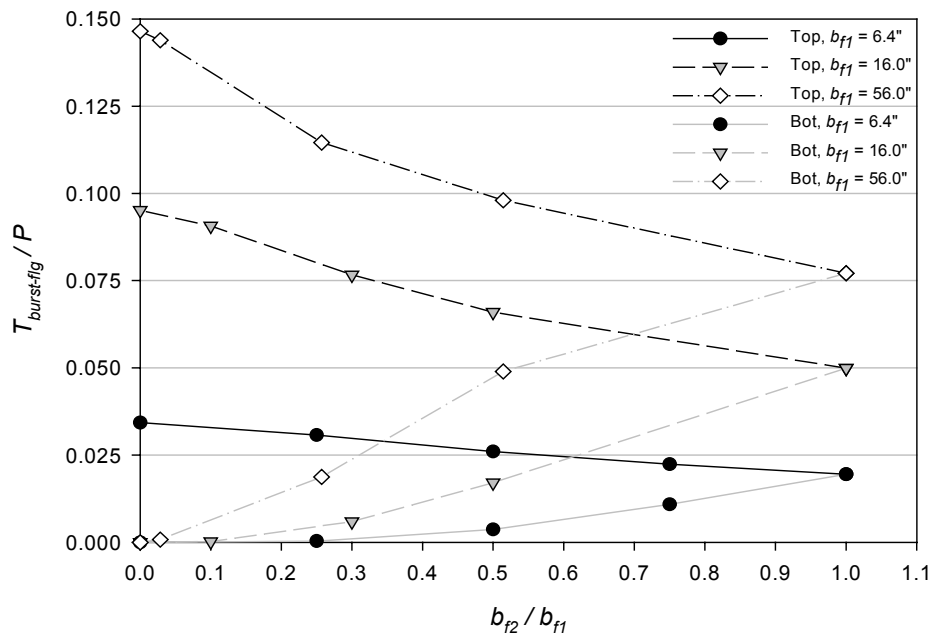


Fig. 4.40 FLANGE BURSTING FORCE vs. FLANGE WIDTH RATIO
 ($a/h_w = 0.20$, $t_w = 1.5$ in. and $t_f/t_w = 1.40$)

4.4.1.1.3 Location of Bursting Force

The presence of the flange in the non-rectangular section not only affects the magnitude of the web bursting force, but also affects the extent of the stress distribution. As illustrated earlier, the stress contour plots of flanged sections indicate a major difference in the distribution of stresses compared to those in the study of rectangular sections. The length of the bursting region in the web along the horizontal axis of the beam extends farther as the width of the flange increases. This section describes the investigation of the bursting force location.

4.4.1.1.3.1 Symmetrical I-Section

Figures 4.41 through 4.43 present the relation between the location of the web bursting force ($d_{burst-web}$) and the thickness ratio for the models of symmetrical I-sections with three different flange widths. The location is divided by the web height (h_w). The plots of web bursting force location obviously vary with the change of the flange thickness. The location of the web bursting force is slightly different among the models with the same a/h_w ratio. It is noted that there is no value of $d_{burst-web}$, which is close to half of the section height as commonly found in the models with a rectangular section. The $d_{burst-web}$ value of the models with the larger flange is larger than those with a narrower flange. The highest magnitude detected in Fig. 4.43 has a distance of $1.08h_w$.

According to Figs. 4.41 to 4.43, the models that have the largest value of $d_{burst-web}$ are those with the thickest flange. The thickness of the flange increases the height of the web. Hence, the web height increases while the anchor plate size remains the same. Since the ratio of a/h_w increases, the magnitude and the location of the bursting force become larger similar to those commonly found in a rectangular study. If considering only the models with the same flange width, the model with the thicker flange has a larger distance to the web bursting force.

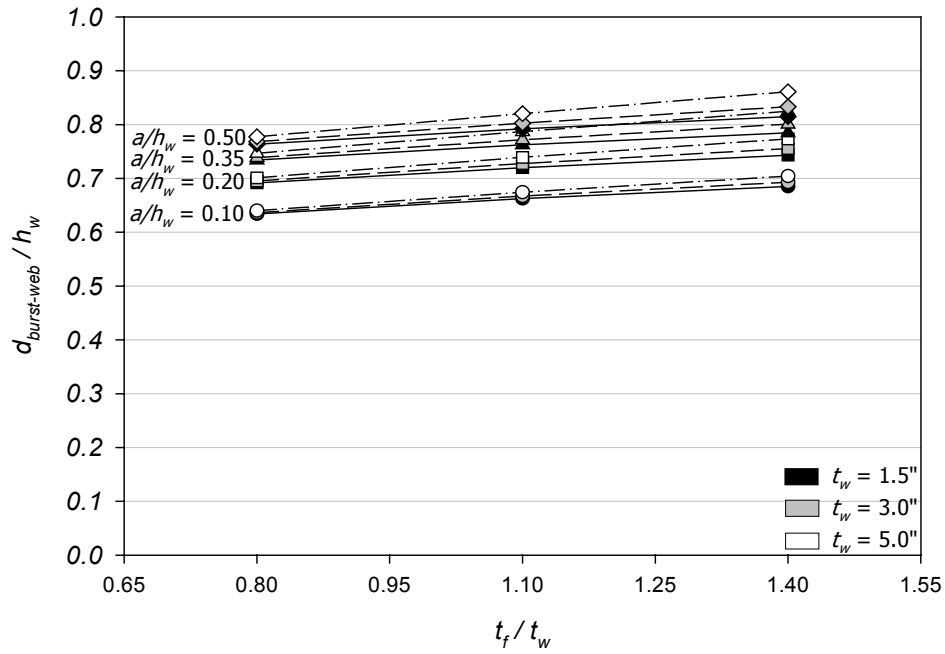


Fig. 4.41 WEB BURSTING FORCE LOCATION vs. THICKNESS RATIO FOR SYMMETRICAL I-SECTION ($b_f = 6.4$ in.)

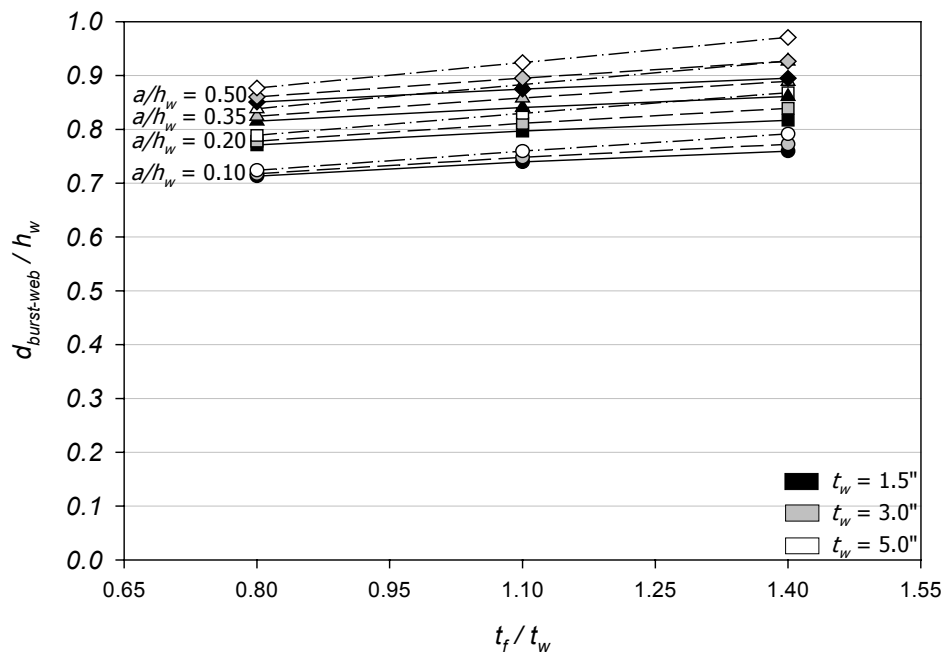


Fig. 4.42 WEB BURSTING FORCE LOCATION vs. THICKNESS RATIO FOR SYMMETRICAL I-SECTION ($b_f = 16.0$ in.)

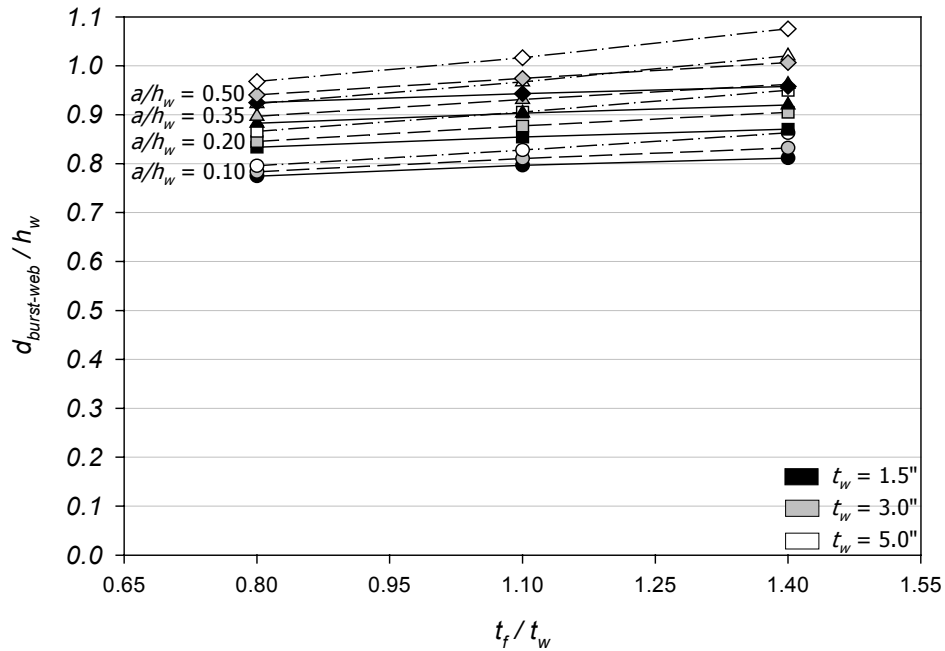


Fig. 4.43 WEB BURSTING FORCE LOCATION vs. THICKNESS RATIO FOR SYMMETRICAL I-SECTION ($b_f = 56.0$ in.)

Figures 4.44 through 4.46 show the relation between the flange bursting force location and thickness ratio. Based on the characteristic of all the plots in each figure, the location of the flange bursting force seems to merge to one value as the thickness ratio reaches the highest value. The largest $d_{burst-flg}$ occurs in the models with the thinnest web. It is also noticed that the models with thin webs also have a rapid change in $d_{burst-flg}$ due to the change of the web thickness, while the ones with the thickest web change at a slower rate. The thinnest web causes the section to have a large value of the ratio between flange width and web thickness and results in more variation of the web bursting force location than those with a thicker web. The plots in Fig. 4.46 show more change in the slope than those in Figs. 4.44 and 4.45. The width of flange, therefore, has a significant effect on the location of the flange bursting force as well. According to all the figures, increases in the thickness of the flange cause the location of the flange bursting force to move closer to the anchor plate. The larger area provided by a thicker flange allows the internal forces to distribute faster in order to reach a uniform stress state within the member.

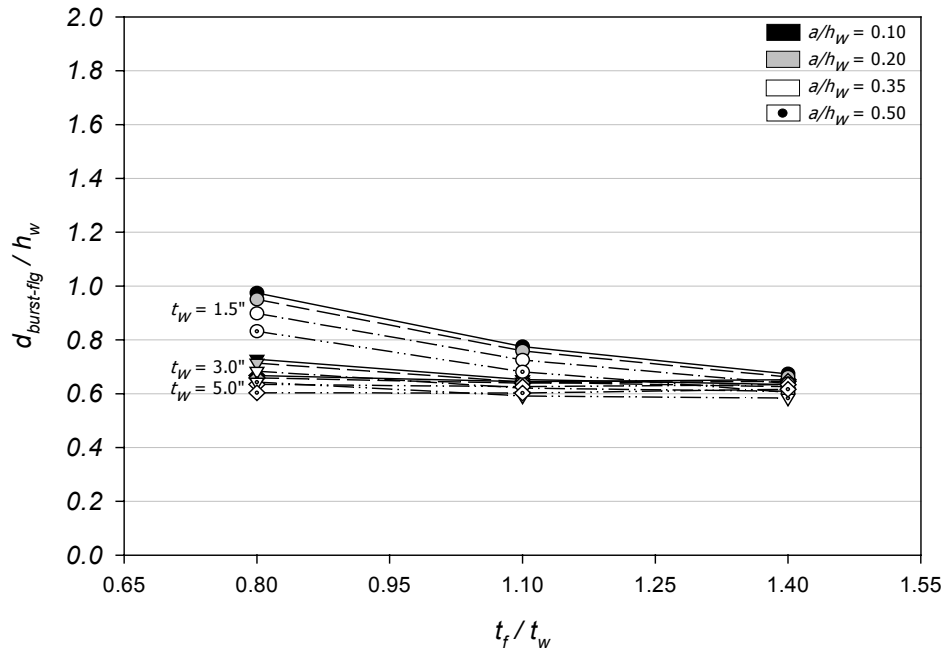


Fig. 4.44 FLANGE BURSTING FORCE LOCATION vs. THICKNESS RATIO FOR SYMMETRICAL I-SECTION ($b_f = 6.4$ in.)

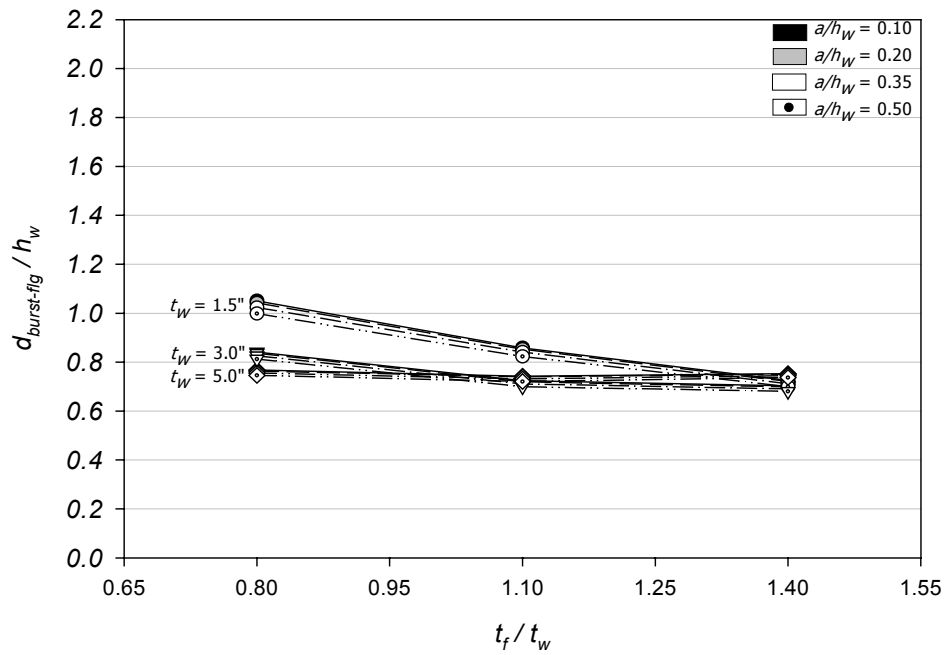


Fig. 4.45 FLANGE BURSTING FORCE LOCATION vs. THICKNESS RATIO FOR SYMMETRICAL I-SECTION ($b_f = 16.0$ in.)

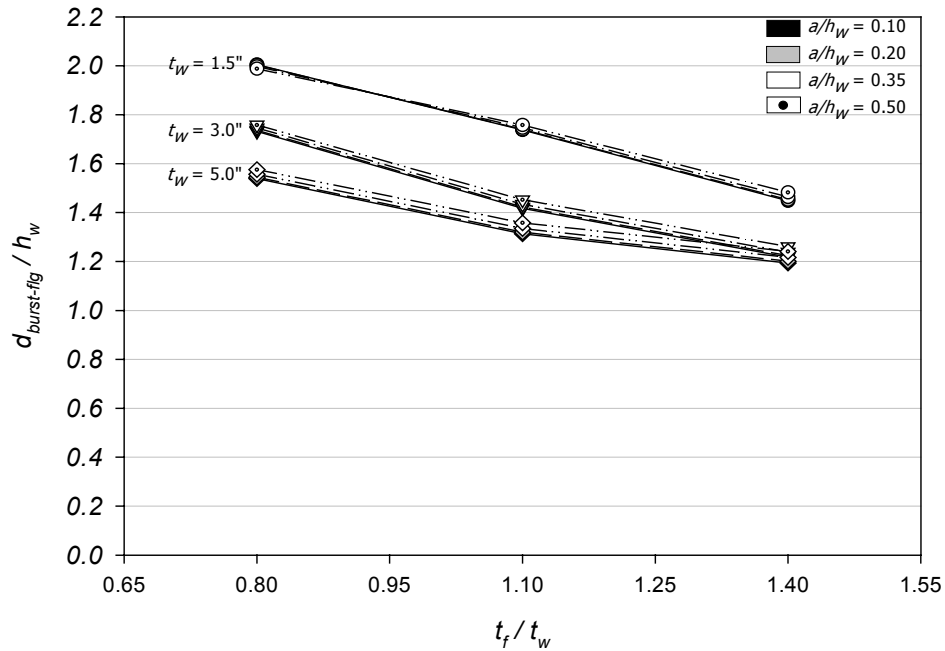


Fig. 4.46 FLANGE BURSTING FORCE LOCATION vs. THICKNESS RATIO FOR SYMMETRICAL I-SECTION ($b_f = 56.0$ in.)

The anchorage ratio is one of the most important parameters in the investigation of bursting force location in anchorage zones. As has been shown in the study of rectangular sections, the equation to determine d_{burst} illustrates the importance of the anchorage ratio. In the present study, the changes in the location of the bursting force in the web and flange due to the change of anchorage ratio is also examined. Fig. 4.47 shows the relation between web bursting force location and the anchorage ratio for the models with the web thickness of 1.5 in. The results from models with three different flange widths are shown in the figure. The plot from a rectangular finite element model and the approximate equation for a rectangular section are given for comparison. As shown in the figure, all plots from the present study have a similar slope. However, this slope is not parallel to that of the plot for a rectangular section. Additionally, the value of the web bursting force location in the present study is much higher than that of a rectangular section. The approximate equation for a rectangular section does not produce a close estimation for the models with symmetrical I-section. However, since all plots of the present study exhibits the same trend, a new formulation for estimating the location of the web bursting force can be developed based on the variables considered in the approximate equation of an anchorage zone in a rectangular section.

Similar to the plots in Fig. 4.31, the plots in Fig. 4.48 indicate that the flange bursting force location is not strongly influenced by the anchorage ratio. In the figure, the models used for the plots are the same as those used in Fig. 4.47. It is noticed that the models with smallest flange width show a slight drop in the magnitude of $d_{burst-flg}$ with respect to the a/h_w ratio, especially in the case of a very thin flange. However, the location of the bursting force in the flange for a flanged section with a narrow flange width may not be as critical as that for a large flange since the magnitude of the bursting force in the section is very small.

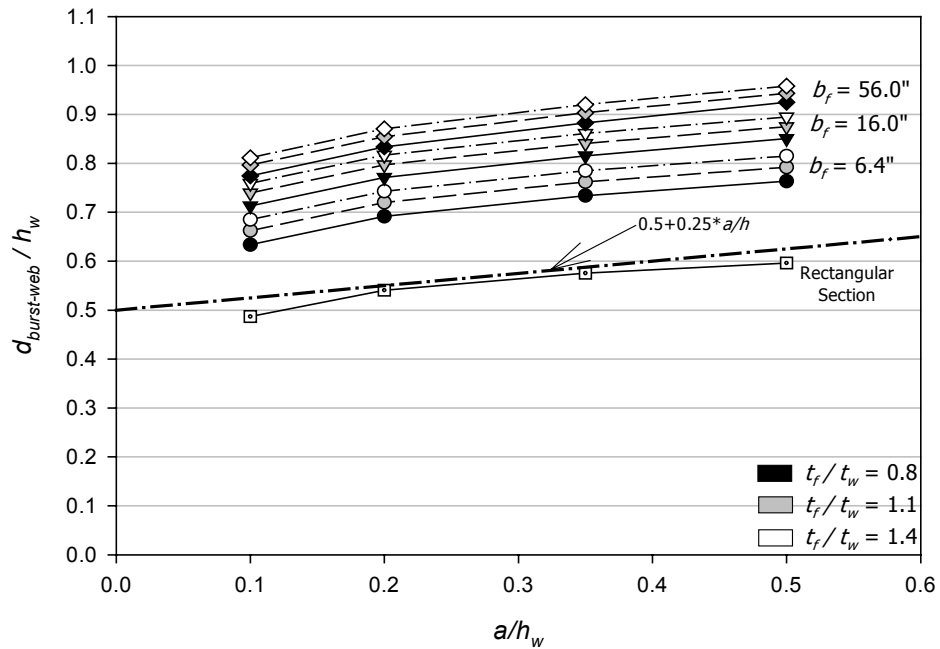


Fig. 4.47 WEB BURSTING FORCE LOCATION vs. ANCHORAGE RATIO FOR SYMMETRICAL I-SECTION ($t_w = 1.5$ in.)

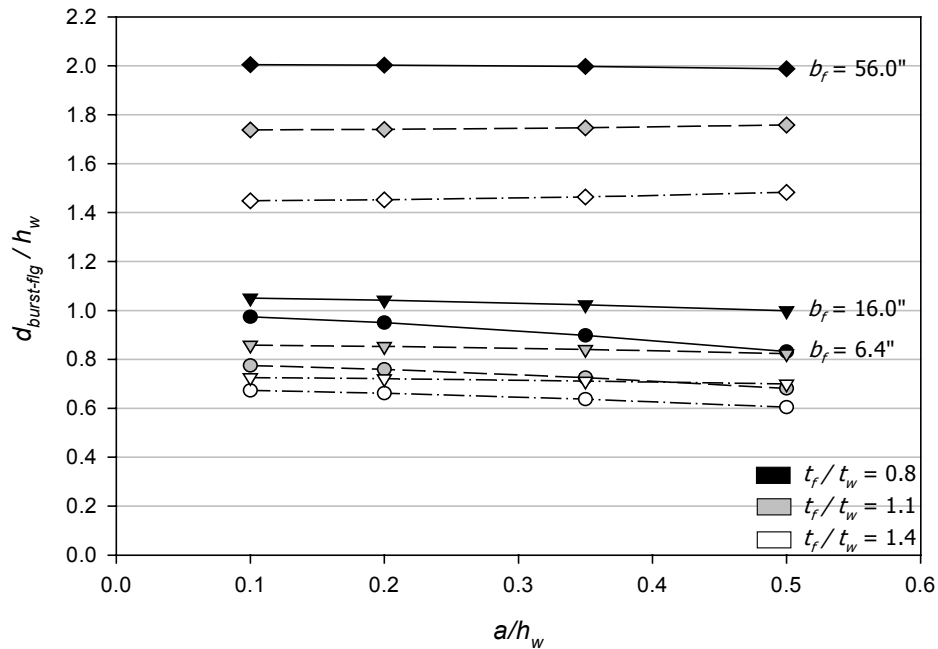


Fig. 4.48 FLANGE BURSTING FORCE LOCATION vs. ANCHORAGE RATIO FOR SYMMETRICAL I-SECTION ($t_w = 1.5$ in.)

Figure 4.49 shows the relation between the location of the web bursting force and the flange width for the models with a web thickness equal to 1.5 in. As can be noticed, the characteristic of each plot in the figure is similar but different in magnitude. The $d_{burst-web}$ value rapidly increases at the beginning and then develops at a slower rate for flange widths greater than 16 in. According to Fig. 4.32, the plots of the web bursting force magnitude for symmetrical I-sections have the same type of variation with increase in the width of the flange. Both web bursting force magnitude and location increase quickly with increases in width for narrow flanges and slightly decrease in rate of increase as the flange width approaches the largest value of 56 in.

Figure 4.50 shows the behavior of the bursting force location in the flange with respect to the width of flange. The variation of the plots is opposite to that which occurs in the web. All plots have low slope for narrow flange width and show increases in the slope as the flange width becomes greater. The models with the same thickness ratio have the same variation.

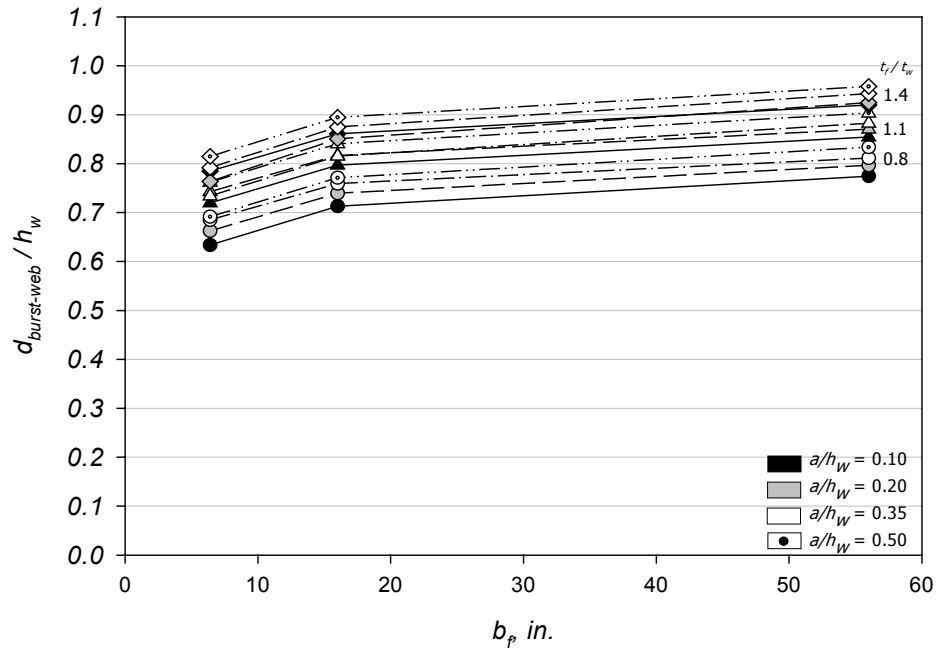


Fig. 4.49 WEB BURSTING FORCE LOCATION vs. FLANGE WIDTH FOR SYMMETRICAL I-SECTION ($t_w = 1.5$ in.)

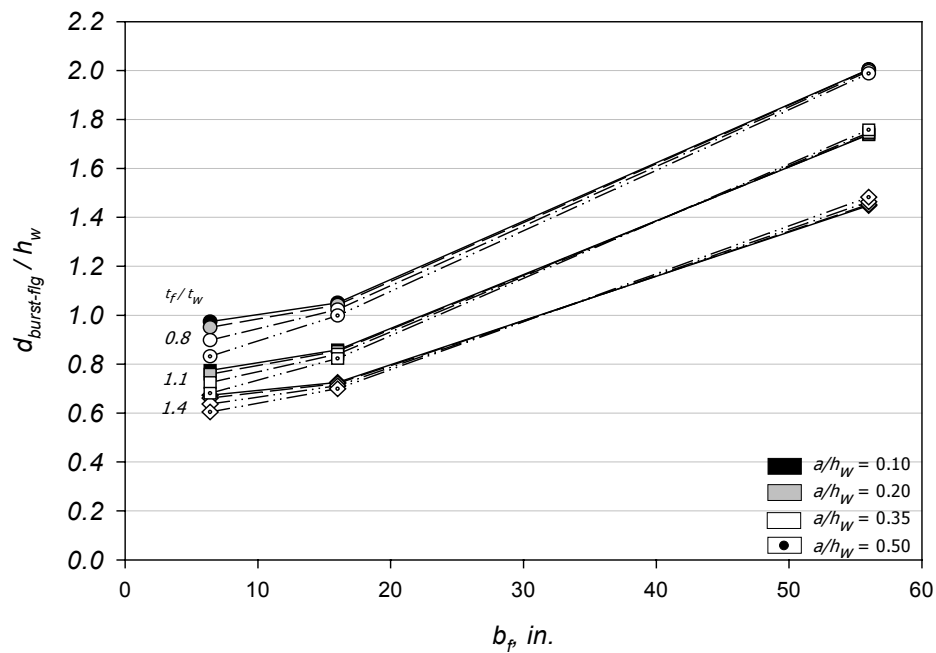


Fig. 4.50 FLANGE BURSTING FORCE LOCATION vs. FLANGE WIDTH FOR SYMMETRICAL I-SECTION ($t_w = 1.5$ in.)

It is clearly seen that the size of the flange in symmetrical I-sections significantly influences the behavior of the bursting force magnitude and location. In the web, the behavior of the bursting force magnitude and location exhibit a similar trend to those in rectangular sections. Since the presence of the flange changes the magnitude and location of the bursting force, the formulations for estimating them should contain the variable of flange dimension. It is noted that all the behaviors of bursting stresses occurring in the flanged section models are related to the dimension of each element comprising a flanged section. Therefore, an initial assumption to develop formulations to calculate bursting force magnitudes and locations of the forces can be made. The forces should depend on the proportion of the member areas in the section.

4.4.1.1.3.2 T-Section

In this section, the bursting force location in the T-section model is investigated. Fig. 4.51 shows the relation between the location of the web bursting force and the thickness ratio of T-section models. Similar to those presented in the study of bursting force, only the models with a flange width equal to 6.4 in. are used for the illustration. All plots also show the same characteristics as those occurring for the study of bursting force magnitude. No significant variation of the location of the web bursting force with the thickness ratio is found in the figure.

Figures 4.52 and 4.53 show the relation of the bursting force location of both the web and flange and the thickness ratio for the models with different flange width. As the t_f/t_w ratio increases, all plots exhibit a slight variation. In Fig. 4.53, as t_f/t_w ratio increases, the location of the flange bursting force in some plots decreases. This is similar to those occurring in symmetrical I-section models. However, the location of the bursting force for the model with the widest flange width has a very high magnitude compared to those of the models with smaller flanges.

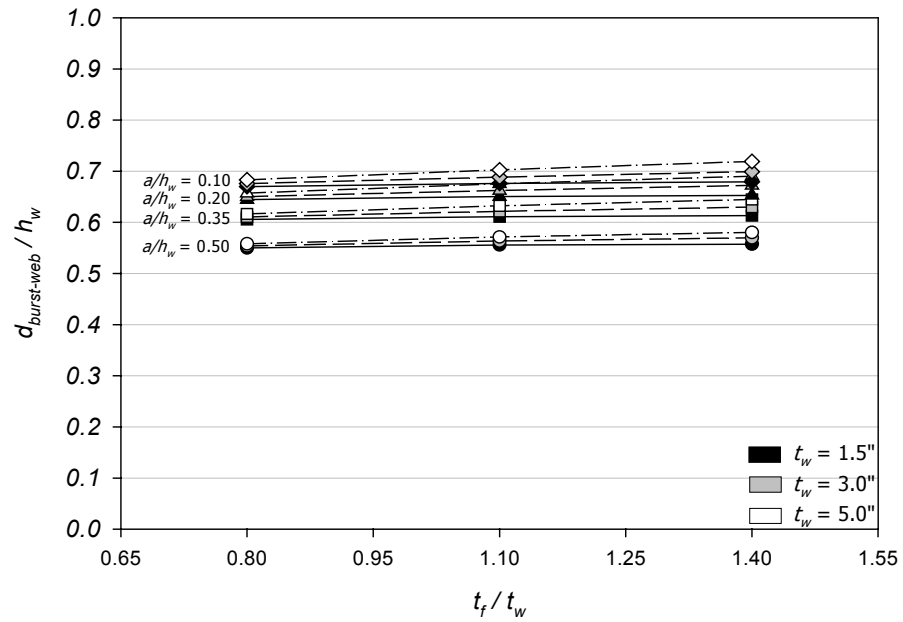


Fig. 4.51 WEB BURSTING FORCE LOCATION vs. THICKNESS RATIO FOR T-SECTION ($b_f = 6.4$ in.)

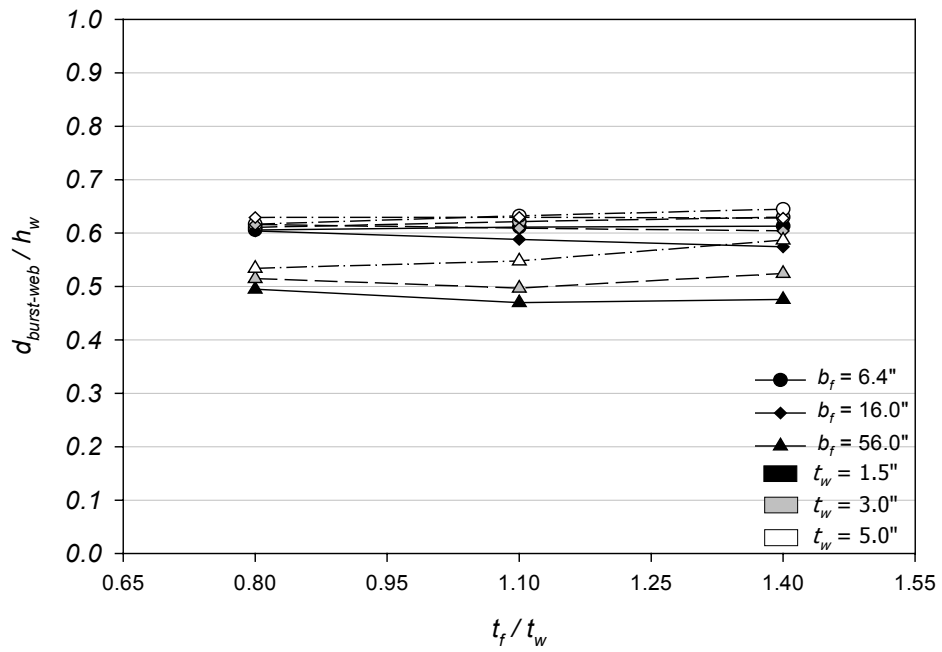


Fig. 4.52 WEB BURSTING FORCE LOCATION vs. THICKNESS RATIO FOR T-SECTION ($a/h_w = 0.20$)

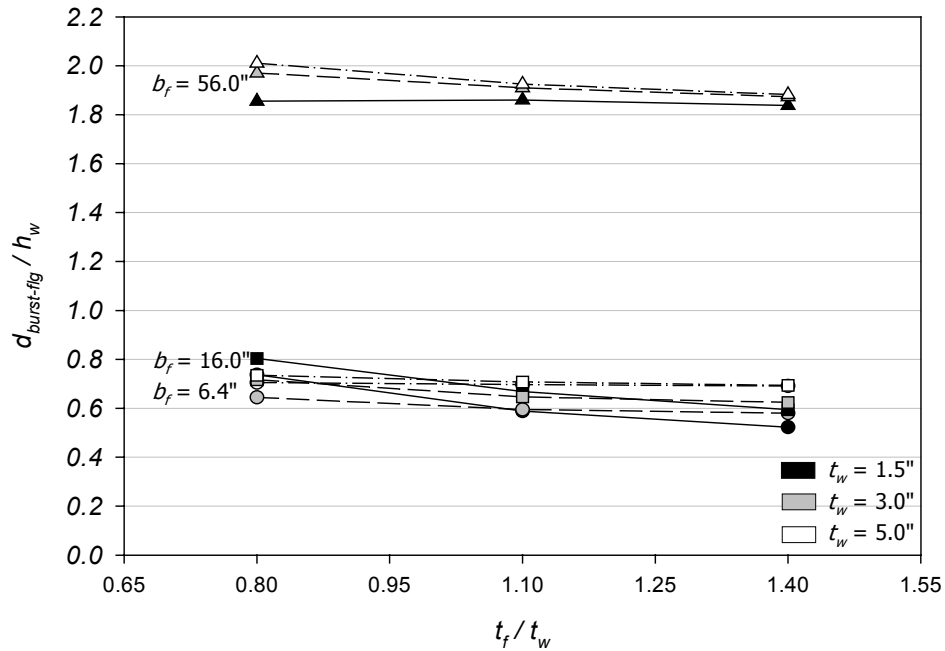


Fig. 4.53 FLANGE BURSTING FORCE LOCATION vs. THICKNESS RATIO FOR T-SECTION ($a/h_w = 0.20$)

In T-sections, the prestressing load is only transferred into one flange, which results in a large magnitude of flange bursting force. Therefore, the large distance of bursting force location in the flange is consistent with the magnitude of the force. For the models with flange widths of 6.4 and 16 in. (see Fig. 4.53), the bursting force location in the flanges of the models is similar. This indicates the significance of the position of the centroid, which affects the location of the bursting force, just as it affects the magnitude of the bursting force in T-sections.

Figure 4.54 shows the bursting force locations in both the web and the flange with respect to the anchorage ratio. As can be seen, the plot of bursting force location in the web looks similar to that for symmetrical section models. For the bursting force location in the flange, the plot obviously decreases as the anchor plate size increases. After comparing the plot with that in the study of symmetrical I-sections, the plot of the models with the same flange geometry in the previous study exhibits the same trend.

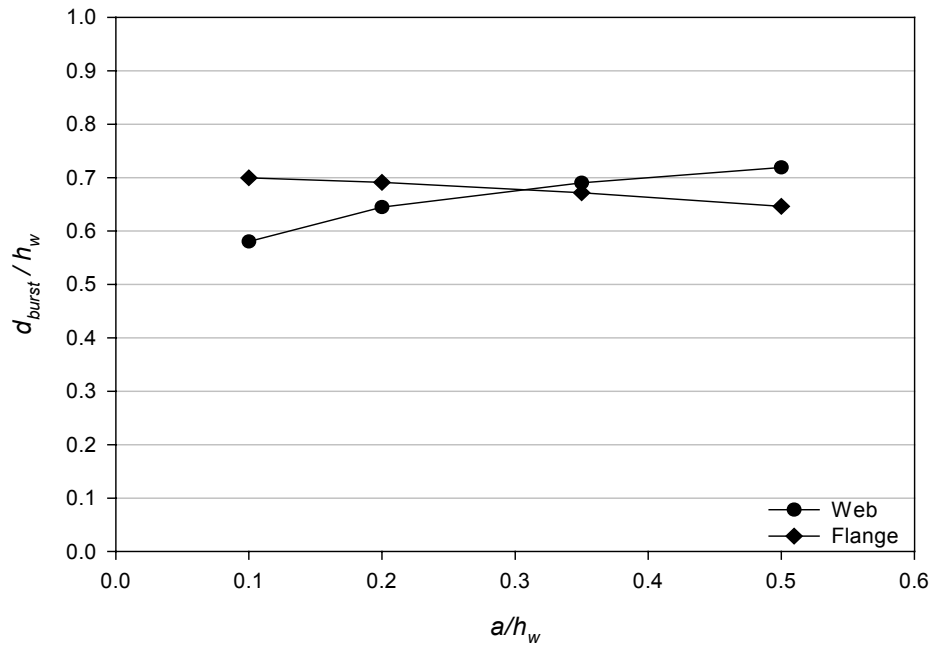


Fig. 4.54 BURSTING FORCE LOCATION vs. ANCHORAGE RATIO FOR T-SECTION
 ($b_f = 6.4$ in., $t_f/t_w = 1.4$, and $t_w = 5$ in.)

In Fig. 4.55, the location of the web bursting force in T-sections shows a different relation to flange width from that in symmetrical I-sections. The location decreases slightly as the flange width increases. This is caused by the reduction of the bursting region because the position of the prestressing force application is close to the center of the flange. The bursting force location in the flange of T-section models has the same variation as those occurring in the study of symmetrical I-sections. However, it has a larger magnitude than the symmetrical I-section models.

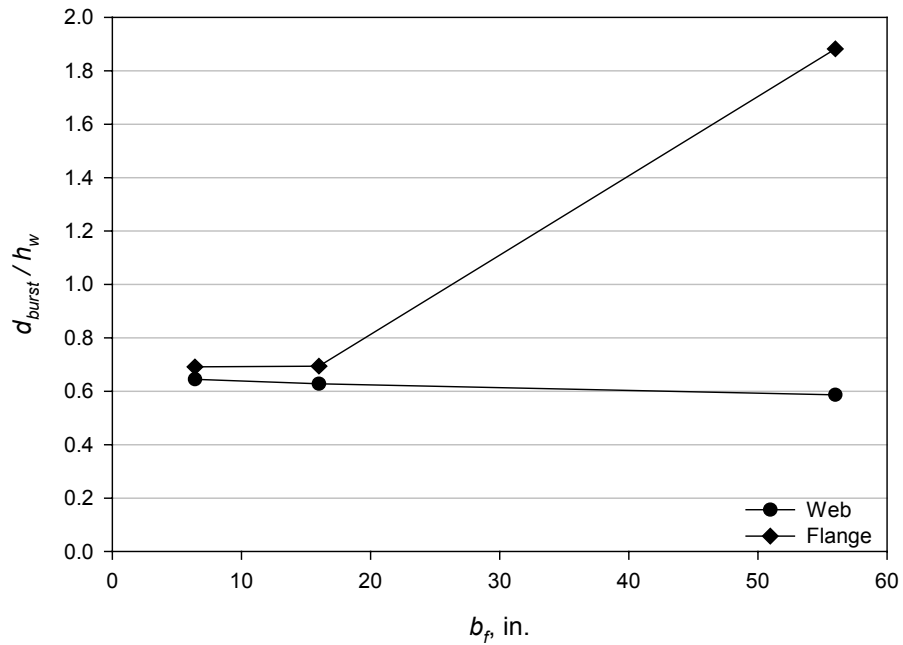


Fig. 4.55 BURSTING FORCE LOCATION vs. FLANGE WIDTH FOR T-SECTION
 ($a/h_w = 0.20$, $t_f/t_w = 1.4$, and $t_w = 5$ in.)

4.4.1.1.3.3 Unsymmetrical I-Section

Just as for the magnitude of the bursting force, the location of the bursting force in unsymmetrical I-section models establishes the transition between symmetrical I-sections and T-sections. Figs. 4.56 and 4.57 show the relation between the bursting force locations in the web and the flange, respectively, and the ratio of the bottom flange width to the top flange width (b_{f2}/b_{f1}). In Fig. 4.56, the relation between the web bursting force location and the b_{f2}/b_{f1} ratio exhibits a variation in the plots similar to those of the bursting force magnitude as shown in Fig. 4.39. In Fig. 4.57, the plots of the bursting force location also exhibit the same trend as plots of bursting force magnitude. These two figures present the relationship among these three types of flanged sections, which are all dependent on the geometric configuration of the flange.

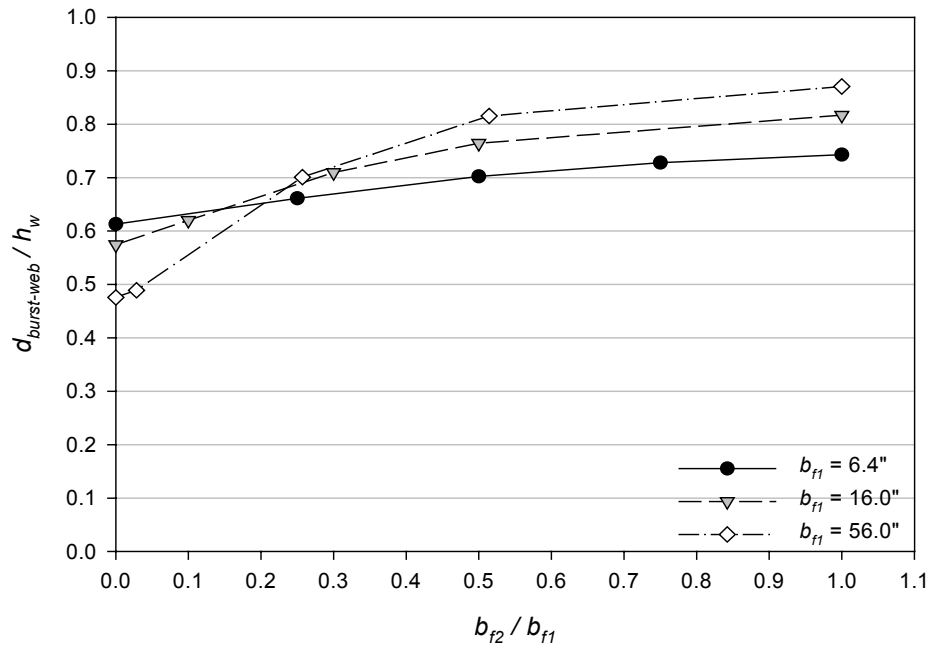


Fig. 4.56 WEB BURSTING FORCE LOCATION vs. FLANGE WIDTH RATIO
 ($a/h_w = 0.20$, $t_w = 1.5$ in., and $t_f/t_w = 1.40$)

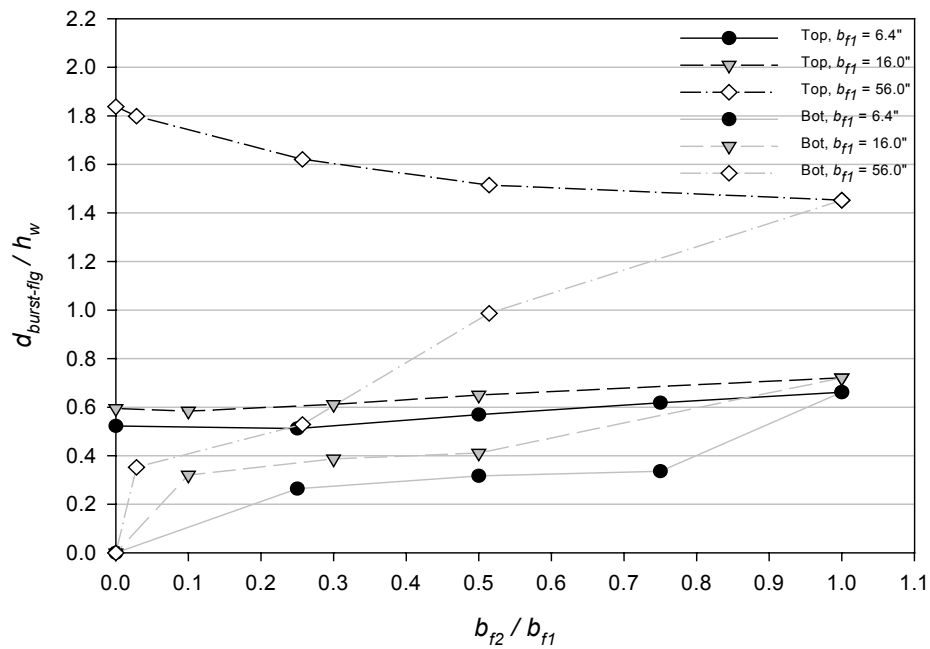


Fig. 4.57 FLANGE BURSTING FORCE LOCATION vs. FLANGE WIDTH RATIO
 ($a/h_w = 0.20$, $t_w = 1.5$ in., and $t_f/t_w = 1.40$)

4.4.1.2 Formulations

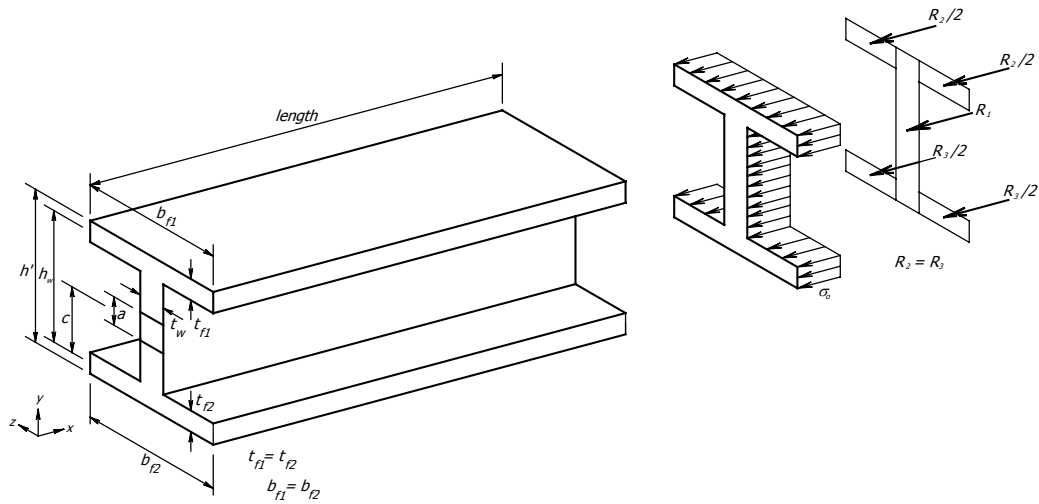
After investigating all flanged sections, it has been shown that the dimension of each member in the section has a major influence on the behavior of the bursting force magnitude and location. The area of the total section, which consists of a web and flanges, is described by the dimensioning parameters such as t_w , h_w , t_f , and b_f . For concentric load configuration, the application of prestressing load results in a uniform stress state at the end of the anchorage zone. The resultant force on each member, web or flange, can be easily calculated by multiplying the area of each member by the magnitude of the uniform stress. This resultant force is then used for the estimation of the bursting force magnitude.

Fig. 4.58 presents the pictures of anchorage zone structures with a uniform stress at the end for all types of flanged sections used in the present study. The geometric variables are also presented in the figure. Two new geometric parameters are introduced consisting of h' and c . The parameter h' is the total height of the flanged section, which is determined from the height of the web plus half of the thickness of each flange. If the bottom flange is not present as in T-section, h' is the height of the web plus half of the top flange thickness only. The value of c is the distance from the section centroid to the center of the bottom flange. If the bottom flange is not present, it is measured from the bottom fiber of the section.

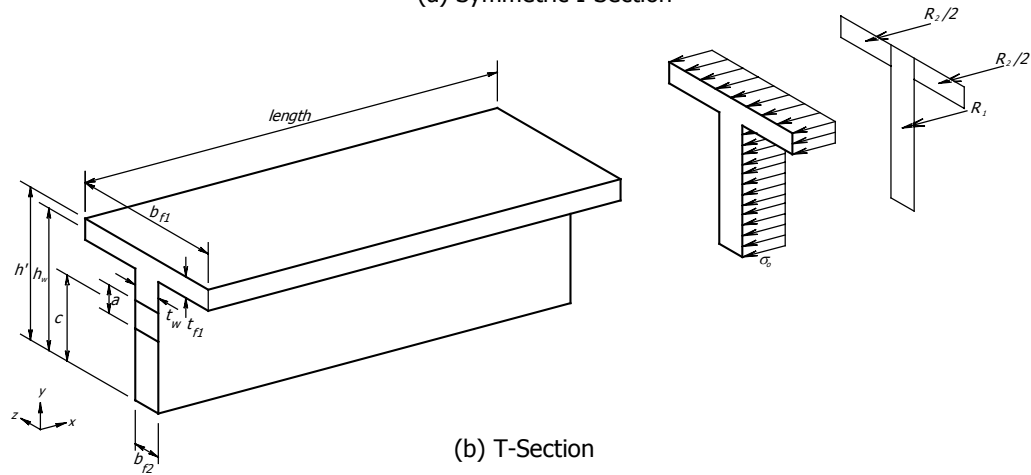
To develop an expression to calculate the bursting force magnitude, an effective tool is the Strut-and-Tie Model (STM) approach. A tie is usually placed in the position where the bursting force occurs. After the structure of a strut-and-tie model is created, the calculation of the forces in the members provides the magnitude of the bursting force in a tie. The method is very effective for the present study since it can relate the external forces to the member forces inside the structure. Based on a uniform stress at the end of the anchorage zone as shown in Fig. 4.58, the external forces can be determined based on each area of the flanged section.

As shown in Fig. 4.58, force R_1 represents the total force occurring in the web including some part of the flange. The area in which the force R_1 applies can be calculated by multiplying the total height of the section (h') with the thickness of the web (t_w). Forces R_2

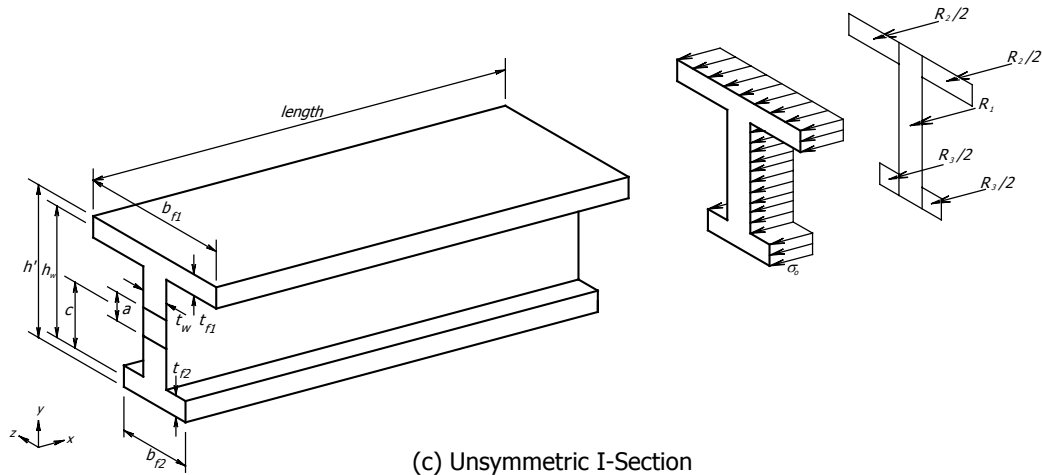
and R_3 represent the forces in part of the top and bottom flange, respectively. The area in which forces R_2 and R_3 apply can be determined by multiplying the thickness of the flange (t_f) with the partial flange width, which is equal to the width of the flange (b_f) minus the thickness of the web (t_w). The magnitudes of R_1 to R_3 for concentrically loaded anchorage zones can be determined from the uniform stress at the end of the anchorage zone multiplied by the corresponding area of the force.



(a) Symmetric I-Section



(b) T-Section



(c) Unsymmetric I-Section

Fig. 4.58 SYMBOLS OF GEOMETRIC PROPERTIES AND RESULTANT FORCES IN MEMBERS OF FLANGED SECTIONS

4.4.1.2.1 Symmetrical I-Section

The formulation presented herein is for the estimation of bursting force magnitude for a symmetrical I-section. Fig. 4.59 shows a side view of the structure of a strut-and-tie model developed for describing the behavior of the forces within a symmetrical flanged section. Based on the finite element study, the members within the model can be located. The secondary nodes ahead of the anchor plate are placed at the distance $a/4$. Since the structure of the model is symmetric about a horizontal axis, the forces can be divided into two equal sets. At the end of the structure, half of the force R_1 and the force R_2 in the flange area are used for each portion of the structure. The structure of the strut-and-tie model in Fig. 4.59 can be considered as two individual trusses. The first truss contains tie 2-5 and the second contains tie 3-6. As can be seen in Fig. 4.59, strut 1-2 is inclined with an angle α_1 . The strut connects the local zone node to the intersection point of the horizontal strut and tie 2-5. In the figure, T_{b1} is the magnitude of the bursting force in tie 2-5. The position of tie 2-5 is at a distance d_{b1} from the prestressing surface.

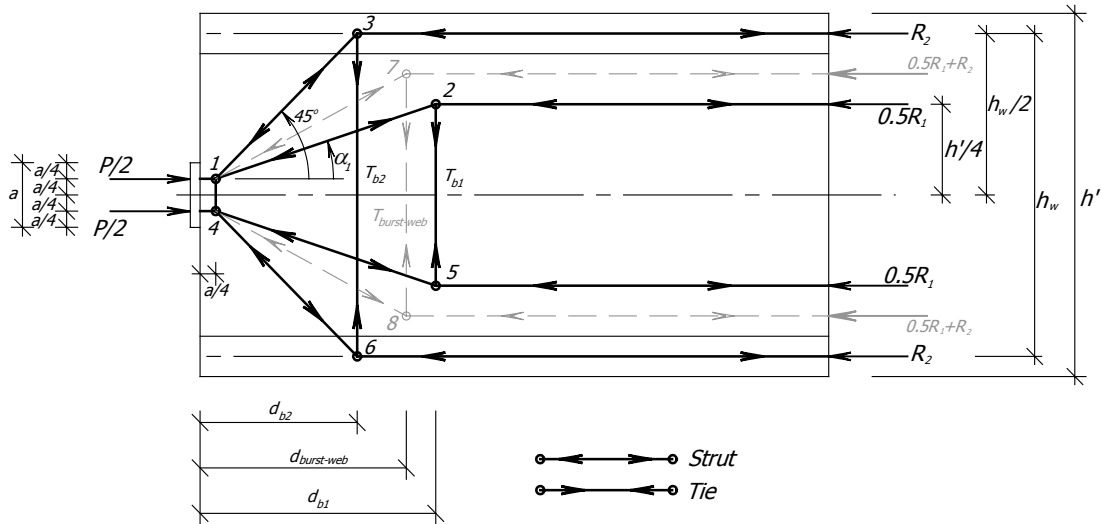


Fig. 4.59 STRUT-AND-TIE MODEL FOR THE FORMULATION OF SYMMETRICAL I-SECTION

The second truss contains tie 3-6. Two inclined struts consisting of struts 1-3 and 4-6 connect the local zone nodes to the centerline of each flange at an angle of 45 degrees. This 45 degree angle is chosen based on the study of the finite element models, which indicate the

direction of the principal compressive stress to be approximately at 45 degrees from a horizontal line. Tie member 3-6 connects the nodes in the top and bottom flanges and is located at a distance d_{b2} from the prestressing surface. The tensile force has magnitude T_{b2} . Nodes 3 and 6 are located at the position where the inclined struts transfer the compressive forces into each flange. In Fig. 4.59, the total web bursting force in the structure ($T_{burst-web}$) is the combination of two tensile forces, T_{b1} and T_{b2} . Therefore the location of the web bursting force ($d_{burst-web}$) is the centroid of the forces T_{b1} and T_{b2} .

According to Fig. 4.58, the values of R_1 and R_2 can be determined from the equations:

$$R_1 = |\sigma_o|(h't_w) \quad (4.1)$$

$$R_2 = |\sigma_o|((b_f - t_w) \times t_f) \quad (4.2)$$

where σ_o is equal to $P/(h't_f + 2(b_f - t_w) \times t_f)$. The relation of angle α_1 to the dimension and the forces in the model can be written as

$$\tan \alpha_1 = \frac{h'/4 - a/4}{d_{b1} - a/4} = \frac{T_{b1}}{R_1/2} \quad (4.3)$$

This leads to the equation

$$d_{b1} = \frac{R_1/2}{T_{b1}} \left(\frac{h'}{4} - \frac{a}{4} \right) + \frac{a}{4} \quad (4.4)$$

The equation for $d_{burst-web}$ can be determined from the centroid of the forces T_{b1} and T_{b2} . Since strut 1-3 has an angle of 45 degrees, the magnitude of T_{b2} equals force R_2 . Similarly distance d_{b2} can be replaced by $h_w/2$. The equation for $d_{burst-web}$ can be determined from the following equation:

$$d_{burst-web} = \frac{T_{b1}d_{b1} + R_2(h_w/2)}{T_{burst-web}} \quad (4.5)$$

By substituting equation (4.4) into equation (4.5), the equation for $T_{burst-web}$ can be written as follows:

$$T_{burst-web} = \left[\frac{R_1}{2} + \left(\frac{2h_w - a}{h' - a} \right) R_2 \right] \left(\frac{h'}{4d_{burst-web} - a} \right) \left(1 - \frac{a}{h'} \right) \quad (4.6)$$

Equation (4.6) can be used to determine the magnitude of the web bursting force of an anchorage zone with symmetrical I-section. However, the value of $d_{burst-web}$ is unknown. Therefore, an expression to estimate the value of $d_{burst-web}$ needs to be created.

It is noted that equation (4.6) can be used to determine the bursting force in a rectangular section anchorage zone as well. If the section of an anchorage zone contains no flange, the thickness and the width of the flange become zero. Therefore the value of R_2 becomes zero. The dimension h' can be replaced by h , which is the height of a rectangular beam. The value of $d_{burst-web}$ can be substituted by the equation to calculate the bursting force location in a rectangular section, which gives the value of $d_{burst-web}$ equal to $h/2+a/4$. By substituting all information, equation (4.6) becomes $R_1/4 \times (1-a/h)$. In a rectangular section, the value of R_1 is equal to P since the area of the flange does not exist. Therefore, the equation is identical to that used for the calculation of T_{burst} in a rectangular section subjected to a concentric load, which is equal to $P/4 \times (1-a/h)$.

Since the previous section already presented the behavior of $d_{burst-web}$, it is known that the flange of a symmetrical I-section has a significant effect on the behavior of $d_{burst-web}$. As can be seen in Fig. 4.49, the variation of each plot of $d_{burst-web}$ from all models is very similar but different in magnitude due to the different thickness ratio. However, to find an accurate equation, a more refined plot needs to be used.

Figure 4.60 shows the behavior of $d_{burst-web}$ with respect to the flange width for a model of a symmetrical I-section. Section detail information is given below Fig. 4.60. After using a refined plot, the variation of $d_{burst-web}$ is illustrated with greater detail. Two approximate equations, named equation (a) and equation (b), are also given for comparison. Equation (a) is created from an exponential function based on the characteristic of the finite element plot. The purpose of using equation (a) is to give a close approximation to the value of $d_{burst-web}$. Equation (b) is created with simple linear equations for the purpose of providing a less complicated mathematical function. As shown in Fig. 4.60, the plot of equation (a) develops very similarly to the finite element result. Only the magnitudes of the plots are different

from each other. For equation (b), the equation is separated into two segments based on the limiting value $b_f = (1.5 \times h_w)$. Both equations give close approximations to the plot from finite element model.

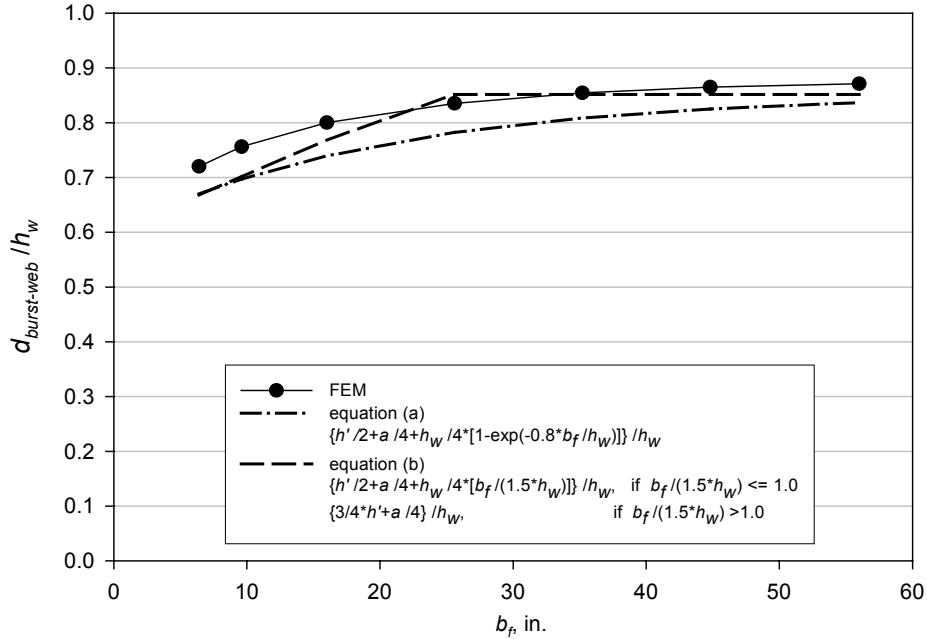


Fig. 4.60 WEB BURSTING FORCE LOCATION vs. FLANGE WIDTH FOR SYMMETRICAL I-SECTION ($t_w = 1.5$ in., $t_f/t_w = 1.4$, and $a/h_w = 0.20$)

Table 4.3 shows a comparison between finite element results and the estimated values using equation (a). The first eight columns next to the name of the model in the table contain geometric information for the model and the next two columns present the values of R_1 and R_2 in terms of P . The next three columns show the bursting force location in the web from the finite element method and from equation (a) along with the percent difference between them. For the magnitude of bursting force, the results from the finite element method and from the equation as well as their percent difference are given in the last three columns. The columns named $d_{burst-wfem}$ and $T_{burst-wfem}$ indicate results from the finite element method, while the columns named $d_{burst-web}$ and $T_{burst-web}$ present those using the approximate equations.

As can be seen from Table 4.3, the estimation based on equation (a) provides a reasonably close value of $d_{burst-web}$ to the result from finite element analysis. The group of models with

the thickness of the web equal to 5 in. contains positive percent differences between $d_{burst-web}$ and $d_{burst-wfem}$. However, they indicate a small number less than 10 percent. The comparison of bursting force magnitude based on the value of $d_{burst-web}$ using equation (a) produces a series of negative percent differences, which occur in the same group that contains positive percent differences of d_{burst} . However, all the values of negative percent differences of these models are very small as well.

Table 4.3 COMPARISON OF $d_{burst-web}$ FOR SYMMETRICAL I-SECTION USING EQUATION (a) SUBJECTED TO CONCENTRIC LOAD

Name	a/h	a	h_w	t_w	t_f/t_w	t_f	b_f	h'	R_1/P	R_2/P	$d_{burst-wfem}$	$d_{burst-web}$	%diff	$T_{burst-wfem}$	$T_{burst-web}$	%diff
		(in.)	(in.)	(in.)	(in.)	(in.)	(in.)	(in.)				/h _w	/h _w	-1 & 2-	/P	/P
FS211A	0.2	3.2	16	1.5	1.1	1.65	6.4	17.65	0.62	0.19	0.7200	0.6700	-6.94	0.2298	0.2506	9.06
FS211H	0.2	3.2	16	1.5	1.1	1.65	9.6	17.65	0.50	0.25	0.7554	0.6969	-7.75	0.2361	0.2616	10.78
FS211B	0.2	3.2	16	1.5	1.1	1.65	16	17.65	0.36	0.32	0.7968	0.7392	-7.22	0.2422	0.2685	10.84
FS211I	0.2	3.2	16	1.5	1.1	1.65	25.6	17.65	0.25	0.38	0.8263	0.7821	-5.36	0.2455	0.2691	9.61
FS211J	0.2	3.2	16	1.5	1.1	1.65	35.2	17.65	0.19	0.40	0.8425	0.8086	-4.03	0.2467	0.2682	8.70
FS211K	0.2	3.2	16	1.5	1.1	1.65	44.8	17.65	0.16	0.42	0.8502	0.8249	-2.97	0.2472	0.2677	8.31
FS211C	0.2	3.2	16	1.5	1.1	1.65	56	17.65	0.13	0.44	0.8545	0.8364	-2.12	0.2474	0.2678	8.25
FS231A	0.2	3.2	16	3	1.1	3.3	6.4	19.3	0.72	0.14	0.7274	0.7216	-0.80	0.2272	0.2286	0.59
FS231H	0.2	3.2	16	3	1.1	3.3	9.6	19.3	0.57	0.21	0.7654	0.7484	-2.22	0.2327	0.2411	3.60
FS231B	0.2	3.2	16	3	1.1	3.3	16	19.3	0.40	0.30	0.8110	0.7908	-2.49	0.2375	0.2498	5.15
FS231I	0.2	3.2	16	3	1.1	3.3	25.6	19.3	0.28	0.36	0.8446	0.8336	-1.31	0.2398	0.2517	4.98
FS231J	0.2	3.2	16	3	1.1	3.3	35.2	19.3	0.21	0.39	0.8616	0.8601	-0.17	0.2405	0.2515	4.57
FS231K	0.2	3.2	16	3	1.1	3.3	44.8	19.3	0.17	0.41	0.8720	0.8765	0.52	0.2409	0.2514	4.35
FS231C	0.2	3.2	16	3	1.1	3.3	56	19.3	0.14	0.43	0.8772	0.8879	1.23	0.2411	0.2517	4.41
FS231A	0.2	3.2	16	5	1.1	5.5	6.4	21.5	0.87	0.06	0.7389	0.7903	6.96	0.2237	0.2070	-7.45
FS231H	0.2	3.2	16	5	1.1	5.5	9.6	21.5	0.68	0.16	0.7795	0.8172	4.84	0.2283	0.2206	-3.37
FS231B	0.2	3.2	16	5	1.1	5.5	16	21.5	0.47	0.26	0.8295	0.8595	3.63	0.2322	0.2303	-0.83
FS231I	0.2	3.2	16	5	1.1	5.5	25.6	21.5	0.32	0.34	0.8681	0.9024	3.95	0.2338	0.2330	-0.33
FS231J	0.2	3.2	16	5	1.1	5.5	35.2	21.5	0.24	0.38	0.8871	0.9289	4.71	0.2341	0.2332	-0.38
FS231K	0.2	3.2	16	5	1.1	5.5	44.8	21.5	0.20	0.40	0.8990	0.9453	5.15	0.2343	0.2333	-0.44
FS231C	0.2	3.2	16	5	1.1	5.5	56	21.5	0.16	0.42	0.9052	0.9567	5.68	0.2343	0.2336	-0.31

Table 4.4 shows a comparison of finite element results and those using equation (b) in Fig. 4.60. The comparison of the models with the web thickness of 1.65 and 3.3 in. indicate a good estimation using equation (b). However, some negative percent differences of the magnitude of bursting force are detected from the comparison of these models. For the models with the web thickness of 5 in., the estimation using equation (b) results in all negative percent differences. The largest negative percent difference detected from the models is -15.70. This occurs in the model with the flange width equal to $1.6h_w$, just after the transition from the first to the second straight line. The finite element plot falls below equation (b) as can be seen in the example in Fig. 4.60. Therefore, it is obviously shown that

the calculation of $d_{burst-web}$ using equation (a) results in a better estimation of $T_{burst-web}$ than that using equation (b)

Table 4.4 COMPARISON OF $d_{burst-web}$ FOR SYMMETRICAL I-SECTION USING EQUATION (b) SUBJECTED TO CONCENTRIC LOAD

Name	a/h	a (in.)	h_w (in.)	t_w (in.)	t_f/t_w	t_f (in.)	b_f (in.)	h' (in.)	R_1/P	R_2/P	$d_{burst-wfem}$	$d_{burst-web}$	%diff	$T_{burst-wfem}$	$T_{burst-web}$	%diff
											/h _w -1-	/h _w -2-	-1 & 2-	/P -3-	/P -4-	-3 & 4-
FS211A	0.2	3.2	16	1.5	1.1	1.65	6.4	17.65	0.62	0.19	0.7200	0.6682	-7.19	0.2298	0.2514	9.38
FS211H	0.2	3.2	16	1.5	1.1	1.65	9.6	17.65	0.50	0.25	0.7554	0.7016	-7.13	0.2361	0.2597	9.98
FS211B	0.2	3.2	16	1.5	1.1	1.65	16	17.65	0.36	0.32	0.7968	0.7682	-3.58	0.2422	0.2577	6.37
FS211I	0.2	3.2	16	1.5	1.1	1.65	25.6	17.65	0.25	0.38	0.8263	0.8773	6.17	0.2455	0.2381	-3.02
FS211J	0.2	3.2	16	1.5	1.1	1.65	35.2	17.65	0.19	0.40	0.8425	0.8773	4.13	0.2467	0.2459	-0.34
FS211K	0.2	3.2	16	1.5	1.1	1.65	44.8	17.65	0.16	0.42	0.8502	0.8773	3.20	0.2472	0.2508	1.45
FS211C	0.2	3.2	16	1.5	1.1	1.65	56	17.65	0.13	0.44	0.8545	0.8773	2.68	0.2474	0.2546	2.88
FS231A	0.2	3.2	16	3	1.1	3.3	6.4	19.3	0.72	0.14	0.7274	0.7198	-1.04	0.2272	0.2292	0.86
FS231H	0.2	3.2	16	3	1.1	3.3	9.6	19.3	0.57	0.21	0.7654	0.7531	-1.61	0.2327	0.2395	2.91
FS231B	0.2	3.2	16	3	1.1	3.3	16	19.3	0.40	0.30	0.8110	0.8198	1.09	0.2375	0.2404	1.19
FS231I	0.2	3.2	16	3	1.1	3.3	25.6	19.3	0.28	0.36	0.8446	0.9547	13.03	0.2398	0.2180	-9.07
FS231J	0.2	3.2	16	3	1.1	3.3	35.2	19.3	0.21	0.39	0.8616	0.9547	10.80	0.2405	0.2252	-6.36
FS231K	0.2	3.2	16	3	1.1	3.3	44.8	19.3	0.17	0.41	0.8720	0.9547	9.48	0.2409	0.2297	-4.67
FS231C	0.2	3.2	16	3	1.1	3.3	56	19.3	0.14	0.43	0.8772	0.9547	8.84	0.2411	0.2331	-3.29
FS231A	0.2	3.2	16	5	1.1	5.5	6.4	21.5	0.87	0.06	0.7389	0.7885	6.72	0.2237	0.2075	-7.23
FS231H	0.2	3.2	16	5	1.1	5.5	9.6	21.5	0.68	0.16	0.7795	0.8219	5.44	0.2283	0.2192	-3.96
FS231B	0.2	3.2	16	5	1.1	5.5	16	21.5	0.47	0.26	0.8295	0.8885	7.12	0.2322	0.2223	-4.26
FS231I	0.2	3.2	16	5	1.1	5.5	25.6	21.5	0.32	0.34	0.8681	1.0578	21.86	0.2338	0.1971	-15.70
FS231J	0.2	3.2	16	5	1.1	5.5	35.2	21.5	0.24	0.38	0.8871	1.0578	19.25	0.2341	0.2034	-13.13
FS231K	0.2	3.2	16	5	1.1	5.5	44.8	21.5	0.20	0.40	0.8990	1.0578	17.67	0.2343	0.2072	-11.56
FS231C	0.2	3.2	16	5	1.1	5.5	56	21.5	0.16	0.42	0.9052	1.0578	16.86	0.2343	0.2102	-10.31

Since it is found that equation (a) of Fig. 4.60 gives a good estimation of the bursting force, it can be used for the calculation of the magnitude of the web bursting force as presented in equation (4.7). Therefore, equation (a) can be rewritten as

$$d_{burst-web} = \frac{h'}{2} + \frac{a}{4} + \frac{h_w}{4} (1 - \exp(-0.8b_f / h_w)) \quad (4.7)$$

The comparison in Table 4.4 indicates that the value of $T_{burst-web}$ is sensitive to the value of $d_{burst-web}$. A larger value of $d_{burst-web}$ compared to the value from the finite element result can cause the magnitude of $T_{burst-web}$ using equation (4.6) to be unconservative. By the application of equation (4.7), a good estimation of a web bursting force magnitude is produced. An additional comparison between the bursting force location and the magnitude of the force for symmetrical I-sections is given in Tables 4.5 and 4.6. As can be noticed from the table, the percent differences indicated in the comparison of bursting force in the last

column contain some negative values. The largest negative percent difference detected from the table is -8.33. This occurs in the case where the thickness of the section is as large as 5 in. while the width of the flange equals 6.4 in. The section contains a shape very close to a rectangular shape. Based on all percent differences from the comparison, equations (4.6) and (4.7) give a satisfying result in the estimation of web bursting force magnitude and the location of the force.

Table 4.5 COMPARISON OF $T_{burst-web}$ AND $d_{burst-web}$ FOR SYMMETRICAL I-SECTION SUBJECTED TO CONCENTRIC LOAD

Name	a/h	a (in.)	h _w (in.)	t _w (in.)	t _f /t _w	t _f (in.)	b _f (in.)	h'	R ₁ /P	R ₂ /P	$d_{burst-wfem}$			$T_{burst-wfem}$		
											/h _w -1-	/h _w -2-	%diff -1 & 2-	/P -3-	/P -4-	%diff -3 & 4-
FS210A	0.2	3.2	16	1.5	0.8	1.2	6.4	17.2	0.69	0.16	0.6915	0.6560	-5.14	0.2247	0.2402	6.93
FS210B	0.2	3.2	16	1.5	0.8	1.2	16	17.2	0.43	0.29	0.7710	0.7252	-5.95	0.2382	0.2603	9.29
FS210C	0.2	3.2	16	1.5	0.8	1.2	56	17.2	0.16	0.42	0.8336	0.8223	-1.35	0.2442	0.2667	9.22
FS220A	0.2	3.2	16	3	0.8	2.4	6.4	18.4	0.77	0.11	0.6949	0.6935	-0.21	0.2234	0.2222	-0.54
FS220B	0.2	3.2	16	3	0.8	2.4	16	18.4	0.47	0.27	0.7780	0.7627	-1.97	0.2358	0.2457	4.20
FS220C	0.2	3.2	16	3	0.8	2.4	56	18.4	0.18	0.41	0.8452	0.8598	1.73	0.2408	0.2545	5.68
FS240A	0.2	3.2	16	5	0.8	4	6.4	20	0.90	0.05	0.7010	0.7435	6.05	0.2213	0.2029	-8.33
FS240B	0.2	3.2	16	5	0.8	4	16	20	0.53	0.23	0.7887	0.8127	3.03	0.2323	0.2296	-1.14
FS240C	0.2	3.2	16	5	0.8	4	56	20	0.20	0.40	0.8660	0.9098	5.06	0.2363	0.2402	1.64
FS310A	0.35	5.6	16	1.5	0.8	1.2	6.4	17.2	0.69	0.16	0.7341	0.6935	-5.54	0.1893	0.2093	10.58
FS310B	0.35	5.6	16	1.5	0.8	1.2	16	17.2	0.43	0.29	0.8154	0.7627	-6.47	0.2058	0.2326	13.00
FS310C	0.35	5.6	16	1.5	0.8	1.2	56	17.2	0.16	0.42	0.8827	0.8598	-2.60	0.2129	0.2424	13.85
FS320A	0.35	5.6	16	3	0.8	2.4	6.4	18.4	0.77	0.11	0.7384	0.7310	-1.00	0.1881	0.1931	2.67
FS320B	0.35	5.6	16	3	0.8	2.4	16	18.4	0.47	0.27	0.8241	0.8002	-2.91	0.2034	0.2194	7.88
FS320C	0.35	5.6	16	3	0.8	2.4	56	18.4	0.18	0.41	0.8967	0.8973	0.07	0.2095	0.2313	10.38
FS340A	0.35	5.6	16	5	0.8	4	6.4	20	0.90	0.05	0.7463	0.7810	4.64	0.1859	0.1758	-5.39
FS340B	0.35	5.6	16	5	0.8	4	16	20	0.53	0.23	0.8383	0.8502	1.42	0.1996	0.2050	2.75
FS340C	0.35	5.6	16	5	0.8	4	56	20	0.20	0.40	0.9225	0.9473	2.69	0.2049	0.2184	6.61
FS510A	0.5	8	16	1.5	0.8	1.2	6.4	17.2	0.69	0.16	0.7636	0.7310	-4.28	0.1591	0.1784	12.09
FS510B	0.5	8	16	1.5	0.8	1.2	16	17.2	0.43	0.29	0.8506	0.8002	-5.93	0.1772	0.2048	15.58
FS510C	0.5	8	16	1.5	0.8	1.2	56	17.2	0.16	0.42	0.9246	0.8973	-2.96	0.1850	0.2181	17.91
FS520A	0.5	8	16	3	0.8	2.4	6.4	18.4	0.77	0.11	0.7682	0.7685	0.03	0.1581	0.1639	3.70
FS520B	0.5	8	16	3	0.8	2.4	16	18.4	0.47	0.27	0.8603	0.8377	-2.63	0.1750	0.1931	10.35
FS520C	0.5	8	16	3	0.8	2.4	56	18.4	0.18	0.41	0.9404	0.9348	-0.59	0.1819	0.2081	14.45
FS540A	0.5	8	16	5	0.8	4	6.4	20	0.90	0.05	0.7774	0.8185	5.29	0.1561	0.1488	-4.66
FS540B	0.5	8	16	5	0.8	4	16	20	0.53	0.23	0.8766	0.8877	1.26	0.1714	0.1805	5.30
FS540C	0.5	8	16	5	0.8	4	56	20	0.20	0.40	0.9680	0.9848	1.74	0.1772	0.1966	10.93

Table 4.6 COMPARISON OF $T_{burst-web}$ AND $d_{burst-web}$ FOR SYMMETRICAL I-SECTION
SUBJECTED TO CONCENTRIC LOAD (continued)

Name	a/h	a	h_w	t_w	t_f/t_w	t_f	b_f	h'	R_1/P	R_2/P	$d_{burst-wfem}$	$d_{burst-web}$	%diff	$T_{burst-wfem}$	$T_{burst-web}$	%diff
											/ h_w	/ h_w	-1 & 2-	/ P	/ P	-3 & 4-
FS211A	0.2	3.2	16	1.5	1.1	1.65	6.4	17.65	0.62	0.19	0.7200	0.6700	-6.94	0.2298	0.2506	9.06
FS211B	0.2	3.2	16	1.5	1.1	1.65	16	17.65	0.36	0.32	0.7968	0.7392	-7.22	0.2422	0.2685	10.84
FS211C	0.2	3.2	16	1.5	1.1	1.65	56	17.65	0.13	0.44	0.8545	0.8364	-2.12	0.2474	0.2678	8.25
FS231A	0.2	3.2	16	3	1.1	3.3	6.4	19.3	0.72	0.14	0.7274	0.7216	-0.80	0.2272	0.2286	0.59
FS231B	0.2	3.2	16	3	1.1	3.3	16	19.3	0.40	0.30	0.8110	0.7908	-2.49	0.2375	0.2498	5.15
FS231C	0.2	3.2	16	3	1.1	3.3	56	19.3	0.14	0.43	0.8772	0.8879	1.23	0.2411	0.2517	4.41
FS251A	0.2	3.2	16	5	1.1	5.5	6.4	21.5	0.87	0.06	0.7389	0.7903	6.96	0.2237	0.2070	-7.45
FS251B	0.2	3.2	16	5	1.1	5.5	16	21.5	0.47	0.26	0.8295	0.8595	3.63	0.2322	0.2303	-0.83
FS251C	0.2	3.2	16	5	1.1	5.5	56	21.5	0.16	0.42	0.9052	0.9567	5.68	0.2343	0.2336	-0.31
FS311A	0.35	5.6	16	1.5	1.1	1.65	6.4	17.65	0.62	0.19	0.7621	0.7075	-7.16	0.1959	0.2204	12.49
FS311B	0.35	5.6	16	1.5	1.1	1.65	16	17.65	0.36	0.32	0.8405	0.7767	-7.58	0.2110	0.2413	14.34
FS311C	0.35	5.6	16	1.5	1.1	1.65	56	17.65	0.13	0.44	0.9035	0.8739	-3.28	0.2168	0.2440	12.52
FS331A	0.35	5.6	16	3	1.1	3.3	6.4	19.3	0.72	0.14	0.7715	0.7591	-1.61	0.1933	0.2006	3.82
FS331B	0.35	5.6	16	3	1.1	3.3	16	19.3	0.40	0.30	0.8582	0.8283	-3.48	0.2062	0.2245	8.86
FS331C	0.35	5.6	16	3	1.1	3.3	56	19.3	0.14	0.43	0.9310	0.9254	-0.60	0.2104	0.2293	8.99
FS351A	0.35	5.6	16	5	1.1	5.5	6.4	21.5	0.87	0.06	0.7868	0.8278	5.22	0.1894	0.1817	-4.08
FS351B	0.35	5.6	16	5	1.1	5.5	16	21.5	0.47	0.26	0.8829	0.8970	1.60	0.2002	0.2071	3.44
FS351C	0.35	5.6	16	5	1.1	5.5	56	21.5	0.16	0.42	0.9670	0.9942	2.81	0.2031	0.2129	4.85
FS511A	0.5	8	16	1.5	1.1	1.65	6.4	17.65	0.62	0.19	0.7918	0.7450	-5.90	0.1668	0.1902	14.03
FS511B	0.5	8	16	1.5	1.1	1.65	16	17.65	0.36	0.32	0.8748	0.8142	-6.92	0.1834	0.2141	16.75
FS511C	0.5	8	16	1.5	1.1	1.65	56	17.65	0.13	0.44	0.9430	0.9114	-3.36	0.1900	0.2201	15.86
FS531A	0.5	8	16	3	1.1	3.3	6.4	19.3	0.72	0.14	0.8024	0.7966	-0.72	0.1644	0.1727	5.09
FS531B	0.5	8	16	3	1.1	3.3	16	19.3	0.40	0.30	0.8949	0.8658	-3.26	0.1788	0.1991	11.36
FS531C	0.5	8	16	3	1.1	3.3	56	19.3	0.14	0.43	0.9740	0.9629	-1.14	0.1840	0.2070	12.48
FS551A	0.5	8	16	5	1.1	5.5	6.4	21.5	0.87	0.06	0.8202	0.8653	5.51	0.1607	0.1563	-2.69
FS551B	0.5	8	16	5	1.1	5.5	16	21.5	0.47	0.26	0.9238	0.9345	1.16	0.1730	0.1839	6.32
FS551C	0.5	8	16	5	1.1	5.5	56	21.5	0.16	0.42	1.0165	1.0317	1.49	0.1767	0.1923	8.81
FS222A	0.2	3.2	16	1.5	1.4	2.1	6.4	18.1	0.57	0.22	0.7429	0.6841	-7.92	0.2332	0.2574	10.41
FS222B	0.2	3.2	16	1.5	1.4	2.1	16	18.1	0.31	0.35	0.8167	0.7533	-7.76	0.2441	0.2723	11.54
FS222C	0.2	3.2	16	1.5	1.4	2.1	56	18.1	0.11	0.45	0.8705	0.8504	-2.30	0.2479	0.2667	7.61
FS242A	0.2	3.2	16	3	1.4	4.2	6.4	20.2	0.68	0.16	0.7552	0.7497	-0.73	0.2290	0.2320	1.32
FS242B	0.2	3.2	16	3	1.4	4.2	16	20.2	0.36	0.32	0.8391	0.8189	-2.41	0.2370	0.2498	5.41
FS242C	0.2	3.2	16	3	1.4	4.2	56	20.2	0.12	0.44	0.9050	0.9160	1.22	0.2388	0.2470	3.47
FS272A	0.2	3.2	16	5	1.4	7	6.4	23	0.85	0.07	0.7733	0.8372	8.26	0.2244	0.2095	-6.62
FS272B	0.2	3.2	16	5	1.4	7	16	23	0.43	0.29	0.8678	0.9064	4.45	0.2309	0.2276	-1.40
FS272C	0.2	3.2	16	5	1.4	7	56	23	0.14	0.43	0.9499	1.0035	5.65	0.2319	0.2257	-2.68
FS322A	0.35	5.6	16	1.5	1.4	2.1	6.4	18.1	0.57	0.22	0.7848	0.7216	-8.06	0.2004	0.2279	13.72
FS322B	0.35	5.6	16	1.5	1.4	2.1	16	18.1	0.31	0.35	0.8611	0.7908	-8.16	0.2135	0.2457	15.07
FS322C	0.35	5.6	16	1.5	1.4	2.1	56	18.1	0.11	0.45	0.9201	0.8879	-3.49	0.2177	0.2433	11.76
FS342A	0.35	5.6	16	3	1.4	4.2	6.4	20.2	0.68	0.16	0.8008	0.7872	-1.70	0.1959	0.2052	4.73
FS342B	0.35	5.6	16	3	1.4	4.2	16	20.2	0.36	0.32	0.8890	0.8564	-3.67	0.2061	0.2254	9.36
FS342C	0.35	5.6	16	3	1.4	4.2	56	20.2	0.12	0.44	0.9623	0.9535	-0.91	0.2084	0.2254	8.17
FS372A	0.35	5.6	16	5	1.4	7	6.4	23	0.85	0.07	0.8248	0.8747	6.05	0.1907	0.1857	-2.65
FS372B	0.35	5.6	16	5	1.4	7	16	23	0.43	0.29	0.9268	0.9439	1.85	0.1990	0.2057	3.38
FS372C	0.35	5.6	16	5	1.4	7	56	23	0.14	0.43	1.0202	1.0410	2.04	0.2004	0.2061	2.81
FS522A	0.5	8	16	1.5	1.4	2.1	6.4	18.1	0.57	0.22	0.8147	0.7591	-6.83	0.1720	0.1983	15.30
FS522B	0.5	8	16	1.5	1.4	2.1	16	18.1	0.31	0.35	0.8946	0.8283	-7.42	0.1867	0.2190	17.29
FS522C	0.5	8	16	1.5	1.4	2.1	56	18.1	0.11	0.45	0.9579	0.9254	-3.39	0.1918	0.2199	14.63
FS542A	0.5	8	16	3	1.4	4.2	6.4	20.2	0.68	0.16	0.8330	0.8247	-1.00	0.1678	0.1784	6.30
FS542B	0.5	8	16	3	1.4	4.2	16	20.2	0.36	0.32	0.9263	0.8939	-3.50	0.1798	0.2011	11.84
FS542C	0.5	8	16	3	1.4	4.2	56	20.2	0.12	0.44	1.0065	0.9910	-1.54	0.1827	0.2037	11.52
FS572A	0.5	8	16	5	1.4	7	6.4	23	0.85	0.07	0.8611	0.9122	5.94	0.1628	0.1619	-0.55
FS572B	0.5	8	16	5	1.4	7	16	23	0.43	0.29	0.9708	0.9814	1.10	0.1726	0.1838	6.53
FS572C	0.5	8	16	5	1.4	7	56	23	0.14	0.43	1.0756	1.0785	0.27	0.1746	0.1864	6.79

In the formulation of the bursting force in the flange of a symmetrical I-section, the STM method can also be employed. Fig. 4.61 shows the strut-and-tie model of a flange. The struts and ties are located in the model based on the result from the finite element study. As previously mentioned in section 4.4.1.1.1, a flange member in some structures may contain more than one bursting stress region. As a result, the strut-and-tie model is developed to have two tie locations, which are located separately based on the position where the force from the web is applied. Since the strut from the web has a 45 degree angle, the position of the applied force is located at a distance equal to the distance between the center of the anchor plate and the center of the flange. The magnitude of the applied force in the direction of the flange axis must be equal to the resultant force R_2 at the end of the flange. The forces $R_2/2$ at the end of the flange are located at the positions shown in Fig. 4.61.

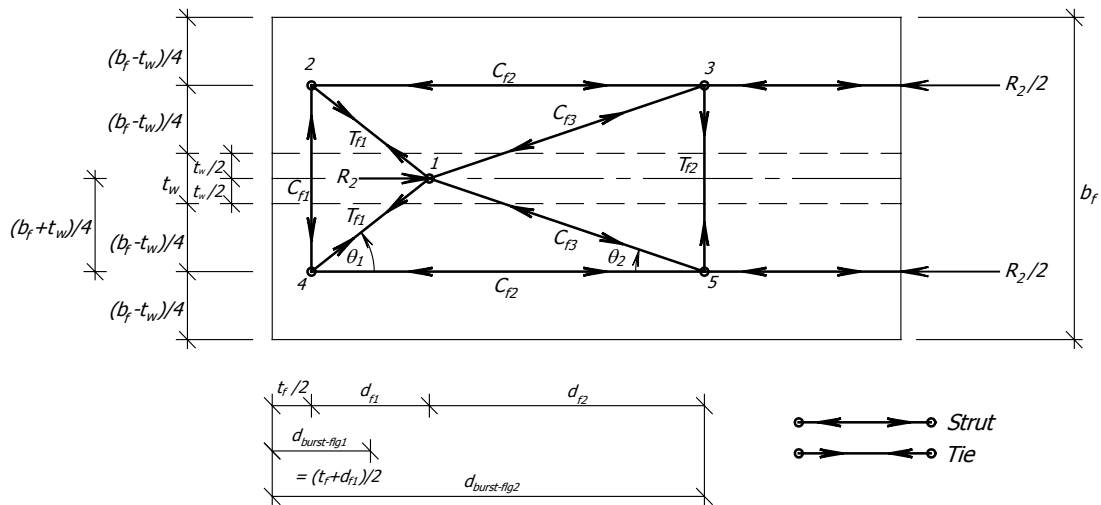


Fig. 4.61 STRUT-AND-TIE MODEL OF THE FLANGE FOR THE FORMULATIONS OF SYMMETRICAL I-SECTION

As can be seen in Fig. 4.61, the location of the applied force R_2 (node 1) is located at the distance of d_{f1} plus $t_f/2$. The distance $t_f/2$ is assigned as half of the width of strut 2-4, which carries a compressive force. The ties 1-2 and 1-4 are constructed based on the tensile forces occurring from a tieback effect because the force R_2 is applied at an intermediate location on the flange. Tie 3-5 is located at the distance d_{f2} from the position of the applied force R_2 . Since the model contains two tie locations, the tensile forces in the transverse direction of the flange are equal to $T_{f1} \sin \theta_1$ and T_{f2} . The position of the force $T_{f1} \sin \theta_1$ is located at the

distance $d_{burst-flg1}$ from the flange surface. Force T_{f2} is located at the distance $d_{burst-flg2}$. By considering equilibrium in the transverse direction of nodes 1 and 3, T_{f2} is equal to $T_{f1} \sin \theta_1$, which also equals $C_{f3} \sin \theta_2$. The equilibrium in the longitudinal direction at node 1 gives the following equation:

$$\frac{R_2}{2} = T_{f2} \left(\frac{1}{\tan \theta_1} + \frac{1}{\tan \theta_2} \right) \quad (4.8)$$

By substituting $\tan \theta_1 = \frac{(b_f + t_w)/4}{d_{f1}}$ and $\tan \theta_2 = \frac{(b_f + t_w)/4}{d_{f2}}$, equation (4.8) can be rewritten as

$$d_{f1} + d_{f2} = \frac{R_2}{T_{f2}} \left(\frac{b_f + t_w}{8} \right) \quad (4.9)$$

Because the location of the applied force R_2 is considered from the 45 degree inclined strut as stated earlier, the distance of the applied force location is equal to $h_w/2$ for the case of a symmetrical I-section. In Fig. 4.61, the distance of the applied force R_2 equals d_{f1} plus $t_f/2$, which also equals $h_w/2$. As a result, the expression for d_{f1} can be written as

$$d_{f1} = \frac{h_w}{2} - \frac{t_f}{2} \quad (4.10)$$

The position of the force $T_{f1} \sin \theta_1$ is located at the distance of $d_{burst-flg1}$, which equals $(d_{f1} + t_f)/2$. By using equation (4.10) for d_{f1} , the equation for determining $d_{burst-flg1}$ can be written as

$$d_{burst-flg1} = \frac{h_w/2}{2} + \frac{t_f}{4} \quad (4.11)$$

Since $d_{burst-flg2}$ equals $d_{f1} + d_{f2} + \frac{t_f}{2}$ (see Fig. 4.61), substituting the value of $d_{f1} + d_{f2}$ from equation (4.9), the equation for $d_{burst-flg2}$ can be written as

$$d_{burst-flg2} = \frac{R_2}{T_{f2}} \left(\frac{b_f + t_w}{8} \right) + \frac{t_f}{2} \quad (4.12)$$

Finally, by finding the centroid of the tensile forces $T_{f1} \sin \theta_1$ and T_{f2} with respect to the prestressing surface, an approximate equation for $d_{burst-flg}$ can be found from the following equation:

$$d_{burst-flg} = \frac{T_{f1} \sin \theta_1 \times d_{burst-flg1} + T_{f2} \times d_{burst-flg2}}{T_{burst-flg}} \quad (4.13)$$

where $T_{f1} \sin \theta_1 = T_{f2} = 0.5T_{burst-flg}$. By substituting equations (4.11) and (4.12) into equation (4.13), the approximate equation for $d_{burst-flg}$

$$d_{burst-flg} = \frac{h_w}{4} + \frac{3}{8}t_f + \frac{R_2}{T_{burst-flg}} \frac{(b_f + t_w)}{8} \quad (4.14)$$

Equation (4.14) contains an unknown, which is the magnitude of $T_{burst-flg}$. The expression to determine the value of $T_{burst-flg}$ can be formulated using the finite element results. After examining the behavior of the flange bursting force to find the best expression to determine the value of $T_{burst-flg}$, it was found that the best equation to describe the behavior of bursting force in a flange is related to the ratio of the force in the flange R_{flg} and the force on the area divided by the centroid of the section where the flange exists (R_{total}). The ratio is named k_f and can be calculated using the expression presented in Fig. 4.62. The expression shown in the figure is for the calculation of the k_f value for the top portion of the section.

The approximate equation used for the estimation of the magnitude of the flange bursting force can be expressed as

$$T_{burst-flg} = 0.15k_f^3 P \quad (4.15)$$

Fig. 4.63 shows an example of the comparison between the plot from finite element results and that using equation (4.15). As can be seen, both plots exhibit a similar trend.

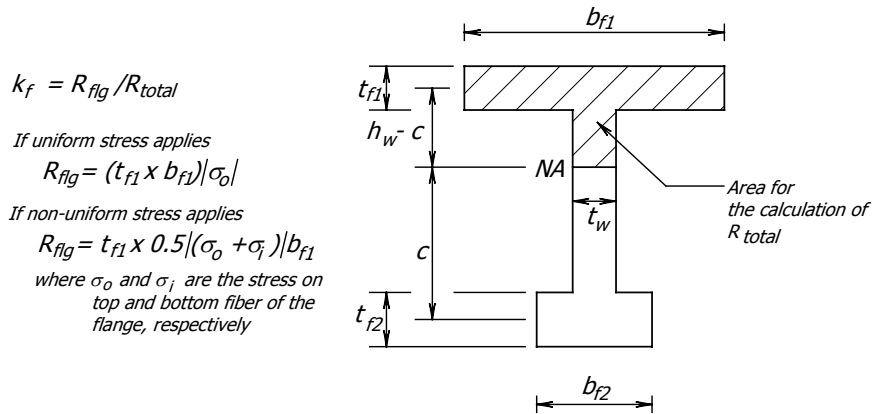


Fig. 4.62 k_f RATIO FOR THE TOP PORTION OF A FLANGED SECTION

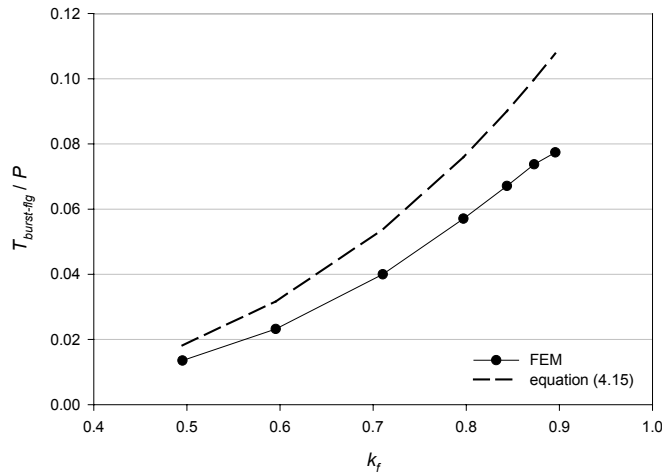


Fig. 4.63 FLANGE BURSTING FORCE LOCATION vs. k_f RATIO FOR SYMMETRICAL I-SECTION
 ($t_w = 1.5$ in., $t_f/t_w = 1.4$, and $a/h_w = 0.20$)

Tables 4.7 and 4.8 show the comparison of finite element results and those using equations (4.14) and (4.15). Since the bursting force in the flange is small in magnitude compared to that in the web, the overestimated bursting force magnitude as indicated by a positive percent difference may not cause problems of reinforcement congestion in a structure due to the small amount of reinforcing steel required. For instance, a percent difference as great as 97.22 percent in a case of the model with the thickness ratio of 1.4, which has the width of flange equal to 6.4 in., only has a magnitude of bursting force equal to $0.0442P$. This number is less than 5 percent of the prestressing force. In the comparisons of $d_{burst-flg}$, the percent differences shown are mostly positive. It should be noted that the

magnitude of the bursting force may result in a small amount of reinforcing steel, which needs to be distributed over a considerable distance on the flange body. After distribution of the steel, the amount of required reinforcement per length may be less than the requirement for temperature reinforcing steel.

Table 4.7 COMPARISON OF $T_{burst-flg}$ AND $d_{burst-flg}$ FOR SYMMETRICAL I-SECTION SUBJECTED TO CONCENTRIC LOAD

Name	a/h	a (in.)	h _w (in.)	t _w (in.)	t _f /t _w	t _f (in.)	b _f (in.)	h' (in.)	R _z /P	k _f	$T_{burst-flg}$			$d_{burst-flg}$		
											$T_{burst-flg}$ /P -1-	$T_{burst-flg}$ /P -2-	%diff -1 & 2-	$d_{burst-flg}$ /h _w -3-	$d_{burst-flg}$ /h _w -4-	%diff -3 & 4-
FS210A	0.2	3.2	16	1.5	0.8	1.2	6.4	17.2	0.16	0.41	0.0091	0.0103	12.17	0.9499	1.0950	15.27
FS210B	0.2	3.2	16	1.5	0.8	1.2	16	17.2	0.29	0.63	0.0315	0.0382	21.22	1.0419	1.1817	13.42
FS210C	0.2	3.2	16	1.5	0.8	1.2	56	17.2	0.42	0.86	0.0580	0.0948	63.46	2.0030	2.1316	6.42
FS220A	0.2	3.2	16	3	0.8	2.4	6.4	18.4	0.11	0.43	0.0124	0.0119	-3.90	0.7137	0.8861	24.16
FS220B	0.2	3.2	16	3	0.8	2.4	16	18.4	0.27	0.65	0.0370	0.0418	12.82	0.8363	1.1239	34.39
FS220C	0.2	3.2	16	3	0.8	2.4	56	18.4	0.41	0.87	0.0625	0.0982	57.09	1.7362	2.1103	21.55
FS240A	0.2	3.2	16	5	0.8	4	6.4	20	0.05	0.46	0.0140	0.0146	4.23	0.6582	0.5251	-20.22
FS240B	0.2	3.2	16	5	0.8	4	16	20	0.23	0.68	0.0403	0.0473	17.51	0.7637	1.0298	34.85
FS240C	0.2	3.2	16	5	0.8	4	56	20	0.40	0.88	0.0681	0.1029	51.11	1.5440	2.0789	34.65
FS310A	0.35	5.6	16	1.5	0.8	1.2	6.4	17.2	0.16	0.41	0.0096	0.0103	6.84	0.8980	1.0950	21.93
FS310B	0.35	5.6	16	1.5	0.8	1.2	16	17.2	0.29	0.63	0.0320	0.0382	19.39	1.0229	1.1817	15.53
FS310C	0.35	5.6	16	1.5	0.8	1.2	56	17.2	0.42	0.86	0.0584	0.0948	62.47	1.9973	2.1316	6.73
FS320A	0.35	5.6	16	3	0.8	2.4	6.4	18.4	0.11	0.43	0.0128	0.0119	-7.43	0.6829	0.8861	29.75
FS320B	0.35	5.6	16	3	0.8	2.4	16	18.4	0.27	0.65	0.0375	0.0418	11.51	0.8256	1.1239	36.13
FS320C	0.35	5.6	16	3	0.8	2.4	56	18.4	0.41	0.87	0.0624	0.0982	57.27	1.7457	2.1103	20.89
FS340A	0.35	5.6	16	5	0.8	4	6.4	20	0.05	0.46	0.0145	0.0146	1.11	0.6346	0.5251	-17.25
FS340B	0.35	5.6	16	5	0.8	4	16	20	0.23	0.68	0.0406	0.0473	16.65	0.7552	1.0298	36.37
FS340C	0.35	5.6	16	5	0.8	4	56	20	0.40	0.88	0.0680	0.1029	51.32	1.5564	2.0789	33.58
FS510A	0.5	8	16	1.5	0.8	1.2	6.4	17.2	0.16	0.41	0.0102	0.0103	0.18	0.8318	1.0950	31.64
FS510B	0.5	8	16	1.5	0.8	1.2	16	17.2	0.29	0.63	0.0326	0.0382	17.08	0.9986	1.1817	18.33
FS510C	0.5	8	16	1.5	0.8	1.2	56	17.2	0.42	0.86	0.0590	0.0948	60.85	1.9877	2.1316	7.24
FS520A	0.5	8	16	3	0.8	2.4	6.4	18.4	0.11	0.43	0.0135	0.0119	-11.84	0.6427	0.8861	37.87
FS520B	0.5	8	16	3	0.8	2.4	16	18.4	0.27	0.65	0.0380	0.0418	9.86	0.8127	1.1239	38.29
FS520C	0.5	8	16	3	0.8	2.4	56	18.4	0.41	0.87	0.0624	0.0982	57.23	1.7580	2.1103	20.04
FS540A	0.5	8	16	5	0.8	4	6.4	20	0.05	0.46	0.0151	0.0146	-2.94	0.6029	0.5251	-12.90
FS540B	0.5	8	16	5	0.8	4	16	20	0.23	0.68	0.0410	0.0473	15.34	0.7457	1.0298	38.09
FS540C	0.5	8	16	5	0.8	4	56	20	0.40	0.88	0.0679	0.1029	51.57	1.5752	2.0789	31.98
FS211A	0.2	3.2	16	1.5	1.1	1.65	6.4	17.65	0.19	0.50	0.0140	0.0182	29.92	0.7588	0.8059	6.20
FS211B	0.2	3.2	16	1.5	1.1	1.65	16	17.65	0.32	0.71	0.0402	0.0538	33.62	0.8524	0.9821	15.21
FS211C	0.2	3.2	16	1.5	1.1	1.65	56	17.65	0.44	0.90	0.0662	0.1078	62.89	1.7398	1.9802	13.82
FS231A	0.2	3.2	16	3	1.1	3.3	6.4	19.3	0.14	0.53	0.0181	0.0218	20.32	0.6426	0.6728	4.70
FS231B	0.2	3.2	16	3	1.1	3.3	16	19.3	0.30	0.73	0.0484	0.0595	22.89	0.7194	0.9468	31.60
FS231C	0.2	3.2	16	3	1.1	3.3	56	19.3	0.43	0.91	0.0759	0.1118	47.32	1.4219	1.9717	38.67
FS251A	0.2	3.2	16	5	1.1	5.5	6.4	21.5	0.06	0.57	0.0189	0.0282	48.81	0.6386	0.4518	-29.25
FS251B	0.2	3.2	16	5	1.1	5.5	16	21.5	0.26	0.77	0.0514	0.0685	33.25	0.7399	0.8876	19.98
FS251C	0.2	3.2	16	5	1.1	5.5	56	21.5	0.42	0.92	0.0803	0.1174	46.21	1.3197	1.9577	48.35
FS311A	0.35	5.6	16	1.5	1.1	1.65	6.4	17.65	0.19	0.50	0.0146	0.0182	25.05	0.7248	0.8059	11.19
FS311B	0.35	5.6	16	1.5	1.1	1.65	16	17.65	0.32	0.71	0.0407	0.0538	32.22	0.8404	0.9821	16.85
FS311C	0.35	5.6	16	1.5	1.1	1.65	56	17.65	0.44	0.90	0.0661	0.1078	62.94	1.7462	1.9802	13.40
FS331A	0.35	5.6	16	3	1.1	3.3	6.4	19.3	0.14	0.53	0.0186	0.0218	17.03	0.6205	0.6728	8.42
FS331B	0.35	5.6	16	3	1.1	3.3	16	19.3	0.30	0.73	0.0486	0.0595	22.54	0.7105	0.9468	33.26
FS331C	0.35	5.6	16	3	1.1	3.3	56	19.3	0.43	0.91	0.0758	0.1118	47.47	1.4335	1.9717	37.55
FS351A	0.35	5.6	16	5	1.1	5.5	6.4	21.5	0.06	0.57	0.0192	0.0282	47.09	0.6252	0.4518	-27.73
FS351B	0.35	5.6	16	5	1.1	5.5	16	21.5	0.26	0.77	0.0516	0.0685	32.88	0.7314	0.8876	21.36
FS351C	0.35	5.6	16	5	1.1	5.5	56	21.5	0.42	0.92	0.0801	0.1174	46.58	1.3348	1.9577	46.66
FS511A	0.5	8	16	1.5	1.1	1.65	6.4	17.65	0.19	0.50	0.0153	0.0182	19.17	0.6809	0.8059	18.35
FS511B	0.5	8	16	1.5	1.1	1.65	16	17.65	0.32	0.71	0.0414	0.0538	30.04	0.8234	0.9821	19.27
FS511C	0.5	8	16	1.5	1.1	1.65	56	17.65	0.44	0.90	0.0661	0.1078	63.13	1.7579	1.9802	12.65
FS531A	0.5	8	16	3	1.1	3.3	6.4	19.3	0.14	0.53	0.0193	0.0218	12.88	0.5911	0.6728	13.83
FS531B	0.5	8	16	3	1.1	3.3	16	19.3	0.30	0.73	0.0487	0.0595	22.25	0.6994	0.9468	35.38
FS531C	0.5	8	16	3	1.1	3.3	56	19.3	0.43	0.91	0.0756	0.1118	47.80	1.4523	1.9717	35.76
FS551A	0.5	8	16	5	1.1	5.5	6.4	21.5	0.06	0.57	0.0197	0.0282	43.38	0.6023	0.4518	-24.98
FS551B	0.5	8	16	5	1.1	5.5	16	21.5	0.26	0.77	0.0517	0.0685	32.48	0.7206	0.8876	23.18
FS551C	0.5	8	16	5	1.1	5.5	56	21.5	0.42	0.92	0.0798	0.1174	47.12	1.3579	1.9577	44.17

Table 4.8 COMPARISON OF $T_{burst-flg}$ AND $d_{burst-flg}$ FOR SYMMETRICAL I-SECTION
SUBJECTED TO CONCENTRIC LOAD (continued)

Name	a/h	a	h_w	t_w	t_f/t_w	t_f	b_f	h'	R_2/P	k_f	$T_{burst-flg}$	$T_{burst-flg}$	%diff	$d_{burst-flg}$	$d_{burst-flg}$	%diff
		(in.)	(in.)	(in.)	(in.)	(in.)	(in.)	(in.)	-1-	-2-	-1 & 2-	-3-	-4-	-3 & 4-		
FS222A	0.2	3.2	16	1.5	1.4	2.1	6.4	18.1	0.22	0.56	0.0195	0.0268	37.09	0.6617	0.6709	1.39
FS222B	0.2	3.2	16	1.5	1.4	2.1	16	18.1	0.35	0.76	0.0499	0.0667	33.60	0.7209	0.8833	22.52
FS222C	0.2	3.2	16	1.5	1.4	2.1	56	18.1	0.45	0.92	0.0771	0.1163	50.78	1.4526	1.9013	30.89
FS242A	0.2	3.2	16	3	1.4	4.2	6.4	20.2	0.16	0.60	0.0226	0.0329	45.33	0.6257	0.5811	-7.12
FS242B	0.2	3.2	16	3	1.4	4.2	16	20.2	0.32	0.79	0.0598	0.0744	24.45	0.6990	0.8651	23.77
FS242C	0.2	3.2	16	3	1.4	4.2	56	20.2	0.44	0.93	0.0863	0.1207	39.81	1.2234	1.9047	55.68
FS272A	0.2	3.2	16	5	1.4	7	6.4	23	0.07	0.67	0.0224	0.0442	97.22	0.6462	0.4356	-32.58
FS272B	0.2	3.2	16	5	1.4	7	16	23	0.29	0.83	0.0602	0.0866	43.96	0.7501	0.8313	10.82
FS272C	0.2	3.2	16	5	1.4	7	56	23	0.43	0.95	0.0883	0.1269	43.74	1.2008	1.9066	58.78
FS322A	0.35	5.6	16	1.5	1.4	2.1	6.4	18.1	0.22	0.56	0.0201	0.0268	33.04	0.6368	0.6709	5.35
FS322B	0.35	5.6	16	1.5	1.4	2.1	16	18.1	0.35	0.76	0.0500	0.0667	33.33	0.7111	0.8833	24.21
FS322C	0.35	5.6	16	1.5	1.4	2.1	56	18.1	0.45	0.92	0.0769	0.1163	51.20	1.4638	1.9013	29.89
FS342A	0.35	5.6	16	3	1.4	4.2	6.4	20.2	0.16	0.60	0.0233	0.0329	41.16	0.6080	0.5811	-4.42
FS342B	0.35	5.6	16	3	1.4	4.2	16	20.2	0.32	0.79	0.0598	0.0744	24.47	0.6907	0.8651	25.26
FS342C	0.35	5.6	16	3	1.4	4.2	56	20.2	0.44	0.93	0.0861	0.1207	40.11	1.2377	1.9047	53.88
FS372A	0.35	5.6	16	5	1.4	7	6.4	23	0.07	0.67	0.0227	0.0442	95.21	0.6335	0.4356	-31.23
FS372B	0.35	5.6	16	5	1.4	7	16	23	0.29	0.83	0.0600	0.0866	44.38	0.7443	0.8313	11.68
FS372C	0.35	5.6	16	5	1.4	7	56	23	0.43	0.95	0.0880	0.1269	44.15	1.2169	1.9066	56.68
FS522A	0.5	8	16	1.5	1.4	2.1	6.4	18.1	0.22	0.56	0.0210	0.0268	27.74	0.6042	0.6709	11.02
FS522B	0.5	8	16	1.5	1.4	2.1	16	18.1	0.35	0.76	0.0500	0.0667	33.29	0.6992	0.8833	26.33
FS522C	0.5	8	16	1.5	1.4	2.1	56	18.1	0.45	0.92	0.0765	0.1163	51.92	1.4826	1.9013	28.25
FS542A	0.5	8	16	3	1.4	4.2	6.4	20.2	0.16	0.60	0.0240	0.0329	37.11	0.5829	0.5811	-0.30
FS542B	0.5	8	16	3	1.4	4.2	16	20.2	0.32	0.79	0.0597	0.0744	24.63	0.6803	0.8651	27.16
FS542C	0.5	8	16	3	1.4	4.2	56	20.2	0.44	0.93	0.0858	0.1207	40.64	1.2604	1.9047	51.12
FS572A	0.5	8	16	5	1.4	7	6.4	23	0.07	0.67	0.0230	0.0442	92.73	0.6163	0.4356	-29.32
FS572B	0.5	8	16	5	1.4	7	16	23	0.29	0.83	0.0597	0.0866	45.10	0.7368	0.8313	12.82
FS572C	0.5	8	16	5	1.4	7	56	23	0.43	0.95	0.0876	0.1269	44.76	1.2413	1.9066	53.60

4.4.1.2.2 T-Section

Since the derivation of the approximate equations for bursting force magnitude and location in webs and flanges of symmetrical I-sections using the STM method has been proven to be effective, the formulations for other types of flanged section can be developed using the STM approach. Since there is no bottom flange in T-sections, the location of the section centroid is located closer to the center of the flange in T-section models. Therefore, the strut-and-tie model needs to be modified.

The strut-and-tie model presented in Fig. 4.59 can be revised to a simpler configuration. By using a total force on each half of the body, which equals $0.5R_1$ plus R_2 , the position of this total force can be relocated to produce a simplified strut-and-tie model within the structure. Fig. 4.64 illustrates the simplified version of the strut-and-tie model used in Fig. 4.59. As can be seen from the figure, the location of the total force now changes to the

distance y_u from the section centroid. This distance can be determined from the centroid of the resultant forces on each portion of the I-section, which is equivalent to a T-shape as shown in Fig. 4.64. The expressions to determine the centroid of the forces y_u can be found in Appendix A. The location of the tie can be calculated directly from equation (4.7).

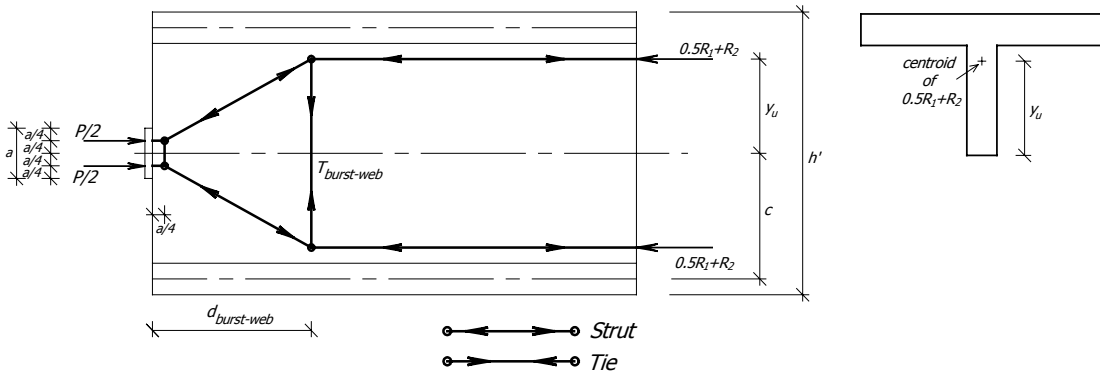


Fig. 4.64 SIMPLIFIED STRUT-AND-TIE MODEL FOR SYMMETRICAL I-SECTION

By using the relation of forces and dimensions in the structure, the equation can be written as

$$\frac{T_{burst-web}}{0.5R_1 + R_2} = \frac{y_u - a/4}{d_{burst-web} - a/4} \quad (4.16)$$

By manipulation of the equation, the equation for estimating the bursting force is

$$T_{burst-web} = (0.5R_1 + R_2) \left(\frac{4y_u}{4d_{burst-web} - a} \right) \left(1 - \frac{a}{4y_u} \right) \quad (4.17)$$

Equation (4.17) results in the same magnitude of web bursting force as that given by equation (4.6).

By employing the same modification method for the strut-and-tie model, the equation for web bursting force in the T-section anchorage zones can also be formulated. Fig. 4.65 shows the strut-and-tie model used for the formulation of the web bursting force. In the figure, the original structure is shown in gray color. The modified model contains unequal forces between the upper portion and lower portion of the structure, which are divided by the

position of the section centroid. The resultant force at the upper portion of the web is designated by γR_1 , where γ can be calculated from $(h'-c)/h'$, which is the proportion of the area in the web where the force γR_1 is determined from the whole area of the web. The resultant force at the lower portion of the web becomes $(1-\gamma)R_1$. Since the forces γR_1 and $(1-\gamma)R_1$ are unequal, the applied prestressing force at the anchorage surface can be divided according to the proportion of the resultant force in the upper and lower portion in order to keep the strut-and-tie model in a stable condition. Therefore, the anchor plate is divided in two different sizes based on the proportion of the forces.

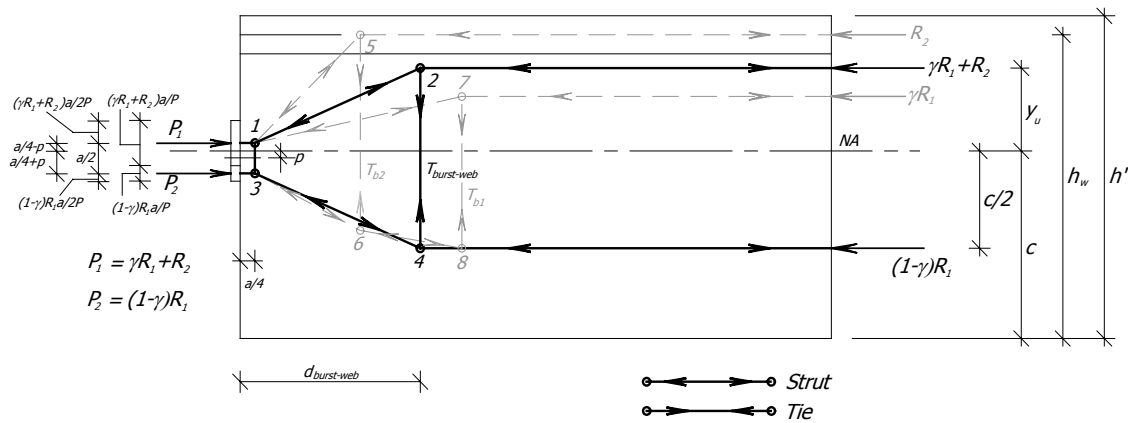


Fig. 4.65 STRUT-AND-TIE MODEL FOR THE FORMULATIONS OF T-SECTION

Since the prestressing load is divided into two separated forces with the proportion based on the resultant forces at the end of model, the location of each separated force is postponed based on the magnitude of the force as shown in Fig. 4.65. The strut-and-tie model is adjusted following the force positions. The distance from the center of anchor plate to the centerline of the model is p , which can be determined using the equation

$$p = (\gamma R_1 + R_2 - 0.5P)a / 2P, \quad (4.18)$$

where γ equals $(h'-c)/h'$ as mentioned earlier. According to the relationship between the forces and dimensions of the model at node 2, the equation can be written as

$$\frac{T_{burst-web}}{\gamma R_1 + R_2} = \frac{y_u - a/4 + p}{d_{burst-web} - a/4} \quad (4.19)$$

After manipulating equation (4.19), the equation to determine the magnitude of the web bursting force is

$$T_{burst-web} = (\gamma R_1 + R_2) \left(\frac{4y_u + 4p}{4d_{burst-web} - a} \right) \left(1 - \frac{a}{4y_u + 4p} \right) \quad (4.20)$$

Another equation to calculate the bursting force can be derived from the equilibrium of the forces and dimensions at node 4. By using an equation similar to (4.19), another expression to estimate the value of $T_{burst-web}$ can be written as

$$T_{burst-web} = (1 - \gamma) R_1 \left(\frac{2c - 4p}{4d_{burst-web} - a} \right) \left(1 - \frac{a}{2c - 4p} \right) \quad (4.21)$$

Equations (4.20) and (4.21) result in the same magnitude of the web bursting force.

In a symmetrical section, the structure of the anchorage zone can be divided into two similar T-shapes. The strut-and-tie models in both the upper and lower portion with respect to the centroidal axis contain the same value of $d_{burst-web}$. However, the same situation cannot be applied to T-sections and unsymmetrical I-sections since the division based on the centroid axis of the section for these two sections does not result in two similar structures. Although equations (4.20) and (4.21) provide exactly the same results of $T_{burst-web}$, the same $d_{burst-web}$ must be used in the calculations. By replacing the height of each portion of T-section for the $h'/2$ term in equation (4.7), the equations, which are shown below, can be written for the formulation of $d_{burst-web}$ in a T-section:

$$d_{burst-web} = (h' - c) + \frac{a}{4} + \frac{h_w}{4} (1 - \exp(-0.8b_{f1} / h_w)) \quad (4.22)$$

$$d_{burst-web} = c + \frac{a}{4} \quad (4.23)$$

Equations (4.22) and (4.23) are used for the calculation of $d_{burst-web}$ in the upper and lower portions, respectively. It should be noted that equation (4.23) equals the estimated location

of the bursting force for a rectangular section with a height equal to $2c$. The results from using equation (4.22) are proven to give a good estimation compared to those from the finite element method as can be seen in Fig. 4.66. In the figure, the plot of equation (4.22) lies beneath the finite element plot but has a similar form. Although the $d_{burst-web}$ value, which is used in the determination of $T_{burst-web}$ in T-section, needs to be considered from both upper and lower portions of the section, only a single value of $d_{burst-web}$ is needed. It is conservative to use the smaller number from both equations (4.22) and (4.23).

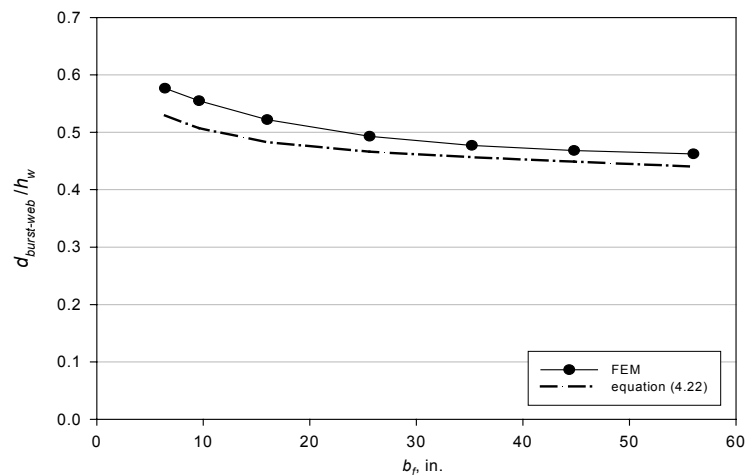


Fig. 4.66 WEB BURSTING FORCE LOCATION vs. FLANGE WIDTH FOR T-SECTION
($t_w = 1.5$ in., $t_f/t_w = 1.4$, and $a/h_w = 0.20$)

Table 4.9 shows the comparison of the finite element results and those using equations (4.20) to (4.23). The $d_{burst-web}$ values in the table are the smaller numbers from equation (4.22) or (4.23). The largest negative percent difference occurring in the table is -2.94 , which is considered as a very small value. Almost all the values of $T_{burst-web}$ are conservative compared to the finite element results. The $d_{burst-web}$ comparison is also quite acceptable. The largest negative percent difference in $d_{burst-web}$, -18.74 percent, occurs in a model that has a conservative value of $T_{burst-web}$ with a magnitude 36.39 percent larger than that of finite element result. Because the required amount of steel from the estimation is larger than the finite element prediction, even though it will be placed at a location closer to the anchor plate according to the estimated value of $d_{burst-web}$, the structure remains conservatively designed. For models with a poor estimation of $T_{burst-web}$ magnitude, the percent difference of $d_{burst-web}$ indicates a very close estimation to the finite element result. This is also acceptable.

Table 4.9 COMPARISON OF $T_{burst-web}$ AND $d_{burst-web}$ FOR T-SECTION
SUBJECTED TO CONCENTRIC LOAD

Name	a/h	a (in.)	h _w (in.)	t _w (in.)	t _f /t _w	t _f (in.)	b _f (in.)	h' (in.)	c (in.)	γ _R /P	(1-γ) _R /P	R _z /P	p	y _u (in.)	$d_{burst-web}$			$T_{burst-web}$		
															/h _w -1-	/h _w -2-	%diff -1 & 2-	/P -3-	/P -4-	%diff -3 & 4-
TS210A	0.2	3.2	16	1.5	0.8	1.2	6.4	16.6	9.77	0.33	0.48	0.19	0.04	4.44	0.6055	0.5453	-9.94	0.2106	0.2432	15.46
TS210B	0.2	3.2	16	1.5	0.8	1.2	16	16.6	11.47	0.18	0.41	0.41	0.15	3.93	0.6037	0.5085	-15.78	0.2090	0.2652	26.87
TS210C	0.2	3.2	16	1.5	0.8	1.2	56	16.6	13.88	0.05	0.23	0.72	0.43	2.08	0.4948	0.4550	-8.03	0.1477	0.2030	37.50
TS220A	0.2	3.2	16	3	0.8	2.4	6.4	17.2	9.61	0.38	0.48	0.14	0.03	4.48	0.6105	0.5928	-2.89	0.2097	0.2209	5.35
TS220B	0.2	3.2	16	3	0.8	2.4	16	17.2	11.39	0.21	0.41	0.38	0.14	4.00	0.6159	0.5509	-10.56	0.2065	0.2448	18.53
TS220C	0.2	3.2	16	3	0.8	2.4	56	17.2	13.86	0.06	0.23	0.71	0.43	2.10	0.5146	0.4933	-4.14	0.1444	0.1871	29.59
TS240A	0.2	3.2	16	5	0.8	4	6.4	18	9.41	0.45	0.49	0.06	0.01	4.56	0.6163	0.6381	3.54	0.2082	0.2036	-2.22
TS240B	0.2	3.2	16	5	0.8	4	16	18	11.30	0.25	0.42	0.33	0.13	4.12	0.6290	0.6065	-3.57	0.2036	0.2237	9.84
TS240C	0.2	3.2	16	5	0.8	4	56	18	13.86	0.07	0.24	0.69	0.42	2.14	0.5339	0.5437	1.85	0.1425	0.1702	19.45
TS310A	0.35	5.6	16	1.5	0.8	1.2	6.4	16.6	9.77	0.33	0.48	0.19	0.07	4.44	0.6445	0.5828	-9.58	0.1714	0.2054	19.82
TS320A	0.35	5.6	16	3	0.8	2.4	6.4	17.2	9.61	0.38	0.48	0.14	0.05	4.48	0.6501	0.6303	-3.04	0.1708	0.1864	9.17
TS340A	0.35	5.6	16	5	0.8	4	6.4	18	9.41	0.45	0.49	0.06	0.02	4.56	0.6571	0.6756	2.83	0.1694	0.1717	1.34
TS510A	0.5	8	16	1.5	0.8	1.2	6.4	16.6	9.77	0.33	0.48	0.19	0.10	4.44	0.6700	0.6203	-7.41	0.1382	0.1677	21.32
TS520A	0.5	8	16	3	0.8	2.4	6.4	17.2	9.61	0.38	0.48	0.14	0.07	4.48	0.6755	0.6678	-1.13	0.1379	0.1519	10.15
TS540A	0.5	8	16	5	0.8	4	6.4	18	9.41	0.45	0.49	0.06	0.03	4.56	0.6830	0.7131	4.41	0.1369	0.1398	2.14
TS211A	0.2	3.2	16	1.5	1.1	1.65	6.4	16.83	10.25	0.30	0.46	0.24	0.06	4.39	0.6110	0.5292	-13.39	0.2128	0.2568	20.67
TS211B	0.2	3.2	16	1.5	1.1	1.65	16	16.83	12.10	0.14	0.37	0.49	0.21	3.54	0.5882	0.4827	-17.94	0.2034	0.2636	32.30
TS211C	0.2	3.2	16	1.5	1.1	1.65	56	16.83	14.34	0.03	0.19	0.78	0.50	1.65	0.4696	0.4403	-6.24	0.1203	0.1755	45.84
TS231A	0.2	3.2	16	3	1.1	3.3	6.4	17.65	10.08	0.35	0.47	0.17	0.05	4.49	0.6213	0.5916	-4.77	0.2106	0.2080	8.27
TS231B	0.2	3.2	16	3	1.1	3.3	16	17.65	12.04	0.18	0.38	0.45	0.20	3.64	0.6089	0.5385	-11.55	0.1977	0.2420	22.41
TS231C	0.2	3.2	16	3	1.1	3.3	56	17.65	14.33	0.04	0.19	0.77	0.50	1.67	0.4967	0.4921	-0.92	0.1184	0.1565	32.20
TS251A	0.2	3.2	16	5	1.1	5.5	6.4	18.75	9.88	0.44	0.49	0.08	0.02	4.69	0.6321	0.6674	5.57	0.2083	0.2029	-2.55
TS251B	0.2	3.2	16	5	1.1	5.5	16	18.75	11.97	0.22	0.39	0.39	0.18	3.80	0.6292	0.6112	-2.86	0.1939	0.2165	11.62
TS251C	0.2	3.2	16	5	1.1	5.5	56	18.75	14.34	0.06	0.19	0.75	0.49	1.70	0.5474	0.5604	2.37	0.1200	0.1379	14.90
TS311A	0.35	5.6	16	1.5	1.1	1.65	6.4	16.83	10.25	0.30	0.46	0.24	0.11	4.39	0.6503	0.5667	-12.86	0.1737	0.2179	25.41
TS331A	0.35	5.6	16	3	1.1	3.3	6.4	17.65	10.08	0.35	0.47	0.17	0.08	4.49	0.6621	0.6291	-4.98	0.1720	0.1935	12.53
TS351A	0.35	5.6	16	5	1.1	5.5	6.4	18.75	9.88	0.44	0.49	0.08	0.04	4.69	0.6752	0.7049	4.39	0.1698	0.1726	1.65
TS511A	0.5	8	16	1.5	1.1	1.65	6.4	16.83	10.25	0.30	0.46	0.24	0.15	4.39	0.6760	0.6042	-10.63	0.1406	0.1790	27.27
TS531A	0.5	8	16	3	1.1	3.3	6.4	17.65	10.08	0.35	0.47	0.17	0.12	4.49	0.6881	0.6666	-3.13	0.1396	0.1590	13.93
TS551A	0.5	8	16	5	1.1	5.5	6.4	18.75	9.88	0.44	0.49	0.08	0.05	4.69	0.7025	0.7424	5.67	0.1378	0.1422	3.20
TS222A	0.2	3.2	16	1.5	1.4	2.1	6.4	17.05	10.67	0.27	0.45	0.29	0.09	4.30	0.6131	0.5172	-15.63	0.2129	0.2656	24.71
TS222B	0.2	3.2	16	1.5	1.4	2.1	16	17.05	12.59	0.12	0.34	0.54	0.26	3.20	0.5742	0.4666	-18.74	0.1940	0.2646	36.39
TS222C	0.2	3.2	16	1.5	1.4	2.1	56	17.05	14.63	0.03	0.16	0.82	0.55	1.36	0.4756	0.4358	-8.37	0.1142	0.1516	32.71
TS242A	0.2	3.2	16	3	1.4	4.2	6.4	18.1	10.50	0.33	0.46	0.21	0.07	4.46	0.6297	0.5936	-5.72	0.2094	0.2314	10.53
TS242B	0.2	3.2	16	3	1.4	4.2	16	18.1	12.53	0.15	0.35	0.50	0.25	3.31	0.6039	0.5355	-11.32	0.1868	0.2320	24.22
TS242C	0.2	3.2	16	3	1.4	4.2	56	18.1	14.64	0.04	0.16	0.80	0.55	1.38	0.5242	0.5012	-4.39	0.1125	0.1312	16.62
TS272A	0.2	3.2	16	5	1.4	7	6.4	19.5	10.32	0.43	0.48	0.09	0.03	4.78	0.6446	0.6922	7.38	0.2063	0.2027	-1.74
TS272B	0.2	3.2	16	5	1.4	7	16	19.5	12.51	0.20	0.36	0.44	0.23	3.49	0.6278	0.6247	-0.50	0.1825	0.2038	11.64
TS272C	0.2	3.2	16	5	1.4	7	56	19.5	14.66	0.05	0.16	0.79	0.54	1.41	0.5867	0.5873	0.12	0.1157	0.1123	-2.94
TS322A	0.35	5.6	16	1.5	1.4	2.1	6.4	17.05	10.67	0.27	0.45	0.29	0.15	4.30	0.6528	0.5547	-15.02	0.1738	0.2259	29.94
TS342A	0.35	5.6	16	3	1.4	4.2	6.4	18.1	10.50	0.33	0.46	0.21	0.11	4.46	0.6721	0.6311	-6.10	0.1708	0.1971	15.40
TS372A	0.35	5.6	16	5	1.4	7	6.4	19.5	10.32	0.43	0.48	0.09	0.05	4.78	0.6902	0.7297	5.72	0.1679	0.1735	3.33
TS522A	0.5	8	16	1.5	1.4	2.1	6.4	17.05	10.67	0.27	0.45	0.29	0.22	4.30	0.6789	0.5922	-12.76	0.1407	0.1862	32.31
TS542A	0.5	8	16	3	1.4	4.2	6.4	18.1	10.50	0.33	0.46	0.21	0.16	4.46	0.6991	0.6686	-4.36	0.1387	0.1629	17.42
TS572A	0.5	8	16	5	1.4	7	6.4	19.5	10.32	0.43	0.48	0.09	0.08	4.78	0.7190	0.7672	6.69	0.1363	0.1444	5.88

The formulations for the determination of the magnitude of the bursting force and the location of the force in the flange of T-sections are similar to those derived for symmetrical I-sections. Based on the 45 degree angle of compressive strut that transfers the force into the flange, the position of the transferring load in the flange of a T-section moves closer to the loaded surface as the distance from the center of the anchor plate to the center of the flange is reduced due to the change in location of the section centroid. Equation (4.14) can be modified for the estimation of $d_{burst-flg}$ in T-sections. By substituting the distance $h_w/2$ by $(h_w - c)$, the equation to determine the location of flange bursting force can be rewritten as

$$d_{burst-flg} = \frac{h_w - c}{4} + \frac{3}{8}t_f + \frac{R_2}{T_{burst-flg}} \frac{(b_f + t_w)}{8} \quad (4.24)$$

Equation (4.24) is also applicable for the calculation of $d_{burst-flg}$ in symmetrical I-section models. The bursting force in the flange can also be determined using equation (4.15) since the change in the position of the load does not affect the calculation of k_f . However, because the centroid of a T-section may be located inside the flange area, the calculation of k_f may lead to a value greater than 1.0, which is unrealistic since the force R_{flg} cannot be greater than the force R_{total} (see Fig. 4.62). Therefore, by applying an upper limit to equation (4.15), the new equation can be rewritten as

$$T_{burst-flg} = 0.15k_f^3P, \quad k_f \leq 1.0, \quad (4.25)$$

where k_f can be determined from R_{flg}/R_{total} .

Table 4.10 presents the comparison of the flange bursting force magnitude and the location of the force from the finite element method and equations (4.24) and (4.25). As can be seen from the table, the estimation of the flange bursting force magnitude using equation (4.25) is conservative in most of the cases. The largest negative percent difference detected in the comparison of $T_{burst-flg}$ is only -3.66 , which is considered quite small. For the comparison of $d_{burst-flg}$, the largest positive percent difference is found in model TS272C. This model has an estimated value of $T_{burst-flg}$ slightly higher than the finite element prediction. This can be considered as an unconservative approximation. However, with a proper reinforcing steel arrangement, this problem can be overcome.

Table 4.10 COMPARISON OF $T_{burst-flg}$ AND $d_{burst-flg}$ FOR T-SECTION
SUBJECTED TO CONCENTRIC LOAD

Name	a/h	a (in.)	h _w (in.)	t _w (in.)	t _f /t _w	t _f (in.)	b _f (in.)	h' (in.)	c (in.)	R _z /P	k _f	$T_{burst-flg}$			$d_{burst-flg}$		
												$T_{burst-flg}$ /P	$T_{burst-flg}$ /P	%diff	$d_{burst-flg}$ /h _w	$d_{burst-flg}$ /h _w	%diff
												-1-	-2-	-1 & 2-	-3-	-4-	-3 & 4-
TS210A	0.2	3.2	16	1.5	0.8	1.2	6.4	16.6	9.77	0.19	0.48	0.0142	0.0162	14.41	0.7370	0.8528	15.71
TS210B	0.2	3.2	16	1.5	0.8	1.2	16	16.6	11.47	0.41	0.76	0.0578	0.0671	16.09	0.8035	0.9365	16.56
TS210C	0.2	3.2	16	1.5	0.8	1.2	56	16.6	13.88	0.72	0.97	0.1274	0.1357	6.47	1.8549	2.4591	32.57
TS220A	0.2	3.2	16	3	0.8	2.4	6.4	17.2	9.61	0.14	0.50	0.0180	0.0184	2.13	0.6449	0.7019	8.84
TS220B	0.2	3.2	16	3	0.8	2.4	16	17.2	11.39	0.38	0.79	0.0631	0.0738	17.03	0.7170	0.8859	23.56
TS220C	0.2	3.2	16	3	0.8	2.4	56	17.2	13.86	0.71	0.98	0.1162	0.1410	21.30	1.9705	2.4156	22.58
TS240A	0.2	3.2	16	5	0.8	4	6.4	18	9.41	0.06	0.53	0.0193	0.0220	13.66	0.7052	0.4340	-38.46
TS240B	0.2	3.2	16	5	0.8	4	16	18	11.30	0.33	0.83	0.0640	0.0845	32.03	0.7352	0.8051	9.51
TS240C	0.2	3.2	16	5	0.8	4	56	18	13.86	0.69	1.00	0.1119	0.1486	32.72	2.0104	2.3529	17.04
TS310A	0.35	5.6	16	1.5	0.8	1.2	6.4	16.6	9.77	0.19	0.48	0.0149	0.0162	8.45	0.6912	0.8528	23.38
TS320A	0.35	5.6	16	3	0.8	2.4	6.4	17.2	9.61	0.14	0.50	0.0185	0.0184	-0.57	0.6197	0.7019	13.26
TS340A	0.35	5.6	16	5	0.8	4	6.4	18	9.41	0.06	0.53	0.0198	0.0220	10.89	0.6822	0.4340	-36.39
TS510A	0.5	8	16	1.5	0.8	1.2	6.4	16.6	9.77	0.19	0.48	0.0168	0.0162	-3.26	0.6125	0.8528	39.24
TS520A	0.5	8	16	3	0.8	2.4	6.4	17.2	9.61	0.14	0.50	0.0191	0.0184	-3.66	0.5887	0.7019	19.23
TS540A	0.5	8	16	5	0.8	4	6.4	18	9.41	0.06	0.53	0.0205	0.0220	7.48	0.6524	0.4340	-33.48
TS211A	0.2	3.2	16	1.5	1.1	1.65	6.4	16.83	10.25	0.24	0.59	0.0234	0.0306	30.46	0.5888	0.6181	4.99
TS211B	0.2	3.2	16	1.5	1.1	1.65	16	16.83	12.10	0.49	0.85	0.0779	0.0926	18.85	0.6683	0.8181	22.40
TS211C	0.2	3.2	16	1.5	1.1	1.65	56	16.83	14.34	0.78	0.99	0.1383	0.1440	4.15	1.8602	2.4999	34.39
TS231A	0.2	3.2	16	3	1.1	3.3	6.4	17.65	10.08	0.17	0.62	0.0280	0.0362	29.26	0.5951	0.5248	-11.80
TS231B	0.2	3.2	16	3	1.1	3.3	16	17.65	12.04	0.45	0.88	0.0822	0.1036	26.03	0.6464	0.7808	20.79
TS231C	0.2	3.2	16	3	1.1	3.3	56	17.65	14.33	0.77	1.00	0.1322	0.1499	13.33	1.9099	2.4642	29.02
TS251A	0.2	3.2	16	5	1.1	5.5	6.4	18.75	9.88	0.08	0.68	0.0273	0.0464	70.00	0.6966	0.3704	-46.83
TS251B	0.2	3.2	16	5	1.1	5.5	16	18.75	11.97	0.39	0.93	0.0812	0.1216	49.79	0.7077	0.7211	1.89
TS251C	0.2	3.2	16	5	1.1	5.5	56	18.75	14.34	0.75	1.00	0.1274	0.1500	17.75	1.9248	2.5361	31.76
TS311A	0.35	5.6	16	1.5	1.1	1.65	6.4	16.83	10.25	0.24	0.59	0.0245	0.0306	24.59	0.5541	0.6181	11.55
TS331A	0.35	5.6	16	3	1.1	3.3	6.4	17.65	10.08	0.17	0.62	0.0284	0.0362	27.40	0.5773	0.5248	-9.09
TS351A	0.35	5.6	16	5	1.1	5.5	6.4	18.75	9.88	0.08	0.68	0.0278	0.0464	66.84	0.6769	0.3704	-45.29
TS511A	0.5	8	16	1.5	1.1	1.65	6.4	16.83	10.25	0.24	0.59	0.0264	0.0306	15.67	0.5057	0.6181	22.23
TS531A	0.5	8	16	3	1.1	3.3	6.4	17.65	10.08	0.17	0.62	0.0288	0.0362	25.67	0.5556	0.5248	-5.54
TS551A	0.5	8	16	5	1.1	5.5	6.4	18.75	9.88	0.08	0.68	0.0284	0.0464	62.98	0.6511	0.3704	-43.12
TS222A	0.2	3.2	16	1.5	1.4	2.1	6.4	17.05	10.67	0.29	0.68	0.0343	0.0465	35.52	0.5227	0.5134	-1.77
TS222B	0.2	3.2	16	1.5	1.4	2.1	16	17.05	12.59	0.54	0.90	0.0952	0.1110	16.68	0.5946	0.7718	29.80
TS222C	0.2	3.2	16	1.5	1.4	2.1	56	17.05	14.63	0.82	1.00	0.1465	0.1482	1.18	1.8376	2.5480	38.66
TS242A	0.2	3.2	16	3	1.4	4.2	6.4	18.1	10.50	0.21	0.72	0.0366	0.0571	55.93	0.5798	0.4522	-22.01
TS242B	0.2	3.2	16	3	1.4	4.2	16	18.1	12.53	0.50	0.94	0.0964	0.1256	30.31	0.6239	0.7451	19.44
TS242C	0.2	3.2	16	3	1.4	4.2	56	18.1	14.64	0.80	1.00	0.1458	0.1500	2.90	1.8736	2.5901	38.24
TS272A	0.2	3.2	16	5	1.4	7	6.4	19.5	10.32	0.09	0.80	0.0336	0.0781	132.29	0.6909	0.3570	-48.33
TS272B	0.2	3.2	16	5	1.4	7	16	19.5	12.51	0.44	1.00	0.0942	0.1500	59.31	0.6939	0.7013	1.06
TS272C	0.2	3.2	16	5	1.4	7	56	19.5	14.66	0.79	1.00	0.1436	0.1500	4.48	1.8823	2.6805	42.41
TS322A	0.35	5.6	16	1.5	1.4	2.1	6.4	17.05	10.67	0.29	0.68	0.0352	0.0465	32.08	0.4994	0.5134	2.81
TS342A	0.35	5.6	16	3	1.4	4.2	6.4	18.1	10.50	0.21	0.72	0.0369	0.0571	54.75	0.5649	0.4522	-19.95
TS372A	0.35	5.6	16	5	1.4	7	6.4	19.5	10.32	0.09	0.80	0.0342	0.0781	128.21	0.6717	0.3570	-46.85
TS522A	0.5	8	16	1.5	1.4	2.1	6.4	17.05	10.67	0.29	0.68	0.0369	0.0465	25.98	0.4651	0.5134	10.39
TS542A	0.5	8	16	3	1.4	4.2	6.4	18.1	10.50	0.21	0.72	0.0371	0.0571	53.93	0.5467	0.4522	-17.29
TS572A	0.5	8	16	5	1.4	7	6.4	19.5	10.32	0.09	0.80	0.0350	0.0781	123.16	0.6462	0.3570	-44.75

4.4.1.2.3 Unsymmetrical I-Section

After the method of a modified strut-and-tie model is proven to be applicable in the formulations for T-sections, the same method is employed in the formulations for unsymmetrical I-sections. By dividing the structure of an unsymmetrical I-section anchorage zone along its centroidal axis, the structure becomes two different T-sections. Fig. 4.67 shows the strut-and-tie model used to formulate the equations for the magnitude of the web

bursting force. The upper portion of the model is the same model as that used in the development of equation (4.20). For the lower portion, the distance from the section centroid to the centroid of the forces in the lower portion is assigned as y_l , which can be determined from the forces $(1-\gamma)R_1$ and R_3 with respect to the section centroid. The value of γ is calculated from $(h'-c-t_{f2}/2)/h'$ and the force R_3 is the resultant force in the bottom flange as illustrated in Fig. 4.58. Other variables are the same as those used in the formulations for the T-section model.

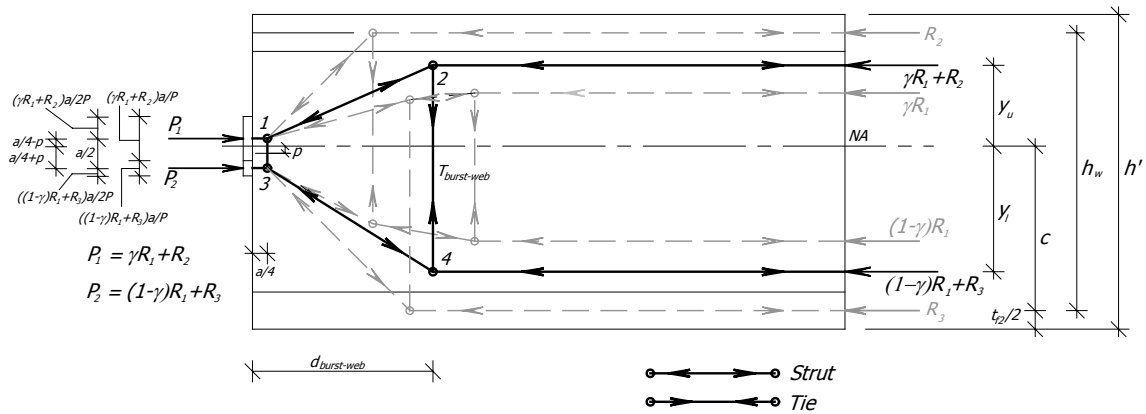


Fig. 4.67 STRUT-AND-TIE MODEL FOR THE FORMULATION OF UNSYMMETRICAL I-SECTION

By using a similar method to that used in the previous formulations, the equation to determine the magnitude of the bursting force based on the lower portion of the strut-and-tie model in Fig. 4.67 is

$$T_{burst-web} = ((1-\gamma)R_1 + R_3) \left(\frac{4y_l - 4p}{4d_{burst-web} - a} \right) \left(1 - \frac{a}{4y_l - 4p} \right) \quad (4.26)$$

This equation gives approximately the same value as the magnitude of web bursting force from equation (4.20). For the formulation of $d_{burst-web}$, equation (4.22) can be applied for the upper portion of the model by including the thickness of bottom flange into the first term of the equation. Equation (4.22) can be used to create the equation of $d_{burst-web}$ for the lower portion by replacing all variables related to the upper portion by those from the lower portion. The equations for the estimation of $d_{burst-web}$ for the top and the bottom portion are

$$d_{burst-web} = (h' - c - \frac{t_{f2}}{2}) + \frac{a}{4} + \frac{h_w}{4} (1 - \exp(-0.8b_{f1} / h_w)) \quad (4.27)$$

$$d_{burst-web} = (c + \frac{t_{f2}}{2}) + \frac{a}{4} + \frac{h_w}{4} (1 - \exp(-0.8b_{f2} / h_w)) \quad (4.28)$$

Similarly to that considered for the estimation of $d_{burst-web}$ in other flanged sections, the smaller value of the $d_{burst-web}$ from equations (4.27) and (4.28) is selected as the location of the web bursting force for an unsymmetrical I-section anchorage zone. Table 4.11 shows the comparison of the results from the finite element method and those using either equations (4.20) or (4.26) and both equations (4.27) and (4.28). The percent differences from the comparison of the bursting force magnitude are all positive numbers. The locations of the web bursting force estimated by using the equations are smaller in distance than those given from the finite element results. With a larger approximated magnitude of bursting force and a closer distance to the prestressing surface compared to those of finite element results, the approximate equations result in a conservative design.

Table 4.11 COMPARISON OF $T_{burst-web}$ AND $d_{burst-web}$ FOR UNSYMMETRICAL I-SECTION SUBJECTED TO CONCENTRIC LOAD

Name	t_w	t_{f1}/t_w	t_{f1}	b_{f1}	b_{f2}	h'	c	V_R	$(1-V)R$	R_2	R_3	p	y_u	y_l	$d_{burst-wfem}$	$d_{burst-web}$	%diff	$T_{burst-wfem}$	$T_{burst-web}$	%diff
US210I	1.5	0.8	1.2	6.4	4.8	17.2	8.43	0.34	0.38	0.16	0.11	0.01	5.21	5.40	0.6787	0.6290	-7.32	0.2222	0.2432	9.45
US210J	1.5	0.8	1.2	6.4	3.2	17.2	8.91	0.34	0.42	0.17	0.06	0.03	4.94	5.28	0.6606	0.5990	-9.32	0.2190	0.2449	11.82
US210K	1.5	0.8	1.2	6.4	1.6	17.2	9.45	0.34	0.47	0.18	0.00	0.04	4.63	5.06	0.6353	0.5654	-11.00	0.2150	0.2447	13.85
US210L	1.5	0.8	1.2	16	8	17.2	9.51	0.21	0.30	0.34	0.15	0.08	5.38	6.57	0.7265	0.6311	-13.14	0.2313	0.2753	19.04
US210M	1.5	0.8	1.2	16	4.8	17.2	10.28	0.20	0.35	0.37	0.08	0.11	4.82	6.39	0.6887	0.5827	-15.39	0.2248	0.2761	22.83
US210N	1.5	0.8	1.2	16	1.6	17.2	11.19	0.19	0.41	0.40	0.00	0.14	4.14	5.93	0.6319	0.5257	-16.80	0.2140	0.2694	25.91
US210O	1.5	0.8	1.2	56	28.8	17.2	10.11	0.08	0.13	0.53	0.26	0.17	5.55	8.54	0.7866	0.6906	-12.20	0.2361	0.2910	23.26
US210P	1.5	0.8	1.2	56	14.4	17.2	11.74	0.07	0.17	0.61	0.15	0.29	4.07	8.71	0.6918	0.5883	-14.95	0.2147	0.2819	31.28
US210Q	1.5	0.8	1.2	56	1.6	17.2	13.72	0.05	0.24	0.72	0.00	0.42	2.23	7.20	0.5126	0.4649	-9.30	0.1560	0.2129	36.45
US211I	1.5	1.1	1.65	6.4	4.8	17.65	8.53	0.31	0.35	0.20	0.14	0.02	5.46	5.75	0.7058	0.6370	-9.74	0.2273	0.2556	12.49
US211J	1.5	1.1	1.65	6.4	3.2	17.65	9.13	0.31	0.40	0.22	0.08	0.04	5.09	5.63	0.6836	0.5994	-12.32	0.2236	0.2589	15.80
US211K	1.5	1.1	1.65	6.4	1.6	17.65	9.82	0.30	0.46	0.23	0.00	0.06	4.66	5.37	0.6503	0.5560	-14.50	0.2184	0.2592	18.67
US211L	1.5	1.1	1.65	16	8	17.65	9.73	0.17	0.26	0.39	0.18	0.10	5.43	7.07	0.7474	0.6313	-15.54	0.2346	0.2882	22.85
US211M	1.5	1.1	1.65	16	4.8	17.65	10.65	0.17	0.31	0.43	0.10	0.15	4.72	6.92	0.6998	0.5738	-18.01	0.2262	0.2888	27.63
US211N	1.5	1.1	1.65	16	1.6	17.65	11.76	0.15	0.37	0.47	0.00	0.20	3.83	6.34	0.6252	0.5043	-19.34	0.2102	0.2768	31.68
US211O	1.5	1.1	1.65	56	28.8	17.65	10.22	0.06	0.10	0.56	0.28	0.19	5.53	8.96	0.8013	0.6974	-12.97	0.2381	0.2937	23.34
US211P	1.5	1.1	1.65	56	14.4	17.65	11.99	0.05	0.14	0.65	0.15	0.33	3.89	9.34	0.6931	0.5871	-15.30	0.2133	0.2811	31.78
US211Q	1.5	1.1	1.65	56	1.6	17.65	14.16	0.03	0.19	0.77	0.00	0.49	1.82	7.54	0.4869	0.4513	-7.30	0.1341	0.1891	41.02
US222I	1.5	1.4	2.1	6.4	4.8	18.1	8.61	0.29	0.33	0.23	0.16	0.03	5.64	6.05	0.7278	0.6462	-11.21	0.2306	0.2642	14.58
US222J	1.5	1.4	2.1	6.4	3.2	18.1	9.31	0.28	0.38	0.25	0.09	0.05	5.19	5.95	0.7021	0.6022	-14.24	0.2265	0.2689	18.71
US222K	1.5	1.4	2.1	6.4	1.6	18.1	10.14	0.28	0.45	0.27	0.01	0.08	4.65	5.65	0.6611	0.5502	-16.77	0.2200	0.2693	22.39
US222L	1.5	1.4	2.1	16	8	18.1	9.89	0.15	0.23	0.43	0.19	0.13	5.45	7.47	0.7641	0.6354	-16.85	0.2356	0.2950	25.21
US222M	1.5	1.4	2.1	16	4.8	18.1	10.92	0.14	0.28	0.47	0.11	0.18	4.62	7.36	0.7092	0.5711	-19.48	0.2253	0.2948	30.84
US222N	1.5	1.4	2.1	16	1.6	18.1	12.18	0.13	0.34	0.53	0.00	0.24	3.55	6.68	0.6200	0.4917	-20.68	0.2037	0.2765	35.76
US222O	1.5	1.4	2.1	56	28.8	18.1	10.30	0.05	0.09	0.58	0.29	0.20	5.51	9.24	0.8153	0.7069	-13.30	0.2377	0.2929	23.22
US222P	1.5	1.4	2.1	56	14.4	18.1	12.14	0.04	0.12	0.68	0.16	0.36	3.77	9.80	0.7007	0.5915	-15.58	0.2102	0.2773	31.93
US222Q	1.5	1.4	2.1	56	1.6	18.1	14.44	0.03	0.16	0.81	0.00	0.54	1.55	7.81	0.4890	0.4476	-8.46	0.1142	0.1682	47.27

Note: All models in the Table contain the dimensions as indicated below:

$$a/h = 0.20, a = 3.2 \text{ in.}, h_w = 16 \text{ in.}$$

In the formulations for the flange bursting force magnitude and location in the flange method derived for both symmetrical I-section and T-section is also applied. Since an unsymmetrical I-section contains two different flanges, the top flange can still employ equation (4.24) by substituting the variable f with $f1$ to indicate the position of the top flange. A new equation to calculate the location of bursting force for the bottom flange can be created by replacing the term $h_w - c$ with c in equation (4.24). Therefore, the equations to estimate $d_{burst-flg}$ can be written as

$$d_{burst-flg} = \frac{h_w - c}{4} + \frac{3}{8}t_{f1} + \frac{R_2}{T_{burst-flg}} \frac{(b_{f1} + t_w)}{8} \quad (4.29)$$

$$d_{burst-flg} = \frac{c}{4} + \frac{3}{8}t_{f2} + \frac{R_3}{T_{burst-flg}} \frac{(b_{f2} + t_w)}{8} \quad (4.30)$$

The value of $T_{burst-flg}$ in each equation is the magnitude of the bursting force for the considered flange. For the estimation of the magnitude of the bursting force in each flange, equation (4.25) is still applicable in an unsymmetrical I-section.

Tables 4.12 and 4.13 show the comparison of the bursting force magnitude and the location of the force in top and bottom of unsymmetrical I-section models, respectively. According to both tables, the estimation of the bursting force magnitude is conservative except for model US211J in Table 4.13. Although the percent difference indicated in the table is -9.86 , the values of $T_{burst-ffem}$ and $T_{burst-flg}$ are less than 0.5 percent of the prestressing force. For the estimation of $d_{burst-flg}$ in the top flange as shown in Table 4.12, the equation gives a larger distance in all models especially in the models with the widest flanges. However, some close estimations of $d_{burst-flg}$ values to the finite element results are found in Table 4.13. Based on all comparisons of the results given in Tables 4.5 to 4.13, the developed equations for each type of flanged sections give a good estimation for the design of concentrically loaded anchorage zones in flanged sections. Additional illustrated examples for the design of anchorage zones with three different sections based on the standard sections given in the PCI Bridge Design Manual (1997) are given in Appendix D.

Table 4.12 COMPARISON OF $T_{burst-flg}$ AND $d_{burst-flg}$ FOR THE TOP FLANGE OF UNSYMMERTRICAL I-SECTION SUBJECTED TO CONCENTRIC LOAD

Name	t_w	t_{f_1}/t_w	t_{f_1}	b_{f_1}	b_{f_2}	h'	c	R_2/P	k_f	$T_{burst-flg}$	$T_{burst-flg}$	%diff	$d_{burst-flg}$	$d_{burst-flg}$	%diff
	(in.)		(in.)	(in.)	(in.)	(in.)	(in.)			/P	/P	-1 & 2-	/h _w	/h _w	-3 & 4-
										-1-	-2-		-3-	-4-	
US210I	1.5	0.8	1.2	6.4	4.8	17.2	8.43	0.16	0.42	0.0102	0.0114	11.62	0.8905	1.0400	16.78
US210J	1.5	0.8	1.2	6.4	3.2	17.2	8.91	0.17	0.44	0.0115	0.0129	11.73	0.8267	0.9752	17.97
US210L	1.5	0.8	1.2	16	8	17.2	9.51	0.34	0.68	0.0409	0.0482	17.59	0.9457	1.0983	16.14
US210M	1.5	0.8	1.2	16	4.8	17.2	10.28	0.37	0.71	0.0472	0.0547	15.80	0.8858	1.0403	17.44
US210O	1.5	0.8	1.2	56	28.8	17.2	10.11	0.53	0.89	0.0767	0.1073	39.98	1.9872	2.3291	17.21
US210P	1.5	0.8	1.2	56	14.4	17.2	11.74	0.61	0.92	0.0940	0.1185	26.08	1.9499	2.4178	24.00
US211I	1.5	1.1	1.65	6.4	4.8	17.65	8.53	0.20	0.51	0.0159	0.0204	28.34	0.7083	0.7665	8.22
US211J	1.5	1.1	1.65	6.4	3.2	17.65	9.13	0.22	0.54	0.0182	0.0234	28.06	0.6531	0.7176	9.87
US211L	1.5	1.1	1.65	16	8	17.65	9.73	0.39	0.76	0.0540	0.0668	23.78	0.7663	0.9378	22.38
US211M	1.5	1.1	1.65	16	4.8	17.65	10.65	0.43	0.80	0.0629	0.0755	19.98	0.7185	0.8983	25.03
US211O	1.5	1.1	1.65	56	28.8	17.65	10.22	0.56	0.93	0.0847	0.1190	40.47	1.7879	2.2324	24.86
US211P	1.5	1.1	1.65	56	14.4	17.65	11.99	0.65	0.95	0.1010	0.1289	27.70	1.8373	2.3769	29.37
US222I	1.5	1.4	2.1	6.4	4.8	18.1	8.61	0.23	0.59	0.0224	0.0301	34.48	0.6181	0.6403	3.59
US222J	1.5	1.4	2.1	6.4	3.2	18.1	9.31	0.25	0.61	0.0260	0.0347	33.21	0.5695	0.6003	5.42
US222L	1.5	1.4	2.1	16	8	18.1	9.89	0.43	0.82	0.0659	0.0814	23.43	0.6495	0.8627	32.82
US222M	1.5	1.4	2.1	16	4.8	18.1	10.92	0.47	0.85	0.0767	0.0913	19.08	0.6112	0.8355	36.69
US222O	1.5	1.4	2.1	56	28.8	18.1	10.30	0.58	0.94	0.0980	0.1262	28.69	1.5147	2.1867	44.36
US222P	1.5	1.4	2.1	56	14.4	18.1	12.14	0.68	0.97	0.1146	0.1350	17.79	1.6210	2.3675	46.05

Note: All models in the Table contain the dimensions as indicated below:

$$a/h = 0.20, a = 3.2 \text{ in.}, h_w = 16 \text{ in.}, t_w = 1.5 \text{ in.}$$

Table 4.13 COMPARISON OF $T_{burst-flg}$ AND $d_{burst-flg}$ FOR THE BOTTOM FLANGE OF UNSYMMERTRICAL I-SECTION SUBJECTED TO CONCENTRIC LOAD

Name	t_w	t_{f_2}/t_w	t_{f_2}	b_{f_1}	b_{f_2}	h'	c	R_3/P	k_f	$T_{burst-flg}$	$T_{burst-flg}$	%diff	$d_{burst-flg}$	$d_{burst-flg}$	%diff
	(in.)		(in.)	(in.)	(in.)	(in.)	(in.)			/P	/P	-1 & 2-	/h _w	/h _w	-3 & 4-
										-1-	-2-		-3-	-4-	
US210I	1.5	0.8	1.2	6.4	4.8	17.2	8.43	0.11	0.33	0.0050	0.0053	6.43	1.1173	1.1834	5.92
US210J	1.5	0.8	1.2	6.4	3.2	17.2	8.91	0.06	0.24	0.0018	0.0020	10.30	0.9200	1.3014	41.45
US210L	1.5	0.8	1.2	16	8	17.2	9.51	0.15	0.42	0.0089	0.0110	23.51	1.1082	1.2118	9.34
US210M	1.5	0.8	1.2	16	4.8	17.2	10.28	0.08	0.28	0.0031	0.0034	11.53	1.4063	1.3913	-1.07
US210O	1.5	0.8	1.2	56	28.8	17.2	10.11	0.26	0.71	0.0338	0.0532	57.38	1.4685	1.3617	-7.27
US210P	1.5	0.8	1.2	56	14.4	17.2	11.74	0.15	0.51	0.0108	0.0197	82.33	1.3440	1.1266	-16.18
US211I	1.5	1.1	1.65	6.4	4.8	17.65	8.53	0.14	0.41	0.0078	0.0101	28.80	0.8879	0.8359	-5.86
US211J	1.5	1.1	1.65	6.4	3.2	17.65	9.13	0.08	0.30	0.0044	0.0040	-9.86	2.1161	0.8781	-58.50
US211L	1.5	1.1	1.65	16	8	17.65	9.73	0.18	0.50	0.0125	0.0184	47.26	0.8939	0.8974	0.39
US211M	1.5	1.1	1.65	16	4.8	17.65	10.65	0.10	0.35	0.0044	0.0064	44.69	1.1373	0.9537	-16.15
US211O	1.5	1.1	1.65	56	28.8	17.65	10.22	0.28	0.77	0.0414	0.0688	66.00	1.1997	1.1584	-3.44
US211P	1.5	1.1	1.65	56	14.4	17.65	11.99	0.15	0.59	0.0144	0.0303	110.88	1.0326	0.8602	-16.69
US222I	1.5	1.4	2.1	6.4	4.8	18.1	8.61	0.16	0.47	0.0109	0.0156	43.33	0.7648	0.6750	-11.74
US222J	1.5	1.4	2.1	6.4	3.2	18.1	9.31	0.09	0.35	0.0037	0.0065	75.16	0.6275	0.6849	9.14
US222L	1.5	1.4	2.1	16	8	18.1	9.89	0.19	0.56	0.0171	0.0262	53.46	0.7638	0.7464	-2.28
US222M	1.5	1.4	2.1	16	4.8	18.1	10.92	0.11	0.41	0.0060	0.0100	67.54	0.9643	0.7496	-22.27
US222O	1.5	1.4	2.1	56	28.8	18.1	10.30	0.29	0.81	0.0490	0.0807	64.85	0.9863	1.0551	6.98
US222P	1.5	1.4	2.1	56	14.4	18.1	12.14	0.16	0.65	0.0188	0.0403	114.52	0.8339	0.7344	-11.92

Note: All models in the Table contain the dimensions as indicated below:

$$a/h = 0.20, a = 3.2 \text{ in.}, h_w = 16 \text{ in.}, t_w = 1.5 \text{ in.}$$

4.4.2 Eccentrically Loaded Anchor Configuration

4.4.2.1 Finite Element Results

4.4.2.1.1 Elastic Stress Distribution

In the present study, the number of models used for the finite element analysis of eccentrically loaded anchorage zone with flanged section is limited due to the possibility of creating some models with large eccentricity as previously stated. In all flanged sections used in the present research, the values of eccentricity are chosen based on the condition of eccentricity inside and outside the kern of the section. For symmetrical I-sections, the eccentricity ratio (e/h_w) consists of two values: 0.10 and 0.40. There is no direction of eccentric load indicated for this type of section since the section is in symmetric condition with respect to the section centroid. For the modeling of a T-section, the e/h_w ratio is limited to three values of +0.10, -0.10, and -0.40. For the models with the eccentricity value of +0.10, the number of the models is limited to a few because of the inadequate space allowed for the modeling of the anchor plate. No condition of eccentricity outside the kern in the upper direction is possible for T-section models. Similarly for the unsymmetrical I-section, only a few models allow the condition of eccentric load outside the kern.

Figure 4.68 presents the stress contour plots for a symmetrical I-section with the flange width equal to 16 in. The model is loaded at an eccentricity of $0.10h_w$. As can be seen in the figure, the bursting stress region in the symmetrical section model occurs ahead of the anchor plate similar to that in a rectangular section. The location of the bursting stresses in each flange is related to the position of the applied load. Since the eccentric load is applied closer to the bottom flange, the bursting stresses in the bottom flange have a larger magnitude than those in the top flange.

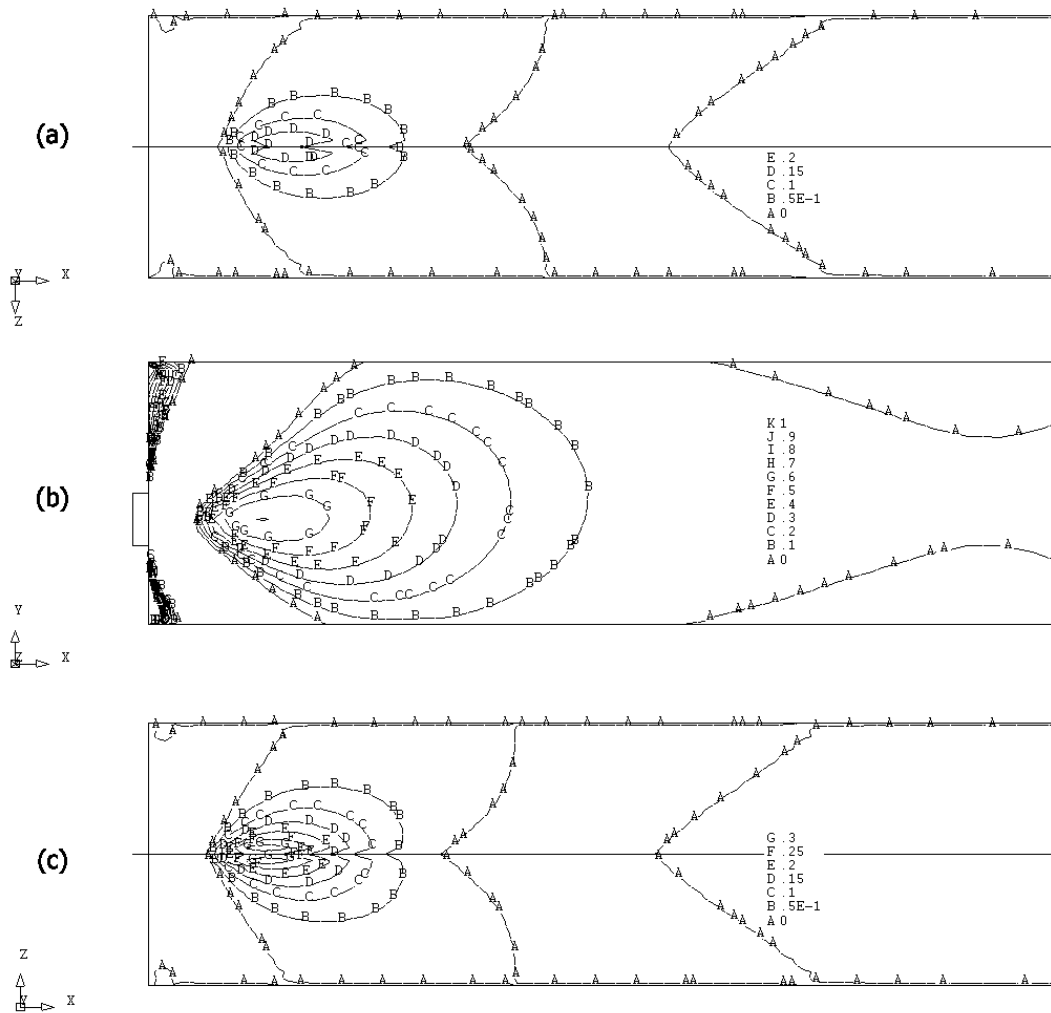


Fig. 4.68 TENSILE STRESSES IN EACH MEMBER OF SYMMETRICAL I-SECTION MODEL WITH $b_f = 16.0$ in. AND $e/h_w = 0.10$

a) TOP FLANGE, b) WEB, AND c) BOTTOM FLANGE (Stress multiplied by σ_O , $A = 228.5$ sq.in.)

In Fig. 4.69, the effect of eccentricity on the flanged section model is even more noticeable. The load is applied at a position with a large eccentricity from the center of the web. The bursting stress region occurs right next to the plane of bottom flange, which results in the bursting stresses in the bottom flange having their position closer to anchorage surface compared to those in Fig. 4.68. The bursting stress region in the top flange is located further away due to the additional space between the location of applied eccentric load and the center of the flange.

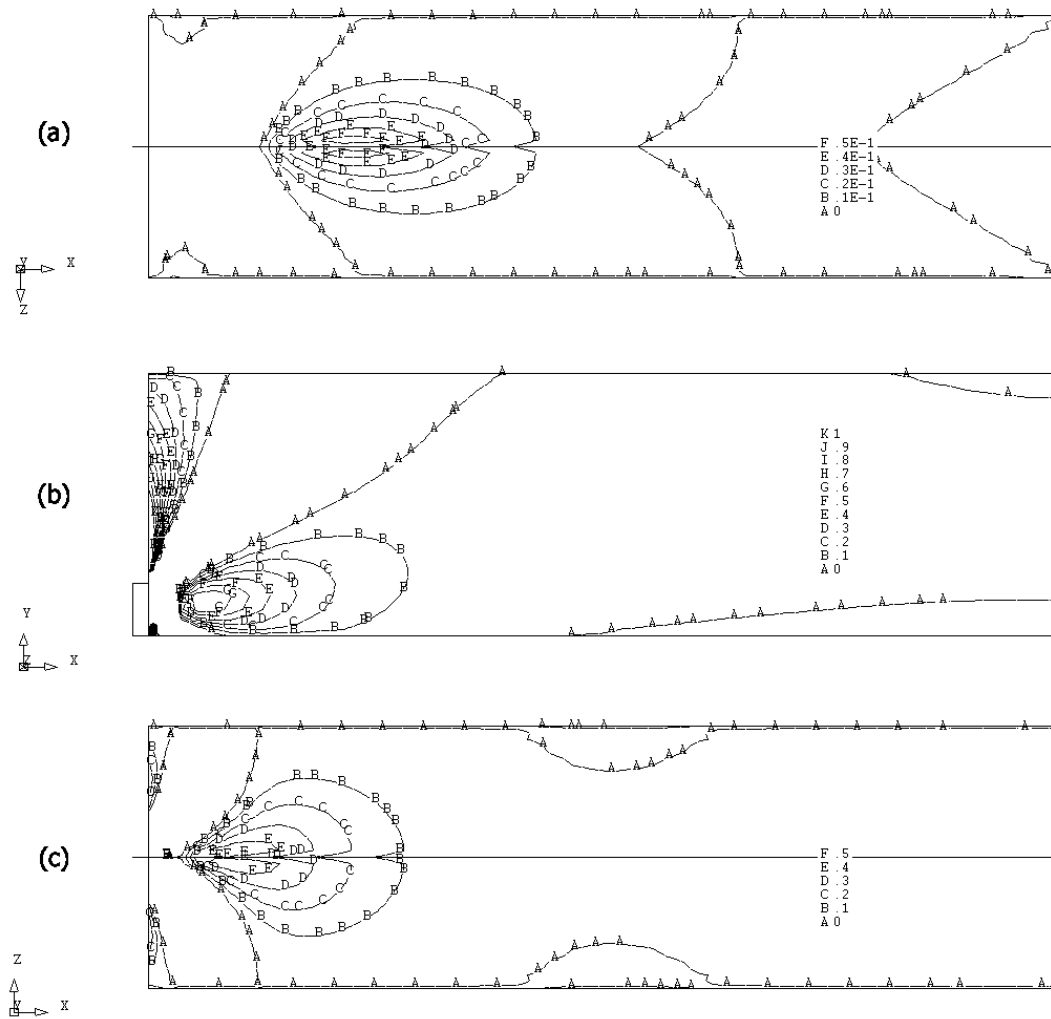


Fig. 4.69 TENSILE STRESSES IN EACH MEMBER OF SYMMETRICAL I-SECTION MODEL WITH $b_f = 16.0$ in. AND $e/h_w = 0.40$

a) TOP FLANGE, b) WEB, AND c) BOTTOM FLANGE (Stress multiplied by σ_o , $A = 228.5$ sq.in.)

Figure 4.70 shows the stress contour plots in the x-x direction of the top flange of the model in Fig. 4.69. It can be seen that almost the whole body of the flange has positive magnitude of stresses (tension) since the application of the eccentric load is located outside the kern of the section. No compression contour is detected within the flange. It is noticed that the stresses in the x-x direction, which is the longitudinal direction of the flange, have a large magnitude in the same region that the bursting stresses in the top flange occur, as can be seen in Fig. 4.69a. The largest stress in the longitudinal direction of the top flange is approximately 6 times its largest stress in the transverse direction.

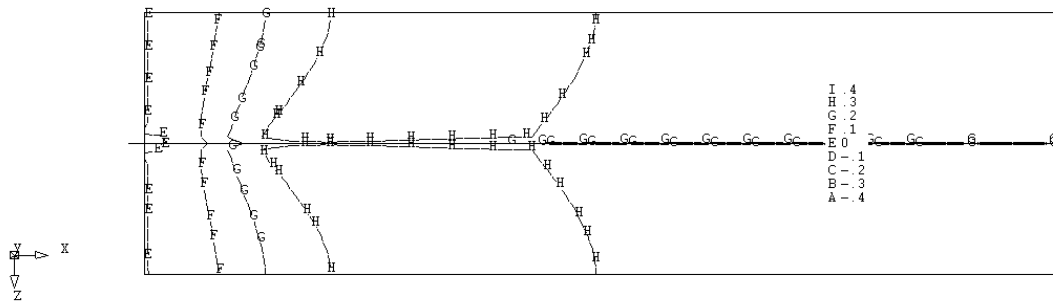


Fig. 4.70 X-X STRESSES IN TOP FLANGE OF SYMMETRICAL I-SECTION MODEL WITH $b_f = 16.0$ in. AND $e/h_w = 0.40$ (Stress multiplied by σ_o , $A = 228.5$ sq.in.)

Figure 4.71 shows the stress contour plots in a T-section model subjected to a load with an eccentricity of $0.10h_w$ in the lower direction with respect to the section centroid. The behavior of the contours does not differ from those of the concentric load configuration. The maximum bursting stresses in the flange occur approximately at the same location as that of the maximum bursting stresses in the web.

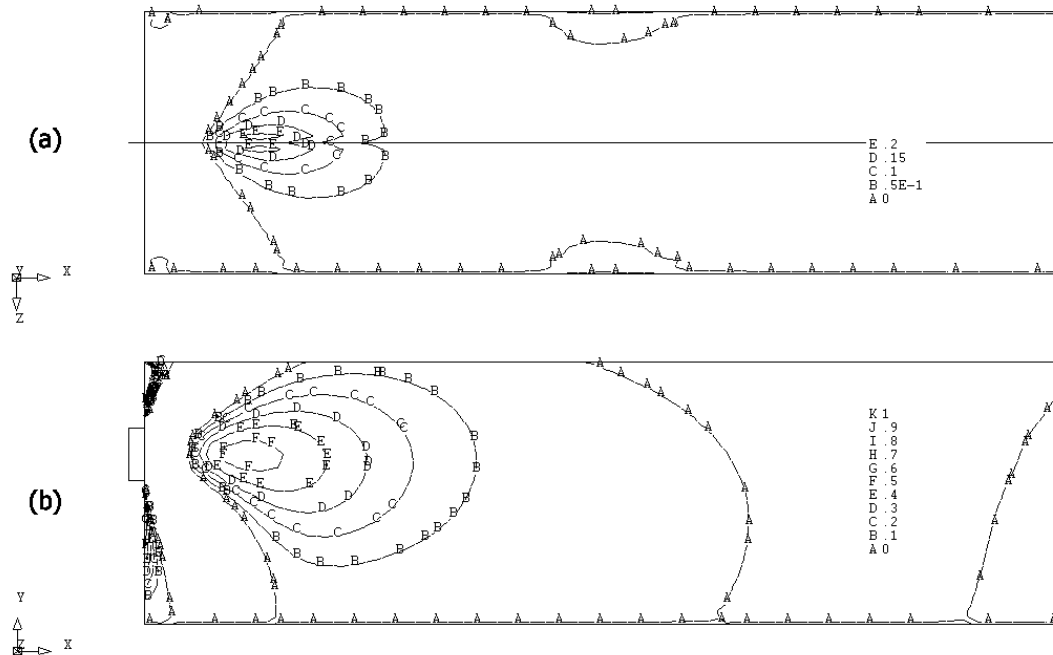


Fig. 4.71 TENSILE STRESSES IN EACH MEMBER OF T-SECTION MODEL WITH $b_f = 16.0$ in. AND $e/h_w = -0.10$
a) TOP FLANGE AND b) WEB (Stress multiplied by σ_o , $A = 154.25$ sq.in.)

For a load applied with an eccentricity outside the kern as shown in Fig. 4.72, the same characteristic of the bursting stresses as that occurring in rectangular sections subjected to eccentric load outside the kern occurs. The stresses in the longitudinal direction of the flange of the T-section are shown in Fig. 4.73. The tensile stresses are distributed over all of the flange body similar to those in a symmetrical I-section. This establishes a similar behavior of both types of flanged sections.

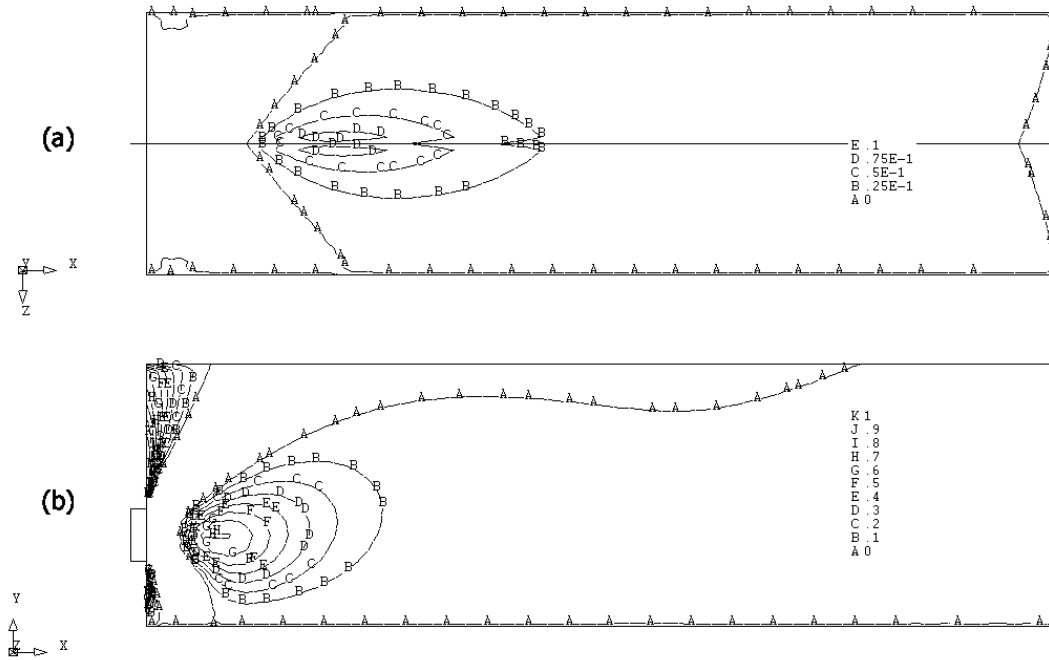


Fig. 4.72 TENSILE STRESSES IN EACH MEMBER OF T-SECTION MODEL WITH $b_f = 16.0$ in. AND $e/h_w = -0.40$
a) TOP FLANGE AND b) WEB (Stress multiplied by σ_o , $A = 154.25$ sq.in.)

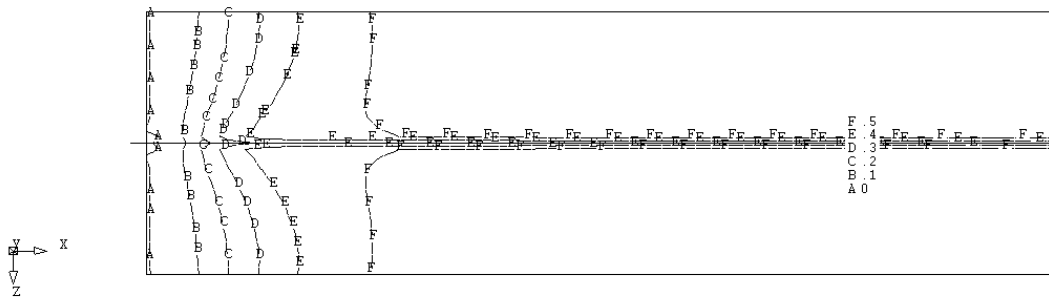


Fig. 4.73 X-X STRESSES IN TOP FLANGE OF T-SECTION MODEL WITH $b_f = 16.0$ in. AND $e/h_w = -0.40$
(Stress multiplied by σ_o , $A = 154.25$ sq.in.)

Figure 4.74 shows the stress contour plots for an unsymmetrical I-section model with an eccentricity of $-0.40h_w$. Similar to those occurring in the symmetrical I-section model in Fig. 4.69, the proximity of the load to the bottom flange results in the bursting stresses in the bottom flange to be located closer to the anchorage surface. The bursting stresses in the top flange occur at a position more distant from the anchorage surface compared to the location of bursting stresses in the model with the same dimensions of the flanges but subjected to a concentric load.

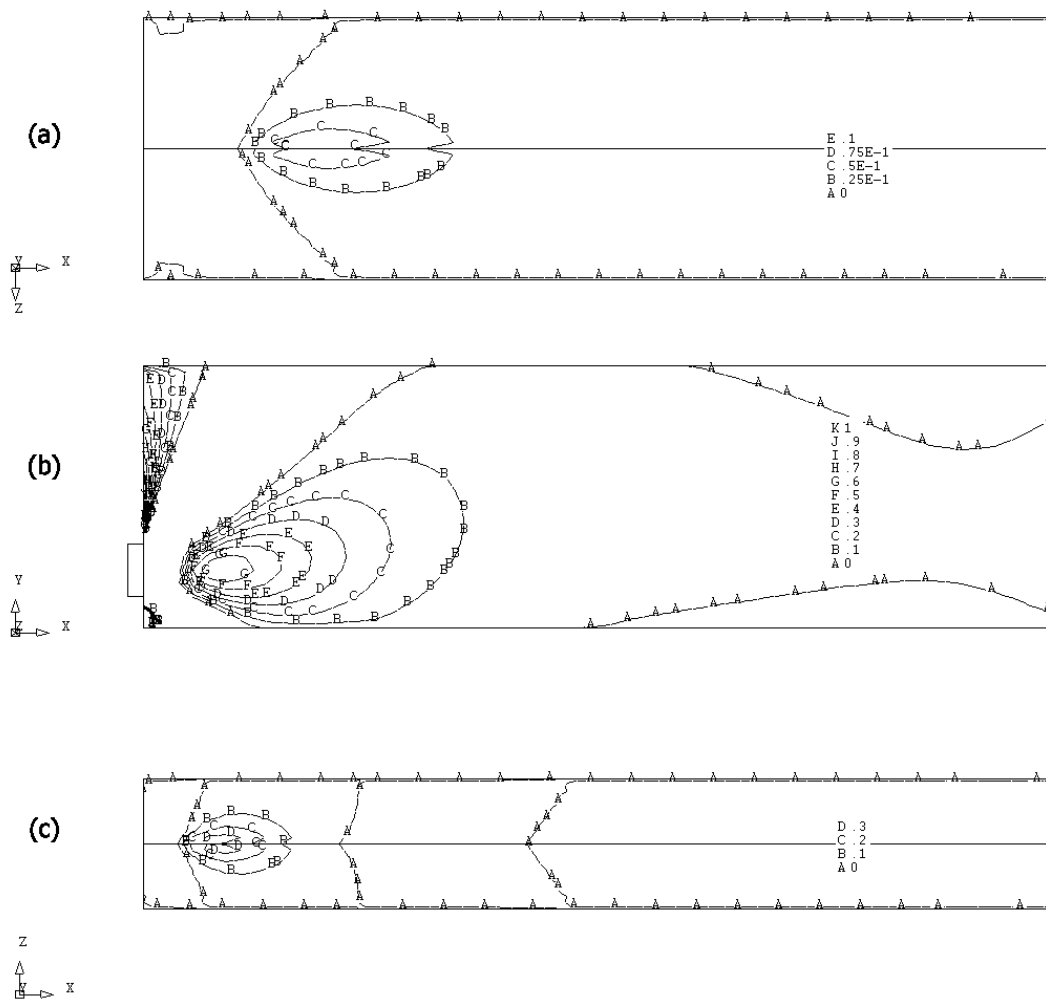


Fig. 4.74 TENSILE STRESSES IN EACH MEMBER OF UNSYMMETRICAL I-SECTION MODEL WITH $b_{f1} = 16$ in., $b_{f2} = 8$ in., AND $e/h_w = 0.40$

a) TOP FLANGE, b) WEB, AND c) BOTTOM FLANGE (Stress multiplied by σ_O , $A = 184.5$ sq.in.)

Based on the elastic stress distributions, it can be seen that the eccentricity of the prestressing load significantly affects the behavior of bursting stresses in the flanges. If the load is located closer to one flange, the magnitude of the bursting stresses in that flange increases and the location of the bursting stress region moves closer to the anchorage surface. On the other hand, in the flange the load is farther from, the bursting stress magnitude is reduced and the location of the stresses is further away from the anchorage surface. A large eccentricity of prestressing load also causes longitudinal tensile stresses to occur in the flange that is further from the load. The determination of longitudinal edge tension is certainly required.

4.4.2.1.2 Bursting Force

It has been shown that the size of a flange significantly affects the magnitude of the bursting force; therefore only the behavior of the bursting force due to the change of flange width is illustrated in this section. More flange widths are used to create more detailed plots. All models in this section contain an anchorage ratio of 0.20, web thickness of 5 in., and a thickness ratio of 1.1.

4.4.2.1.2.1 Symmetrical I-Section

Since a prestressing load is applied eccentrically, the plots for bursting force in the top and bottom flanges exhibit a different behavior. Fig. 4.75 shows the relation between the magnitude of bursting force in each member of a symmetrical I-section and the width of the flange for the eccentricity of $0.10h_w$. As can be seen, the behavior of the plot for the bursting force magnitude in the web is similar to those of concentrically loaded symmetrical I-sections. However, the plots of the top and bottom flanges are distinguished from each other. The top flange contains a smaller magnitude of the force compared to that in the bottom flange, which is closer to the load than the top flange. This corresponds to the behavior of stresses in each flange that was previously illustrated.

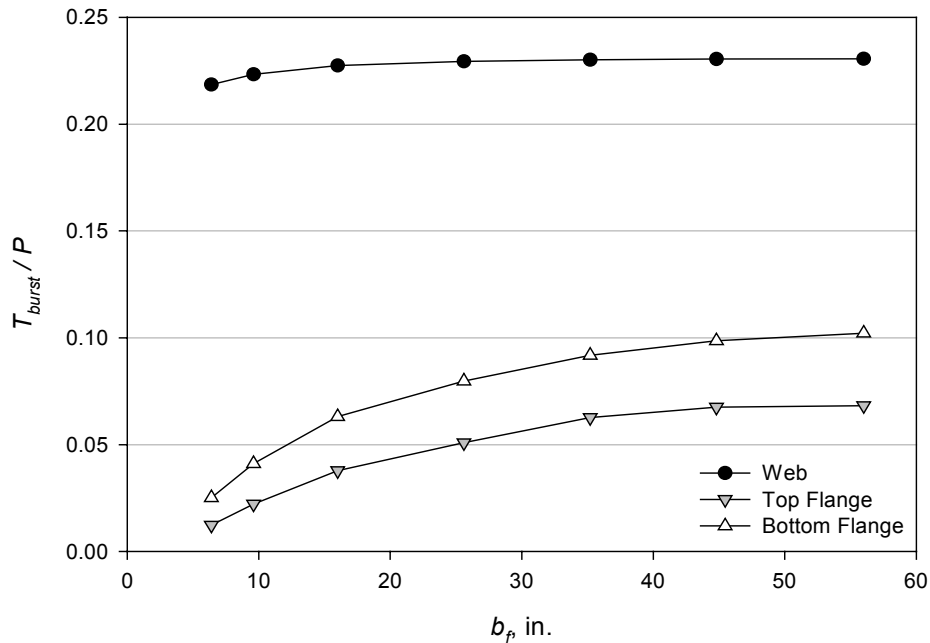


Fig. 4.75 BURSTING FORCE vs. FLANGE WIDTH FOR SYMMETRICAL I-SECTION WITH $e/h_w = 0.10$ ($a/h_w = 0.20$, $t_w = 5$ in., and $t_f/t_w = 1.10$)

Figure 4.76 presents the plots of the bursting force for the models of symmetrical I-sections relative to the flange width subjected to an e/h_w ratio of 0.40. Since the prestressing load is applied at a large eccentricity, the load is closer to the bottom flange. For flange widths greater than 15 in. the magnitude of the bursting force in the bottom flange is larger than that in the web while the magnitude of the bursting force in the top flange remains the smallest. The largest value of bursting force in the bottom flange is $0.1408P$. Comparing to $0.1118P$ that occurs in the web, it can be seen that the magnitude of the bursting force in the bottom flange is 20.6 percent larger. The top flange for this model has a bursting force equal to $0.0601P$.

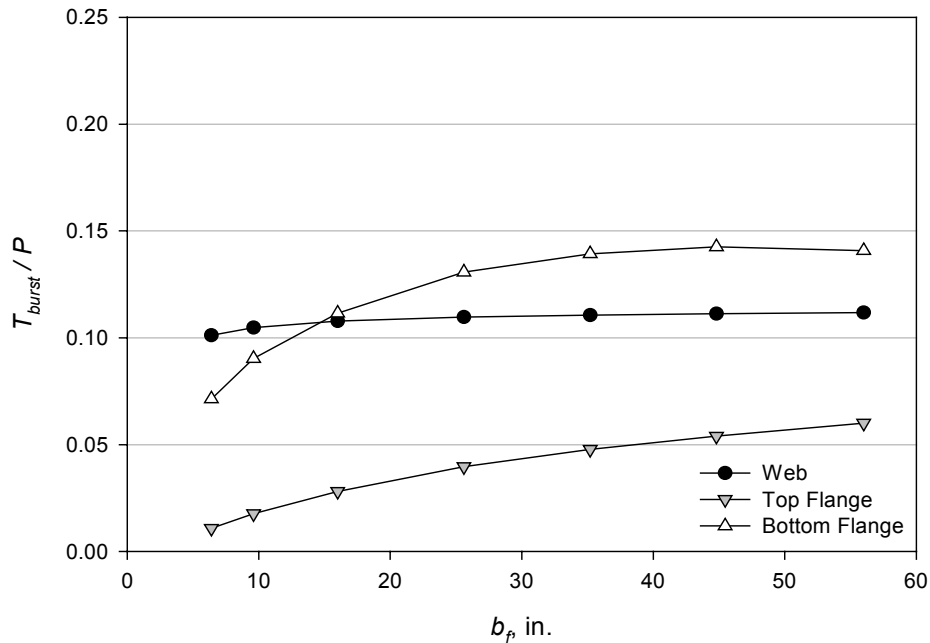


Fig. 4.76 BURSTING FORCE vs. FLANGE WIDTH FOR SYMMETRICAL I-SECTION WITH $e/h_w = 0.40$
 ($a/h_w = 0.20$, $t_w = 5$ in., and $t_f/t_w = 1.10$)

4.4.2.1.2.2 T-Section

Figure 4.77 presents the plots of the bursting force in a T-section model subjected to a load with an eccentricity of $-0.10h_w$. The plots are very similar to those occurring in the concentric load case. The plot for the bursting force in the web slopes downward as the flange width increases, while the bursting force magnitude in the flange becomes higher. For the application of an eccentric load with a small eccentricity in the upper portion of the model, the behavior of the bursting force is quite similar to the case of a concentrically loaded T-section anchorage zone when the position of the load is very close to the center of the flange as has been illustrated previously.

Figure 4.78 shows the behavior of the bursting force of T-section models subjected to an eccentric prestressing load applied outside kern below the section centroid with an e/h_w value of -0.40 . Since the longitudinal tensile stresses occur on the top flange in this model, there is no internal compressive force applied into the body of the flange, which is assumed to be the cause of the bursting force occurring within the flange body. However, the plot of the

bursting force in the top flange indicates a high value. When the model has a flange width larger than 36 in., the bursting force in the flange is larger than that in the web. The flange bursting force for the model with the widest flange has a magnitude as high as $0.2741P$, which is considered to be a very large amount of force. By determining the longitudinal tensile force in the top flange of this model based on the simple beam theory, the magnitude of longitudinal force determined is $0.3226P$. The bursting force in the flange is approximately 0.85 times the magnitude of the longitudinal tensile force in the flange of the same model. Therefore, it would be conservative to use the magnitude of the longitudinal tensile force to determine the amount of transverse reinforcing steel in the flange in the case of a flanged section subjected to a highly eccentric prestressing load.

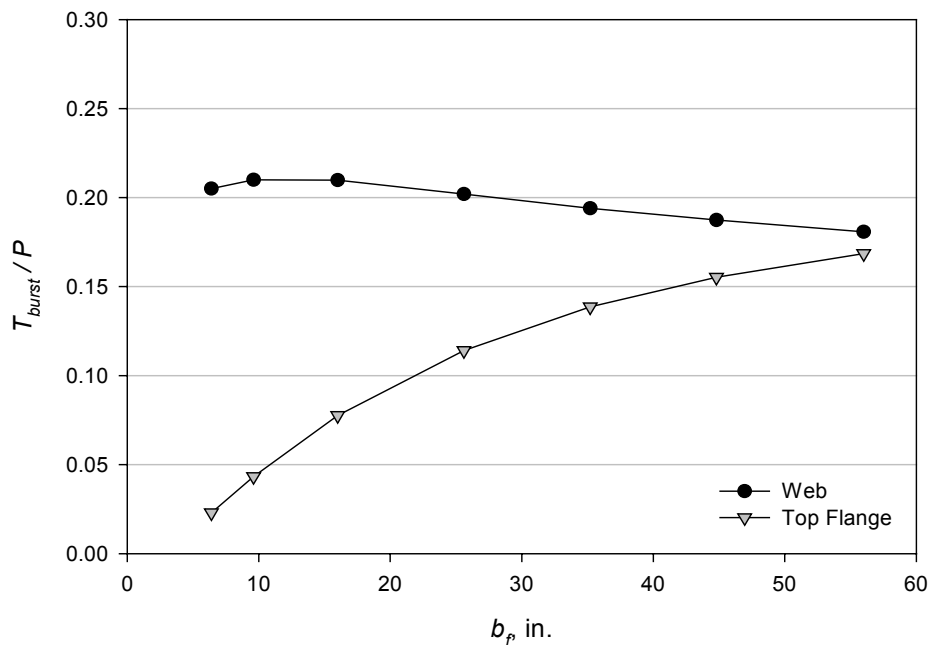


Fig. 4.77 BURSTING FORCE vs. FLANGE WIDTH FOR T-SECTION WITH $e/h_w = -0.10$
 ($a/h_w = 0.20$, $t_w = 5$ in., and $t_f/t_w = 1.10$)

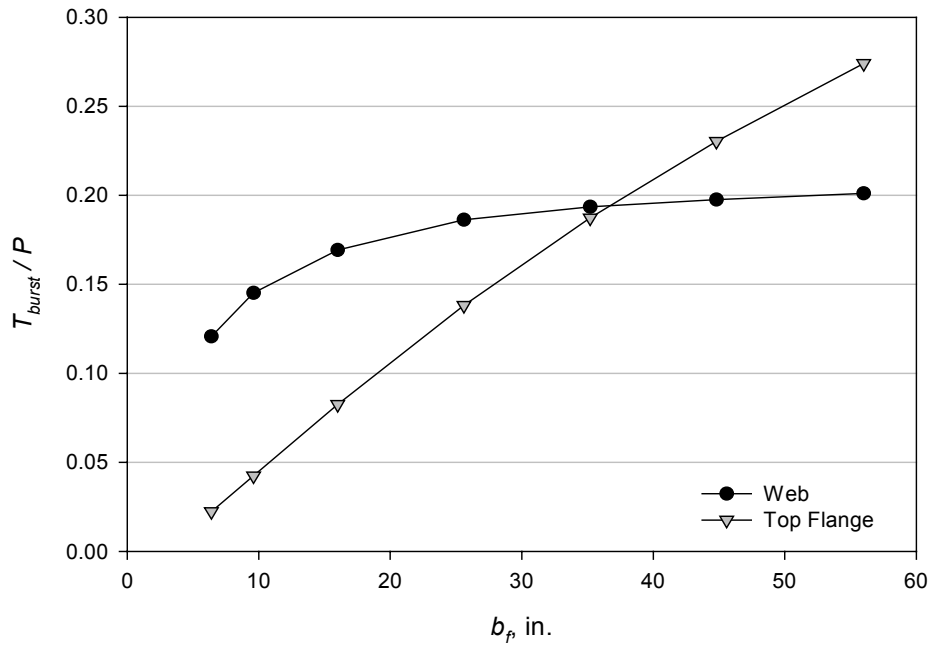


Fig. 4.78 BURSTING FORCE vs. FLANGE WIDTH FOR T-SECTION WITH $e/h_w = -0.40$
 ($a/h_w = 0.20$, $t_w = 5$ in., and $t_f/t_w = 1.10$)

4.4.2.1.2.3 Unsymmetrical I-Section

Figure 4.79 shows the relation between the bursting force magnitude of each member within a flanged section relative to the flange width ratio b_{f2}/b_{f1} for the models with two top flange widths: 16 in. and 56 in. Since the prestressing load is not applied at the center of the section centroid, the magnitudes of the bursting forces in both the top and bottom flanges do not equal at the ratio of b_{f2}/b_{f1} equals to 1.0. However, the variation of the plots from the flange width ratio of 0 to 1.0 establishes that the behavior of the bursting force in each part of the section is similar to that in concentrically loaded unsymmetrical I-sections.

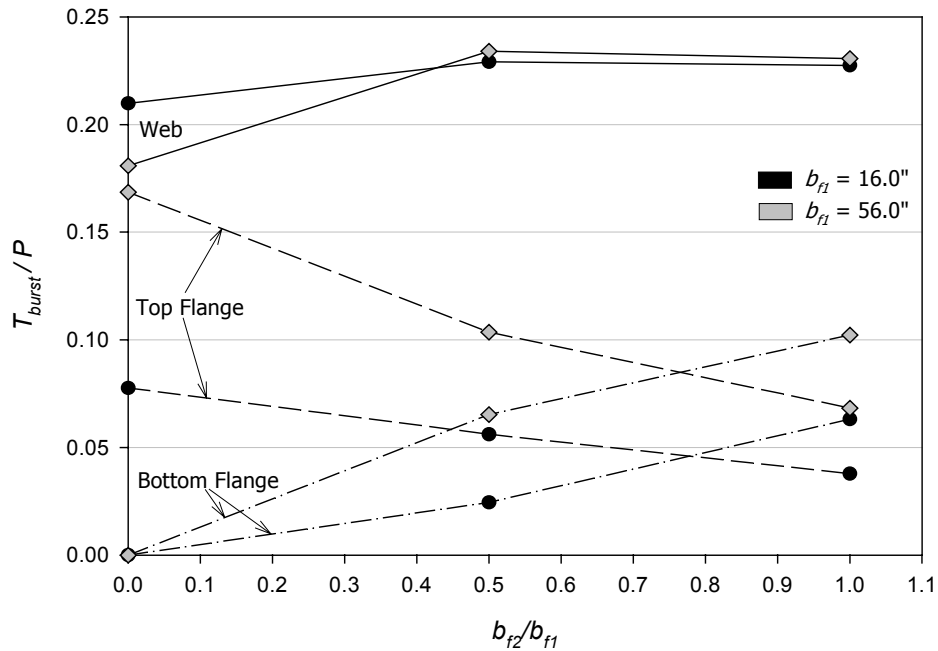


Fig. 4.79 BURSTING FORCE vs. FLANGE WIDTH RATIO WITH $e/h_w = -0.10$
 ($a/h_w = 0.20$, $t_w = 5$ in. and $t_f/t_w = 1.10$)

4.4.2.1.3 Location of Bursting Force

4.4.2.1.3.1 Symmetrical I-Section

Figure 4.80 shows the relation between the location of the bursting force in both the web and flanges on a symmetrical I-section anchorage zone subjected to an eccentric load with an eccentricity of $0.10h_w$. Similar to what occurs in the plots of the bursting force magnitude, the plots are similar to those from the concentric load case except the locations of bursting force of top and bottom flange are different. The location of the bursting force in the bottom flange is further away from the anchorage surface than the location of bursting force in the top flange, which corresponds to the stress distribution illustrated previously.

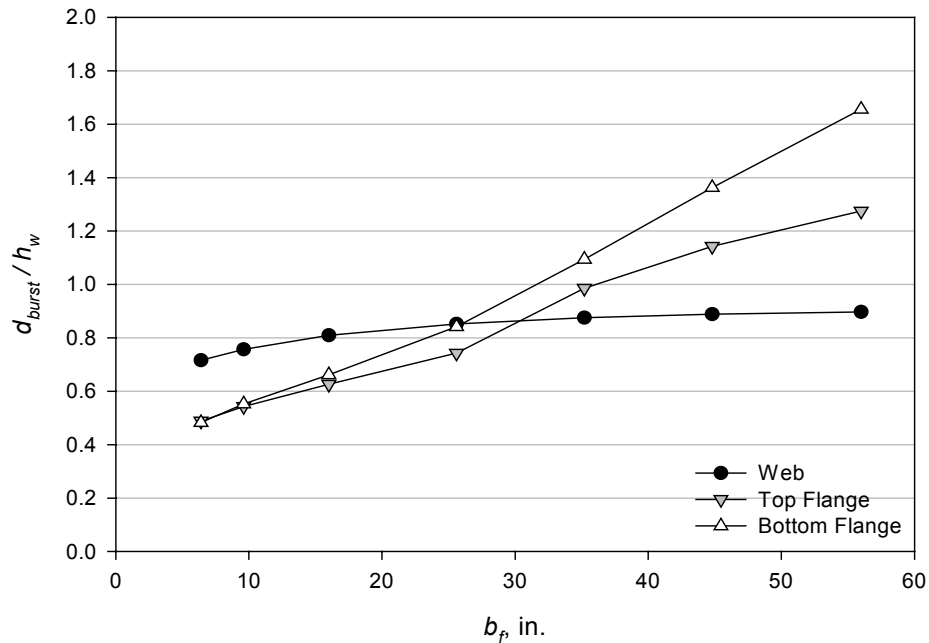


Fig. 4.80 BURSTING FORCE LOCATION vs. FLANGE WIDTH FOR SYMMETRICAL I-SECTION WITH $e/h_w = 0.10$
 ($a/h_w = 0.20$, $t_w = 5$ in., and $t_f/t_w = 1.10$)

As the eccentricity becomes larger, the plots of the locations of the bursting force in both the top and bottom flanges exhibit very different characteristics. Fig. 4.81 shows the locations of bursting forces in the web and flanges of symmetrical section models relative to the flange width. As can be seen, the distance of the bursting force in the top flange is much larger than in the bottom flange. The location of the bursting force in the top flange is the location of tensile stress induced by the longitudinal tensile stresses that occur in the flange, which result from the application of an eccentric load outside the kern. The plot of the bursting force location in the bottom flange is similar to the plot of the bursting force location in the flange subjected to internal compressive forces, which are transferred from the web.

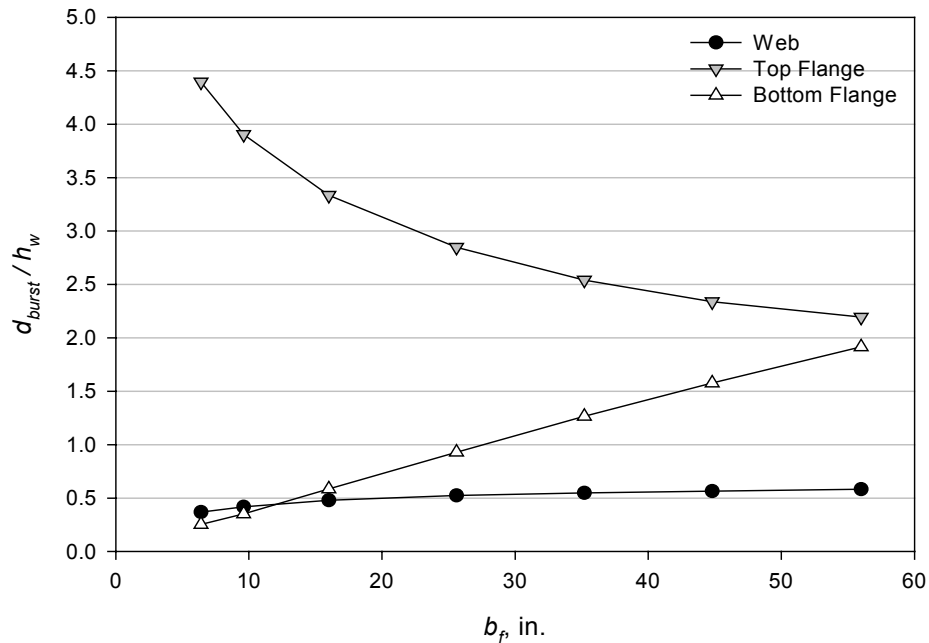


Fig. 4.81 BURSTING FORCE LOCATION vs. FLANGE WIDTH FOR SYMMETRICAL I-SECTION WITH $e/h_w = 0.40$ ($a/h_w = 0.20$, $t_w = 5$ in., and $t_f/t_w = 1.10$)

4.4.2.1.3.2 T-Section

Similar to those from the symmetrical I-section models, the plots of the bursting force location for T-section models with an eccentricity of $-0.10h_w$ are similar to those for concentrically loaded T-section models as can be seen in Fig. 4.82. However, the location of the flange bursting force is relatively large compared to that of the web. With an eccentric load applied far away from the flange, the load requires additional length to propagate the internal forces to the flange. This results in a greater distance from the location to the anchorage surface. The behavior of the bursting force location in models subjected to an eccentric load outside the kern is presented in Fig. 4.83. As the eccentricity increases to a position outside the kern, the location of the bursting force in the web slightly decreases with respect to that in Fig. 4.82. However, the location of the bursting force in the flange becomes much further from the prestressing surface. The smallest flange bursting force location in Fig. 4.83 is approximately 3.25 times the height of the web.

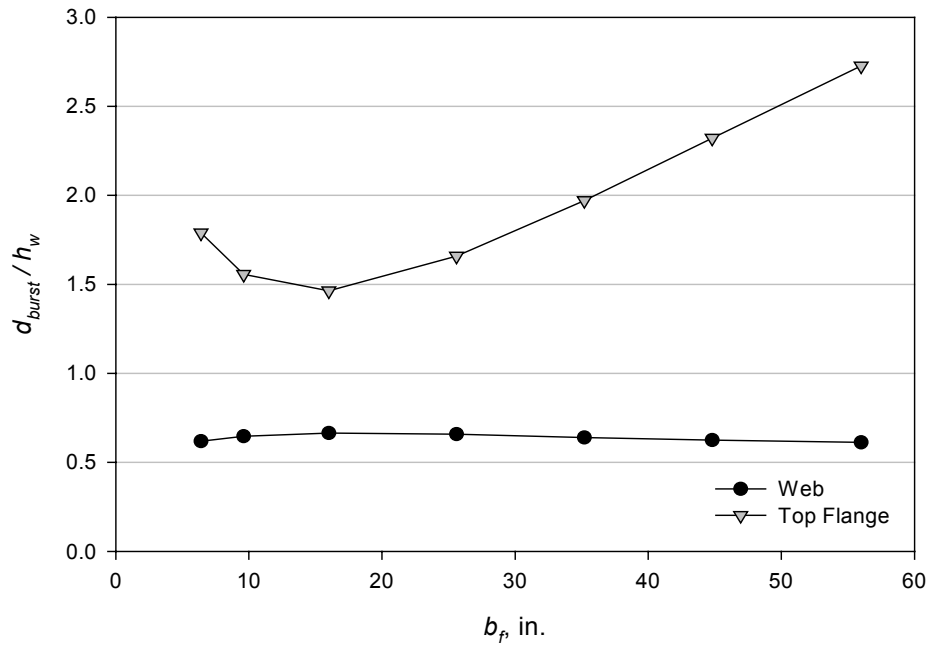


Fig. 4.82 BURSTING FORCE LOCATION vs. FLANGE WIDTH FOR T-SECTION WITH $e/h_w = -0.10$
 ($a/h_w = 0.20$, $t_w = 5$ in., and $t_f/t_w = 1.10$)

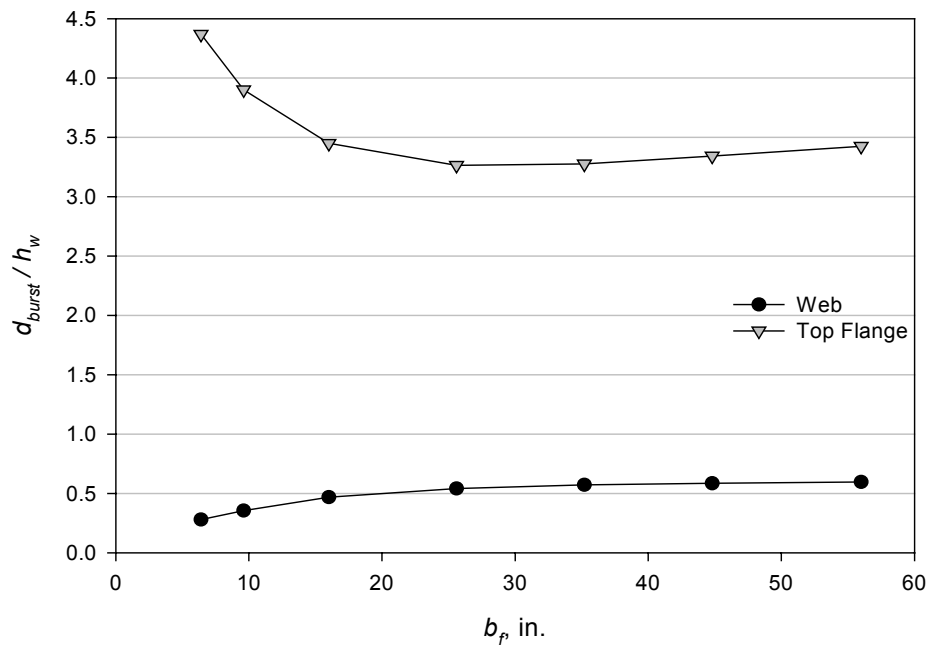


Fig. 4.83 BURSTING FORCE LOCATION vs. FLANGE WIDTH FOR T-SECTION WITH $e/h_w = -0.40$
 ($a/h_w = 0.20$, $t_w = 5$ in., and $t_f/t_w = 1.10$)

4.4.2.1.3.3 Unsymmetrical I-Section

Figure 4.84 shows the relation between the location of the bursting force in each member and the flange width ratio for models with eccentricity within the kern. As shown, the locations of the bursting force in unsymmetrical I-section models develop with a similar trend as those of the magnitudes of the force. Although the largest distance of bursting force occurs in the top flange, the distance decreases as the flange width ratio increases, similar to the plot of bursting force magnitude of the top flange as shown in Fig. 4.79. The plots of bursting force location in Fig. 4.84 illustrate the relationship among three types of flanged sections used in this study similar to those presented in Fig. 4.79.

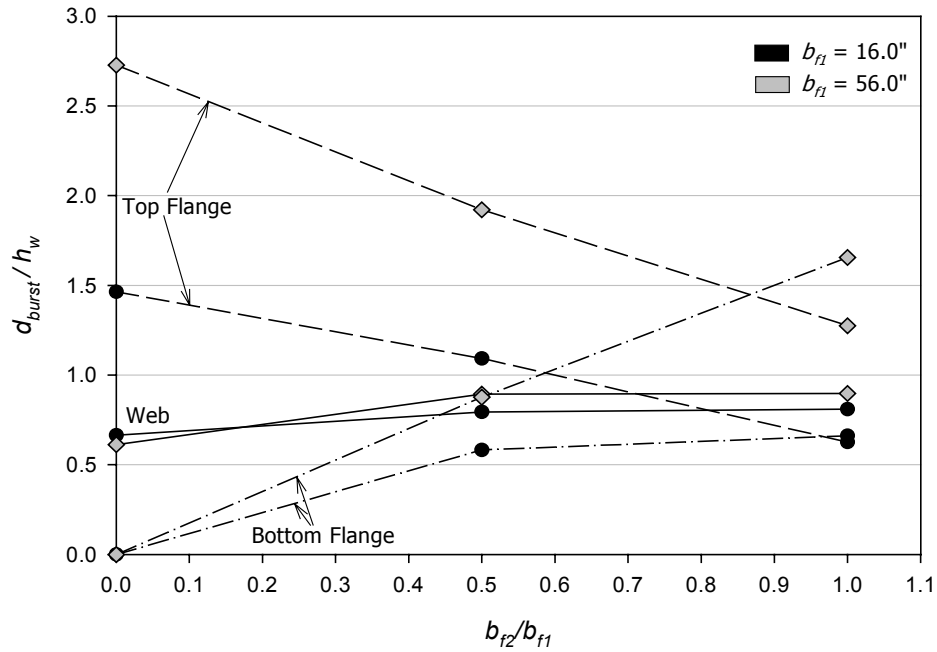


Fig. 4.84 BURSTING FORCE LOCATION vs. FLANGE WIDTH RATIO WITH $e/h_w = -0.10$
 ($a/h_w = 0.20$, $t_w = 5$ in., and $t_{f1}/t_w = t_{f2}/t_w = 1.1$)

4.4.2.2 Formulations

This section presents the formulations of bursting force magnitude and location for an eccentrically loaded anchorage zone in a flanged section. For an eccentric load application, the positions of the resultant forces at the end of the strut-and-tie model in Fig. 4.67 change. This is because the stress at the end of the structure is not uniform but instead varies linearly as can be seen in Fig. 4.85. The resultant forces in each area of the member can be determined using classical beam theory. In Fig. 4.85, a strut-and-tie model used in the formulations of bursting force for an unsymmetrical section can be employed in the formation of the approximate equations of bursting force in this section. The stress used for the calculation of the resultant forces is determined from the stress at each level of the flanged section as shown in Fig. 4.85. The stress at each fiber of the top flange is named as σ_{to} and σ_{ti} , which represent the stresses at outer fiber and inner fiber of the top flange, respectively. The stresses σ_{bo} and σ_{bi} represent the stresses at outer fiber and inner fiber of the bottom flange, respectively. The stress σ_e is the stress at the level of the eccentric load. All stresses are negative in compression and positive in tension and can be determined using the expression based on simple beam theory as

$$\sigma = -\frac{P}{A_f} \pm \frac{My}{I_f} \quad (4.31)$$

In equation (4.31), σ is the stress at distance y from the centroid, M is the total moment about the section centroid, A_f is the total area of a flanged section, and I_f is the moment inertia of the same section. In Fig. 4.85, e is the eccentricity, which is positive in the upward direction and negative in the other direction with respect to the centroid axis.

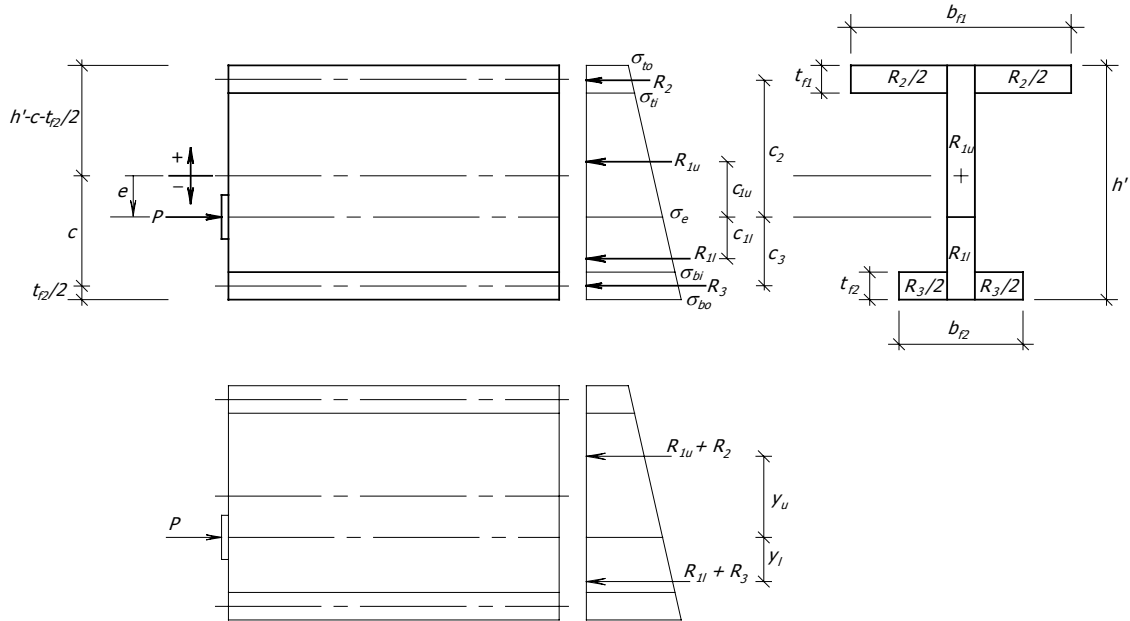


Fig. 4.85 FREE BODY FOR THE CALCULATION OF RESULTANT FORCES FOR ECCENTRIC LOAD CASE

Since the shape of the stress diagram does not remain a rectangular shape, the centroid of the resultant forces is not located at the center of the area of each member. By considering the position of each resultant force with respect to the location of the prestressing load, the distance from the load to the resultant force is assigned by using a c character with a subscript corresponding the considered resultant force. For example, if the resultant load R_2 is considered, the distance from the prestressing force to the force R_2 is assigned as c_2 . The location of each resultant force with respect to the position of the prestressing load can be determined using the expressions presented in Appendix A. For the resultant forces on the web of the section, since the stress diagram is a trapezoidal shape, γR_l and $(1-\gamma)R_l$ are renamed R_{lu} and R_{ll} , respectively. The expressions to determine the magnitudes of all resultant forces in Fig. 4.85 are

$$R_{lu} = \frac{1}{2} |(\sigma_{to} + \sigma_e)| \left(h' - c - \frac{t_{f2}}{2} - e \right) t_w \quad (4.32)$$

$$R_{ll} = \frac{1}{2} |(\sigma_e + \sigma_{bo})| \left(c + \frac{t_{f2}}{2} + e \right) t_w \quad (4.33)$$

$$R_2 = \frac{1}{2}(\sigma_{to} + \sigma_{ti})(b_{f1} - t_w)t_{f1} \quad (4.34)$$

$$R_3 = \frac{1}{2}(\sigma_{bi} + \sigma_{bo})(b_{f2} - t_w)t_{f2} \quad (4.35)$$

Similar to those used in the formulations of concentric load configuration, the centroids of the resultant forces in the upper and lower portions of the flanged section are used in the modified strut-and-tie model as presented in sections 4.4.1.2.2 and 4.4.1.2.3. As can be seen from Fig. 4.85, the locations of the centroids in the upper and lower portions are represented by y_u and y_l , respectively, and their expressions can be found in Appendix A. By substituting the new variables into equations (4.20) and (4.26), the new equations can be rewritten as

$$T_{burst-web} = (R_{1u} + R_2) \left(\frac{4y_u + 4p}{4d_{burst-web} - a} \right) \left(1 - \frac{a}{4y_u + 4p} \right) \quad (4.36)$$

$$T_{burst-web} = (R_{1l} + R_3) \left(\frac{4y_l - 4p}{4d_{burst-web} - a} \right) \left(1 - \frac{a}{4y_l - 4p} \right) \quad (4.37)$$

By including the eccentricity term in the formulations of the web bursting force location, equations (4.27) and (4.28) can also be rewritten as

$$d_{burst-web} = (h' - c - \frac{t_{f2}}{2} - e) + \frac{a}{4} + \frac{h_w}{4} (1 - \exp(-0.8b_{f1} / h_w)) \quad (4.38)$$

$$d_{burst-web} = (c + \frac{t_{f2}}{2} + e) + \frac{a}{4} + \frac{h_w}{4} (1 - \exp(-0.8b_{f2} / h_w)) \quad (4.39)$$

Equation (4.38) is used for the $d_{burst-web}$ in the upper portion while equation (4.39) presents the $d_{burst-web}$ value for the lower portion. The $d_{burst-web}$ used in equations (4.36) and (4.37) is the smaller value of equations (4.38) and (4.39). Note that the equation developed herein can also be used in the estimation of the magnitude and the location of the bursting force in a rectangular section as well. By substituting all the variables of a rectangular section into equations (4.36) to (4.39), the same equations as those used in the design of a rectangular section result.

Table 4.14 shows the comparison of the results from the finite element analysis and those using equations (4.36) to (4.39) for symmetrical I-section subjected to both eccentric loads inside and outside the kern. The column $max\ e$ in Table 4.14 indicates the position of the kern with respect to the section centroid. According to the percent difference of $d_{burst-wfem}$ and $d_{burst-web}$, the result using equations (4.38) and (4.39) gives a very close estimation to that from the finite element analysis. Almost all the percent difference values are negative except the model EIS52A. The model is subjected to an eccentric load outside the kern. The percent differences of the magnitudes of web bursting force are all positive, which indicates a conservative approximation. Among the models with large eccentricity, the models EIS52A and EIS52H contain negative resultant forces as can be seen in the column R_2/P . These negative values indicate that large magnitudes of longitudinal tensile forces occur in the whole area of the top flanges of these two models.

Table 4.14 COMPARISON OF $T_{burst-web}$ AND $d_{burst-web}$ FOR SYMMETRICAL I-SECTION SUBJECTED TO ECCENTRIC LOAD

Name	b_f (in.)	e/h_w	e (in.)	$max\ e$ (in.)	R_{1u} /P	R_{1l} /P	R_2 /P	R_3 /P	p (in.)	y_u (in.)	y_l (in.)	$d_{burst-wfem}$ /h _w	$d_{burst-web}$ /h _w	%diff	$T_{burst-wfem}$ /P	$T_{burst-web}$ /P	%diff
												-1-	-2-	-1 & 2-	-3-	-4-	-3 & 4-
<i>Eccentric Inside Kern</i>																	
EIS51A	6.4	0.10	1.60	3.91	0.41	0.46	0.04	0.08	-0.07	5.96	5.04	0.7160	0.6903	-3.58	0.2186	0.2278	4.23
EIS51H	9.6	0.10	1.60	4.42	0.33	0.35	0.12	0.20	-0.08	6.67	5.39	0.7570	0.7172	-5.26	0.2233	0.2422	8.46
EIS51B	16	0.10	1.60	4.96	0.23	0.24	0.20	0.33	-0.10	7.48	5.74	0.8093	0.7595	-6.15	0.2274	0.2515	10.59
EIS51I	25.6	0.10	1.60	5.35	0.16	0.16	0.26	0.41	-0.12	8.09	5.98	0.8518	0.8024	-5.80	0.2294	0.2531	10.34
EIS51J	35.2	0.10	1.60	5.55	0.12	0.12	0.30	0.46	-0.13	8.42	6.10	0.8749	0.8289	-5.26	0.2301	0.2525	9.72
EIS51K	44.8	0.10	1.60	5.67	0.10	0.10	0.32	0.49	-0.13	8.63	6.17	0.8882	0.8453	-4.83	0.2305	0.2521	9.37
EIS51C	56	0.10	1.60	5.77	0.08	0.08	0.33	0.51	-0.14	8.79	6.22	0.8967	0.8567	-4.46	0.2306	0.2521	9.31
<i>Eccentric Outside Kern</i>																	
EIS52A	6.4	0.40	6.40	3.91	0.47	0.41	-0.01	0.14	-0.08	2.60	2.15	0.3672	0.3903	6.29	0.1012	0.1432	41.59
EIS52H	9.6	0.40	6.40	4.42	0.38	0.30	-0.01	0.33	-0.21	3.40	2.00	0.4180	0.4172	-0.20	0.1047	0.1511	44.24
EIS52B	16	0.40	6.40	4.96	0.28	0.19	0.01	0.52	-0.34	4.68	1.89	0.4791	0.4595	-4.08	0.1078	0.1557	44.37
EIS52I	25.6	0.40	6.40	5.35	0.19	0.13	0.04	0.64	-0.43	6.08	1.83	0.5237	0.5024	-4.07	0.1097	0.1553	41.59
EIS52J	35.2	0.40	6.40	5.55	0.15	0.09	0.05	0.70	-0.47	7.09	1.81	0.5480	0.5289	-3.50	0.1106	0.1541	39.36
EIS52K	44.8	0.40	6.40	5.67	0.12	0.08	0.06	0.74	-0.50	7.85	1.79	0.5652	0.5453	-3.53	0.1112	0.1536	38.07
EIS52C	56	0.40	6.40	5.77	0.10	0.06	0.07	0.77	-0.52	8.53	1.78	0.5820	0.5567	-4.36	0.1118	0.1536	37.34

Note: All models in the Table contain the dimensions as indicated below:

$$a/h = 0.20, a = 3.2 \text{ in.}, h_w = 16 \text{ in.}, t_w = 5 \text{ in.}, t_f/t_w = 1.1, t_f = 5.5 \text{ in.}, h' = 21.5 \text{ in.}, c = 8 \text{ in.}$$

Tables 4.15 and 4.16 show the comparison of the results between finite element method and the approximate equations for T-sections and unsymmetrical I-sections, respectively. As can be seen from both tables, some estimations of web bursting force location are very similar to those from finite element method. Based on the model, which contains negative

percent difference of the $d_{burst-web}$, the estimated magnitude of the force for the same model is higher than that achieved from finite element analysis. However, the combination of those values of $d_{burst-web}$ and $T_{burst-web}$ should produce conservative designs. There are three cases in which the estimation of $T_{burst-web}$ gives a negative percent difference, but the percent differences occurring are very small, less than 3 percent. In conclusion, the estimation of the bursting force magnitude and location using equations (4.36) to (4.39) is acceptable for eccentrically loaded anchorage zones in a flanged section.

Table 4.15 COMPARISON OF $T_{burst-web}$ AND $d_{burst-web}$ FOR T-SECTION
SUBJECTED TO ECCENTRIC LOAD

Name	b_f (in.)	c (in.)	e/h_w	e (in.)	$max\ e$ (in.)	R_{1u} /P	R_{1l} /P	R_2 /P	p (in.)	y_u (in.)	y_l (in.)	$d_{burst-wfem}$ /h _w	$d_{burst-web}$ /h _w	%diff -1 & 2-	$T_{burst-wfem}$ /P	$T_{burst-web}$ /P	%diff -3 & 4-
<i>Eccentric Inside Kern in Upper Portion</i>																	
ETS53A	6.4	9.88	0.10	1.60	3.07	0.46	0.44	0.10	0.09	3.96	5.00	0.6378	0.5730	-10.17	0.1971	0.2170	10.11
ETS53H	9.6	10.78	0.10	1.60	2.87	0.33	0.40	0.27	0.17	3.50	5.33	0.6556	0.5432	-17.13	0.1867	0.2191	17.39
ETS53B	16	11.97	0.10	1.60	2.44	0.21	0.32	0.48	0.30	2.58	5.61	0.6960	0.5112	-26.55	0.1578	0.1930	22.31
<i>Eccentric Inside Kern in Lower Portion</i>																	
ETS51A	6.4	9.88	-0.10	-1.60	3.42	0.42	0.53	0.05	-0.05	4.96	4.37	0.6189	0.5963	-3.66	0.2051	0.2201	7.35
ETS51H	9.6	10.78	-0.10	-1.60	3.88	0.34	0.51	0.16	-0.01	5.05	4.87	0.6465	0.6583	1.83	0.2100	0.2135	1.65
ETS51B	16	11.97	-0.10	-1.60	4.32	0.23	0.46	0.31	0.06	4.74	5.54	0.6647	0.7112	6.99	0.2099	0.2040	-2.77
ETS51I	25.6	13.00	-0.10	-1.60	4.44	0.15	0.40	0.44	0.16	4.13	6.17	0.6583	0.6898	4.79	0.2020	0.2042	1.08
ETS51J	35.2	13.61	-0.10	-1.60	4.34	0.11	0.36	0.53	0.23	3.65	6.56	0.6398	0.6783	6.01	0.1940	0.1966	1.35
ETS51K	44.8	14.01	-0.10	-1.60	4.17	0.09	0.32	0.59	0.28	3.28	6.84	0.6249	0.6694	7.12	0.1874	0.1884	0.52
ETS51C	56	14.34	-0.10	-1.60	3.96	0.07	0.29	0.64	0.33	2.96	7.09	0.6122	0.6604	7.87	0.1808	0.1796	-0.64
<i>Eccentric Outside Kern in Lower Portion</i>																	
ETS52A	6.4	9.88	-0.40	-6.40	3.42	0.56	0.47	-0.02	0.05	1.58	1.82	0.2803	0.2771	-1.13	0.1208	0.1233	2.04
ETS52H	9.6	10.78	-0.40	-6.40	3.88	0.51	0.51	-0.02	-0.02	2.42	2.31	0.3551	0.3388	-4.58	0.1453	0.1690	16.36
ETS52B	16	11.97	-0.40	-6.40	4.32	0.41	0.54	0.05	-0.07	3.54	2.97	0.4690	0.4219	-10.05	0.1693	0.2051	21.15
ETS52I	25.6	13.00	-0.40	-6.40	4.44	0.32	0.55	0.14	-0.08	4.31	3.57	0.5426	0.4957	-8.64	0.1863	0.2180	16.98
ETS52J	35.2	13.61	-0.40	-6.40	4.34	0.26	0.54	0.20	-0.06	4.55	3.93	0.5726	0.5408	-5.56	0.1936	0.2178	12.52
ETS52K	44.8	14.01	-0.40	-6.40	4.17	0.23	0.52	0.25	-0.04	4.59	4.17	0.5861	0.5713	-2.53	0.1976	0.2142	8.43
ETS52C	56	14.34	-0.40	-6.40	3.96	0.20	0.51	0.29	-0.01	4.53	4.37	0.5967	0.5964	-0.05	0.2011	0.2088	3.83

Note : All models in the Table contain the dimensions as indicated below:

$$a/h = 0.20, a = 3.2 \text{ in.}, h_w = 16 \text{ in.}, t_w = 5 \text{ in.}, t_f/t_w = 1.1, t_f = 5.5 \text{ in.}, h' = 18.75 \text{ in.}$$

Table 4.16 COMPARISON OF $T_{burst-web}$ AND $d_{burst-web}$ FOR UNSYMMETRICAL I-SECTION
SUBJECTED TO ECCENTRIC LOAD

Name	b_{f1} (in.)	b_{f2} (in.)	h' (in.)	c (in.)	e/h_w	e (in.)	$max\ e$ (in.)	R_{1u} /P	R_{1l} /P	R_2 /P	R_3 /P	p (in.)	y_u (in.)	y_l (in.)	$d_{burst-wfem}$ /h _w	$d_{burst-web}$ /h _w	%diff -1 & 2-	$T_{burst-wfem}$ /P	$T_{burst-web}$ /P	%diff -3 & 4-
<i>Eccentric Inside Kern In Upper Portion</i>																				
EUS53L	16	8	21.5	9.91	0.10	1.60	3.68	0.23	0.31	0.40	0.06	0.20	4.26	7.20	0.7121	0.6403	-10.09	0.2051	0.2439	18.93
EUS53O	56	28.8	21.5	10.31	0.10	1.60	4.24	0.08	0.12	0.63	0.18	0.33	4.09	9.77	0.8042	0.7125	-11.40	0.2030	0.2405	18.44
<i>Eccentric Inside Kern In Lower Portion</i>																				
EUS51L	16	8	21.5	9.91	-0.10	-1.60	-5.27	0.25	0.37	0.26	0.12	0.01	6.25	6.43	0.7943	0.8235	3.68	0.2291	0.2239	-2.25
EUS51O	56	28.8	21.5	10.31	-0.10	-1.60	-6.56	0.09	0.13	0.45	0.33	0.06	6.81	7.96	0.8935	0.9125	2.13	0.2340	0.2371	1.32
<i>Eccentric Outside Kern In Lower Portion</i>																				
EUS52L	16	8	21.5	9.91	-0.40	-6.40	-5.27	0.34	0.39	0.05	0.21	-0.16	5.22	3.44	0.5863	0.5235	-10.70	0.1798	0.2231	24.08
EUS52O	56	28.8	21.5	10.31	-0.45	-7.20	-6.56	0.14	0.13	0.14	0.59	-0.35	8.31	3.22	0.6734	0.6068	-9.89	0.1769	0.2242	26.76

Note : All models in the Table contain the dimensions as indicated below:

$$a/h = 0.20, a = 3.2 \text{ in.}, h_w = 16 \text{ in.}, t_w = 5 \text{ in.}, t_f/t_w = 1.1, t_f = 5.5 \text{ in.}, h' = 21.5 \text{ in.}$$

Equation (4.25) for the estimation of flange bursting force magnitude is also applicable for anchorage zones with flanged sections subjected to eccentric loads. Since the stresses which occur in the flange are not uniform, as the stresses which occur in the concentrically loaded section, the calculation of the k_f ratio in the equation needs to use the stress values on the top and bottom fibers of the considered flange. The method to calculate this k_f ratio for the case in which a non-uniform stress is present on the flange, can also employ the expression presented in Fig. 4.62.

For the determination of the flange bursting force location, the equations used for the calculation of $d_{burst-flg}$ as presented in equation (4.29) and (4.30) are modified by adding eccentricity into the first term of each equation. Therefore, the equations to determine the $d_{burst-flg}$ values can be rewritten as

$$d_{burst-flg} = \frac{h_w - c - e}{4} + \frac{3}{8}t_{f1} + \frac{R_2}{T_{burst-flg}} \frac{(b_{f1} + t_w)}{8} \quad (4.40)$$

$$d_{burst-flg} = \frac{c + e}{4} + \frac{3}{8}t_{f2} + \frac{R_3}{T_{burst-flg}} \frac{(b_{f2} + t_w)}{8} \quad (4.41)$$

Table 4.17 shows the comparison of the magnitude and the location of the bursting force in the top flange of symmetrical I-section models subjected to eccentric loads. Only the results from the models subjected to an eccentric load within the kern are given in the table. The estimation of the flange bursting force magnitude is conservative in almost every case. Only a small negative percent difference occurs in model EIS51A. The estimated locations of bursting force are larger than the values from finite element result in all models. However, a proper arrangement of reinforcing steel will help redistribute bursting stresses, which is described at the end of this chapter.

For the comparison in Table 4.18, the estimated values for the magnitude and location of the bursting force result in positive percent differences, except one case in the model EIS51A. It should be noted that by setting the limitation for the k_f value as presented in equation (4.25), the estimated values for $T_{burst-flg}$ in the bottom flange of the models subjected to an eccentric load outside the kern will be conservative. Although the model EIS52A

exhibits a percent difference as large as 110.17, the magnitude of the flange bursting force in this model is considered to be the lowest among all models with the same load configuration.

Table 4.17 COMPARISON OF $T_{burst-flg}$ AND $d_{burst-flg}$ FOR THE TOP FLANGE OF SYMMETRICAL I-SECTION SUBJECTED TO ECCENTRIC LOAD

Name	b_f (in.)	e/h_w	e (in.)	$max\ e$ (in.)	R_{1u} /P	R_2 /P	k_f	$T_{burst-flg}$	$T_{burst-flg}$	%diff	$d_{burst-flg}$	$d_{burst-flg}$	%diff
								/P	/P	-1 & 2-	/h _w	/h _w	-3 & 4-
<i>Eccentric Inside Kern</i>													
EIS51A	6.4	-0.1	-1.6	-3.91	0.41	0.04	0.43	0.0123	0.0123	-0.36	0.4883	0.5945	21.73
EIS51H	9.6	-0.1	-1.6	-4.42	0.33	0.12	0.55	0.0222	0.0243	9.79	0.5427	0.8267	52.33
EIS51B	16	-0.1	-1.6	-4.96	0.23	0.20	0.67	0.0378	0.0459	21.37	0.6260	0.9983	59.48
EIS51I	25.6	-0.1	-1.6	-5.35	0.16	0.26	0.77	0.0509	0.0687	35.05	0.7426	1.1957	61.02
EIS51J	35.2	-0.1	-1.6	-5.55	0.12	0.30	0.82	0.0627	0.0838	33.67	0.9854	1.3910	41.17
EIS51K	44.8	-0.1	-1.6	-5.67	0.10	0.32	0.86	0.0675	0.0943	39.57	1.1425	1.5882	39.01
EIS51C	56	-0.1	-1.6	-5.77	0.08	0.33	0.88	0.0682	0.1030	50.94	1.2749	1.8197	42.74

Note: All models in the Table contain the dimensions as indicated below:

$$a/h = 0.20, a = 3.2 \text{ in.}, h_w = 16 \text{ in.}, t_w = 5 \text{ in.}, t_f/t_w = 1.1, t_f = 5.5 \text{ in.}, h' = 21.5 \text{ in.}, c = 8 \text{ in.}$$

Table 4.18 COMPARISON OF $T_{burst-flg}$ AND $d_{burst-flg}$ FOR THE BOTTOM FLANGE OF SYMMETRICAL I-SECTION SUBJECTED TO ECCENTRIC LOAD

Name	b_f (in.)	e/h_w	e (in.)	$max\ e$ (in.)	R_{1l} /P	R_3 /P	k_f	$T_{burst-flg}$	$T_{burst-flg}$	%diff	$d_{burst-flg}$	$d_{burst-flg}$	%diff
								/P	/P	-1 & 2-	/h _w	/h _w	-3 & 4-
<i>Eccentric Inside Kern</i>													
EIS51A	6.4	-0.1	-1.6	-3.91	0.46	0.08	0.69	0.0252	0.0493	95.91	0.4826	0.3766	-21.96
EIS51H	9.6	-0.1	-1.6	-4.42	0.35	0.20	0.77	0.0411	0.0677	64.66	0.5525	0.5712	3.38
EIS51B	16	-0.1	-1.6	-4.96	0.24	0.33	0.84	0.0631	0.0903	42.97	0.6614	0.8256	24.83
EIS51I	25.6	-0.1	-1.6	-5.35	0.16	0.41	0.90	0.0797	0.1079	35.30	0.8412	1.1476	36.42
EIS51J	35.2	-0.1	-1.6	-5.55	0.12	0.46	0.92	0.0918	0.1175	27.97	1.0940	1.4550	33.00
EIS51K	44.8	-0.1	-1.6	-5.67	0.10	0.49	0.94	0.0986	0.1236	25.30	1.3625	1.7579	29.02
EIS51C	56	-0.1	-1.6	-5.77	0.08	0.51	0.95	0.1022	0.1283	25.60	1.6557	2.1091	27.39

Eccentric Outside Kern

EIS52A	6.4	-0.4	-6.4	-3.91	0.41	0.14	1.00	0.0714	0.1500	110.17	0.2531	0.2364	-6.58
EIS52H	9.6	-0.4	-6.4	-4.42	0.30	0.33	1.00	0.0903	0.1500	66.10	0.3516	0.4068	15.69
EIS52B	16	-0.4	-6.4	-4.96	0.19	0.52	1.00	0.1115	0.1500	34.53	0.5853	0.7214	23.25
EIS52I	25.6	-0.4	-6.4	-5.35	0.13	0.64	1.00	0.1307	0.1500	14.73	0.9298	1.1755	26.42
EIS52J	35.2	-0.4	-6.4	-5.55	0.09	0.70	1.00	0.1393	0.1500	7.68	1.2646	1.6234	28.37
EIS52K	44.8	-0.4	-6.4	-5.67	0.08	0.74	1.00	0.1426	0.1500	5.17	1.5770	2.0690	31.20
EIS52C	56	-0.4	-6.4	-5.77	0.06	0.77	1.00	0.1408	0.1500	6.52	1.9147	2.5876	35.14

Note: All models in the Table contain the dimensions as indicated below:

$$a/h = 0.20, a = 3.2 \text{ in.}, h_w = 16 \text{ in.}, t_w = 5 \text{ in.}, t_f/t_w = 1.1, t_f = 5.5 \text{ in.}, h' = 21.5 \text{ in.}, c = 8 \text{ in.}$$

Table 4.19 presents the comparison of the magnitude and the location of the flange bursting force for T-section models subjected to an eccentric load. Only one eccentricity case is given in the table, which is the model subjected to an eccentric load inside the kern in the lower portion. For the case of eccentric load applied in the upper portion, the results from finite element indicate a very large magnitude since the load is applied almost directly to the centroid of the top flange. The approximate equations cannot be used for this case. Special consideration should be given to the design of the bursting steel in the flange, treating it as a concentric load applied directly onto the center of the flange, similar to the method that is used for the design of a rectangular section. The estimation for the case of small eccentricity shown in the table gives a conservative value of $T_{burst-flg}$ in two cases. The largest negative percent difference is detected in the model with the magnitude of bursting force equal to approximately 2 percent of the magnitude of the prestressing load. The comparison of the location of the force for the small eccentricity case shows that the estimated value gives a shorter distance of the $d_{burst-web}$ than that of finite element result. Based on all estimated values, the results given in Table 4.19 are slightly unconservative since the shorter distance of bursting steel is indicated and the amount of steel is close to the requirement given from the finite element prediction. However, it is considered to be acceptable if the arrangement of the bursting steel is properly handled.

Table 4.19 COMPARISON OF $T_{burst-flg}$ AND $d_{burst-flg}$ FOR T-SECTION SUBJECTED TO ECCENTRIC LOAD

Name	b_f (in.)	c	e/h_w (in.)	e (in.)	$max\ e$	R_{1u} /P	R_2 /P	k_f	$T_{burst-fem}$ /P -1-	$T_{burst-flg}$ /P -2-	%diff -1 & 2-	$d_{burst-fem}$ /h _w -3-	$d_{burst-flg}$ /h _w -4-	%diff -3 & 4-
<i>Eccentric Inside Kern</i>														
ETS51A	6.4	9.88	-0.1	-1.6	-3.42	0.42	0.05	0.50	0.0230	0.0189	-17.83	1.7889	0.4916	-72.52
ETS51H	9.6	10.78	-0.1	-1.6	-3.88	0.34	0.16	0.66	0.0434	0.0431	-0.62	1.5566	0.6462	-58.48
ETS51B	16	11.97	-0.1	-1.6	-4.32	0.23	0.31	0.83	0.0776	0.0844	8.73	1.4636	0.8116	-44.55
ETS51I	25.6	13.00	-0.1	-1.6	-4.44	0.15	0.44	0.92	0.1141	0.1177	3.07	1.6587	1.1035	-33.47
ETS51J	35.2	13.61	-0.1	-1.6	-4.34	0.11	0.53	0.96	0.1386	0.1328	-4.19	1.9714	1.4435	-26.78
ETS51K	44.8	14.01	-0.1	-1.6	-4.17	0.09	0.59	0.98	0.1553	0.1405	-9.55	2.3213	1.8125	-21.92
ETS51C	56	14.34	-0.1	-1.6	-3.96	0.07	0.64	0.99	0.1685	0.1452	-13.87	2.7268	2.2662	-16.89

Note : All models in the Table contain the dimensions as indicated below:

$$a/h = 0.20, a = 3.2 \text{ in.}, h_w = 16 \text{ in.}, t_w = 5 \text{ in.}, t_f/t_w = 1.1, t_f = 5.5 \text{ in.}, h' = 18.75 \text{ in.}$$

Table 4.20 shows the comparison of the magnitude and the location of bursting force for the top flange for unsymmetrical I-section models subjected to eccentric load. Table 4.21 shows the comparison of the same variables for the bottom flange of the models. The estimation is not given for the top flange of the models subjected to an eccentric load outside the kern. According to the percent differences given in both tables, the formulations developed in equation (4.25), (4.40) and (4.41) provide a level of conservatism for the estimation of the bursting force magnitude in the flanges and provide a direction for the development of a steel reinforcement pattern in the flange based on the values of $d_{burst-flg}$.

Table 4.20 COMPARISON OF $T_{burst-flg}$ AND $d_{burst-flg}$ FOR THE TOP FLANGE OF UNSYMMETRICAL I-SECTION SUBJECTED TO ECCENTRIC LOAD

Name	b_{f1}	b_{f2}	c	e/h_w	e	R_{1u}/P	R_2/P	k_f	$T_{burst-flg}/P$	$T_{burst-flg}/P$	%diff	$d_{burst-flg}/h_w$	$d_{burst-flg}/h_w$	%diff
									-1-	-2-	-1 & 2-	-3-	-4-	-3 & 4-
<i>Eccentric Inside Kern in Upper Portion</i>														
EUS53L	16	8	9.91	0.10	1.60	0.23	0.40	0.92	0.0769	0.1162	51.06	0.6161	0.7589	23.18
EUS53O	56	288	10.31	0.10	1.60	0.08	0.63	0.98	0.1199	0.1414	17.92	1.8283	2.3149	26.61
<i>Eccentric Inside Kern in Lower Portion</i>														
EUS51L	16	8	9.91	-0.10	-1.60	0.25	0.26	0.74	0.0561	0.0617	10.05	1.0926	0.9383	-14.12
EUS51O	56	288	10.31	-0.10	-1.60	0.09	0.45	0.92	0.1035	0.1169	12.93	1.9211	2.0837	8.47

Note: All models in the Table contain the dimensions as indicated below:
 $a/h = 0.20$, $a = 3.2$ in., $h_w = 16$ in., $t_w = 5$ in., $t_f/t_w = 1.1$, $t_f = 5.5$ in., $h' = 21.50$ in.

Table 4.21 COMPARISON OF $T_{burst-flg}$ AND $d_{burst-flg}$ FOR THE BOTTOM FLANGE OF UNSYMMETRICAL I-SECTION SUBJECTED TO ECCENTRIC LOAD

Name	b_{f1}	b_{f2}	c	e/h_w	e	R_{1l}/P	R_3/P	k_f	$T_{burst-flg}/P$	$T_{burst-flg}/P$	%diff	$d_{burst-flg}/h_w$	$d_{burst-flg}/h_w$	%diff
									-1-	-2-	-1 & 2-	-3-	-4-	-3 & 4-
<i>Eccentric Inside Kern in Upper Portion</i>														
EUS53L	16	8	9.91	0.10	1.60	0.31	0.06	0.42	0.0125	0.0113	-9.38	0.6819	0.8369	22.74
EUS53O	56	288	10.31	0.10	1.60	0.12	0.18	0.73	0.0441	0.0576	30.37	1.1327	1.1278	-0.44
<i>Eccentric Inside Kern in Lower Portion</i>														
EUS51L	16	8	9.91	-0.10	-1.60	0.37	0.12	0.65	0.0245	0.0409	67.00	0.5827	0.5564	-4.52
EUS51O	56	288	10.31	-0.10	-1.60	0.13	0.33	0.86	0.0653	0.0951	45.73	0.8764	1.1739	33.94
<i>Eccentric Outside Kern in Lower Portion</i>														
EUS52L	16	8	9.91	-0.40	-6.40	0.39	0.21	0.93	0.0534	0.1223	128.88	0.3950	0.3591	-9.08
EUS52O	56	288	10.31	-0.45	-7.20	0.13	0.59	0.99	0.1133	0.1458	28.69	0.9596	1.2460	29.85

Note: All models in the Table contain the dimensions as indicated below:
 $a/h = 0.20$, $a = 3.2$ in., $h_w = 16$ in., $t_w = 5$ in., $t_f/t_w = 1.1$, $t_f = 5.5$ in., $h' = 21.50$ in.

4.4.3 Inclined and Inclined Eccentrically Loaded Anchor Configurations

4.4.3.1 Finite Element Results

4.4.3.1.1 Elastic Stress Distribution

Since the behavior of concentrically loaded and eccentrically loaded anchorage zones in flanged sections has been examined, the main objective in this section is to investigate the behavior of anchorage zones subjected to an inclined load, which can be classified as inclined concentric load and inclined eccentric load. It is known from the behavior of a rectangular anchorage zone subjected to an inclined concentric load that the inclination of the load causes shear forces to occur within the structure and causes the stress distribution within the structure to deviate corresponding to the direction of the load. In a flanged section anchorage zone, the application of a prestressing load creates internal forces within the web that propagate into the flanges. The magnitude of the bursting force in the flange is affected by the position of the load as illustrated in the behavior of eccentrically loaded anchorage zones in section 4.4.2.

Figure 4.86 presents a symmetrical section model with a flange width of 16 in. subjected to a 6 degree inclined concentric load in which the load points in a downward direction toward the bottom flange. The stress contour plots shown are presented as a factor of the uniform stress on the structure. According to Fig. 4.86, the tensile stress contours occurring in the top and bottom flanges of the model are slightly different from each other. As can be noticed, the magnitude of the largest tensile stress in the bottom flange is larger than the highest stress in the top flange. For the bursting stresses in the web, the pattern of the stress distribution looks similar to the stress distribution in the web that occurred in other flanged sections subjected to a concentric load. The maximum bursting stress in each member of the model occurs at approximately the same location with respect to the prestressing surface.

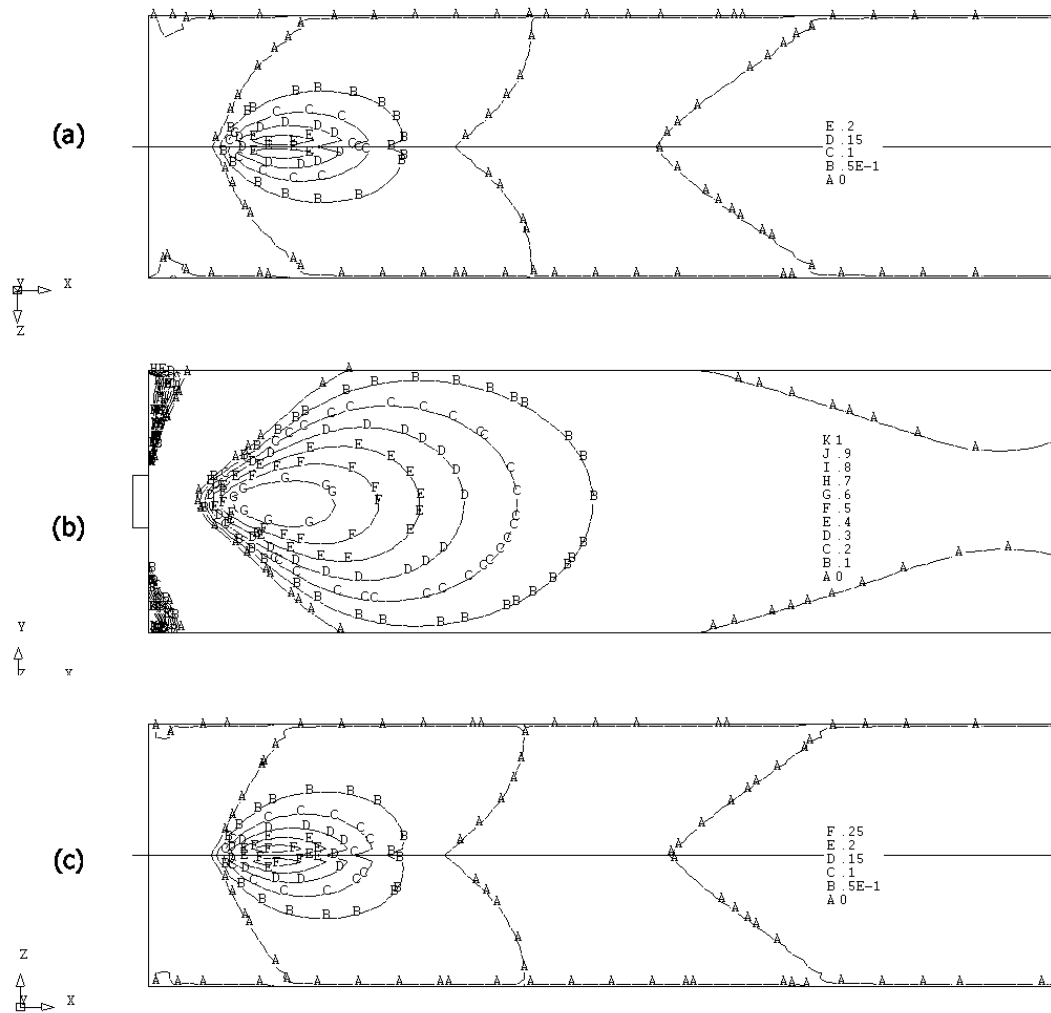


Fig. 4.86 TENSILE STRESSES IN EACH MEMBER OF SYMMETRICAL I-SECTION MODEL WITH $b_f = 16.0$ in. SUBJECTED TO 6 DEGREE INCLINED CONCENTRIC LOAD
 a) TOP FLANGE, b) WEB, AND c) BOTTOM FLANGE (Stress multiplied by σ_o , $A = 228.5$ sq.in.)

Figure 4.87 shows the stress contour plots for the model subjected to an inclined load at the location of $0.10h_w$ below the section centroid. Since the inclined load is placed closer to the bottom flange, the magnitude of the tensile stress in the bottom flange is clearly larger than that in the top flange. The location of the maximum tensile stress in the top flange occurs more distant from anchorage surface. The bursting region in the web is located ahead of the position where the load is applied. As can be noticed, the eccentricity of a prestressing load affects the stresses more than inclination.

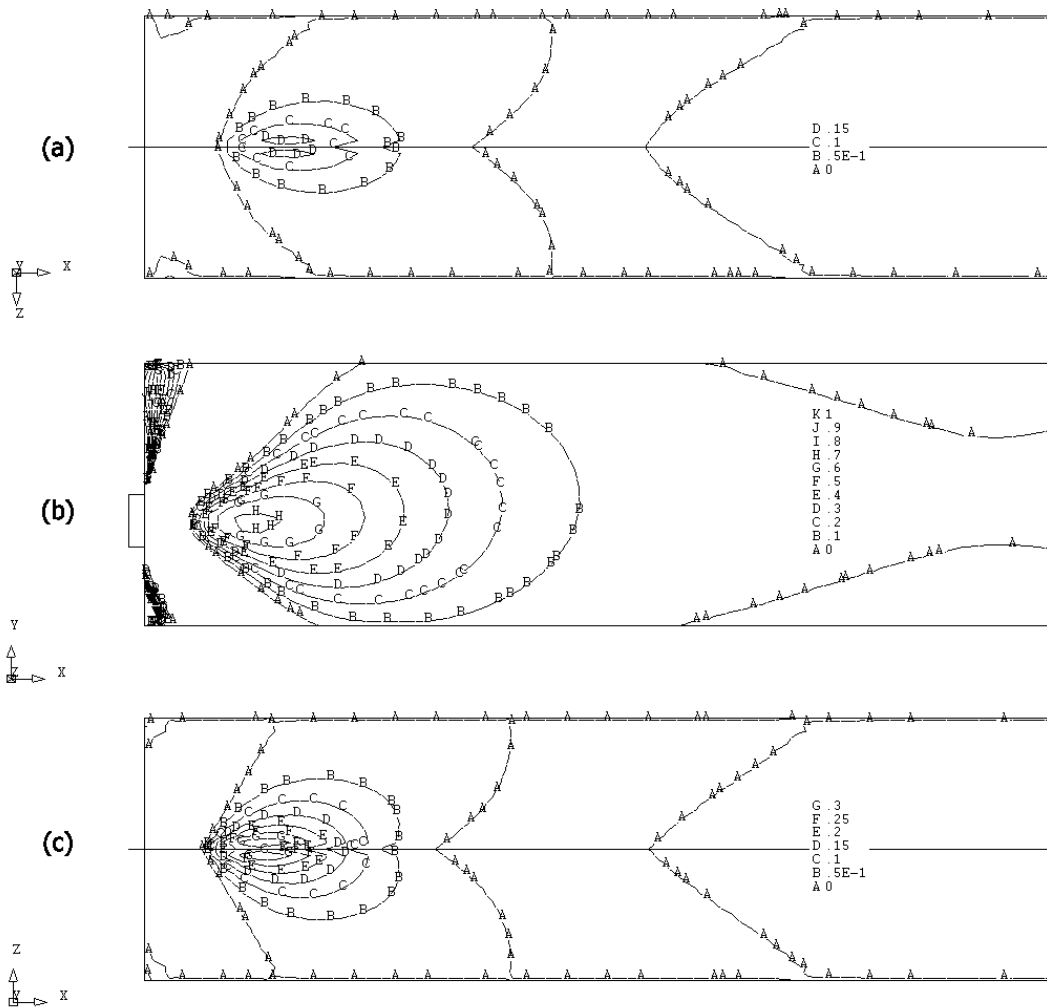


Fig. 4.87 TENSILE STRESSES IN EACH MEMBER OF SYMMETRICAL I-SECTION MODEL WITH $b_f = 16.0$ in. SUBJECTED TO 6 DEGREE INCLINED ECCENTRIC LOAD WITH $e/h_w = -0.10$
 a) TOP FLANGE, b) WEB, AND c) BOTTOM FLANGE (Stress multiplied by σ_0 , $A = 228.5$ sq.in.)

Figure 4.88 shows another case of inclined eccentric load configuration. The model in the figure is subjected to an inclined load above the section centroid. The prestressing load is inclined downward while the position of the load is above the centroid. The largest tensile stress in the top flange is larger than that of the bottom flange. Although the load points toward the bottom flange, the position of the load closer to the top flange results in a larger magnitude of bursting force in the top flange than the magnitude of the force in the bottom flange. In the case of 6 degree inclined load, the position of the load has more influence on the magnitude of flange bursting force than the inclination of the load.

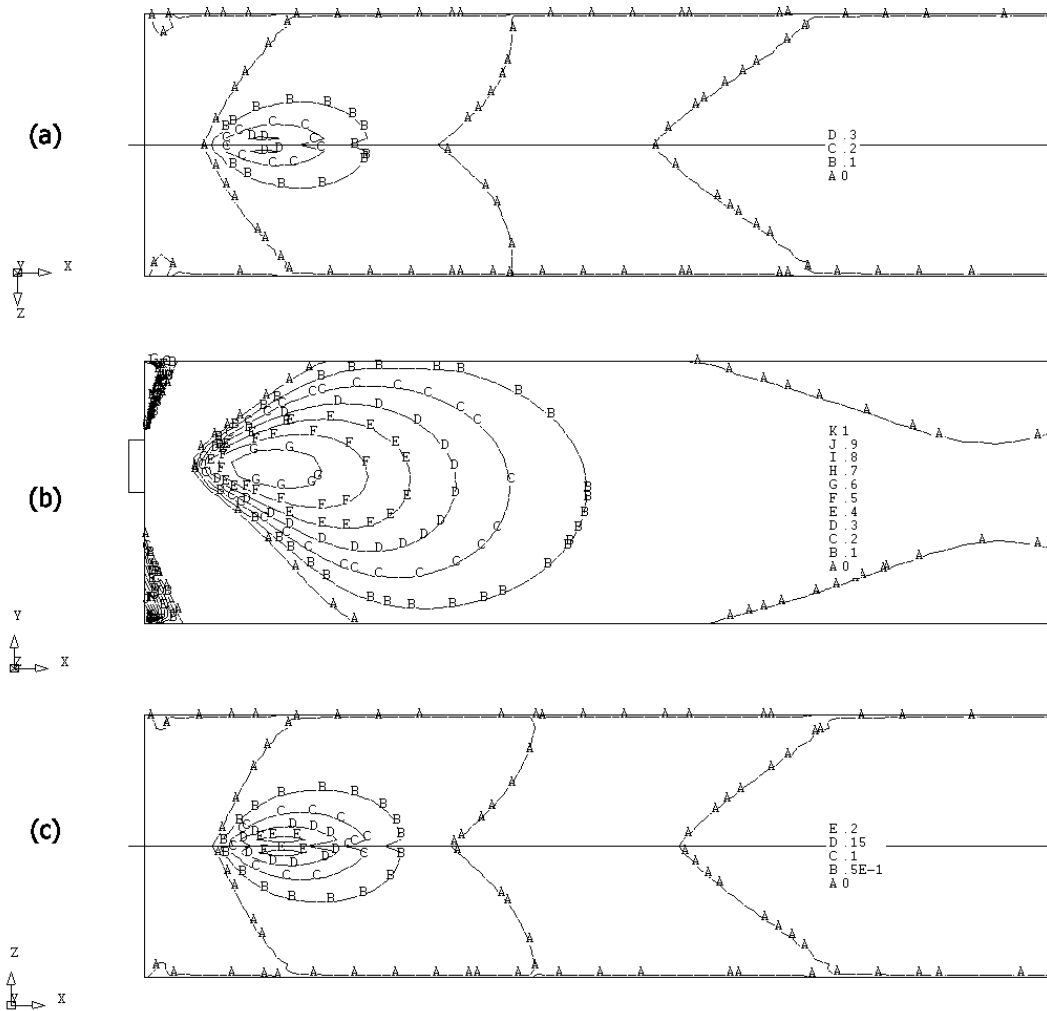


Fig. 4.88 TENSILE STRESSES IN EACH MEMBER OF SYMMETRICAL I-SECTION MODEL WITH $b_f = 16.0$ in. SUBJECTED TO 6 DEGREE INCLINED ECCENTRIC LOAD WITH $e/h_w = +0.10$
a) TOP FLANGE, b) WEB, AND c) BOTTOM FLANGE (Stress multiplied by σ_o , $A = 228.5$ sq.in.)

An anchorage zone in a T-section under the application of an inclined eccentric load with an e/h_w ratio of -0.10 is shown in Fig. 4.89. As shown, the behavior of tensile stresses is similar to that of the model with the same geometric configuration but subjected to a horizontal load as presented in Fig. 4.71. Because the load points in the direction away from the top flange, the bursting stresses in the flange of model in Fig. 4.89 have a smaller magnitude compared to the stresses occurring in the model of Fig. 4.71.

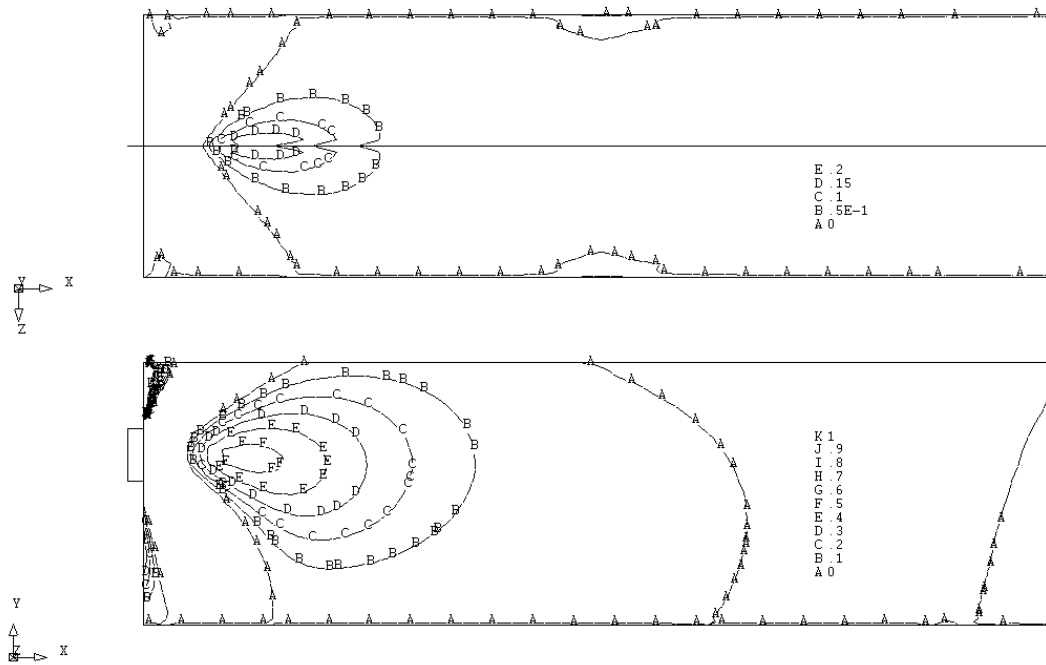


Fig. 4.89 TENSILE STRESSES IN EACH MEMBER OF T-SECTION MODEL WITH $b_f = 16.0$ in. SUBJECTED TO 6 DEGREE INCLINED ECCENTRIC LOAD WITH $e/h_w = -0.10$
 a) TOP FLANGE AND b) WEB (Stress multiplied by σ_o , $A = 154.25$ sq.in.)

Figure 4.90 shows the stress contour plots of an unsymmetrical I-section subjected to an inclined eccentric load. The top flange width is 16 in. while the bottom flange width is 8 in. A prestressing load is applied at an eccentric location of $-0.10h_w$ below the section centroid. Fig. 4.91 is given for a comparison with Fig. 4.90. The model in Fig. 4.91 has the same geometric configuration except it contains a support reaction at the bottom flange. The bearing plate for the support reaction has a length of $0.10h_w$, and the thickness is equal to the web of the model. As can be seen, the presence of the reaction force obviously influences the stress distribution in the model. The tensile stresses in the bottom flange of the model with the reaction force are larger than the other and the bursting stress region in the web is located slightly higher due to the application of the reaction force. However, the high magnitude of stresses in the bottom flange may be the result of strain compatibility in the surrounding region of the flange close to the position that the reaction force is applied. Since the presence of the support reaction is not a major focus of the present study, this type of structure is not mentioned in great detail.

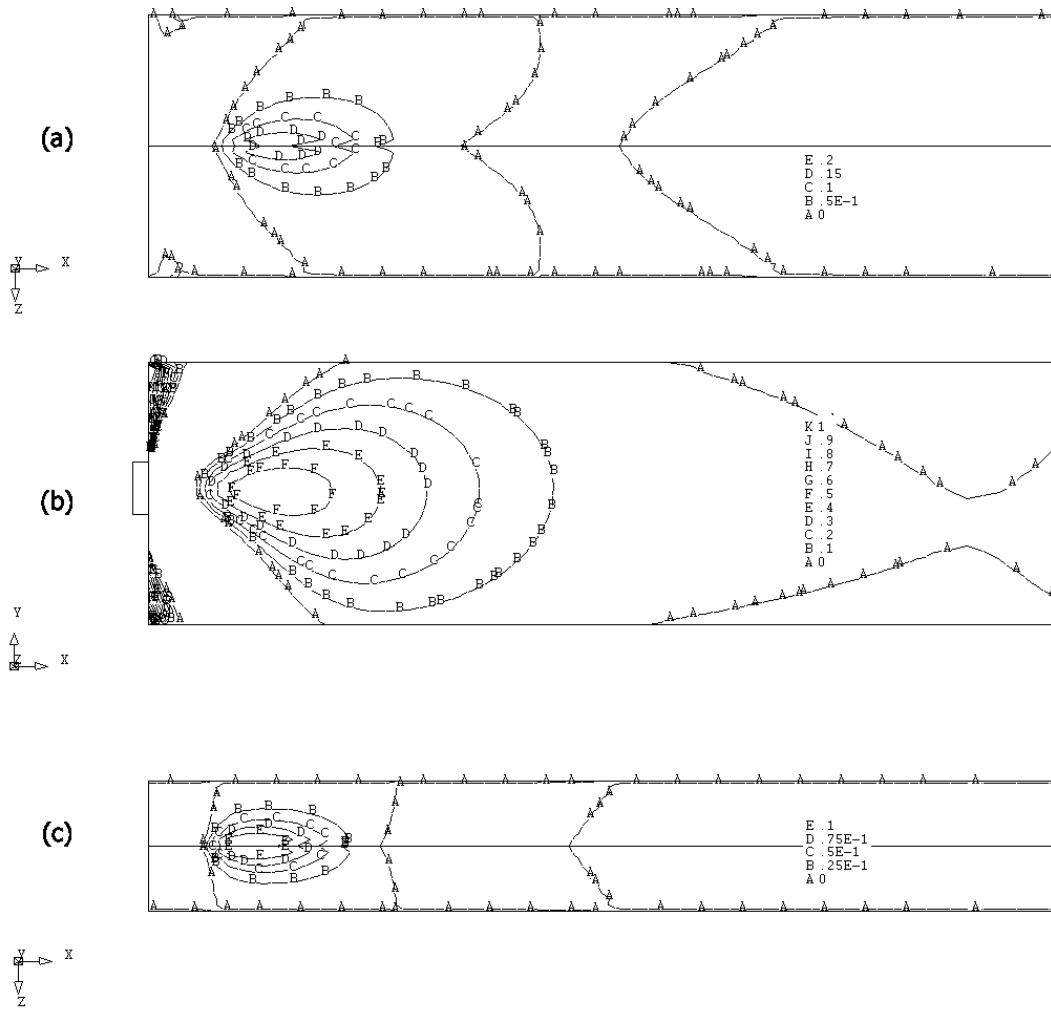


Fig. 4.90 TENSILE STRESSES IN EACH MEMBER OF UNSYMMETRICAL I-SECTION MODEL WITH $b_f = 16.0$ in. SUBJECTED TO 6 DEGREE INCLINED ECCENTRIC LOAD WITH $e/h_w = -0.10$
 a) TOP FLANGE, b) WEB, AND c) BOTTOM FLANGE (Stress multiplied by σ_o , $A = 184.5$ sq.in.)

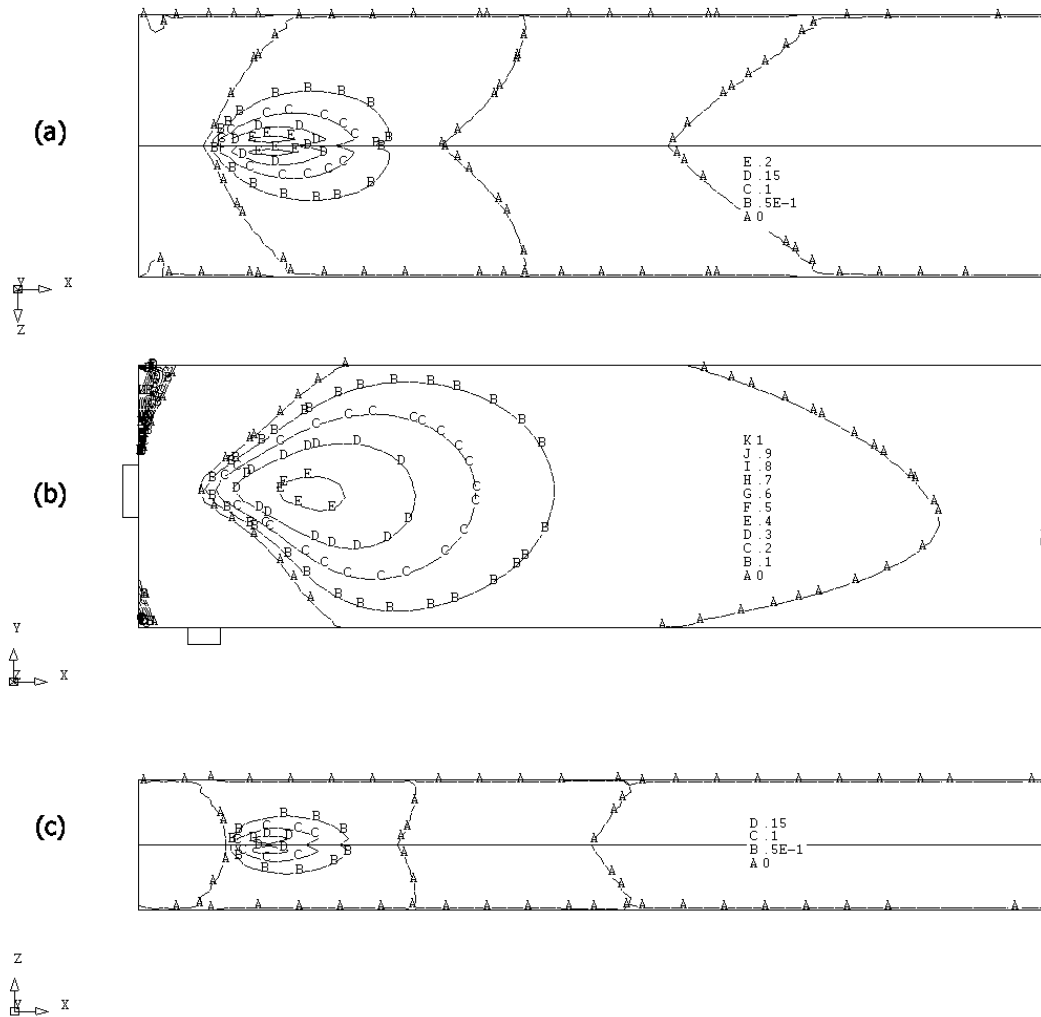


Fig. 4.91 TENSILE STRESSES IN EACH MEMBER OF UNSYMMETRICAL I-SECTION MODEL
 SUBJECTED TO 6 DEGREE INCLINED ECCENTRIC LOAD AND A SUPPORT REACTION
 WITH $R/P = 0.15$, $b_{f1} = 16$ in., $b_{f2} = 8$ in., AND $e/h_w = -0.10$
 a) TOP FLANGE, b) WEB AND c) BOTTOM FLANGE (Stress multiplied by σ_o , $A = 184.5$ sq.in.)

4.4.3.1.2 Bursting Force

In this section, the behavior of symmetrical models subjected to four load configurations are chosen for comparison. Three of them have 6 degree inclination, and eccentricity ratio of -0.10 , 0.0 , and $+0.10$. The fourth configuration is horizontal concentric.

Figure 4.92 and 4.93 show the relation between the magnitude of bursting force and the flange width for three symmetrical I-section models subjected to four different load configurations, which consist of horizontal concentric, inclined concentric, inclined eccentric below the section centroid, and inclined eccentric above the section centroid. The plots of bursting force magnitudes in the web and the top flange are shown in Fig. 4.92 while the plots for the bottom flange are shown in Fig. 4.93. The inclination angle used in the model subjected to an inclined load is chosen as 6 degrees and the eccentricity ratio for both eccentric load cases is $0.10h_w$.

According to Fig. 4.92, the plot for the inclined concentric load case (indicated with 6 deg., $e/h_w = 0.00$) lies high above the plot from the horizontal concentric load case (indicated with 0 deg., $e/h_w = 0.00$). Similar to the behavior of a rectangular section subjected to an inclined load, the magnitude of the bursting force increases as the inclination increases. The difference between the magnitudes of these two plots is as high as 0.055 times the magnitude of prestressing load. Considered in terms of the vertical component of the prestressing load ($P \sin 6$), this value of $0.055P$ is approximately equal to $0.53 \times P \sin 6$. In a rectangular section, the vertical component of prestressing load presented in the formulations of bursting force magnitude is equal to $0.40 \times P \sin 6$. It is apparent that the inclination of a prestressing load results in an increase in the magnitude of the bursting force in the web of a flanged section to a larger degree than in a rectangular section.

In Fig. 4.92, the plot of the web bursting force magnitude of the model with inclined concentric load lies in between the plots from the two models with inclination and eccentricity. When the inclined load points toward the bottom flange and is located close to the bottom flange as well, the bursting force in the web slightly increases in magnitude as can be seen in Fig. 4.92. However, when the load is located closer to the top flange while its inclination remains unchanged, the magnitude of bursting force in the web is smaller. It can be noticed that when the load points toward the closest flange, the magnitude of the web bursting force is larger than when it points away from the flange. Therefore, the inclination angle has a significant effect on eccentric load cases.

The bursting force magnitude within the flange depends on the direction and the position of the load, similar to other models presented before. As the load is placed closer to the flange, it is known that the magnitude of the bursting force in the flange increases. If an inclined load points directly toward the flange, the magnitude of the bursting force in the flange increases even more than the model subjected to an eccentric load with no inclination.

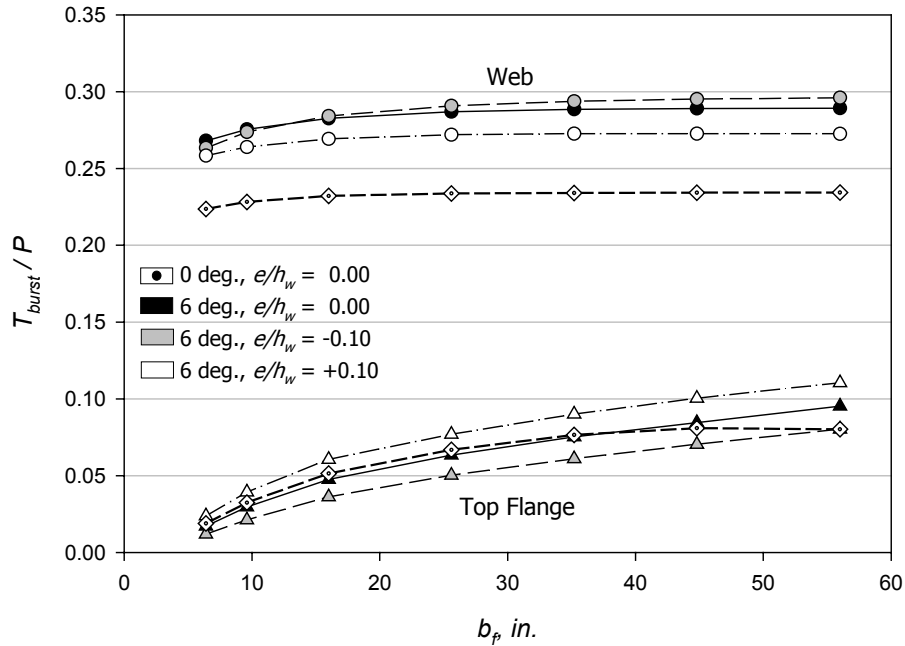


Fig. 4.92 BURSTING FORCE vs. FLANGE WIDTH FOR INCLINED CONCENTRIC AND INCLINED ECCENTRIC LOAD, WEB AND TOP FLANGE ($a/h_w = 0.20$, $t_w = 5$ in., and $t_f/t_w = 1.10$)

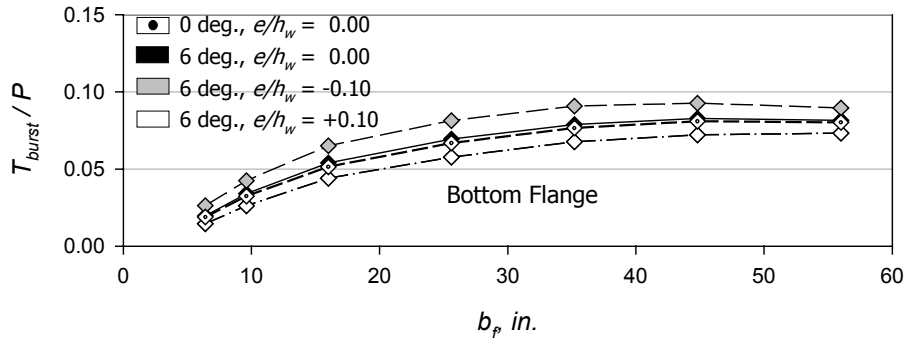


Fig. 4.93 BURSTING FORCE vs. FLANGE WIDTH FOR INCLINED CONCENTRIC AND INCLINED ECCENTRIC LOAD, BOTTOM FLANGE ($a/h_w = 0.20$, $t_w = 5$ in., and $t_f/t_w = 1.10$)

4.4.3.1.3 Location of Bursting Force

Similar to those presented in section 4.4.3.1.2, the presentation of the behavior of bursting force location presents information that is found to be different from that presented before. The relation of the bursting force location and the flange width for four different models similar to those presented in Fig. 4.92 is shown in Fig. 4.94. Fig. 4.94 only presents the plots for bursting force location in the web and the top flange. The plots of the location of the web bursting force follow the same sequence as the plots of bursting force magnitudes in Fig. 4.92. The plot from the horizontal concentric load case (0 deg., $e/h_w = 0.00$) lies below the plot from the inclined concentric load case (6 deg., $e/h_w = 0.00$) with a difference of approximately $0.13h_w$. This is equivalent to $1.24 \times h_w \sin 6$, which can be used to describe an inclination effect in the formulations of $d_{burst-web}$. Compared to the term $0.25 \times h_w \sin \alpha$ in the approximate equation for the magnitude of d_{burst} in a rectangular section, the effect of inclination of a prestressing load on the location of the web bursting force in a flanged section is much greater.

The largest distance of the web bursting force occurs in the model that has an inclined load applied below the section centroid while the smallest distance appears in the model with the load applied above the section centroid. For the location of the flange bursting force, the plots are similar to those of the models subjected to other load configurations.

Figure 4.95 presents the relation between the bursting force location in the bottom flange and the flange width. By comparing the plots from the top flange to those from the bottom flange as shown in Fig. 4.94, it can be seen that the plots have a distinct relation to each other. If the location of the bursting force in the top flange is greater than the others, the location in the bottom is the smallest.

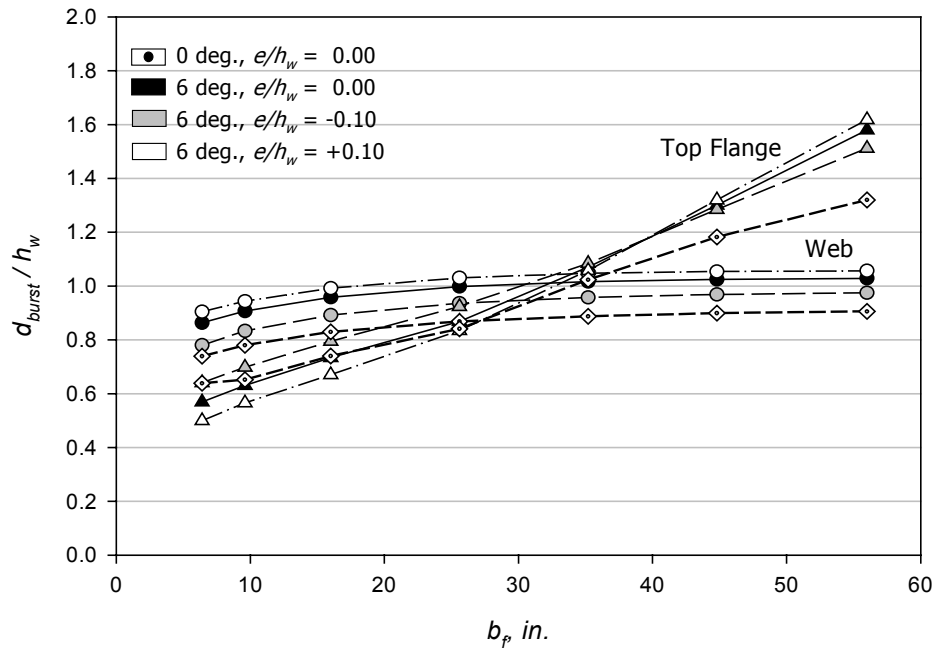


Fig. 4.94 BURSTING FORCE LOCATION vs. FLANGE WIDTH FOR INCLINED CONCENTRIC AND INCLINED ECCENTRIC LOAD, WEB AND TOP FLANGE ($a/h_w = 0.20$, $t_w = 5$ in., and $t_f/t_w = 1.10$)

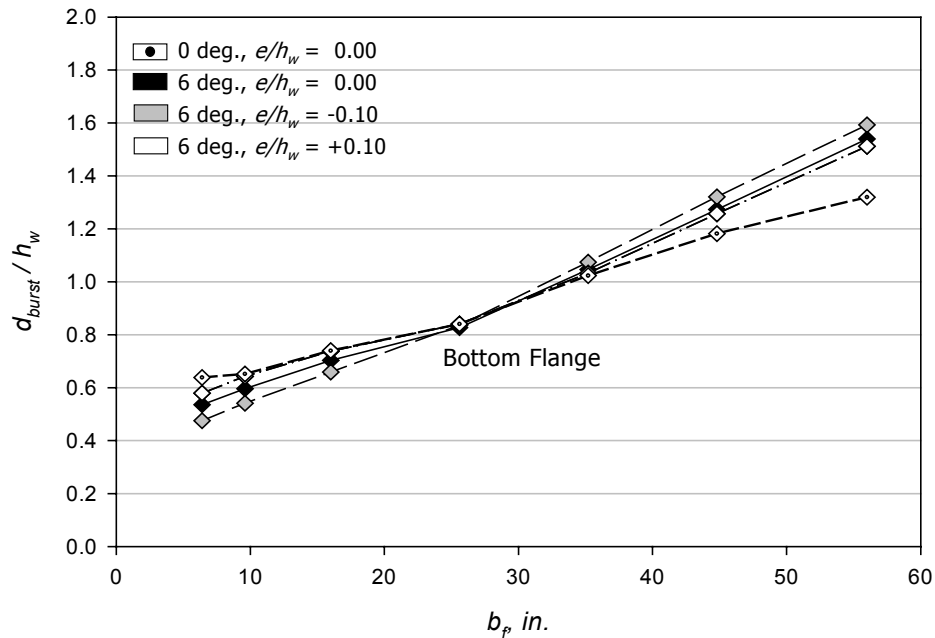


Fig. 4.95 BURSTING FORCE LOCATION vs. FLANGE WIDTH FOR INCLINED CONCENTRIC AND INCLINED ECCENTRIC LOAD, BOTTOM FLANGE ($a/h_w = 0.20$, $t_w = 5$ in., and $t_f/t_w = 1.10$)

4.4.3.2 Formulations

As presented in the finite element study, an inclined load causes the internal forces to transfer more into the bottom flange. However, the only influence on the behavior of the bursting force in the flange is the increase of the magnitude of the transferring force from the web into the flange. Therefore, the formulations of flange bursting force are not affected by the results from the present study. For the web of the section, the direction of the prestressing load affects the behavior of the bursting stresses in the same way as was seen in the study of inclined load configurations on rectangular sections. Since the inclined load is applied onto the web, the vertical component of the load influences the magnitude and the location of bursting force in the web directly. As has been known for the effect of inclination angle, it causes a shearing force to occur at the end of the section. Therefore, the formulations of bursting force for flanged sections in the present study must include the effect of vertical force in the equations.

Figure 4.96 shows a free body diagram of an anchorage zone subjected to an inclined eccentric load. The shearing stress diagram shown at the end of the structure is resulted from the vertical component of the inclined load. Because the cross-section of the structure contains flange members, the shearing forces need to be determined from the stress volume on each member of the section, including flanges and web. In order to use the STM approach to derive the formulations of bursting force magnitude and location, the normal forces and shearing forces need to be determined from the stress diagrams at the end of the structure. The normal forces are determined from the normal stress diagrams, which are created from the stresses calculated from equation (4.31). The magnitude of total moment used in the equation needs to include the moment from the vertical component of the prestressing load. The shearing forces are determined from stress diagrams in each member of the flanged section as well, which are complex geometric shapes. After all forces have been determined, the alignments of the struts of the strut-and-tie model used for the development of the formulations can be located based on these forces, in the same way as presented for the improved STM method in section 3.5.2.2.2. The method to develop the formulations in this section, therefore, requires significant effort to achieve the solution of one problem.

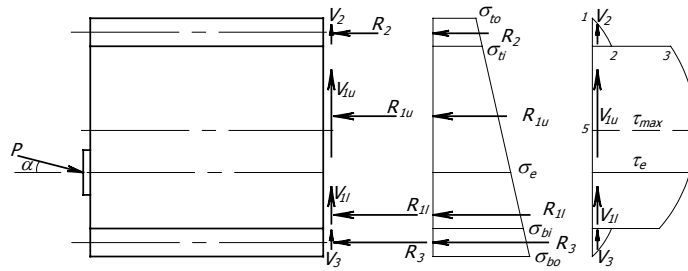


Fig. 4.96 FREE BODY FOR THE CALCULATION OF RESULTANT FORCES INCLUDING SHEARING FORCES

The modified strut-and-tie model for a flanged section as presented in section 4.4.1.2.3 assumes the total resultant forces to act at the upper and lower portions of the model. The total resultant forces are determined from the combination of the forces in the web and the flange. The influence from the presence of the flange is already included into the consideration in the form of a resultant force from the flange. Therefore, the method of combining the forces as being used in the modified strut-and-tie model is proven to be effective for the formulations for flanged sections as presented in equations (4.36) and (4.37). Equations (4.36) or (4.37) are applicable for horizontal concentrically loaded anchorage zones. If the structure is subjected to an inclined load, an influence from the inclination angle of the load needs to be added into the equations.

Since the method used to formulate the equation to calculate the web bursting force magnitude for inclined loaded anchorage zone with a flanged section is rather complicated, a simplified equation needs to be found. Based on the study with finite element method, the effect of inclination angle is found in the term of the vertical component of a prestressing load as illustrated in section 4.4.3.1.2. With the inclination of the load, the magnitude of the bursting force increases from that of horizontal concentric load case with the value of 0.53 times the vertical component of the load. The term representing the effect of inclination can be added into the equation that is used for determining the bursting force magnitude of an anchorage zone subjected to a concentric load with no inclination.

Since the bursting force magnitude provided by equations (4.36) and (4.37) can only be used for an anchorage zone subjected to a prestressing load with no inclination angle, the term of inclination effect is added into the equations in order to be able to be used for an

inclined load case. Equations (4.36) or (4.37) are comparable to the first term in equation (3.8) from the study of a rectangular section. The second term, which represents the inclination effect, can be added into the equations of bursting force magnitude of a flanged section. As a simplification, the term representing the inclination effect for a flanged section can be approximated as $0.6P \sin \alpha$. Therefore, the new equations for $T_{burst-web}$ can be rewritten as

$$T_{burst-web} = (R_{1u} + R_2) \left(\frac{4y_u + 4p}{4d_{burst-web} - a} \right) \left(1 - \frac{a}{4y_u + 4p} \right) + 0.6P \sin \alpha \quad (4.42)$$

$$T_{burst-web} = (R_{1l} + R_3) \left(\frac{4y_l - 4p}{4d_{burst-web} - a} \right) \left(1 - \frac{a}{4y_l - 4p} \right) + 0.6P \sin \alpha \quad (4.43)$$

The forces R_{1u} , R_{1l} , R_2 , and R_3 are determined from the normal stresses, which are calculated from the horizontal component of the prestressing load. Similarly, the equations used to determine the $d_{burst-web}$ as presented in equation (4.38) and (4.39) can also be modified to include the effect of inclination angle similar to the third term of equation (3.7) in the study of a rectangular section. As illustrated in section 4.4.3.1.3, the effect of the inclination angle in the equation used to estimate the location of the web bursting force from the study of finite element method can be approximated as $h_w/4 \times \sin \alpha$ for a conservative formulation. Therefore the equations to determine $d_{burst-web}$ can be rewritten as

$$d_{burst-web} = (h' - c - \frac{t_{f2}}{2} - e) + \frac{a}{4} + \frac{h_w}{4} (1 - \exp(-0.8b_{f1} / h_w)) + \frac{h_w}{4} \sin \alpha \quad (4.44)$$

$$d_{burst-web} = (c + \frac{t_{f2}}{2} + e) + \frac{a}{4} + \frac{h_w}{4} (1 - \exp(-0.8b_{f2} / h_w)) + \frac{h_w}{4} \sin \alpha \quad (4.45)$$

Similar to those presented for the formulations of other load configurations, the smaller value of equations (4.44) and (4.45) is used in equations (4.42) and (4.43).

Tables 4.22 to 4.24 present the comparison of finite element results and the results using equations (4.42) to (4.45) for three types of model subjected to inclined concentric and inclined eccentric load. In Table 4.22, the estimation of the location of the force using the

equations results in a shorter distance from the prestressing surface than the result of finite element model. When considering the magnitude of the bursting force, the estimation from the equations gives conservative results for almost every case compared to the finite element result. The model II251A is found to provide an unconservative estimation of $T_{burst-web}$ with the percent difference of -1.83 , which is considered as a very small number. Therefore, the approximation of bursting force magnitude and location using equations (4.42) to (4.45) is effective for the design of anchorage zones with symmetrical I-section subjected to an inclined load.

Table 4.22 COMPARISON OF $T_{burst-web}$ AND $d_{burst-web}$ FOR SYMMETRICAL I-SECTION SUBJECTED TO INCLINED CONCENTRIC AND INCLINED ECCENTRIC LOAD

Name	b_f (in.)	e/h_w	e (in.)	$max\ e$ (in.)	R_{1u} /P	R_{1l} /P	R_2 /P	R_3 /P	p (in.)	y_u (in.)	y_l (in.)	α ($^\circ$)	$d_{burst-wfem}$	$d_{burst-web}$	%diff	$T_{burst-wfem}$	$T_{burst-web}$	%diff
													/h _w	/h _w	-1 & 2-	/P	/P	-3-
<i>Inclined Eccentric in Upper Portion</i>																		
IEI53A	6.4	0.10	1.60	3.91	0.46	0.41	0.08	0.04	0.06	5.04	5.96	6	0.8992	0.7165	-20.32	0.2569	0.2806	9.23
IEI53H	9.6	0.10	1.60	4.42	0.35	0.33	0.20	0.12	0.08	5.39	6.67	6	0.9378	0.7433	-20.74	0.2625	0.2947	12.29
IEI53B	16	0.10	1.60	4.96	0.24	0.23	0.33	0.20	0.10	5.74	7.48	6	0.9864	0.7857	-20.35	0.2677	0.3042	13.60
IEI53I	25.6	0.10	1.60	5.35	0.16	0.16	0.41	0.26	0.12	5.98	8.09	6	1.0246	0.8285	-19.14	0.2705	0.3062	13.18
IEI53J	35.2	0.10	1.60	5.55	0.12	0.12	0.46	0.30	0.12	6.10	8.42	6	1.0414	0.8550	-17.90	0.2712	0.3058	12.78
IEI53K	44.8	0.10	1.60	5.67	0.10	0.10	0.48	0.32	0.13	6.17	8.63	6	1.0479	0.8714	-16.84	0.2712	0.3056	12.69
IEI53C	56	0.10	1.60	5.77	0.08	0.08	0.50	0.33	0.13	6.22	8.79	6	1.0503	0.8828	-15.95	0.2710	0.3057	12.81
<i>Inclined Concentric</i>																		
II251A	6.4	0.00	0.00	-3.91	0.43	0.43	0.06	0.06	0.00	5.70	5.70	6	0.8585	0.8165	-4.90	0.2666	0.2617	-1.83
II251H	9.6	0.00	0.00	-4.42	0.34	0.34	0.16	0.16	0.00	6.22	6.22	6	0.9015	0.8433	-6.46	0.2739	0.2750	0.41
II251B	16	0.00	0.00	-4.96	0.23	0.23	0.26	0.26	0.00	6.77	6.77	6	0.9528	0.8857	-7.05	0.2811	0.2847	1.27
II251I	25.6	0.00	0.00	-5.35	0.16	0.16	0.34	0.34	0.00	7.16	7.16	6	0.9926	0.9285	-6.45	0.2854	0.2877	0.80
II251J	35.2	0.00	0.00	-5.55	0.12	0.12	0.38	0.38	0.00	7.36	7.36	6	1.0109	0.9550	-5.53	0.2870	0.2881	0.40
II251K	44.8	0.00	0.00	-5.67	0.10	0.10	0.40	0.40	0.00	7.48	7.48	6	1.0189	0.9714	-4.66	0.2875	0.2883	0.27
II251C	56	0.00	0.00	-5.77	0.08	0.08	0.42	0.42	0.00	7.58	7.58	6	1.0228	0.9828	-3.91	0.2877	0.2887	0.34
<i>Inclined Eccentric in Lower Portion</i>																		
IEI53A	6.4	-0.10	-1.60	-3.91	0.41	0.46	0.04	0.08	-0.07	5.96	5.04	6	0.7756	0.7165	-7.62	0.2619	0.2806	7.16
IEI53H	9.6	-0.10	-1.60	-4.42	0.33	0.35	0.12	0.20	-0.09	6.67	5.39	6	0.8281	0.7433	-10.24	0.2723	0.2947	8.25
IEI53B	16	-0.10	-1.60	-4.96	0.23	0.24	0.20	0.33	-0.11	7.48	5.74	6	0.8868	0.7857	-11.40	0.2826	0.3042	7.63
IEI53I	25.6	-0.10	-1.60	-5.35	0.16	0.16	0.26	0.41	-0.12	8.09	5.98	6	0.9308	0.8285	-10.99	0.2892	0.3062	5.87
IEI53J	35.2	-0.10	-1.60	-5.55	0.12	0.12	0.30	0.46	-0.13	8.42	6.10	6	0.9521	0.8550	-10.20	0.2921	0.3058	4.69
IEI53K	44.8	-0.10	-1.60	-5.67	0.10	0.10	0.32	0.48	-0.14	8.63	6.17	6	0.9629	0.8714	-9.50	0.2936	0.3056	4.09
IEI53C	56	-0.10	-1.60	-5.77	0.08	0.08	0.33	0.50	-0.14	8.79	6.22	6	0.9694	0.8828	-8.93	0.2945	0.3057	3.83

Note : All models in the Table contain the dimensions as indicated below:

$$a/h = 0.20, a = 3.2 \text{ in.}, h_w = 16 \text{ in.}, t_w = 5 \text{ in.}, t_f/t_w = 1.1, t_f = 5.5 \text{ in.}, h' = 21.5 \text{ in.}, c = 8 \text{ in.}$$

For the comparison of T-section models in Table 4.23, all the estimations of bursting force magnitudes give conservative results compared to those from the finite element analysis. There is no negative percent difference of the bursting force magnitude found in the table. This indicates an effective estimation of the bursting force magnitude in the T-section model. For the location of the bursting force, equations (4.44) and (4.45) provide a shorter distance

in all models as well. In some cases, the estimation results in the percent difference as much as -42.86 percent, which is considered as a large value. As the bursting force estimation is conservative, a short distance of the force location is acceptable. For unsymmetrical I-section, the equations provide a good estimation as well as can be seen in Table 4.24. The location of the force from the estimation is also shorter than those achieved from the finite element analysis. In conclusion, equations (4.42) to (4.45) are effective in the approximation of both magnitude and location of bursting force in a flanged section anchorage zone subjected to an inclined load.

Table 4.23 COMPARISON OF $T_{burst-web}$ AND $d_{burst-web}$ FOR T-SECTION SUBJECTED TO INCLINED CONCENTRIC AND INCLINED ECCENTRIC LOAD

Name	b_f (in.)	c (in.)	e/h_w	e (in.)	$max e$ (in.)	R_{1u} /P	R_{1l} /P	R_2 /P	p (in.)	y_u (in.)	y_l (in.)	α (°)	$d_{burst-wfem}$ /h _w	$d_{burst-web}$ /h _w	%diff -1 & 2-	$T_{burst-wfem}$ /P	$T_{burst-web}$ /P	%diff -3 & 4-
<i>Inclined Eccentric in Upper Portion</i>																		
IET53A	6.4	9.88	0.10	1.60	3.07	0.45	0.44	0.10	0.09	3.96	5.00	6	0.8201	0.5991	-26.95	0.2345	0.2680	14.29
IET53H	9.6	10.78	0.10	1.60	2.87	0.33	0.39	0.27	0.16	3.50	5.33	6	0.8587	0.5694	-33.69	0.2218	0.2693	21.39
IET53B	16	11.97	0.10	1.60	2.44	0.21	0.31	0.48	0.29	2.58	5.61	6	0.9335	0.5373	-42.44	0.1884	0.2439	29.47
<i>Inclined Concentric</i>																		
IT251A	6.4	9.88	0.00	0.00	3.42	0.43	0.48	0.08	0.02	4.69	4.94	6	0.7486	0.6935	-7.37	0.2442	0.2561	4.88
IT251H	9.6	10.78	0.00	0.00	3.88	0.33	0.45	0.21	0.07	4.46	5.39	6	0.7986	0.6694	-16.18	0.2439	0.2677	9.77
IT251B	16	11.97	0.00	0.00	4.32	0.22	0.39	0.39	0.17	3.80	5.99	6	0.8559	0.6373	-25.54	0.2323	0.2681	15.41
IT251I	25.6	13.00	0.00	0.00	4.44	0.14	0.31	0.54	0.29	2.97	6.50	6	0.9078	0.6160	-32.14	0.2092	0.2485	18.77
IT251J	35.2	13.61	0.00	0.00	4.34	0.10	0.26	0.64	0.37	2.41	6.80	6	0.9448	0.6044	-36.03	0.1888	0.2273	20.38
IT251K	44.8	14.01	0.00	0.00	4.17	0.08	0.22	0.70	0.43	2.02	7.01	6	0.9806	0.5956	-39.27	0.1713	0.2093	22.23
IT251C	56	14.34	0.00	0.00	3.96	0.06	0.19	0.75	0.49	1.70	7.17	6	1.0266	0.5865	-42.86	0.1534	0.1925	25.48
<i>Inclined Eccentric in Lower Portion</i>																		
IET51A	6.4	9.88	-0.10	-1.60	-3.42	0.41	0.53	0.05	-0.05	4.96	4.37	6	0.6307	0.6224	-1.31	0.2325	0.2714	16.73
IET51H	9.6	10.78	-0.10	-1.60	-3.88	0.33	0.51	0.15	-0.02	5.05	4.87	6	0.6972	0.6845	-1.83	0.2411	0.2661	10.35
IET51B	16	11.97	-0.10	-1.60	-4.32	0.23	0.46	0.30	0.06	4.74	5.54	6	0.7784	0.7373	-5.28	0.2454	0.2577	5.00
IET51I	25.6	13.00	-0.10	-1.60	-4.44	0.15	0.40	0.44	0.15	4.13	6.17	6	0.8310	0.7160	-13.84	0.2394	0.2575	7.54
IET51J	35.2	13.61	-0.10	-1.60	-4.34	0.11	0.36	0.53	0.22	3.65	6.56	6	0.8538	0.7044	-17.50	0.2311	0.2501	8.24
IET51K	44.8	14.01	-0.10	-1.60	-4.17	0.09	0.32	0.58	0.28	3.28	6.84	6	0.8650	0.6956	-19.59	0.2233	0.2421	8.39
IET51C	56	14.34	-0.10	-1.60	-3.96	0.07	0.29	0.63	0.32	2.96	7.09	6	0.8714	0.6865	-21.22	0.2154	0.2336	8.45

Note : All models in the Table contain the dimensions as indicated below:

$$a/h = 0.20, a = 3.2 \text{ in.}, h_w = 16 \text{ in.}, t_w = 5 \text{ in.}, t_f/t_w = 1.1, t_f = 5.5 \text{ in.}, h' = 18.75 \text{ in.}$$

Table 4.24 COMPARISON OF $T_{burst-web}$ AND $d_{burst-web}$ FOR UNSYMMETRICAL I-SECTION SUBJECTED TO INCLINED CONCENTRIC AND INCLINED ECCENTRIC LOAD

Name	b_{f1} (in.)	b_{f2} (in.)	c (in.)	e/h_w	e (in.)	$max e$ (in.)	R_{1u} /P	R_{1l} /P	R_2 /P	R_3 /P	p (in.)	y_u (in.)	y_l (in.)	α (°)	$d_{burst-wfem}$ /h _w	$d_{burst-web}$ /h _w	%diff -1 & 2-	$T_{burst-wfem}$ /P	$T_{burst-web}$ /P	%diff -3 & 4-
<i>Inclined Eccentric in Upper Portion</i>																				
IEU53L	16	8	9.91	0.10	1.60	3.68	0.23	0.31	0.39	0.06	0.20	4.26	7.20	6	0.9596	0.6664	-30.55	0.2370	0.2952	24.57
IEU53O	56	28.8	10.31	0.10	1.60	4.24	0.08	0.12	0.63	0.18	0.32	4.09	9.77	6	1.0442	0.7387	-29.26	0.2295	0.2930	27.67
<i>Inclined Concentric</i>																				
IUS51L	16	8	9.91	0.00	0.00	-5.27	0.24	0.34	0.33	0.09	0.10	5.39	7.07	6	0.9216	0.7664	-16.84	0.2605	0.2941	12.90
IUS51O	56	28.8	10.31	0.00	0.00	-6.56	0.08	0.13	0.54	0.25	0.19	5.50	9.05	6	1.0318	0.8387	-18.72	0.2636	0.3029	14.91
<i>Inclined Eccentric in Lower Portion</i>																				
IEU51L	16	8	9.91	-0.10	-1.60	-5.27	0.25	0.37	0.26	0.12	0.01	6.25	6.43	6	0.9022	0.8497	-5.83	0.2721	0.2783	2.26
IEU51O	56	28.8	10.31	-0.10	-1.60	-6.56	0.09	0.13	0.45	0.33	0.06	6.81	7.96	6	1.0201	0.9387	-7.98	0.2807	0.2917	3.92

Note : All models in the Table contain the dimensions as indicated below:

$$a/h = 0.20, a = 3.2 \text{ in.}, h_w = 16 \text{ in.}, t_w = 5 \text{ in.}, t_f/t_w = 1.1, t_f = 5.5 \text{ in.}, h' = 21.5 \text{ in.}$$

In addition to the study of inclined concentrically and inclined eccentrically loaded, the formulations in equations (4.42) to (4.45) are modified by adding another term, which represents the effect of a support reaction as has been studied in Chapter 3. The last terms in equations (3.7) and (3.8) are adopted into the formulations of $T_{burst-web}$ and $d_{burst-web}$ in order to examine the applicability of determining the bursting force magnitude and the location of the force in an anchorage zone with the presence of support reaction. The new equations can be written as

$$T_{burst-web} = (R_{1u} + R_2) \left(\frac{4y_u + 4p}{4d_{burst-web} - a} \right) \left(1 - \frac{a}{4y_u + 4p} \right) + 0.6P \sin \alpha + \frac{R}{P} (0.25 - 5 \sin \alpha) \quad (4.46)$$

$$T_{burst-web} = (R_{1l} + R_3) \left(\frac{4y_l - 4p}{4d_{burst-web} - a} \right) \left(1 - \frac{a}{4y_l - 4p} \right) + 0.6P \sin \alpha + \frac{R}{P} (0.25 - 5 \sin \alpha) \quad (4.47)$$

$$d_{burst-web} = (h' - c - \frac{t_{f2}}{2} - e) + \frac{a}{4} + \frac{h_w}{4} (1 - \exp(-0.8b_{f1} / h_w)) + \frac{h_w}{4} \sin \alpha + \frac{R}{P} h_w (1.5 - 10 \sin \alpha) \quad (4.48)$$

$$d_{burst-web} = (c + \frac{t_{f2}}{2} + e) + \frac{a}{4} + \frac{h_w}{4} (1 - \exp(-0.8b_{f2} / h_w)) + \frac{h_w}{4} \sin \alpha + \frac{R}{P} h_w (1.5 - 10 \sin \alpha) \quad (4.49)$$

Six models are especially created in order to compare the results from finite element method and those using equations (4.46) to (4.49). Three models in this study have a top flange width equal to 16 in. and the bottom flange equal to 8 in. Another three models have the flange widths of 56 in. and 28.8 in. for the top and the bottom flange, respectively. In each set of three models, the magnitudes of the reaction force, which are applied to the models, consist of $0.05P$, $0.10P$, and $0.15P$. Table 4.25 presents the comparison result of this study. The column R/P presents the magnitude of the reaction force in terms of P . As can be seen from the table, the estimation using equations (4.46) to (4.49) provides a very conservative result with the percent difference as high as 64.35 percent in one case. The locations of the bursting force from the estimation agree well with those from the finite element analysis. However, since the present study does not focus on the study of a flanged section with the presence of support reaction, the formulations presented in equation (4.46) to (4.49) are not recommended for the general design of anchorage zones with flanged sections.

A further study with a wider range of parameters needs to be conducted before the use of equations (4.46) to (4.49) can be recommended.

Table 4.25 COMPARISON OF $T_{burst-web}$ AND $d_{burst-web}$ FOR UNSYMMETRICAL I-SECTION SUBJECTED TO INCLINED ECCENTRIC LOAD AND A SUPPORT REACTION

Name	b_{f_1} (in.)	b_{f_2} (in.)	c (in.)	e/h_w	e (in.)	$max\ e$ (in.)	$R_{1,u}$ /P	$R_{1,l}$ /P	R_2 /P	R_3 /P	p (in.)	y_u (in.)	y_l (in.)	α ($^\circ$)	R /P	$d_{burst-efem}$	$d_{burst-web}$	%diff	$T_{burst-efem}$	$T_{burst-web}$	%diff
																/h _w	/h _w	-1 & 2-	/P	/P	-3 & 4-
IRU51A	16	8	9.91	-0.10	-1.60	-5.27	0.25	0.37	0.26	0.12	0.01	6.25	6.43	6	0.05	0.8903	0.8724	-2.00	0.2282	0.2378	4.22
IRU51B	16	8	9.91	-0.10	-1.60	-5.27	0.25	0.37	0.26	0.12	0.01	6.25	6.43	6	0.10	0.8548	0.8951	4.72	0.1798	0.2185	21.53
IRU51C	16	8	9.91	-0.10	-1.60	-5.27	0.25	0.37	0.26	0.12	0.01	6.25	6.43	6	0.15	0.8581	0.9179	6.97	0.1351	0.1996	47.69
IRU51D	56	288	10.31	-0.10	-1.60	-6.56	0.09	0.13	0.45	0.33	0.06	6.81	7.96	6	0.05	1.0085	0.9614	-4.67	0.2342	0.2515	7.40
IRU51E	56	288	10.31	-0.10	-1.60	4.24	0.09	0.13	0.45	0.33	0.06	6.81	7.96	6	0.10	0.9703	0.9841	1.42	0.1822	0.2324	27.55
IRU51F	56	288	10.31	-0.10	-1.60	4.24	0.09	0.13	0.45	0.33	0.06	6.81	7.96	6	0.15	0.9311	1.0069	8.14	0.1300	0.2136	64.35

Note: All models in the Table contain the dimensions as indicated below:

$$a/h = 0.20, \alpha = 3.2 \text{ in.}, h_w = 16 \text{ in.}, t_w = 5 \text{ in.}, t_f/t_w = 1.1, t_f = 5.5 \text{ in.}, h' = 21.5 \text{ in.}$$

In the estimation of the flange bursting force magnitude and location, the calculation of the k_f ratio (see Fig. 4.62) is different from the calculation in the previous two sections. Since an inclined load is applied, the moment that is used to calculate stresses on the flange body as presented in equation (4.31) needs to consider the vertical component of the inclined load. The distance used to determine the moment due to the vertical force should be located appropriately in order to achieve a reasonable method to calculate the bursting force. Since the derivation of the equations (4.42) to (4.45) are based on the assumption that the transferring force from the web is applied at an angle of 45 degrees from the center of the anchor plate. The distance to the application of the force is equal the length from the center of the anchor plate to the center of the flange. For example, if the top flange is considered, this distance is equal to $h_w - c - e$. By applying this location of the transferring force to the calculation of stresses, the forces that are used for the calculation of k_f can be determined.

Tables 4.26 and 4.27 show the comparison of the results from finite element analysis and the equation to approximate the magnitude of the bursting force and the location of the force. For the top flange in Table 4.26, the results from the approximate equations provide conservative values for the magnitude of the force for almost all cases. In the two unconservative models, the busting force magnitudes are found to be quite small. The approximation of the bursting force location gives a larger distance compared to the result

from finite element method, which is similar to the comparisons of $d_{burst-flg}$ that have been presented so far. Similar comparison results are found in Table 4.27. The estimation of flange bursting force magnitude in one case produces a large percent difference as high as 99.4 percent, but the value from the finite element result of the same model indicates a very small magnitude as well.

Table 4.26 COMPARISON OF $T_{burst-flg}$ AND $d_{burst-flg}$ FOR THE TOP FLANGE OF SYMMETRICAL I-SECTION SUBJECTED TO INCLINED CONCENTRIC AND INCLINED ECCENTRIC LOAD

Name	b_f (in.)	e/h_w	e (in.)	$max e$ (in.)	α (°)	R_{1u} /P	R_2 /P	k_f	$T_{burst-fem}$	$T_{burst-flg}$	%diff	$d_{burst-fem}$	$d_{burst-flg}$	%diff
									/P	/P	-1 & 2-	/h _w	/h _w	-3 & 4-
<i>Inclined Eccentric in Upper Portion</i>														
IEI53A	6.4	0.1	1.6	3.91	6	0.42	0.07	0.68	0.0238	0.0468	96.59	0.4997	0.3683	-26.29
IEI53H	9.6	0.1	1.6	4.42	6	0.32	0.18	0.76	0.0393	0.0654	66.18	0.5653	0.5500	-2.71
IEI53B	16	0.1	1.6	4.96	6	0.22	0.30	0.84	0.0607	0.0884	45.66	0.6701	0.7858	17.26
IEI53I	25.6	0.1	1.6	5.35	6	0.15	0.38	0.89	0.0770	0.1064	38.30	0.8345	1.0841	29.91
IEI53J	35.2	0.1	1.6	5.55	6	0.11	0.42	0.92	0.0900	0.1164	29.25	1.0574	1.3689	29.46
IEI53K	44.8	0.1	1.6	5.67	6	0.09	0.45	0.94	0.1004	0.1226	22.13	1.3196	1.6496	25.01
IEI53C	56	0.1	1.6	5.77	6	0.07	0.47	0.95	0.1106	0.1275	15.29	1.6181	1.9751	22.06
<i>Inclined Concentric</i>														
II251A	6.4	0	0	3.91	6	0.48	0.07	0.60	0.0196	0.0318	62.49	0.5355	0.4562	-14.82
II251H	9.6	0	0	4.42	6	0.37	0.18	0.69	0.0341	0.0486	42.64	0.5966	0.6801	14.01
II251B	16	0	0	4.96	6	0.25	0.30	0.78	0.0540	0.0722	33.67	0.7034	0.9275	31.86
II251I	25.6	0	0	5.35	6	0.17	0.38	0.85	0.0694	0.0929	33.77	0.8273	1.2237	47.92
II251J	35.2	0	0	5.55	6	0.13	0.42	0.89	0.0789	0.1050	33.12	1.0463	1.5047	43.81
II251K	44.8	0	0	5.67	6	0.11	0.44	0.91	0.0829	0.1129	36.23	1.2727	1.7817	40.00
II251C	56	0	0	5.77	6	0.09	0.46	0.93	0.0816	0.1192	46.11	1.5397	2.1032	36.60
<i>Inclined Eccentric in Lower Portion</i>														
IEI53A	6.4	-0.1	-1.6	-3.91	6	0.36	0.03	0.37	0.0120	0.0075	-37.25	0.6404	0.6512	1.69
IEI53H	9.6	-0.1	-1.6	-4.42	6	0.29	0.09	0.49	0.0213	0.0176	-17.06	0.6981	0.8559	22.61
IEI53B	16	-0.1	-1.6	-4.96	6	0.21	0.16	0.63	0.0363	0.0379	4.35	0.7943	0.9734	22.55
IEI53I	25.6	-0.1	-1.6	-5.35	6	0.15	0.21	0.74	0.0504	0.0609	20.91	0.9237	1.1218	21.44
IEI53J	35.2	-0.1	-1.6	-5.55	6	0.11	0.24	0.80	0.0611	0.0767	25.63	1.0834	1.2788	18.03
IEI53K	44.8	-0.1	-1.6	-5.67	6	0.09	0.26	0.84	0.0705	0.0879	24.81	1.2841	1.4408	12.20
IEI53C	56	-0.1	-1.6	-5.77	6	0.07	0.28	0.87	0.0803	0.0974	21.28	1.5115	1.6333	8.06

Note : All models in the Table contain the dimensions as indicated below:

$$a/h = 0.20, a = 3.2 \text{ in.}, h_w = 16 \text{ in.}, t_w = 5 \text{ in.}, t_f/t_w = 1.1, t_f = 5.5 \text{ in.}, h' = 21.5 \text{ in.}, c = 8 \text{ in.}$$

Table 4.27 COMPARISON OF $T_{burst-flg}$ AND $d_{burst-flg}$ FOR THE BOTTOM FLANGE OF SYMMETRICAL I-SECTION SUBJECTED TO INCLINED CONCENTRIC AND INCLINED ECCENTRIC LOAD

Name	b_f (in.)	e/h_w	e (in.)	$max\ e$ (in.)	α ($^\circ$)	R_{11} /P	R_3 /P	k_f	$T_{burst-flg}$ /P -1-	$T_{burst-flg}$ /P -2-	%diff -1 & 2-	$d_{burst-flg}$ /h _w -3-	$d_{burst-flg}$ /h _w -4-	%diff -3 & 4-
<i>Inclined Eccentric in Upper Portion</i>														
IEI53A	6.4	0.1	1.6	3.91	6	0.45	0.05	0.47	0.0146	0.0154	5.83	0.5793	0.5750	-0.75
IEI53H	9.6	0.1	1.6	4.42	6	0.35	0.13	0.57	0.0262	0.0284	8.32	0.6425	0.8181	27.33
IEI53B	16	0.1	1.6	4.96	6	0.25	0.23	0.70	0.0440	0.0505	14.59	0.7375	1.0158	37.74
IEI53I	25.6	0.1	1.6	5.35	6	0.17	0.29	0.79	0.0577	0.0730	26.59	0.8407	1.2403	47.53
IEI53J	35.2	0.1	1.6	5.55	6	0.13	0.33	0.84	0.0676	0.0876	29.62	1.0325	1.4582	41.22
IEI53K	44.8	0.1	1.6	5.67	6	0.10	0.35	0.87	0.0721	0.0976	35.43	1.2565	1.6762	33.41
IEI53C	56	0.1	1.6	5.77	6	0.09	0.37	0.89	0.0733	0.1060	44.49	1.5120	1.9313	27.73
<i>Inclined Concentric</i>														
II251A	6.4	0	0	3.91	6	0.48	0.07	0.60	0.0196	0.0318	62.49	0.5355	0.4562	-14.82
II251H	9.6	0	0	4.42	6	0.37	0.18	0.69	0.0341	0.0486	42.64	0.5966	0.6801	14.01
II251B	16	0	0	4.96	6	0.25	0.30	0.78	0.0540	0.0722	33.67	0.7034	0.9275	31.86
II251I	25.6	0	0	5.35	6	0.17	0.38	0.85	0.0694	0.0929	33.77	0.8273	1.2237	47.92
II251J	35.2	0	0	5.55	6	0.13	0.42	0.89	0.0789	0.1050	33.12	1.0463	1.5047	43.81
II251K	44.8	0	0	5.67	6	0.11	0.44	0.91	0.0829	0.1129	36.23	1.2727	1.7817	40.00
II251C	56	0	0	5.77	6	0.09	0.46	0.93	0.0816	0.1192	46.11	1.5397	2.1032	36.60
<i>Inclined Eccentric in Lower Portion</i>														
IEI53A	6.4	-0.1	-1.6	-3.91	6	0.51	0.09	0.70	0.0263	0.0524	99.40	0.4754	0.3875	-18.49
IEI53H	9.6	-0.1	-1.6	-4.42	6	0.39	0.23	0.78	0.0424	0.0706	66.44	0.5413	0.5988	10.63
IEI53B	16	-0.1	-1.6	-4.96	6	0.26	0.37	0.85	0.0650	0.0927	42.50	0.6586	0.8773	33.21
IEI53I	25.6	-0.1	-1.6	-5.35	6	0.17	0.46	0.90	0.0813	0.1097	34.87	0.8353	1.2305	47.31
IEI53J	35.2	-0.1	-1.6	-5.55	6	0.13	0.51	0.93	0.0908	0.1190	31.02	1.0741	1.5675	45.93
IEI53K	44.8	-0.1	-1.6	-5.67	6	0.11	0.54	0.94	0.0927	0.1248	34.57	1.3209	1.8996	43.81
IEI53C	56	-0.1	-1.6	-5.77	6	0.09	0.56	0.95	0.0896	0.1293	44.24	1.5928	2.2844	43.42

Note : All models in the Table contain the dimensions as indicated below:

$$a/h = 0.20, a = 3.2 \text{ in.}, h_w = 16 \text{ in.}, t_w = 5 \text{ in.}, t_f/t_w = 1.1, t_f = 5.5 \text{ in.}, h' = 21.5 \text{ in.}, c = 8 \text{ in.}$$

For the comparison of flange bursting force and the location of the force in T-section models, all the results from all inclined load configurations are given in Table 4.28. There are two cases in the table in which the results from the finite element analysis provide unusually large values. The models (IT251C and IET51C) contain a very large flange, which causes the centroid of the section to be at the center of the flange. This finite element model may produce an incorrect result, which might not occur if the model had a more sophisticated element type. For the $d_{burst-flg}$ value, the estimation gives a smaller distance than that of finite element method. This should provide a conservative approximation when combining with the overestimated bursting force magnitudes.

Table 4.28 COMPARISON OF $T_{burst-flg}$ AND $d_{burst-flg}$ FOR THE FLANGE OF T-SECTION
SUBJECTED TO INCLINED CONCENTRIC AND INCLINED ECCENTRIC LOAD

Name	b_f	c	e/h_w	e	$max\ e$	α	R_{1u}	R_2	k_f	$T_{burst-fem}$	$T_{burst-flg}$	%diff	$d_{burst-fem}$	$d_{burst-flg}$	%diff
	(in.)	(in.)		(in.)	(in.)	(°)	/P	/P		/P	/P	-1 & 2-	/h _w	/h _w	-3 & 4-
<i>Inclined Eccentric in Upper Portion</i>															
IET53A	6.4	9.878	0.1	1.6	3.42	6	0.43	0.09	0.82	0.0306	0.0818	166.94	0.4369	0.2285	-47.70
IET53H	9.6	10.78	0.1	1.6	3.88	6	0.32	0.25	0.93	0.0594	0.1212	103.96	0.4501	0.3295	-26.79
IET53B	16	11.97	0.1	1.6	4.32	6	0.20	0.46	1.00	0.0923	0.1500	62.56	0.5701	0.5571	-2.28
<i>Inclined Concentric</i>															
IT251A	6.4	9.878	0	0	3.42	6	0.39	0.07	0.65	0.0236	0.0418	77.31	0.4905	0.2504	-48.95
IT251H	9.6	10.78	0	0	3.88	6	0.31	0.19	0.80	0.0438	0.0765	74.72	0.5312	0.3600	-32.22
IT251B	16	11.97	0	0	4.32	6	0.21	0.37	0.93	0.0736	0.1203	63.44	0.6410	0.5536	-13.64
IT251I	25.6	13	0	0	4.44	6	0.13	0.52	0.99	0.0989	0.1459	47.61	0.9732	0.8901	-8.55
IT251J	35.2	13.61	0	0	4.34	6	0.10	0.62	1.00	0.1060	0.1500	41.47	1.3959	1.3060	-6.44
IT251K	44.8	14.01	0	0	4.17	6	0.07	0.68	1.00	0.1012	0.1500	48.16	1.8251	1.7625	-3.43
IT251C	56	14.34	0	0	3.96	6	0.06	0.73	1.00	0.3451	0.1500	-56.53	4.3421	2.3099	-46.80
<i>Inclined Eccentric in Lower Portion</i>															
IET51A	6.4	9.878	-0.1	-1.6	-3.42	6	0.36	0.04	0.44	0.0165	0.0127	-23.15	0.5680	0.3247	-42.83
IET51H	9.6	10.78	-0.1	-1.6	-3.88	6	0.30	0.13	0.62	0.0326	0.0359	9.92	0.6101	0.4414	-27.66
IET51B	16	11.97	-0.1	-1.6	-4.32	6	0.22	0.27	0.81	0.0601	0.0793	31.83	0.7475	0.6014	-19.54
IET51I	25.6	13	-0.1	-1.6	-4.44	6	0.15	0.41	0.92	0.0847	0.1153	36.12	1.0796	0.8849	-18.03
IET51J	35.2	13.61	-0.1	-1.6	-4.34	6	0.11	0.50	0.96	0.0924	0.1316	42.53	1.4742	1.2126	-17.75
IET51K	44.8	14.01	-0.1	-1.6	-4.17	6	0.08	0.56	0.98	0.0876	0.1398	59.64	1.9039	1.5685	-17.62
IET51C	56	14.34	-0.1	-1.6	-3.96	6	0.07	0.61	0.99	0.3700	0.1449	-60.85	4.4538	2.0075	-54.93

Note : All models in the Table contain the dimensions as indicated below:

$$a/h = 0.20, a = 3.2 \text{ in.}, h_w = 16 \text{ in.}, t_w = 5 \text{ in.}, t_f/t_w = 1.1, t_f = 5.5 \text{ in.}, h' = 18.75 \text{ in.}$$

Tables 4.29 and 4.30 give the comparisons of flange bursting force magnitude and location of unsymmetrical I-section models. The results given in the table are similar to those present in Tables 4.26 and 4.27, which are given for the comparison of symmetrical I-section. Most of the estimated magnitudes of bursting force shown in both Tables 4.29 and 4.30 are conservative. The approximation of the location of bursting force provides a larger value compared to that of finite element method for every model. Therefore, based on all the comparison of results from Tables 4.26 to 4.30, the method to determine the bursting force magnitude in the flange based on the assumed location where force is transferred from the web is acceptable. For the approximation of flange bursting force location, it was found to be larger than the results of finite element in some cases, which may result in an improper reinforcing arrangement if the distribution of the reinforcement is based on the value from the estimation. However, the study of nonlinear analysis can help in finding an effective reinforcing steel arrangement.

Table 4.29 COMPARISON OF $T_{burst-flg}$ AND $d_{burst-flg}$ FOR THE TOP FLANGE OF UNSYMMETRICAL I-SECTION SUBJECTED TO INCLINED CONCENTRIC AND INCLINED ECCENTRIC LOAD

Name	b_{f1}	b_{f2}	c	e/h_w	e	a	R_{1u}/P	R_2/P	k_f	$T_{burst-flg}/P$ -1-	$T_{burst-flg}/P$ -2-	%diff -1 & 2-	$d_{burst-flg}/h_w$ -3-	$d_{burst-flg}/h_w$ -4-	%diff -3 & 4-
<i>Inclined Eccentric in Upper Portion</i>															
IEU53L	16	8	9.91	0.10	1.60	6	0.22	0.37	0.92	0.0753	0.1154	53.13	0.6118	0.7313	19.52
IEU53O	56	28.8	10.31	0.10	1.60	6	0.07	0.60	0.98	0.1274	0.1412	10.79	1.7505	2.2257	27.15
<i>Inclined Concentric</i>															
IUS51L	16	8	9.91	0.00	0.00	6	0.22	0.30	0.83	0.0600	0.0863	43.87	0.6811	0.7924	16.33
IUS51O	56	28.8	10.31	0.00	0.00	6	0.08	0.50	0.95	0.1123	0.1295	15.33	1.7077	2.0741	21.46
<i>Inclined Eccentric in Lower Portion</i>															
IEU51L	16	8	9.91	-0.10	-1.60	6	0.23	0.22	0.72	0.0481	0.0557	15.83	0.7456	0.9073	21.70
IEU51O	56	28.8	10.31	-0.10	-1.60	6	0.08	0.41	0.91	0.0945	0.1144	21.07	1.6116	1.9384	20.28

Note : All models in the Table contain the dimensions as indicated below:
 $a/h = 0.20$, $a = 3.2$ in., $h_w = 16$ in., $t_w = 5$ in., $t_f/t_w = 1.1$, $t_f = 5.5$ in., $h' = 21.5$ in.

Table 4.30 COMPARISON OF $T_{burst-flg}$ AND $d_{burst-flg}$ FOR THE BOTTOM FLANGE OF UNSYMMETRICAL I-SECTION SUBJECTED TO INCLINED CONCENTRIC AND INCLINED ECCENTRIC LOAD

Name	b_{f1}	b_{f2}	c	e/h_w	e	a	R_{1l}/P	R_2/P	k_f	$T_{burst-flg}/P$ -1-	$T_{burst-flg}/P$ -2-	%diff -1 & 2-	$d_{burst-flg}/h_w$ -3-	$d_{burst-flg}/h_w$ -4-	%diff -3 & 4-
<i>Inclined Eccentric in Upper Portion</i>															
IEU53L	16	8	9.91	0.10	1.60	6	0.37	0.08	0.49	0.0142	0.0172	21.20	0.6505	0.7915	21.67
IEU53O	56	28.8	10.31	0.10	1.60	6	0.14	0.23	0.77	0.0449	0.0678	51.07	0.8388	1.2292	46.55
<i>Inclined Concentric</i>															
IUS51L	16	8	9.91	0.00	0.00	6	0.39	0.11	0.58	0.0204	0.0295	45.02	0.6074	0.6575	8.24
IUS51O	56	28.8	10.31	0.00	0.00	6	0.14	0.30	0.82	0.0559	0.0840	50.15	0.8355	1.2375	48.11
<i>Inclined Eccentric in Lower Portion</i>															
IEU51L	16	8	9.91	-0.10	-1.60	6	0.41	0.14	0.66	0.0259	0.0436	67.91	0.5673	0.5752	1.40
IEU51O	56	28.8	10.31	-0.10	-1.60	6	0.15	0.37	0.87	0.0666	0.0974	46.39	0.8518	1.2631	48.29

Note : All models in the Table contain the dimensions as indicated below:
 $a/h = 0.20$, $a = 3.2$ in., $h_w = 16$ in., $t_w = 5$ in., $t_f/t_w = 1.1$, $t_f = 5.5$ in., $h' = 21.5$ in.

4.5 Examples Using Nonlinear Analysis

Since the formulations for the determination of bursting force magnitude and location for anchorage zones in a flanged section have been established, a more sophisticated method needs to be used in order to verify the formulations. Moreover, since a recommended pattern of bursting steel arrangement is not yet provided, the study of various bursting steel patterns within a non-rectangular anchorage zone structure helps to provide the best solution for an effective steel arrangement. Therefore, nonlinear analysis is employed for the study of a non-rectangular anchorage zone in the present research. Similar to the examples using nonlinear analysis that were presented in Chapter 3, the applicability of using nonlinear finite element method to study an available experimental work is examined before using the nonlinear finite element method to verify the effectiveness of the approximate equations developed in the design of a non-rectangular anchorage zone.

In this section, two examples using nonlinear finite element analysis are demonstrated. The first example involves the comparison of an experimental work conducted by Sanders (1990) to a nonlinear finite element model. The goal is to examine the applicability of using nonlinear analysis to model a flanged section anchorage zone and compare the behavior of bursting steel within the finite element model to the available experimental results. The second example is related to the use of the approximate equations to design a non-rectangular anchorage zone structure. The anchorage zone structure used in the second example was chosen from a recommended design example of a box girder bridge presented in the PTI Anchorage Zone Design Manual (Wollmann et al., 2000).

4.5.1 Example Based on Sanders' Experimental Specimen

4.5.1.1 Problem Illustration

In Sanders' experimental study of an eccentrically loaded anchorage zone, a T-beam specimen named F1 was chosen from the tested series. This specimen contains two anchorage devices and it was subjected to two prestressing loads in the direction parallel to the specimen axis. The dimensions and reinforcement detailing of specimen F1 are shown in

Fig. 4.97. As can be seen from the figure, specimen F1 contains two anchor plates at the positions indicated. The centroid of the loads is located at a distance of 26 in. from the bottom of the specimen while the centroid of the section is located at 21.30 in. from the bottom surface as well. The eccentricity ratio of the load is equal to +0.15 of the height of the web, which is 31.875 in. The magnitudes of the loads on anchors A and B were both equal to one half of the total prestressing load applied on the specimen. The reinforcing steel arrangement in the specimen is also given in Fig. 4.97b and c.

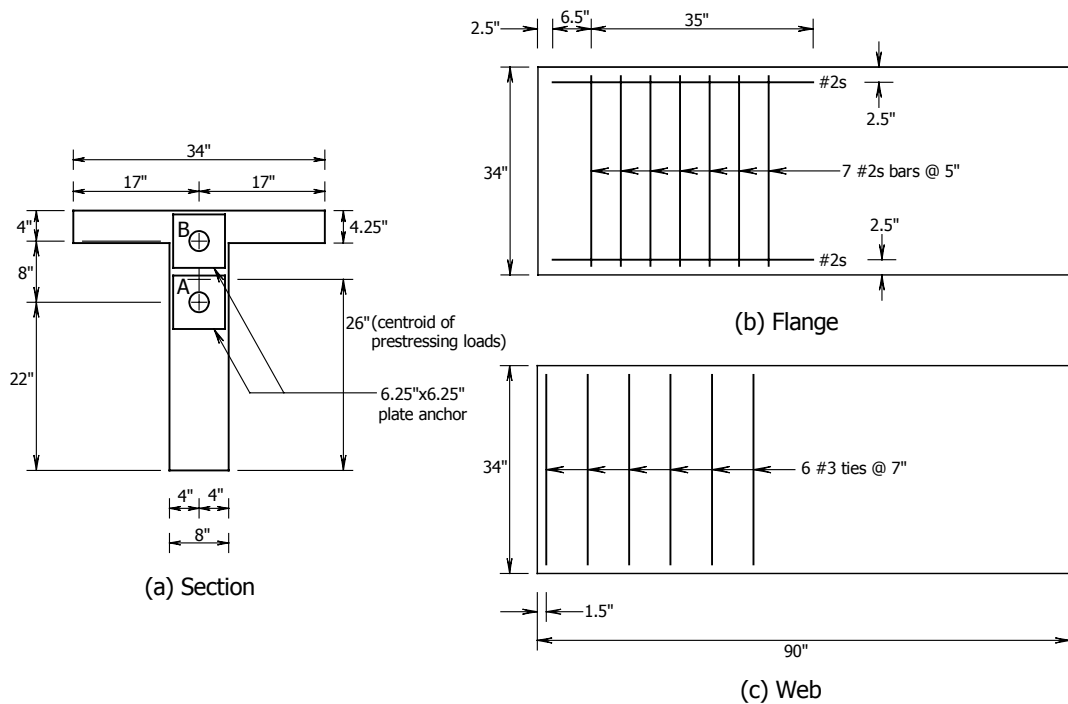


Fig. 4.97 SPECIMEN F1 FROM SANDERS' EXPERIMENTAL WORK

The material properties and the capacity of specimen F1 are given in Table 4.31. The ultimate load of the specimen was 248 kips. The material properties given in Table 4.31 are applied to the constitutive material models used in the nonlinear finite element analysis in this example. The tensile strength of concrete used in the finite element analysis is calculated based on the splitting tensile strength of concrete indicated in the table.

Table 4.31 EXPERIMENTAL DATA OF F1 FROM SANDERS' RESEARCH (1990)

Specimen : F1	
Concrete,	
Strength (f_{ci}'), psi :	4540
Splitting Strength (f_{sp}), psi :	316
Reinforcement,	
Bar #2s:	
Modulus of Elasticity, ksi :	28900
Yield Strength (f_y), psi :	75100
Area, sq.in. :	0.044
Yield Strain (microstrain) :	2600
Bar #3:	
Modulus of Elasticity, ksi :	27500
Yield Strength (f_y), psi :	60000
Area, sq.in. :	0.11
Yield Strain (microstrain) :	2200
Load Capacity,	
Web:	
Anchor "A" :	
\$ Cracking Load (kips)* :	145/175
Anchor "B" :	
\$ Cracking Load (kips) :	None
Flange :	
\$ Cracking Load (kips) :	165
Ultimate Load (kips) :	248
	* indicated for both side of the web

Since the finite element model used in this study is created by using a shell element CQ40S as mentioned in Chapter 1, there is a problem modeling the anchor plate to have the same size as the anchor plate in the specimen. Since the web of the model has a height of 31.875 in. as stated earlier, the anchor plate B extends beyond the height of the web. In order to be able to model the anchor plate in the position of anchor B, the size of the plate must be reduced to 3.75 in. instead of 6.25 in. according to the specimen. Therefore, two versions of a finite element model were constructed for the present nonlinear analysis study. The first model named SDTS01 was created in order to maintain the size of the lower anchor plate close to the real size of anchor plate A in specimen F1. The second model named SDTS02 was created in order to keep the sizes of the anchor plates in the finite element models equal to each other. These two models contain exactly the same material constitutive models. The pictures of both finite element models are given in Fig. 4.98. In order to keep the size of the elements consistent to other elements within the model body, the width of the lower plate in model SDTS01 is 6 in. The width of the lower plate in model SDTS02 is 3.75 in. in order to be similar to the size of the upper plate.

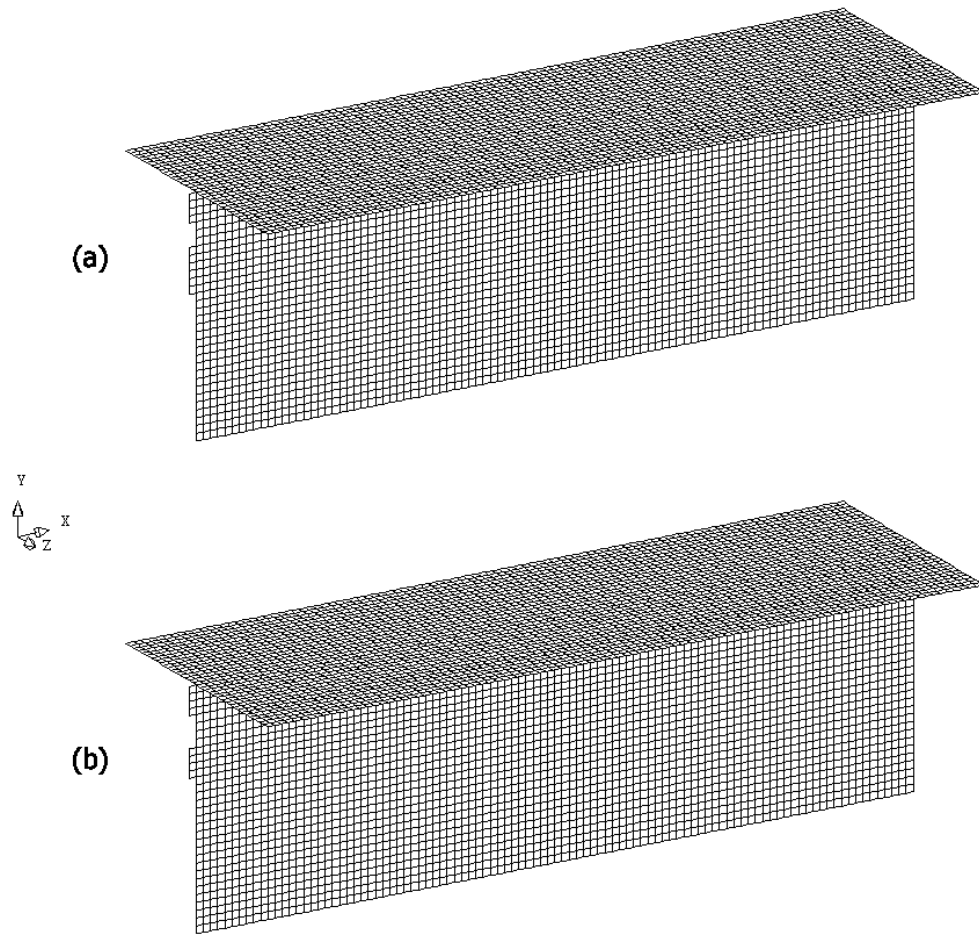


Fig. 4.98 MODELS USED FOR NONLINEAR ANALYSIS EXAMPLE a)SDTS01 AND b)SDTS02

The confining region of concrete ahead of each anchor plate is the same width as the width of the plate and extends 8 in. into the body of the model. The strength of the confined concrete is determined based on a lateral stress of 1.2 ksi as recommended by Roberts (1990). The tensile strength of concrete was determined from the percent reduction from the whole width of the beam reduced by the diameter of the duct. The compressive and tensile strength of the concrete have a linear relationship following the linear tension cut-off model. Linear tension softening and variable shear retention criteria were applied for concrete cracking model.

The arrangement of reinforcing steel bars used in the models followed the same pattern of reinforcement in specimen F1 as shown in Fig. 4.97. For the steel constitutive property, the

Von Mises yield criterion was adopted and two yield strengths, 60 ksi and 75.1 ksi, were used according to the strength of the No. 3 and No. 2s bars, respectively. All steel plate models have a tensile strength of 60 ksi. The same iteration scheme as those used in chapter two was applied. The convergence criterion in this example was modified to increase the speed of computation by using all available convergence criteria including force, displacement, and internal energy, for each iteration. The loads on both anchor plates were applied simultaneously with the 10 load steps and they were set to reach the tenth step at the magnitude of 248 kips, which is the ultimate load of specimen F1.

4.5.1.2 Nonlinear Analysis Result

In specimen F1, the cracking region occurred close to anchor B and the cracks propagated within the flange along the tendon path to the end of the specimen. The cracking occurred in front of both anchors A and B after the applied load reached the ultimate load level. According to the report given from the experiment, the failure originated at a region close to anchor B and then propagated to anchor A. Cracking severely damaged the top surface of the flange and small cracks were found at the outer edge of the flange. For nonlinear analysis results, the cracking patterns occurring in both models indicate a similarity to that which occurred in specimen F1. Figs. 4.99 and 4.100 show the cracking strain vectors at the final load step of the models SDTS01 and SDTS02, respectively. The magnitude of the load at the final load step for model SDTS01 is 232 kips, which equals a factor of 0.935 times the ultimate load of specimen F1. The magnitude of the load from model SDTS02 equals a factor of 0.934 times the ultimate load of specimen F1. According to Figs. 3.99 and 3.100, the cracking patterns are similar to that which occurred in specimen F1. As can be noticed in Figs. 4.99b and 4.100b, the length of the vector indicates the magnitude of the cracking strain. Because the anchor plate size on the lower anchor of model SDTS02 is smaller than the size of the lower anchor plate of model SDTS01, larger magnitude of the strains occur within the body of model SDTS02. As a result, the web body of model SDTS02 shows a longer extension of cracks than those occurring in model SDTS01. However, the cracking pattern on the flange bodies of both models looks similar to each other.

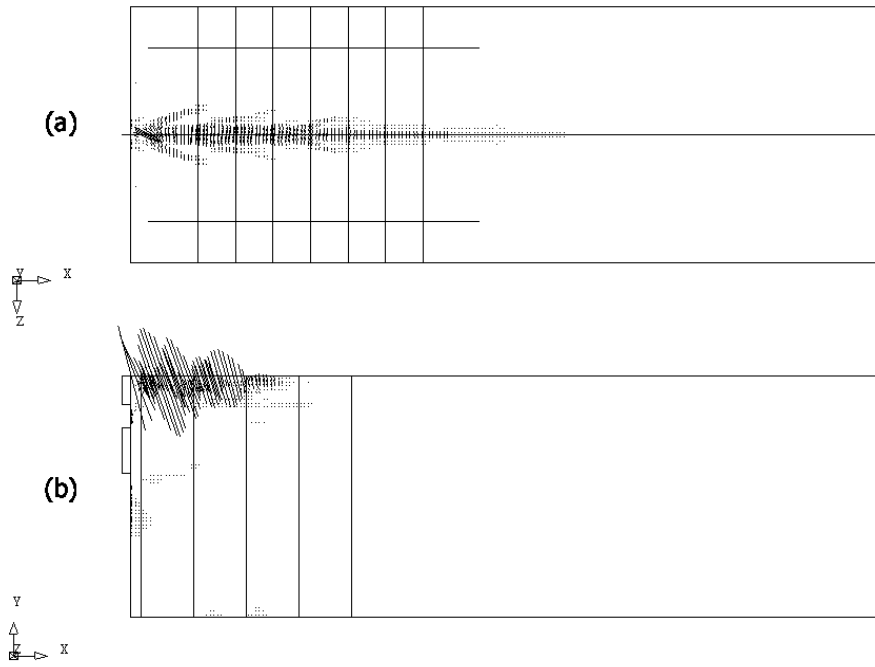


Fig. 4.99 CRACKING STRAIN VECTORS IN MODEL SDTS01 a) FLANGE AND b) WEB

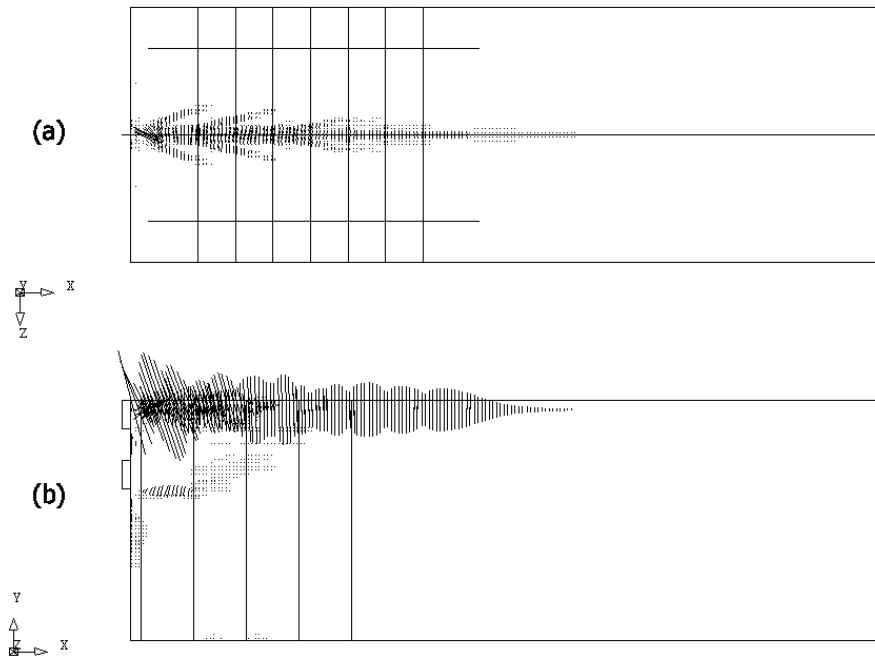


Fig. 4.100 CRACKING STRAIN VECTORS IN MODEL SDTS02 a) FLANGE AND b) WEB

According to the cracking strain vectors shown in Fig. 4.99 and 4.100, both models show a similar cracking behavior to that which occurred in specimen F1. However, the results from the models cannot indicate the cracking pattern that occurs after the applied load passes the level of 248 kips, which is the ultimate load level of specimen F1. Therefore, crack near the region of anchor plate A cannot be detected by the nonlinear analysis result.

Figures 4.101 and 4.102 show the plots of bursting strains occurring in the flange close to anchor plate B from Sanders' specimen F1. Figs. 4.103 and 4.104 present the plots of flange bursting strains from models SDTS01 and SDTS02, respectively. The plots from the experiment indicate that the steel bars at the locations of 9, 14, 19, 24, and 29 in. from the loading surface pass their yield strain as the load reaches the ultimate level. However, the plots from the nonlinear analysis from both Figs. 4.103 and 4.104 show only two bars at the location of 14 in. and 19 in. from the loading surface pass their yield strain. Since the analyses of both models were terminated before the load passed the level of 248 kips, it is possible that other bars whose strains remain under the yield point may have yielded at the next load step, which failed to converge.

Figures 4.105 and 4.106 show the experimental plots of web reinforcement bursting strains near anchor plates A and B, respectively. In Fig. 4.105, the plots indicate that three bars at the positions of 2, 8.5, and 15.5 in. pass their yield strains while the other two bars show reduced strains as the load reaches the ultimate level. Similarly to Fig. 4.105, the plots in Fig. 4.106 exhibit similar results but with more variation of the plots than in Fig. 4.105. Figs. 4.107 and 4.108 show the plots of bursting strains in the web reinforcing bars from model SDTS01 for the locations near anchor plates A and B, respectively. Figs. 4.109 and Fig. 4.110 show similar plots to those in Figs. 4.107 and 4.108 from model SDTS02. The behaviors of the web bursting bar strains near anchor plate A from both models are very similar in that they show a small development of strains with respect to increasing load as can be seen from Figs. 4.107 and 4.109. However, the web bursting bar strains near anchor plate B show some larger increases as the load increases than those occurring near anchor plate A as can be seen in Fig. 4.108 and 4.110.

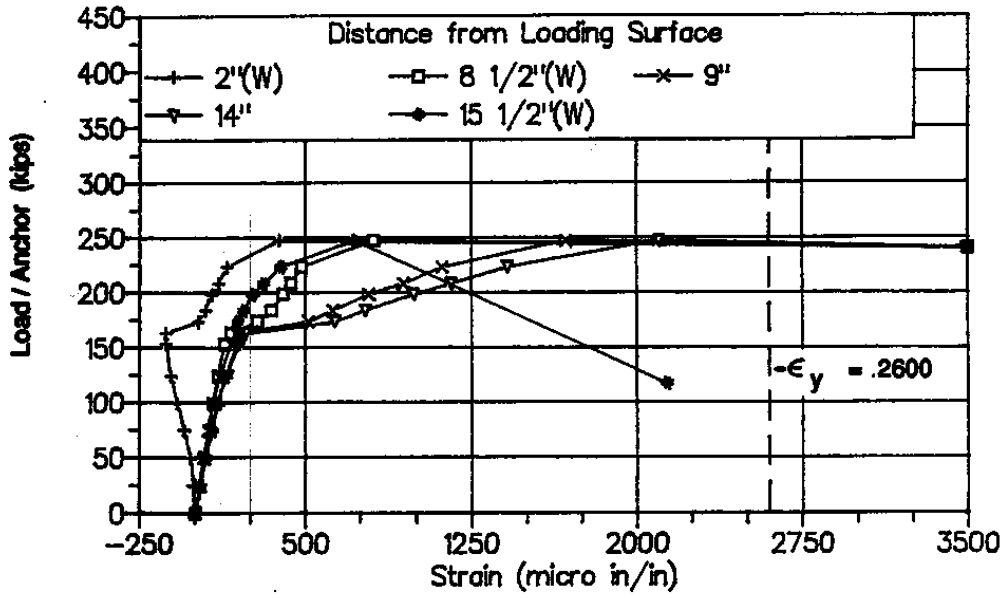


Fig. 4.101 FLANGE REINFORCEMENT BURSTING STRAINS NEAR ANCHOR B FROM SANDERS' SPECIMEN F1 (SANDERS, 1990)

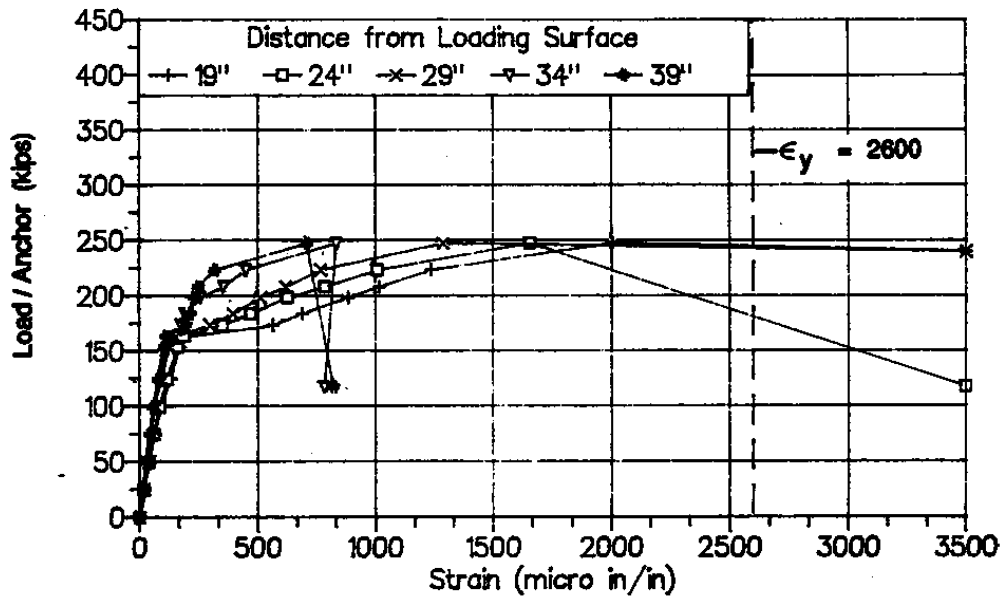


Fig. 4.102 FLANGE REINFORCEMENT BURSTING STRAINS DISTANT FROM ANCHOR B FROM SANDERS' SPECIMEN F1 (SANDERS, 1990)

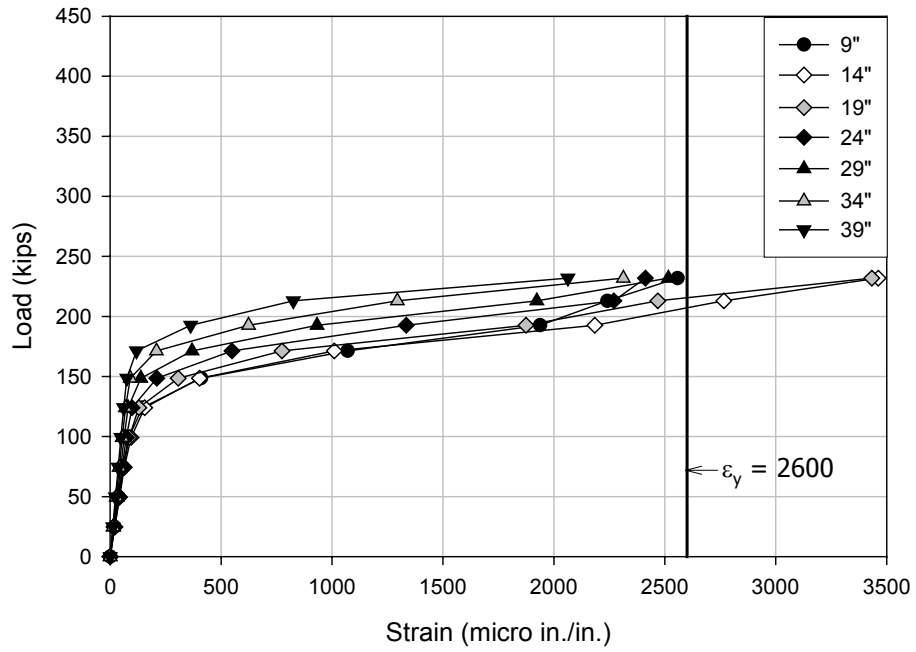


Fig. 4.103 FLANGE REINFORCEMENT BURSTING STRAINS FROM MODEL SDTS01

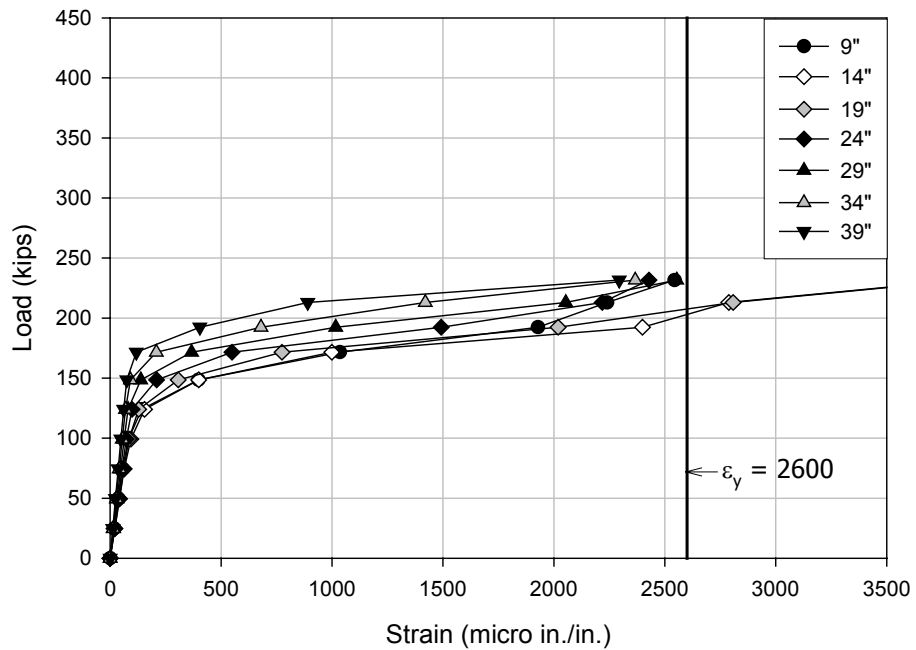


Fig. 4.104 FLANGE REINFORCEMENT BURSTING STRAINS FROM MODEL SDTS02

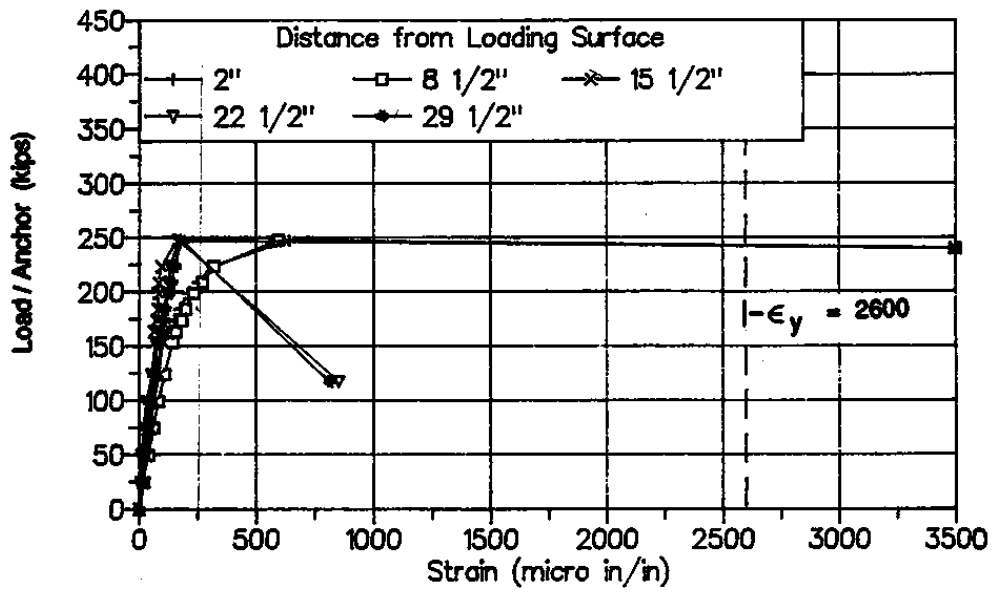


Fig. 4.105 WEB REINFORCEMENT BURSTING STRAINS NEAR ANCHOR A
FROM SANDERS' SPECIMEN F1 (SANDERS, 1990)

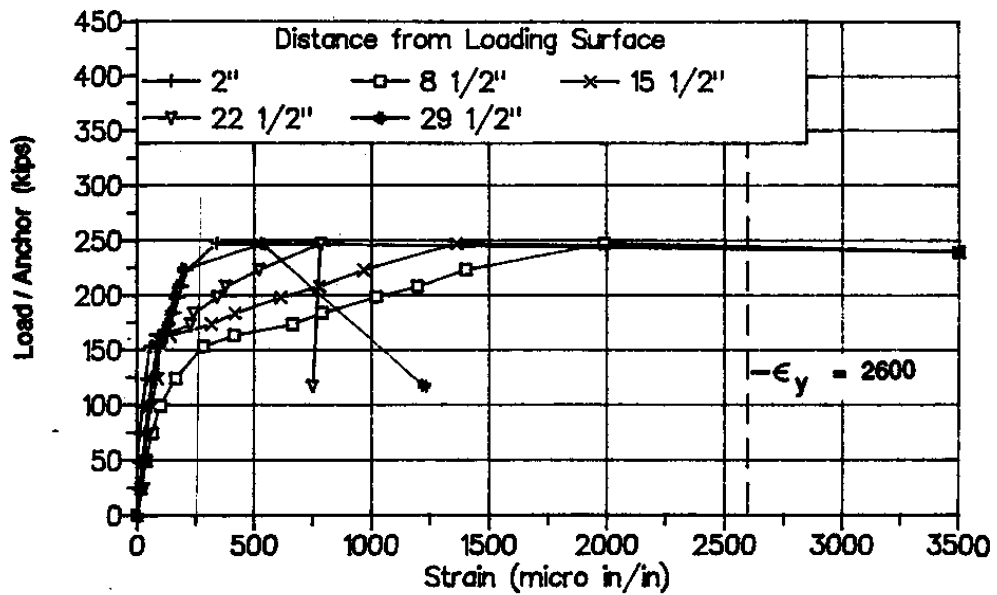


Fig. 4.106 WEB REINFORCEMENT BURSTING STRAINS NEAR ANCHOR B
FROM SANDERS' SPECIMEN F1 (SANDERS, 1990)

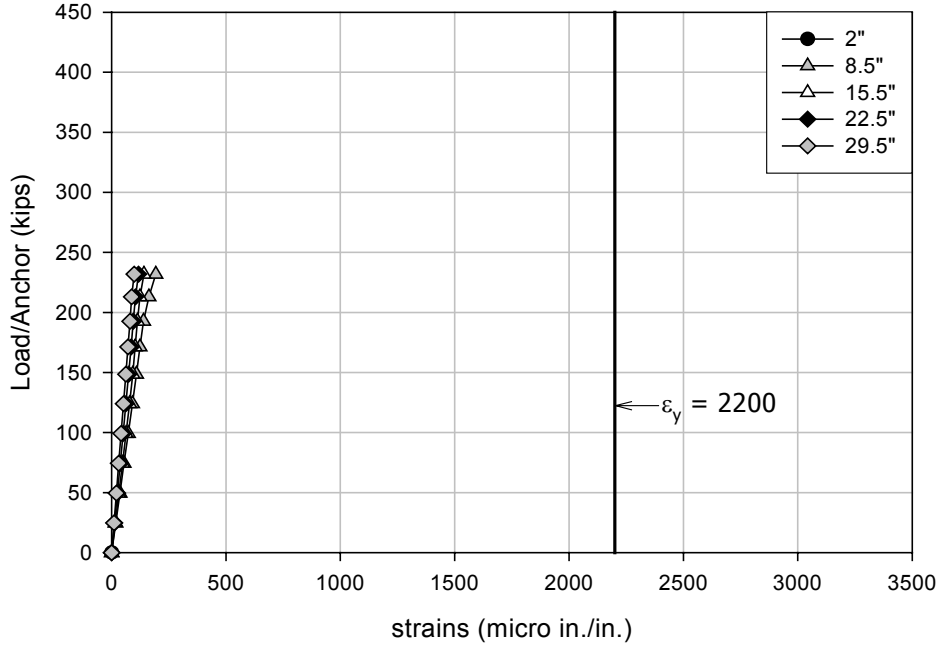


Fig. 4.107 WEB REINFORCEMENT BURSTING STRAINS NEAR ANCHOR A FROM MODEL SDTS01

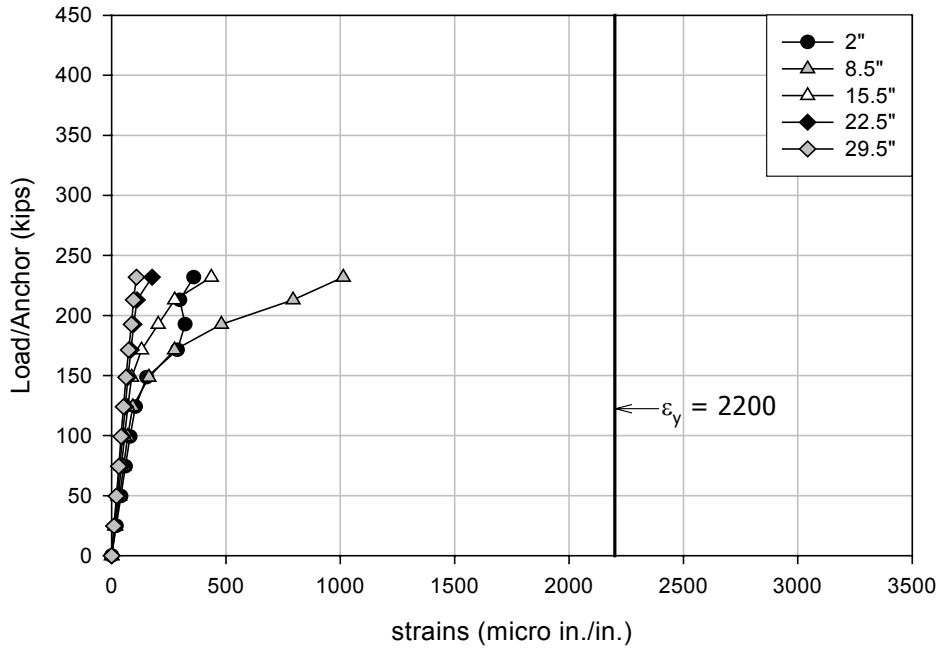


Fig. 4.108 WEB REINFORCEMENT BURSTING STRAINS NEAR ANCHOR B FROM MODEL SDTS01

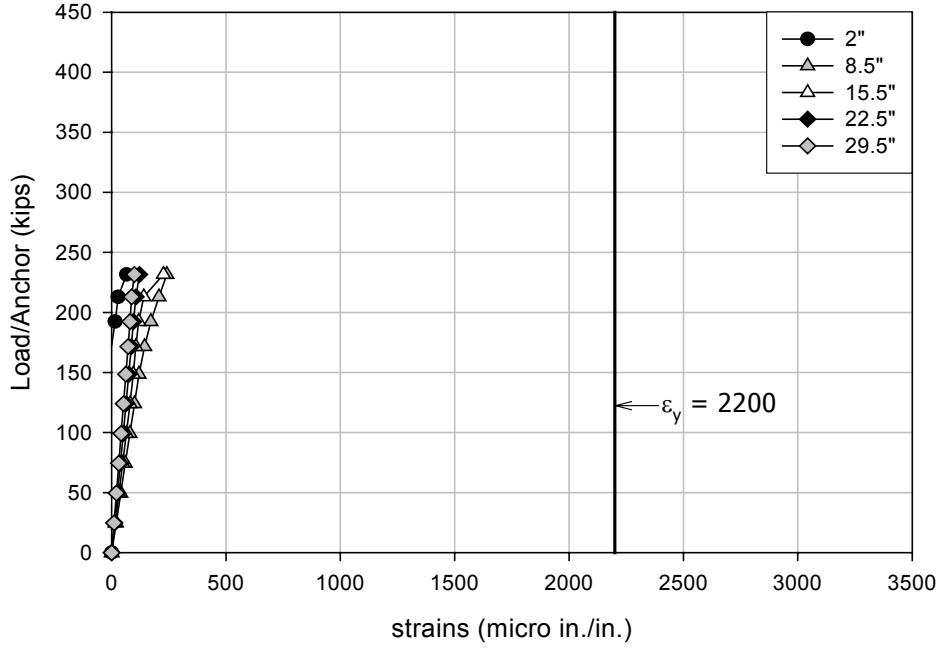


Fig. 4.109 WEB REINFORCEMENT BURSTING STRAINS NEAR ANCHOR A FROM MODEL SDTS02

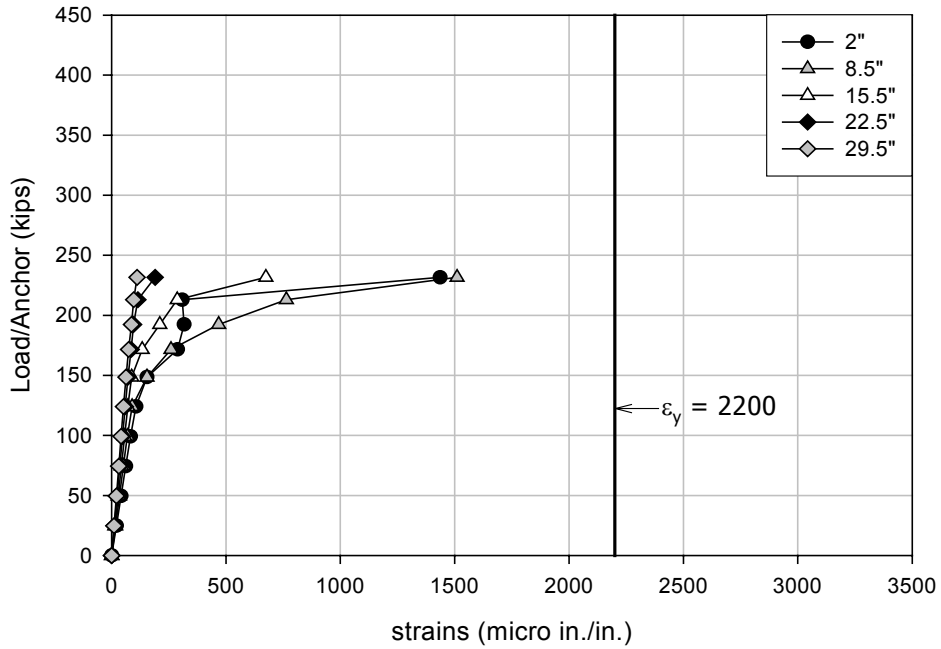


Fig. 4.110 WEB REINFORCEMENT BURSTING STRAINS NEAR ANCHOR B FROM MODEL SDTS02

As can be seen from the comparison results presented thus far, although the results from nonlinear analysis cannot show the behavior of the bar strains after the ultimate load is reached, the results are similar in many ways to the results from the experimental work. The magnitude of the load at the final load step, which can be considered as the ultimate load of the finite element model, is very similar to the ultimate load achieved by the specimen. The bars that yielded at the final load step in the model have the same position as the bars that yielded in the experiment. Based on this study, a nonlinear finite element method can provide a similar result to the result from the experimental work by Sanders in the case of an anchorage zone in a flanged section.

4.5.2 Example Based on Box Girder Bridge with Internal Tendons Presented in PTI Manual

The following example illustrates the design of an anchorage zone in a flanged section using the methodology developed in this chapter. The flanged section anchorage zone structure used in this example is chosen from the design example of a box girder bridge with internal tendons presented in the PTI manual excerpt (Wollmann et al., 2000). A box girder bridge is considered as an appropriate example for the design illustration in this study since it is a popular structure used in the construction of transportation systems particularly in California. Moreover, the geometric configuration of the box girder bridge structure presented in the example of the PTI manual excerpt contains a complex geometric configuration, which is useful for the clarification of the current design methodology. After the amount of reinforcing steel is determined in the design, a nonlinear analysis is conducted in order to compare the anchorage zone model based on the design method presented in the PTI manual excerpt and the design using the approximate equations presented in this chapter. Another model with a different steel reinforcement pattern is examined in order to study the method of reinforcing steel arrangement for an anchorage zone with a flanged section.

4.5.2.1 Problem Illustration

Figure 4.111 shows the details and dimensions of the box girder bridge from the design example presented in the PTI manual excerpt. The section that is selected for the present example is taken from a part of the whole section of the box girder bridge as can be seen in Fig. 4.111a and b. The considered section has a web height of 75.5 in. and a flange width of 140 in. The thickness of each member within the section is presented in the figure. The web of the considered section has a tapered width as can be seen in Fig. 4.111c. The width at the anchorage surface is approximately 24 in. at the location of section A-A as shown. The length of the tapered part of the web is 200 in. with a width of 12 in. at the end. Three anchorage devices are installed at the surface of the web with dimensions as indicated in Fig. 4.111d.

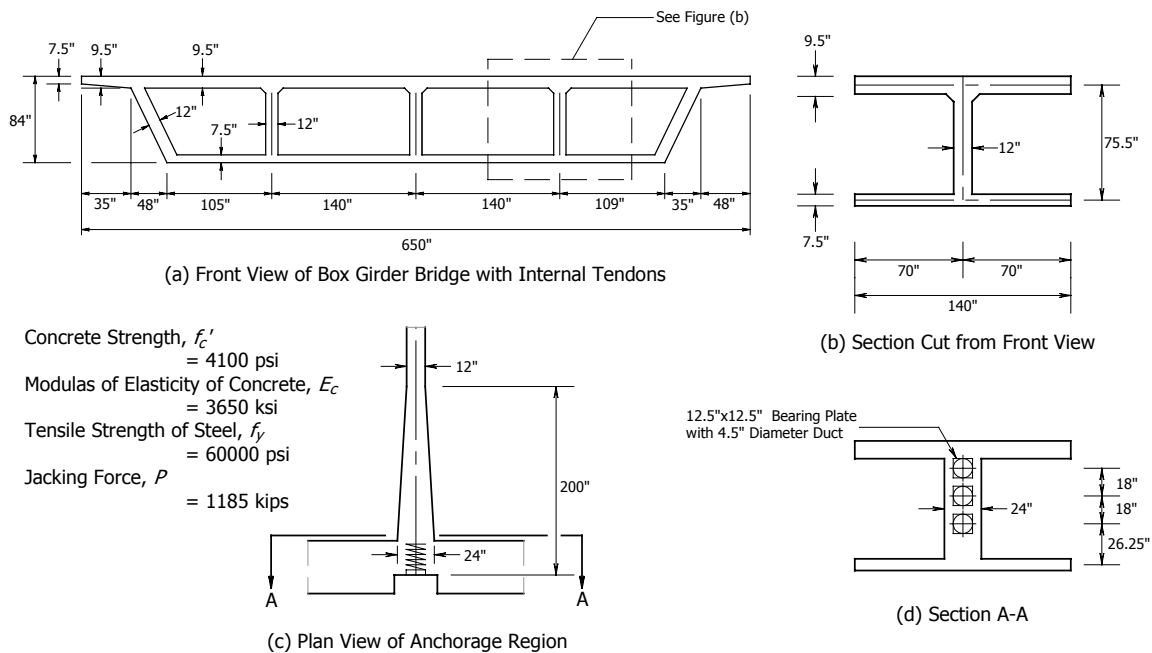


Fig. 4.111 BOX GIRDER BRIDGE DETAILS AND DIMENSIONS

4.5.2.2 Design of Bursting Reinforcement

Since the anchorage zone in this example contains three anchorage devices, according to the AASHTO Standard Specifications (2002), a grouped anchor can be considered if the spacing between the center of each adjacent anchor plate is less than 1.5 of the anchor plate

size. The size of anchor plate in this example is 12.5 in. and the spacing between adjacent plates is 18 in. The spacing of 18 in. is less than $1.5 \times 12.5 = 18.75$ in., therefore all three anchors can be combined as a group anchor with the magnitude of prestressing load equal to $1.2 \times 3 \times 1185 = 4266$ kips as a factored load. The anchor plate size equals $12.5 + 18 \times 2 = 48.5$ in. Since the thickness of the web is tapered, the section centroid, the area of the section, and the moment of inertia that need to be determined vary along the length of this tapered part of the web. Therefore, an average value was used of the thickest and the thinnest parts of this tapered web, which are equal to 24 in. and 12 in., respectively. Therefore, the average thickness of the web becomes $(24+12)/2 = 18$ in. The section centroid with respect to the center of the flange (c), the area of the section (A_f), and its moment of inertia (I_f) equal 40.53 in., 3586 sq.in., and 3830317 in.^4 , respectively.

Since the centroid of the section is 40.53 in., the prestressing load is located above the section centroid with a distance of $26.25 + 18 - 40.53 = 3.72$ in. as the eccentricity of the load (e). Therefore, the structure is classified as an eccentrically loaded anchorage zone in an unsymmetrical I-section. Since the total height of the section equals 84 in., the height of the web (h_w) is 75.5 in., and the width of both top and bottom flanges are equal to 140 in. These variables are ready to be used for determining the value of $d_{burst-web}$. As presented in equations (4.44) and (4.45), the value of $d_{burst-web}$ is taken from the smaller value of these two equations. Therefore, the $d_{burst-web}$ can be determined as follows:

From equation (4.44),

$$\begin{aligned} d_{burst-web} &= (h' - c - t_{f2} / 2 - e) + a / 4 + h_w / 4 \times (1 - \exp(-0.8b_{f1} / h_w)) + h_w / 4 \times \sin \alpha \\ &= (84 - 40.53 - 7.5 / 2 - 3.72) + 48.5 / 4 + 75.5 / 4 \times (1 - \exp(-0.8 \times 140 / 75.5)) + 0 \\ &= 62.72 \text{ in.} \end{aligned}$$

From equation (4.45),

$$\begin{aligned} d_{burst-web} &= (c + t_{f2} / 2 + e) + a / 4 + h_w / 4 \times (1 - \exp(-0.8b_{f2} / h_w)) + h_w / 4 \times \sin \alpha \\ &= (40.53 + 7.5 / 2 + 3.72) + 48.5 / 4 + 75.5 / 4 \times (1 - \exp(-0.8 \times 140 / 75.5)) + 0 \\ &= 74.72 \text{ in.} \end{aligned}$$

Therefore, the value of $d_{burst-web}$ becomes 62.72 in. The next step is to calculate the forces R_{1u} , R_{1l} , R_2 , and R_3 in order to use in the estimation of $T_{burst-web}$ in equation (4.42) and (4.43).

Since the forces depend on the stresses on the section as can be seen in Fig. 4.85, the stress at each level of the section needs to be determined before the calculation of the forces can be performed. Based on equation (4.31), the stress at each level of the section can be written as

$$\begin{aligned}
 \sigma_{io} &= P_u \left(-1/A_f - e(h'-c-t_{f2}/2)/I_f \right) \\
 &= 4266 \left(-1/3586 - 3.72(84 - 40.53 - 7.5/2)/3830317 \right) = -1.3542 \text{ ksi} \\
 \sigma_{ii} &= P_u \left(-1/A_f - e(h'-c-t_{f2}/2-t_{f1})/I_f \right) \\
 &= 4266 \left(-1/3586 - 3.72(84 - 40.53 - 7.5/2 - 9.5)/3830317 \right) = -1.3149 \text{ ksi} \\
 \sigma_e &= P_u \left(-1/A_f - e^2/I_f \right) \\
 &= 4266 \left(-1/3586 - 3.72^2/3830317 \right) = -1.2050 \text{ ksi} \\
 \sigma_{bi} &= P_u \left(-1/A_f - e(c-t_{f2}/2)/I_f \right) \\
 &= 4266 \left(-1/3586 - 3.72(40.53 - 7.5/2)/3830317 \right) = -1.0372 \text{ ksi} \\
 \sigma_{bo} &= P_u \left(-1/A_f - e(c+t_{f2}/2)/I_f \right) \\
 &= 4266 \left(-1/3586 - 3.72(40.53 + 7.5/2)/3830317 \right) = -1.0061 \text{ ksi}
 \end{aligned}$$

Therefore, the forces R_{1u} , R_{1l} , R_2 , and R_3 can be determined as follows:

$$\begin{aligned}
 R_{1u} &= 1/2 \left((\sigma_{io} + \sigma_e) \right) (h' - c - t_{f2}/2 - e) \times t_w \\
 &= 1/2 \left((-1.3542 - 1.2050) \right) (84 - 40.53 - 7.5/2 - 3.72) \times 18 = 829 \text{ kips} \\
 R_{1l} &= 1/2 \left((\sigma_e + \sigma_{bo}) \right) (c + t_{f2}/2 + e) \times t_w \\
 &= 1/2 \left((-1.2050 - 1.0061) \right) (40.53 + 7.5/2 + 3.72) \times 18 = 955 \text{ kips} \\
 R_2 &= 1/2 \left((\sigma_{io} + \sigma_{ii}) \right) (b_{f1} - t_w) \times t_{f1} \\
 &= 1/2 \left((-1.3542 - 1.3149) \right) (140 - 18) \times 9.5 = 1549 \text{ kips} \\
 R_3 &= 1/2 \left((\sigma_{bi} + \sigma_{bo}) \right) (b_{f2} - t_w) \times t_{f2} \\
 &= 1/2 \left((-1.0372 - 1.0061) \right) (140 - 18) \times 7.5 = 935 \text{ kips}
 \end{aligned}$$

The location of each force can be determined by using the expression presented in Appendix A and they can be written as follows:

$$c_{1u} = [(\sigma_e + 2\sigma_{io}) / (3\sigma_e + 3\sigma_{io})] (h' - c - t_{f2}/2 - e) \times t_w$$

$$= [(1.2050 + 2 \times 1.3542) / (3 \times 1.2050 + 3 \times 1.3542)] (84 - 40.53 - 7.5 / 2 - 3.72) \times 18$$

$$= 18.35 \text{ in.}$$

$$c_{1l} = [1 - (2\sigma_e + \sigma_{bo}) / (3\sigma_e + 3\sigma_{bo})] (c + t_{f2} / 2 + e) \times t_w$$

$$= [1 - (2 \times 1.2050 + 1.0061) / (3 \times 1.2050 + 3 \times 1.0061)] (40.53 + 7.5 / 2 + 3.72) \times 18$$

$$= 23.28 \text{ in.}$$

$$c_2 = [(\sigma_{ti} + 2\sigma_{to}) / (3\sigma_{ti} + 3\sigma_{to})] \times t_{f1} + (h' - c - t_{f2} / 2 - t_{f1} - e)$$

$$= [(1.3149 + 2 \times 1.3542) / (3 \times 1.3149 + 3 \times 1.3542)] \times 9.5$$

$$+ (84 - 40.53 - 7.5 / 2 - 9.5 - 3.72)$$

$$= 31.27 \text{ in.}$$

$$c_3 = [1 - (2\sigma_{bi} + \sigma_{bo}) / (3\sigma_{bi} + 3\sigma_{bo})] \times t_{f2} + (c - t_{f2} / 2 + e)$$

$$= [1 - (2 \times 1.0372 + 1.0061) / (3 \times 1.0372 + 3 \times 1.0061)] \times 7.5 + (40.53 - 7.5 / 2 + 3.72)$$

$$= 44.23 \text{ in.}$$

As all the positions of the resultant forces are determined, the locations of forces $R_{1u} + R_2$ and $R_{1l} + R_3$ can be determined from the centroid of each force the upper and lower portions, respectively. According to the expression to determine y_u and y_l in Appendix A, the calculation can be written as

$$y_u = (R_{1u} \times c_{1u} + R_2 \times c_2) / (R_{1u} + R_2)$$

$$= (829 \times 18.35 + 1547 \times 44.23) / (829 + 1547) = 26.76 \text{ in.}$$

$$y_l = (R_{1l} \times c_{1l} + R_3 \times c_3) / (R_{1l} + R_3)$$

$$= (955 \times 23.28 + 935 \times 44.23) / (955 + 935) = 33.64 \text{ in.}$$

The value of p can be determined based on the force $R_{1u} + R_2$ and the calculation can be written as

$$p = ((R_{1u} + R_2) / P_u - 0.5) \times a / 2$$

$$= ((829 + 1547) / 4266 - 0.5) \times 48.5 / 2 = 1.38 \text{ in.}$$

The value of $T_{burst-web}$ can be found by using either equation (4.42) or (4.43). By substituting all variables in both equations, the equations can be written as

$$\begin{aligned}
T_{burst-web} &= (R_{1u} + R_2) \left(\frac{4y_u + 4p}{4d_{burst-web} - a} \right) \left(1 - \frac{a}{4y_u + 4p} \right) + 0.6P \sin \alpha \\
&= (829 + 1547) \left(\frac{4 \times 26.76 + 4 \times 1.38}{4 \times 62.72 - 48.5} \right) \left(1 - \frac{48.5}{4 \times 26.76 + 4 \times 1.38} \right) + 0 \\
&= 752 \text{ kips} \\
T_{burst-web} &= (R_{1l} + R_3) \left(\frac{4y_l - 4p}{4d_{burst-web} - a} \right) \left(1 - \frac{a}{4y_l - 4p} \right) + 0.6P \sin \alpha \\
&= (955 + 935) \left(\frac{4 \times 33.64 - 4 \times 1.38}{4 \times 62.72 - 48.5} \right) \left(1 - \frac{48.5}{4 \times 33.64 - 4 \times 1.38} \right) + 0 \\
&= 752 \text{ kips}
\end{aligned}$$

Since the magnitude of $T_{burst-web}$ has been determined, the amount of bursting reinforcement in the web can be calculated. The tensile strength of steel is 60 ksi as indicated in Fig. 4.111, therefore the required cross-sectional area of steel can be determined as follows:

$$A_{s-web} = T_{burst-web} / (0.85 \times f_y) = 752 / (0.85 \times 60) = 14.75 \text{ sq.in.}$$

After the amount of bursting steel has been calculated, the pattern of steel arrangement needs to be selected. As presented in Chapter 3, the recommended reinforcing steel arrangement presented in the AASHTO specifications is rather complicated. Therefore, the pattern of steel arrangement in this study is based on a simpler method to select the steel bars and their spacing.

As illustrated in the part of the investigation to study steel reinforcement patterns of Chapter 3, the distribution of a group of bars with the same bar size and an equal spacing between each bar over the region that extends for the length of $2d_{burst}$ from the prestressing surface is found to be acceptable. Therefore, the same pattern is used for the layout of bursting steel reinforcement in the present study. Since the required cross-sectional area of steel is equal to 14.75 sq.in., a set of 16 stirrups of No. 6 bars is chosen as the reinforcing steel in the web of the present example. The total area provided by the selected steel bars is equal to 14.08 sq.in., which is smaller than the required reinforcing steel by less than 5 percent. These 16 stirrups are distributed uniformly with a spacing of 8 in. starting at the position of 8 in. from the prestressing surface. According to the AASHTO specifications, 2

percent of the highest prestressing load in the group is used as the spalling reinforcement. Therefore, an additional No. 6 bar stirrup is added the location of 1.5 in. from the loading surface.

The next step in the design of the anchorage zone in the present example is the estimation of bursting steel in both flanges of the structure. Since there is no vertical force applied onto the structure, the stresses used in the calculation of k_f in equation (4.25) are the same as the stresses used in the design of the web bursting steel as illustrated previously. Only the stresses at the extreme fiber of each flange are needed in the determination of k_f , therefore the value of k_f for the top flange can be calculated as

$$\begin{aligned} k_f &= 1/2[(\sigma_{to} + \sigma_{ti})]b_{f1}t_{f1}/(R_{1u} + R_2) \\ &= 1/2[(-1.3542 - 1.3149)](140)(9.5)/(829 + 1547) = 0.7470 \leq 1.0 \end{aligned}$$

Therefore, the value of $T_{burst-flg}$ for the top flange can be determined as

$$\begin{aligned} T_{burst-flg} &= 0.15k_f^3P_u \\ &= 0.15(0.7470^3)(4266) = 266 \text{ kips} \end{aligned}$$

The amount of bursting reinforcement in the top flange can be calculated as

$$A_{s-flg} = 266/(0.85 \times 60) = 5.22 \text{ sq.in.}$$

Since the comparison between the location of flange bursting force from the finite element analysis and the approximate equations as presented in equation (4.29) and (4.30) indicated that the estimation of $d_{burst-flg}$ using the approximate equations may not give a close prediction to the result from finite element, the bursting steel within the flange member needs to be arranged by considering the pattern of tensile stresses that actually occur in the flange body.

As the method of using a strut-and-tie model to develop the formulations of $d_{burst-flg}$ is based on the pattern of stresses within the flange body, which is indicated from the finite element study. Two regions in which the bursting stresses occur are divided by the position of the applied transferring force from the web. Since both regions have their corresponding bursting forces located at the location of $d_{burst-flg1}$ and $d_{burst-flg2}$ as can be seen in Fig. 4.61, the bursting steel can be arranged based on these two locations. As the bursting forces in both

regions contain the same magnitude of the force in the transverse direction of the flange, the total bursting steel in the flange can be divided in half and positioned at the locations of $d_{burst-flg1}$ and $d_{burst-flg2}$. The first half of the total amount of bursting steel is distributed over the distance of $2d_{burst-flg1}$ while the second half spreads over the distance of $2(d_{burst-flg2} - 2d_{burst-flg1})$. Since the distance of $2d_{burst-flg1}$ covers on the front part of the flange with respect to the position of the applied transferring load, the 50 percent of the bursting steel that is reinforced in this part can protect the concrete from the cracks that originate close to the loading surface and propagate along the axis of the flange. If the cracks propagate past the bursting steel in the front part, the bursting steel in the second part can still work to arrest the cracks, which continue into this part with a small magnitude of cracking stress. Therefore, equation (4.11) and (4.12), which are used for the calculation of $d_{burst-flg1}$ and $d_{burst-flg2}$, need to be employed for the arrangement of flange bursting steel.

Since the anchorage zone of the present example is within an unsymmetrical I-shape, the term $h_w/2$ needs to be modified to be applicable to the structure. By replacing the term $h_w - c - e$, equation (4.11) can be rewritten as

$$d_{burst-flg1} = \frac{h_w - c - e}{2} + \frac{t_{f1}}{4} \quad (4.50)$$

Therefore, the arrangement of bursting steel in the top flange of the anchorage zone in the present example can be determined from the following calculation:

$$\begin{aligned} d_{burst-flg1} &= (h_w - c - e)/2 + t_{f1}/4 \\ &= (75.5 - 40.53 - 3.72)/2 + 9.5/4 = 18 \text{ in.} \end{aligned}$$

Therefore, fifty percent of the bursting steel in the top flange is distributed over the distance of 36 in. from the loading surface. The location of the other fifty percent of the bursting steel can be determined based on the following calculation:

$$\begin{aligned} d_{burst-flg2} &= R_2 / 8 \times [(b_{f1} + t_w)/(0.5T_{burst-flg})] + t_{f1} / 2 \\ &= 1547 / 8 \times [(140 + 18)/(0.5 \times 266)] + 9.5 / 2 = 120 \text{ in.} \end{aligned}$$

Based on the value of $d_{burst-flg2}$, the second part starts from the position of 36 in. from the loading surface and extends to a distance equal to $2 \times (120 - 36) = 168$ in. It is noticed that with the amount of steel equal to $0.5(5.22) = 2.61$ sq.in. distributed over the length of 168 in., it results in an amount of steel per cross-sectional area of concrete equals to $2.61/(120 \times 9.5) = 0.0016$. This number is less than the requirement of temperature reinforcing steel per cross-sectional area of concrete, which equals 0.0018. As a result, two layers of five No. 5 bars with a spacing of 8 in. starting at 8 in. from the loading surface and two layers of No. 3 bar at a spacing of 12 in. starting at the position of 48 in. from the loading surface are selected for the bursting reinforcement of the top flange of anchorage zone in this example.

For the design of bursting reinforcement of the bottom flange, the method of determining the required reinforcing steel is similar to the method used for the top flange as presented previously. The k_f value of the bottom flange needs to be determined from the stresses at the extreme fibers of bottom flange. Therefore, the calculation of k_f can be written as

$$\begin{aligned} k_f &= 1/2[(\sigma_{bo} + \sigma_{bi})b_f t_{f2} / (R_{1l} + R_3)] \\ &= 1/2[(-1.0372 - 1.0061)(140)(7.5) / (955 + 935)] = 0.5676 \leq 1.0 \end{aligned}$$

Therefore, the value of $T_{burst-flg}$ for the bottom flange can be determined as

$$\begin{aligned} T_{burst-flg} &= 0.15k_f^3 P_u \\ &= 0.15(0.5676^3)(4266) = 117 \text{ kips} \end{aligned}$$

The required bursting steel for the bottom flange is equal to the result of the calculation

$$A_{s-flg} = 117 / (0.85 \times 60) = 2.29 \text{ sq.in.}$$

Fifty percent of this amount of bursting steel is distributed over the length of $2d_{burst-flg1}$ in which the equation to calculate for the value of $d_{burst-flg1}$ of the bottom flange can be found by substituting the term $h_w/2$ in equation (4.11) with $c + e$. Therefore, the equation to calculate the $d_{burst-flg1}$ for the bottom flange can be rewritten as

$$d_{burst-flg1} = \frac{c + e}{2} + \frac{t_f}{4} \quad (4.51)$$

Therefore, by substituting all variables into equation (4.51), the value of $d_{burst-flg1}$ is calculated as

$$\begin{aligned} d_{burst-flg1} &= (c + e) / 2 + t_{f2} / 4 \\ &= (40.53 + 3.72) / 2 + 7.5 / 4 = 24 \text{ in.} \end{aligned}$$

Fifty percent of the bursting steel in the bottom flange is distributed over the length of $2(24) = 48$ in. from the loading surface. Similar to the top flange, the value of $d_{burst-flg2}$ can be calculated using equation (4.12). The value of $d_{burst-flg2}$ is determined from the following calculation:

$$\begin{aligned} d_{burst-flg2} &= R_3 / 8 \times [(b_{f2} + t_w) / (0.5T_{burst-flg})] + t_{f2} / 2 \\ &= 935 / 8 \times [(140 + 18) / (0.5 \times 117)] + 7.5 / 2 = 319 \text{ in.} \end{aligned}$$

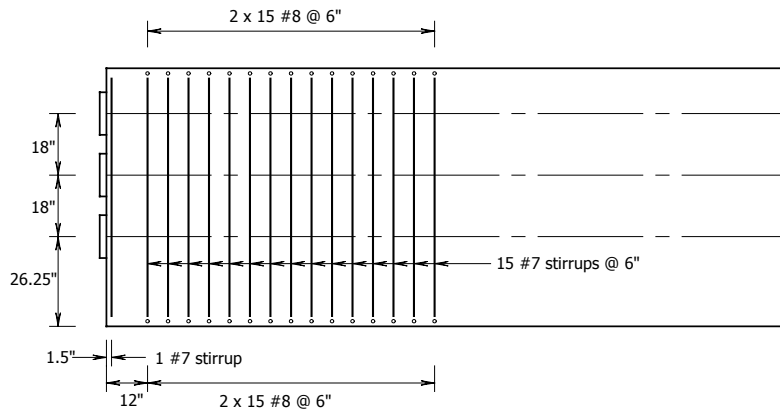
Another fifty percent of the bursting steel in the bottom flange is distributed over the length of $2 \times (319 - 48) = 542$ in. continued from the location of 48 in. from the loading surface. Similar to the bursting steel arrangement in the top flange, the distribution of one half of the required bursting steel area over the bottom flange section with the size of 542×7.5 sq.in. is undoubtedly less than the required temperature reinforcement. Therefore, the arrangement of bursting steel for the bottom flange can be two layers of five bars of No. 4 with a spacing of 8 in. starting from the location of 8 in. from the loading surface and two layers of No. 3 bar at a spacing of 12 in. continued from the location of 48 in. from the loading surface.

Figure 4.112 shows the reinforcement details of three anchorage zone models used for nonlinear analysis study in this chapter. Fig. 4.112a shows the detail of the reinforcement in the model based on the example of the box girder bridge from the PTI manual excerpt Fig. 4.112b shows the reinforcement pattern from the present design study. The model in Fig. 4.112c is given for comparison with the first two structures. The reinforcement in Fig. 4.112c is modified by increasing the amount of web reinforcing steel of the model in Fig. 4.112b by 20 percent in order to study the strength of the anchorage zone if the reinforcement within region from the anchorage surface to $d_{burst-web}$ contains 60 percent of the required amount of bursting steel. This 60 percent of the required bursting steel area is chosen from the study of linear elastic finite element analysis, which indicates that 60 percent of the magnitude of the bursting force occurs within the distance of d_{burst} from the loading surface.

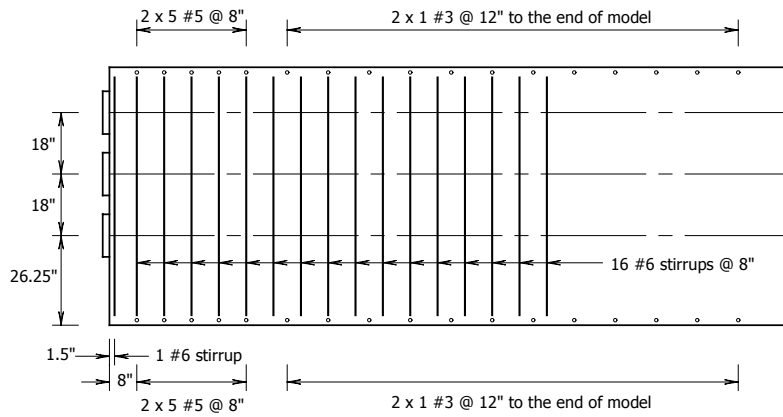
In order to avoid a complicated method of steel arrangement, the model in Fig. 4.112c is constructed to have a uniformly distributed reinforcement with only one bar size larger than the first two models. As a result, the area of reinforcing steel in the third model is 20 percent greater than the steel used in the second model.

For the finite element models of the present study, the material properties used for all three models are identical. The compressive strength of concrete has a magnitude of 4100 psi and the confined concrete strength was calculated based on a 1.2 ksi lateral stress, similar to the confined concrete strength used in the previous nonlinear analysis examples. Since the anchorage zone in this study contains three anchorage devices, which can be considered as a grouped anchor, the confined region in the finite element models has a width equal to three times the spacing between the center of each anchorage plate. The length of the confined region extends from the anchorage surface to a distance of 18 in. The web thickness of the all models is divided into three parts according to the tapered shape of the web in the structure. The first part beginning from the anchorage surface to a distance of 90 in. has a thickness of 24 in. The next part of the web continued past the end of the first part for a length of 54 in. has a thickness of 18 in. The last part extending to the end of the model has a web thickness of 12 in. All models have a length of 212 in. All bars used in the models have a tensile strength equal to 60 ksi.

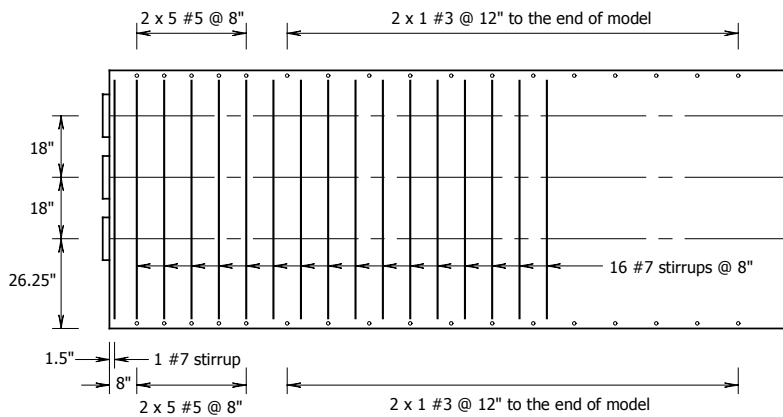
The cracking model used in this example is similar to that used in the previous example as well. Linear tension cut-off, linear tension softening and variable shear retention were chosen for the concrete constitutive behavior while a Von Mises yield criterion was applied for the steel. The modified Newton-Rhapson iteration scheme with arc-length method similar to that used in the previous nonlinear studies along with combined convergence criteria were adopted in the present nonlinear analysis.



(a) PTI Example



(b) Present Design Example



(c) Additional Model Example

Fig. 4.112 REINFORCEMENT DETAILS FOR NONLINEAR ANALYSIS STUDY

4.5.2.3 Nonlinear Analysis Result

Figure 4.113 shows the cracking strain contour plots of the model constructed based on the PTI manual. The factor of the jacking load at the final step was equal to 1.64, which is equivalent to 5380 kips. The cracks occur in the web at the upper region close to the web-flange interface and the lower region in the direction toward the bottom flange as can be seen in Fig. 4.113b. In the upper region, the cracks extend beyond the last stirrup of the web bursting steel. The cracks in the top flange are concentrated at the anchorage surface and propagate into the body of the flange with a very small magnitude of strain (see Fig. 4.113a). In the bottom flange, the cracking strain has a lower magnitude compared to that in the web and the top flange (see Fig. 4.113c). The cracks in the bottom flange occur at a distance far removed from the anchorage surface.

Figure 4.114 shows the cracking strain contour plots of the model reinforced by the bursting steel developed from the present design example. The final load was 1.29 times the jacking load or 4586 kips. This magnitude is much smaller than that of the previous model. However, it indicates that this model has a higher capacity than the factored load, which is determined by using a factor of 1.20. However, the factor 1.29 is less than $1.20/0.85 = 1.41$, which is the conventional load factor 1.20 divided by resistance factor 0.85. Therefore, the amount of bursting steel in the model is slightly unconservative. The cracks that occur in the web also mostly appear close to the interface line between the web and the top flange as can be seen in Fig. 4.114b. The cracks do not propagate past to the last stirrup of the web. The cracks in both the top and bottom flange occur at locations similar to those in the model based on the PTI example.

Using the larger amount of reinforcement in the web, the capacity of the anchorage zone increases significantly to 6150 kips or 1.73 times the magnitude of the jacking load. As can be seen in Fig. 4.115, the cracks now extend deeper toward the end of the model. However, the extent of the cracks is not beyond the last stirrup. This indicates that the steel at the position furthest away from the loading surface is not affected by the prestressing load, similar to the second model. The cracking strains on the top and the bottom flange also occur at similar locations to those found in the other models.

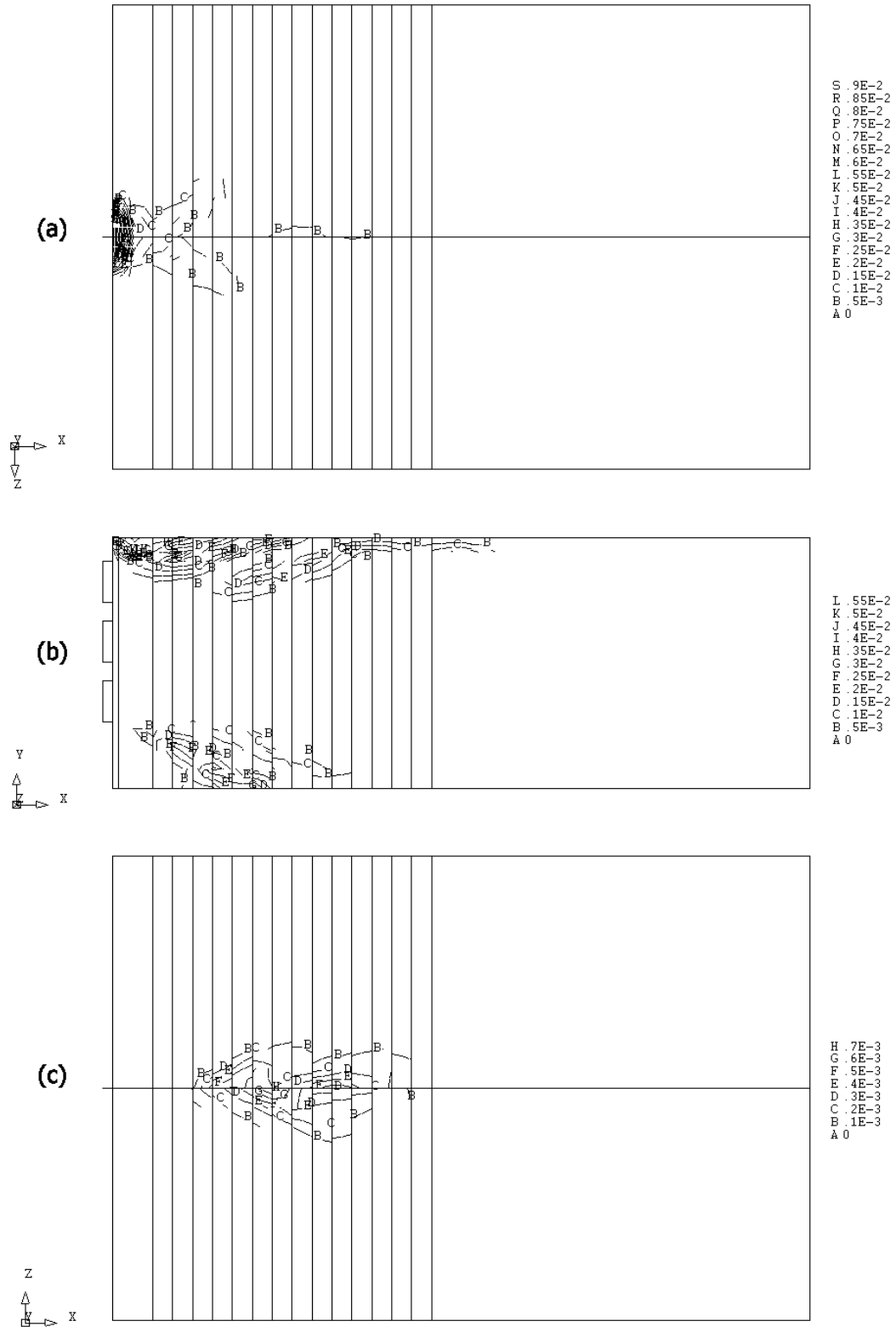


Fig. 4.113 CRACKING STRAIN CONTOUR PLOTS FOR MODEL BASED ON PTI EXAMPLE
a) TOP FLANGE, b) WEB, AND c) BOTTOM FLANGE

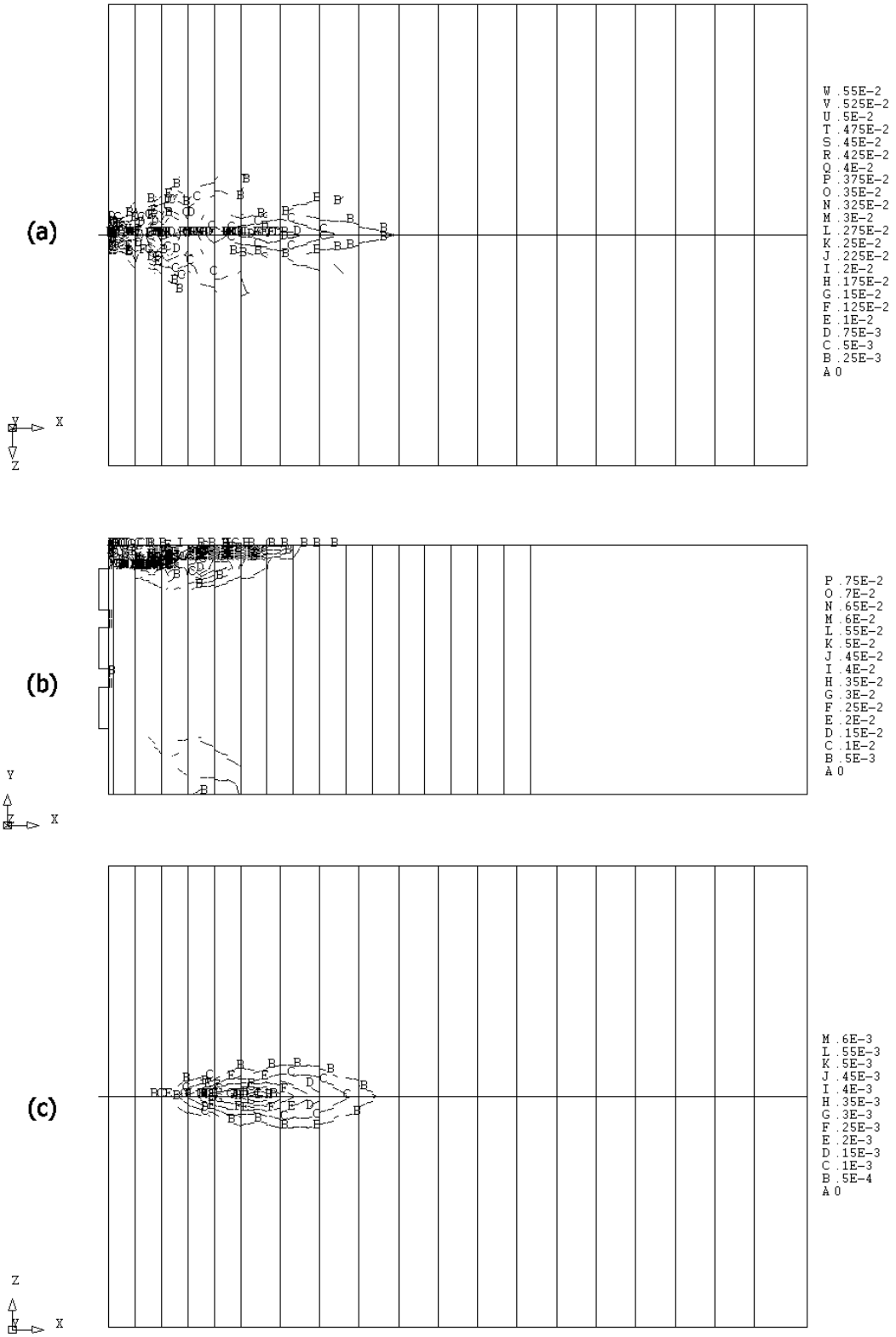


Fig. 4.114 CRACKING STRAIN CONTOUR PLOTS FOR MODEL BASED ON PRESENT DESIGN EXAMPLE
a) TOP FLANGE, b) WEB, AND c) BOTTOM FLANGE

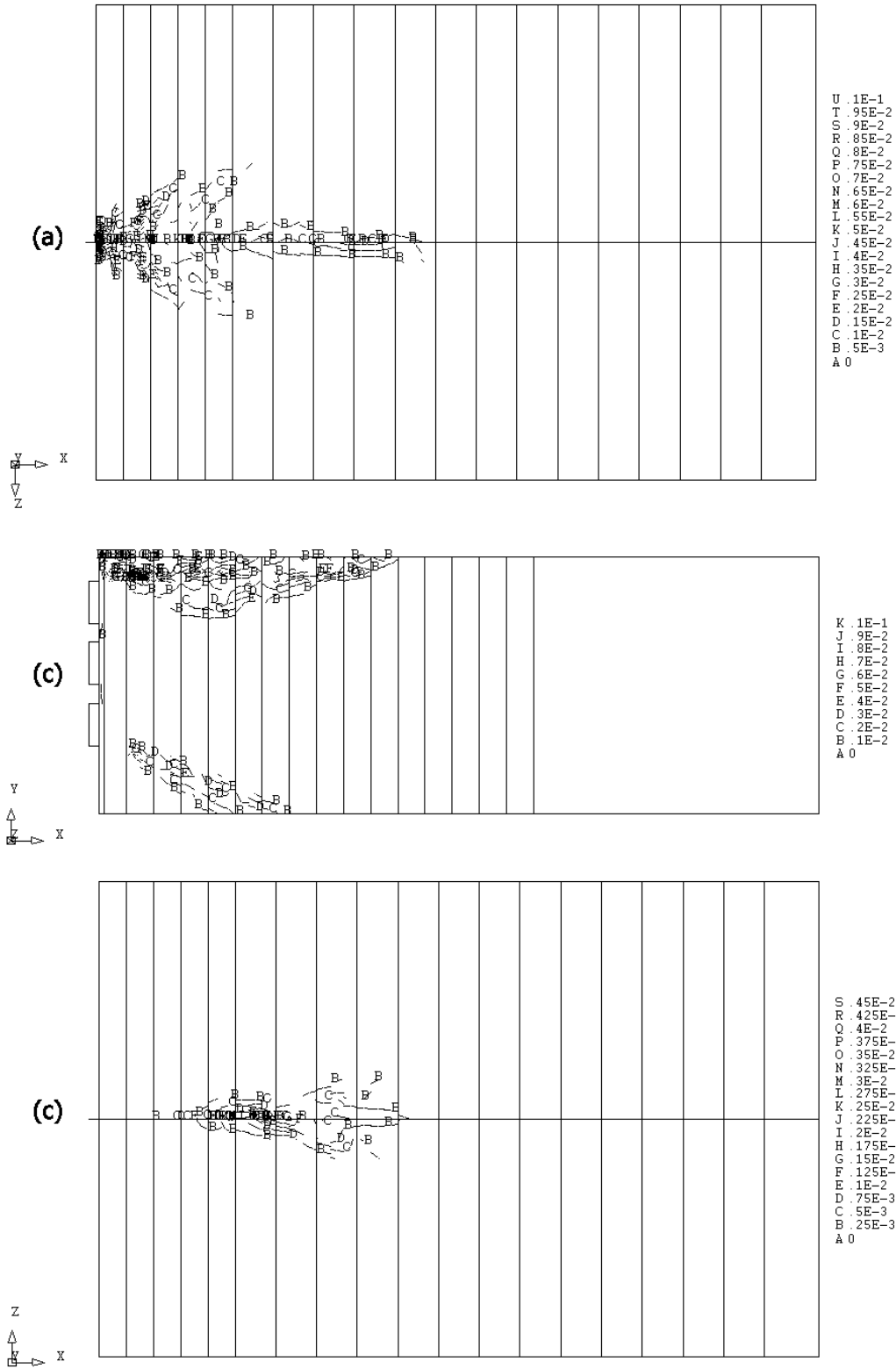


Fig. 4.115 CRACKING STRAIN CONTOUR PLOTS FOR MODEL BASED ON THE MODIFICATION OF PRESENT DESIGN EXAMPLE, a) TOP FLANGE, b) WEB, AND c) BOTTOM FLANGE

Figure 4.116 shows the tensile stress in the reinforcing bars at the level close to the interface line between web and flange with respect to the increasing of the jacking load for the model from the PTI example. The height at which the magnitudes of tensile stresses are taken is located at 71.25 in. from the centerline of the bottom flange. As can be seen, the stirrup at the location of 12 in. yields at a load of 5546 kips. All stirrups in this model start to increase their tensile stresses rapidly after the load passes 5261 kips. The stirrup at the closest position to the anchorage surface of the model exhibits the most variation of stress. Unlike the behavior of the tensile stresses in the bursting steel in Fig. 4.116, the model reinforced with the amount of reinforcement based on the present design example has two stirrups that yield after the load passes 4586 kips, which is the final load level for this model (see Fig. 4.117). The first stirrup from the loaded surface in this model also shows the most variation among all stirrups in the model. This stirrup passes its yield strength as the load increases to 4337 kips, which is equivalent to a factor of 1.22 times the magnitude of the jacking load. The reason that more stirrups in the second model pass their yield points as the load increases to the level where the stirrups of the first model remain under their yield strength is that the size of the stirrups in the second model is smaller than those used in the first model. The spacing of the stirrups in the second model is also wider than that of the first model, which allows more available space for a crack to originate due to the increasing of the load.

With the larger web stirrups in the third model, the capacity of the model increases. As can be seen in Fig. 4.118, the modified model still has two stirrups that pass their yield point similar to the second model. However, the load level at which those stirrups begin to pass the yield point is higher than that occurring in the second model. After these stirrups pass the yield strength of steel at a load equal to 5013 kips, the tensile stresses in these stirrups level out. The stirrups at locations more distant away from the anchorage surface in both the second and third model show a small variation in the stress as the load increases. The stirrup at the furthest location from the anchorage surface in these two models exhibits a linear variation, which indicates that this stirrup does not become effective as the applied load on the anchorage reaches its final level. However, the results from the nonlinear analysis prove

that the anchorage zone has adequate capacity to resist the conventional factored load, with a factor of 1.20.

When considering the magnitude of the load at service (jacking) load level, the stirrups in the model from the PTI example (Fig. 4.116) show stress increases in more bars than those occurring in the other two models (Figs. 4.117 and 4.118). The magnitudes of stresses of the stirrups in the first model vary gradually while those of the two bars that are closest to the anchorage surface in the other two models are obviously distinct from all the rest of the stirrups. Since the spacing in the second and third model is larger than that of the first model, more distance between the bars allow the cracks to be wider and causes the stress in the steel in the first two bars to increase before the cracks propagate deeper into the body of the anchorage zone and result in increasing the stresses in the latter bars. The bar spacing clearly affects the stress behavior of the reinforcing steel at the service load level.

Figure 4.119 shows a comparison of the tensile stress in each bar at the final load step for the three models. The tensile stresses shown in the figure are taken at the position of 71.25 in. from the center of the bottom flange similar to those used in Fig. 4.116 to 4.118. As shown, the plots of all models show a similar characteristic in that the highest tensile stress occurs in the stirrup that is located closest to the loading surface. The tensile stress in the next stirrup is smaller. The smallest tensile stress typically occurs in the stirrup that is positioned at the furthest location from the loading surface. All the bars in the model based on the PTI example have a higher tensile stress compared to the stresses in the stirrups of the second model, which is based on the present design example. However this is to be expected because the magnitude of the final load from the first model is higher than that from the second model. Because the nonlinear analysis was terminated at the factor of 1.29 times the jacking load due to a possible violation of any material constitutive equation occurring during the analysis process, the stirrups from the location of 48 in. to the end of the arrangement do not exhibit a high level of stress as can be seen in Fig. 4.119. They are not affected by the cracks, which had not propagated to this location when the termination of the analysis occurred. The region in which the violation of material constitutive models occurred should be the region where a large cracking strain or a high level of tensile stress exists. Based on the behavior of cracking strains, the region close to the anchorage surface between

the edge of the anchor plate and the center of the top flange appears to be the region where the material constitutive equations of the finite element model are violated. Therefore, it can be stated that the design of a web bursting reinforcement pattern should also consider the region between the anchorage plate and the flange body close to the loading surface in addition to a typical method used for the design of the reinforcement arrangement within the bursting region ahead of the anchor plate.

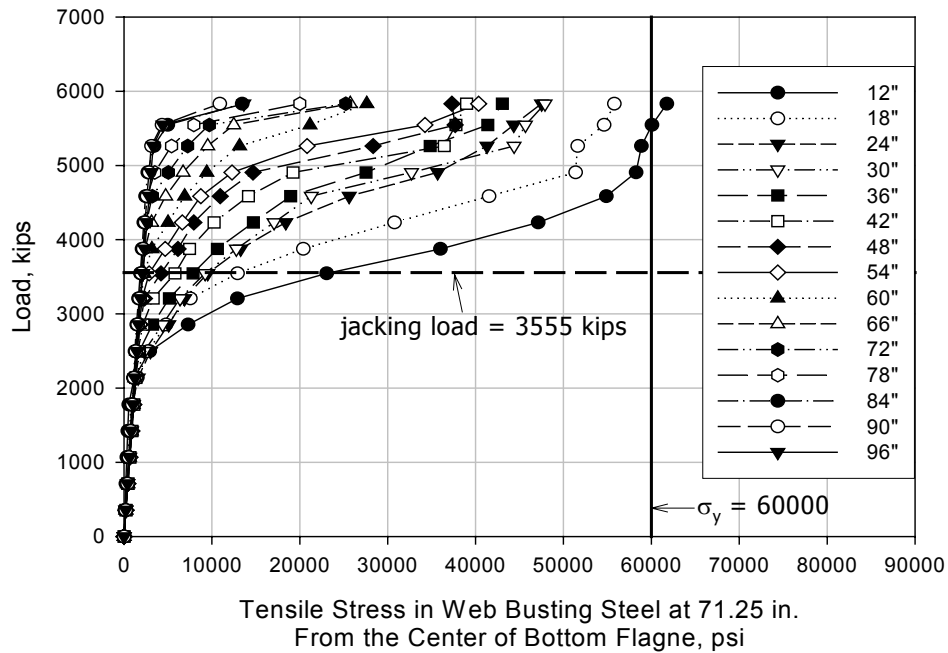


Fig. 4.116 TENSILE STRESSES IN THE WEB BURSTING STEEL FOR ALL LOAD STEPS FOR MODEL BASED ON PTI EXAMPLE

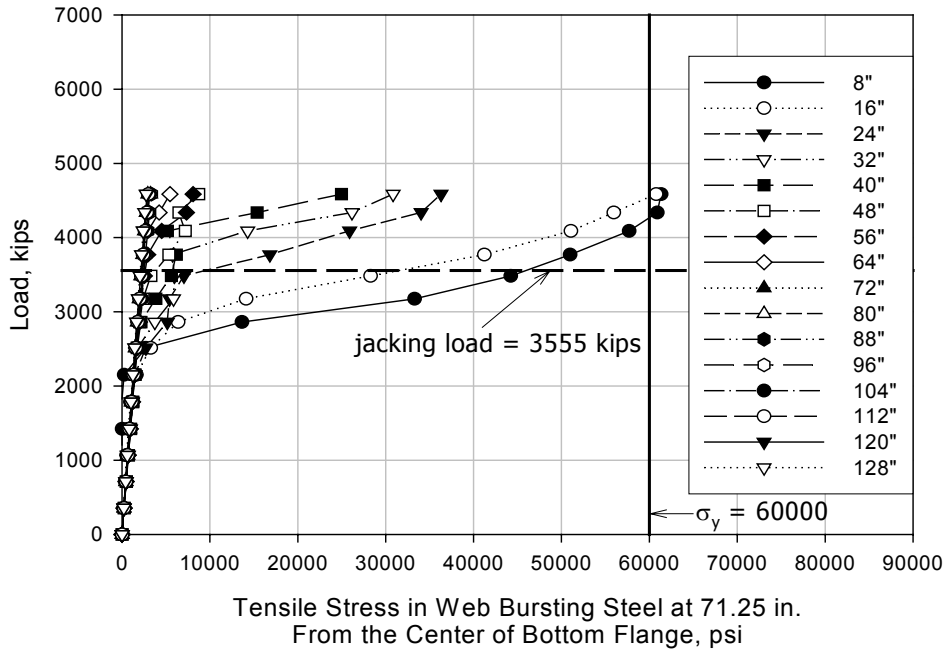


Fig. 4.117 TENSILE STRESSES IN THE WEB BURSTING STEEL FOR ALL LOAD STEPS FOR MODEL BASED ON PRESENT DESIGN EXAMPLE

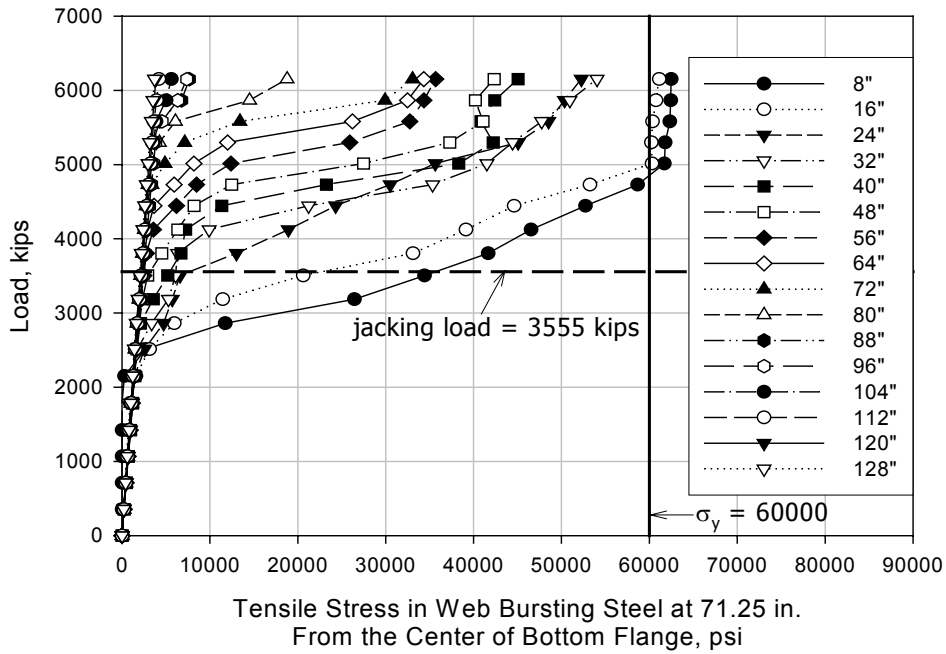


Fig. 4.118 TENSILE STRESSES IN THE WEB FOR ALL LOAD STEPS FOR MODEL BASED ON THE MODIFICATION OF PRESENT DESIGN EXAMPLE

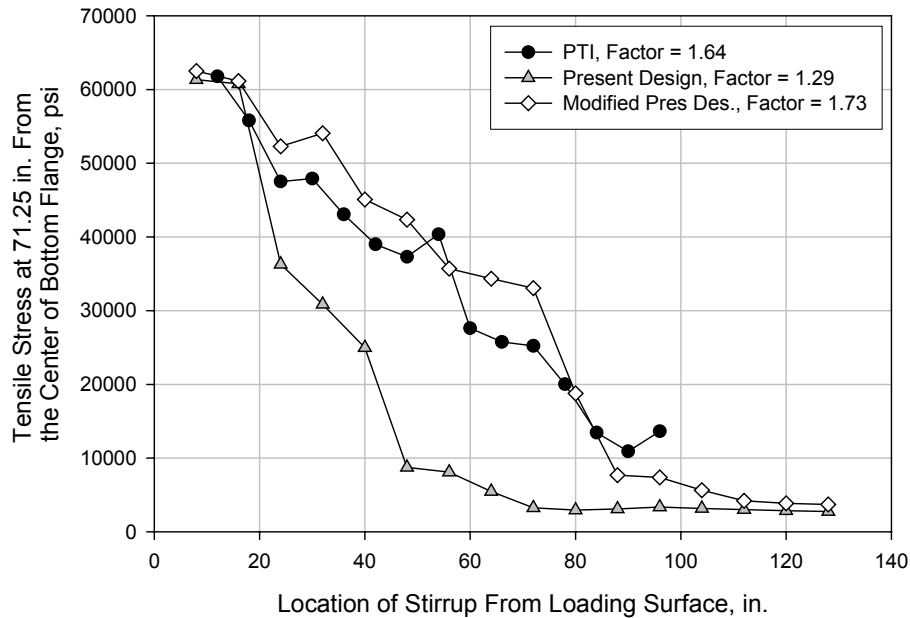


Fig. 4.119 COMPARISON OF TENSILE STRESSES ALONG THE HORIZONTAL LINE AT THE FINAL LOAD STEP

In the top and the bottom flange of the structure, the magnitude of the cracking strains within the body of the flanges are rather small relative to those occurring in the web as can be seen in Figs. 4.113 to 4.115. However, the finite element results indicate a concentrated region of cracking occurring near the front surface of the top flange. These cracks may be the result of the load, which is placed close to the top flange and causes a crushing failure in this location. Therefore, special consideration should be taken for the reinforcement of the flange as well. Figs. 4.120 and 4.121 show the stresses at the final load step in the bursting steel of the top flange from the model based on the PTI example and the model based on the present design example, respectively. As can be seen, the highest tensile stresses occur in the bars located at 24 in. in the first model and 52 in. in the second model. Both bars have stresses that are much less than the tensile strength of steel. However, the bars that have the largest stresses are close to the location of the first flange reinforcement region, which covers the distance of 36 in. from the loading surface, according to the present reinforcing steel arrangement for the flange developed in this example.

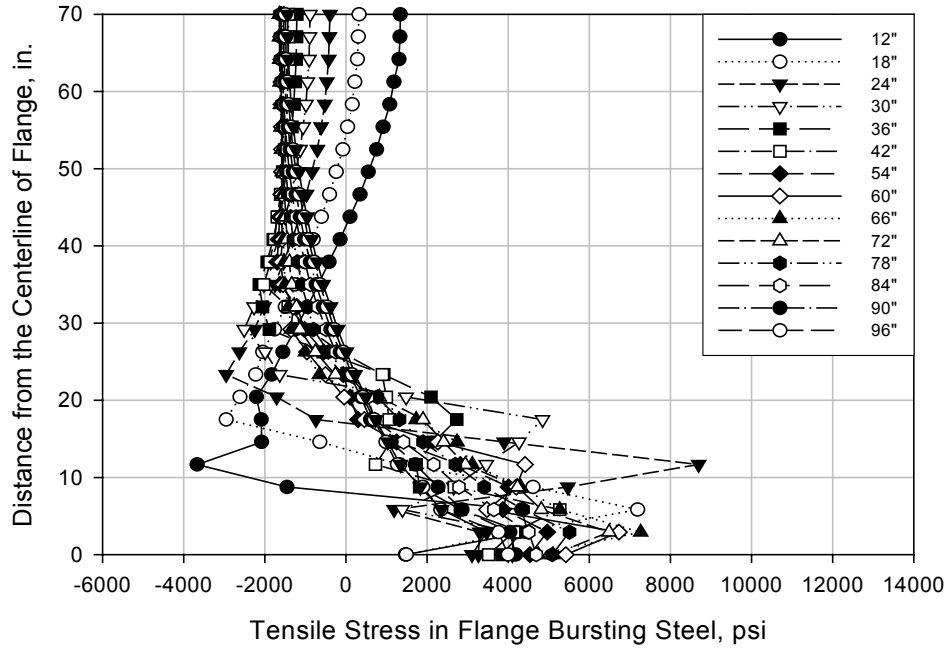


Fig. 4.120 TENSILE STRESSES IN THE TOP FLANGE BURSTING STEEL FOR MODEL BASED ON PTI EXAMPLE

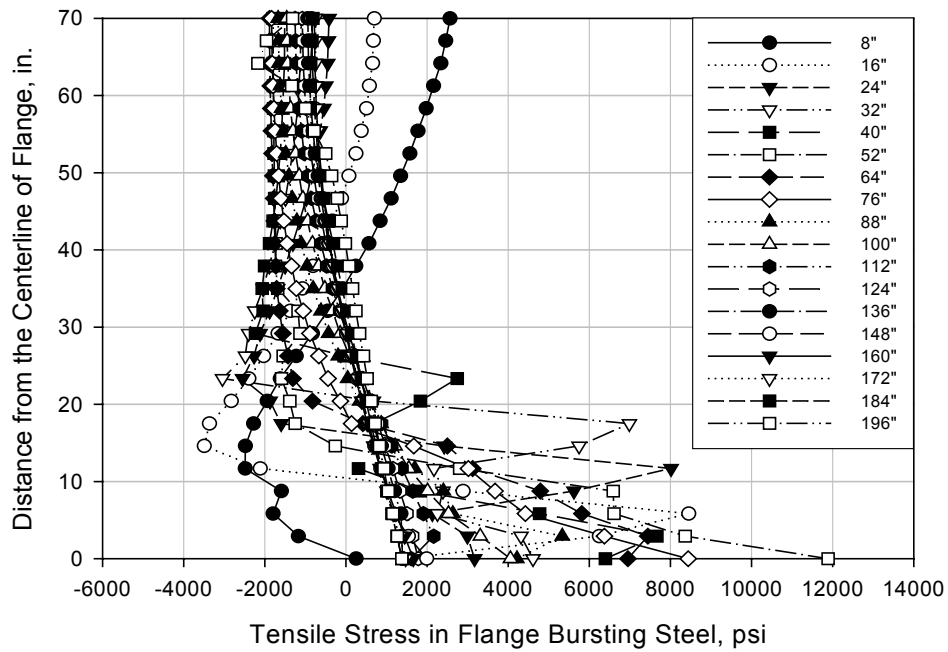


Fig. 4.121 TENSILE STRESSES IN THE TOP FLANGE BURSTING STEEL FOR MODEL BASED ON PRESENT DESIGN EXAMPLE

4.5.3 Summary

Based on three methods of reinforcing steel arrangement in the second example, it is found that each method provides a different advantage. The model based on the PTI example has a smaller spacing of reinforcement and its bursting steel is distributed over a shorter distance than the other two models. The load magnitude at the final load step of the model is higher than the second model, which has the bursting steel distributed further and uses a smaller bar size. However, the amount of bursting steel in the second model is smaller than that of the first model by almost 22 percent. The final load of the second model is still able to resist a factored load with the factor of 1.2. As the bursting steel bar size of the second model is modified to have a larger diameter with all other reinforcement detailing of the model remaining the same, the final load of the third model increases even higher than that of the first model. However, the propagation of the cracks in the web of the third model does not extend to the last stirrups. Therefore, it can be stated that an effective reinforcement of bursting steel within the web of the anchorage zone in a flanged section can be achieved from a uniform distribution of the steel and the use of a large bar diameter at the region close to the anchorage surface. A small spacing between each bar also helps the cracks to propagate deeper into the body of the anchorage zone and results in an effective use of all bursting stirrups within the structure. Based on the length of the crack propagation occurring in the first model, the distance of $2d_{burst-web}$ is applicable for the distribution of steel bars in order to cover the length of the crack propagation. Furthermore, a special consideration should be provided for the design of an anchorage zone structure that contains a wide region of anchorage surface such as a grouped anchor. The prestressing load may not affect the bursting steel under the grouped anchor as much as the steel within the region between the anchor axis and the web-flange interface line. Since the region can possibly be the weak zone of the structure, the reinforcement pattern of this region should be carefully selected.

For the reinforcement within the flange, the reinforcement pattern based on the present design method is proven to be adequate for the resistance of the bursting force within the flange body. Since the transferring forces from the web to the flange are distributed along the interface line, the reinforcement arrangement all over the body of the flange is found to be appropriate. For two separated regions of the flange reinforcement, the first region close

to the anchorage surface contains more steel per length than the second region. From the nonlinear analyses, this region contains a high magnitude of cracking strains as can be seen in Fig. 4.113a, 4.114a, and 4.115a, which indicates a significant need for reinforcement. Therefore, the appropriateness of the method of separating two regions for the flange reinforcement is confirmed.

According to the elastic stress distribution, tensile stresses also occur in the first region of the flange that are a result of a tieback effect as mentioned in section 4.4.1.2.1. Reinforcement in the longitudinal direction in this region of the flange should be provided. In fact, the transferring of the forces from the web to the centerline of the flange does not act as a point load as has been assumed in the strut-and-tie model for flanged section. The tensile forces in the longitudinal direction of the flange in a real structure may not be as critical as it appears from the strut-and-tie model. However, if the longitudinal reinforcement of the flange for this region is desired, it is recommended to extend to the length of the first region, which is equal to $2d_{burst-flgl}$, since the tieback forces only occur within this region. In the front region of the flange where the flange edge connects to the loaded surface of the web, the compressive stresses resulting from strain compatibility in this region may cause cracks to occur within the front edge of the flange. Therefore, special reinforcement of this front edge may be required.

4.6 Discussions and Recommendations

As the presentation of the investigation of anchorage zones in flanged sections has been given in this chapter, a new approach for the design of a non-rectangular anchorage zone is proposed. The formulations for determining bursting force magnitude and the location of the force for both the web and flange are demonstrated. The verification of the formulations for each load configuration is given. Since the formulations are developed based on the use of Strut-and-Tie Model approach, a modified version of the methodology using strut-and-tie models for the design of a non-rectangular anchorage zone is also found. Finally, an

effective method of bursting steel arrangement using nonlinear analysis is investigated and recommended.

4.6.1 Design Recommendations

4.6.1.1 Design Using Strut-and-Tie Model Method

Generally the method of using the STM approach in the design of anchorage zones in non-rectangular sections as previously found in any code provisions including the PTI Anchorage Zone Design manual (Wollmann et al., 2000) assumes the location of the tie in the web to be placed at a distance of approximately one half of the height of the section. Only one tie member within the web of the structure is used to connect both horizontal struts that exist in the web and in the flange. The application point of the transferring force from the local zone node to the flange is defined at the intersection between the tie and the centerline of the flange. Another set of strut-and-tie models is created within the body of the flanges. Based on the same assumption, the location of the tie within the flange is positioned at a distance from the application point of the transferring force. Then all the bursting forces within the model can be found. However, since the present study has found an effectiveness of using the STM approach to develop the formulations for the design of anchorage zones in non-rectangular sections, a modified method of locating the ties in both web and flanges can be employed.

By starting with the calculation of external forces similar to the method of determining the resultant forces as presented in sections 4.4.1.2 and 4.4.2.2, all external forces can be found at the beginning of the design. By using equations (4.44) and (4.45), the location of the tie in the web can be assumed based on this value. Fig. 4.122 shows the strut-and-tie model developed for an anchorage zone in a non-rectangular section. As can be seen in Fig. 4.122a, the structure of the strut-and-tie model in the web can be separated into two sets consisting of the set that connects the forces γR_I and $(1-\gamma)R_I$ into the model and another set that is created based on the forces in the flanges. Tie 2-4 represents the bursting force resulting from the forces in the flanges. Tie 5-6 represents the bursting force that is caused by the forces γR_I and $(1-\gamma)R_I$.

The assumption of the inclined strut that is connected from the local zone node to the flange with a 45 degree angle can be only used for the formulation of the approximate equations of $T_{burst-web}$. However, it may not be applicable for the development of the strut-and-tie model of a non-rectangular section because in some cases, the resultant force in the flange may be very large. The use of a 45 degree inclined strut results in an unrealistically large magnitude of bursting force in tie 2-4, which cannot be bigger than the value of $T_{burst-web}$. Therefore, an appropriate value of the inclination angle must be determined.

As previously illustrated in section 4.4, the location of the total bursting force can be determined by using the smaller value of $d_{burst-web}$ provided by equations (4.44) and (4.45). By first assuming the location of tie 5-6, the location of tie 2-4 can be found by the relationship of the location of the total bursting force and the bursting forces from both ties as

$$T_{burst-web} = \frac{T_{b1}d_{b1} + T_{b2}d_{b2}}{d_{burst-web}} \quad (4.52)$$

Since $T_{burst-web}$ is equal to $T_{b1} + T_{b2}$, by substituting $T_{burst-web}$ into equation (4.52), the rearrangement of equation (4.52) leads to the equation

$$\frac{T_{b1}}{T_{b2}} = \frac{d_{b2} - d_{burst-web}}{d_{burst-web} - d_{b1}} \quad (4.53)$$

According to Fig.4.122a, the angles α_1 and α_2 are the angles of struts 1-2 and 1-5, respectively. Since T_{b1} equals to $R_2 \tan \alpha_1$ and T_{b2} equals to $\gamma R_1 \tan \alpha_2$, equation (4.53) can be rewritten and the angle α_1 can be found using the equation

$$\tan \alpha_1 = \frac{\gamma R_1}{R_2} \times \frac{d_{b2} - d_{burst-web}}{d_{burst-web} - d_{b1}} \tan \alpha_2 \quad (4.54)$$

Since the locations of ties 2-4 and 5-6 are set, the geometry of the model within the web can be constructed.

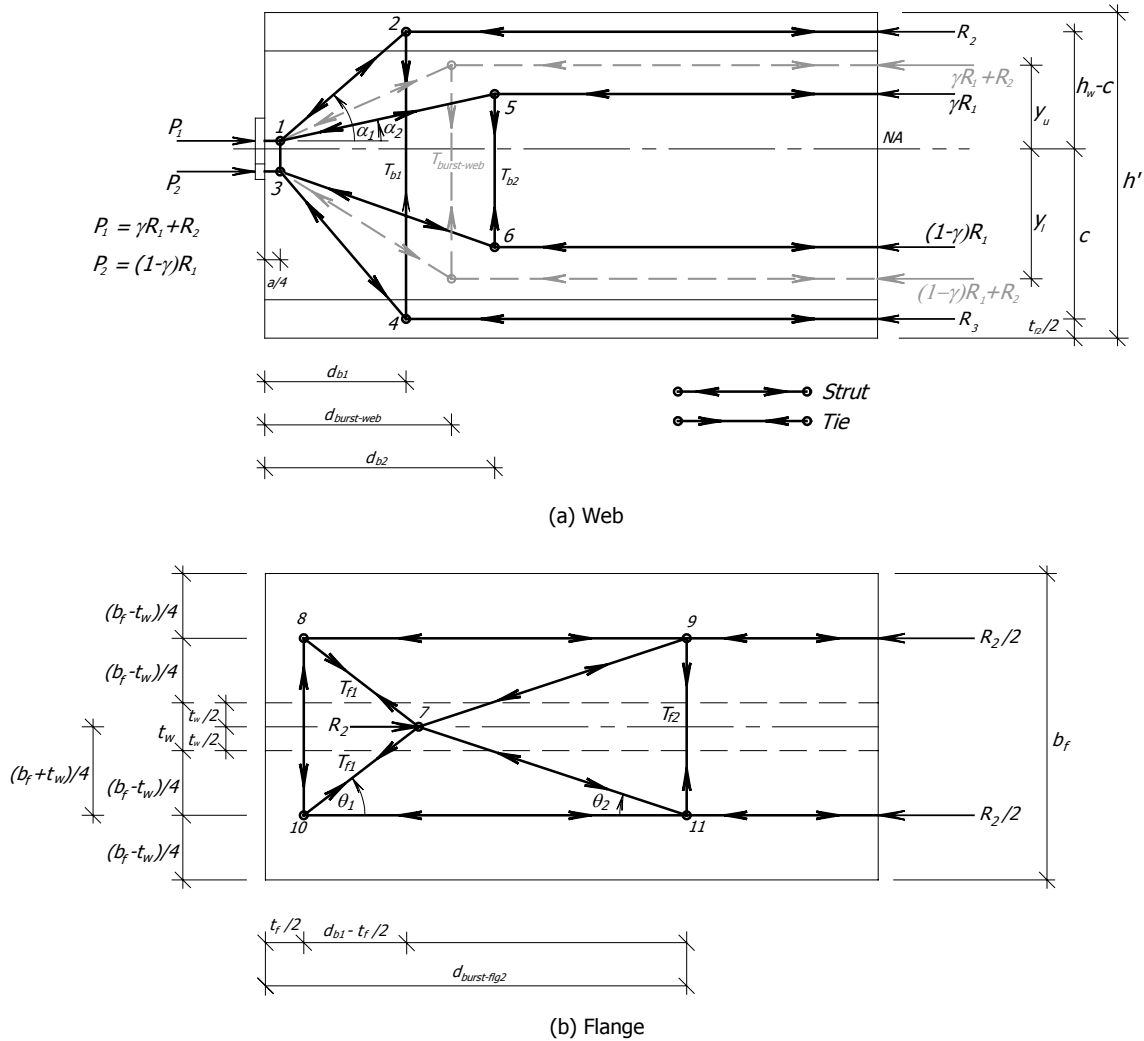


Fig. 4.122 STRUT-AND-TIE MODEL FOR A NON-RECTANGULAR SECTION

For the strut-and-tie model in the top flange (see Fig. 4.122b), the application point of the transferring force from strut 1-2 is already known from the value of d_{b1} . The structure of the model is similar to that presented in section 4.4.1.2.1. Two sets of ties consisting of the ties 7-8 and 7-10, which are used to resist the tieback force in the front part of the flange, and the tie 9-11, which is used to withstand the bursting force in the flange, are presented in the model. The position of strut 8-10 can be located at a distance equal to one half of the flange thickness as seen in Fig. 4.122b. One half of the force R_2 can be located at the center of each side of the flange extending from the surface of the web. The location of the tie 9-11 can be found using equation (4.12). Therefore, the geometry of the strut-and-tie model in the top flange is achieved. The method of constructing the strut-and-tie model in the top flange can

be used for the creation of the model for the bottom flange as well. Therefore, the design of an anchorage zone in a non-rectangular section based on a modified STM method is established.

4.6.1.2 Design Using Approximate Equations

The present study of anchorage zones in a non-rectangular sections is developed based on four load configurations: concentric, eccentric, inclined concentric, and inclined eccentric. The formulations of the approximate equations employ the STM approach as well as the information provided by the finite element study. As has been developed and verified, the design of an anchorage zone with a non-rectangular section can be accomplished using a series of equations presented in section 4.4. At the beginning of the design procedure, equations (4.44) and (4.45) are used for determining the location of the bursting force in the web ($d_{burst-web}$), which is needed for the calculation of the bursting force magnitude in the web ($T_{burst-web}$) as presented in equations (4.42) and (4.43). The calculation of web bursting force magnitude involves several calculations needed to determine the resultant forces and the geometric variables. For the design of bursting steel in the flange, the magnitude of bursting force can be found using equation (4.25) and the method of flange bursting steel arrangement employs the values provided by equations (4.12), (4.50), and (4.51). The calculation of flange bursting force in equation (4.25) also involves the calculation of stress as well.

4.6.2 Detailing Recommendations

As illustrated in the examples using nonlinear analysis, an acceptable arrangement of reinforcing steel within the web and the flanges of anchorage zones in non-rectangular sections can be achieved based on the location of the bursting forces in the web and flanges. In the web, a uniform distribution of bursting steel over the length of $2d_{burst-web}$ from the anchorage surface is found to be practical. The resulting anchorage zone will have adequate strength capacity to withstand the conventional factored load. A more convenient method to manipulate the spacing and the bar size is also achieved. For the bursting reinforcement in the flange, the method of arranging the steel is developed based on the behavior of the stresses occurring in the flange body. Two separate regions of reinforcement are defined

according to the behavior of the two bursting stress regions. Based on the distances of the bursting force locations from both regions, fifty percent of the total bursting steel required for the flange is located over the full length of the first region, which is equal to $2d_{burst-flg1}$. The other fifty percent of the total flange bursting steel is uniformly distributed for the distance of $2(d_{burst-flg2} - 2d_{burst-flg1})$ continued from the first region. The method can be used to improve the effectiveness of steel arrangement instead of uniformly distributing the flange bursting steel over a length without regard for the behavior of stresses, which occur in the body of the flange based on the finite element study.

CHAPTER 5

MODIFIED RECCOMENDATIONS TO AASHTO

The present study focuses on the investigation of anchorage zones with complex configurations, which are not currently addressed in the AASHTO Standard Specifications (2002). The investigation of rectangular sections was presented in Chapter 3, and several modified recommendations are proposed and shown to be useful in order to develop more effective methodologies for rectangular anchorage zone design. As can be seen in Article 9.21.6.3 in the Specifications, the approximate stress analyses and design of rectangular sections gives guidance for anchorage zone design using approximate equations to determine the magnitude and location of the bursting force. However, several changes can be made to achieve a better rectangular anchorage zone design. Furthermore, Article 9.21.3.4.5 addresses the method of detailing bursting steel reinforcement that is found to be rather complicated as stated in the previous chapters. A more practical arrangement for bursting steel can also be used in the specifications. In addition to the design of rectangular sections, the present study also provides recommendations for the design of non-rectangular anchorage zones as illustrated in Chapter 4. The design methodologies using both the approximate equations based on linear elastic finite element study and the Strut-and-Tie Model are given.

5.1 Design Recommendations for Rectangular Sections

In the AASHTO Standard Specifications (2002), Article 9.21.3.4.5 states that the reinforcement is to be distributed ahead of the loaded surface along both sides of the tendon throughout a distance taken as the lesser of $2.5d_{burst}$ for the plane considered and 1.5 times the corresponding lateral dimension of the section, where d_{burst} is determined using equation (9-38) (see equation (1.6) in Chapter 1). The spacing of the reinforcement is not to be greater than either 24.0 bar diameters or 12.0 in. Based on the nonlinear finite element study, it is found that the distribution of bursting reinforcement can be taken from the loaded surface

along both sides of the tendon throughout a distance of $2d_{burst}$ for the considered plane with a uniform spacing with the spacing smaller than both 24.0 bar diameters and 12.0 in. without causing problems of steel congestion. An improved value of d_{burst} can be determined from equation (5.2), which is modified from equation (3.7) presented in Chapter 3. Since a uniform spacing is selected, the centroid of the bursting steel is located at d_{burst} from the loaded surface. The new method of bursting steel arrangement provides more convenience in handling the bursting reinforcement within a rectangular section. The smaller spacing helps reduce the possibility that cracking that will occur within the anchorage zone after the prestressing load reaches a level beyond the service limit state.

Article 9.21.4, about the application of the Strut-and-Tie Model approach to the design of the general zone, gives guidance on general geometries of strut-and-tie models for anchorage zones subjected to various types of load configurations. The location of the tie within the model is generally assigned at the distance $h/2$ ahead of the anchor plate, where h is the width of the anchorage zone. The present study produces an improved equation to calculate d_{burst} as presented in equation (5.2). It can be used in defining the location of the tie in the strut-and-tie model. Other methods to determine the external forces and the alignment of the struts within the model follow those presented in the specifications. With the presence of a support reaction, an additional strut member needs to be added vertically from the center of the bearing plate to intersect other members above the bearing plate within the model as shown in Fig. 5.1. The location where the main compressive strut approaches the end of the anchorage zone can be calculated from the centroid of the normal stress diagram as shown in the figure.

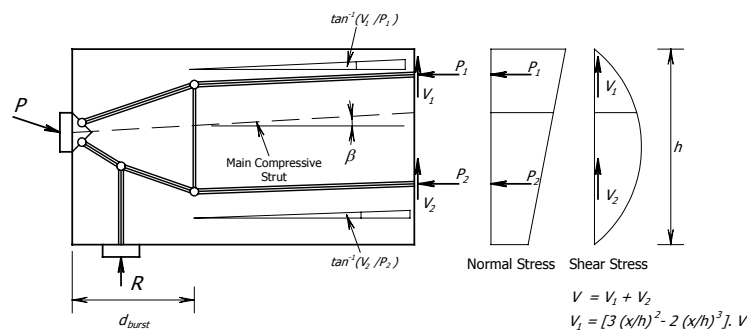


Fig. 5.1 STRUT-AND-TIE MODEL FOR ANCHORAGE ZONE WITH A SUPPORT REACTION

Article 9.21.6.3 in the specifications presents the method of using approximate equations developed based on the finite element study conducted by Burdet (1990). The equations are used for the calculation of the bursting force (T_{burst}) and the location of the force (d_{burst}) as presented in equations (9-37) and (9-38) (equations (1.5) and (1.6)). The study of rectangular anchorage zones with the presence of a support reaction illustrated in Chapter 3 gives modified equations to account for the effect of the support reaction as follows:

$$T_{burst} = 0.25 \Sigma P_u \left(1 - \frac{a}{h-2e}\right) + 0.4 \Sigma (P_u \sin \alpha) + R (0.25 - 5 \sin \alpha) \geq 0.125 \Sigma P_u \quad (5.1)$$

$$d_{burst} = 0.5 (h-2e) + 0.25 a + 0.25 (h-2e) \sin \alpha + \frac{R}{\Sigma P_u} (h-2e) (1.5 - 10 \sin \alpha) \quad (5.2)$$

where T_{burst} is the tensile force in the anchorage zone acting ahead of the anchorage device and transverse to the tendon axis (kips), P_u is the factored tendon force (kips), d_{burst} is the distance from anchorage device to the centroid of the bursting force, T_{burst} (in.), a is the lateral dimension of the anchorage device or group of devices in the direction considered (in.), e is the eccentricity of the anchorage device or group of devices with respect to the centroid of the cross-section, always taken as positive (in.), h is the lateral dimension of the cross-section in the direction considered (in.), α is the angle of inclination of the tendon force with respect to the centerline of the member, always taken as positive, and R is the reaction force applied at the bottom surface of the anchorage zone (kips).

5.2 Design Recommendations for Non-Rectangular Sections

Since the design of an anchorage zone with a non-rectangular section is not currently addressed in the AASHTO Specifications, the newly developed methodologies from Chapter 4 can be used in order to achieve an effective approximation of the bursting force and the location of the force for non-rectangular anchorage zones. Based on an irregular shape of a flanged section, the geometry of the section needs to be transformed into a section constructed from a set of individual rectangular sections as presented in Fig. 5.2 in order to be applied into the equations used to determine the bursting force and location of the force for both the web and flange of the section.

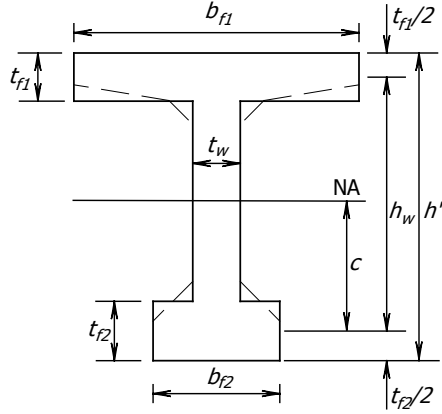


Fig. 5.2 TRANSFORMED NON-RECTANGULAR SECTION

In Fig. 5.2, h' is the total height of the section, h_w is the web height of the section, considered from the center of the top flange to the center of the bottom flange, c is the distance from the centroid of the section to the center of the bottom flange, t_w is the thickness of the web, b_{f1} and b_{f2} are flange widths of the top and bottom flange, respectively, and t_{f1} and t_{f2} are thicknesses of the top and bottom flange, respectively. The further calculations of stresses and the locations of resultant forces on the section are based on these parameters.

5.2.1 Design Recommendations of the Web

Either of the equations presented below can be used for the determination of the web bursting force:

$$T_{burst-web} = (R_{1u} + R_2) \left(\frac{4y_u + 4p}{4d_{burst-web} - a} \right) \left(1 - \frac{a}{4y_u + 4p} \right) + 0.6\Sigma(P_u \sin \alpha) \quad (5.3)$$

$$T_{burst-web} = (R_{1l} + R_3) \left(\frac{4y_l - 4p}{4d_{burst-web} - a} \right) \left(1 - \frac{a}{4y_l - 4p} \right) + 0.6\Sigma(P_u \sin \alpha) \quad (5.4)$$

where $T_{burst-web}$ is the tensile force in the web of the non-rectangular anchorage zone acting ahead of the anchorage device and transverse to the tendon axis (kips), R_{1u} is the resultant force in the web part of the section, calculated from the volume of the stress diagram occurring in the area of the web considered from the location of the applied prestressing load

to the topmost fiber of the flange (kips), R_2 is the resultant force in the top flange of the section, calculated from the volume of the stress diagram occurring in the partial area of the top flange considered from the part of the top flange that extends from the surface of the web on both sides of the flange (kips), R_{1l} is the resultant force in the web part of the section, calculated from the volume of the stress diagram occurring in the area of the web considered from the location of the applied prestressing load to the lowest fiber of the flange (kips), R_3 is the resultant force in the bottom flange of the section, calculated from the volume of the stress diagram occurring in the partial area of the bottom flange considered from the part of the bottom flange that extends from the surface of the web on both sides of the flange (kips), y_u and y_l are the locations of the centroids of the resultant forces within the upper and lower portions of the section, respectively, which are separated based on the location of the prestressing load (in.), p is the distance from the center of the anchor plate to the centerline of the strut-and-tie model developed in the formulations, which can be determined from $p = (\gamma R_1 + R_2 - 0.5P)a / 2P$ (in.), a is the lateral dimension of the anchorage device or group of devices in the direction considered (in.), α is the angle of inclination of a tendon force with respect to the centerline of the member; always taken as positive, and $d_{burst-web}$ is the distance from the anchorage device to the centroid of the bursting force (in.), which can be calculated using the smaller value from the following equations:

$$d_{burst-web} = (h' - c - \frac{t_{f2}}{2} - e) + \frac{a}{4} + \frac{h_w}{4} (1 - \exp(-0.8b_{f1} / h_w)) + \frac{h_w}{4} \sin \alpha \quad (4.44) \text{ or } (5.5)$$

$$d_{burst-web} = (c + \frac{t_{f2}}{2} + e) + \frac{a}{4} + \frac{h_w}{4} (1 - \exp(-0.8b_{f2} / h_w)) + \frac{h_w}{4} \sin \alpha \quad (4.45) \text{ or } (5.6)$$

where e is the eccentricity of the anchorage device or group of devices with respect to the centroid of the cross-section (in.), positive if located above the centroid of the section and negative if located below the centroid of the section. In the calculation of the resultant forces (R_{1u} , R_{1l} , R_2 , and R_3), if an inclined prestressing load is present, the calculation of stresses on the section must consider only the horizontal component of the load.

The distribution of web bursting reinforcement is taken from the loaded surface over the distance of $2d_{burst-web}$ with a uniform spacing. The spacing shall be smaller than both 24.0 bar

diameters and 12.0 in. without causing the problem of steel congestion. Special consideration should be taken if the anchorage device is placed close to the center of the nearest flange.

5.2.2 Design Recommendations of the Flange

The following equation is used for the calculation of the flange bursting force:

$$T_{burst-flg} = 0.15k_f^3 \Sigma P_u, \quad k_f \leq 1.0, \quad (5.7)$$

where $T_{burst-flg}$ is the tensile force in the flange in the non-rectangular anchorage zone (kips), k_f is the ratio of the force within the flange R_{flg} to the total force within the divided portion of the section with respect to the location of the prestressing load where the force within the flange exists (R_{total}). Both R_{flg} and R_{total} are determined from the volume of the stress diagram within the considered portion (in.). If the inclined prestressing load applies, the determination of the stresses must also consider the vertical component of the load.

The location of the flange bursting reinforcement is divided into two regions, which are based on the calculations of $d_{burst-flg1}$ and $d_{burst-flg2}$ as follows:

For the top flange,

$$d_{burst-flg1} = \frac{h_w - c - e}{2} + \frac{t_{f1}}{4} \quad (4.50) \text{ or } (5.8)$$

$$d_{burst-flg2} = \frac{R_2}{T_{burst-flg}} \left(\frac{b_{f1} + t_w}{4} \right) + \frac{t_{f1}}{2} \quad (5.9)$$

For the bottom flange,

$$d_{burst-flg1} = \frac{c + e}{2} + \frac{t_{f2}}{4} \quad (4.51) \text{ or } (5.10)$$

$$d_{burst-flg2} = \frac{R_3}{T_{burst-flg}} \left(\frac{b_{f2} + t_w}{4} \right) + \frac{t_{f2}}{2} \quad (5.11)$$

where $d_{burst-flg1}$ is the location of the tensile force within the first reinforced region (in.), $d_{burst-flg2}$ is the location of the tensile force within the second reinforced region immediately continued from the end of the first region (in.).

The flange bursting reinforcement within the first reinforced region can be arranged by using half of the required flange bursting reinforcement distributed over the distance of $2d_{burst-flg1}$ from the surface of the anchorage zone with a uniform spacing. The second half of the flange bursting steel in the second reinforced region is continued from the first region for a distance of $2(d_{burst-flg2}-2d_{burst-flg1})$. The spacing shall be smaller than both 24.0 bar diameters and 12.0 in. without causing the problem of steel congestion. It is recommended to place the first reinforcing steel bar at a location close to the front edge of the flange.

In a highly eccentric prestressing load case, a longitudinal edge tensile force may occur at the top or the bottom flange of the structure. The determination the longitudinal tensile force can be done by using simple beam theory. The amount of reinforcing steel in the longitudinal direction, which is used to resist the tensile force, can also be used in the transverse direction of the flange, uniformly distributed over the distance $2d_{burst-web}$ from the loaded surface.

5.2.3 Design Recommendations Using the Strut-and-Tie Model Method

Based on the finite element analysis of non-rectangular sections, modified recommendations for the design of anchorage zones using Strut-and-Tie Modeling were developed. Fig. 5.3 (Fig. 4.122 in Chapter 4) gives the detailing information for a strut-and-tie model used for the design of non-rectangular anchorage zones. The geometry of the strut-and-tie model within the web of the anchorage zone can be assumed using the equation

$$\tan \alpha_1 = \frac{\gamma R_1}{R_2} \times \frac{d_{b2} - d_{burst-web}}{d_{burst-web} - d_{b1}} \tan \alpha_2 \quad (4.54) \text{ or } (5.11)$$

where α_1 and α_2 are the angles of the inclined struts within the web as can be seen in Fig. 5.3, d_{b1} is the distance to the tie that connects the horizontal struts within both flanges considered from the loaded surface (in.), d_{b2} is the distance to the tie that connects the

horizontal struts within the web considered from the loaded surface (in.). The value of $d_{burst-web}$ can be determined using the smaller value of equation (5.5) and (5.6).

The procedure to calculate the resultant forces and the location of the forces at the end of the model is similar to those presented in section 5.2.2. However, if an inclined prestressing load is applied on the anchorage zone, special consideration in the calculation of stresses to include the effect of inclination of the load is required. For the strut-and-tie model of the flange, the determination of $d_{burst-flg2}$ employs the use of equations (5.9) and (5.11).

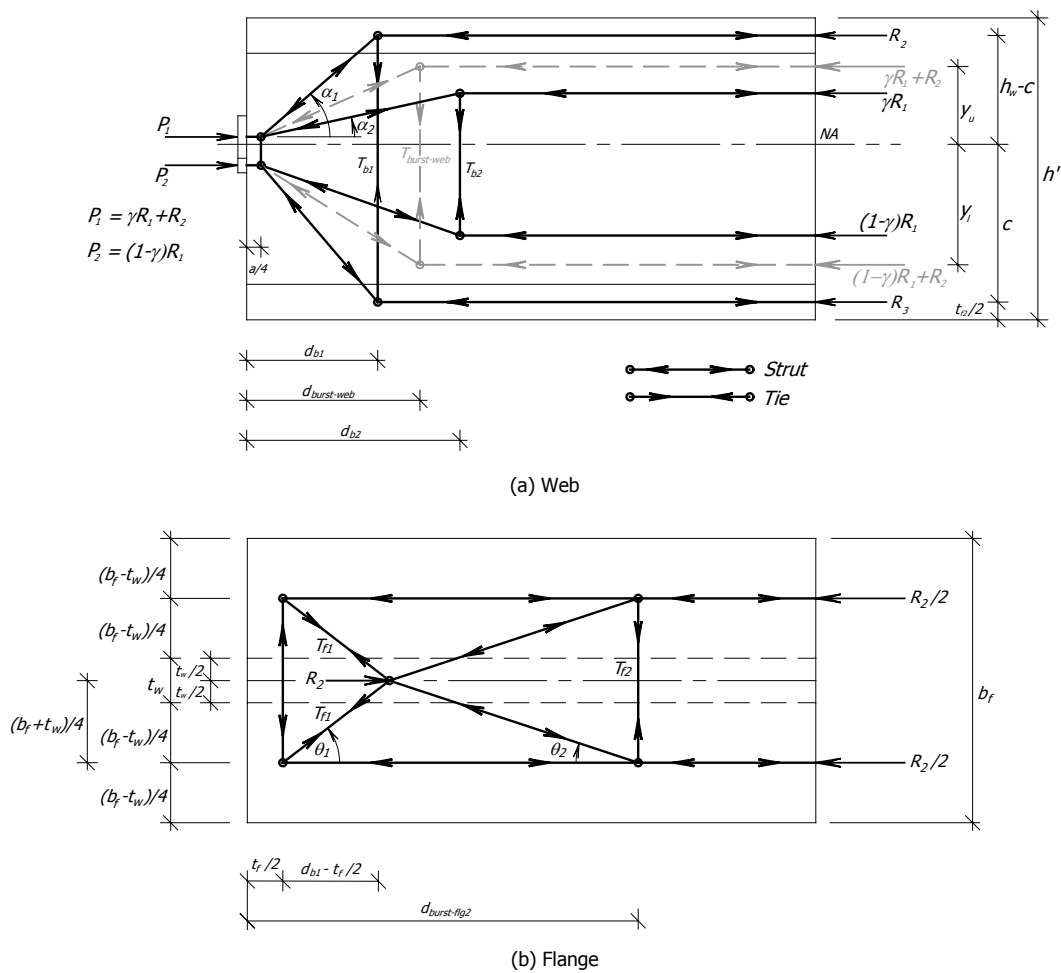


Fig. 5.3 STRUT-AND-TIE MODEL FOR A NON-RECTANGULAR SECTION

CHAPTER 6

CONCLUSIONS

6.1 General Conclusions

The present study is the investigation of anchorage zone configurations that are not currently addressed in the AASHTO Standard Specifications (2002). The main objectives of the overall study were:

- To investigate the behavior of anchorage zones with the presence of a support reaction and non-rectangular anchorage zones under four load configurations including concentric, eccentric, inclined, and inclined eccentric.
- To evaluate the applicability of the anchorage zone design methodologies addressed in the AASHTO Standard Specifications (2002) to the design of anchorage zones with a support reaction.
- To improve the simplified equations for the design of rectangular anchorage zones with a support reaction and produce new equations for the design of anchorage zones in non-rectangular sections.
- To recommend effective bursting steel arrangement for anchorage zones based on nonlinear finite element analysis.

At the beginning of the study, a finite element program with the capability to conduct nonlinear analyses of reinforced concrete structures was selected and evaluated by comparing the results from the analyses with two available published researches: Foster and Rogowsky (1996, 1997) and Sanders (1990) (Chapter 2). The nonlinear analysis results produced good correlations to those from the available researches. Therefore the program was used for the investigations of anchorage zones in the present study.

6.1.1 Design of Rectangular Anchorage Zones with the Presence of a Support Reaction

In the investigation of rectangular anchorage zones with the presence of a support reaction (Chapter 3), four load configurations were selected, including concentric, inclined concentric, eccentric, and inclined eccentric. The bursting force (T_{burst}) and the location of the force (d_{burst}) in the anchorage zones were determined and compared to those produced by the equations presented in the AASHTO Specifications (2002), which are presented as equations (1.5) and (1.6) in Chapter 1. The preparation of the models used in the investigation, which can be useful for designers wishing to use the method of using a finite element analysis in the design of anchorage zones with a support reaction, was given. Several parameters related to the geometric configuration of anchorage zones and the presence of support reaction were discussed. In the study of concentrically loaded anchors, adding the effect of anchor plate size into the formulations of d_{burst} was found to give a better prediction in the determination of d_{burst} than that of equation (1.6). The effect of the support reaction was applied into the formulations of T_{burst} and d_{burst} .

In the study of inclined concentrically loaded anchors, the effect of the inclination angle of the prestressing load was included into the formulations and the terms representing the effect of the inclination angle in the new formulations was found to be different from those presented in equations (1.5) and (1.6). After the study of eccentrically loaded anchors, the symmetric prism approach was applied into the development of the new formulations. Finally, after the inclined eccentrically loaded anchor was investigated, approximate equations for the design of anchorage zones with the presence of a support reaction were established as presented in equations (3.8) and (3.7).

During the development of the formulations in each load configuration, the comparison of the results from the equations of both the AASHTO Specifications (2002) and the newly developed equations to those of the finite element method was given. A better agreement with the finite element result was achieved from the use of the new equations. After the new approximate equations of T_{burst} and d_{burst} were established, a nonlinear finite element analysis was used in finding a method of bursting steel arrangement that is less complicated than that

given in the AASHTO Specifications. A uniform distribution of bursting steel over the distance of $2d_{burst}$ from the anchorage surface was found to be effective for the arrangement of bursting steel in a rectangular anchorage zone with the presence of support reaction. During the illustration of the anchorage zone design examples, an improved method of using the STM approach in the design of anchorage zones with a support reaction was also proposed. As a contribution from this study, the improved recommendations to the AASHTO Specifications (2002) were presented in section 5.1 of Chapter 5.

6.1.2 Design of Non-Rectangular Anchorage Zones

New methodologies for the design of non-rectangular anchorage zones were developed and discussed in Chapter 4. The study of non-rectangular anchorage zones was also conducted with four load configurations: concentric, eccentric, inclined, and inclined eccentric. The geometries of the non-rectangular sections used in the study were selected from the available standard sections presented in the PCI Bridge Design Manual (1997). The preparation of the finite element models used for the study provides useful guidance for creating a finite element model of non-rectangular sections for the designers of non-rectangular anchorage zones if the finite element method is used. Both load-related and geometry-related parameters were chosen to cover all possible geometric and load configurations which can occur in a non-rectangular anchorage zone.

During the investigation, it was found that the presence of the flange was very important for the behavior of the bursting force and the location of the force. The distribution of bursting stresses within the web of non-rectangular sections extends for a greater distance compared to that in rectangular sections. Based on the changes in distribution of the stresses caused by the presence of the flange, the formulations of the web bursting force ($T_{burst-web}$) were created by using the Strut-and-Tie Model approach. However, the determination of $T_{burst-web}$ requires the value of the distance of web bursting force ($d_{burst-web}$), which must be calculated from the equation developed based on the finite element results. The final equations for the calculation of $T_{burst-web}$ and $d_{burst-web}$ were presented in equations (4.42) to (4.45).

The STM method was also applied for the formulations for flange bursting force. The magnitude of the flange bursting force ($T_{burst-flg}$) was developed based on the finite element results and the equation to determine $T_{burst-flg}$ was given in equation (4.25). As the development of the equation to determine the location of flange bursting force ($d_{burst-flg}$) using the STM method continued, it was found that using only a single location of the total flange bursting force might not provide a conservative bursting steel arrangement. Therefore, after using a nonlinear finite element analysis to study the arrangement of reinforcing steel in non-rectangular anchorage zones, a modified arrangement method was found for the bursting steel reinforcement within the flange of a non-rectangular section. After the nonlinear analyses of the selected non-rectangular anchorage zones were conducted, the method of bursting steel arrangement was found to be acceptable. The recommendations for using the STM method for the design of a non-rectangular anchorage zone are also given.

The reinforcement arrangement within the web of a non-rectangular section is similar to that used for a rectangular section. A uniform distribution of bursting steel over the distance of $2d_{burst-web}$ from the loaded surface was found to be effective. The arrangement of the flange bursting steel can be divided into two regions based on the stress behavior that occurred within the flange, which was found in the finite element results. Half of the required flange bursting steel is distributed over the distance of $2d_{burst-flg1}$ from the loaded surface and the second half of the bursting steel is continued from the first half with a uniform distribution over the distance of $2(d_{burst-flg2}-2d_{burst-flg1})$. The equations to calculate the value of $d_{burst-flg1}$ and $d_{burst-flg2}$ are presented as equations (5.8) to (5.11) in Chapter 5. The recommendations to the AASHTO Specifications (2002) for the design of non-rectangular anchorage zones were presented in section 5.2 of Chapter 5.

6.2 Recommendations for Further Research

6.2.1 Experimental Research for Rectangular Anchorage Zone with a Support Reaction

Due to a limited number of the experimental studies of anchorage zones with a support reaction, only a few parameters of an anchorage zone with a support reaction were

investigated using a physical testing method. The only available experimental work presented in this study is the research conducted by Wollmann (1992). Therefore, more parameters related to anchorage zones with the presence of a support reaction need to be investigated by using experimental methods in order to provide supportive information for the design of anchorage zones with a support reaction.

6.2.2 Non-Rectangular Anchorage Zones

The recommendations for the further research of non-rectangular anchorage zones are as follows:

- A finite element study of non-rectangular anchorage zones with other load configurations such as multiple anchors and curved tendons.
- A finite element study of non-rectangular anchorage zones with the presence of a support reaction.
- An experimental study of non-rectangular anchorage zones with a wider variety of geometric configurations without and with a support reaction.
- An experimental study of non-rectangular anchorage zones with a wider variety of load configurations without and with a support reaction.

REFERENCES

- Abeles, P.W. and Bardhan-Roy, B.K. (1981). *Prestressed Concrete Designer's Handbook*, 3rd Ed., Charlesworth & Co Ltd.
- Adeghe L.N. and Collins M.P. (1986). "A Finite Element Model for Studying Reinforced Concrete Detailing Problems." *Publication No. 18-12*, Department of Civil Engineering, University of Toronto, 66-74.
- Al-Manaseer, A.A., and Philips, D.V. (1987) "Numerical Study of Some Post Cracking Material Parameters Affecting Nonlinear Solutions in RC Deep Beams." *Canadian Journal of Civil Engineering*, 14, 655-666.
- American Association of State Highway Transportation Officials (AASHTO). (1994) *Standard Specifications for Highway Bridges*, 1st Ed.
- American Association of State Highway Transportation Officials (AASHTO). (2002) *Standard Specifications for Highway Bridges*, 1st Ed.
- American Concrete Institute. (1983). *Building Code Requirements for Reinforced Concrete*, ACI 318-83, Detroit.
- American Concrete Institute. (1983). *Commentary on Building Code Requirements for Reinforced Concrete*, ACI 318R-83, Detroit.
- Breen, J.E., Burdet, O., Roberts, C., Sanders, D., and Wollmann, G. (1994). *Anchorage Zone Reinforcement for Post-Tensioned Concrete Girders*, NCHRP Report 356, Transportation Research Board, Washington D.C.
- Budiono, B., Gilbert, R.I., and Foster, S.J. (1993). *Tests on Partially Prestressed Beam-Column Connections Under Cyclic Loads*, ACMSM, University of Wollongong, Australia.
- Burdet, O.A. (1990). *Analysis and Design of Post-Tensioned Anchorage Zones Concrete Bridges*, Ph.D. Dissertation, University of Texas at Austin.
- Chandrupatla, T.R., and Belegundu, A. (1997). *Introduction to Finite Elements in Engineering*, 2nd Ed., Prentice hall, New Jersey.
- Chen, W.F. (1982). *Plasticity in Reinforced Concrete*, McGraw-Hill Book Company, New York.
- Collins, M.P., and Mitchell, D. (1997). *Prestressed Concrete Structures*, Response Publications, Canada.

Cope, R. J., Rao, P.V., and Clar, L.A. (1979). "Nonlinear Design of Concrete Bridge Slabs Using Finite Element Procedures." *CSCE-ASCE-ACI-CEB International Symposium*, University of Waterloo, Waterloo, Ontario, 379-407.

Cornelissen, H.A.W., Hordijk, D.A., and Reinhardt, H.W. (1986). "Experimental Determination of Crack Softening Characteristics of Normal Weight and Lightweight Concrete." *Heron*, 31(2).

Darwin, D., and Pecknold, D.A. (1977). "Nonlinear Biaxial Stress-Strain Law for Concrete." *Journal of the Engineering Mechanics Division*, ASCE, 103(EM2), 229-241.

DIANA Finite Element Analysis, User's Manual, Release 7.2. (2000). *Element Library*, TNO Building and Construction Research, Delft, The Netherlands.

DIANA Finite Element Analysis, User's Manual, Release 7.2. (2000). *Introduction and Utilities*, TNO Building and Construction Research, Delft, The Netherlands.

DIANA Finite Element Analysis, User's Manual, Release 7.2. (2000). *Linear Static Analysis*, TNO Building and Construction Research, Delft, The Netherlands.

DIANA Finite Element Analysis, User's Manual, Release 7.2. (2000). *Nonlinear Analysis*, TNO Building and Construction Research, Delft, The Netherlands.

DIANA Finite Element Analysis, User's Manual, Release 7.2. (2000). *Pre- and Postprocessing*, TNO Building and Construction Research, Delft, The Netherlands.

Egeberg, J.L. (1968). "A Finite Element Investigation of the Anchorage Zones of Prestressed Concrete Beams." *Publication No. 363*, Department of Civil Engineering, University of California, Berkeley.

Falconer, B.A. (1990). *Post-Tensioning Anchorage Zones in Bridge Decks*, M.S. Thesis, The University of Texas at Austin.

Foster, S. (1992). "An Application of the Arc Length Method Involving Concrete Cracking." *International Journal for Numerical Methods in Engineering*, 33, 269-285.

Foster, S.J. (1992). *The Structural Behavior of Reinforced Concrete Deep Beams*, Ph.D. Dissertation, the School of Civil Engineering, University of New South Wales.

Foster, S.J., Budiono, B., and Gilbert, R.I. (1996). "Rotating Crack Finite Element Model for Reinforced Concrete Structures." *International Journal for Computational Structures*, 58(1), 43-50.

Foster, S.J., and Rogowsky, D.M. (1996). "Design of Concrete Panels Subject to Bursting Tension Forces Resulting From In-Plane Concentrated Loads." *UNICIV Report No. R-347*, The University of New South Wales.

Foster, S.J., and Rogowsky, D.M. (1997). "Bursting Forces in Concrete Panels Resulting From In-Plane Concentrated Loads." *Magazine of Concrete Research*, 49(180), 231-240.

Gergely, P., and Sozen, M.A. (1967). "Design of Anchorage Zone Reinforcement in Prestressed Concrete Beams." *PCI Journal*, 12(2), 63-75.

Guyon, Y. (1953). *Prestressed Concrete*, Parsons, London.

Hillerborg, A., Mod er, M., and Petersson, P.E. (1976). "Analysis of Crack Formation and Crack Growth in Concrete by Means of Fracture Mechanics and Finite Elements." *Cement and Concrete Research*, 6(6), 773-782.

Iyengar, K.T.S.R. (1961). "Some Three-Dimensional Problems in Elasticity." *Proceedings of the Seventh Conference on Theoretical and Applied Mechanics*, Bombay, 165-206.

Johansson, M. (2000). "Nonlinear Finite-Element Analysis of Concrete Frame Corners." *Journal of Structural Engineering*, ASCE, 126(2), 190-199.

Kwan, W.P. and Billington, S.L. (2001). "Simulation of Structural Concrete Under Cyclic Load." *Journal of Structural Engineering*, ASCE, 127(12), 1391-1401.

Leonhardt, F. (1964). *Prestressed Concrete Design and Construction*, 2nd Ed., Wilhelm Ernst & Sohn, Berlin, Germany.

Lundgren, K., and Magnusson, J. (2001). "Three-Dimensional Modelling of Anchorage Zones in Reinforced Concrete." *Journal of Engineering Mechanics*, ASCE, 127(7), 693-699.

MacGreger, J.G. (1997). *Reinforced Concrete Mechanics and Design*, 3rd Ed., Prentice Hall, New Jersey.

Magnel, G. (1954). *Prestressed Concrete*, 3rd Ed., McGraw Hill, New York.

Magnusson, J. (2000). *Bond and Anchorage of Ribbed Bars in High-Strength Concrete*, Ph.D. Thesis, Division of Concrete Structures, Chalmers University of Technology, G teborg, Sweden.

Menn, C. (1990). *Prestressed Concrete Bridges*, Birkh user Verlag AG, Basel, Germany.

M rsch E. (1924). " ber die Berechnung der Gelenkquader." *Beton Eisen*, 23(12m), 156-161.

Nilson, A.H. (1978). *Design of Prestressed Concrete*, 2nd Ed., John Wiley & Sons, Inc. Canada.

Ngo, D., and Scordelis, A.C. (1967). "Finite Element Analysis of Reinforced Concrete Beams." *American Concrete Institute Journal*, 64(3), 152-164.

Ottosen, N.S. (1977). "A Failure Criterion for Concrete." *Journal of the Engineering Mechanics Division*, ASCE, 104(EM4), 527-535.

Post-Tensioning Institute. (1999). *Post-Tensioning Manual*, 5th Ed.

Ramakrishnan, V., and Ananthanarayana, Y. (1978). "Ultimate Strength of Deep Beams in Shear." *Journal of the American Concrete Institute*, 55, 87-98.

Ricketts, D.R. (1985). *Ultimate Behaviour of Continuous Deep Reinforced Concrete Beams*, M.S. Thesis, Department of Civil Engineering, The University of Alberta.

Roberts, C.L. (1990). *Behavior and Design of the Local Anchorage Zone in Post-Tensioned Concrete*, M.S. Thesis, University of Texas at Austin.

Sanders, D.H. (1990). *Design and Behavior of Anchorage Zones in Post-Tensioned Concrete Members*, Ph.D. Dissertation, University of Texas at Austin.

Schlaich, J., Schafer, K., and Jennewein, M. (1987). "Toward a Consistent Design of Reinforced and Prestressed Concrete Structures." *PCI Journal*, 32(3), 74-151.

Sritharan, S., Priestley, M.J.N., and Seible, F. (1996). "Seismic Response of Column/Cap Beam Tee Connections with Cap Beam Prestressing." *Report No. SSRP-96/09*, Division of Structural Engineering, University of California at San Diego, La Jolla, California.

Su, X., and Zhu, B. (1994). "Algorithm for Hysteresis Analysis of Prestressed-Concrete Frames." *Journal of Structural Engineering*, ASCE, 120(6), 1732-1744.

Tabatabai, S.M.R., and Mosalam, K.M. (2000). "Computational Platform for Non-Linear Analysis/Optimal Design of Reinforced Concrete Structures." *Engineering Computations*, 18(5/6), 726-743.

Tesar M. (1932). "Détermination expérimentale des tensions dans les extrémités des pièces prismatiques munies d'une semi-articulation." *International Vereinigung für Brückenbau und Hochbau*, Zürich, 1, 497-506.

Thorenfeldt, D., Thomaszewic, A., and Jensen, J.J. (1987). "Mechanical Properties of High-Strength Concrete and Applications in Design." *Proc. Symp. On Utilization of High-Strength Concrete*, Tapir Publishers, Stavanger, Norway, 149-159.

Vecchio, F.J., and Collins, M.P. N. (1986). "The Modified Compression Field Theory for Reinforced Concrete Elements Subjected to Shear." *American Concrete Institute Journal Proceedings*, 83(22), 219-231.

Wollmann, G.P. (1992). *Anchorage Zones in Post-Tensioned Concrete Structures*, Ph.D. Dissertation, University of Texas at Austin.

Wollmann, G.P., and Roberts-Wollmann, C.L. (2000). *Anchorage Zone Design, Preprint of Chapter VIII, Post-Tensioning Manual*, 6th Ed., Post-Tensioning Institute.

Yettram, A.L., and Robbins, K. (1969). "Anchorage Zone Stresses in Axially Post-Tensioned Members of Uniform Rectangular Section." *Magazine of Concrete Research*, 21(67), 103-122.

Yettram, A.L., and Robbins, K. (1971). "Anchorage Zone Stresses in Axially Post-Tensioned I-Section Members with End-Blocks." *Magazine of Concrete Research*, 23(74), 37-42.

Yettram, A.L., and Robbins, K. (1970). "Anchorage Zone Stresses in Post-Tensioned Uniform Members with Eccentric and Multiple Anchorages." *Magazine of Concrete Research*, 22(73), 209-218.

Zieliński, J. and Rowe, R.E. (1960). "An Investigation of the Stress Distribution in the Anchorage Zone of Post-Tensioned Concrete Members." *Research Report No.9*, London, Cement and Concrete Association, 32.

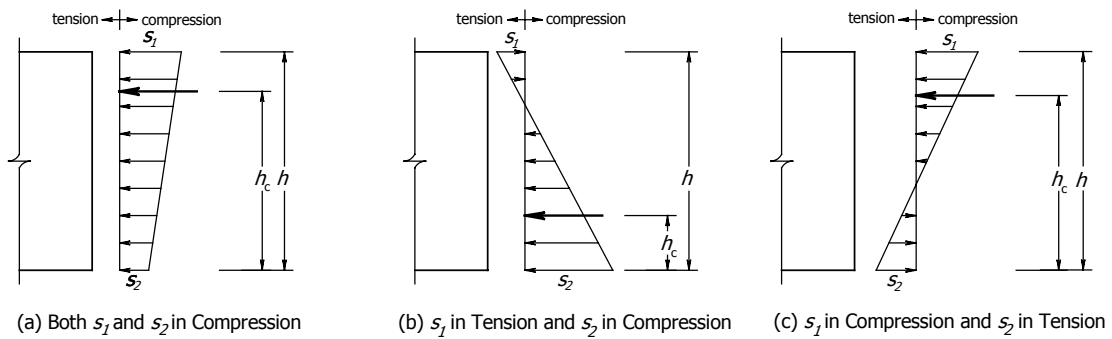
Zienliński, J. and Rowe, R.E. (1962). "The Stress Distribution Associated with Groups of Anchorages in Post-Tensioned Concrete Members." *Research Report No. 13*, London, Cement and Concrete Association, 39.

APPENDIX A

GENERAL EXPRESSIONS

A.1 Centroid of Compressive Stress Diagram

The stresses occurring at the considered section of an anchorage zone can be classified into three types as shown in Fig. A.1. The equations used to determine the location of the centroid of the compressive stress diagram with respect to the bottom surface of the beam are presented below.



Note : Both s_1 and s_2 are absolute values of stress at the top and bottom fiber, respectively.

Fig. A.1 COMPRESSIVE STRESS DIAGRAMS

a) If both s_1 and s_2 are in compression

$$h_c = \left[\frac{2s_1 + s_2}{3(s_1 + s_2)} \right] h, \quad (\text{A.1a})$$

b) If s_1 is in tension and s_2 is in compression

$$h_c = \left[\frac{s_2}{3(s_1 + s_2)} \right] h, \quad (\text{A.1b})$$

c) If s_1 is in compression and s_2 is in tension

$$h_c = \left[\frac{2s_1 + 3s_2}{3(s_1 + s_2)} \right] h, \quad (\text{A.1c})$$

A.2 Kern of Non-Rectangular Sections

The kern of a non-rectangular section measured in the vertical direction can be calculated using simple beam theory. Since the stress at the extreme fiber when the load is at the kern is zero, the equation of simple beam theory can be written as shown below:

$$\frac{P}{A} = \frac{My}{I} \quad (\text{A.2})$$

where P is prestressing force (kips), A is area of the non-rectangular section, M is moment about the centroid of the non-rectangular section (Pe), y is distance from the centroid of the non-rectangular section to the extreme fiber where the considered stress occurs, and I is moment of inertia of the non-rectangular section. The parameters within the non-rectangular are as shown in Fig. A.2.

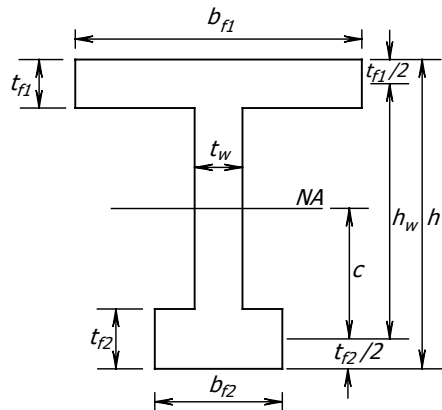


Fig. A.2 PARAMETERS WITHIN NON-RECTANGULAR SECTION

The moment of inertia of the section (I) can be calculated using the equation

$$I = \frac{t_w h^3}{12} + t_w h' \left(c + \frac{t_f}{2} - \frac{h'}{2} \right) + \frac{(b_{f1} - t_w) t_{f1}^3}{12} + (b_{f1} - t_w) t_{f1} (h_w - c)^2 + \frac{(b_{f2} - t_w) t_{f2}^3}{12} + (b_{f2} - t_w) t_{f2} c^2 \quad (\text{A.2})$$

The area of the section (A) can be calculated using the equation

$$A = t_w h' + (b_{f1} - t_w) t_{f1} + (b_{f2} - t_w) t_{f2} \quad (\text{A.3})$$

a) For symmetrical I-sections, the value of y for both upper and lower portions of the section is equal to $h'/2$. Therefore, the kern of the section can be determined from the equation

$$e = \frac{2I}{Ah'} \quad (\text{A.3})$$

b) For T-sections, the value of y in the upper portion of the section is equal to $h'-c$ and the value of y in the lower portion equals c . Therefore, the kern of the section for both directions of the T-section can be determined from the equations below.

For the kern above the centroid of the section,

$$e = \frac{I}{Ac} \quad (\text{A.4})$$

For the kern below the centroid of the section,

$$e = \frac{I}{A(h'-c)} \quad (\text{A.5})$$

c) For unsymmetrical I-sections, the value of y in the upper portion of the section is equal to $h'-c-t_{f2}/2$ and the value of y in the lower portion of the section equals $c+t_{f2}/2$. The kern of the unsymmetrical I-section can be determined using the equations shown below.

For the kern above the centroid of the section,

$$e = \frac{2I}{A(2c+t_{f2})} \quad (\text{A.6})$$

For the kern below the centroid of the section,

$$e = \frac{2I}{A(2h'-2c-t_{f2})} \quad (\text{A.7})$$

A.3 Centroid of the Resultant Force

The expressions to determine the centroids of resultant forces on a non-rectangular section can be developed based on the geometry of a trapezoidal shape. Fig. A.3 shows the pictures of free body diagrams of the non-rectangular section. The location of each resultant force, consisting of R_{1u} , R_{1l} , R_2 , and R_3 , with respect to the centroid of the section can be seen in Fig. A.3a. The locations of the total resultant force on the upper portion of the section $R_{1u}+R_2$ and the lower portion of the section $R_{1l}+R_3$ with respect to the centroid of the section are shown in Fig. A.3b.

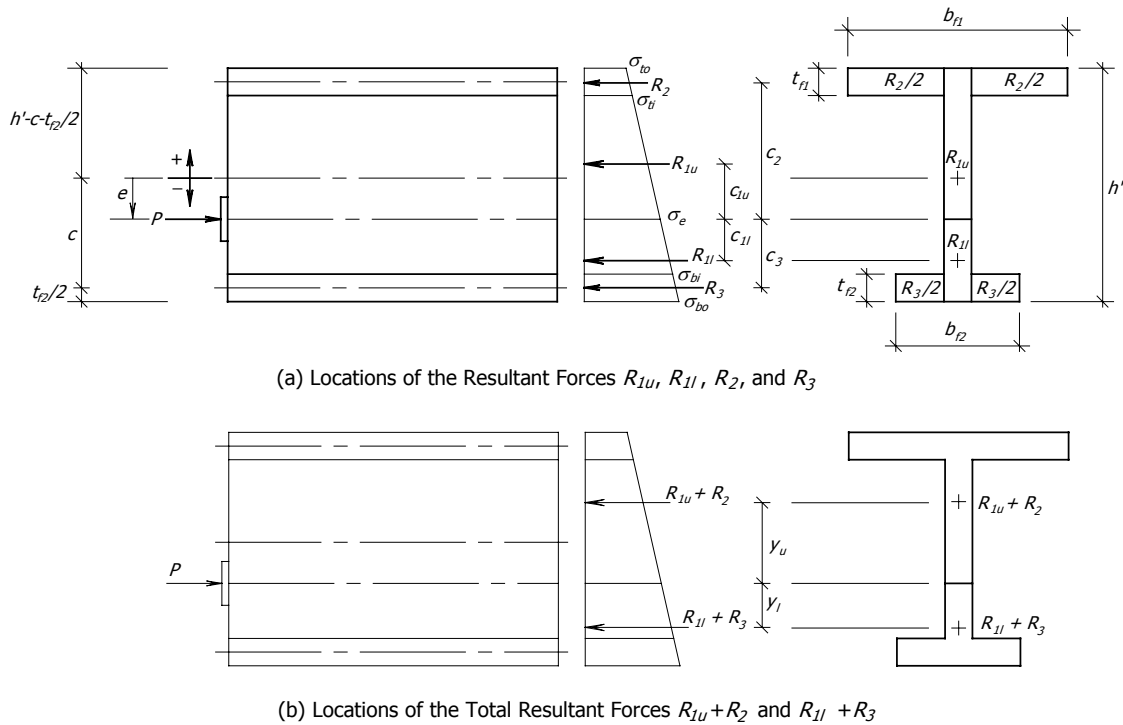


Fig. A.3 FREE BODY FOR THE CALCULATION OF THE LOCATIONS OF RESULTANT FORCES

The stress on each fiber of the section is positive in tension and negative in compression. The equations to calculate the location of each resultant force, c_{1u} , c_{1l} , c_2 , and c_3 , as shown in Fig. A.3a can be written as

$$c_{1u} = \left(\frac{\sigma_e + 2\sigma_{to}}{3\sigma_e + 3\sigma_{to}} \right) \left(h' - c - \frac{t_{f2}}{2} - e \right) \quad (\text{A.8})$$

$$c_{1l} = \left(1 - \frac{2\sigma_e + \sigma_{bo}}{3\sigma_e + 3\sigma_{bo}} \right) \left(c + \frac{t_{f2}}{2} + e \right) \quad (\text{A.9})$$

$$c_2 = \left(\frac{\sigma_{ti} + 2\sigma_{to}}{3\sigma_{ti} + 3\sigma_{to}} \right) t_{f1} + \left(h' - c - \frac{t_{f2}}{2} - t_{f1} - e \right) \quad (\text{A.10})$$

$$c_2 = \left(1 - \frac{2\sigma_{bi} + \sigma_{bo}}{3\sigma_{bi} + 3\sigma_{bo}} \right) t_{f2} + \left(c - \frac{t_{f2}}{2} + e \right) \quad (\text{A.11})$$

The equations to calculate the locations of the total resultant force in the upper portion, y_u , and the lower portion, y_l , are

$$y_u = \frac{R_{1u} \times c_{1u} + R_2 \times c_2}{R_{1u} + R_2} \quad (\text{A.12})$$

$$y_l = \frac{R_{1l} \times c_{1l} + R_3 \times c_3}{R_{1l} + R_3} \quad (\text{A.13})$$

APPENDIX B

TABLES OF RESULTS

B.1 Comparison of T_{burst} on Horizontal and Inclined Strut Line

Table B.1 shows the comparison between tensile forces determined from the integration of tensile stresses along a horizontal line (T_{b-hor}) and on an inclined line along a main compressive strut (T_b). According to the heading of each table, some parameters can be obtained from Fig. 3.9 in Chapter 3. Besides the parameters previously described, the column β_{hor} presents the angle of zero for a horizontal line and T_{b-hor} indicates the tensile force taken from the integration along a horizontal line.

As can be seen, almost all percent differences shown in each table are positive except some numbers in Table B.1b. The positive percent difference means the tensile force given from an inclined compressive strut have a higher value than that from the integration along a horizontal line. The negative value in Table B.1b (inclined concentric load) is for the case in which the magnitude of the support reaction is equal to 10 percent of the prestressing load. The vertical component of the inclined load with 6 degree angle has the closest value to the magnitude of the reaction force. The integration of the stresses along the lines that contain a very close angle between horizontal line and compressive strut line (close to zero degrees) may result in negative percent differences. However, this proves that the difference between the smaller tensile force normal to the compressive strut and the tensile force normal to the horizontal line of this case can be considered negligible. Note in Table B.1c that the percent differences in some cases become very large when an eccentric load is applied.

Table B.1a CONCENTRIC LOAD CASE

	<i>P</i>	<i>h</i> (in.)	<i>t</i> (in.)	<i>a/h</i>	<i>α</i> (deg.)	<i>e/h</i>	<i>e</i> (in.)	<i>R/P</i>	<i>b/h</i>	<i>l</i> (in.)	<i>r.s.h</i> (in.)	σ_t (psi)	σ_b (psi)	<i>h_c</i> (in.)	β_{hor} -1-	<i>T_{b-hor}</i> -2-	β -3-	<i>T_b</i> -4-	% Diff. -2&4-
Concentric	1	16	1	0.10	0	0	0	0.05	0.125	2	24	-0.0906	-0.0344	9.20	0.00	0.2280	2.64	0.2354	3.16
	1	16	1	0.10	0	0	0	0.10	0.125	2	24	-0.1188	-0.0062	10.40	0.00	0.2141	5.27	0.2422	11.59
	1	16	1	0.10	0	0	0	0.15	0.125	2	24	-0.1469	0.0219	11.36	0.00	0.2003	7.36	0.2550	21.45
	1	16	1	0.10	0	0	0	0.05	0.125	4	24	-0.0906	-0.0344	9.20	0.00	0.2237	2.45	0.2312	3.27
	1	16	1	0.10	0	0	0	0.10	0.125	4	24	-0.1188	-0.0062	10.40	0.00	0.2056	4.90	0.2343	12.27
	1	16	1	0.10	0	0	0	0.15	0.125	4	24	-0.1469	0.0219	11.36	0.00	0.1874	6.84	0.2432	22.94
Concentric	1	16	1	0.20	0	0	0	0.05	0.125	2	24	-0.0906	-0.0344	9.20	0.00	0.1843	2.64	0.1914	3.74
	1	16	1	0.20	0	0	0	0.10	0.125	2	24	-0.1188	-0.0062	10.40	0.00	0.1750	5.27	0.2020	13.35
	1	16	1	0.20	0	0	0	0.15	0.125	2	24	-0.1469	0.0219	11.36	0.00	0.1662	7.36	0.2182	23.85
	1	16	1	0.20	0	0	0	0.05	0.125	4	24	-0.0906	-0.0344	9.20	0.00	0.1785	2.45	0.1859	4.01
	1	16	1	0.20	0	0	0	0.10	0.125	4	24	-0.1188	-0.0062	10.40	0.00	0.1635	4.90	0.1918	14.77
	1	16	1	0.20	0	0	0	0.15	0.125	4	24	-0.1469	0.0219	11.36	0.00	0.1485	6.84	0.2034	26.98
Concentric	1	16	1	0.35	0	0	0	0.05	0.125	2	24	-0.0906	-0.0344	9.20	0.00	0.1446	2.64	0.1516	4.60
	1	16	1	0.35	0	0	0	0.10	0.125	2	24	-0.1188	-0.0062	10.40	0.00	0.1383	5.27	0.1638	15.57
	1	16	1	0.35	0	0	0	0.15	0.125	2	24	-0.1469	0.0219	11.36	0.00	0.1328	7.36	0.1823	27.14
	1	16	1	0.35	0	0	0	0.05	0.125	4	24	-0.0906	-0.0344	9.20	0.00	0.1384	2.45	0.1457	5.05
	1	16	1	0.35	0	0	0	0.10	0.125	4	24	-0.1188	-0.0062	10.40	0.00	0.1254	4.90	0.1529	18.01
	1	16	1	0.35	0	0	0	0.15	0.125	4	24	-0.1469	0.0219	11.36	0.00	0.1134	6.84	0.1666	31.92
Concentric	1	16	1	0.50	0	0	0	0.05	0.125	2	24	-0.0906	-0.0344	9.20	0.00	0.1104	2.64	0.1171	5.77
	1	16	1	0.50	0	0	0	0.10	0.125	2	24	-0.1188	-0.0062	10.40	0.00	0.1055	5.27	0.1303	19.06
	1	16	1	0.50	0	0	0	0.15	0.125	2	24	-0.1469	0.0219	11.36	0.00	0.1018	7.36	0.1494	31.88
	1	16	1	0.50	0	0	0	0.05	0.125	4	24	-0.0906	-0.0344	9.20	0.00	0.1039	2.45	0.1111	6.52
	1	16	1	0.50	0	0	0	0.10	0.125	4	24	-0.1188	-0.0062	10.40	0.00	0.0924	4.90	0.1194	22.64
	1	16	1	0.50	0	0	0	0.15	0.125	4	24	-0.1469	0.0219	11.36	0.00	0.0824	6.84	0.1341	38.55

Table B.1b INCLINED CONCENTRIC LOAD CASE

	<i>P</i>	<i>h</i> (in.)	<i>t</i> (in.)	<i>a/h</i>	<i>α</i> (deg.)	<i>e/h</i>	<i>e</i> (in.)	<i>R/P</i>	<i>b/h</i>	<i>l</i> (in.)	<i>r.s.h</i> (in.)	σ_t (psi)	σ_b (psi)	<i>h_c</i> (in.)	β_{hor} -1-	<i>T_{b-hor}</i> -2-	β -3-	<i>T_b</i> -4-	% Diff. -2&4-
Inclined Concentric	1	16	1	0.10	6	0	0	0.05	0.250	2	24	-0.0266	-0.0977	6.47	0.00	0.2241	-3.36	0.2324	3.59
	1	16	1	0.10	6	0	0	0.10	0.250	2	24	-0.0547	-0.0696	7.68	0.00	0.2105	-0.70	0.2104	-0.05
	1	16	1	0.10	6	0	0	0.15	0.250	2	24	-0.0828	-0.0415	8.89	0.00	0.1965	1.95	0.2025	2.95
	1	16	1	0.10	6	0	0	0.05	0.250	4	24	-0.0217	-0.1026	6.26	0.00	0.2200	-3.55	0.2233	1.49
	1	16	1	0.10	6	0	0	0.10	0.250	4	24	-0.0498	-0.0745	7.47	0.00	0.2018	-1.08	0.2017	-0.04
	1	16	1	0.10	6	0	0	0.15	0.250	4	24	-0.0779	-0.0464	8.68	0.00	0.1836	1.38	0.1883	2.48
Inclined Concentric	1	16	1	0.20	6	0	0	0.05	0.250	2	24	-0.0266	-0.0977	6.47	0.00	0.1806	-3.36	0.1888	4.33
	1	16	1	0.20	6	0	0	0.10	0.250	2	24	-0.0547	-0.0696	7.68	0.00	0.1717	-0.70	0.1716	-0.04
	1	16	1	0.20	6	0	0	0.15	0.250	2	24	-0.0828	-0.0415	8.89	0.00	0.1627	1.95	0.1682	3.24
	1	16	1	0.20	6	0	0	0.05	0.250	4	24	-0.0217	-0.1026	6.26	0.00	0.1751	-3.55	0.1841	4.91
	1	16	1	0.20	6	0	0	0.10	0.250	4	24	-0.0498	-0.0745	7.47	0.00	0.1599	-1.08	0.1598	-0.10
	1	16	1	0.20	6	0	0	0.15	0.250	4	24	-0.0779	-0.0464	8.68	0.00	0.1449	1.38	0.1497	3.15
Inclined Concentric	1	16	1	0.35	6	0	0	0.05	0.250	2	24	-0.0266	-0.0977	6.47	0.00	0.1412	-3.36	0.1492	5.36
	1	16	1	0.35	6	0	0	0.10	0.250	2	24	-0.0547	-0.0696	7.68	0.00	0.1352	-0.70	0.1351	-0.03
	1	16	1	0.35	6	0	0	0.15	0.250	2	24	-0.0828	-0.0415	8.89	0.00	0.1295	1.95	0.1348	3.92
	1	16	1	0.35	6	0	0	0.05	0.250	4	24	-0.0217	-0.1026	6.26	0.00	0.1352	-3.55	0.1439	6.05
	1	16	1	0.35	6	0	0	0.10	0.250	4	24	-0.0498	-0.0745	7.47	0.00	0.1220	-1.08	0.1218	-0.19
	1	16	1	0.35	6	0	0	0.15	0.250	4	24	-0.0779	-0.0464	8.68	0.00	0.1101	1.38	0.1148	4.09
Inclined Concentric	1	16	1	0.50	6	0	0	0.05	0.250	2	24	-0.0266	-0.0977	6.47	0.00	0.1072	-3.36	0.1150	6.79
	1	16	1	0.50	6	0	0	0.10	0.250	2	24	-0.0547	-0.0696	7.68	0.00	0.1025	-0.70	0.1025	-0.03
	1	16	1	0.50	6	0	0	0.15	0.250	2	24	-0.0828	-0.0415	8.89	0.00	0.0987	1.95	0.1036	4.74
	1	16	1	0.50	6	0	0	0.05	0.250	4	24	-0.0217	-0.1026	6.26	0.00	0.1010	-3.55	0.1093	7.67
	1	16	1	0.50	6	0	0	0.10	0.250	4	24	-0.0498	-0.0745	7.47	0.00	0.0893	-1.08	0.0890	-0.29
	1	16	1	0.50	6	0	0	0.15	0.250	4	24	-0.0779	-0.0464	8.68	0.00	0.0793	1.38	0.0839	5.47

Table B.1c ECCENTRIC AND INCLINED ECCENTRIC LOAD CASE

	P	h (in.)	t (in.)	a/h	α (deg.)	e/h	e (in.)	R/P	b/h	l (in.)	t.s.h (in.)	σ_t (psi)	σ_b (psi)	h_c (in.)	β_{hor} -1-	T_{b-hor} -2-	β -3-	T_b -4-	% Diff. -2&4-
Eccentric, $l = 2'$	1	16	1	0.20	0	0.4	6.4	0.15	0.125	2	24	-0.2969	0.1719	1262	0.00	0.1493	-3.91	0.2074	28.00
	1	16	1	0.20	0	0.25	4	0.15	0.125	2	24	-0.2406	0.1156	1240	0.00	0.0786	0.88	0.1285	38.81
	1	16	1	0.20	0	0.1	1.6	0.15	0.125	2	24	-0.1844	0.0594	1197	0.00	0.0001	5.20	0.0130	98.98
	1	16	1	0.20	0	-0.1	-1.6	0.15	0.125	2	24	-0.1094	-0.0156	1000	0.00	0.1619	7.88	0.2258	28.28
	1	16	1	0.20	0	-0.25	-4	0.15	0.125	2	24	-0.0531	-0.0719	760	0.00	0.0896	7.88	0.1454	38.39
	1	16	1	0.20	0	-0.4	-6.4	0.15	0.125	2	24	0.0031	-0.1281	521	0.00	0.0639	7.90	0.0691	7.49
Eccentric, $l = 4'$	1	16	1	0.10	0	0.4	6.4	0.15	0.250	4	24	-0.2969	0.1719	1262	0.00	0.1634	-3.63	0.2010	18.70
	1	16	1	0.10	0	0.25	4	0.15	0.250	4	24	-0.2406	0.1156	1240	0.00	0.1239	0.81	0.1306	5.11
	1	16	1	0.10	0	0.1	1.6	0.15	0.250	4	24	-0.1844	0.0594	1197	0.00	0.0260	4.83	0.0332	21.74
	1	16	1	0.10	0	-0.1	-1.6	0.15	0.250	4	24	-0.1094	-0.0156	1000	0.00	0.1974	7.33	0.2368	16.66
	1	16	1	0.10	0	-0.25	-4	0.15	0.250	4	24	-0.0531	-0.0719	760	0.00	0.1763	7.33	0.1831	3.71
	1	16	1	0.10	0	-0.4	-6.4	0.15	0.250	4	24	0.0031	-0.1281	521	0.00	0.1215	7.34	0.1296	6.21
Incl. Eccentric, $l = 2'$	1	16	1	0.20	6	0.4	6.4	0.15	0.125	2	24	-0.2320	0.1077	1236	0.00	0.1483	-4.49	0.1524	28.00
	1	16	1	0.20	6	0.25	4	0.15	0.125	2	24	-0.1761	0.0518	1188	0.00	0.0807	-0.27	0.0834	38.81
	1	16	1	0.20	6	0.1	1.6	0.15	0.125	2	24	-0.1201	-0.0042	1049	0.00	0.0000	1.95	0.0000	98.98
	1	16	1	0.20	6	-0.1	-1.6	0.15	0.125	2	24	-0.0455	-0.0788	729	0.00	0.1650	1.95	0.1686	28.28
	1	16	1	0.20	6	-0.25	-4	0.15	0.125	2	24	0.0104	-0.1347	495	0.00	0.0990	2.09	0.1018	38.39
	1	16	1	0.20	6	-0.4	-6.4	0.15	0.125	2	24	0.0663	-0.1907	396	0.00	0.0873	5.18	0.0925	7.49
Incl. Eccentric, $l = 4'$	1	16	1	0.10	6	0.4	6.4	0.15	0.250	4	24	-0.2271	0.1028	1233	0.00	0.1568	-4.23	0.1630	18.70
	1	16	1	0.10	6	0.25	4	0.15	0.250	4	24	-0.1712	0.0469	1181	0.00	0.1102	-0.38	0.1093	5.11
	1	16	1	0.10	6	0.1	1.6	0.15	0.250	4	24	-0.1152	-0.0091	1028	0.00	0.0067	1.38	0.0134	21.74
	1	16	1	0.10	6	-0.1	-1.6	0.15	0.250	4	24	-0.0406	-0.0837	708	0.00	0.1871	1.38	0.1923	16.66
	1	16	1	0.10	6	-0.25	-4	0.15	0.250	4	24	0.0153	-0.1396	481	0.00	0.1617	1.65	0.1604	3.71
	1	16	1	0.10	6	-0.4	-6.4	0.15	0.250	4	24	0.0712	-0.1956	391	0.00	0.0961	4.71	0.1043	6.21

APPENDIX C

TENSILE STRESSES IN WEB

C.1 Tensile Stresses in the Web of Symmetrical I-Sections

Figure C.1 shows the tensile stresses within the web of Symmetrical I-sections with three flange widths.

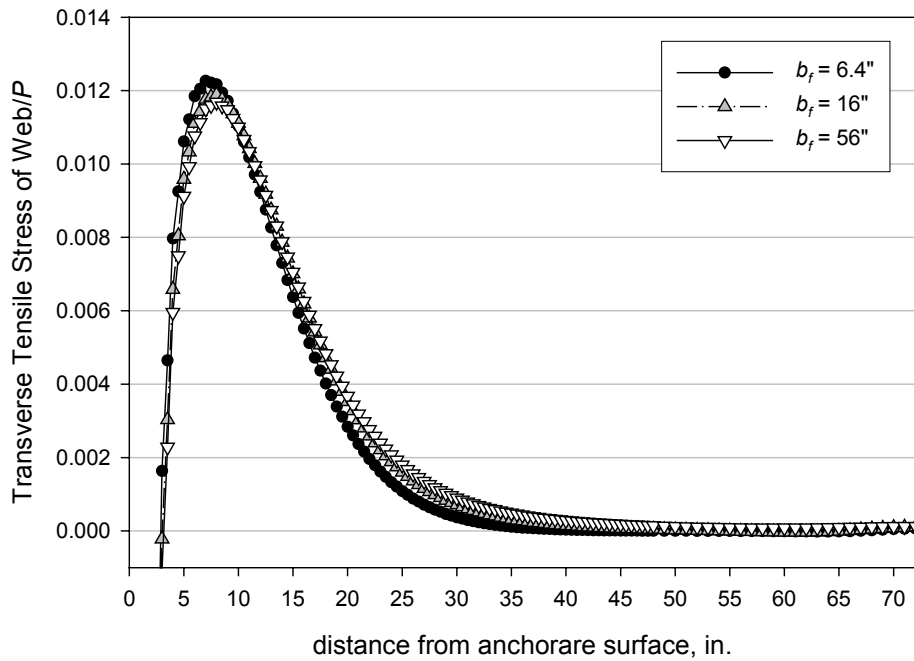


Fig. C.1 TENSILE STRESSES IN WEB OF SYMMETRICAL I-SECTION MODEL WITH THREE FLANGE WIDTHS ($t_w = 1.5''$, $t_f/t_w = 1.1$, and $a/h_w = 0.20$)

APPENDIX D

DESIGN EXAMPLES OF NON-RECTANGULAR ANCHORAGE ZONES

Three design examples for concentrically loaded anchorage zones selected from the standard sections provided in the PCI Bridge Design Manual (1997) are presented in this Appendix. The selected sections contain three different special characteristics of the section consisting of ones with the thickest flange, the thinnest web, and the widest flange from all the available standard sections presented in the manual. The anchorage ratio of all the examples is chosen as the closest value to the a/h_w ratio of 0.20.

D.1 Section with the Thickest Flange

The section that contains the thickest flange is the AASHTO I-Beam Type VI, which has the thickest dimension for the bottom flange as can be seen in Fig. D.1. Fig. D.1a shows the original section taken from the manual (PCI, 1997). In order to be able to apply the formulations developed in section 4.4.1.2, the section must be transformed into the section as shown in Fig. D.1b.

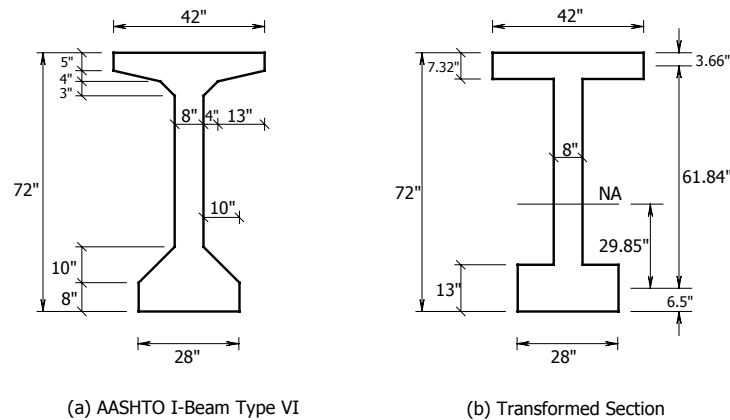


Fig. D.1 SECTION WITH THE THICKEST FLANGE

The prestressing load has the magnitude of P kips. The anchor plate size (a) for this problem is chosen as approximately 12.8 in. Since the prestressing load is applied concentrically at the centroid of the section, the stress at the considered section is uniform ($\sigma_o = P/A = P/1084.88$ ksi). Therefore, the values of γR_1 , $(1-\gamma)R_1$, R_2 , R_3 , p , y_u , and y_l can be calculated as follow:

$$\begin{aligned}
 R_1 &= |\sigma_o|(h' t_w) \\
 \gamma R_1 &= |\sigma_o|(h'-c - t_{f2}/2)t_w = |\sigma_o|(72-29.85-13/2) \times 8 = 0.2629P \text{ kips} \\
 (1-\gamma)R_1 &= |\sigma_o|(c + t_{f2}/2)t_w = |\sigma_o|(29.85+13/2) \times 8 = 0.2680P \text{ kips} \\
 R_2 &= |\sigma_o|(b_{f1} - t_w)t_{f1} = |\sigma_o|(42-8) \times 7.32 = 0.2294P \text{ kips} \\
 R_3 &= |\sigma_o|(b_{f2} - t_w)t_{f2} = |\sigma_o|(28-8) \times 13 = 0.2397P \text{ kips} \\
 p &= (\gamma R_1 + R_2 - 0.5P)a / 2P = (0.2629+0.2294-0.5) \times 12.8/2 = -0.05 \\
 y_u &= (\gamma R_1 \times (72 - 29.85 - 13/2) / 2 + R_2 \times (61.84 - 29.85)) / (\gamma R_1 + R_2) = 24.43 \text{ in.} \\
 y_l &= ((1-\gamma)R_1 \times (29.85 + 13/2) / 2 + R_3 \times 29.85) / ((1-\gamma)R_1 + R_3) = 23.69 \text{ in.}
 \end{aligned}$$

In the calculation of the web bursting force $T_{burst-web}$, the value of $d_{burst-web}$ can be calculated as the smaller value of equations (4.27) and (4.28).

$$\begin{aligned}
 d_{burst-web} &= (h'-c - \frac{t_{f2}}{2}) + \frac{a}{4} + \frac{h_w}{4} (1 - \exp(-0.8b_{f1} / h_w)) \\
 &= (72-29.85-13/2)+12.8/4+61.84/4 \times (1-\exp(-0.8 \times 42/61.84)) = 45.32 \text{ in.} \\
 d_{burst-web} &= (c + \frac{t_{f2}}{2}) + \frac{a}{4} + \frac{h_w}{4} (1 - \exp(-0.8b_{f2} / h_w)) \\
 &= (29.85+13/2)+12.8/4+61.84/4 \times (1-\exp(-0.8 \times 28/61.84)) = 44.24 \text{ in.}
 \end{aligned}$$

Therefore, $d_{burst-web}$ is equal to 44.24 in. This value can be substituted into equation (4.20) or (4.26) with all the values calculated previously. Therefore, $T_{burst-web}$ can be calculated as shown below:

$$\begin{aligned}
T_{burst-web} &= (\gamma R_1 + R_2) \left(\frac{4y_u + 4p}{4d_{burst-web} - a} \right) \left(1 - \frac{a}{4y_u + 4p} \right) \\
&= (0.2629P + 0.2294P) \left(\frac{4 \times 24.43 + 4 \times (-0.05)}{4 \times 44.24 - 12.8} \right) \left(1 - \frac{12.8}{4 \times 24.43 + 4 \times (-0.05)} \right) \\
&= 0.2541P \text{ kips}
\end{aligned}$$

$$\begin{aligned}
T_{burst-web} &= ((1 - \gamma)R_1 + R_3) \left(\frac{4y_l - 4p}{4d_{burst-web} - a} \right) \left(1 - \frac{a}{4y_l - 4p} \right) \\
&= (0.2680P + 0.2397P) \left(\frac{4 \times 23.69 - 4 \times (-0.05)}{4 \times 44.24 - 12.8} \right) \left(1 - \frac{12.8}{4 \times 23.69 - 4 \times (-0.05)} \right) \\
&= 0.2541P \text{ kips}
\end{aligned}$$

For the calculation of the flange bursting force $T_{burst-flg}$ and the location of the force $d_{burst-flg}$, the section contains both top and bottom flanges. Since equation (4.25) is used for the calculation of $T_{burst-flg}$, the calculations of $T_{burst-flg}$ and $d_{burst-flg}$ for the top flange can be illustrated as shown below:

$$T_{burst-flg} = 0.15k_f^3 P, \quad k_f \leq 1.0,$$

where $k_f = R_{flg}/R_{total} = |\sigma_o|(b_{f1}t_{f1})/(\gamma R_1 + R_2) = (42 \times 7.32/1084.88)/(0.2629 + 0.2294) = 0.58 \leq 1.0$. Therefore,

$$T_{burst-flg} = 0.15 \times 0.58^3 \times P = 0.0286P \text{ kips}$$

The value of $d_{burst-flg}$ for the top flange can be calculated using equation (4.29) as shown below:

$$\begin{aligned}
d_{burst-flg} &= \frac{h_w - c}{4} + \frac{3}{8}t_{f1} + \frac{R_2}{T_{burst-flg}} \frac{(b_{f1} + t_w)}{8} \\
&= \left(\frac{61.84 - 29.85}{4} \right) + \frac{3}{8} \times 7.32 + \frac{0.2294P}{0.0286P} \times \frac{(42 + 8)}{8} = 60.86 \text{ in.}
\end{aligned}$$

With a similar method but using the variables from the bottom flange, the values of $T_{burst-flg}$ and $d_{burst-flg}$ can be determined as $0.0433P$ kips and 37.25 in., respectively. The comparison

of the results using the approximate equations as presented above and those predicted by using the finite element analysis can be seen in Table D.1.

Table D.1 COMPARISON FOR EXAMPLE D.1

	<i>Web</i>		<i>Top Flange</i>		<i>Bottom Flange</i>	
	T_{burst}	d_{burst}	T_{burst}	d_{burst}	T_{burst}	d_{burst}
<i>FEM</i>	0.2322	47.1676	0.0260	44.4051	0.0350	34.0443
<i>Approx. Eq.</i>	0.2541	44.2388	0.0286	60.8559	0.0433	37.2473
<i>% Diff</i>	9.45	-6.21	10.12	37.05	23.73	9.41

D.2 Section with the Thinnest Web

Fig. D.2 shows an AASHTO Bulb-Tee Type BT-72, which has the thinnest web among the standard sections presented in the PCI Bridge Design Manual (1997). Similarly to those presented in Fig. D.1, Fig. D.2a shows the original standard section from the manual while Fig. D.2b presents the transformed section used for the calculation of the bursting forces and locations of the forces in all members within the section.

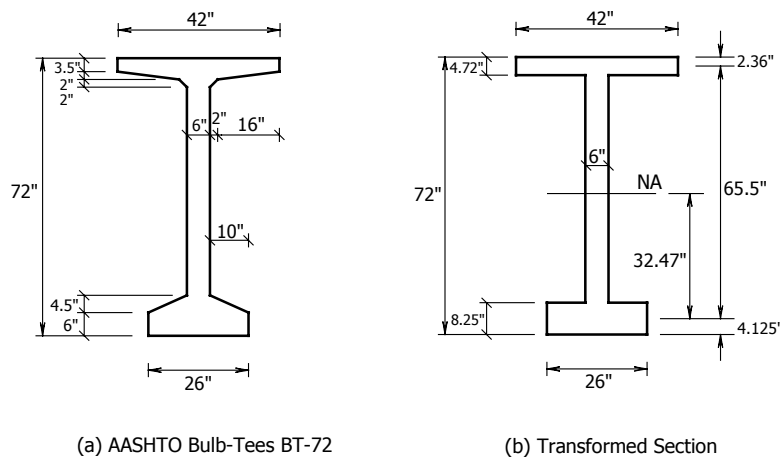


Fig. D.2 SECTION WITH THE THINNEST WEB

The height anchor plate used in this example equals 12.8 in. and the area of the section equals 766.89 sq.in. With the same design procedure used in the previous example, the values of all variables can be presented

$$\begin{aligned}\gamma R_1 &= |\sigma_o|(h'-c-t_{f2}/2)t_w = |\sigma_o|(72-32.47-8.25/2) \times 6 = 0.2770P \text{ kips} \\ (1-\gamma)R_1 &= |\sigma_o|(c+t_{f2}/2)t_w = |\sigma_o|(32.47+8.25/2) \times 6 = 0.2863P \text{ kips} \\ R_2 &= |\sigma_o|(b_{f1}-t_w)t_{f1} = |\sigma_o|(42-6) \times 4.72 = 0.2216P \text{ kips} \\ R_3 &= |\sigma_o|(b_{f2}-t_w)t_{f2} = |\sigma_o|(26-6) \times 8.25 = 0.2152P \text{ kips} \\ p &= (\gamma R_1 + R_2 - 0.5P)a/2P = (0.2770+0.2216-0.5) \times 12.8/2 = -0.01 \\ y_u &= (\gamma R_1 \times (72 - 32.47 - 8.25/2)/2 + R_2 \times (65.5 - 32.47))/(\gamma R_1 + R_2) = 24.52 \text{ in.} \\ y_l &= ((1-\gamma)R_1 \times (32.47 + 8.25/2)/2 + R_3 \times 32.47)/((1-\gamma)R_1 + R_3) = 24.38 \text{ in.}\end{aligned}$$

Therefore, the smaller value of $d_{burst-web}$ from the following calculations is used:

$$\begin{aligned}d_{burst-web} &= (72-32.47-8.25/2)+12.8/4+65.5/4 \times (1-\exp(-0.8 \times 42/65.5)) = 45.17 \text{ in.} \\ d_{burst-web} &= (32.47+8.25/2)+12.8/4+65.5/4 \times (1-\exp(-0.8 \times 26/65.5)) = 44.25 \text{ in.}\end{aligned}$$

By substituting $d_{burst-web}$ equal to 44.25 in. into either equation (4.20) or (4.25), the value of $T_{burst-web}$ becomes $0.2588P$ kips. Similarly, the calculation of $T_{burst-flg}$ and $d_{burst-flg}$ for both top and bottom flanges of the section can be illustrated as shown below:

For the top flange,

$$\begin{aligned}k_f &= R_{flg}/R_{total} = (4.72 \times 42 / 766.89)/(0.2770 + 0.2116) = 0.52 \leq 1.0 \\ T_{burst-flg} &= 0.15 \times 0.52^3 \times P = 0.0209P \text{ kips}\end{aligned}$$

Therefore, the value of $d_{burst-flg}$ is equal to

$$d_{burst-flg} = \left(\frac{65.5 - 32.47}{4} \right) + \frac{3}{8} \times 4.72 + \frac{0.2216P}{0.0209P} \times \frac{(42 + 6)}{8} = 73.61 \text{ in.}$$

The values of $T_{burst-flg}$ and $d_{burst-flg}$ for the bottom flange are equal to $0.0260P$ kips and 44.27 in., respectively. Table D.2 shows the comparison of the results calculated above to those using the finite element method.

Table D.2 COMPARISON FOR EXAMPLE D.2

	<i>Web</i>		<i>Top Flange</i>		<i>Bottom Flange</i>	
	T_{burst}	d_{burst}	T_{burst}	d_{burst}	T_{burst}	d_{burst}
<i>FEM</i>	0.2334	47.7296	0.0195	57.6919	0.0216	38.7378
<i>Approx. Eq.</i>	0.2588	44.2489	0.0209	73.6102	0.0260	44.2724
<i>% Diff</i>	10.88	-7.29	7.30	27.59	20.69	14.29

D.3 Section with the Widest Flange

The section with the widest flange that can be found from the standard sections presented in the PCI Bridge Design Manual (1997) is the AASHTO Deck Bulb-Tee Type BT-35c as shown in Fig. D.3a. The transformed section is presented in Fig. D.3b. To maintain the anchorage ratio of 0.20, the anchor plate size used in this example equals 5.60 in. The area of the section equals 1048.2 sq.in. The calculations for the web bursting force and the location of the force as well as those for the flanges are similar to those presented in the previous examples which are presented below:

$$\gamma R_1 = |\sigma_o|(h'-c-t_{f2}/2)t_w = |\sigma_o|(35-20.93-7.5/2) \times 6 = 0.0591P \text{ kips}$$

$$(1-\gamma)R_1 = |\sigma_o|(c+t_{f2}/2)t_w = |\sigma_o|(20.93+7.5/2) \times 6 = 0.1413P \text{ kips}$$

$$R_2 = |\sigma_o|(b_{f1}-t_w)t_{f1} = |\sigma_o|(96-6) \times 7.73 = 0.6637P \text{ kips}$$

$$R_3 = |\sigma_o|(b_{f2}-t_w)t_{f2} = |\sigma_o|(25-6) \times 7.5 = 0.1360P \text{ kips}$$

$$p = (\gamma R_1 + R_2 - 0.5P)a/2P = (0.0591+0.6637-0.5) \times 5.6/2 = 0.62$$

$$y_u = (\gamma R_1 \times (35 - 20.93 - 7.5/2)/2 + R_2 \times (27.38 - 20.93))/(\gamma R_1 + R_2) = 6.35 \text{ in.}$$

$$y_l = ((1 - \gamma)R_1 \times (20.93 + 7.5 / 2) / 2 + R_3 \times 20.93) / ((1 - \gamma)R_1 + R_3) = 16.55 \text{ in.}$$

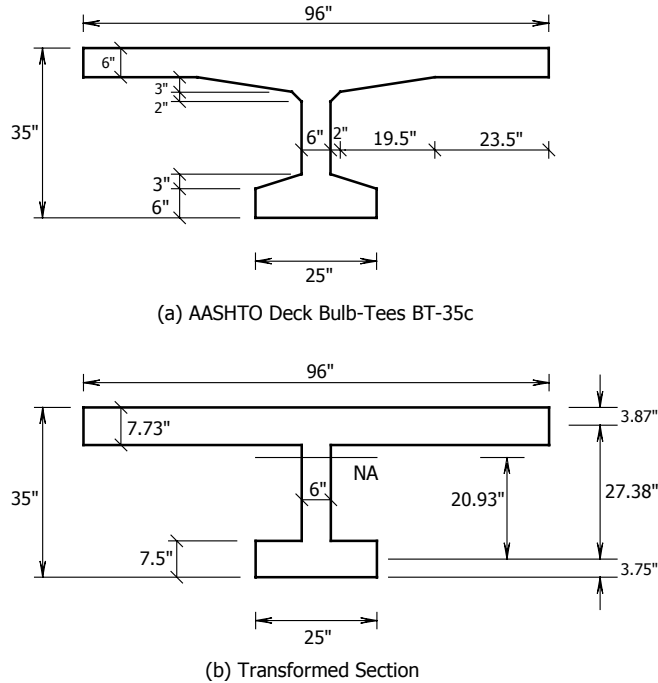


Fig. D.3 SECTION WITH THE WIDEST FLANGE

The value of $d_{burst-web}$ can be determined from the smaller value determined from the calculations presented below:

$$d_{burst-web} = (35 - 20.93 - 7.5 / 2) + 5.6 / 4 + 27.38 / 4 \times (1 - \exp(-0.8 \times 96 / 27.38)) = 18.15 \text{ in.}$$

$$d_{burst-web} = (20.93 + 7.5 / 2) + 5.6 / 4 + 27.38 / 4 \times (1 - \exp(-0.8 \times 25 / 27.38)) = 29.62 \text{ in.}$$

Therefore, using $d_{burst-web}$ equal to 18.15 in either equation (4.20) or (4.25), $T_{burst-web}$ is equal to $0.2404P$ kips. With the same calculation steps as those presented in the previous examples, the value of $T_{burst-flg}$ and $d_{burst-flg}$ of the top can be presented as shown below:

$$k_f = R_{flg} / R_{total} = (7.73 \times 96 / 1048.2) / (0.0591 + 0.6637) = 0.98 \leq 1.0$$

$$T_{burst-flg} = 0.15 \times 0.98^3 \times P = 0.1410P \text{ kips}$$

Therefore, the value of $d_{burst-flg}$ is equal to

$$d_{burst-flg} = \left(\frac{35 - 20.93}{4} \right) + \frac{3}{8} \times 7.73 + \frac{0.6637P}{0.1410P} \times \frac{(96 + 6)}{8} = 64.55 \text{ in.}$$

The values of $T_{burst-flg}$ and $d_{burst-flg}$ for the bottom flange are equal to $0.0403P$ kips and 21.11 in., respectively. Table D.3 shows the comparison of the results calculated above to those using the finite element method.

Table D.3 COMPARISON FOR EXAMPLE D.3

	<i>Web</i>		<i>Top Flange</i>		<i>Bottom Flange</i>	
	T_{burst}	d_{burst}	T_{burst}	d_{burst}	T_{burst}	d_{burst}
<i>FEM</i>	0.2016	20.0243	0.1039	40.0945	0.0219	17.4522
<i>Approx. Eq.</i>	0.2404	18.1480	0.1410	64.5454	0.0403	21.1140
<i>% Diff</i>	19.28	-9.37	35.66	60.98	83.98	20.98

VITA

Songwut Hengprathanee was born on December 28, 1973 in Khon Kaen, a northeastern province of Thailand. He received a Bachelor's degree from Kasetsart University at Bangkok in 1995. After completing his Bachelor's degree, he earned a chance to work in an international civil engineering consulting company named Pyramid Development International Co. Ltd. There he participated in the project of the fourth state expressway of Thailand named the Bang Na-Bang Pli-Bang Pakong Expressway. It was the first time that he was impressed by the ability of using the finite element method for the study of civil engineering structures and the applicability of the Strut-and-Tie Model method for the design of bridge superstructures. In 1997, he became a faculty member of the Department of Civil Engineering at Kasetsart University, his former school. In 1998, he was granted a scholarship from the Royal Thai Government to study for Master's and Doctoral degrees in the United States. In 2000, he pursued his Master's degree at Ohio University at Athens. He then continued his Doctoral degree in Civil and Environmental Engineering at Virginia Polytechnic Institute and State University. After receiving his Doctoral degree, he will remain as a faculty member at Kasetsart University in Bangkok, Thailand.